ATMOSPHERE, IONOSPHERE, SAFETY

Part 1

Kaliningrad
2018

IMMANUEL KANT BALTIC FEDERAL UNIVERSITY
SEMENOV INSTITUTE OF CHEMICAL PHYSICS, RAS
PUSHKOV INSTITUTE OF TERRESTRIAL MAGNETISM, IONOSPHERE
AND RADIO WAVE PROPAGATION, RAS

ATMOSPHERE, IONOSPHERE, SAFETY

Proceedings
of VI International conference

Part 1

Kaliningrad
2018

UDK 550.51
BBK 552.44
A92

The conference AIS-2018 was supported by Russian Foundation for Basic Researches (Grant No. 18-03-20020); the VarSITI program and the program «5-100» for improving competitiveness at Immanuel Kant Baltic Federal University.

A92 **Atmosphere, ionosphere, safety** / edited by I. V. Karpov, O.P. Borchevkina. — Kaliningrad, 2018. — Pt. 1 — 360 p.
ISBN 978-5-9971-0490-0 (Pt. 1)
ISBN 978-5-9971-0491-7

Proceedings of International Conference "Atmosphere, ionosphere, safety" (AIS-2018) include materials reports on: (1) — response analysis of the atmosphere — ionosphere to natural and manmade processes, various causes related geophysical phenomena and evaluate possible consequences of their effects on the human system and process; (2) — to study the possibility of monitoring and finding ways to reduce risk. Scientists from different countries and regions of Russia participated in the conference. Attention was given to questions interconnected with modern nanotechnology and environmental protection. Knowledge of the factors influencing the atmosphere and ionosphere can use them to monitor natural disasters and to establish the appropriate methods on this basis.

Content of the reports is of interest for research and students specializing in physics and chemistry of the atmosphere and ionosphere.

UDK 550.51
BBK 552.44

ISBN 978-5-9971-0490-0 (Pt. 1)
ISBN 978-5-9971-0491-7

ATMOSPHERIC-IONOSPHERIC RELATIONS

Review on Some Aspects of the Solar-Terrestrial Coupled Systems

Clezio M. Denardini[1], Juliano Moro[2,3], and Laysa C. A. Resende[1]

[1]National Institute for Space Research (INPE), S. J. Campos-SP, Brazil
[2]Southern Regional Space Research Center in collaboration with the LACESM/CT-UFSM, Santa Maria-RS, Brazil
[3]State Key Laboratory of Space Weather, National Space Science Center, Chinese Academy of Science (CAS), Beijing, China

Abstract. In the present paper we present a discussion about some aspects of the solar-terrestrial system coupling based on some recent studies of energetic particles precipitation at the South American Magnetic Anomaly and the cosmic noise absorption seem by image riometers, and abnormal enhancement of the equatorial sporadic E-layers (Esq) density during the recovery phase of magnetic storm.

Introduction. Several studies have been reported in the past and recently dealing with the solar-terrestrial systems interactions due to the solar activity effect and the terrestrial magnetosphere-ionosphere response to these effects. *Prölss* [1] has published a review with respect to this topic. However, he limited his review to the ionospheric F-region only mostly constrained to the chemical aspects due to changes in the circulation pattern. In addition, most of the analysis concerned about changes in the ionospheric density only (named ionospheric storm) due to geomagnetic storms, which in turn is the response of the Earth's magnetosphere (geomagnetic field) to a solar event (e. g. solar flare; Coronal Mass Ejection — CME; and High Speed Stream — HSS). In this sense, a positive ionospheric storm is defined as increases in the electron density with respected the observed electron density during a normal quiet day at the same season and local time. Negative ionospheric storm is exactly the opposite of positive ionospheric storms, i. e. it is defined by the decrease in the electron density when compared to the observed electron density during a normal quiet day.

We kwon that prompt penetrating electric fields (PPEF), atmospheric gravity waves (AGW) propagating up to the E-region heights, and 2-day wave in the E-region electric fields are also able to modify the ionospheric density at the E-region (limited to some latitudinal ranges) from several separated studies [2—4]. Indeed, even the F region will have its electron density modifies due PPEF to

equatorial E-region leading to changes in to the fountain effect. In addition, climatological studies that define ionospheric background conditions [5, 6] as well as regional peculiarities [7, 8] have to be taken into account when analyzing the complex solar-terrestrial coupled system. In summary, these few studies support our point that there are several scenarios and events that have to be considered in a coupled system perspective. Modernly, this solar-terrestrial coupled systems point of view of analyzing the near Earth space (being it the magnetosphere, ionosphere or neutral atmosphere) has evolved to the concept of space weather (see [9] and references therein). Correspondingly, we provide the Fig. 1 to illustrate what we call the most obvious sketch showing the interconnection between the solar-terrestrial systems.

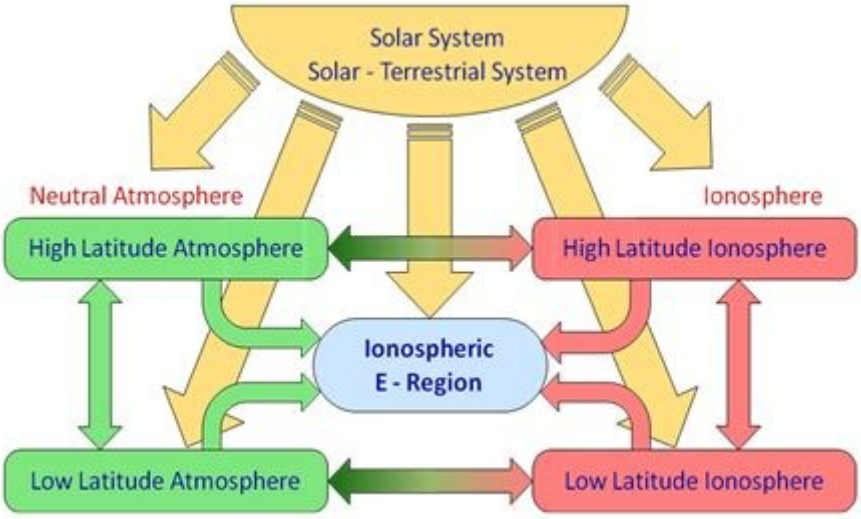

FIGURE 1. The most obvious sketch showing the interconnection between the solar-terrestrial systems.

This sketch covers most of the connections between the systems, having the ionospheric E-region as a terminator/connecting node. However, in the present paper we intend to investigate only two aspects of the solar-terrestrial coupled system with regard to space weather effects. We present a discussion based on some recent studies of energetic particles precipitation at the South American Magnetic Anomaly (SAMA) [10] and the Cosmic Noise Absorption (CNA) seem by image riometers [11, 12]. In addition, we discuss an abnormal enhancement of the equatorial sporadic E-layers density during the recovery phase of geomagnetic storm [13, 14].

Studies with respect to the CNA has been made since the early 50's, when [15] showed that CNA could be split into two components, one occurring at D-region heights and another occurring at the F-region heights [16]. The last one is often neglected because the critical frequencies of the F layer (*fo*F2) are 5—10 times the

lower than the riometer operational frequency, usually around 38 MHz. However, [17, 18] and [19] suggested that the CNA at the F-region heights could be as significant as the CNA in others ionospheric regions. In these cases, *fo*F2 can be higher than 7 MHz. Investigations of the latitudinal variation of the relative CNA at the F-region heights to the CNA in others ionospheric regions revealed that this above conclusion is valid for low latitudes only. Indeed, the contribution of the F-region to the CNA is proportional to $(foF2)^4$, among other factors [16]. Considering that *fo*F2 has a clear variations with latitude, having a maximum at about 15° in both North and South magnetic latitudes and decreasing to half of it in latitudes greater than 60°, it is assumed that the effects of the F-region in the CNA do not surpass 1/16 close to our observations site. Therefore, besides being certainly true for the auroral region [20], it is reasonable to assume that almost all the CNA measured by the riometers is due to energetic particles precipitation at the D-region height. This is the case for the observation made at the Southern Space Observatory (SSO; 29.4ºS; 53.1ºW; 480 m a.s.l.), São Martinho da Serra (RS), Brazil. In order to exemplify that, we show some results of a correlation between the CNA images obtained at the SSO and the flux of electrons and protons precipitation measured by the Medium Energy Proton and Electron Detector (MEPED) on-board the Polar Operational Environment Satellite (POES).

With respect to the studies of the presence of Es layers during disturbed periods, it has been already a matter of investigations carried out in a study by [21], where they investigate of the presence of Es layers during disturbed periods covering several magnetic storms on the solar cycle 20 over Cachoeira Paulista (SP), Brazil. They compiled the total frequency (*ft*Es) and the blanketing frequency (*fb*Es) and shown well-defined enhancements of the electron density of appreciable magnitude, which were observed 1—3 days after the initiation of the storms. At that time, they had classified the sporadic layers associated with the *ft*Es/*fb*Es enhancements as being type “a”. Subsequently, after a careful study of winds and recombination rates, they associated the electron density sudden enhancement to particle precipitations from the Van Allen Radiation Belts due to the SAMA presence in this region. The *fb*Es enhancements were observed in other regions in the Brazilian sector, like the recent study by [22] for São Luís (MA), Brazil, (2.3ºS, 44.2ºW, dip: –3.3), a transition equatorial region. However, they did not observed sporadic layers of the “a” type. After a careful analysis considering several characteristics of the ionogram traces (e. g. height, shape, size, slant), they classified the sporadic layers associated with the *fb*Es enhancements as being a type “c”. Such layer is associated with the tidal wind shears [23] that they stated to be the cause of its formation.

In order to support this statement, they investigated electron density enhancements in terms of the atmosphere dynamics based on magnetic signature of the equatorial electrojet (EEJ) current using magnetometer data, which was feasible since São Luís was an equatorial region at that time. [22] also considered that [24] established that extreme solar flares might cause sudden changes in the ionospheric ionization, which can lead to global distribution changes. They, shown that

enhancements of X-ray and UV radiation intensity, which are observed during chromospheric flares, cause sudden increases in the process of formation of free electrons, increasing the electron density in ionosphere layers. Therefore, [22] checked for correlation between the occurrence of flares and the associated sporadic E layer density enhancement during the days before, during and subsequent to the December 2003 magnetic storm. Latter, a more comprehensive study has been presented by [13] that encompassed all the abnormal *fb*Es enhancements in equatorial Es layers during magnetic storms of solar cycle 23.

Finally, through these two phenomena (energetic particles precipitation at the SAMA leading to cosmic noise absorption, and abnormal enhancement of the equatorial sporadic E-layers) of the space weather we would like to review some aspects solar-terrestrial coupled systems.

Instrumentation and Methods. The instrument designed to evaluate the CNA under the SAMA region is the Relative Ionospheric Opacity Meters (Riometer), which is essentially a very sensitive radio receivers that have been used since the early 60's [18, 25—30]. The present one, used in this study, is an Imaging Riometer for Ionospheric Studies (IRIS), which has the advantage to observe the CNA in images. The basic features of the IRIS are found in [31]. The operation of an IRIS is based on determining the Quiet Day Curve (QDC) and comparing it with the curve observed during an absorption event. The detailed methodology for this procedure has been extensively discussed for several authors [15, 26, 32—37].

In order to investigate the abnormal enhancement of the equatorial sporadic E-layers density and its effects in the E-region, we have used a digital ionosonde and two magnetometers. Data from the digital sounders at São Luís (MA) was used to determine the ionospheric frequency parameters and to classify the types of ionospheric sporadic layers. It was operated every 15 minutes sending consecutive pulses in the frequencies range from 0.5 to 30 MHz, with 0.5 MHz of frequency step. Magnetometers installed at the two sites, SLZ and Vassouras (VSS, 3.9° S, 38.4° W, dip: –13.3), were used to monitor the Earth's magnetic field at the rate of one measurement per second. However, we have only used the one-minute averaged *H* component measurements from these two sites. Thus, we determined the strength of the magnetic effect of the EEJ current at the ground level (named EEJ ground strength for simplification). The basic treatment of the magnetic data at each station is based on to eliminate outlier values from the measured components, based on a 3rd order polynomial fitting. Then, the five quietest days in the month are chosen and their local midnight values averaged ($<H_{00LT}>$). Thereafter, the H component variations are normalized to the difference between the *H* component values and the mean midnight values for the five quietest days providing the ΔH, i. e., $\Delta H_{SLZ} = H_{SLZ} - <H_{00LT@SLZ}>$. Finally, the diurnal variation of the EEJ ground strength is estimated by taking the difference between the ΔH values measured at the dip equator station (ΔH_{SLZ}) and that at a station nearby the dip equator but outside the EEJ influence (ΔH_{VSS}). [2] and [38] explained the treatment applied to the magnetic data and it used to determine the ΔH values in more details.

Results. Energetic particles precipitation at the SAMA:

With regard to the space weather effects related to CNA observed within IRIS, [29] have observed an absorption event during the main phase of the intense geomagnetic storm occurred on 22 and 23 September 1999 (Dst = –164 nT) by the IRIS (38.2 MHz) at the SSO, Southern of Brazil. We have reprocessed the same data set and we found the special distribution and temporal evolution of the event as presented in Fig. 2. Each image is obtained at ~2 min interval and represents a 300 x 300 km horizontal area in the IRIS field of view at about 100 km of altitude. This figure clearly shows a quite weak area of absorption appearing at southwestern region of the first image suddenly that becomes a strong area connecting the western field of view of the IRIS with the Northern area that means low latitudes. Differential analysis of the images evolution revealed that this northward elongated structure is migrating eastward with a drift velocity of about 250 m/s. Also, it is getting weaker as the main phase of the magnetic storm evolves.

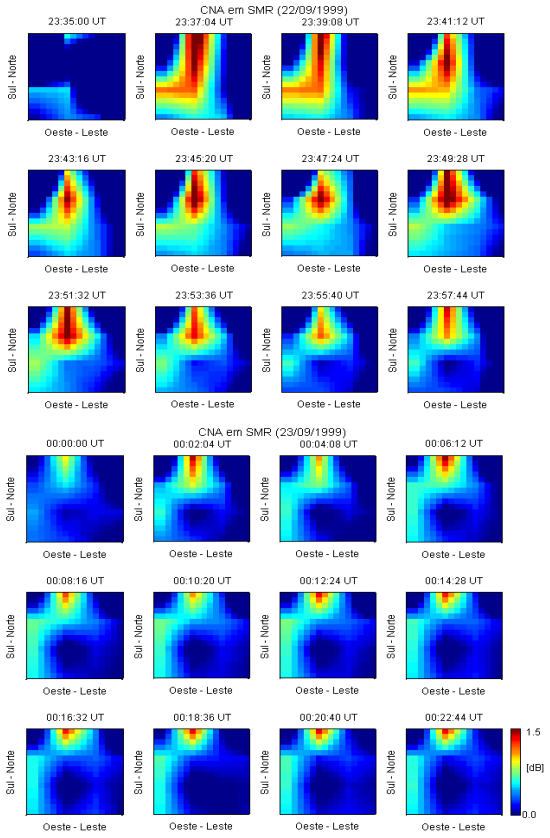

FIGURE 2. Images of the CNA images obtained during the main phase of the geomagnetic storm occurred on 22 and 23 September 1999 by the IRIS (38.2 MHz) at the SSO. The color scale gives the intensity of the CNA in dB.

Ionospheric data (not shown here) were acquired for the same period at the closest digisonde available, i. e., at Cachoeira Paulista (CP), which is ~1,000 km far away from the SSO. No abortion effects were observed there. Therefore, despite we have no reason to confirm that this CNA event observed in the IRIS data at the SSO is due to particles precipitation, we cannot discard this possibility as well. If we assume a background electric field of about 1.8 mV/m, we will find that electrons precipitating in the SAMA must have energy around 20 keV. Such intensity of the electric field is reasonable for the E-region height if we consider Disturbance Dynamo Electric Fields (DDEF) associated with a magnetic storm or sub-storms.

Unfortunately, the CNA measured in this example was not contrasted against the measurement of energetic particles made by the Medium Energy Proton and Electron Detector (MEPED) on board of the POES satellite since there were no data available from this detector during this event. However, [29] attributed this CNA to electrons flux with energy of the order of ~20 keV. In addition, [31] performed such correlation between the CNA and the energetic electron flux in two energy channels (>30 and >300 keV) and the proton flux in three energy channels (80—240, 800—2500 and >6900 keV) during a moderate geomagnetic storm that occurred on September 3, 2008.

Therefore, following the analysis proposed by [31], we integrated all the CNA inside each frame and correlated with measurement of energetic particles made by the MEPED detector, on board of the POES satellite. An example of a contour map of electron flux within the energy range of lower 30 keV derived from the POES satellite at 840 km of altitude is shown in Fig. 3. The red square on the map shown the area illuminated by the IRIS antenna.

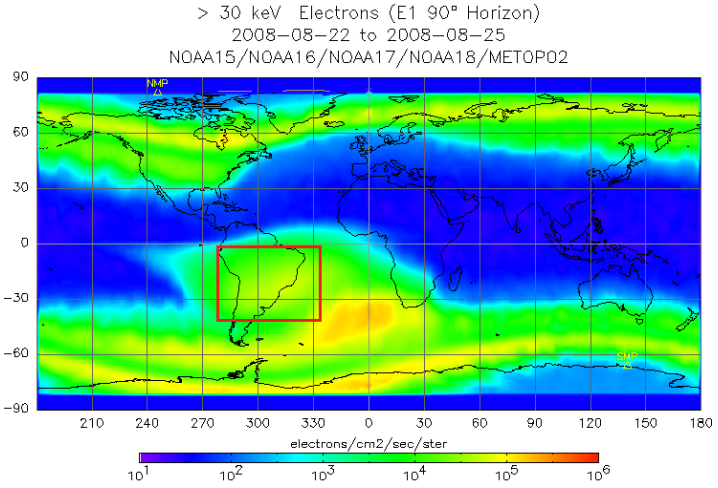

FIGURE 3. Contour map of electron flux within the energy range of lower 30 keV derived from the POES satellite at 840 km of altitude, with area illuminated by the IRIS antenna limited by the red dashed square. AFTER: Modified from [39].

In our analysis, we considered only those particles measure in the region of the satellite orbit corresponding to the projection of the field of view overhead the IRIS. Both MEPED detectors (the one aligned to the zenith and the one aligned with the horizontal satellite path) were considered in the analysis. All the measurement of the different particles (electrons and protons) within all measured energy ranges were taken into account. The best fit (95%) was found between electron flux distribution within the energy range of between 30 and 300 keV and the four-day running averaged max CNA values detected by the IRIS installed at the SSO (Fig. 4). Therefore, we attribute the occurrence of this CNA event to particle precipitation in the SAMA region.

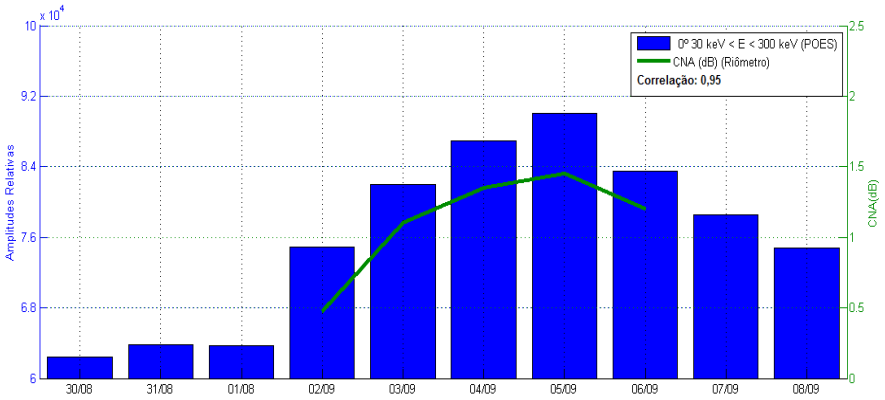

FIGURE 4. Histogram of electron flux distribution within the energy range of between 30 and 300 keV detected over the SAMA region derived from the POES satellite at 840 km of altitude (blues bars) and the four-day running averaged max CNA values detected by the imaging riometer installed at the SSO (green line).

Abnormal enhancement of the equatorial sporadic E-layers:

With respect to space weather effects related associated with abnormal enhancements of the equatorial sporadic E-layers density during the recovery phase of magnetic storm, we show the variation of the *fb*Es (green line) and *ft*Es (brown line) at SLZ on the middle panel of Fig. 5. On the top panel of the same figure is shown the variation of the Dst index, and the variation of the X-ray solar radiation intensity measured in the range 0.5—4.0 Angstrom (red line) and 1.0—8.0 Angstrom (blue line) from October 26 to November 3, 2003. All the data are referred in Universal Time (UT). The Dst intensity variation is given in nT and its linear scale is shown in the left vertical axis of the top panel. Both *fb*Es and *fb*Es are given in MHz and their linear scale is shown in the left vertical axis of the middle panel. The X-ray solar radiation intensity in both bands is given in W/m^2 and their logarithmic scale is shown in the left vertical axis of the bottom panel. Also, on the right vertical axis of the bottom panel it is shown a classification of the flare according to the intensity reached by the peak of the X-ray flux [40].

During the magnetic super storm occurred on October 2003, the behavior of these frequency parameters changed the background profile. From October 29 to 31, the digisonde registered sequentially smaller values in the *ft*Es maximum daily peak (identified by the dotted line in the middle panel of Fig. 5). Also, an anomalous intensification of the ionospheric density (determined from the *fb*Es) that exceeded the typical ambient background values for local time and location could be seen some days after the main phase of the storm (identified in the middle panel of Fig. 5 by the arrow labeled with the letters A, B and C).

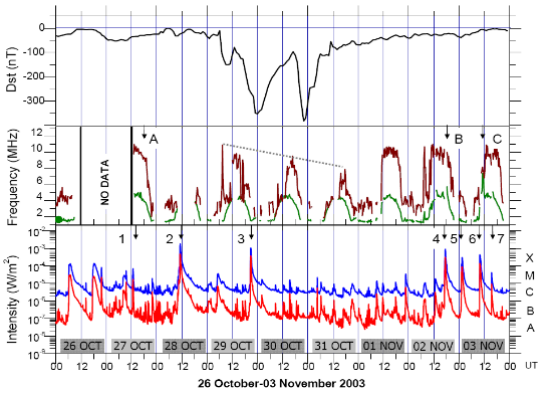

FIGURE 5. Variation of the Dst index on the top, the variation of the fbEs (green line) and ftEs (brown line) at São Luís on the middle panel, and the variation of the X-ray solar radiation intensity measured in the range 0.5—4.0 Angstrom (red line) and 1.0—8.0 Angstrom (blue line) from October 26 to November 3.

The sequentially smaller values of the *ft*Es maximum daily peak started on the initial phase of the magnetic storm and lasted until the beginning of the recovery phase. On October 29, *ft*Es maximum daily peak reached ~10 MHz around midday; it decreased to 9.5 MHz on October 30 and decreased to 8 MHz on October 31. Afterwards, the value of the *ft*Es maximum daily peak returned to the typical level of 11 MHz (normally found around local midday). Despite being a remarkable characteristic of the frequency parameters measured during this event, we were not able to collect enough evidences to provide a definitive explanation for the declination in the *ft*Es daily peak measured during the main phase of the super storm. Nevertheless, from the magnetic measurement of the EEJ ground strength (presented in Fig. 6) we identified that during the period when the declination in the *ft*Es maximum daily was measured the EEJ current was very weak, meaning weak EEJ polarization electric field. Thereafter, we suggest that an electromagnetic rearrangement on the Sq system, i. e., Disturbance Dynamo effects could be ruling over the equatorial environment at the E-region heights during that period. This is supported by the fact that the *ft*Es is a parameter taken from the equatorial sporadic E layer (Es_q), which is associated to EEJ plasma instabilities, which are in turn driven by the EEJ electric field that we state to be weak during that period.

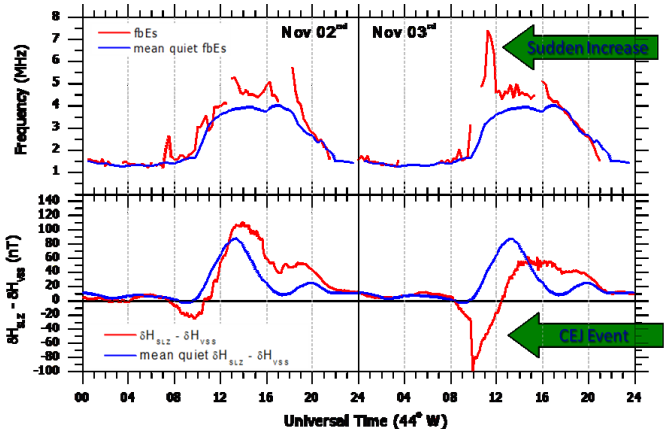

FIGURE 6. Diurnal variation of fbEs and the effect of the chain of the induced equatorial electrojet in the ground in days 02 and 03 of November. The blue line shows the average secular variation of the same parameters above for the calm period of 10 the 12 of October.

With respect to the anomalous intensification of the ionospheric density, observed thought of the sudden peaks in the *fb*Es parameter (used as a proxy of the *fo*E), two main interpretation rises from these impressive increases in the electron density. We concentrated in the peaks during the recovery phase of the October 2003 super storm (B and C). The first interpretation deals with radio signal absorption (in the HF band) commonly known to happen in the D-region. We verified the evolution of the type of Es layer during the event occurred on November 3 (not shown here) considering the influence of the X-ray radiation due to burst solar events. We investigated the increases of the X-ray radiation in ranges 0.5—4.0 and 1.0—8.0 Angstrom using measurement by XRS at the GOES 10 (arrow 1 to 7 in the lower panel of Fig. 5). However, we no longer have a definitive answer. Therefore, we will keep these two possibilities as probable explanations for the observed abnormal electron density enhancement of the equatorial sporadic E-layers density during the recovery phase of the magnetic storm. Furthermore, to support this hypothesis, we know that an extra amount of X-ray or EUV solar radiation could have increased the D-region density leading to an increase of its opacity for a lower wavelength electromagnetic signal propagating upward [16, 18, 27]. In this case, the lower frequencies of the digisonde would be blocked and the *fb*Es no longer can be used as a proxy of the *fo*E. Therefore, the results we are interpreting as electron density increases at the E-region height are indeed a response of the D-region density to sudden X-ray and/or EUV solar radiation.

On the other hands, the second interpretation is thought in term of the dominant process that is ruling the Es formation at the time of the sudden intensification. Whichever was the explanation, the present result still is an evidence of the reaction of the ionospheric-thermospheric system to space weather forces. Supporting the second hypothesis, we mentioned that we observed a suddenly

appearance of the type "c" sporadic layer (Es_c) that replaced the normally observed sporadic layers of the type "q" (Es_q). In addition, we know that the different types of sporadic layer are classified according to the different mechanisms of formation and location that they are observed. Moreover, the Es_c is an E-region ionization enhancements that are associated with vertical shear caused by apposite horizontal neutral winds at the E-region height normally identifies in middle latitudes [41].

Lastly, these two possible explanations for this event, the radio signal absorption (commonly known to happen in the D-region), while the second points out that the changes of the types of sporadic layer, which leads to different mechanisms of formation and a competition in the aspects of the solar-terrestrial system coupling.

Conclusions. We identified two kind of event associated with space weather that were measured during magnetic storms in the Brazilian sector, both at low latitudes. We observed a CNA event on during the main phase of the intense geomagnetic storm occurred on 22 and 23 September 1999 (Dst = –164 nT) by the IRIS (38.2 MHz) at the SSO, Southern of Brazil, drifting eastward with at about 250 m/s and getting weaker as the main phase of the magnetic storm evolves. Calculated the energy of the probable precipitating particles and checking within the MEPED detector on-board of the POES satellite, we attribute the occurrence of this CNA event to the energetic particle precipitation in the SAMA region. We also were able to identify a sequence of smaller values for the *fi*Es maximum daily peak from October 29 to 31, explained as an effect of the Disturbance Dynamo in response to the energy injection dues to the super magnetic storm. Moreover, an anomalous intensification of the ionospheric density (determined from the fbEs) that exceeded the normal ambient background values for local time and location could be seen some days after the main phase of the storm. Two possible explanations were raised for this event. The first one deals with the radio signal absorption (commonly known to happen in the D-region), while the second points out that the changes of the types of sporadic layer, which leads to different mechanisms of formation.

Acknowledgments: *C. M. Denardini thanks to CNPq/MCTIC (Grant 303121/2014-9), to FAPESP (Grant 2012/08445-9). J. Moro thanks to China-Brazil Joint Laboratory for Space Weather (CBJLSW). L. C. A. Resende thanks to CNPq/MCTIC (Grant 405334/2017-6) and FAPESP (grant 2014/11198-9).*

1. G.W. Prölss, Magnetic storm associated perturbations of the upper atmosphere: recent results obtained by satellite-borne gas analyzers, *Rev. Geophys. Space Phys*., 1980, 18, pp. 183—202.

2. C.M. Denardini, M.A. Abdu, H.C. Aveiro et al., Counter electrojet features in the Brazilian sector: simultaneous observation by radar, digital sounder and magnetometers, *Ann. Geophysicae*, 2009, 27(4), pp. 1593—1603.

3. H.C. Aveiro, C.M. Denardini, and M.A. Abdu, Climatology of gravity waves–induced electric fields in the equatorial E region, *J. Geophys. Res*., 2009, 114 (A11308), doi:10.1029/2009JA014177.

4. H.C. Aveiro, C.M. Denardini, and M.A. Abdu, Signatures of 2-day wave in the E-region electric fields and their relationship to winds and ionospheric currents, *Ann. Geophysicae*, 2009, 27(2), pp. 631—638.

5. C.M. Denardini, M.A. Abdu, E.R. de Paula et al., Seasonal characterization of the equatorial electrojet height rise over Brazil as observed by the RESCO 50 MHz back-scatter radar, *J. Atmos. Sol.-Terr. Phys*., 2005, 67(17—18), pp. 1665—1673.

6. E. B. Shume, C. M. Denardini, E. R. de Paula, and N. B. Trivedi, Variabilities of the equatorial electrojet in Brazil and Peru, *J. Geophys. Res.*, 2009, doi:10.10292009JA014984.

7. C. M. Denardini, M. A. Abdu, and J. H. A. Sobral, Detection of three distinct regions in the equatorial electrojet in the Brazilian sector, *Brazil. J. Geophys.*, 2003, 21(1), pp. 65—74.

8. C. M. Denardini, M. A. Abdu, E. R. de Paula et al., VHF radar observations of the dip equatorial E-region during sunset in the Brazilian sector, *Ann. Geophysicae — Atmos. Hydrospheres and Space Sci.*, 2006, 24(6), pp. 1617—1623.

9. C. M. Denardini, S. Dasso, and J. Gonzalez-Esparza, A Review on space weather in Latin America. 3. Development of space weather forecasting centers, *Adv. Space Res*., 2016, 58(10), pp. 1960—1967, doi:10.1016/j.asr.2016.03.011.

10. M. A. Abdu, I. S. Batista, A. J. Carrasco, and C. G. M. Brum, South Atlantic Magnetic Anomaly ionization: A review and a new focus on electrodynamics effects in the equatorial ionosphere, *J. Atmos. Sol. Terr. Phys*., 2005, 67, pp. 1643—1657.

11. J. Moro, C. M. Denardini, M. A. Abdu et al., A comparison of two different techniques for deriving the quiet day curve from SARINET riometer data*, Ann. Geophys*., 2012, 30, pp. 1159—1168.

12. J. Moro, C. M. Denardini, M. A. Abdu et al., Latitudinal dependence of cosmic noise absorption in the ionosphere over the SAMA region during the September 2008 magnetic storm, *J. Geophys. Res*., 2012, 117, A06311, doi:10.1029/2011JA017405.

13. L. C. A. Resende, C. M. Denardini, and I. S. Batista, Abnormal fbEs enhancements in equatorial Es layers during magnetic storms of solar cycle 23, *J. Atmos. Sol.-Terr. Phys*., 2013, 102, pp. 228—234, doi:10.1016/j.jastp.2013.05.020.

14. C. M. Denardini, L. C. A. Resende, J. Moro, and S. S. Chen, Occurrence of the blanketing sporadic E layer during the recovery phase of the October 2003 superstorm, *Earth, Planets and Space*, 2016, 68(80), pp. 1—9, doi:10.1186/s40623-016-0456-7.

15. A.P. Mitra and C.A. Shain, The measurement of ionospheric absorption using observation of 18.3 mc/s cosmic radio noise, *J. Atmos. Sol.-Terr. Phys*., 1953, 4, pp. 204—218.

16. M. A. Abdu, Galactic radio noise attenuation in the ionosphere, Ph. D. Thesis, The Gujarat University, Ahmedabad, India, 1966, 147 p.

17. K. R. Ramanathan, R. V. Bhonsle, and D. D. Degaonkar, Effect of electron-ion collisions in the F region of the ionosphere on the absorption of cosmic radio noise at 25 Mc/s at Ahmedabad: Changes in absorption associated with magnetic storms, *J. Geophys. Res.*, 1961, 66, pp. 2763—2771.

18. M. A. Abdu, S. S. Degaonkar, and K. R Ramanathan, Attenuation of galactic radio noise at 25 MHz and 21.3 MHz in the ionosphere over Ahmedabad during 1957—1964, *J. Geophys. Res.*, 1967, 72, pp. 1547—1554.

19. R. I. Kressman, Riometer studies at South Georgia, *Br. Antarct. Surv. Bull*., 1976, 43, pp. 15—23.

20. T. J. Rosenberg, Z. Wang, A. S. Rodger et al., Imaging riometer and HF radar measurements of drifting F region electron density structures in the polar cap, *J. Geophys. Res*., 1993, 98, pp. 7757—7764.

21. I. S. Batista and M. A. Abdu, Magnetic storm delayed sporadic E enhancements in the Brazilian geomagnetic anomaly*, J. Geophys. Res*., 1977, 82(29), pp. 4777—4783.

22. L. C. A. Resende and C. M. Denardini, Equatorial sporadic E-layer abnormal density enhancement during the recovery phase of the December 2006 magnetic storm: A

case study, *Earth Planets and Space*, 2012, 64(4), pp. 345—351, doi:10.5047/eps.2011.10.007.

23. N. Wakai, H. Ohyama, and T. Koizumi, *Manual of Ionogram Scaling*, Revised Edition, Radio Research Laboratory, Tokyo, 1986, 120 p.

24. E. L. Afraimovich, A. T. Altyntsev, E. A. Kosogorov et al., Ionospheric effects of the solar flares of September 23, 1998 and July 29, 1999 as deduced from global GPS network data, *J. Atmos. Solar-Terr. Phys*., 2001, 63, pp. 1841—1849.

25. C. G. Little and H. Leinbach, The riometer-a device for continuous measurements of ionospheric absorption, *Proceedings of the IRE*, 1959, 46, pp. 320—325.

26. B. Lusignan, Cosmic noise absorption measurements at Stanford, California, and Pullman, Washington, *J. Geophys. Res.*, 1960, 65, pp. 3895—3902.

27. M. A. Abdu, S. Ananthakrishnan, E. F .Coutinho et al., Azimuthal drift and precipitation of electrons into the South Atlantic Geomagnetic Anomaly during an SC Magnetic storm, *J. Geophys. Res.*, 1973, 78, pp. 5830—5836.

28. M. Nishino, Y. Tanaka, T. Oguti et al., Initial observations results with imager riometer at NY-Alesud (L = 16*)*, *NIPR Symp. Upper Atmosphere Physics*, 1993, 6, pp. 47—61.

29. M. Nishino, K. Makita, K. Yumoto et al., Unusual ionospheric absorption characterizing energetic electron precipitation into the South Atlantic Magnetic Anomaly, *Earth, Planets, and Space*, 2002, 54, pp. 907—916.

30. M. Nishino, K. Makita, K. Yumoto et al., Energetic particle precipitation in the brazilian geomagnetic anomaly during the "Bastille Day Storm" of July 2000, *Earth, Planets, and Space*, 2006, 58, pp. 607—616.

31. J. Moro, C. M. Denardini, M. A. Abdu et al., Correlation between the cosmic noise absorption calculated from the SARINET data and the energetic particles measured by MEPED: Simultaneous observations over SAMA region, *Adv. Space Res*., 2013, 51(9), pp. 1692—1700, doi:10.1016/j.asr.2012.11.030.

32. A. Fredriksen and R. B.Dyce, Ionospheric absorption investigations at Hawaii and Johnston Island, *J. Geophys. Res.*, 1960, 65, pp. 1177—1181.

33. W. R. Steiger and J. W. Warwick, Observations of cosmic radio noise at 18 mc/s in Hawaii, *J. Geophys. Res.*, 1961, 66, pp. 57—66.

34. R. Heisler and G. L. Hower, Riometer quiet day curves, *J. Geophys. Res.*, 1967, 72, pp. 5485—5490.

35. R. J. Armstrong, F. T. Berkey, and T. Melbye, The day to night absorption ratio in auroral zone riometer measurements, *Planet Space Sci.e*, 1977, 25, pp. 1193—1198.

36. S. Krishnaswamy, D. L. Detrick, and T. Rosenberg, The inflection point method of determining riometer quiet day curves, *Radio Sci.*, 1985, 20(20), pp. 123—136.

37. Y. Tanaka, K. Makita, M. Nishino, and T. Ookawa, Development of data analysis program for imaging riometer by using MATLAB, *Bulletin of science and engineering*, *Takushoku University*, 2007, 10(1), pp. 61—66.

38. C. M. Denardini, S. S. Chen, L. C. A. Resende et al., The Embrace Magnetometer Network for South America: Network Description and Its Qualification, *Radio Sci.*, 2018, 53, pp. 1—32, doi:10.1002/2017RS006477.

39. SWPC.The NOAA POES (TIROS) Medium Energy Proton and Electron Detector. 325 Broadway, Boulder CO 80305, USA: NOAA Space Weather Prediction Center, 2001. Avaliable: http://www.swpc.noaa.gov/pmap/PoesSem.html. Access on: 24 November 2017.

40. B. V. Somov and S. I. Syrovatskii, Magnetically driven motions in solar corona, *Soviet Phys*., 1972, 34, pp. 332—335.

41. J. D. Whitehead, Recent Work on Mid-Latitude and Equatorial Sporadic-E, *J. Atmos. Sol.-Terr. Phys.*, 1989, 51(5), pp. 401—424.

Coupling between Neutral and Ionized Atmosphere and Transient Changes of Electron Densities in the Upper Atmosphere

Jaroslav Chum

Institute of atmospheric Physics, Czech Academy of Sciences, Boční II/1401, 14131 Prague, Czech Republic

Introduction. Disturbances of electron densities in the ionosphere will be studied in this paper. Experimental data, based mainly on the continuous Doppler sounding will be presented and compared with theoretical expectations and numerical simulations. A special attention will be paid to internal atmospheric gravity waves (GWs), infrasound and sudden ionospheric disturbances (SIDs) associated with solar flares as these processes represent examples of mechanisms that cause local perturbations of electron densities. Acoustic-gravity waves represent an important coupling mechanism as they transfer momentum and energy between different atmospheric layers [1]. They might also couple the solid Earth with the ionosphere during earthquakes [2, 3]. Solar flares, namely the ionizing X-ray and EUV fluxes, cause transient imbalance between ion-electron production rate and loss processes. In addition, they are responsible for enhanced ionization in the lower ionosphere, especially in the D-layer, where the collision between neutral particles and electrons are frequent, which results in increased attenuation of sounding radio waves. A role of the ionospheric and atmospheric electric field will also be mentioned.

Continuous Doppler sounding (CDS). The CDS is a relatively simple and cheap method to investigate dynamics of the ionosphere. It is based on precise measurement of Doppler shift that experiences a continuous sine wave reflecting from the ionosphere. It can be shown that the Doppler shift mainly depends on the time change of electron density, $\partial N/\partial t$, in the region of reflection [4]. Using equation of continuity, the $\partial N/\partial t$ term can be decomposed as

$$\frac{\partial N}{\partial t} = -\nabla N \cdot u_P - N(\nabla \cdot u_P) + P - L, \tag{1}$$

where u_P is the radial velocity of plasma motion, P is electron production, *e. g.*, owing to photoionization, and L represents losses of free electrons [5]. The first term on the right hand side of equation (1) represent the advection (e. g., the up and down motion of the reflecting level), the second term arises from compression of plasma and the third term (P-L) is caused by an imbalance between production rate and losses of free electrons (e. g., recombination). The advection usually dominates during the plasma motion owing to GWs (via collisions with neutral particles) or if plasma moves owing to ExB drift (if an electric field across the magnetic field is present). The compression might be dominant when compressional waves as

infrasound act on ionospheric plasma. This was observed during earthquakes [3, 6]. Finally, the *P-L* term might be dominant during X-ray and EUV solar flares [7].

The CDS is especially useful to study perturbation on short time scales as the time resolution is several seconds or tens of seconds, depending on the time intervals over which the spectral analysis is performed. It is advantageous to operate the CDS close to an ionospheric sounder to know the reflection height (note that the CDS does not measure the reflection height). The Institute of Atmospheric Physics, Czech Republic, currently operates an international network of CDSs. The CDS were installed in in the Czech Republic (~50.3° N, 14.5° E), Taiwan (~23.9° N, 121.2° E), northern Argentina (~26.8° S, 65.2° W), and South Africa (~34.4° S, 19.2° E). The multi-point CDS systems were installed in each country; the system consists of at least three transmitters and one receiver in each country. The time delays between the corresponding signatures observed on different sounding paths (transmitter-receiver pairs) can be used to calculate propagation velocities of GWs.

GW propagation and their observation. An example of GW observation in the Czech Republic and analysis of propagation will be presented. There are three multi-point CDS systems operating at frequencies of 3.59, 4.65, and 7.04 MHz in the Czech Republic; waves of individual frequencies reflect at different heights, provided that the sounding frequency is lower than the critical frequency. So, the propagation of GWs can be studied in 3D in the Czech Republic, using the time (phase) delays between corresponding signatures observed on different sounding paths as these time delays are observed both in the horizontal and vertical directions.

Figures 1a and 1b show the Doppler shift spectrograms recorded on 5 July 2014 from 19:30 to 21:00 at frequencies 4.65 MHz and 7.04 MHz, respectively. The frequencies of individual transmitters are mutually offset by about 4 Hz to avoid frequency overlap and to be able to display them in one Doppler shift spectrogram by performing only one spectral analysis. Each Doppler shift spectrogram contains signals from three different transmitters. GWs can be easily recognized on each signal path (transmitter-receiver pair). In addition, ground waves are visible as straight horizontal lines for the upper sounding path in both spectrograms. The signals (Doppler shifts) were approximated by single valued functions of time for each sounding path and the propagation velocities were computed by slowness method as described in [8]; the slowness method was generalized for the 3D case. The results of the slowness analysis are presented in Figures 1c and 1d in the form of the normalized slowness maps. The map in Fig. 1c presents the horizontal cross-section through the maximum of energy in the 3D space of slowness components and the map in Fig 1d displays the corresponding vertical cross-section. The slowness is the inverse of phase velocity. The darker color in the map, the more energy propagates with the given slowness (velocity) components. The dominant wave (most of the energy) propagated approximately north-westward with velocity of about 114 m/s. The apparent horizontal velocity

was about 139 m/s as the phase velocity vector was directed obliquely downward; the angle between the horizontal plane and wave vector was about 35°. It should be reminded that the downward phase vector means that the energy (group velocity) propagated upward in the case of GWs [1]. So, the observed GWs were generated at lower altitudes, perhaps their primary origin could be in the troposphere. The heights of observation (reflection), determined from nearby ionospheric sounder were around 220, 230 and 255 km for the CDS operating at 3.59, 4.65 and 7.04 MHz, respectively.

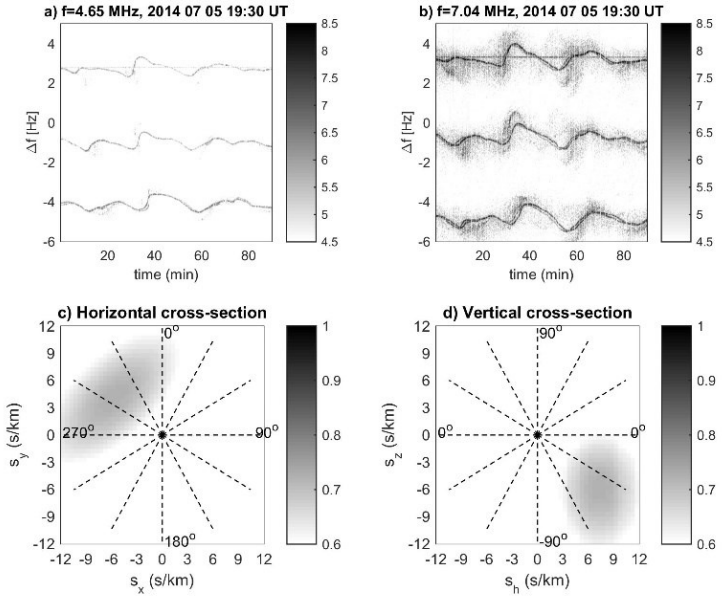

FIGURE 1. Example of GW observation and its analysis. Doppler shift spectrogram recorded from 19:30 to 21:00 UT on 5 July 2014 by the multi-point CDS system operating at frequency 4.65 (a) and 7.04 MHz (b), and the normalized energies in the space of slowness components for the horizontal (c) and vertical (d) cross-section through the maximum. See the text for more details.

Infrasound observation in the ionosphere. Unlike the GWs, the infrasound observations in the ionosphere are rare. Usually, they can be associated with ground surface movement caused by significant earthquakes or with large and severe weather system in the troposphere as typhoons, large convective cells or passages of distinct fronts [3]. Examples of coseismic infrasound in the ionosphere, observed far (~9000 km) from the epicenter and relatively close (~800 km) from the epicenter are presented in Fig. 2. Figure 2a shows the Doppler shift spectrogram recorded in the Czech Republic from 6:00 to 7:00 UT on 11 March 2011. Several distinct wave packets can be easily recognized in this spectrogram. It was shown [6] that these wave packets are well correlated with vertical velocity v_z

of the ground surface movement measured in the Czech Republic. The wave packets observed by CDS at the altitude around 210 km are observed with about 9 min delays with respect to the wave packets of v_z observed on the ground. This time delay is consistent with expected (simulated) time for vertically propagating infrasound waves. The packets of v_z correspond to P, S, SS and Rayleigh seismic waves [6] triggered by the *M*9.0 Tohoku earthquake with epicenter at about 9000 km distance. Figure 2b shows the Doppler shift spectrogram recorded in northern Argentina on 16 September 2015 from 22:45 to 23:45 after *M*8.3 earthquake with epicenter at about 800 km horizontal distance. The character of the ionospheric response is completely different. The main reason for that are nonlinear phenomena that results from large amplitude of infrasound waves in the upper atmosphere [3, 6]. The results of numerical simulations based on the solution of continuity, momentum and heat equation for realistic viscous and compressional atmosphere are consistent with the observation. The nonlinear phenomena lead to the change of the original wave packet, including its frequency content, during its propagation in the upper atmosphere [2, 3].

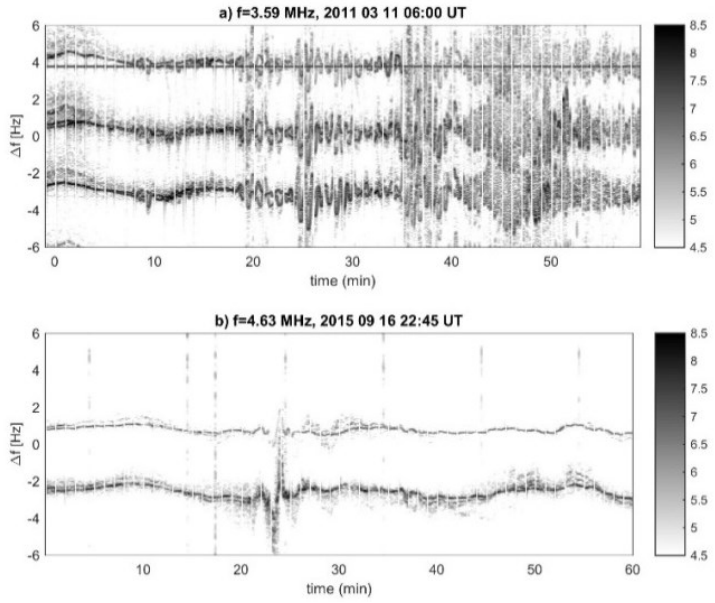

FIGURE 2. Doppler shift spectrograms showing infrasound waves recorded in the Czech Republic on 11 March 2011 from 6:00 to 7:00 UT (a) and in northern Argentina on 16 September 2015 from 22:45 to 23:45 UT.

Electron density changes during X-ray and EUV solar flares. Solar flares are associated with a large increase of ionizing flux in the EUV and X-ray spectral range. The rapid increase of ionization flux results in imbalance between electron-ion production rate and electron losses and hence in sudden frequency deviation in

CDS measurements [5, 7]. In addition, the enhanced X-ray flux causes increase of electron density in the D region, which results in the enhanced attenuation of radio waves. For very strong X-ray flares, the attenuation is so large that the signal to noise ratio decreases significantly and the received signal might not be recognized in the noise. This concerns both the CDS and ionospheric sounders dedicated for measurements of electron profile. The attenuation depends strongly on sounding frequency; the lower frequency, the higher attenuation. So, the information is first lost at lower frequencies during the X-ray flares.

Conclusions. Several phenomena that cause transient local changes of electron densities were discussed; references to more detailed studies were provided. Special attention was given to acoustic-gravity waves and their coupling to ionospheric plasma. The examples of observation were based on continuous Doppler sounding.

Acknowledgments. The international collaborations with colleagues in Taiwan and Argentina that make it possible to operate CDS in these countries is acknowledged, namely the support by J. Y. Liu (Taiwan) and M. A. Cabrera (Argentina). The collaboration with other colleagues from the Institute of Atmospheric Physics, Prague, namely with J. Baše and J. Laštovička, is acknowledged. The support under the project 18-01969S by the Czech Science Foundation is acknowledged.

1. Fritts, D. C., Alexander, M. J. (2003), Gravity wave dynamics and effects in the middle atmosphere, *Rev. Geophys., 41*(1), 1003, doi:10.1029/2001RG000106.

2. Chum, J., Cabrera, M. A., Mosna, Z., Fagre, M., Base, J., Fiser, J., 2016b. Nonlinear acoustic waves in the viscous thermosphere and ionosphere above earthquake. *J. Geophys. Res., 121*, *12*, doi:10.1002/2016JA023450.

3. Chum, J., J.-Y. Liu, K. Podolská, T. Šindelářová (2017), Infrasound in the ionosphere from earthquakes and typhoons, *J. Atmos. Sol. Terr. Phys.*, doi:/10.1016/j.jastp.2017.07.022

4. Davies, K., J. Watts, Zacharisen, D. (1962), A study of F2-layer effects as observed with a Doppler technique, *J. Geophys. Res.,* 67, 2, doi:10.1029/JZ067i002p00601

5. Liu, J. Y., C. S. Chiu, and C. H. Lin (1996), The solar flare radiation responsible for sudden frequency deviation and geomagnetic fluctuation, *J. Geophys. Res*., 101(A5), 10,855–10,862, DOI:10.1029/95JA03676.

6. Chum, J., Hruska, F. Zednik, J., Lastovicka, J. (2012), Ionospheric disturbances (infrasound waves) over the Czech Republic excited by the 2011 Tohoku earthquake, *J. Geophys. Res., 117*, A08319, doi:10.1029/2012JA017767.

7. Laštovička, J., and J. Chum (2017), A review of results of the international ionospheric Doppler sounder network, *Adv. Space Res.*, DOI: http://dx.doi.org/10.1016/j.asr.2017.01.032

8. Chum, J., F. A. M. Bonomi, J. Fišer, M. A. Cabrera, R. G. Ezquer, et al. Propagation of gravity waves and spread F in the low-latitude ionosphere over Tucumán, Argentina, by continuous Doppler sounding: first results. (2014), *J. Geophys. Res. Space Phys. 119*:6954—6965, DOI:10.1002/2014JA020184

Results of the Studies of the Lower Ionosphere by the Method of the Radio Wave Back Scattering on Natural and Artificial Irregularities of the Ionospheric Plasma

Nataliya V. Bakhmetieva, Gennady I. Grigoriev, and Ariadna V. Tolmacheva

Radiophysical Research Institute Nizhny Novgorod State University, 25/12a, Bol'shaya Pecherskya St., Nizhniy Novgorod, 603950, Russia

Introduction. We present the main results of the studies of the Earth's lower ionosphere in the altitude range 60—130 km, obtained by the method of partial reflections and by resonance scattering of radio waves on artificial periodic irregularities of the ionospheric plasma. The method of partial reflections (PR) is the radar sounding of the lower ionosphere in the range of decameter waves. It is based on the backscattering of radio waves by natural plasma irregularities created by the atmospheric turbulence. PR technique allows one to obtain an information about the electron density and inhomogeneity parameters at altitudes of 60-90 km. At present, the theory of applying of the PR technique is well developed. The method of differential absorption is the most widespread. According to it the electron concentration is determined by the ratio of the amplitudes of the ordinary and the extraordinary components of the scattered signal. The method of partial reflections does not require the use of powerful transmitters. It has a high temporal resolution which allows analyzing fast variations of ionosphere parameters. At present, only two PR facilities work in Russia. One of them is the mid-latitude NIRFI facility witch located in Vasil'sursk township (56.15° N; 46.10° E) near Nizhny Novgorod. Another high-latitude facility belongs to the Polar Geophysical Institute located in Tumanny township (68.91°N; 46.10°E) [1].

The method of resonance scattering of radio waves on artificial periodic irregularities (API) of the ionospheric plasma developed in NIRFI [2] is the relatively new method for ionosphere diagnostics. Many years of experimental and theoretical researches have shown the API technique is one of the most informative methods for studying of the Earth's lower ionosphere. It allows us to determine many characteristics of ionized and neutral components of the lower ionosphere with a great accuracy, including the electron density profile, the temperature and the density of the neutral atmosphere, the frequency of ion-molecular collisions, the velocity of vertical regular and turbulent plasma motions, the altitude of the turbopause, the relative density of negative oxygen ions and the density of atomic oxygen and excited molecular oxygen in the $^1\Delta_g$ state in the *D*-region. In addition, the method based on the radio waves scattering on APIs allows one to determine the parameters of internal gravity waves that affect characteristics of scattered signals, to study the irregular structure of the lower ionosphere, including the stratification of the regular *E*-layer. API technique allows one to detect weak sporadic ionization layers which are not available for detection by an ordinary

ionosonde; to investigate the features of the sunrise and sunset phenomena and the solar eclipse phenomena in the lower ionosphere and additional layers of the electron density from the lower part of the *D*-region to the height of the maximum of the *F*-layer.

1. Results of investigation of the D-region of the ionosphere by the method of partial reflections. One of the parameter of the *D*-region is the height profile of the electron density. The $N(h)$-profile is determined by the differential absorption method [1]. For that measurements of the altitude dependences of the amplitudes of the magnetoionic components $A_0(h)$ and $A_x(h)$ of the scattered signal are required. The partial reflections technique makes it possible to determine the height profile of the electron density in the range of 60—90 km. The measurements were carried out using NIRFI PR facility consisting of a transmitter emitting pulses of 25 μs duration with a pulsed power of 50 kW at the frequency of 2.95 MHz, a transceiver antenna having 12 dipoles in each of the two linear polarizations and the receiver with the 70 kHz band. Sounding of the ionosphere was carried out with the repetition rate 25 or 50 Hz. The 12-bit ADC was used for recording of scattered signals. A step of the height data registration was 0.7 or 1.4 km. Here are the main results. At mid-latitudes temporal variations of the $N(t)$ density in the height range of 70—90 km during the day followed the cosine of the Sun zenith angle with an exponent close to unity, which is much higher than the values found earlier (~0.5). At heights of 71—76 km the electron density in autumn (September) is higher than in summer (June).

Reaction of the D-region to chromospheric flares. Investigations of the lower ionosphere during the chromospheric flare on the Sun observed in April 2004 were carried out. It was found in joint NIRFI and PGI observations that the electron density at altitudes of 60—70 km grew in proportion to the intensity of X-ray radiation during the flare. In this case, the recombination law must be regarded as linear.

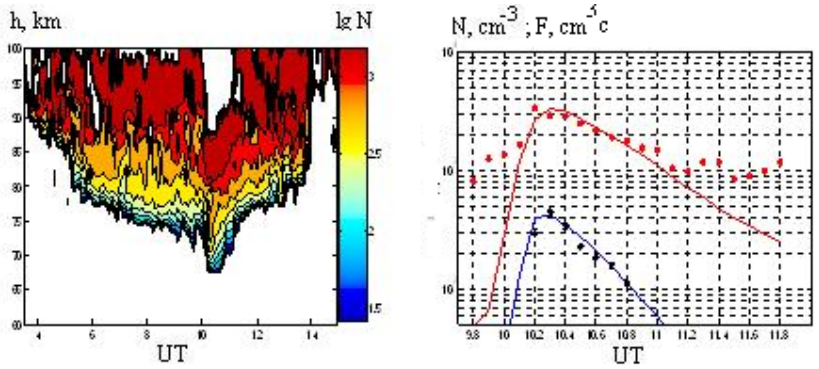

FIGURE 1. The electron density measured in Nizhny Novgorod by the PR technique (left panel); X-ray fluxes and electron density at heights of 71 km and 83 km during the chromospheric flare on April 8, 2004 (right panel).

To explain the linear law a hypothesis has been put forward that the main process of electron losses in the *D*-region is caused not by the dissociative recombination but by the recombination of electrons and ions on aerosol particles and on a meteor dust. It is shown the linear law can be caused by the plasma recombination on dust particles with the radius of $r \approx 10^{-5}$ cm with the dust concentration of the order of 30—100 cm^{-3}. The determination of the electron loss factor can prove to be an effective method for measuring the dust concentration in the mesosphere.

The D-region during a solar eclipse. The response of the ionosphere to partial solar eclipses was studied in Vasil'sursk on March 29, 2006 with a maximum eclipse phase φ=0.696 and August 1, 2008 with a maximum phase φ=0.653. In 2006, the signals scattered by natural irregularities of the *D*-region were recorded by PR, and by the method of simultaneous recording of PR scattering signals and API signals scattered in 2008. The results of observations of both eclipses are generally in good agreement with each other. It was found the electron density in the *D*-region the decreased 3—4 times or more during the eclipse. At heights of 75—77 km the response of the ionosphere, that is, the attainment of a minimum of the electron density, lagged behind the maximum phase of the eclipse on the Earth by no more than 2—4 minutes, but at the altitude of 85—90 km this delay was 20—24 minutes. It is shown in the Figure 2.

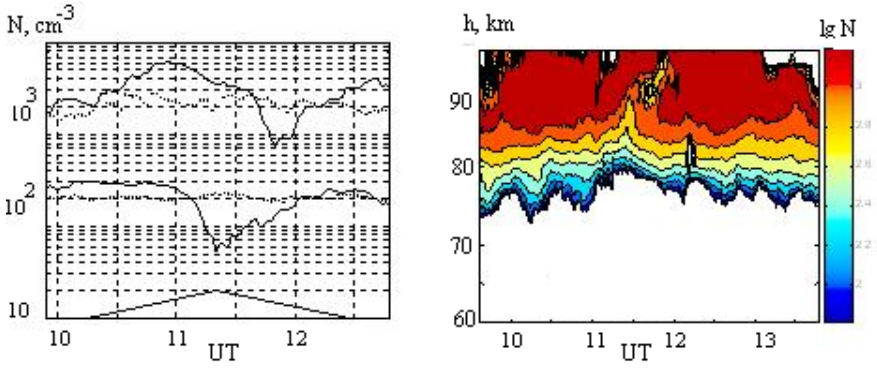

FIGURE 2. The temporal variations of the electron density during the solar eclipse on March 29, 2006 (the upper curve for the altitude 91 km, the lower one for 77 km, the points correspond to the next day) is shown on the left panel. The electron density-time-height plot in the *D*-region during the eclipse on August 1, 2008 is shown on the right panel.

Estimates show that the delay time and the magnitude of the decrease in the electron concentration during the eclipse differ significantly at different altitudes, which supports the linear recombination coefficient at the bottom of the *D*-region and the quadratic in its upper part.

2. Results of the studies of the ionospheric D- and E-regions by the API technique. The API technique uses the effect of powerful high-frequency radio emission on the ionospheric plasma with a purpose of creating artificial periodic

irregularities of the electron density, a sounding of the periodic structure with probe radio waves during the relaxation of irregularities after the heating termination, the measuring the amplitude and phase of the API scattered signal, determining the characteristics of the ionosphere and the neutral atmosphere from these data, parameters of sporadic ionization clouds, velocities and scales of wave and turbulent motions. To API create and sounding the SURA heating facility with frequencies of 4.7 and 5.6 MHz is used. For receiving the scattered signals, the receiving part of the PR facility is used. The height-temporal dependences of the API relaxation time are used to determine large number characteristics of the ionosphere and neutral atmosphere [2].

Sunset and sunrise phenomena in the D-region. The API technique was used to study the sunset and sunrise processes in the summer mid-latitude *D*-region. An example of range-time-amplitude plot of the API scattered signal on 12—13 August 2015 is shown in Fig. 3. The asymmetry of the altitude-time dependences of the amplitude and the relaxation time of the API scattered signal is detected. At altitudes below 65 km the signal amplitude growth at the sunrise began with a time-lag in relation to altitudes of 70—75 km, forming a kind of "step". Probably, the delay in the appearance of signals at altitudes below 65 km is due to the delay in the growth of the concentration of excited oxygen, which plays a primary role in the detachment processes at these heights. In this case the appearance of the "step" can be connected with the penetration of a part of the spectrum of solar radiation into the lower heights in the wavelength range λ=220—280 nm, which causes the appearance of oxygen molecules in the $^1\Delta_g$ state. In addition, there is a significant increase in the "dip" in the amplitude of the scattered signal at the altitudes between the *D*- and the *E*-regions at the sunrise. In the calculations it was found that the concentration of atomic oxygen should increase by 2—3 times at sunrise, and the lower boundary of the height of the appearance of atomic oxygen can be reduced by 5—7 km.

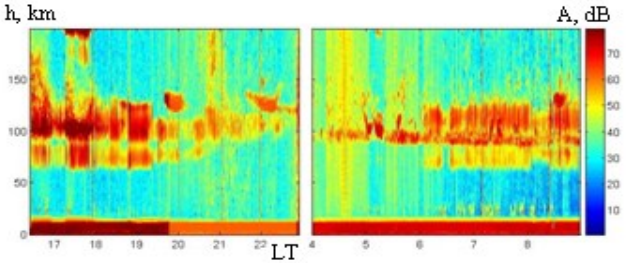

FIGURE 3. Amplitude of the signal scattered by the API during the sunrise and sunrise period August 12—13, 2015.

The temperature and density of the neutral component. Velocity of vertical plasma motion. Based on measurements of the amplitude and the phase of the API scattered signal the temperature T and density ρ of the neutral component, the velocity of vertical plasma motion V at heights of the lower

ionosphere are determined [2]. An example of simultaneous temperature and velocity variations is shown in Fig. 4. At the heights of the lower ionosphere the vertical plasma velocity is equal to the velocity of the neutral component.

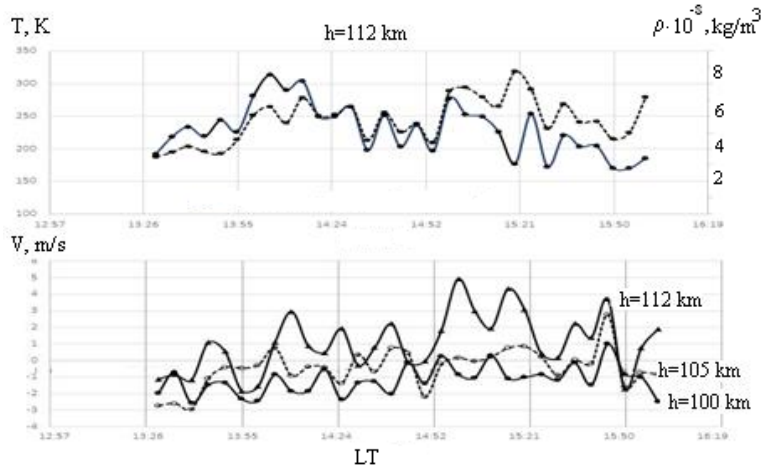

FIGURE 4. Dependence of temperature (solid line) and density (dashed line) of the neutral component on time at the height 112 km (upper panel) and the velocities of vertical movement at three heights 100, 105 and 112 km (bottom panel) 27.09.2016.

Time dependences of the ionosphere parameters show intense wave movements of different periods from minutes to hours, most likely associated with the propagation of internal gravity waves (IGW), which include waves with periods exceeding 5—10 minutes. It is clearly seen that these variations have a pronounced wave-like mode. Characteristic periods of 10—15 minutes are observed against a background of slower processes with a period of up to 1.5 hours. Amplitudes of waves reach to 50 K in the temperature and 3 m/s in the vertical velocity. Wave movements of large scales are more pronounced with the altitude increasing. It is the characteristic IGW signature. As a rule, the amplitude of the vertical velocity increases with altitude, which is also typical feature for variations in parameters due to atmospheric wave's effect. Obtained altitude profiles of the neutral temperature and density and the profiles of the vertical plasma velocity have a scale of 5 km to 15 km.

The work supported of the State task of the Ministry of Education and Science of the Russian Federation for Project No. 5.8092.2017/8.9.

1. V. V. Belikovich et al, *Radiophysics and Quantum Electronics*, Vol. 46, No. 3, 2003, Vol. 46. No. 3, pp. 162—171.

2. V. V. Belikovich, E. A. Benediktov, A. V. Tolmacheva, and Bakhmet'eva N. V., Ionospheric Research by Means of Artificial Periodic Irregularities — Copernicus GmbH, 2002, Katlenburg-Lindau, Germany, p. 160.

Stimulated Electromagneic Emissions of the Ionosphere: Main Properties and Diagnostic Possibilities

Savely M. Grach

Radiophysics Faculty, Lobachesky University, Gagarin Avenue 23, Nizhny Novgorod, 603950, Russia

One of the most interesting and informative manifestations of the artificial ionospheric turbulence arising near the reflection level of powerful HF radio waves is the generation of stimulated electromagnetic emission of the ionosphere (SEE). The SEE is known as a noise low-intensity (from −50 to −90 dB) component in the spectrum of the powerful radio-wave signal (pump wave) reflected from the ionosphere. The SEE occupies the frequency range of several tens (in some cases, up to several hundreds) of kilohertz near the pump wave frequency and demonstrates a rich spectral structure. The spectral components of SEE are formed due to different nonlinear interactions of high-frequency plasma waves and low-frequency perturbations arising due to HF pumping ionospheric plasma.

The following is discussed in the lecture:

- SEE properties for short-term (1—100 ms) HF pumping of the ionosphere;
- the main SEE spectral features during long-term (quasi-stationary) ionosphere HF-pumping
- SEE dependence of the ratio between the pump wave frequency f_0 and multiple electron cyclotron frequency sf_{ce} (s=2,3,4,6,7) between successive gyroharmonics;
- behavior of stimulated electromagnetic emission in a small vicinity of multiple electron cyclotron resonances;
- new SEE features obtained for large pump power at EISCAT, HAARP and Sura facilities;
- using SEE during specially elaborated diagnostic schemes of pumping (diagnostic SEE, DSEE) for identifying of nonlinear plasma processes in the HF-pumped ionosphere;
- diagnostics of both low frequency (plasma density irregularities) and high frequency (plasma waves) artificial ionospheric turbulence with DSEE;
- using SEE in combination with other diagnostic tools such as artificial optical emission and multifrequency Doppler sounding.

The statement is based on the results of numerous original papers summarized in the review [1].

The work was supported by Russian Science Foundation, grant 14-12-00706.

1. S.M. Grach, E.N. Sergeev, E.V. Mishin, A.V. Shindin, Dynamic properties of ionospheric plasma turbulence driven by high-power high-frequency radiowaves, *Physics — Uspekhi,* 2016, 59 (11), pp. 1091—1128, DOI:https://doi.org/10.3367/UFNe.2016.07.037868.

The Evolution of the Ozone Layer Under Influence of the Natural and Anthropogenic Factors

Eugene V. Rozanov[1,2,3]

[1]*Physikalisch-Meteorologishes Observatorium, Davos, World Radiation Center (PMOD/WRC), Dorfstrasse 33, 7260 Davos Dorf, Switzerland.*
[2]*Institute for Atmospheric and Climate Science, Swiss Federal Institute of Technology (IAC ETHZ), Universittstrasse 16, 8092, Zurich, Switzerland.*
[3]*Western Department of Pushkov Institute of Terrestrial Magnetism, Ionosphere and Radio Waves Propagation, Russian Academy of Sciences, Kaliningrad, Russia*

Introduction. The presence of the ozone layer in the Earth's atmosphere is important for the protection of the biological objects from the dangerous solar ultraviolet radiation (SUV). The absorption of the SUV by the ozone molecules heats up the air above the tropopause forming stable layer called stratosphere, where the temperature gradually increases until approximately 50 km. The ozone distribution in the atmosphere is driven by different chemical and transport processes. The ozone in the stratosphere is produced by recombination of the atomic oxygen atoms produced from the molecular oxygen photolysis. The ozone can be catalytically destroyed by reactive chemical species such as nitrogen, hydrogen, chlorine or bromine oxides (RO_x, where R = N, H, Cl or Br). The intensity of these cycles depends on the properties of the radicals, conditions of terminal reactions and the atmospheric state. In general, the intensity of the ozone destruction cycles increases in warmer environment. The primary sources of RO_x have natural (e. g., CH_4) or anthropogenic origin (e. g., CF_2Cl_2). These source gases have very long life time in the troposphere, but after penetration to the stratosphere they are destroyed by the enhanced above the ozone layer SUV producing RO_x. Recently it was discovered that even very short-lived species (e. g., CH_2Br_2) can contribute to stratospheric halogen radical burdens via the vertical transport of their degradation products. During the night time in the absence of SUV RO_x are converted to rather passive reservoir species (e. g., HNO_3, $ClONO_2$). The reservoir species can be converted back to reactive form by either photolysis during the day time or heterogeneous reactions in the presence of solid/liquid atmospheric aerosol particles. There are other processes like lightning or ionization by precipitating energetic particles producing NO_x directly in the atmosphere. The transport processes also play crucial role in the shaping of the vertical and horizontal distributions of the ozone in the atmosphere. The ozone transport by meridional circulation from the main production area in the tropical middle stratosphere to the middle latitudes explains the poleward displacement of the total vertical column ozone content (TOC) maximum in during winter-spring seasons. Thus, the evolution of the ozone layer depends on many natural and anthropogenic factors,

physical processes and their interactions making the simulation of the ozone evolution very complicated. More details about the processes related to the ozone layer evolution can be found in text books [1, 2].

Ozone layer depletion. During the second half of the 20th century the long-term ozone trends was mostly controlled by anthropogenic emission of halogen containing ozone destroying substances (hODS). Chlorine oxides produced from hODS in the stratosphere are the most dangerous for ozone in the upper stratosphere and lower stratosphere over high latitudes. The catalytic cycles involving chlorine containing radicals are very efficient in the upper stratosphere in the normal conditions, while in the lower stratosphere heterogeneous reactions on/in aerosol particles are necessary to convert reservoir species: HCl and $ClONO_2$ to Cl_2 during the polar night. After sunrise, fast photolysis of Cl_2 produces reactive chlorine radicals, which destroy ozone creating ozone hole over the polar regions. The ozone hole is the most pronounced in the southern hemisphere where the cold and isolated from middle latitudes environment facilitates extensive chlorine activation. Because of small natural emission of hODS these processes became important only when the production of anthropogenic hODS started in 1960's and intensified after 1980.

Figure 1 illustrates the simulated by the CCM SOCOL [3] and observed [4] ozone trend for the last 20 years of 20th century. The areas of high ozone sensitivity to hODS are clearly visible in the high latitude upper stratosphere and southern lower stratosphere. The discovery of the ozone hole [5] led to strong limitation on different hODS production introduced in 1987 by Montreal protocol and its amendments (MPA), have a dramatic impact on the future of the ozone layer. The simulated with the CCM SOCOL global mean TOC evolution is shown in the Fig. 2 (left panel) for the period from 1960 to 2100 for the cases with and without implemented MPA.

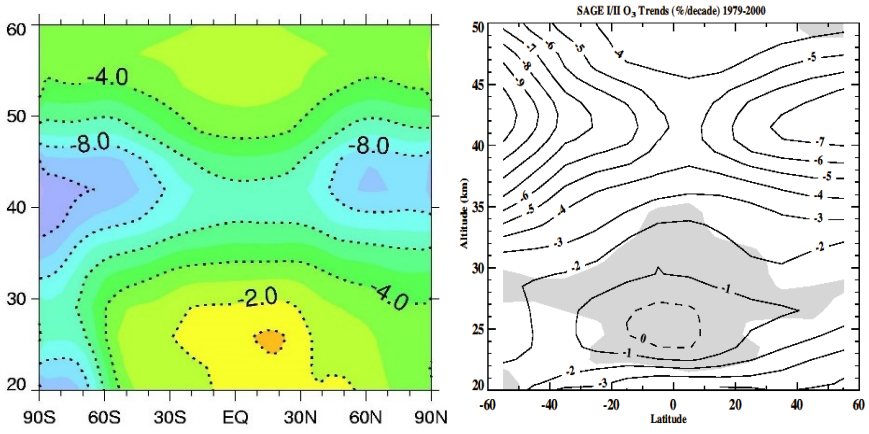

FIGURE 1. The simulated with the CCM SOOCL (left) and observed (WMO, 2002, right) zonal mean ozone mixing ratio trends (%/decade) for the period 1979—2000.

Ozone layer recovery. While all models predict bright future of the ozone layer in of 21st century [6], the current state of the ozone layer recovery has not been robustly established for all layers in the observation data. As expected from the model simulations, the recent analysis of the ozone observations confirms the beginning of the recovery phase in the upper stratosphere. Figure 3 (upper panel) shows that the ozone recovery started in approximately 1998 in the both satellite observations and model simulations. In the lower stratosphere, the situation is more complicated because the efficiency of halogen catalytic cycles there is smaller (see Fig. 1) and the internal variability of the ozone field is higher. Figure 3 (lower panel) reveals continuous negative trend with no traces of ozone recovery in the observation data, while the models robustly show that the ozone decrease stopped after 1998. Ball et al. [7] (Fig. 1) showed that the observed ozone depletion in the lower stratosphere covers wide latitudinal belt from 50°S to 50°N. Such a striking disagreement inspires a search for the missing processes or unaccounted driving factors in models, because the future ozone recovery cannot be confirmed if some serious problem with models exists. The analysis of recent publications allows to suggest several candidates such as (i) intensification of the meridional circulation in warming climate; (ii) decline of the solar activity; (iii) influence of bromine containing very-short lived species; (iv) emissions of unaccounted by MPA halogen containing gases; (v) increase of the aerosol loading.

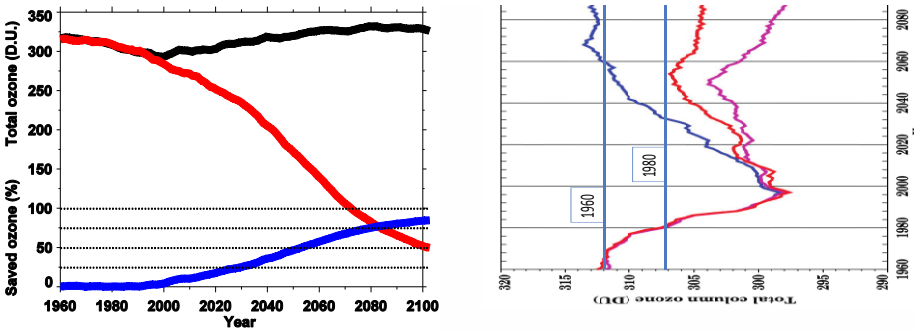

FIGURE 2. Left panel: Time evolution of the global and annual mean TOC (D.U.) for the reference (black) and no Montreal protocol (red) simulations. Total ozone saved by the Montreal Protocol limitations (%) is represented by the blue line. Adapted from [8]. Right panel: Simulated global annual mean total column ozone (in Dobson units) from 1960 to 2100. The blue line represents a case with constant solar activity. Red/Pink lines represent the case with a strong decline of the solar activity for weak/strong strength scenarios of SSI evolution (see [9] for the experiments description). Adapted from [10].

The influence of the meridional circulation strength was analyzed in the publications (e. g., Zubov et al. [3] Fig. 1c). It was shown that more intensive upward ozone transport in the tropical stratosphere leads to strong ozone depletion between the tropopause and 30 hPa layers in the latitudinal band 30°S — 30°N. This effect cannot explain the observed ozone depletion in much wider latitudinal belt shown by [7].

Possible decline of the solar activity (e. g., Anet et al. [9]) and consequent decrease of the oxygen photolysis. Figure 2 (right panel) shows that this effect may lead to substantial delay or even full cancellation of the TOC recovery in the future. However, in this case the vertical structure of the ozone depletion with maximum effects in the middle stratosphere around 10 hPa ([11], Fig. 8) does not coincide with the observations and cannot help to explain them.

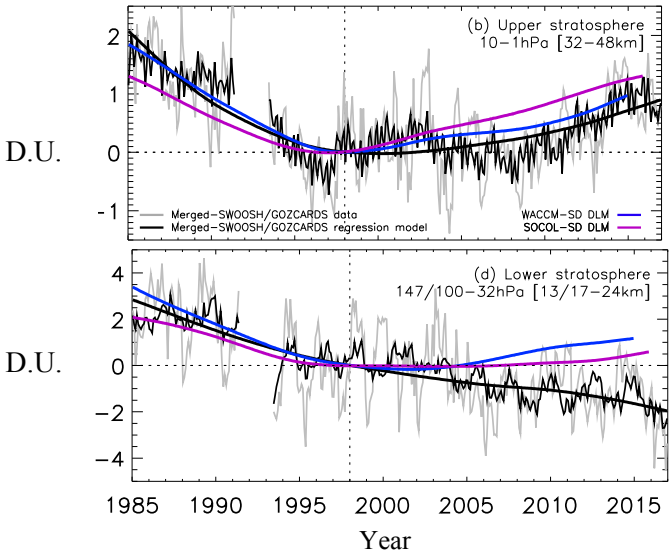

FIGURE 3. Near-global (60°S — 60°N) partial column ozone anomalies (D.U.) relative to 1998 mean. Deseasonalised and regression model time series are given for the Merged-SWOOSH/GOZCARDS composite (grey and black, respectively) for upper (upper panel) and lower (lower panel) stratosphere. The non-linear trend is shown by the smoothly varying thick black line. The results for WACCM-SD (blue) and SOCOL-SD (purple) models are also shown. Adapted from [7].

The effects of halogen containing VSLS was studied by [12]. They demonstrated that the absence of VSLS in models can lead to about 2—6% ozone depletion in the latitude band 60°S — 60°N mostly due to ozone loss in the upper troposphere/lower stratosphere (see their Fig. 2). The vertical structure of the ozone depletion by VSLS mimics the observed. However, the magnitude of VSLS effects is increasing in the poleward direction, which does not fully agree with observed features (see [7], Fig. 1). The disagreement of the latitudinal structure also characterizes the general effects of long-lived new or unaccounted by MPA hODS, which tend to maximize over the cold high-latitude polar lower stratosphere or in the upper stratosphere. For example, the TOC decrease caused by CH_2Cl_2 emissions is only about 1 D.U. in the tropical area, while in the polar atmosphere it can reach 14 D.U. in 2050 (see [13], Fig. 4). The situation can be changed if

aerosol loading is high, because the heterogeneous reactions are able to facilitate more intensive ozone destruction by additional hODS. However, during the analyzed period (1998—2015) available observations show only small positive trend caused by increasing volcanic activity or anthropogenic activity [14].

Conclusions. The understanding and prediction of the ozone layer evolution are very challenging, because the ozone evolution is driven by multitude of physical/chemical and dynamical processes and their interactions. The ozone depletion during the second half of 20th century caused by hODS has been stopped by MPA in the upper stratosphere and over the high southern latitudes. However, the observation shows that the ozone depletion in the lower stratosphere started in 1980's continues until now partially compensating the ozone recovery in the middle and upper stratosphere. The presence of some positive trend in the tropospheric TOC makes it difficult to clearly see total column ozone recovery. The negative ozone trend in the lower stratosphere is not simulated by most of the state-of-the-art chemistry-climate model, therefore, several listed in the text or new causes of this phenomenon should be carefully investigated in the nearest future. Considering potential danger for the complete total ozone recovery some new limitation on the ODS production should be considered by science community and policymakers.

Acknowledgments: This review paper was prepared with the financial support of the Russian Science Foundation grant № 17-17-01060.

1. G. P. Brasseur and S. Solomon, *Aeronomy of the Middle Atmosphere: Chemistry and Physics of the Stratosphere and Mesosphere*, 3rd ed., Springer, 2005, 644 p.

2. J. Seinfeld and S. Pandis, *Atmospheric Chemistry and Physics: From Air Pollution to Climate Change*, 2nd edition, J. Wiley, 2006, 1203 p.

3. V. Zubov, E. Rozanov, T. Egorova et al., Role of external factors in the evolution of the ozone layer and stratospheric circulation in 21st century, *Atmos. Chem. Phys.*, 2013, 13, pp. 4697—4706, doi:10.5194/acp-13-4697-2013.

4. WMO, Scientific Assessment of Ozone Depletion: 2002, World Meteorological Organization Global Ozone Research and Monitoring Project, 2003, Report No. 47.

5. J. C. Farman, B. G. Gardiner, and J. D. Schaklin, Large losses of the total ozone in Antarctica reveal seasonal ClOx/NOx interaction, *Nature*, 1985, 315, pp. 207—210.

6. WMO, World Meteorological Organization: Scientific assessment of ozone depletion: 2010, Global Ozone Research and Monitoring Project, Geneva, Switzerland, 2011, Report No. 52.

7. W. T. Ball, J. Alsin, D. J. Mortlock et al., Evidence for a continuous decline in lower stratospheric ozone offsetting ozone layer recovery, *Atmos. Chem. Phys.*, 2018, 18, pp. 1379—1394, doi: 10.5194/acp-18-1379-2018.

8. T. Egorova, E. Rozanov, J. Gröbner et al., Montreal Protocol benefits simulated with CCM SOCOL, *Atmos. Chem. Phys.*, 2013, 13, pp. 3811—3823.

9. J. Anet, E. V. Rozanov, S. Muthers et al., Impact of a potential 21st century "grand solar minimum" on surface temperatures and stratospheric ozone, *Geophys. Res. Lett.*, 2013, 40, pp. 4420—4425, doi:10.1002/grl.50806.

10. E. Rozanov, K. Tourpali, H. Schmidt, and B. Funke, Long-term variations of solar activity and their impacts: From the Maunder Minimum to the 21st century, *Sparc newsletter*, 2016, 46, pp. 15—20.

11. P. Arsenovic, E. Rozanov, J. Anet et al., Implications of potential future grand solar minimum for ozone layer and climate, *Atmos. Chem. Phys. Discuss.*, 2017, doi: 10.5194/acp-2017-818.

12. R. Hossaini, M. Chipperfield, S. Montzka et al., Efficiency of short-lived halogens at influencing climate through depletion of stratospheric ozone, *Nature Geosci.*, 2015, 8, pp. 186—190, doi:10.1038/ngeo2363.

13. R. Hossaini, M. Chipperfield, S. Montzka et al., The increasing threat to stratospheric ozone from dichloromethane, *Nature Communications*, 2017, 8, doi: 10.1038/ncomms.

14. S. Kremser, L. W. Thomason, M. Von Hobe et al., Stratospheric aerosol: Observations, processes, and impact on climate, *Rev. Geophys.*, 2016, 54, pp. 278—335.

3d Numerical Simulations of Ionized and Neutral Atmospheric Chemical Composition up To 90 km from the Ground With Global Photochemical Model Charm-I

Alexei A. Krivolutsky, Lidiya A. Cherepanova, Tatyana Yu. Vyushkova, and Alexander I. Repnev

Laboratory for Atmospheric Chemistry and Dynamics, Roshydromet, Central Aerological Observatory, Pervomayskata Str. 3, Dolgoprudny, 141700, Russia

It is well-known [1] that middle atmosphere (10—100 km) isunder strong control of solar UV radiation and also under energetic particles control inside Polar Regions. So that, the ozonosphere and lower ionosphere (D-region, 50—90 km) are very sensitive to these radiation. As we know there are two different ways exist to study chemical ionized and neutral composition at these altitudes now: satellite observations and numerical model using. We present here the results of model simulations obtained with new three-dimentional global photochemical numerical model developed at the Laboratory for Atmospheric Chemistry and Dynamics of Central Aerological Observatory [2]. This model CHARM-I (Chemical Atmospheric Research Model with Ions) permits to reproduce global ozone and other neutral speciesjointly with electron density and positive and negative ions. Short description of the model and some results of simulations are presented in this paper.

Short model description. This model was described in paper [2], but presented version has some additional ionized negative compounds.

List of neutral compounds looks like as follow:

“Families members”

Ox = O_3 + O(^{3}P) + O(^{1}D);

$NOy = N + NO + NO_2 + NO_3 + 2N_2O_5 + HNO_3 + HO_2NO_2 + ClNO_3 + N(^2D)$;
$HOx = H + OH + HO_2 + 2H_2O_2$;
$Cly = Cl + ClO + ClOO + OClO + ClNO_3$,

"Other species"

CH_3O_2, CH_3O_2H, CH_3O, CHO, CO, $O_2(^1\Delta_g)$.

"Gas-sources"

CH_4, CO_2, N_2O, CF_2Cl_2, $CFCl_3$, H_2, Cl_4, Cl_2, CH_3Cl, CH_2Cl, O_2, H_2O.

Corresponding list of ionized compounds looks like as follow:

"Positive ions"

$O_2^+ O_2^+(H_2O) H_3^+OH_3^+O\ (H_2O)H_3^+O\ (H_2O)_3H_3^+O$
$(H_2O)_4\ H_3^+O\ (H_2O)_2NO^+N_2\ NO^+CO_2NO^+(H_2O)$
$NO^+(H_2O)_2NO^+(H_2O)_3N^+$ $N2^+$

"Negative ions and electrons"

$[e]O_2^-\ O_3^-O_4^-CO_4^-\ O^-\ OH^-HCO_3^-\ NO_3^-\ NO_2^-$

Joint number of photochemical reaction including the reaction of ionization in the model equals 242. Ionization of NOis initiated by short UV (L-α). Corresponding well-known formula for its calculations is:

$$q_{Ly-\alpha}(z) = \sigma_{NO}^{i} n(NO) I_{\infty}(Ly-\alpha) \exp\left[-\sigma^{a}(O_2)\int_{z}^{\infty} n(O_2)dzCh(z,\chi)\right],$$

Ionization of $O_2(^1\Delta_g)$ in range 102,7—111,8 nm is calculated by the following way:

$$q(z)=n(O_2(^1\Delta_g))\{0{,}549\cdot10^{-9}\exp(-2{,}406\cdot10^{-20}N(O_2)+2{,}614\cdot10^{-9}* \\ *\exp(-8{,}508\cdot10^{-20}N(O_2))\}(sm^{-3}s^{-1})$$

where:

$$N(O_2) = \int_{z}^{\infty} n(O_2)dzCh(z,\chi).$$

Ionization by Galactic Cosmic Rays is also is took into account (parameterization is used).

Dissociation rates by UV are recalculated after each hour of integration in the model. The greed looks like as follow: vertical — 2 km; latitude — 5°; longitude — 10°. Time-step of integration is in range: 100—500 sec. To describe the global transport of chemical species Prather's scheme was used [3]. Global 3D of wind components and temperature fields has been calculated with Middle Atmosphere GCM ARM [4].

We present the results below, which illustrate global distribution of ozone (as the exampleof neutral species), electron density and vertical structure of several ions. We will show also the response of lower ionosphere to solar eleven-year forcing in UV radiation.

Results of simulations. Figure 1 shows global monthly mean distribution of ozone mixing ratio (ppm v) simulated with CHARM-I. This result is in god correspondence with observations and with simulations with other models (but

without ions) [1]. So that, we can conclude that model reproduce neutral species well. It should be mentioned that CHARM-I is the development of the model CHARM, which is does not include ion chemistry.

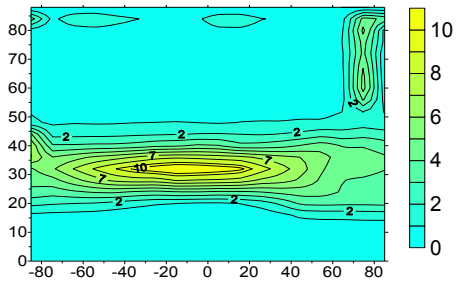

FIGURE 1. Global distribution of ozone mixing ratio (simulation with CHARM-I)

Figure 2 illustrates global distribution of electron concentration at 80 km in summer (00-00 UT).

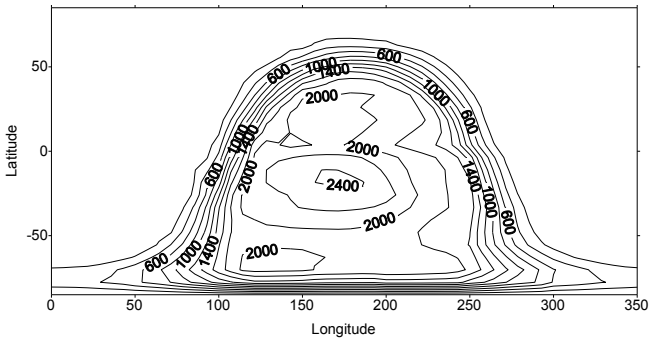

FIGURE 2. Global distribution of electron concentrations at 80 km in summer (00-00 UT) (simulation with CHARM-I)

Figure 3 shows the distribution (concentration) of one positive ions — O_2^+ simulated with CHAM-I.

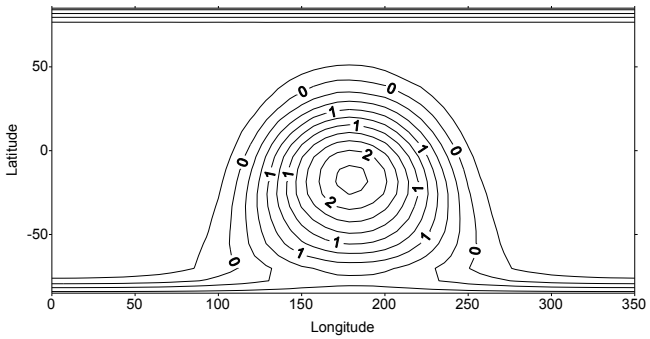

FIGURE 3. The distribution (concentration) of one of the positive ions — O_2^+.

Figures 4, 5 show selected vertical profiles ofpositiveand negative ions at middle latitudes (afternoon) simulated with CHAM-I. It should be mentioned that presented profiles of ions are in a good correspondence with rocket measurements [1].

1st March (noon)

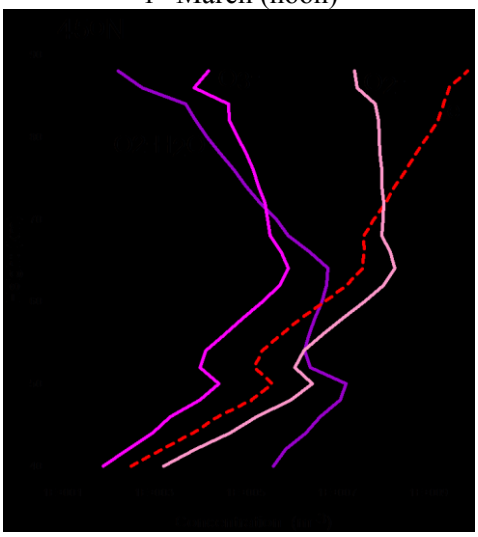

FIGURE 4. Selected vertical profiles ofpositive ions at middle latitudes (afternoon) simulated with CHAM-I. (simulation with CHARM-I).

1st March (noon)

FIGURE 5. Selected vertical profiles ofpositive ions at middle latitudes (afternoon) simulated with CHAM-I. (simulation with CHARMR-I).

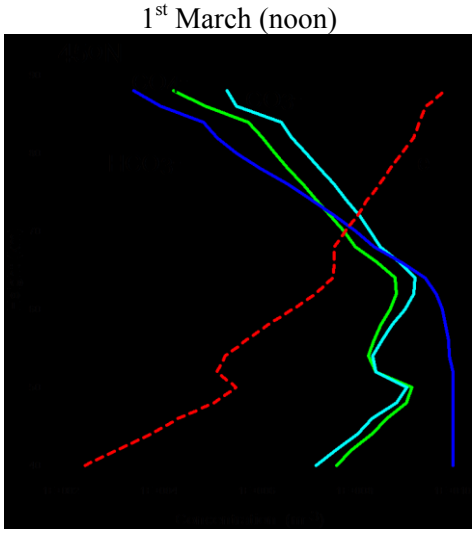

FIGURE 6. Selected vertical profiles of negative ions and electrons at middle latitudes (afternoon) simulated with CHAMR-I.

Figure 7 illustrates changes (%) at 80 km in electron density causedby UV variations during 23rd cycle of solar activity (minima minus maxima). Satellite observations realizedby SIM instrument (Solar Irradiance Monitor) was used for simulations with CHARM-I (summer). One can see that the area of effect is localized inside afternoon region and equals about 30% with minus (we moved from minima 2009 to maxima 2003 of solar cycle).

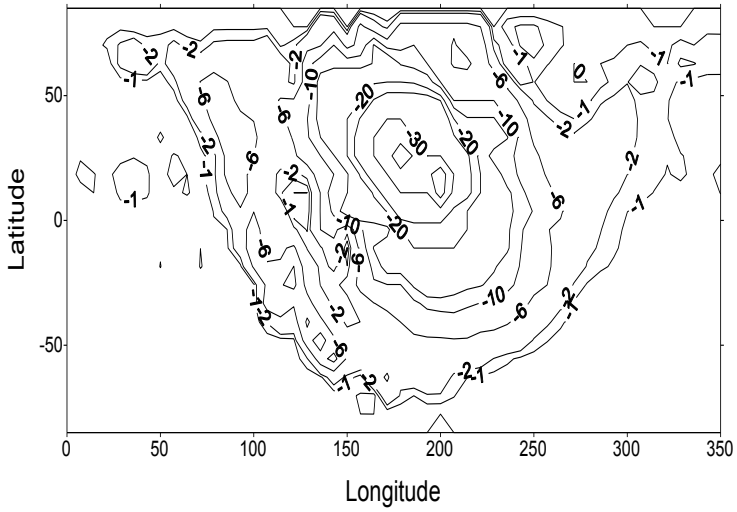

FIGURE 7. Changes (%) at 80 km in electron density causedby UV variations during 23rd cycle of solar activity (minima minus maxima) simulated by CHARM-I.

Concluding remarks. So that, we can conclude that presented results based on a new global photochemical numericalmodel CHARM-I, which describesthe interaction between neutral and ionized chemical compounds in middle atmosphere including D-region of the lower ionosphere, suggest the opportunity to have a new look on a problem ofbetter understand D-region behavior. It seems that this model is a perspective instrument for solving different important problems of radio wave propagation in this area of ionosphere.

1. G. Brasseur and S. Solomon. Aeronomy and Physics of the Middle Atmosphere, Springer, 2005, 644 p.

2. A. A. Krivolutsky, L. A. Cherepanova., T. Yu. Vyushkova., A. I. Repnev, The Three-Dimensional Numerical Model CHARM-I: The Incorporation of Processes in the Ionospheric D-region, *Geomagnetism and Aeronomy*, 2015, 55(4), pp. 468—487.

3. A. A. Krivolutsky, L. A Cherepanova et al., Global circulationof the Earth's atmosphere at altitudes from 0 to 135 km simulated with ARM model. Consideration of the solar activity contribution. *Geomagnetism and Aeronomy*, 2015, 55(6) , pp. 468—487.

4. A. A. Krivolutsky, T. Yu.Vyushkova et al., The Three-Dimensional Photochemical Model CHARM. Incorporation of Solar Activity, *Geomagnetism and Aeronomy*, 2015, 55(1), pp. 59—88.

5. M. Prather, Numerical advection by conservation of second-order moments, *J. Geophys. Res*., 1986, 91, pp. 6671—6681.

Laboratory Experiments in Atmospheric Chemistry

Igor I. Morozov[1], Evgenii S. Vasiliev[1], Grigorii V. Karpov[1], Alexey G. Syromyatnikov[2], and Nadezhda I. Butkovskaya[1]

[1]Semenov Institute of Chemical Physics RAS, Moscow, 119991, Russia
[2]Department of Physics, Moscow State University, Moscow, 119991, Russia

Introduction. The report will cover the processes occurring in the gas phase, the water and on the surface of sea salts. Three different experimental techniques are used to study these processes. Reactions in water, gases and aerosols, involving hydroxyl radicals are playing an important role by defining air quality in the atmosphere. Processes of hydration of ions halogenated organic acids in solution are one of the fundamental problems of hydrochemistry. Multiple processes taking place in the water involving ions and ion clusters are controlled by them.

Oxidation of halogenated hydrocarbons in the troposphere leads to generation of a number of secondary pollutants, including halogenated acids. Halogenated carboxylic acids are widely distributed in the environment. Some of the products of atmospheric degradation of chlorofluorocarbons (CFC), such as trifluoroacetic acid

(TFA), difluoroacetic acid (DFA), and monofluoroacetic acid (MFA) are extremely toxic substances. Formation of these acids presents an environmental threat, since all classes of CFC replacements, even hydrofluorocarbons, can generate them. Formation of hazardous substances from relatively safe precursors proceeds via a rather complicated scheme including processes in both gas and aqueous phase, as well as heterogeneous processes involving aerosols.

Ion hydration is an important stage of liquid-phase reactions. It determines the ion mobility, thus affecting reaction rates. Consequently, both non-hydrated ions and ions with a hydrate shell must be taken into account in the consideration of the processes of ion diffusion and migration. In particular, hydration should be taken into account in the study of the reactions in aerosols, which play an important role in atmospheric chemistry. The circulation of non-organic bromine in the marine boundary layer is of interest [1]. Bromides present in sea water are emitted into the atmosphere from the ocean surface as sea salt aerosols. It has been suggested that cluster processes with participation of bromine ions play a certain role in the destruction of the atmospheric ozone [2]. At present, however, such processes have not been well-studied.

A mass-spectrographic method electrospraying electrolyte solutions in vacuum (ESESV) was used to determine the enthalpy of hydration of bromine ions by different numbers of water molecules. The mass-spectra of negative ions from aqueous solutions of NaBr were measured over the temperature range of 15—50 C and showed that the most intense peaks correspond to the hydrated bromine ions with one and two water molecules. It was found that the Van't Hoff equation holds for bromine hydrates containing up to three water molecules, whereas addition of the fourth water molecule leads to a violation of the Van't Hoff equation. The enthalpy of bromine ion hydration by the first and the second water molecules was found to be –(28.5 ± 1.7) and –(21 ± 4.2) kJ mol-1, respectively.

In the present work we examine the hydrated bromine ions contained in aqueous solutions of NaBr. In aqueous solutions of bromine salts the processes of hydration and dehydration of the negative bromine ions take place:

$$Br^-(H_2O)_n + H_2O \leftrightarrow Br^-(H_2O)_{(n+1)}, \quad n=0, 1, 2, ..$$

According to the Van't Hoff principle [10], under equilibrium conditions the logarithm of the ratio of $Br^-(H_2O)_n$ to $Br^-(H_2O)_{n+1}$ ion concentrations is a linear function of the reciprocal temperature of the solution. In the mass-spectrographic method of electrospraying electrolyte solutions in vacuum used in our experiments, the ion concentrations in the solution are represented by the intensities of the corresponding mass-spectral peaks, and the Van't Hoff equation can be written as follows:

$$Ln(I_n/I_{(n+1)}) = Const + (\Delta H_{n,(n+1)}/RT), \quad (1)$$

where I_n and $I_{(n+1)}$ are the intensities of the mass-spectral peaks corresponding to $Br^-(H_2O)_n$ and $Br^-(H_2O)_{n+1}$ ions, respectively; n is the number of water molecules in

the hydrate shell; R is the universal gas constant, and T is the solution temperature. The enthalpy of attachment of one more water molecule to the $Br^-(H_2O)_n$ ion, $\Delta H_{n,(n+1)}$, can be determined from Equation (1).

Experimental methods. A flow reactor connected to a molecular beam mass spectrometer was used in the study of gas and heterogeneous processes. Two methods were used to study the processes in water: laser flash photolysis and evaporation of solution into a vacuum chamber of a mass spectrograph.

Let's consider here in more detail the mass-spectrographic method of electrospraying electrolyte solutions in vacuum.

This method was used in the present work. The essence of the method is that the electrolyte solution under analysis is continuously carried into the high-vacuum chamber of a mass-spectrograph through a capillary. A high voltage of several kilovolts is applied to the capillary. At a certain rate of the electrolyte flow, electrospraying of the solution occurs on the exit tip of the capillary, which leads to the emission of ions from the solution into the gas-phase. The charge sign of the emitted ions is of the same sign as that of the high voltage, hence, the ESESV method can be used for the analysis of both positive and negative ions. The emitted ions pass through an energy filter, giving a monoenergetic ion beam, which then passes through a magnetic field, producing a mass-spectrum. As electrospraying is a pulse process, the mass-spectra is recorded by accumulation of the ion signal on a photo-plate or photographic film.

The hydration enthalpy was determined for each isotope using two abovementioned methods of data processing. Accordingly, for each temperature we obtained four ΔH values, which averaging gave the following results:

$$Br^- + H_2O \leftrightarrow Br^-(H_2O) \qquad \Delta H_{0,1} = (-28.5 \pm 1.7) \text{ kJ mol}^{-1}$$

$$Br^-(H_2O) + H_2O \leftrightarrow Br^-(H_2O)_2 \qquad \Delta H_{1,2} = (-21.0 \pm 4.2) \text{ kJ mol}^{-1}$$

$$Br^-(H_2O)_2 + H_2O \leftrightarrow Br^-(H_2O)_3 \qquad \Delta H_{2,3} = (-7.5 \pm 3.3) \text{ kJ mol}^{-1}$$

The values obtained differ significantly from the enthalpies for gas-phase clustering measured by Hiraoka et al. Sremaniak et al. used the enthalpy data from Hiraoka et al. to find the parameters for the MD computer simulation on $Br^-(H_2O)_n$ clusters. The simulation showed that the Br^- ion is located on the surface of the water clusters. This result confirmed the conclusion of their previous work [5], that Br^- ions are not solvated in small water clusters, but instead are attached to the water cluster. This conclusion was based on a good agreement between the E_{stab} calculated by MD methods and experimental E_{stab} from the molecular jet study of Markovich et al. Since our results for n =1–3 correspond to the hydration in bulk solution, it can be supposed that the cumulative enthalpies, $-\Delta H_n$ (28.5, 49.5, 57.0 kJ mol^{-1}), for this process are approximately one half of the enthalpies for gas-phase formation of $Br^-(H_2O)_n$ clusters (49, 97.6, 145.3 kJ mol^{-1}) as obtained by Hiraoka et al.

fig. 1a

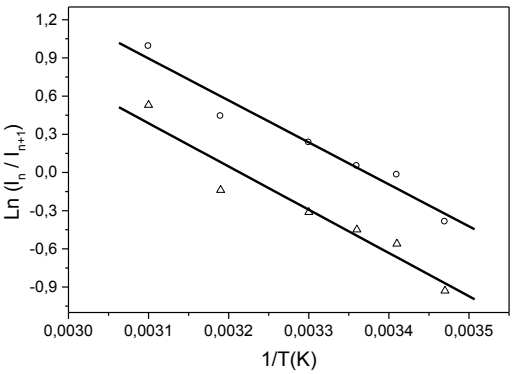

FIGURE 1. Temperature dependences for hydration of bromine ions in water.

Uptake of ClO radicals. The uptake of ClO radicals on KBr, NaCl and NaBr dry solid films was studied at 1 Torr pressure of helium over the temperature range 290—350 K using a flow tube technique with a modulated molecular beam mass spectrometer as the detection method. A Pyrex tube with the deposited salt sample was introduced into the flow reactor along its axis. The ClO uptake coefficient on KBr surface did not depend on temperature within the experimental accuracy of ~ 20 %. Chlorine oxide radicals were prepared using reaction of Cl with ozone. It was found out that the ClO uptake coefficient strongly depended on ozone concentration. The uptake coefficient at T = 293 K and $[O_3] = 4.6 \times 10^{13}$ molecule cm^{-3} were found to be: $(9.6 \pm 5.7) \times 10^{-4}$, $(3.7 \pm 1.5) \times 10^{-4}$ and $(12.3 \pm 3.6) \times 10^{-4}$ for KBr, NaCl and NaBr, respectively. Bromine containing species were not observed during the interaction of ClO radicals with KBr film. The results obtained indicate that the ClO loss through heterogeneous interaction with salt surface is not sufficiently rapid to compete with gas-phase self-reaction in the atmosphere.

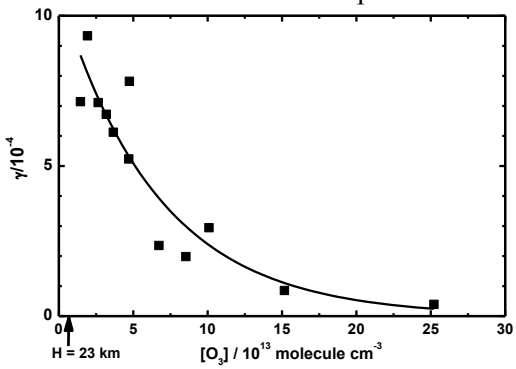

FIGURE 2. Uptake coefficient of ClO radicals vs ozone concentration**.**

The measurements of the ClO uptake coefficient, γ, on KBr, NaCl and NaBr salt surfaces, simulating atmospheric aerosols containing components of ocean water, were carried out. At room temperature, similar γ values were obtanined for KBr and NaBr, whereas somewhat lower value was found for NaCl surface. Mass spectral analysis of the products of the heterogeneous interaction of ClO with KBr film did not reveal formation of bromine-containing gaseous products. The main observed products of the surface reaction were of HCl and HOCl that can be explained by the presence of surface adsorbed water and its participation in the heterogeneous process. The measurements of the uptake coefficient of ClO on the surface of KBr salt over the 323—353 K temperature range did not show a noticeable temperature dependence. However, a significant dependence of γ on ozone concentration was observed.

The report will also be discussed in detail on the reactions in the gas phase and in the aquatic environment.

The work was supported by the grant 16-05-00432 of the Russian Foundation for Basic Research, Department of Chemistry of the RAS and the state task for ICP RAS 0082-2014-0012, № АААА-А17-117040310008-5.

1. G.V. Karpov, O. A.Vinogradova, E. S. Vasilev et al., *Chimicheskaya Bezopastnost*, 2017, 1(2), 192 p. (in Russian)

2. I. I. Morozov, E. S. Vasilev, G. V. Karpov, Elementarnye chimicheskie procesi atmosphernoy chimii, Trudi 21 Vserossiiskoy skoli-konferencii molodich uchenich «Sostav atmospheri. Atmosphernoe electrichestvo. Klimaticheskie procesi», Borok, 2017, pp. 6—7. (in Russian)

3. G. V. Karpov, E. S. Vasiliev, I. I. Morozov et al., *Int. J. Chem. Kin.*, 2016, 48(8), pp. 442—448.

4. N. E. Strokova, S. V. Savilov, I. I. Morozov, T. V. Yagodovskaya, V. V. Lunin, *J. Phys. Chem*., 2015, 89, 1, 33.

5. I. I. Morozov, E. S. Vasiliev, V. D. Knyazev, G. V. Karpov, *J. Phys. Chem*., A, 2014, 4013.

6. G. V. Karpov, I. I. Morozov, E. S. Vasiliev et al., *Chem. Phys. Lett.*, 2013, 586, pp. 40—43.

7. E. S. Vasiliev, E. E. Loukhovitskaya, I. I. Morozov et. al., *J. Phys. Chem*. A, 2012, 116, pp. 6107−6112.

8. E. S. Vasiliev, V. D. Knyazev, E. S. Savelieva, I. I. Morozov, *Chem. Phys. Lett*., 2011, 45.

9. E. S. Vasiliev, V. D. Knyazev, I. I. Morozov, Chem. *Phys. Lett.*, 2011, 512, 172.

10. E. Loukhovitskaya, Yu. Bedjanian, I. Morozov, G. Le Bras, *Phys. Chem. Chem.Phys*., 2009, 11, 7896 p.

Influence of Relief and Oceans on the Global Electric Circuit

Valery V. Denisenko[1,2], Michael J. Rycroft[3,4], and R. Giles Harrison[5]

[1]Institute of Computational Modelling, Federal Research Center "Krasnoyarsk Science Center", Siberian Branch of the Russian Academy of Sciences, 660036 Krasnoyarsk, Russia
[2]Siberian Federal University, 660041 Krasnoyarsk, Russia
[3]CAESAR Consultancy, Cambridge CB3 9HW, UK
[4]Centre for Space, Atmospheric and Oceanic Science, University of Bath, Bath BA2 7AY, UK
[5]Department of Meteorology, University of Reading, Earley Gate, Reading RG6 6BB, UK

Introduction. Modern views on the Global Electric Circuit are described, for example, in reviews [1, 2]. The generator in the Circuit is the set of all thunderstorms and showerclouds occurring on the Earth. Storm clouds are mainly discharged with lightning, carrying charges to the land and onto other clouds, but there also exists a current flowing into the upper atmosphere and further up into the ionosphere.

The total current into the ionosphere is on average a thousand amperes or more. This generator creates a potential difference of about 300 kV between two good conductors: the ionosphere and the ground. Since the atmosphere is also a conductor, though a relatively poor one, charges return through it from the ionosphere to the ground. This vertical current of about 2 pA/m^2 density is referred to as the fair-weather current. It is associated with a vertical electric field, whose strength under fair-weather conditions is about 130 V/m near the ground.

The purpose of the model developed is to take into account the relief of the Earth's surface and the increase of conductivity above the sea surface.

The electric conductivity equation. The basic equations for the steady state electric field $\mathbf{E}$ and current density $\mathbf{j}$ are Faraday's law, the charge conservation law, and Ohm's law. The electric potential V can be introduced so that $\mathbf{E} = -grad\, V$. Then the system of the equations is reduced to the electric conductivity equation

$$-div\left(\hat{\sigma}\, grad\ V\right) = 0. \tag{1}$$

The lower boundary of the atmosphere is the Earth's surface. We use spherical geodetic coordinates r, ϑ, φ, and height above mean sea level h. We use the data base [3], that gives height $h_g(\vartheta, \varphi)$ above the mean sea level at the grid in geodetic coordinates ϑ, φ with a step-size of 0.1^o. The mean sea level is the surface $r = R_s(\vartheta, \varphi)$ with function $R_s(\vartheta, \varphi)$ defined in the World Geodetic System WGS 84 [4]. Our model of the topography is presented in details in [5].

Since the conductivity of air near the surface is much larger than the conductivity of ground or salt water, the Earth is usually regarded as an ideal conductor, i.e. there is a constant value of the electric potential at the Earth's surface

$$V(\vartheta, \varphi)\ \Big|_{h_g(\vartheta, \varphi)} = -V_0, \tag{2}$$

where the value of the constant V_0 is defined by a balance between distant disturbed weather thunderstorm generators which drive current into the ionosphere and downward fair weather currents.

Separation of ionospheric and atmospheric conductors. Since the ionospheric conductivity is many orders of magnitude larger than that of the atmosphere, the ionosphere can be approximately simulated as an ideal conductor at large heights $h > h_I$. Test calculations show that $h_I > 80$ km is enough to make only a very small influence on atmospheric electric fields. Then the boundary condition takes the form

$$V(\vartheta, \varphi)\ \Big|_{h=h_I} = 0. \tag{3}$$

It completes the Dirichlet boundary value problem (1—3) for the atmosphere, simulated as a conductor between two ideal conductors. Such a problem has a unique solution when the constant V_0 is given.

1-D model of the atmospheric conductor. The models of large scale electric fields and currents between ground and ionosphere [6, 7] show that more than 99% of the voltage is presented below 50 km, and that the currents are almost vertical there, we consider the currents in the atmosphere to be vertical. The the atmospheric electric fields are then vertical, too, because the conductivity is scalar there. Accordingly we use the flat 1-D approximation of the 3-D equation (1) and shift the boundary condition (3) from height $h_I > 80\,\text{km}$ to $h_0 = 50\,\text{km}$. The the boundary value problem (1—3) then takes the form

$$-\frac{d}{dh}\left(\sigma(h)\frac{d}{dh}V(h)\right)=0,\quad V(\vartheta,\varphi)\;\big|_{h=h_0}=0,\quad V(\vartheta,\varphi)\;\big|_{h=h_g(\vartheta,\varphi)}=-V_0\,. \qquad (4)$$

The solution $V(h)$ of the problem (4) must have indexes ϑ,φ since the input values depend on coordinates. We omit the indices ϑ,φ for brevity. The solution gives the strength of the vertical electric field $E(h)=-dV(h)/dh$ and the current density $j=-\sigma(h)\,E(h)$. By virtue of equation (4), the current density j does not vary with height, and hence j is a function only of the coordinates ϑ,φ. The last property allows us to reduce the solution of the problem (4) to the integration over height:

$$-V_0 = j(\vartheta,\varphi)\int_{h_g(\vartheta,\varphi)}^{h_0}\frac{dh}{\sigma(h)}\,. \qquad (5)$$

This integral is the resistance of the atmospheric vertical column with unit area ($1\ \text{m}^2$) cross-section between the ground and the ionosphere

$$\rho(\vartheta,\varphi) = j(\vartheta,\varphi)\int_{h_g(\vartheta,\varphi)}^{h_0}\frac{dh}{\sigma(h)}\,.$$

The inverse value is the conductance of the same atmospheric vertical column $\Sigma(\vartheta,\varphi)=1/\rho(\vartheta,\varphi)$.

Height distribution of conductivity in the atmosphere. Thin lines in Fig. 1a show the height distributions of the conductivity $\sigma(h)$, proposed for fair weather above ground by empirical models [8, 9, 10]. The real values of σ can be several times different from the model ones [9]. Since we do not have strong arguments in favor of any one of these models, here we use the averaged distribution shown by the bold line in the same figure. It is constructed in such a way that it does not contradict the three models and satisfies two conditions $\sigma(0)=1.54\cdot10^{-14}$ S/m, $\rho(0)=1.25\cdot10^{17}\,\Omega\cdot\text{m}^2$. The first condition ensures, under fair weather, a vertical

current density $j_0 = 2\,\text{pA/m}^2$ when the vertical electric field strength equals $E_0 = 130\,\text{V/m}$. The second condition, by virtue of (5), provides a potential difference between ground and the ionosphere of $V_0 = 250\,\text{kV}$ for the same E_0. The given values of E_0, j_0, V_0 are considered to be typical for the global electrical circuit [1].

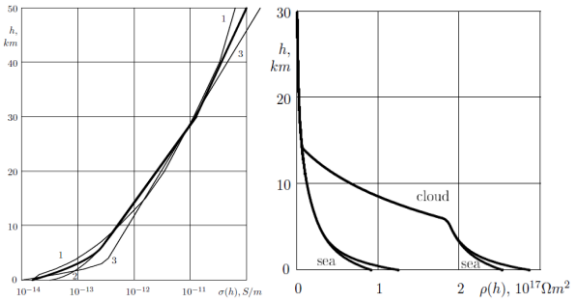

FIGURE 1. a — models of the height distributions of the conductivity for fair weather above the ground. Thin lines: 1 — [8], 2 — [9], 3 — [10]. Bold line — our model that is designed as some average. b — Resistance of the atmospheric vertical column with 1 m^2 cross-section between the ionosphere and ground that is at a height h above the sea level. The curves "cloud" represent the cases when the conductivity at heights $h = 5-15$ km is decreased. The curves "sea" show the resistances above sea with and without clouds.

Global distribution of conductivity in the atmosphere. In our model, $\rho(\vartheta, \varphi)$ is determined by two factors. Firstly, of them is the height of the Earth's surface $h_g(\vartheta, \varphi)$ gives the lower limit of integration in (5). The resistance ρ decreases with increasing altitude of the ground surface, shown as a function of the height above the surface, $h = h_g(\vartheta, \varphi)$, in Fig. 1b. It corresponds to Fig. 6 in [1]. We can see that the atmosphere above 30 km does not contribute.

Secondly, the reason for $\rho(\vartheta, \varphi)$ variations is the increased conductivity in the lower atmosphere above the sea. According to [10], the conductivity above the sea surface is twice that above the continental surface, until this difference disappears at an altitude of 2—4 km. Since the surface layer, in which the conductivity rapidly increases with altitude, in our model, as well as in the models [8, 9] is substantially smoother than model [10], we make the difference between ground and sea equal to zero above 6 km, while it is negligible above 4 km.

One more modification is due to the decrease of conductivity inside clouds. In accordance with model [8], due to cloudiness, the conductivity decreases by a factor of 5—10 at altitudes of 5—15 km. So the total resistance from the ground at sea level to the ionosphere increases by a factor about two as the curves "cloud" in Fig. 1b show. The curves "sea" show the resistances above sea with and without clouds. We do not include clouds in the model in this paper.

The total current through the atmosphere can be obtained by integrating over the sphere. Due to the linearity of the problem (4) with respect to V_0, the total current I is proportional to V_0. The resistance R of the atmosphere as a whole is defined by the relation $-V_0 = RI$. It can be calculated as

$$\frac{1}{R} = R_E^2 \int \Sigma(\vartheta, \varphi) \sin(\vartheta)\, d\vartheta\, d\varphi .$$

This gives $R = 180\,\Omega$, comparable with $R = 190\,\Omega$ to $R = 300\,\Omega$ found in other models [11]. Many factors like volcanos and radon production above the ground are analyzed in those models. Our model is not so sophisticated. These modelled R values depend on the cloud abundance and properties. If clouds are everywhere $R = 496\,\Omega$, or, when absolutely absent, $R = 175\,\Omega$. So clouds could vary the total resistance of the atmosphere by a factor of about 2.8. If the Earth is an oceanless sphere $R = 245\,\Omega$ corresponding to the fair weather value $\rho(0) = 1.25 \cdot 10^{17}\,\Omega \cdot \mathrm{m}^2$ for our model of conductivity. If the surface of the Earth were at the sea level, $h_g(\vartheta, \varphi) = 0$ everywhere and no clouds exist, these formulae would give $R = 195\,\Omega$ instead of $R = 175\,\Omega$. The average value of Σ is about $1.1 \cdot 10^{-17}\,\mathrm{S/m}^2$ and Σ is increased above mountains. Similar features are also described in [11,12].

Conclusions. Thus, the relief reduces the total resistance of the atmosphere by about 11%. The local resistance of a vertical column of the atmosphere over high mountain ranges is reduced much more, up to 7.5 times over the mountains with 6 km height. The increased conductivity above the oceans decreases the total resistance of the atmosphere by about one third. Cloud absence or abundance modifies the resistance of the atmosphere by a factor of 3.

The research is supported by Russian Foundation for Basic Research (project 18-05-00195).

1. M. J. Rycroft, R. G. Harrison, K. A. Nicoll, E. A. Mareev, An overview of Earth's global electric circuit and atmospheric conductivity, *Space Sci. Rev.,* 2008, 137, 83—105. DOI: 10.1007/s11214-008-9368-6.

2. E. A. Mareev, Achievements and prospects of the global electric circuit, *Phys. Usp.*, 2010, 53. 504—534. DOI: 10.3367/UFNr.0180.201005h.0527.

3. GLOBE Task Team and others (D. A. Hastings, P. K. Dunbar, et al.), eds., 1999. The Global Land One-kilometer Base Elevation (GLOBE) Digital Elevation Model, Version 1.0. National Oceanic and Atmospheric Administration, National Geophysical Data Center, 325 Broadway, Boulder, Colorado 80305-3328, U.S.A. Digital data base on the World Wide Web (URL: http://www.ngdc.noaa.gov/mgg/topo/globe.html) and CD-ROMs.

4. World Geodetic System 1984 (WGS 84). http://earth-info.nga.mil/GandG/wgs84/

5. V. V. Denisenko, O. E. Yakubailik, The income of topography to the resistance of the global atmospheric conductor, *Solar-Terrestrial Physics,* 2015, 1(1), 104—108. DOI: 10.12737/6044.

6. V. V. Denisenko, Electric current penetration from a thunderstorm cloud into the ionosphere at the geomagnetic equator. Editors: V. N. Troyan et al. *Proceedings of the 10-th International Conference "Problems of Geocosmos"*. St. Petersburg. 2014. pp. 82—87.

7. V. V. Denisenko, Electric current penetration from a thunderstorm cloud into the middle-latitude ionosphere. Editors: V. N. Troyan et al. *Proceedings of the 10-th International Conference "Problems of Geocosmos"*. St. Petersburg. 2014. pp. 76—81.

8. M. J. Rycroft, A. Odzimek, Effects of lightning and sprites on the ionospheric potential, and threshold effects on sprite initiation, obtained using an analog model of the global atmospheric electric circuit, *J. Geophys. Res.,* 2010, 115, A00E37, DOI: 10.1029/2009JA014758.

9. *Handbook of Geophysics*. The Macmillan Company, New York. 1960.

10. O. Molchanov, M. Hayakawa, *Seismo-electromagnetics and related phenomena: History and latest results,* TERRAPUB, Tokyo, 2008. 190 p.

11. B. A. Tinsley, L. Zhou, Initial results of a global circuit model with variable stratospheric and tropospheric aerosols, *J. Geophys. Res.,* 2006, 111, D16205, DOI: 10.1029/2005JD006988.

12. M. J. Rycroft, S. Israelsson, C. Price, The global atmospheric electric circuit, solar activity and climate change, *J. Atmos. Sol. Terr. Phys.,* 2000, 62, 1563—1576, DOI: 10.1016/S1364-6826(00)00112-7.

Flux Enhancements of >30 keV Electrons Beneath the Radiation Belt: a Statistical Study for 1998—2016

Alla Suvorova[1,3], Alex Dmitriev[2,3]

[1]GPS Science and Application Research Center, National Central University, Jhongli, Taiwan
[2]Institute of Space Science, National Central University, Jhongli, Taiwan
[3]Skobeltsyn Institute of Nuclear Physics, Lomonosov Moscow State University, Moscow, Russia

Introduction. In the region beneath the inner radiation belt (RB) at drift shells L<1.2, in a so-called forbidden zone, particle flux intensity has long been considered as stably tenuous because of RB losses in atmospheric collisions in the vicinity of the South Atlantic anomaly (SAA). Figure 1a shows a global map with weak fluxes of >30 keV electrons in the forbidden zone obtained from measurements on board the NOAA/POES satellites at orbital height of ~850 km. In 2012, the concept of stable forbidden zone had changed when strong enhancements of >30 keV electron fluxes were found in the region [1] (see Fig. 1, b—d). The flux enhancements are peculiar to locally trapped electrons in the low/medium energy range from 10 to 300 keV and vary between 10^4 and 10^7 el/(cm^2 s sr) [2]. These electrons can form transient (unstable) population [3]. Later, the study [4] found

flux enhancements of 100s keV electrons in the inner RB at L~1.2. The authors [5] experimentally proved that the enhanced "forbidden" energetic electrons (FEE) originate from the inner RB.

The studies [1, 2, 5—7] convincingly showed that the energetic electrons ionize the upper atmospheric gas at low latitudes during FEE enhancement events. The study [3] proposed that the FEE phenomenon may play important role in such process as radio signal distortion in the low-latitudinal ionosphere and surface charging of LEO spacecrafts. A mechanism of transport of RB electrons to the forbidden zone is still puzzling, and a study of the FEE occurrence is required.

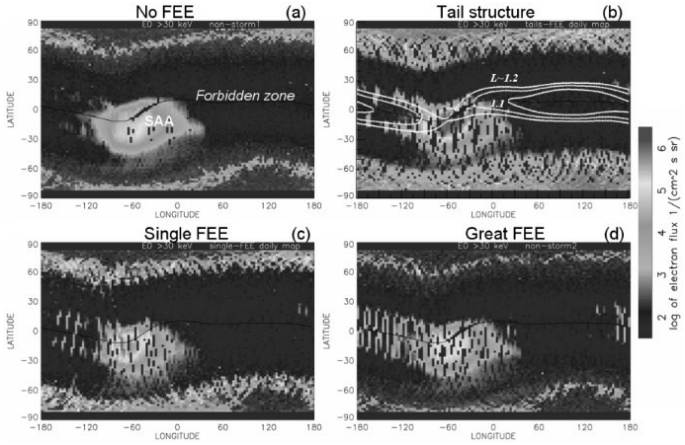

FIGURE 1. Patterns of daily global maps of distributions of >30 keV electrons with: (a) very weak fluxes in the forbidden zone, (b) tails-like FEE enhancements, (c) single-FEE, (d) great-FEE. White lines show drift shells L=1.1, 1.15 and 1.2 in IGRF-2005 model.

Data. We specify statistical characteristics of the >30 keV FEE enhancements using data collected from the NOAA/POES satellites during the last 2 solar cycles, from 1998 to 2016. Near the equator, the locally trapped electrons were measured by the detector that pointed to the Zenith. The threshold for flux enhancements was established at 10^3 (cm^2 s sr)$^{-1}$ (see details in [8]). We considered 1750 daily maps with enhancements and distinguish three different patterns shown in Fig. 1(b—d).

The tails-FEE daily map has enhancements only at low latitudes (Fig. 1b). The single-FEE map contains enhancements at the equator during one satellite pass (Fig. 1c). The great-FEE is observed during consequent equatorial passes of one satellite or different satellites (Fig. 1d). A great enhancement can also has 1—2 equatorial passes but of extremely high intensity of >10^5 (cm^2 s sr)$^{-1}$. We have selected 213 great-FEE, 317 single-FEE, and 1220 tails-FEE daily maps. The great FEE enhancements are of particular interest because of the prominent ionizing effect.

Results. We analyzed yearly, monthly, and diurnal variations of FEE enhancements. Figure 2 shows variations of occurrence of single/great-FEE

enhancements. In Fig. 2(a, b), we determined numbers of daily maps with the FEE enhancements in each year and month. In Fig. 2a, the FEE variations for both solar cycles show similar patterns: the FEE occurrence rate anticorrelates with solar cycle. In Fig. 2b, monthly variation of great-FEE occurrence rate shows the presence of two maxima and two minima. Major peak extends from May to September and minor peak is observed in December and January. Equal minima are observed in February-April and October-November. Thus, the FEE annual variation is opposite to a seasonal variation of geomagnetic activity with equinoctial maxima [9].

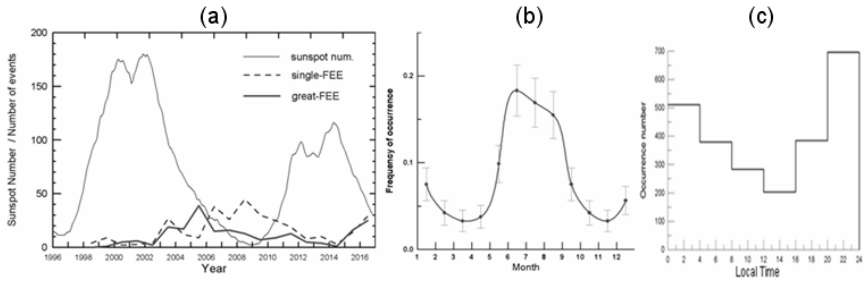

FIGURE 2. Occurrence rate of FEE enhancements: (a) solar-cycle variation single and great FEE days from 1998 to 2016, (b) annual variation for great-FEE days, (c) diurnal variation for single/great FEE fluxes.

The diurnal variation was analysed on the basis of time profiles of single/great FEE enhancements detected by each POES satellite along its orbital passes crossing the dip equator (see details in [8]). The threshold for flux enhancements was established at 10^4 $(cm^2\ s\ sr)^{-1}$. The SAA region at longitudes from -110° to 0° was excluded from analysis. We have collected 2465 equatorial passes with duration of ~20 min and extend within ±30° latitudinal interval. The vast majority of the enhanced fluxes occurred in the Western Hemisphere, over the eastern Pacific. Figure 2c presents local time distributions for the 2465 passes with enhanced fluxes. The FEE occurrence rate peaks around the local midnight (20—4 LT). The night peak is fully consistent with a scenario of particle injections from the magnetotail to the inner magnetosphere during substorms. In studies [1, 5], a fast radial transport of particles in the E cross B fields was suggested as a most probable mechanism for deeper injections of electrons into the forbidden zone after strong substorms.

Discussion. The FEE enhancements occur frequently during magnetospheric disturbances [2, 3]. Hence, the statistical characteristics of enhancements of >30 keV electrons at L<1.2 can relate to the solar wind drivers and intrinsic parameters of the ionosphere-magnetosphere system. The characteristics and efficiency of the solar wind drivers change with solar cycle [10]. Therefore, it is quite expected, that the yearly variation of the FEE occurrence results from solar

cycle changes of the solar wind conditions affecting the substorms and geomagnetic activity. But an additional analysis is required for the unusual FEE monthly variation. Figure 3 (a—c) presents distributions of the solar wind and geomagnetic conditions for the great FEE days and total statistics from the OMNI database. More than 85% of the FEE events occurred under fast solar wind (V>450 km/s), high substorm activity (AL> 150 nT), and enhanced interplanetary electric field perturbations ($V\delta B$>1.5 mV/m). The annual variations of these parameters are shown in Fig. 3(d—f). It seems, only the monthly variation of V shows up some features similar to those of FEE (Fig. 2b).

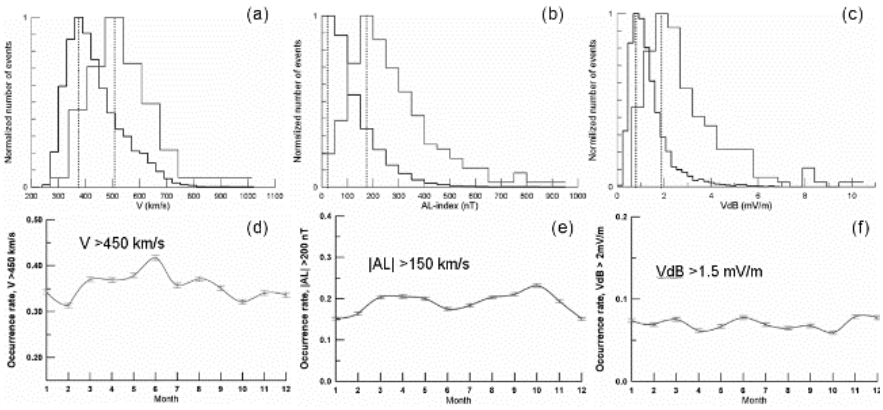

FIGURE 3. (Top) Normalized statistical distributions of (a) the solar wind speed V, (b) AL index, and (c) interplanetary electric field fluctuation VdB during the whole period 1998—2016 and during the great-FEE days. Daily averages are used. (Bottom) Annual variations of occurrence rate of (d) V>450 km/s, (e) |AL|>150 nT, and (f) VdB>1.5 mV/m.

We assume that intrinsic parameters, such as the auroral ionosphere conductance, which depends on the solar illumination [11], could be responsible for the annual variation of FEE occurrence. At local noon, the solar flux intensity I changes as the sine of colatitude θ (Fig. 4a). The cumulative solar flux in solid angle $\partial\Omega$ is determined as $f(\theta)=I\sin\theta\partial\Omega$, where $\theta=|\Psi|+18$, Ψ is a dipole tilt angle and average angular size of the auroral oval is ~18°, then we obtain:

$$f(\theta) = I\sin^2\theta\partial\theta\partial\varphi \;\propto\; \sin^2(|\Psi|+18). \qquad (1)$$

The cumulative flux maximized at noon and varied with UT. We suppose that the FEE injection occurs at 0 LT at the longitude of 105°E (Fig. 4e). Calculation by (1) for 17 UT presented in Fig. 4c. We assume that both the dipole tilt and fast solar wind control the FEE annual variation. The resultant variation ($V\cdot f$) is very similar to the FEE monthly variation both in shape and in amplitude (Fig. 4d). Thus, the assumption about drivers and conditions for FEE occurrence are reasonable.

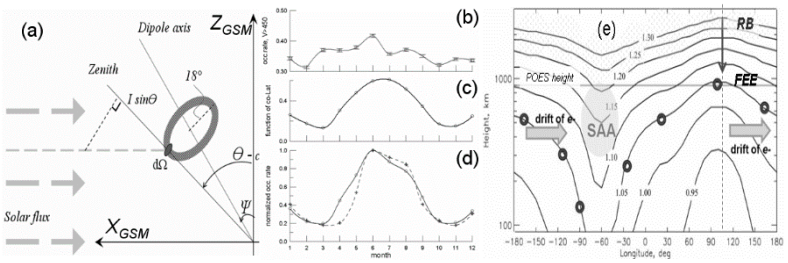

FIGURE 4. (a) Solar illumination I of auroral ionosphere under sunlit. Annual variations of occurrences of (b) V>450 km/s, (c) f= $\sin^2(|\Psi|+18)$, (d) the great-FEE days (dashed curve) and convolution function $V{\cdot}f$ (solid curve). (e) Drift L-shells at the geomag. equator.

Acknowledgments. *The work was supported by grant MOST 105-2811-M-008-048 and partially MOST 106-2811-M-008-050 to National Central University.*

1. A. V. Suvorova, L.-C. Tsai, and A. V. Dmitriev, On relation between mid-latitude ionospheric ionization and quasi-trapped energetic electrons during 15 December 2006 magnetic storm, *Planet. Space Sci.*, 2012, 60(1), pp. 363—369, doi:10.1016/j.pss.2011.11.001.

2. A. V. Suvorova, A. V. Dmitriev, L.-C. Tsai, et al., TEC evidence for near-equatorial energy deposition by 30 keV electrons in the topside ionosphere, *J. Geophys. Res.*, 2013, 118, pp. 4672—4695, doi:10.1002/jgra.50439.

3. A. V. Suvorova and A. V. Dmitriev, Radiation aspects of geomagnetic storm impact below the radiation belt, *In Cyclonic and geomagnetic storms: Predicting factors, formation and environmental impacts*, ed. V. Banks, NOVA Sci.Pub., Inc., NY, 2015, pp. 19—75.

4. H. Zhao and X. Li, Modeling energetic electron penetration into the slot region and inner radiation belt, *J. Geophys. Res.*, 2013, 118, pp. 6936—6945.

5. A. V. Suvorova, C.-M. Huang, H. Matsumoto, et al. Low-latitude ionospheric effects of energetic electrons during a recurrent magnetic storm, *J. Geophys. Res.*, 2014, 119.

6. A. V. Suvorova, C.-M. Huang, A. V. Dmitriev, et al., Effects of ionizing energetic electrons and plasma transport in the ionosphere during the initial phase of the December 2006 magnetic storm, *J. Geophys Res.*, 2016, 121, pp. 5880—5896.

7. A. V. Dmitriev, A. V. Suvorova, M. V. Klimenko, et al., Predictable and unpredictable ionospheric disturbances during St. Patrick's Day magnetic storms of 2013 and 2015 and on 8—9 March 2008, *J. Geophys. Res.*, 2016, 122, pp. 2398—2432.

8. A. V. Suvorova, Flux enhancements of >30 keV electrons at low drift shells L<1.2 during last solar cycles, *J. Geophys. Res.*, 2017, 122, doi:10.1002/2017JA024556.

9. C. T. Russell and R. L. McPherron, Semiannual variation of geomagnetic activity, *J. Geophys. Res.*, 1973, 78(1), pp. 92—10.

10. A. V. Dmitriev, A. V. Suvorova, and I. S. Veselovsky, Statistical Characteristics of the Heliospheric Plasma and Magnetic Field at the Earth's Orbit during Four Solar Cycles 20—23, *In Handbook on solar wind: Effects, dynamics and interactions*, Ed. H. Johannson, NOVA Science Publishers, Inc., New York, 2009, pp. 81—144.

11. W. Lyatsky, P. T. Newell, and A. Hamza, Solar illumination as cause of the equinoctial preference for geomagnetic activity, *Geophys. Res. Lett.*, 2001, 28(12).

Joint Use the Upper and Lower Atmosphere Models for Reproduction the Response to 2009 Sudden Stratospheric Warming Event

Maxim V. Klimenko[1,2], Fedor S. Bessarab[1,2], Timofey V. Sukhodolov[1,3,4], Dmitry V. Kulyamin[1,5], Vladimir V. Klimenko[1], Yuriy N. Korenkov[1], Irina E. Zakharenkova[1], Nicolay V. Chirik[1,2], Pavel A. Vasiliev[1,2], Hauke Schmidt[6], Bernd Funke[7], and Eugene V. Rozanov[1,3,4]

[1]West Department of Pushkov Institute of Terrestrial Magnetism, Ionosphere and Radio Wave Propagation Russian Academy of Sciences, 236017, Kaliningrad, Russia
[2]Immanuel Kant Baltic Federal University, 236016, Kaliningrad, Russia
[3]Physikalisch-Meteorologisches Observatorium, World Radiation Center, Davos, Switzerland
[4]Institute for Atmospheric and Climate Science, ETH Zurich, Zurich, Switzerland
[5]Institute of Numerical Mathematics Russian Academy of Sciences, Moscow, Russia
[6]Max Planck Institute for Meteorology, Hamburg, Germany
[7]Instituto de Astrofısica de Andalucia, CSIC, Granada, Spain

Introduction. In spite of the recent progress in model developments the disagreement exists between model simulation and observations of the upper atmosphere response to Sudden Stratospheric Warming (SSW) events due to some spatial and temporal model limitations and the absence of fully non-linear interaction between stationary planetary waves, atmospheric tides, and gravity waves [1]. As example, the morning-noon 2009 SSW increase in the electron density at low latitudes, that have been recently discussed in observational studies [2] are absent or much smaller in model results [3—5]. The thermospheric/ ionospheric dynamics is not completely reproduced in the model studies due to the lack of understanding of the correct source of disturbances at mesospheric altitudes during SSW event and/or some model simplifications.

For the current study we performed upper atmosphere model runs using the middle atmosphere model output to specify perturbations in neutral parameters at the mesopause in order to reproduce the global thermospheric and ionospheric disturbances during 2009 SSW event. To test the simulation results we used neutral temperature observed by MIPAS instrument, electron content from GPS TEC and *foF*2 provided by radio occultation measurements. To detect the response of the upper atmosphere to stratospheric warming, we used the deviations of the selected parameters from their monthly and zonal mean values.

Statement of the problem. For the upper atmosphere modeling we used the first principles Global Self-Consistent Model of the Thermosphere, Ionosphere and Protonosphere (GSM TIP) [6] that was developed in WD IZMIRAN (Kaliningrad, Russia). This model calculates time-dependent global three-dimensional distributions of temperature, composition and velocity vector of neutral gas; the density, temperature, and velocity vectors of atomic and molecular ions and electrons; and two-dimensional distribution of electric potential, both of

ionospheric and magnetospheric origin. The GSM TIP model has been used to study the global thermsopheric and ionospheric response to 2009 January SSW event [5, 7].

For the calculation of the state and variability of the lower and middle atmosphere, we used the HAMMONIA model (Hamburg Model of the Neutral and Ionized Atmosphere). This model belongs to the class of general circulation and chemistry models and is intended for calculating interactions between circulation, radiation and chemistry to represent the state and variability of the atmosphere. A detailed description of the model can be found in [8]. HAMMONIA was applied to analyze the effects of sudden stratospheric warmings on the downward transport of thermospheric nitrogen oxides [9] and the state of the ionosphere [1]. As another low and middle atmosphere model we used INM RAS general circulation model that is a well-developed free-running version [10] of atmospheric unit of INMCM climate models [11]. This version of INM RAS atmospheric model calculated the atmospheric dynamics (horizontal and vertical winds), temperature and water distributions for Earth surface to mesospheric upper boundary (at the altitude around 90 km) and takes into account all key physical process in middle atmosphere (include new versions of gravity wave drag parameterizations, new radiative processes calculation, etc.).

To simulate the January 2009 sudden stratospheric warming event we use the HAMMONIA model with assimilation of the observed meteorological fields. The INM model was used in free running mode. The global distribution of the neutral temperature, wind velocities and neutral density at an altitude of 80 km, obtained in the both lower atmosphere models, were used as the lower boundary conditions in the GSM TIP model for calculating the upper atmosphere state. These data were adopted by GSM TIP every 1 hour after proper space and time interpolation. The calculations were carried out for the period from 1 to 31 January 2009, which includes sudden stratospheric warming around 23—26 January.

Results. Comparison of Tn deviations from the monthly mean over the northern polar cap (70—90° N) in the altitude range 0—80 km in January 2009 obtained from the MIPAS observations and the HAMMONIA and INM model results (Fig. 1) showed a good qualitative agreement.

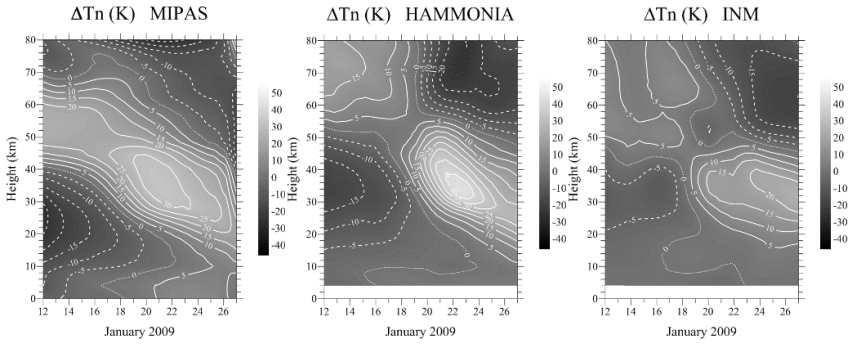

FIGURE 1. Deviations of the neutral temperature from the average values on January 12—27, 2009 according to the MIPAS observations (left), the assimilated HAMMONIA model results (in the middle) and INM free model-run results (right).

The model/data results indicate that in January 2009 there was a stratospheric warming in the northern polar cap, accompanied by a mesospheric cooling. According to observations, Tn in the stratosphere increases up to 30 K on January 21, while the HAMMONIA model produce 40 K warming by January 23, and INM model — 20 K by January 27. Note that MIPAS observations covered only a small zonal sector (20°W — 70°E and 160°E — 110°W).

Fig. 2 shows the absolute deviations of Tn from the January mean value in the altitude region of 80—170 km over the high latitudes. Observation data show a large area (80—100 km) of a significant cooling, a slight warming at altitudes between 100 and 140 km and some cooling above 140 km on January 20—22.

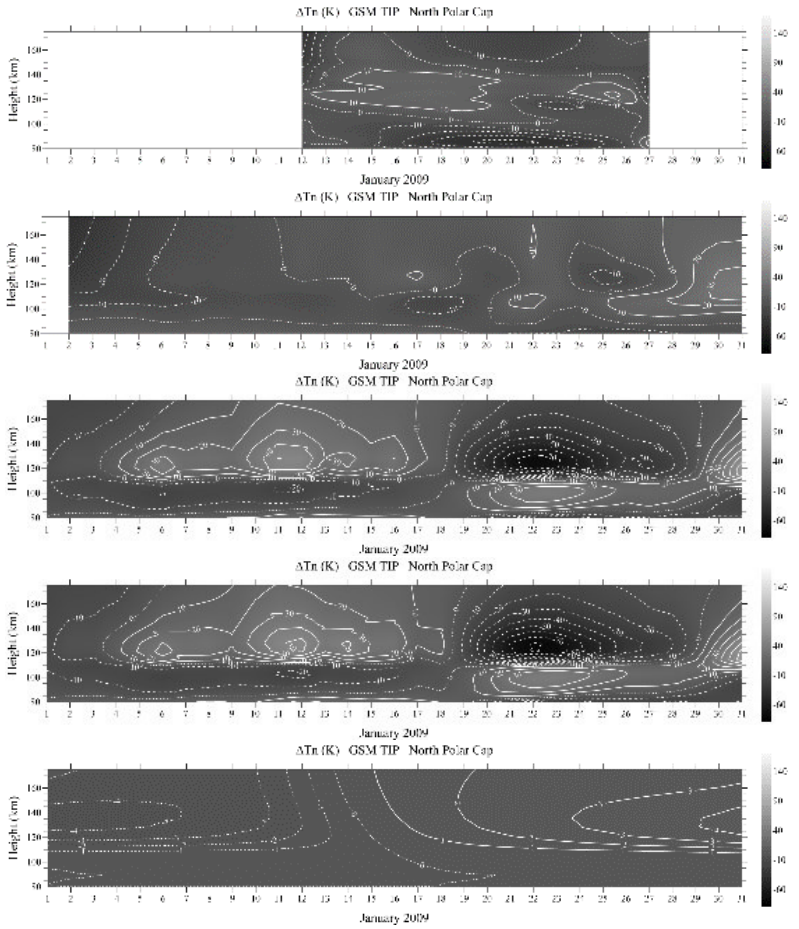

FIGURE 2. Day-to-day variation of vertical profiles of daily zonal mean neutral temperature disturbances obtained using: (a) MIPAS observation data; (b—e) GSM TIP model results. GSM TIP model results were obtained using lower boundary conditions from the INM model (b) and from the HAMMONIA model (c—e): (c) and (d) with and without taking into account the changes in the Solar zenith angle; (e) without taking into account day-to-day changes in the GSM TIP lower boundary conditions.

In the lower thermosphere, the perturbations of neutral temperature have a quasi-wave character with a wavelength of about 40 km in height. The GSM TIP results driven by the INM boundary conditions are in qualitative agreement with the observation. The results of the GSM TIP driven by the HAMMONIA do not agree so well with MIPAS data. So, we conclude that free running INM model allows better simulating thermospheric response to SSW. We performed calculations with the GSM TIP with and without the change in the day number and day-to-day variations at the lower boundary.

It can be seen that the change in the solar zenith angle does not have a noticeable effect on the thermospheric temperature, and all temperature perturbations are associated with a change at the lower boundary.

Fig. 3 shows the evolution of the absolute deviations of the latitudinal profiles of the mean daily average values of *foF*2 and TEC from their monthly averages in January 2009, obtained from GSM TIP (for the same variants as in Fig. 2) and from observations. In general, the transition from negative perturbations of *foF*2 and TEC to positive in the northern hemisphere and, conversely, from positive perturbations to negative in the Southern Hemisphere is common to the model/data results.

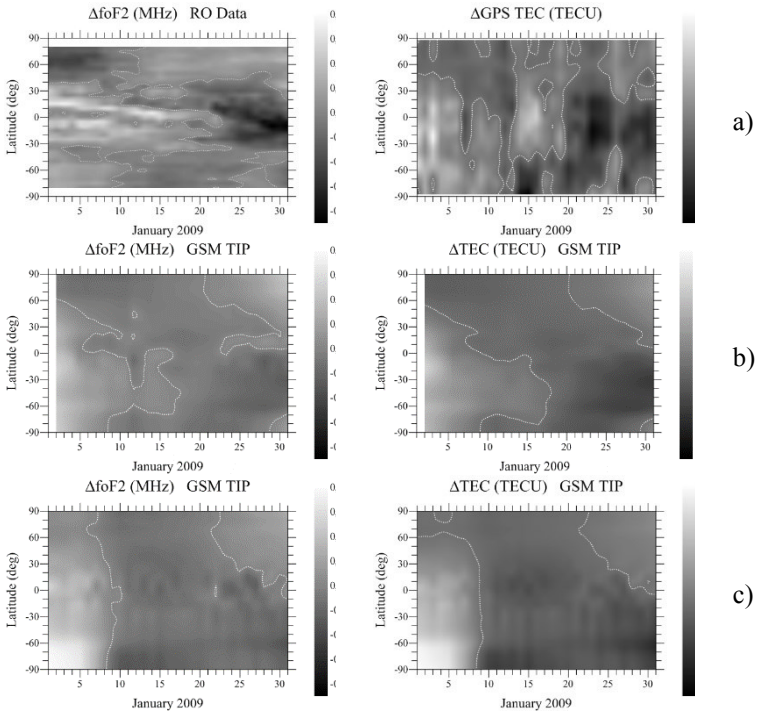

FIGURE 3. Absolute deviations of daily zonal mean *foF*2 (left) and TEC (right) from their monthly averages values in January 2009, obtained: (a) in RO and GPS observations; (b—e) GSM TIP model results. The panels (b—e) are presented by the same way as in Fig. 2 (End of figure see on p. 54).

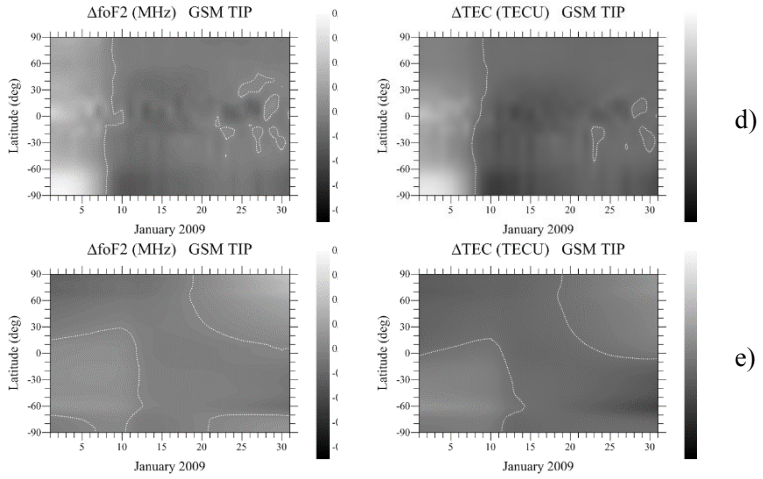

FIGURE 3. Beginning of the figure see on p. 53.

The bottom panel of Fig. 3 shows the time evolution of these ionospheric parameters caused by the seasonal variation in solar zenith angle. So, the general structure of perturbations of *foF*2 and TEC is associated with seasonal variations. However, there are also deviations from seasonal changes that are associated with changes at the lower boundary, and presumably may be caused by stratospheric warming. It is important to note that the *foF*2 and TEC perturbations obtained with the GSM TIP using the lower boundary from the INM are in better agreement with the observations. It can be assumed that in the free running INM model the necessary tidal structures are generated at the mesospheric heights, which produce correct perturbations of the ionospheric parameters. During the passage of stratospheric warming, these deviations of *foF*2 and TEC are formed at the mid latitudes of the northern hemisphere and especially near the equator and are predominantly negative, which agrees with earlier estimates. Positive perturbation of *foF*2 according to observation data reaches its maximum near the equator, and according to the results of model calculations are shifted to the southern hemisphere.

This investigation was performed with the financial support from the Russian Science Foundation grant № 17-17-01060.

1. N. Pedatella, T.-W. Fang, H. Jin et al., Multimodel comparison of the ionosphere variability during the 2009 sudden stratosphere warming, *J. Geophys. Res.*, 2016, 121, pp. 7204—7225.

2. J. L. Chau, L. P. Goncharenko, B. G. Fejer, and H. L. Liu, Equatorial and low latitude ionospheric effects during sudden stratospheric warming events, *Space Sci. Rev.*, 2012, doi: 10.1007/s11214-011-9797-5.

3. L. P. Goncharenko, J. L. Chau, H.-L. Liu, and A. J. Coster, Unexpected connections between the stratosphere and ionosphere, *Geophys. Res. Lett.*, 2010, 37, L10101, doi:10.1029/2010GL043125.

4. H. Jin, Y. Miyoshi, D. Pancheva et al., Response of migrating tides to the stratospheric sudden warming in 2009 and their effects on the ionosphere studied by a whole atmosphere-ionosphere model GAIA with COSMIC and TIMED/SABER observations, *J. Geophys. Res.*, 2012, 117, A10323, doi:10.1029/2012JA017650.

5. M. V. Klimenko, V. V. Klimenko, F. S. Bessarab et al., Study of the thermospheric and ionospheric response to the 2009 sudden stratospheric warming using TIME-GCM and GSM TIP models — first results, *J. Geophys. Res.*, 2015, 120, pp. 7873—7888, doi:10.1002/2014JA020861.

6. A. A. Namgaladze, Yu. N. Korenkov, V. V. Klimenko et al., Global model of the thermosphere-ionosphere-protonosphere system, *PAGEOPH,* 1988, 127(2/3), pp. 219—254.

7. F. S. Bessarab, Yu. N. Korenkov, M. V. Klimenko et al., Modeling the effect of Sudden Stratospheric Warming within the thermosphere-ionosphere system, *J. Atmos. Solar-Terr. Phys.*, 2012, 90—91, pp. 77—85, doi:10.1016/j.jastp.2012.09.005.

8. H. Schmidt, G. P. Brasseur, M. Charron et al., The HAMMONIA chemistry climate model: Sensitivity of the mesopause region to the 11-year solar cycle and CO2 doubling, *J. Climate*, 2006, 19, pp. 3903—3931.

9. K. Meraner and H. Schmidt, Transport of Nitrogen Oxides through the winter mesopause in HAMMONIA. *J. Geophys. Res.*, 2016, 121, pp. 2556—2570.

10. D. V. Kulyamin and V. P. Dymnikov, The atmospheric general circulation model with a hybrid vertical coordinate, *Russian J. Numerical Analysis and Mathematical Modelling*, 2014, 29(6), pp. 355—373.

11. E. M. Volodin, E. V. Mortikov, S. V. Kostrykin et al., Simulation of the present-day climate with the climate model INMCM5, *Climate Dynamics*, 2017, 49, pp. 3715—3734, doi:10.1007/s00382-017-3539-7.

Ionospheric Effects of Sudden Stratospheric Warmings and Geomagnetic Storms Observed with the Signals of Geostationary Navigational Satellites

Ekaterina A. Kozlovtseva[1], Grigoriy A. Kurbatov[1], Artem M. Padokhin[1], and Anna S. Yasyukevich[2]

[1]Department of Atmospheric Physics, Faculty of Physics, Lomonosov Moscow State University, 119991, Moscow, Russia
[2]Institute of Solar–Terrestrial Physics SB RAS, 664033, Irkutsk, Russia

In the Earth's ionosphere, complex physical processes occur that cause a strong variability in the parameters of the ionospheric plasma at various spatial and temporal scales. Most of the ionospheric variability can be explained by such powerful and well-studied mechanisms as solar ionizing radiation and geomagnetic

activity. Nevertheless, a significant part of the ionospheric variability can be associated with processes in the lower atmosphere (strong meteorological storms, tropical cyclones and hurricanes, sudden stratospheric warming), which in some cases is comparable to the variability caused by geomagnetic factors. Thus, the study of interrelations and interactions in the troposphere — stratosphere — mesosphere — thermosphere — ionosphere is of great importance for predicting the state of the ionospheric plasma and understanding the physics of the processes taking place in it.

Among the meteorological factors affecting the ionosphere, a special role is played by sudden stratospheric warming (SSW), which is the strongest phenomena in the high latitude stratosphere, predominantly in the northern hemisphere, occurring quite regularly in the winter season, which allows to study the influence of the processes taking place in middle atmosphere on ionosphere. Large number of studies of the ionospheric effects of SSWs have been carried out recently using various sounding methods (ionosondes, ISRs, GNSS sounding), which made it possible to reveal the main features of the SSW influence on the ionosphere. Nevertheless, each such event is unique, which necessitates the continuation of research, both in terms of accumulating experimental data, and in developing methods for diagnosing ionospheric disturbances caused by the SSW.

With the development of GNSS (Global Navigational Satellite Systems) and SBAS (Satellite Based augmentation systems) constellations, the coherent multi-frequency L band transmissions are now available from a number of geostationary satellites. These signals can be used for ionospheric total electron content TEC estimations in the same way as widely used GPS/GLONASS signals. At the same time, geostationary satellites have the advantage of a fixed ionospheric pierce points, in comparison with the moving pierce points for GPS / GLONASS, which allows continuous TEC monitoring along a given direction in the ionosphere. In connection with it, geostationary satellites of COMPASS/Beidou system play the most important role, as they provide the best TEC noise pattern among all current geostationary GNSS and SBAS satellites [1].

The purpose of this work is to use the signals of geostationary COMPASS / BeiDou satellites to study the day-to-day variability of TEC in themidlatitude and equatorial ionosphere under calm and disturbed heliogeophysical conditions, especially during recent geomagnetic storms and SSWs [2].

To study the TEC variability during the strong (G3) geomagnetic storm of May 28, 2017, the data of three receivers of the IGS-MGEX network were used: the mid-latitude JFNG station of the Northern Hemisphere, the near-equatorial KARR station of the Southern Hemisphere and the SIN1 equatorial station. Geostationary Compass-G3 satellite signals were used to estimate TEC. The geometry of the experiment is shown in Fig. 1a. The data for the period May 22 — June 5, 2017 were analyzed. Geomagnetic indices Kp and Dst are superimposed in Fig. 1b—d. It can be seen that on May 28 (the 148th day) during the storm main phase, the Kp index reached values of 7 at 03-06UT, while the Dst index reached –122nT. Figs. 1b—d show the variability of the relative slant TEC for each of the

stations under consideration in the coordinates (DOY, UT) in the form of 2D maps. During the storm main phase, a positive anomaly is observed in TEC data from all three stations, and its intensity decreases towards the geomagnetic equator. In this case, the observed anomaly of TEC in the southern hemisphere is almost twice as high as in the northern hemisphere and reaches ~ 30TECU. Thus, we observe an asymmetry in the ionospheric response to the geomagnetic storm in the northern and southern hemispheres, caused by a complex combination of processes responsible for the occurrence of positive and negative ionospheric disturbances.

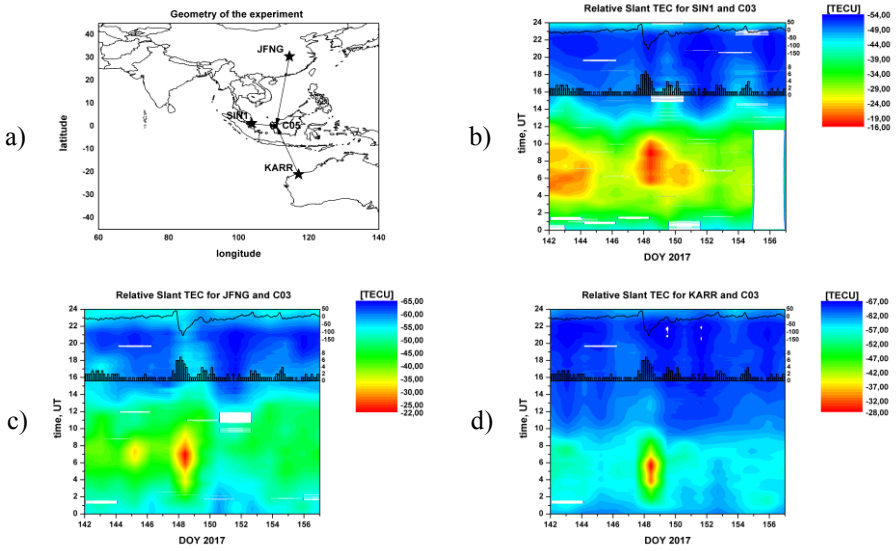

FIGURE 1. The geometry of the experiment (a) and the variations of the relative slant TEC during the strong (G3) geomagnetic storm on May 28, 2017, according to the data of the geostationaryBeiDou-G3 satellite and receivers SIN1 (b), JFNG (c), KARR (d), geomagnetic indices Kp and Dst.

We also present TEC variations in equatorial and midlatitude ionosphere during minor and major final SSW of February and March, 2016 (see Fig. 2). For this study we also used data from three receivers of the IGS-MGEX network: mid-latitude KZN2 and DYNG stations and the SIN1 equatorial station. First two stations used signals of geostationary Compass-G5 satellite for TEC estimation, the last one used signals of Compass-G3 satellite.

The geometry of the experiment is presented in Fig. 2a. For each station, the interval from January 1 to March 3, 2016 was considered. TEC variations for each station together with the stratospheric (10 mbar level) temperature at the North Pole and mean zonal windat 60Nare presented in Fig. 2b—d. For each station we observe intensive positive TEC anomaly during SSW event, which corresponds to the results of the previous studies [3, 4]. An important feature of the events we considered is the absence of an intense negative TEC anomaly in the afternoon

hours reported in previous studies [3]. The geomagnetic situation in the period under review varied from calm to moderately perturbed. Note that during the period of the second SSW, G2 geomagnetic storm occurred, the Dst index reached values of 100 nT. This suggests that the TEC variations observed during this period can not be solely related to the effect of the SSW, but are the response of the ionosphere to a combination of disturbing factors from above and from below. The observed TEC anomalies lasted for about one week after SSW peak and had the amplitudes comparable to those typically observed during moderate geomagnetic storms (see fig. 1). This result shows the importance of the atmosphere — ionosphere coupling for description of the ionospheric electron density distribution.

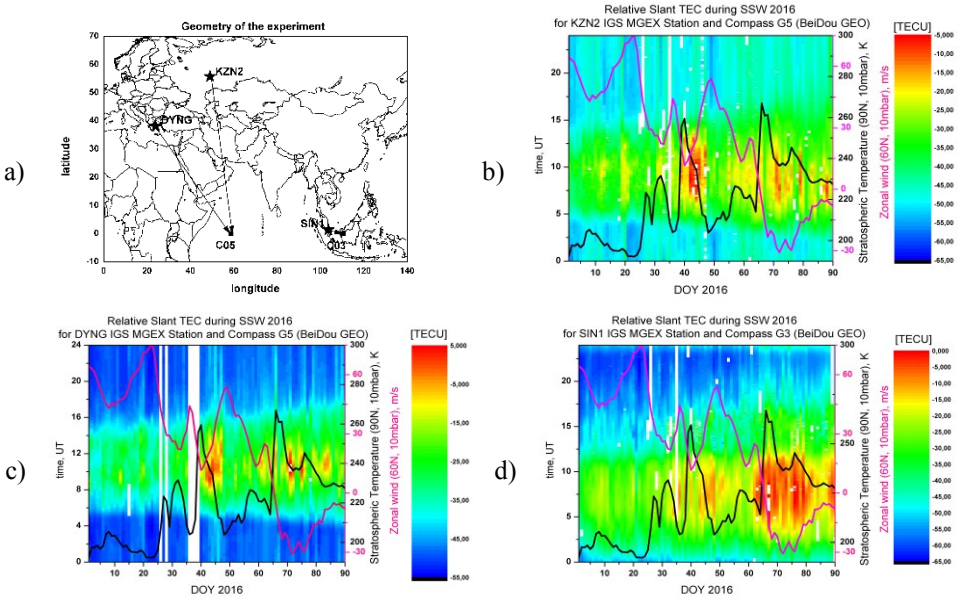

FIGURE 2. The geometry of the experiment (a) and the variations of the relative slant TEC during the SSW in winter of 2016,according to the data of the geostationaryBeiDou satellites and receivers KZN2 (b), DYNG (c), and SIN1 (d) together with the stratospheric (10 mbar) temperature (black curves) and mean zonal windat 60N (pink curves).

Our results show the possibilities and potential for using the dual-frequency coherent signals of the COMPASS / BeiDou geostationary satellites to study TEC variability in the ionosphere at various spatial and temporal scales in calm and disturbed heliogeophysical conditions. The growing number of receivers, as well as dual-frequency geostationary satellites in constellations of navigation systems, makes it possible in the future to use this type of data for continuous TEC monitoring.

The work was supported by the Russian Science Foundation (project 17-77-20087) and Russian Foundation for Basic Research (project 18-35-00663).

1. V. E. Kunitsyn, A. M. Padokhin et al.,. Ionospheric TEC estimation with the signals of various geostationary navigational satellites, *GPS Solutions,* 2016, 20 (4), pp. 877—884.

2. G. A. Kurbatov, E. A. Kozlovtzeva et al., Application of the signals of COMPASS/BeiDou geostationary satellites for the studies of ionospheric effects of geomagnetic storms and sudden stratospheric warmings, *Memoirs of the Faculty of Physics*, 2017, 4, 1740502.

3. L. P. Goncharenko, A. J. Coster, J. L Chau et al., Impact of sudden stratospheric warmings on equatorial ionization anomaly, *J. Geophys. Res*., 2010, 115, P. A00G07. doi:10.1029/2010JA015400.

4. A. S Polyakova, M. A Chernigovskaya., N. P. Perevalova, Ionospheric Effects of Sudden Stratospheric Warmings in Eastern Siberia Region, *J. Atm. Solar-Terr. Phys*, 2014. 120, pp. 15—23, doi: 10.1016/j.jastp.2014.08.011.

To The Problem of Estimating Accuracy of Atmosphere Perturbations Diagnostics by Projection Operators Method

Sergey B. Leble, Sergey D. Vereshchagin, Irina S. Vereshchagina

Institute of Physical, Mathematical Sciences and IT Technologies,
Immanuel Kant Baltic Federal University, ul. A. Nevskogo, 14, Kaliningrad, 236016, Russia

Introduction. In geophysics and oceanology, an atmosphere disturbance is a superposition of waves and non-wave components of different time and space scales. Even in a one-dimensional problem an observation in some point vicinity may contain acoustic waves propagating upward and downward as well as so-called entropy mode, that correspond to zero frequency if one neglect dissipation [1]. One-dimensional atmosphere is an important model of typical wave phenomena, related directly to some real dynamics with large horizontal scale, launched for example by tsunami or earthquake.

Conventionally, the problem is solved by spectral analysis, that cannot give answer for some principle questions such as direction of propagation. The application of the inverse problem method can be found in the works [2], [3]. In the paper [2] to restore the shape of the source, it is shown that an increase in the number of receivers located within the characteristic search dimensions and the receiver's getting to the direction of the main signal significantly affects the quality of the result. In the paper [3] it is proved that the initial state of the ocean surface is uniquely determined by the mode of oscillation of one of the points of the surface. In [4] we proposed a method for diagnosing wave perturbations on the basis of the method of projection operators, which was presented in the monograph [1] and developed in a number of works by the authors, including [5—6].

Formulation of the problem. The method of design the projection operators is based on the idea of dividing the solution space into subspaces corresponding to different branches of the dispersion relation. The linearized

system of equations of hydrodynamics is written in a matrix form and by the same token we determine the evolution operator and after the Fourier transform we find the eigenvalues and eigenvectors corresponding to different branches of the dispersion relation. In this paper we restrict ourselves by the one-dimensional exponential atmosphere. We also exclude the entropy mode.

Projection operators. To separate the "up" and "down" wave modes projection operators approach is used. Projection operators were derived in both discrete and continuous cases. In the continuous case they take the form

$$P_{1,2} = \begin{pmatrix} \frac{k+1}{2k} & \pm\frac{i\gamma\omega}{(\gamma-1)k} \\ \pm\frac{i\omega(\gamma-1)}{\gamma k} & \frac{k+1}{2k} \end{pmatrix} \quad (1)$$

and in the discrete case they are calculated numerically as array of values in each point separately. Where $k = \sqrt{4\omega^2 - 1}$

An evaluation of measurements errors. To control the correctness of wave diagnostic both approaches uses the wave energy. Specifically the energy of the modes after separation is calculated and then sum of it is compared to the initial full energy of the mixed mode state. But since we generally cannot return back to the (x, t) -space (or (ξ,τ)-space in the terms of dimensionless system) standard formulas for energy could not be used. So we had to derive equations for the energy in the Fourier-space, where all our modes are described.

In the case of continual method the energy correctness could be proven directly. Energy take the form

$$E(\xi) = \rho_0 g H \int_{-\infty}^{\infty} \left[\frac{1}{\gamma}\omega^2 \tilde{Q}(\xi,\omega)^2 - \frac{2}{\gamma} I\omega \tilde{Q}(\xi,\omega)\tilde{\phi}(\xi,\omega) + \frac{(\gamma-1)-\gamma\omega^2}{(\gamma-1)^2}\tilde{\phi}(\xi,\omega)^2 \right] d\omega$$

Where $\tilde{Q} = \int_{-\infty}^{\infty}(\tilde{p} - \tilde{\phi})\, d\tau$ variable introduced to simplify equations,$\tilde{\varphi}$is a Fourier transform of

$$\phi = \frac{\left(p' - \gamma\frac{\bar{p}}{\bar{\rho}}\rho'\right) exp\left(\frac{z}{H}\right)}{p_0}$$

p and ρ is pressure and density, bar over variable denote background values in unperturbed atmosphere, while dash denote perturbation. z is height and H is the uniform atmosphere height, while ω is the dimensionless frequency in Fourier-space.

In the discrete method case the formula have the same form only with sum over all the model points instead of integration, but its correctness can only be checked for the specific cases and only approximately. The test results show good agreements of sum of mode's energies with initial energy in the all testes cases.

A real measurement gives an information about ψcomponents with errors and only in a finite number of time points. So we should estimate a distance between a representative observation and a space of, say, right waves.

Let us introduce a norm in the vector space of solutions $\psi = \begin{pmatrix} Q \\ \phi \end{pmatrix}$, decaying at infinities exponentially. It is directly verified by means of

$$\|\psi\|^2 = \frac{E}{\rho g H} = (\psi, \psi) \tag{2}$$

Such way a Banach space ψ is introduced to normalize the vectors, and estimate distances in the space of $\psi \in \Psi$. Given a sequence of time $t_i,\ i = 1..n$, generates a sequence of vectors, by measurements, which form 2n-dimensional vector$\in R^{2n}$. Using an appropriate Fourier transform produce data in omega domain $\tilde{\phi}(0, t_i)$ with the norm

$$\|\phi\|^2 = \sum_{i=1}^{N} \left[\frac{1}{\gamma} \omega^2 \tilde{Q}(\xi, \omega)^2 - \frac{2}{\gamma} I\omega \tilde{Q}(\xi, \omega)\tilde{\phi}(\xi, \omega) + \frac{(\gamma - 1) - \gamma\omega^2}{(\gamma - 1)^2} \tilde{\phi}(\xi, \omega)^2 \right] d\omega$$

that should determine a closest vector solutions $\psi_{1,2}$via minimum of the functional

$$I = ||\psi_{1,2} - P_{1,2}\varphi(0, \omega_i)||_n$$

We treat this condition as variational principle

$$\min_{\psi_{1,2} \in \Psi_{1,2}} I,$$

in a n-dimensional space with the norm correspondent to L_2 with the Euler equations

$$\frac{\partial I}{\partial \psi_{1,2}} = 0.$$

In reality the presence of errors of measurements do not give zero identically even if the wave is purely right. The deviation of the real data from the ideal may be characterized by

$$||\varphi_{1,2} - P_{1,2}\tilde{\varphi}(0, \omega_i)||_n = \delta$$

the correspondent calibration may be performed by the specially organized experiment.

An admixture of a left wave in a superposition of the both may be noticed if the $||\varphi - P_{1,2}\varphi||_n$ exceeds the typical error.

Final form of the reconstruction is a standard procedure of spline or other inverse problem in a chosen a priori physically reasonable space. Note, that arrival time needs a priori information about "zero" time event. An instability from velocity value errors should also be taken into account, error from arrival time determination grows with ct.

Acknowledgments: The work is supported by the RFBR grants No. 18-05-00184 (Leble S. B.)

1. S. B. Leble Nonlinear waves in waveguides with stratification, Springer-Verlag, Berlin, 1991.

2. T. A. Voronina, Determination of the spatial distribution of oscillation sources by remote measurements at a finite number of points, *Siberian Journal of Computational Mathematics*, 2004, 7(3), pp. 203—211.

3. V. G. Romanov, P. S. Moshkalev, One-dimensional inverse problem of determining the source of tsunami, *Siberian Journal of Industrial Mathematics*, 2011. 14, 3(47), pp. 87—99.

4. S. B. Leble, S. D. Vereshchagin, I. S. Vereshchagina, Diagnostics of atmospheric disturbances using projection operators method, *Chim.Phys* (in the press).

5. Leble S., A. Perelomova, Problem of proper decomposition and initialization of acoustic and entropy modes in a gas affected by the mass force, *Applied Mathematical Modeling*, 2013, 37(3), pp. 629—635.

6. S. Leble, I. Vereshchagina, http://arxiv.org/abs/1403.7751

First results of the Entire Atmosphere Global Model (EAGLE)

Timofei V. Sukhodolov[1,2,3], Fedor S. Bessarab[1], Nicolay V. Chirik[1], Bernd Funke[4], Maxim V. Klimenko[1], Vladimir V. Klimenko[1], Yuriy N. Korenkov[1], Dmitry V. Kulyamin[1,5], Katharina Meraner[6], Hauke Schmidt[6], Pavel A. Vasiliev[1], Irina E. Zakharenkova[1], and Eugene V. Rozanov[1,2,3]

[1]West Department of Pushkov Institute of Terrestrial Magnetism, Ionosphere and Radio Wave Propagation RAS, Kaliningrad, Russia, email: office@wdizmiran.ru
[2]Physikalisch-Meteorologisches Observatorium, World Radiation Center, Davos, Switzerland
[3]Institute for Atmospheric and Climate Science, ETH Zurich, Zurich, Switzerland
[4]Instituto de Astrofısica de Andalucia, CSIC, Granada, Spain
[5]Research Computing Center, Lomonosov Moscow State University, Moscow, Russia
[6]Max Planck Institute for Meteorology, Hamburg, Germany

Introduction. The Earth's ionosphere is a complex system of coupled dynamical, radiative and chemical processes. Ionospheric variability is mostly defined by the solar radiation flux and geomagnetic activity, but still a significant part of it (~20%) is associated with the forcing coming from the lower and middle atmosphere [1]. Main mechanisms responsible for this connection are planetary waves, atmospheric tides, and gravity waves [2]. A proper representation of all these processes is crucial for understanding the ionosphere itself and its connection to the lower layers.

Historically, numerical models of the upper atmosphere layers (>80 km) and the lower atmosphere layers (<80 km) progressed almost independently just prescribing the lower/upper boundary conditions, which is usually a very rough approximation of all the physics happening below/above. With a rising knowledge about atmospheric sciences related to progress, both, in measurements and models, it became clear that interrelation between atmospheric layers is important and needs to be addressed explicitly. Here, we present a step in this direction with a focus on the ionosphere by showing our first results of the Entire Atmosphere Global Model (EAGLE) that combines models of the upper and the lower atmosphere.

Methods. To calculate the state and variability of the lower and middle atmosphere, we use the HAMMONIA model (Hamburg Model of the Neutral and Ionized Atmosphere). This model is mostly based on the fifth version of the general circulation model of the atmosphere ECHAM5, but also contains several important additions, such as the extension of the top boundary up to 250 km, inclusion of the chemical module MOZART3, and others [3], which allow a good representation of the lower thermosphere. HAMMONIA is applied here with a horizontal resolution of ~2x2˚ and 119 vertical layers from the ground up to ~200—250 km. State and variability of the upper atmosphere are calculated by the Global Self-consistent Model of the Thermosphere, the Ionosphere and the Protonosphere (GSM TIP) [4]. This model is based on the system of quasi-hydrodynamic equations of continuity, motion and heat balance for neutral and charged particles of the cold near-earth plasma in conjunction with the equation for the electric potential in the altitude range from 80 km to geocentric distance of ~15 earth radii and the horizontal resolution of 5x5°.

For coupling the two models, we programmed a coupler interface that prepares fields of both models to be transited to each other in the overlap region (~80—200 km) and allows to run parallel (HAMMONIA) and non-parallel (GSM TIP) codes simultaneously. In future, it is also planned to transfer nitrogen oxide production and Joule heating from GSM TIP to HAMMONIA, but here, as a first step, we discuss only the one-way coupling through specification of the GSM TIP temperature and neutral wind fields. Neutral density is specified only at 80 km as a lower boundary condition. We used January 2009 as a period of interest, due to its high dynamical activity, represented as a strong sudden stratospheric warming, and due to availability of reliable observations.

Results. Figure 1 shows vertical structure of the zonal mean temperature in January 2009 in the upper mesosphere/lower thermosphere region. One of the characteristic features of this region is an existence of the cold summer mesopause, which is mostly a result of momentum deposition from gravity waves. HAMMONIA (Fig. 1B) perfectly reproduces this region compared to the MIPAS observations (Fig. 1A), since the model dynamics is continuous from the surface. Decoupled GSM TIP model (Fig. 1C), forced by prescribed hourly temperature and density fields at 80 km, cannot reproduce this region and shows a clear lack of

cooling at the polar summer mesopause, which also leads to a cold shift of the above temperatures. This is due to a missing wave forcing information that is necessary to generate a vortex around 90—100 km in the summer high latitudes. Based on this, we have chosen to couple HAMMONIA and GSM TIP in the region 80—120 km, which allows to have a realistic mesopause and to forward further up signals from the lower atmosphere (Fig. 1D). Results from the coupled model EAGLE show the best agreement with the MIPAS observations in the 80—175 km range compared to the decoupled HAMMONIA and GSM TIP models. This illustrates the importance of the coupling processes and necessity of a combined model, our work on which is to be continued.

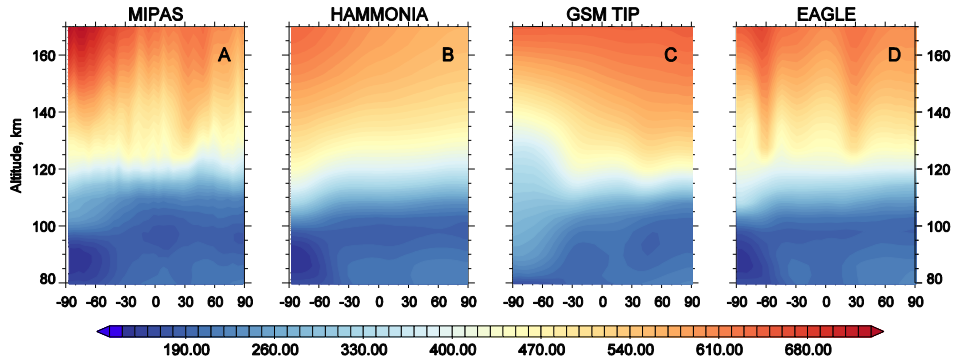

FIGURE 1. January 2009 monthly mean zonal mean temperature from 80 to 175 km. A — MIPAS observations; B — HAMMONIA; C — GSM TIP; D — EAGLE.

This investigation was performed with the financial support from the Russian Science Foundation grant № 17-17-01060.

1. J. M. Forbes, S. E. Palo, and X. Zhang, Variability of the ionosphere, *J. Atmos. Sol. Terr. Phys*., 2000, 62, pp. 685—693, doi:10.1016/S1364-6826(00)00029-8.

2. J. L. Chau, L. P. Goncharenko, B. G. Fejer, and H.-L. Liu, Equatorial and Low Latitude Ionospheric Effects During Sudden Stratospheric Warming Events, *Space Sci. Rev*., 2012, 168, pp. 385—417, doi: 10.1007/s11214-011-9797-5.

3. H. Schmidt, G. P. Brasseur, M. Charron et al., The HAMMONIA chemistry climate model: Sensitivity of the mesopause region to the 11-year solar cycle and CO2 doubling, *J. Climate*, 2006, 19, pp. 3903—3931.

4. A. A. Namgaladze, Yu. N. Korenkov, V. V. Klimenko et al., Global model of the thermosphere-ionosphere-protonosphere system, *Pure and Applied Geophysics (PAGEOPH)*, 1988, 127(2/3), pp. 219—254.

5. L. G. Björn, The cold summer mesopause, *Adv. Space Res.*, 1984, 4(4), pp. 145—151.

6. B. Funke, M. Lopez-Puertas, D. Bermejo-Pantaleon et al., Evidence for dynamical coupling from the lower atmosphere to the thermosphere during a major stratospheric warming, *Geophys. Res. Lett*., 2010, 37(13), doi:10.1029/2010GL043619.

Changes in the Middle and Upper Atmosphere Parameters During the 2013 Major Stratospheric Warming

Anna S. Yasyukevich[1], Yury Yu. Kulikov[2], Maxim V. Klimenko[2,3], Vladimir V. Klimenko[2], Fedor S. Bessarab[2], Yury N. Korenkov[2], and Valery N. Marichev[4]

[1]*Institute of Solar-Terrestrial Physics SB RAS, 664033, Irkutsk, Russia*
[2]*Kaliningrad Branch of N. V. Pushkov IZMIRAN RAS, 236010, Kaliningrad, Russia*
[3]*Immanuel Kant Baltic Federal University, 236016, Kaliningrad, Russia*
[4]*V. E. Zuev Institute of Atmospheric Optics SB RAS, 634055, Tomsk, Russia*

Introduction. The period of December 2012 — January 2013 is of special interest for the study of solar-terrestrial and atmospheric-ionospheric relations physics, due to the almost simultaneous increase in solar activity and the formation of sudden stratospheric warming (SSW). Stratospheric warming is a strong increase in the temperature of the polar and subpolar stratosphere in winter lasting for several days or even weeks. The warming is characterized by the "explosive" nature and the phenomenon intensity can reach up to 30°C or more. The influence of stratospheric warming on the meteorological parameters distribution in the troposphere, surface atmospheric layer and, consequently, on the weather has a rather extensive experimental and theoretical background [1]. Studies of the possible SSW-related effects in the layers of the upper atmosphere, such as the mesosphere, thermosphere and ionosphere, need carrying out on a wider scale. Experimental and modeling results demonstrated SSW-related global changes in the atmosphere dynamics and composition at all the heights from the stratosphere to the thermosphere [2—3]. The consequences of modern works have also shown that SSW could have a considerable effect on the ionospheric plasma distribution [4—9]. However, there have been only a few attempts of complex studying the SSW effects simultaneously in different atmospheric layers so far. In this work we present the results of observations of various parameters in the middle and upper atmosphere in the Northern Asia region during the period of December 2012 — January 2013, when the major SSW event took placed.

The basis of our study was a complex experiment (lidar and ozonometric observations), conducted during the period considered in Tomsk [10]. The data of this experiment were supplemented by the ionospheric parameters observations. We considered variations in the critical frequency and peak height of the ionospheric F2-layer (*foF*2) from ionosonde measurements in Tomsk and Irkutsk, as well as the behavior of the total electron content (TEC) based on the phase dual-frequency GPS/GLONASS receivers' data. The vertical TEC were calculated from the initial series by the method described in [11].

Figure 1 shows the distribution of the stratospheric temperature at the 10 hPa (~ 30 km) level, as well as the isolines of geopotential height from the NCEP/NCAR reanalysis data. The temperature of the stratosphere began to rise from December 21, 2012. The maximum temperature increase exceeded 70°C during January 3—6, 2013 and was registered in the Northern Asia region (Fig. 1 b, c). The reverse of the zonal mean zonal wind direction at 60°N latitude occurred on January 6, the warming was considered to become the "major" type on this day One can also clearly observe the displacement and splitting of the circumpolar vortex during this event. The stratospheric circulation returned to normal mode by the end of January.

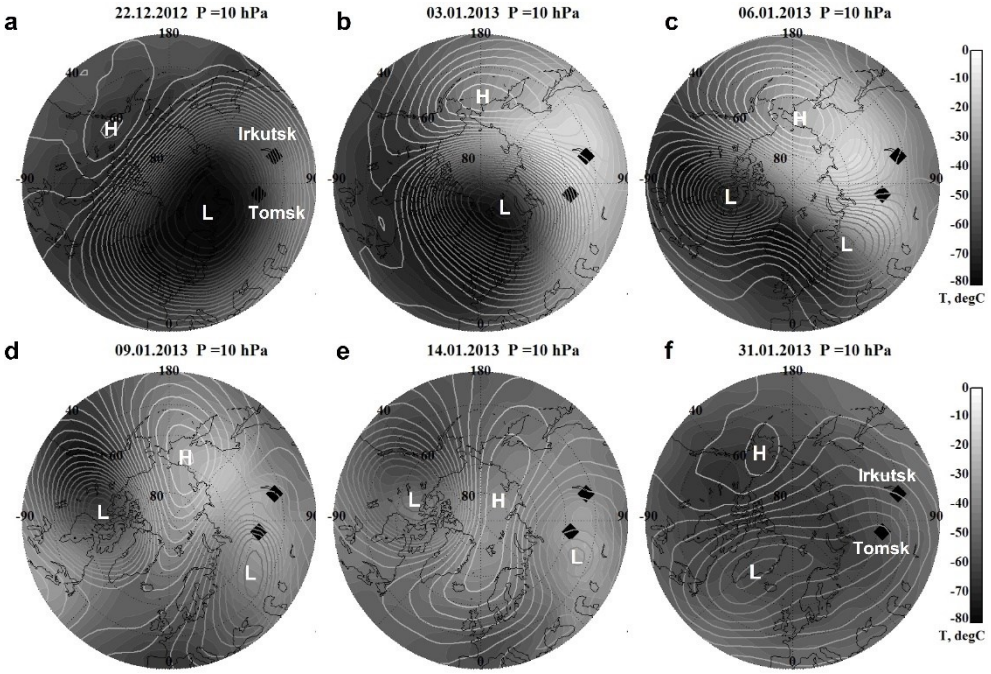

FIGURE 1. Distribution of the stratospheric temperature, as well as isolines of the geopotential height at the 10 hPa (~ 30 km) level. Rhombuses mark the Irkutsk and Tomsk locations.

During the period under consideration, stratospheric ozone measurements were carried out in Tomsk using a mobile microwave (MMW) ozonometr [12], as well as lidar observations of the stratospheric temperature. The obtained results are shown in Fig. 2 jointly with the distributions of the parameters from satellite MLS/AURA measurements and ERA Interim reanalysis data. One can see significant variations in the ozone concentration and temperature of the stratosphere during the SSW. After the SSW warming peak (January 6) the ozone concentration was observed to increase up to 1.5—2 times at 25 and 60 km altitudes (Fig. 2 a, d). On the contrary, at the lower stratosphere during the SSW evolution phase (December 21 — January 2)

one can see a considerable decrease in the O_3 concentration by approximately 50% compared to previous days (Fig. 2a). There was also an increase in the amplitude of ozone fluctuations. The observed period was featured also by the absence of a correlation between the stratospheric temperature and O_3 concentration behavior at the 25 km altitude (Fig. 2 a, b).

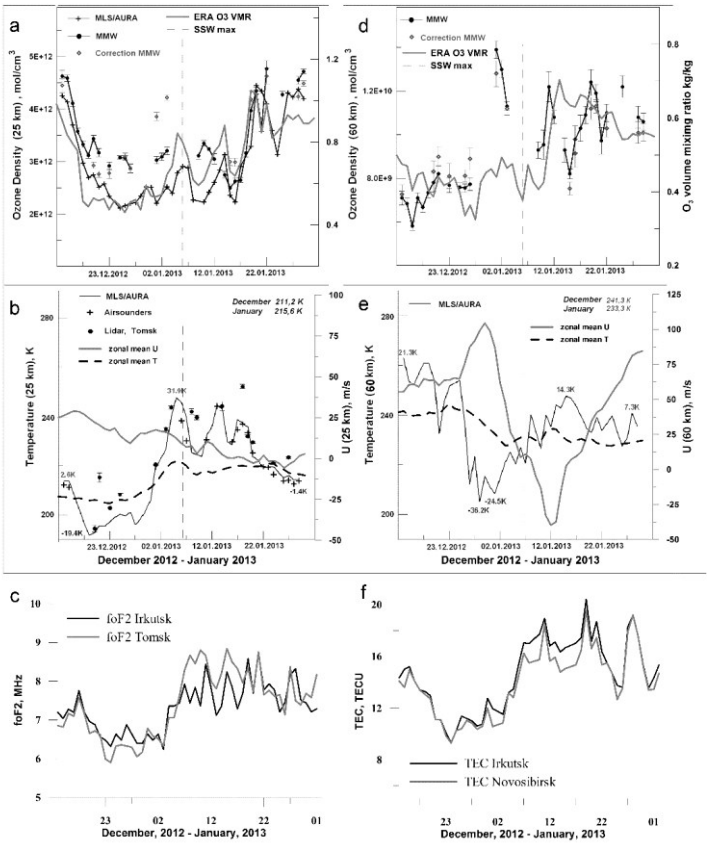

FIGURE 2. Distributions in: ozone concentration at 25 km (a) and 60 km (d) altitudes, temperature of lower (c) and upper stratosphere (e) in Tomsk from experimental and reanalysis data (see the legends); midday critical frequency of ionospheric F2-layer (c) as well as total electron content (f) in Tomsk and Irkutsk. Vertical dashed lines on the panels indicate the SSW peak.

The revealed ozone behavior in the lower stratosphere is, probably, associated with the processes of destruction of the circumpolar vortex during the SSW and the transfer of cold air masses from the Atlantic. At the upper stratosphere the ozone concentration changes are caused basically by variations in the temperature. The obtained significant ozone fluctuations during the SSW indicate the origin of a tidal wave that can affect the ionosphere.

Significant variations were also observed in midday ionospheric critical frequency and TEC behavior (Fig. 2 c, f). The difference between foF2 and TEC values before and after the SSW peak was 1.5 and 2 times, respectively. The analysis showed that the recorded increase in the ionospheric electron density during the considered period cannot be completely explained by changes in the solar activity level. Increased values of solar activity were observed from December 29 till January 18 with a maximum on January 11. However, a significant enhancement in the value of ionospheric parameters was still observed for more than 20 days after the $F_{10.7}$ had decreased down to the mean level. However, the SSW-related stratospheric dynamic disturbances lasted until early February, which matched the duration of the ionospheric variations observed.

Similar changes were registered for the neutral composition of the thermosphere. There was a significant increase in the O/N_2 ratio, measured by satellite GUVI/TIMED instrument, during the SSW peak and within 20 days after it. The positive O/N_2 response was recorded at latitudes greater than 30°N and was most pronounced in the high-latitude region where the warming development took place. This O/N_2 behavior correlated with the revealed variations in the ionospheric electron density.

The obtained results indicate that the ionospheric effects to SSW in the middle and high-latitude regions are caused by changes in the neutral composition at the thermospheric altitudes. Variations in the neutral composition of the thermosphere can be related either to changes in direct penetration of wave disturbances (mainly tides), which are amplified during SSW at the mesosphere/lower thermosphere height; or be the result of neutral gas vertical transfers produced by SSW-indused secondary circulation. This issue requires further detailed studies, involving experimental data and modeling efforts.

The work is supported by the RFBR grants No. 16-35-60018 (Yasyukevich A. S.) and 18-05-00594 (Ratovsky K. G., Klimenko M. V.— ionosonde data analysis), and the RSF grant No. 17-17-01060 (Korenkov Yu. N., Klimenko V. V., Bessarab F. S. — statement of the model problem). The authors enclose their gratitude to the NOAA/OAR/ESRL PSD, USA and to European Centre for Medium-Range Weather Forecasts for the Reanalysis data, to the Aerospace Corporation and The Johns Hopkins University, USA for GUVI/TIMED data. Irkutsk Station vertical sounding data were recorded by the Angara Multiaccess Center facilities at ISTP SB RAS. The author also thanks K. G. Ratovsky and S. N. Kolesnik for the ionosondes' data provided.

1. J. Kidston, A. A. Scaife, S. C. Hardiman et al., Stratospheric influence on tropospheric jet streams, storm tracks and surface weather, *Nature Geoscience*, 2005, doi:10.1038/ngeo2424.

2. H.-L. Liu and R. G. Roble, A study of a self-generated stratospheric sudden warming and its mesospheric–lower thermospheric impacts using the coupled TIME-GCM/CCM3, *J. Geophys. Res.*, 2002, 107(D23), 4695, doi:10.1029/2001JD001533.

3. I. Medvedeva, A. Medvedev, K. Ratovsky et al, Comprehensive study of disturbances of the neutral atmosphere and ionosphere parameters over Eastern Siberia during the 2013 January major sudden stratospheric warming, *Adv. Space Res.*, 2015, 56, pp. 1877—1885, doi: 10.1016/j.asr.2015.06.008.

4. L. P. Goncharenko, J. L. Chau, H. L. Liu, and A. J. Coster, Unexpected connections between the stratosphere and ionosphere, *Geophys. Res. Lett.*, 2010, 37, L10101, doi: 10.1029/2010GL043125.

5. M. V. Klimenko, V. V. Klimenko, F. S. Bessarab et al., Study of the thermospheric and ionospheric response to the 2009 sudden stratospheric warming using TIME-GCM and GSM TIP models: First results, *J. Geophys. Res. Space Phys.*, 2015, 120, doi:10.1002/2014JA020861.

6. D. Pancheva and P. Mukhtarov, Stratospheric warmings: The atmosphere — ionosphere coupling paradigm, *J. Atmos. Sol.-Terr. Phys.*, 2011, 73, pp. 1697—1702, doi: 10.1016/j.jastp.2011.03.006.

7. A. S. Polyakova, M. A. Chernigovskaya, and N. P. Perevalova, Ionospheric Effects of Sudden Stratospheric Warmings in Eastern Siberia Region, *J. Atmos. Sol.-Terr. Phys.*, 2014, 120, pp. 15—23, doi:10.1016/j.jastp.2014.08.011.

8. B. G. Shpynev, V. I. Kurkin, K. G. Ratovsky et al., High-midlatitude ionosphere response to majorstratospheric warming, *Earth Planets and Space,* 2015, 67(18), doi: 10.1186/s40623-015-0187-1.

9. E. Yiğit, P. K. Knížová, K. Georgieva, and W. Ward, A review of vertical coupling in the Atmosphere–Ionosphere system: Effects of waves, sudden stratospheric warmings, space weather, and of solar activity, *J. Atmos. Sol.-Terr. Phys.*, 2016, 141, pp. 1—12, doi:10.1016/j.jastp.2016.02.011.

10. V. N. Marichev, G. G. Matvienko, A. A. Lisenko et al, Microwave and optical observation of ozone and temperature of the middle atmosphere during stratospheric warming at Western Siberia, *Atmospheric and Oceanic Optics,* 2014, 27(1), pp. 46—52 (in Russian).

11. Yu. V. Yasyukevich, A. A. Mylnikova, and A. S. Polyakova, Estimating the total electron content absolute value from the GPS/GLONASS data, *Results in Physics*, 2015, 5, pp. 32—33, doi:10.1016/j.rinp.2014.12.006.

12. Y. Y. Kulikov, A. A. Krasilnikov, V. G. Ryskin et al., Ground-based microwave instrument to research of stratospheric ozone (some results of observations), *Proc. XXX Annual Seminar, Apatity,* 2007, pp. 218—221.

Modeling of Ionospheric Disturbances Caused by Meteorological Storms

Pavel A. Vasilev[1], Ivan V. Karpov[1, 2], and Olga P. Borchevkina[1, 2]

[1]Immanuel Kant Baltic Federal University, Kaliningrad, 236041 Russia
[2]Pushkov Institute of Terrestrial Magnetism, Ionosphere, and Radio Wave Propagation, West Department, Russian Academy of Sciences, Kaliningrad, 236017 Russia

Introduction. The characteristics of ionosphere disturbances that occurred during the meteorological storms passage were identified in observation of the ionospheric parameters. These disturbances are manifested in decreasing the values

of Total Electron Content (TEC) and increasing the amplitudes of their variations with the periods of gravity waves (GW) [1]. An example of such an ionosphere reaction on the passage of a meteorological storm is given in [1]. The physical processes that determine such an ionosphere reaction, remain insufficiently studied. However, the main hypotheses connect the causes of such changes in the state of the ionosphere with the thermosphere processes, that are initiated by the propagation of GW from the region of meteorological disturbance. Theoretical studies of the processes of GW propagation from the lower atmosphere to the upper show that waves with periods close to the Brunt-Väisälä period can propagate up to heights of the thermosphere and ionosphere [2, 3]. The dissipation of such waves in the upper atmosphere leads to the formation of local heating regions in the thermosphere, which can affect the ionization-recombination processes in the ionosphere.

Description of the numerical experiment. The purpose of this article was to test this assumption. For this purpose, numerical experiments were performed using the theoretical model GSM TIP, which allows to calculate global distributions of thermospheric and ionospheric parameters. The version of the model, which was used, covers heights from 80 to 500 km with uneven vertical steps and latitude-longitude steps 5 degrees [4]. The initial conditions were set in such way that the state of the atmosphere corresponded to the end of December.

Several calculations have been made that simulate the daily dynamics of the unperturbed atmosphere in the absence of a source, as well as the effect of a point source of heating on the upper atmosphere. An additive to the temperature ΔT was been used as a source of additional heating of the thermosphere, defined as:

$$\Delta T = A * \exp\left(-\frac{|r - r_0|}{H}\right) \quad (1)$$

where r is the height, r_0 = 180 km is the height of the source maximum, H is the height of the homogeneous atmosphere. The height of the additional heating source r_0 and the amplitude factor A were selected from qualitative estimates of the results [3]. The source was determined at the point with coordinates 45 N, 15 E.

In accordance with the GW's theory, the polarization relations for large-scale waves with a frequency, which is much lower than the Brunt–Väisälä frequency, make it possible to determine the density perturbation associated with GW [5]:

$$\frac{\Delta T_d}{T} = -\frac{\Delta \rho_d}{\rho} \quad (2)$$

where ΔT_d and $\Delta \rho_d$ are additions to temperature and density, respectively, T and ρ are their background values.

Results of the experiment. The simulation covered a daily interval, starting from midnight to UT. The source was switched on immediately in the first variant of the calculation and the worked during entire simulation period. In the second case, the source was switched on at 10 UT, and also worked until the end of the calculation. In both cases, the reaction of the thermospheric parameters was

manifested during the first hour of calculations, and the maximum heating was achieved six hours after the source was switched on, was about 70 degrees and slightly fluctuated near this mark until the end of the calculation.

For convenience of analysis, we will consider additives to various parameters in comparison with the unperturbed state. Figure 1 shows the latitude-longitude distributions of the foF2 additive at 6 (a) and 16 (b) hours after the start of the calculation of the first variant.

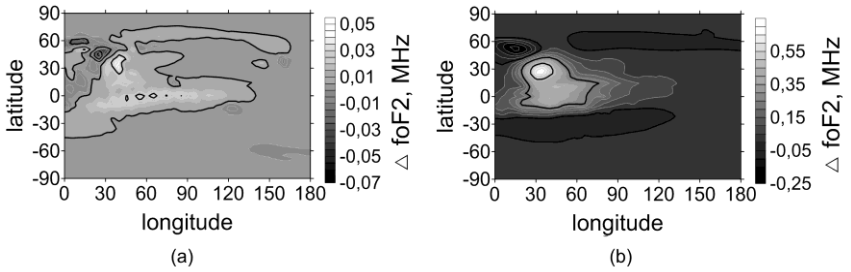

FIGURE 1. The distribution of the additive to foF2 in 6 (a) and 16 UT (b).

From the comparison of the foF2 distributions at night (Fig.1, a) and day (Fig.1, b) it can be seen that the magnitude of ionospheric effects from the operation of the source at night is many times less than the day. Besides, with local point heating, the effects manifest themselves at a great distance, including in the equatorial zone where some periodic structure is observed at night (Fig. 1, a).

At the same time, the daily effects from the source, that worked 6 and 16 hours, differ slightly. Let's consider this issue separately, constructing temporary variations of key dynamic parameters at the point of the maximum negative effect of foF2 near the source (Fig. 2).

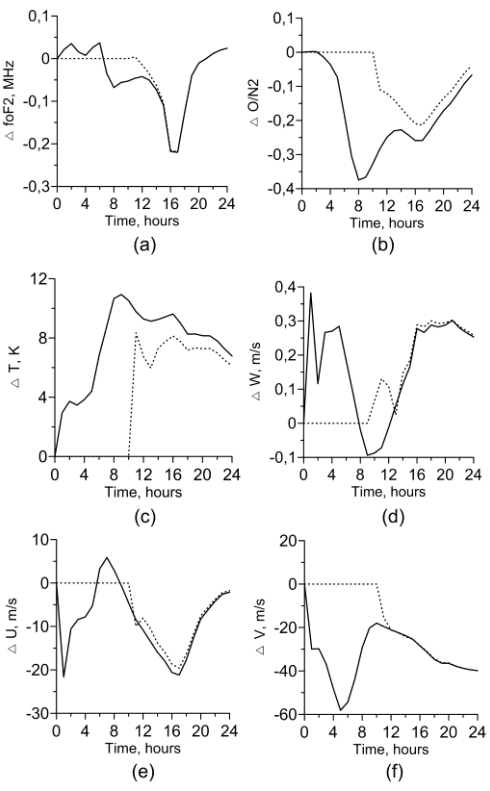

FIGURE 2. The graphs of additives to foF2 (a), the ratio of the concentration of atomic oxygen to the concentration of molecular nitrogen (b), temperature (c), vertical (d), meridional (e) and zonal (f) velocities for calculations with a source operating with 0 UT (solid line) and 10 UT (dashed line).

It follows that, deviations of all key parameters in both cases have a similar dynamics, generating similar effects, starting at 12 UT.

In addition, some parameters, such as additions to temperature (Fig.2, c), the ratio of concentrations of atomic oxygen to the concentration of molecular nitrogen (Fig.2, b) and meridional velocity (Fig.2, e) decrease by the end of the calculation, demonstrating a decline in the corresponding activity. This effect can be caused by the transfer of matter from the source region, in connection with which the density in it falls, and the magnitude of the effects decreases with it.

Conclusions. The results of calculations show, that the inclusion of an additional source of perturbations simulating the effect of GW dissipation leads to a decrease in the electron concentration at the maximum of the F layer of the ionosphere. In this case, in spite of sufficiently large perturbations of the main dynamic parameters, the night ionospheric disturbances are much less pronounced than the daytime ones. This can be explained by the fact that dissipative processes are faster at night than during the day. At the same time, both nighttime and daytime ionospheric effects from a point source at medium latitudes rather quickly spread to the equatorial region, occupying a large spatial interval, both in latitudes and longitudes. Both at night and in the daytime at low latitudes, there is some increase in foF2, and directly above the middle latitude source of the disturbance is its decrease.

This work was financially supported by the RFBR grant 17-05-00574 (Karpov I. V.), grant 18-05-00184 (Borchevkina O. P.) and the grant of the RSF № 17-17-01060 (Vasilev P. A.).

1. O. P. Borchevkina and I. V. Karpov, Ionospheric irregularities during periods of meteorological disturbances, *Geomagn. Aeron.*, 2017, 57(5), pp. 670—675.

2. M. P. Hickey, R. L. Walterscheid, and G. Schubert, Gravity wave heating and cooling of the thermosphere: Roles of the sensible heat flux and viscous flux of kinetic energy, *J. Geophys. Res.*, 2011, 116, A12326, doi:10.1029/2010JA 016792.

3. I. V. Karpov and S. P. Kshevetskii, Numerical study of heating the upper atmosphere by acoustic-gravity waves from a local source on the Earth's surface and influence of this heating on the wave propagation conditions, *J. Atmos. Sol.-Terr. Phys.*, 2017, 164, pp. 89—96.

4. A. A. Namgaladze, Yu. N. Korenkov, V. V. Klimenko et al., Global numerical model of thermosphere, ionosphere and protosphere of the Earth, *Geomagn. Aeron.*, 1990, 30(4), pp. 612—619.

5. G. I. Grigoryev, Acoustic-gravity waves in the Earth's atmosphere (review). *Radiophys. Quantum Electronics*, 1999, 42(1), pp. 3—24.

The Effect on Ionospheric Electron Density of Polarized Modes of Lightning Induced EM Waves

Ramazan Atıcı[1], Esat Güzel[2], and Selçuk Sağır[3]

[1]Faculty of Education, Mus Alparslan University, 49250 Mus, Turkey
[2]Department of Physics, Faculty of Sciences, Firat University, 23119 Elazig, Turkey,
[3]Department of Electronics and Automation, Vocational School, Mus Alparslan University, 49100 Mus, Turkey

Introduction. The lightning discharges (cloud-to-ground (CG), intracloud (IG), cloud-to-air (CA) and cloud-to-cloud (CC)) originated from troposphere directly affect lower ionosphere and upper mesosphere through the fields (quasi-electrostatic field and EM field) that they formed [1]. The EM wave radiated from lightning discharges leads to changes on the electron temperature, ionization frequency, attachment frequency and electron collision frequency [2, 3]. Also these discharges increase ionosphere conductivities. Thanks to that , propagation of the radio waves at the very low frequency band (Very Low Frequency, VLF) is affected from that. Therefore, the EM wave at VLF band radiated from the lightning provides a remote measurement opportunity to provide information about D-region dynamics whose measurement opportunity is limited and hard compared to other regions of the ionosphere [4—6]. In this study, the effect of lightning originated EM waves on the lower ionosphere electron density was reviewed. Glukhov-Pasko-Inan (GPI)[7] model that is a useful method was used to review the change in this electron density. By adding the two-body attachment and electron detachment, this model has developed and more comprehensive results were obtained.

Theoratical Backround. Heating up the electrons by EM fields causes important changes on the chemical balance of the lower ionosphere [8]. The electrons that were speeded up by lightning originated electrical fields changed the electron density by ionizing the neutrals and making changes on the two-three body electron attachment. By this way, the quaternary model of lower ionosphere that was included in the three-body attachment was used by Rodriguez and Inan [9]. This model was especially more useful when only detailed behaviors of the electron density were interested in. To simplify the model, one dimensional model was thought and it was accepted that all physical quantities are only dependent on the height[9]. We concluded this study by taking the acceptances stated here. Rodriguez and Inan [9] expressed the chemical processes between the particles with the below mentioned equations [7]:

$$\frac{dN_e}{dt} = Q_0 + \gamma N^- - v_a N_e - \alpha_d N_e N^+ - \alpha_d^c N_e N_x^+ \quad (1)$$

$$\frac{dN^-}{dt} = v_a N_e - \gamma N^- - \alpha_i N^- (N^+ + N_x^+) \quad (2)$$

$$\frac{dN^+}{dt} = Q_0 - AN^+ - \alpha_d N_e N^+ - \alpha_i N^- N^+ \quad (3)$$

$$\frac{dN_x^+}{dt} = -\alpha_d^c N_e N_x^+ + BN^+ - \alpha_i N^- N_x^+ \quad (4)$$

Here N_e, N^+, N^- ve N_x^+ respectively shows the numerical densities of electrons, primary positive ions (NO^+ and O_2^+), negative ions (O_2^-, CO_3^-, NO_2^-, NO_3^-) and positive cluster ions or proton hydrates ($H^+(H_2O)_n$). Q_0 is steady external ionizer source, α_d and α_d^c are the effective coefficients of recombination of primary positive ions and water cluster ions with the electron. α_i is the neutralizing coefficient that is effective for all species of positive ions with negative ions. v_a is the effective attachment frequency. A is the effective frequency of transformation of the primary positive ions (especially NO^+) to the water cluster ions and γ is the electron detachment frequency. The reaction ratios, coefficients and their dependence to T_e and T_n electron and neutral temperature are shown in Table 1. For the stable state of (1) — (4) equations, the ratio of N^- to N_e was obtained by deducting N^+ and N_x^+ from Equation (1) by accepting the charge neutrality as ($N_e+N^- = N^+ + N_x^+$).

TABLE 1. Reaction ratios and coefficients of D region [9].

Coefficients ($m^3\ s^{-1}$)
$\alpha_d = 3 \times 10^{-13}$ (Glukhov et al., 1992)
$\alpha_d^c = 3 \times 10^{-12} (T_n / T_e)^{0.08}$
$\alpha_i = 1 \times 10^{-13}$
Ratios (s^{-1})
$v_a = v_{a3} = 10^{-43} N_{N_2} N_{O_2} + k_{O_2} (N_{O_2})^2$
$k_{O_2} = K T_e^{-0.65} exp\left[-\frac{a_1}{T_e} - \left(\frac{a_2}{T_e}\right)^2 - \left(\frac{a_3}{T_e}\right)^3\right]$
$K = 1.1617 \times 10^{-39} - 3.4665 \times 10^{-42} T_n + 3.2825 \times 10^{-45} T_n^2$
$a_1 = 781.93 - 3.2964\ T_n$
$a_2 = -191.59 + 3.7646\ T_n - 4.5446 \times 10^{-3} T_n^2$
$a_3 = -76.834 + 1.2277 \times 10^{-2} T_n - 7.6427 \times 10^{-3} T_n^2 + 1.7856 \times 10^{-5} T_n^3$
$A = 10^{-43} N_T^2$, $N_T = N_{N_2} + N_{O_2}$ total neutral density
$\gamma \cong \left(8.6 \times 10^{-16} e^{-6000/T_n} N_T + 2.5 \times 10^{-16} N_{ac}\right) s^{-1}$, $N_{ac} = N_O + N_N$

The electron temperatures (T_e) used in these calculations was obtained from the balance between lost-gained processes and in this study we used the Atici et al. (2016) heating model.

Results of calculations. The date used in the study was obtained within Elazıg ($38^o\ 41'$ K and $39^o\ 13'$ D) province of Turkey. The neutral density and temperature values used in the calculations were taken from web site of (http://omniweb.gsfc.nasa.gov/vitmo/msis_vitmo.html) MSISE-90 (Mass Spectro-meter-Incoherent-Scatter) model. The electron density at lower ionosphere at night

was calculated by using $N_e(z) = 1.43 \times 10^{13} e^{[(-0.15h')+(\beta-0.15)(z-h')]}$ equation as it was not to obtain it with International Reference Ionosphere (IRI) at the range of 50—80 km. Here, h' is the reference height as km and a parameter that defines sharpness of the electron density depending upon the height given as β km^{-1} [10]. For night conditions, $\beta = 0.5$ km^{-1} and $h' = 85$ or 87 km [9, 11, 12]. The electron density values between 80—120 km were obtained for the local time (LT) 2400 on 21 June 2001 by using the internet compiler of IRI- model (http://ccmc.gsfc.nasa.gov/modelweb/models/iri_vitmo.php).

Ionization of the ionosphere by lightning originated VLF EM waves were calculated by using equations (1—4). The results that were obtained when both detachment reaction that occurred due to active species of the electrons and two-body attachment reaction were included into GPI model were given at Fig. 1. As seen from Figure 1, a decrease was occurred at the electron density up to the height (72.6 km) when O and N atoms were started to be seen on lower ionosphere at night for polarized modes of EM wave. Three-body attachment of the electrons was resulted from dominant loss mechanism at these heights. After that height (72.5 km), the electron density were immediately increased. The electron density were increased up to approximately 5.5 times of its base state values at about 80—85 km. We can say that electron detachment at approximately 72—85 km was dominant on the attachment in that case. This result was in accordance with the results of the previous studies [13, 14]. As especially two-body attachment of electron had been started to effective after electron density reached its peak value, a decrease occurred at electron density depending on the electrical field values of EM waves. By this way, it can be said that electron attachment processes is dominant on the detachment at approximately 85—95 km. As two-body attachment process was dominant mechanism at relatively high electrical fields, the decrease at electron density in the high electrical field was increased.

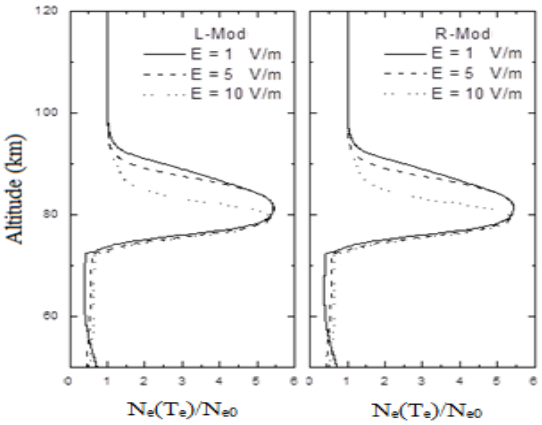

FIGURE 1. The effect of L and R modes of lightning VLF EM wave on lower ionosphere electron density when both two-body attachment reaction and associative detachment reaction of the electrons were included.

The relaxation period of the electron density at D region was at 10—100 s. The electrical field ionization cycle based on the lightning is approximately 6 μs at this region. These fields lead to change of electron density by producing so many ionization within this interaction period [2, 3, 5, 15]. Although realtivelly small ionization occurred within the interaction period as we used electrical field values of lightning originated VLF EM wave at 1—10 V/m in this study, the increase at electron density reached to important values. Also as well as associative detachment reactions of O^- ions [13, 14] were an additional source of electrons, reaction of O_2^- ions with active species by the effect of lightning originated VLF EM waves may be other source of electrons.

Conclusions. The effect of lightning originated electrical fields on the electron density of the lower ionosphere was calculated by means of GPI model. The two-body attachment of electrons and electron detachment processes from active species (O and N atom) were included into this model. The results that were obtained with the inclusion of these aforementioned processes are as stated below:

1. The electron density at lower ionosphere reached to high values even at relatively lower electrical field values. In the calculation, the three-body attachment of the electron for lightning electrical field values was at 50—73 km, associative detachment from active species was at 72—85 km and two-body attachment of electrons was at 85—95 km.

2. It was observed that the detachment was almost at the same level for all wave modes of E field effect of the lightning originated VLF EM wave due to a very sensitive electron affinity (~0,43 eV) of O_2^- [16]. In spite of that, it was calculated that two-body attachment of the electrons was acutely dependent on the electrical field.

3. Also, VLF EM wave radiated from the lightning may lead to so many ionizations within the interaction period (~100 μs). This situation may lead to an accumulation in the ionization and therefore a visible density change even at relatively lower electrical field values as proposed by previous studies [2, 3, 5, 15]. In this study, while a relatively lower ionization that we used its electrical field values of lightning originated VLF EM wave at 1—10 V/m occurred, it was detected that electron density reached up to 5.5 timed of its base state due to accumulation and associative detachment reaction of O_2^- ion with the active species.

1. C. Haldoupis, et al., *Long-lastingD-region ionospheric modifications, caused by intense lightning in association with elve and sprite pairs.* Geophys. Res. Lett., 2012, 39(16).

2. Y.N. Taranenko, U. Inan, and T. Bell, *The interaction with the lower ionosphere of electromagnetic pulses from lightning: Excitation of optical emissions,* Geophys. Res. Lett., 1993, 20(23), pp. 2675—2678.

3. Y.N. Taranenko, U.S. Inan, and T.F. Bell, *Interaction with the lower ionosphere of electromagnetic pulses from lightning: heating, attachment, ionization*, 1993, pp. 1539—1542.

4. U.S. Inan, , S.A. Cummer, and R.A. Marshall, *A survey of ELF and VLF research on lightning-ionosphere interactions and causative discharges,* J.Geophys.Res.: Space Phys., 2010, 115(A6).

5. R.A. Marshall, U.S. Inan, and T. Chevalier, *Early VLF perturbations caused by lightning EMP-driven dissociative attachment,* Geophys. Res. Lett., 2008, 35(21).
6. R.A. Marshall, *An improved model of the lightning electromagnetic field interaction with the D-region ionosphere,* J.Geophys.Res.: Space Phys., 2012, 117(A3).
7. V. Glukhov, V. Pasko, and U. Inan, *Relaxation of transient lower ionospheric disturbances caused by lightning-whistler-induced electron precipitation burst,.* J. Geophys.l Res.: Space Phys., 1992, 97(A11), pp. 16971—16979.
8. V.P. Pasko, U.S. Inan, and T.F. Bell, *Ionospheric effects due to electrostatic thundercloud fields,* J.Atmos. Sol.-Terr. Phys., 1998, 60(7), pp. 863—870.
9. J.V. Rodriguez, and U.S. Inan, *Electron density changes in the nighttime D region due to heating by very-low-frequency transmitters,* Geophys. Res. Lett., 1994, 21(2), pp. 93—96.
10. J.R. Wait, and K.P. Spies, *Characteristics of the Earth-ionosphere waveguide for VLF radio waves,* 1964: US Dept. of Commerce, National Bureau of Standards: for sale by the Supt. of Doc., US Govt. Print. Off.
11. U.S. Inan, et al., *Ionospheric modification with a VLF transmitter.* Geophys. Res. Lett., 1992, 19(20), pp. 2071—2074.
12. W.L. Poulsen, U.S. Inan, and T.F. Bell, *A multiple-mode three-dimensional model of VLF propagation in the Earth-ionosphere waveguide in the presence of localized D region disturbances,* J. Geophys. Res, 1993, 98(A2), pp. 1705—1717.
13. N. Liu, *Multiple ion species fluid modeling of sprite halos and the role of electron detachment of O^- in their dynamics,* J. Geophys. Res.: Space Phys., 2012. 117(A3).
14. A. Luque, and F. Gordillo-Vázquez, *Mesospheric electric breakdown and delayed sprite ignition caused by electron detachment,* Nature Geosci., 2012, 5(1), pp. 22—25.
15. J.V. Rodriguez, U.S. Inan, and T.F. Bell, *D region disturbances caused by electromagnetic pulses from lightning,* Geophys. Res. Lett., 1992. 19(20), pp. 2067—2070.
16. N.G. Lehtinen, and U.S. Inan, *Possible persistent ionization caused by giant blue jets,* Geophys. Res. Lett., 2007, 34(8).

Antropogenic Ionospheric Disturbances in the Central Economic Region of Russia

Victor I. Zakharov[1,2], Yaroslav A. Ilyushin[1,3]

[1]Atmospheric Physics Department, Physical Faculty, Moscow State University, GSP-2, Lengory Moscow, 119992, Russia
[2]A.M.Obukhov Institute of Atmospheric Physics Russian Academy of Sciences Pyzhyovskiy pereulok, 3, Moscow, 119017, Russia
[3]Institute of Radio-engineering and Electronics, ulitza Mokhovaya, 11/7, Moscow, 125009, Russia

Introduction. Currently in the whole world big attention is paid to the state of natural environment and techniques of instrumental monitoring of it. Continuously growing human population and anthropogenic load on the nature, intensive exploitation and consumption of natural resources results in degradation of the natural environment. The most dramatic situations occur in highly populated areas

with well developed industrial and urban infrastructure, such as Central Economic Region of Russia.

For that reason, techniques of the instrumental monitoring of the atmospheric dynamics in the city and the region become especially important. These techniques should combine both in situ measurements and remote sensing of the atmospheric parameters, providing characterization of the environment in average at different scales.

Measuring and data processing technique. Method of detection of ionospheric disturbances, applied in this study, is based on the utilization of combination of two registered phases L1 and L2 of the signals of the Global Navigational Satellite System (GNSS) beacons and further signal filtration for the detection of waves with typical periods longer than 5 minutes [1—4]

$$I = \frac{1}{40.308} \frac{f_1^2 f_2^2}{f_1^2 - f_2^2} \left[\left(L_1 \lambda_1 - L_2 \lambda_2 \right) + K + \delta L \right], \quad (1)$$

where f_1, f_2 are operating frequencies of the Global Positioning System (GPS), respectively 1575.42 and 1227.6 MHz, L1, L2 are the signal phases at these frequencies, λ_1, λ_1 are the wavelengths, m. K is a constant due to phase definition ambiguity, δ L is an instrumental error of phase path difference measurement. The time derivative of the Total Electron Content (TEC) dI/dt is a key informative parameter of the method. This allows to detect quasi-periodical signals without elimination of the phase definition ambiguity.

For detection of the wave structures, the whole receiver network on the ground is structured into cells of three receiving stations each, at which the minimal data set sufficient for the processing is measured. For the analysis, series of measured TEC values (1), derived from phase measurements at each station in the cell, are used together with corresponding zenith and azimuth angles, known from sp3-files of navigational data. Assessment of the accuracy of the GPS interferometry technique and its modification [1, 5, 6], applied here, yields for the azimuth angle accuracy not worse ±15 degrees, i. e. the 30 degrees sector in the worst geophysical situation. Important property of the method is its selectivity. This means that only those traveling ionospheric disturbances (TID) are detected, which move in the directions, not coincident with the observation direction.

In the present work, TID parameters were retrieved from three point registration of GPS signals, registered on nine stations GPS receiving network of the Moscow region. The network included three IGS stations [7] and six stations of navigational and geodetic support system of Moscow region [8]. Analysis shows, that for the satisfactory results not less than 6—8 measuring cells of three stations each should be used in the given network configuration.

Maximal amplitude of electron concentration variations are observed at the height of maximal electron concentration of the F2 ionospheric layer [2, 3], which is assumed to be constant and equal to 250 km during the whole period under investigation [9]. The projection of crossing point of the TID moving direction and

level of maximal ionospheric concentration is called the sub-ionospheric point [1—4]. This technique allows determination if the TID position in the geographic coordinate system with the accuracy 0.5 degree or better [1, 6].

Ionospheric disturbances revealed with correlation technique are then verified by the cluster analysis [5]. In the work we separated the clusters of the structures, i.e. TID with similar characteristic, observed not less that in three cells simultaneously. In fact, cluster analysis enables effective filtering of the TID not only in the space of their positions in the ground projections, but also in the space of velocities and directions.

As indicators of the ionospheric perturbed state due to solar-terrestrial connections in this study, we considered geomagnetic indices and indices of the solar activity [9]. During the whole observational period, the indices Kp and Dst characterize the ionospheric situation as moderately perturbed and account for it in the interpretation of the obtained data.

Main results. In this work, we present the results of the continuous radio-interferometric analysis of GPS signals, registered during the summer period of 2010 year (97 days) on the Moscow regional GPS receiving network. We show that revealed TID group around the Moscow and form the ring-shaped pattern. We consider empirical functions of the TID parameters (motion velocity and observed periods). We show that observed distributions of TID are formed by acoustical-gravitational waves and can be connected with a specific thermal regime in Moscow region during the summer of 2010, in particular the urban heat island (UHI), caused by blocking anticyclone [10—12].

In the present study, we attempted to resolve internal structure of the TID spatial pattern, to retrieve the signatures of the corresponding structure of the heat source. In the Central Economic Region of Russia, the second largest industrial cluster except of Moscow city is Tula, the administrative center of Tula region separated from Moscow by a 200 km distance. Energy consumption of the Tula industrial cluster is roughly 10 times less than Moscow energy consumption. Thus we expect proportionally less efficiency of the TID generation by the Tula city. Both cities are located within the ring of TID, revealed in the Central Economic Region of Russia with our methods. Analysis of the internal structure is not easy task, because of the limited accuracy of the direction of the TID motion determination.

However, large amount of statistical data, collected in the 2010 summer (4000 events) allowed us to filter the raw data with better precision. We searched for the TID, which could be related to the acoustical-gravity waves coming from the source in the known location at 45012’ N; 37037’ E (Tula city). After that, we selected the most reliable data with minimal errors, which allow locate the source with the accuracy better than distance between Moscow and Tula cities.

Our analysis unambiguously shows inhomogeneous structure of the TID ring around the Moscow and reveals contributions of neighboring sources. For Tula, we estimate its TID generation efficiency and contribution to the total TID field at 5—6% level of the whole background. Note that it is a bit less than our expectations based on energetic budget estimate, which predict corresponding efficiency at 10% level.

The TIS identified by us as generated by Tula, also group in the ring structure. Despite not the best configuration of the Moscow GPS network in 2010, it was still capable to provide the statistical data sufficient for localization of different TID sources and assessment of their contributions.

Our analysis shows that local anthropogenically driven atmospheric processes have complicated structure and should not be regarded as a result of action of a single source. Therefore, obtained results are very promising, because give us a hope for well planned and developed experiment for localization and identification of separate TID sources with GPS interferometry methods.

Conclusions and remarks. Complicated structure of the TID ring-shaped pattern is established and determined from thorough data analysis. Contributions of regional industrial centers surrounding Moscow are separated and estimated from the common TID field, formed mostly by the Moscow city itself. Estimated efficiency of TID generation by local sources is in good agreement with theoretical expectations derived from energy budget considerations [13].

Obtained results indicate close interaction between atmospheric and ionospheric disturbances in Moscow region and surrounding regions, which can be related to mesoscale processes of air mass transport in the atmosphere.

Acknowledgments. This research was supported by the Russian Science Foundation grant 17-77-20087 "Study of long period perturbations in the ionosphere, lower atmosphere and ocean by means of GNSS sounding" and RFBR grant 16-05-01024 (ZVI, archive GPS-data analysis).

1. B Hoffman-Wellenhoft,GPS Theory and Practice.. New York, Springer-Verlag Vienna 1998.

2.E. L. Afraimovich and N. P. Perevalova, GPS-monitoring Earth's upper atmosphere. Irkutsk, SB RAS, 2006.

3. M. Hernandez-Pajares, J. M. Juan, and J. Sanz, Medium-scale travelling ionospheric disturbances affecting GPS measurements: Spatial and temporal analysis, *J. Geophys. Res.,* 2006, 111, A07S11, doi:10.1029/2005JA011474.

4. V. I. Zakharov and V. E. Kunitsyn, Regional features of atmospheric manifestations of tropical cyclones according to ground-based GPS network data, *Geomagnetism and Aeronomy,* 2012, 52 (4), pp. 533—545, doi: 10.1134/S0016793212040160.

5. V. I. Zakharov, and P. A. Budnikov, The Application of cluster analysis to the processing of GPS interferometry data, *Moscow University Physics Bull,* 2012*,* 67 (1), pp. 26—33, doi:10.3103/S0027134912010262.

6. Yu. V. Yasyukevich, V. I. Zakharov et al., The Response of the Ionosphere to the Tohoku_Oki Earthquake of March 11, 2011 as Estimated by Different GPS-Based Methods, *Geomagnetism and Aeronomy,* 2015, 55(1), pp. 108—117, doi: 10.1134/ S0016793214060218

7. http://www.sopac.ucsd.edu

8. The system of navigation and geodetic support of Moscow, http://sngo.mggt.ru

9. http://spidr.ngdc.noaa.gov/spidr/

10. G. I. Gorchakov, E. N. Kadygrov, V. E Kunitsyn et al., The Moscow heat island in the blocking anticyclone during summer 2010, *Doklady of the Russian Academy of Science. Earth Science section*. 2014, 456(II), pp. 736—740, doi: 10.1134/S1028334X14060233

11. V. I. Zakharov and G. I. Gorchakov, GPS observation of traveling ionospheric disturbances related to Moscow megacity, *Advances in Space Research*, 2017, 59(2), pp. 614—618.

12. V. I. Zakharov, V. E. Kunitsyn, G. I. Gorchakov, A Ring of Traveling Ionospheric Disturbances around Moscow Megapolis, *Doklady Earth Sci*., 2017, 472(2), pp. 241—243, doi: 10.1134/S1028334X17020258.

13. Ya. A. Ilyushin, V. I. Zakharov, A. L. Gavrik et al., Development of complex methods for regional atmospheric monitoring based on space-borne and ground-based registration of navigational signals, *Abstracts of the Seventh Moscow Solar System Symposium 7M-S3,* Moscow: Space Research Institute, 2016.

Contribution of Mathematical Approximations to Estimation of Parameters of Phase Frequency Dispersion for Transionospheric Radio Propagation

Dmitry V. Ivanov [1], Vladimir A. Ivanov [1], Natalia V. Ryabova [1], Maria I. Ryabova [2], Aleksey A. Kislitsin [1]

[1] Volga State University of Technology, Yoshkar-Ola, Russia
[2] Bauman Moscow State Technical University, Moscow, Russia

Introduction. At present there is an actual problem of expansion of the radio frequency band in the space communication systems and radar the Earth from space. However, it causes dispersive distortions of system characteristics of transionospheric channels and, as a result, distortion of signals. Solving this problem is impossible without a comprehensive study the effect of frequency dispersion at a new position. Frequency dispersion is related to the frequency dependence of phase speed of propagation of a wave in the medium. Differences the phase speeds of the spectral components of signals can lead to disturbances of the phase-frequency characteristics of spectrum and signal distortion, up to complete its "destruction" [1—6]. It is known that the dispersion is caused by the frequency dependence of the refractive index of a medium. Transionospheric propagation is possible at frequencies above the critical frequency of the ionosphere. Therefore transionospheric propagation theory has its own characteristics associated with this condition. They are manifested in the fact that the refractive index can be represented as form at the powers of the ratio of the plasma frequency to the frequency of propagation waves. The components of the refractive index are considered as approximations to the refractive index. In this regard, there is a need to study the contribution of each approximation at parameters of dispersion.

The **aim** of this research is study of the effects of frequency dispersion in transionospheric radio channels and estimate the contribution of each approximation at parameters of dispersion in the equations for the phase taper.

General framework of the theory of frequency dispersion of the phase taper of wave at transionospheric propagation. In general, in a channel with a limited frequency band B_{ch} and a central frequency $\bar{f} = (f_1 + f_2)/2$, the PFC can be presented as follows:

$$\varphi(\omega) = \varphi(\bar{\omega}) + \varphi'_{\omega} \cdot \Omega + \varphi''_{\omega} \cdot \frac{\Omega^2}{2!} + \varphi'''_{\omega} \cdot \frac{\Omega^3}{3!} + \ldots \approx$$
$$\approx \varphi(\bar{f}) + 2\pi\tau_{g|_0} \cdot (F) + \pi s_{|_0} (F)^2 + \frac{\pi}{3} v_{|_0} (F)^3, \quad F \in \left[-\frac{B_{ch}}{2}, \frac{B_{ch}}{2} \right] \tag{1}$$

In this case there is a phase dispersion of the 1st, 2nd and 3rd orders, where $\tau_{g|_0}$, $s_{|_0}$, $v_{|_0}$ dispersion parameters $F = f - \bar{f}$.

Studying significant distortions of transionospheric wideband signals requires to analyze equations of the refractive index and the phase taper [7—9]. It is known that in the equilibrium state, electrons perform an oscillatory motion in the plasma with a frequency called the plasma frequency. Transionospheric propagation is possible when the wave frequency exceeds the plasma frequency of the ionosphere maximum, i. e. $\left(\frac{\omega_p^2(z)}{\omega^2} \right) < 1$. In this case, gyrofrequency is neglected and the equation of the refractive index is represented using expansion in a Taylor series as a sum of powers of relation $\left(\frac{\omega_p^2(z)}{\omega^2} \right)$:

$$n(z) = \sqrt{1 - \left(\frac{\omega_p^2(z)}{\omega^2} \right)} \approx 1 - \frac{1}{2}\left(\frac{f_p^2(z)}{f^2} \right) - \frac{1}{8}\left(\frac{f_p^2(z)}{f^2} \right)^2 - \frac{1}{16}\left(\frac{f_p^2(z)}{f^2} \right)^3 \ldots =$$
$$= 1 - \frac{1}{2} \cdot \left(\frac{k \cdot N}{f^2} \right) - \frac{1}{8} \cdot \left(\frac{k \cdot N}{f^2} \right)^2 - \frac{1}{16} \cdot \left(\frac{k \cdot N}{f^2} \right)^3 \ldots \tag{2}$$

Then, the phase taper caused by the transionospheric propagation can be presented as follows:

$$\phi(\omega) = \frac{1}{c} \int_s \left[\omega \cdot n(\omega, z) \right] dz \approx \omega \int_s \frac{dz}{c} - \left[\frac{1}{f} \overbrace{\frac{\pi\kappa}{c} \int_s N_e(z) dz} + \frac{1}{f^3} \overbrace{\frac{\pi k^2}{4c} \int_s N_e^2(z) dz} + \right.$$

$$+\frac{1}{f^5}\overbrace{\frac{\pi k^3}{8c}\int_s N_e^3(z)dz}\Bigg] = \omega\int_s \frac{dz}{c} - \left[\frac{\alpha_1}{f} + \frac{\alpha_2}{f^3} + \frac{\alpha_3}{f^5}\right]. \quad (3)$$

We took the first three derivatives of the phase function with respect to the frequency at a point $\bar{f}$ to obtain the characteristics of frequency dispersion:

$$\tau_g(f) = \frac{d\varphi}{d\omega}(f) = \frac{1}{2\pi}\left[2\pi\int_s \frac{dz}{c} + \frac{\alpha_1}{f^2} + 3\frac{\alpha_2}{f^4} + 5\frac{\alpha_3}{f^6} + \ldots\right], \quad (4a)$$

$$s(f) = \frac{d\tau_g}{df}(f) = -\frac{1}{\pi}\left[\frac{\alpha_1}{f^3} + 6\frac{\alpha_2}{f^5} + 15\frac{\alpha_3}{f^7} + \ldots\right], \quad (4b)$$

$$v(f) = \frac{d^2\tau_g}{df^2}(f) = \frac{3}{\pi}\left[\frac{\alpha_1}{f^4} + 10\frac{\alpha_2}{f^6} + 35\frac{\alpha_3}{f^8} + \ldots\right]. \quad (4c)$$

The values $\tau_g(\bar{f}),\ s(\bar{f}),\ v(\bar{f})$ are the parameters of the channel phase dispersion at the fixed frequency $f = \bar{f}$.

Evaluate of significance of various approximations for dispersive characteristic oftransionospheric channel. Each of formulas (4a) — (4b) represents the sum of various approximations. Their significance is determined primarily by the frequency value. To optimize the calculations it is important to evaluate the frequency range for which individual approximations are important. Obviously, the first summand in (4) is independent of frequency and therefore does not effect the distortion of wideband signals. The second summand will be significant at high frequencies. Influence of the third and fourth summands will be significant with approach to a critical frequency of the ionosphere.

We investigated the contribution of approximations by numerical method. To evaluate the integrals in coefficients $\alpha_1, \alpha_2, \alpha_3$ it is necessary to calculate integrals of the profile of the electron density, its square and cube. To do this, we used a well-established model NeQuick [https://t-ict4d.ictp.it/nequick2]. The integrals of the profiles were calculated by rectangles method. In this case the region of the profile from 70 to 1000 km was divided into two parts from 70 to 500 and from 500 km to 1000 km. Then the first part was divided by points into equal parts with step 10 km, and the second part — with step 50 km. We used the following expressions:

$$\int_s N_e(z)dz = 10^4 \cdot \sum_{i=7}^{49} N_{ei} + 5\cdot 10^4 \sum_{i=50}^{59} N_{ei} \quad (5a)$$

$$\int_s N_e^2(z)dz = 10^4 \cdot \sum_{i=7}^{49} (N_{ei})^2 + 5\cdot 10^4 \sum_{i=50}^{59} (N_{ei})^2 \quad (5b)$$

$$\int_s N_e^3(z)dz = 10^4 \cdot \sum_{i=7}^{49}(N_{ei})^3 + 5 \cdot 10^4 \sum_{i=50}^{59}(N_{ei})^3 \quad (5c)$$

Calculations showed that the value of the integrals in the coefficients $\alpha_1, \alpha_2, \alpha_3$ will much vary at changing geophysical situation (time of day, season, solar activity). Therefore, the results of study of dependencies (4) will partials.

For general solutions that satisfy to requirements of engineering evaluations, we considered, dependences on relative frequencies, that are equal ratio of an absolute frequency to a critical frequency f_{cr} of the ionosphere $\hat{f} = f / f_{cr}$. Indeed, by adopting a simplified two-parameter model of the ionosphere, in which the parameters satisfy to condition: $\int_s N_e(z)dz = N_m \cdot H_1$ (where N_m — the density for the global maximum of profile, H_1 — effective thickness of the ionosphere), we can see that all ratios $\alpha_1 / f^2, \alpha_2 / f^4, \alpha_3 / f^6$ depend on the relative frequency, because $kN_m = f_{cr}^2$ and $\int_s N_e^2(z)dz = N_m^2 \cdot H_2$ and $\int_s N_e^3(z)dz = N_m^3 \cdot H_3$.

Hypothesis about the dispersion characteristics dependence on relative frequency was used to obtain a common solution. At first, significance of approximations for DC (4) was investigated with the use of the hypothesis. We used the comparison of exact and approximate solutions for dependences of DC on the relative frequency. The exact solution was obtained using the formula:

$$\tau(\hat{f}) = \frac{1}{c}\left(10^4 \cdot \sum_{i=7}^{49} \frac{1}{\sqrt{1 - \frac{1}{\hat{f}^2} \cdot \frac{f_{0i}^2}{f_{cr}^2}}} + 5 \cdot 10^4 \cdot \sum_{i=50}^{59} \frac{1}{\sqrt{1 - \frac{1}{\hat{f}^2} \cdot \frac{f_{0i}^2}{f_{cr}^2}}} + z_0 \right), \quad (6)$$

where f_0 — plasma frequency; z_0 — height of the start of layer.

The first (high frequency approximation), second and third approximations were calculated using the formulas:

$$\tau_1(\hat{f}) = \frac{z_s}{c} + \frac{\alpha_1}{2\pi \cdot \hat{f}^2 \cdot f_{cr}^2}, \quad (7)$$

$$\tau_2(\hat{f}) = \frac{z_s}{c} + \frac{1}{2\pi}\left(\frac{\alpha_1}{\hat{f}^2 \cdot f_{cr}^2} + \frac{\alpha_2}{\hat{f}^4 \cdot f_{cr}^4} \right), \quad (8)$$

$$\tau_3(\hat{f}) = \frac{z_s}{c} + \frac{1}{2\pi}\left(\frac{\alpha_1}{\hat{f}^2 \cdot f_{cr}^2} + \frac{\alpha_2}{\hat{f}^4 \cdot f_{cr}^4} + \frac{\alpha_3}{\hat{f}^6 \cdot f_{cr}^6}\right), \quad (9)$$

where z_s — distance from the Earth to the spacecraft.

The results of calculations of dependences of DC on the relative frequency for exact and approximate solutions are shown at Fig. 1.

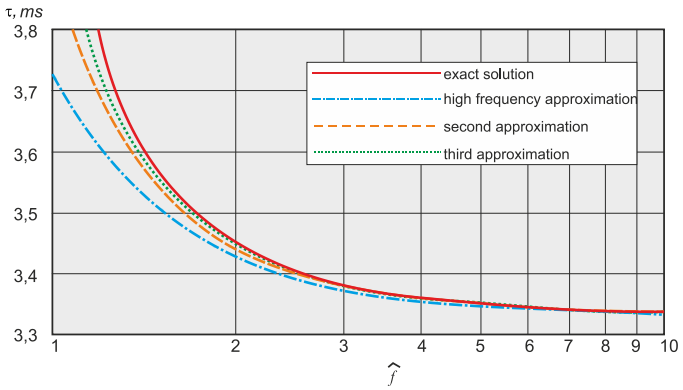

FIGURE 1. Dependencies of DC for exact solution and different approximations Analysis of the data showed that the first approximation is valid at $\hat{f} > 6$, the second $6 > \hat{f} > 4{,}5$ and the third $4{,}5 > \hat{f} > 3$.

Conclusions. We discussed the general framework of the theory of frequency dispersion of the phase taper. Formulas are obtained for components of dispersion through the approximation of a refractive index of a wave at a satellite-to-Earth link. Dependencies were obtained to evaluate dispersion parameters of various orders by the integral characteristics of electron density profile. It is shown that dependences of dispersion characteristics on the frequency ratio (critical frequency of the ionosphere to average channel frequency) have common features.

This work was supported by the grant № 15-07-05280 from the Russian Foundation for Basic Research; the grants № 8.2817.2017/ПЧ, № 3.4074. 2017/ПЧ from the Ministry of Education and Science of the Russian Federation.

1. D. V. Ivanov, V. A. Ivanov, N. N. Mikheeva et al., Propagation of broadband HF signals in a medium with nonlinear dispersion, *Journal of Communications Technology and Electronics*, 2015, 60(11), pp. 1205—1214.

2. V. A. Ivanov, D. V. Ivanov, M. I. Ryabova et al., Broadband signal distortion in the ionosphere, caused by nonlinear frequency dispersion, *Vestnik of Volga State University of Technology. Ser.: Radio Engineering and Infocommunication Systems*, 2013, 2(18), pp. 5—15.

3. D. V. Ivanov, V. A. Ivanov, N. V. Ryabova et al., Fiber material dispersion effect on a matched compression of an optical pulse with frequency modulation, *Proc. SPIE 10342, Optical Technologies for Telecommunications* 2016, 103420E, 2017, doi: 10.1117/12.2270754.

4. P.S. Cannon, K. Groves, D.J. Fraser et al., Signal distortion on VHF/UHF transionospheric paths: First results from the wideband ionospheric distortion experiment, *Radio Sci*., 41, RS5S40, doi:10.1029/2005RS003369.

5. P.K. Banerjee, R.S. Dabas, and B.M. Reddy, C and L band transionospheric scintillation experiment: Some results for applications to satellite radio systems*, Radio Sci.,* 1992, 27(6), pp. 955—969.

6. Kretov, N.V., T.Y. Ryshkina, and L.V. Fedorova, Dispersive distortions of transionospheric broadband VHF signals, *Radio Sci*., 1992, 27(4), pp. 491—495.

7. N.A. Armand, V.M. Smirnov, Distortion of radar pulses by the martin ionosphere, *Radio Science*, 2003, 38(5).

8. N.A. Armand, Propagation of broadband signals in dispersive media, *Journal of Communications Technology and Electronics*, 2003, 48(9), pp. 1045—1057.

9. K.G. Budden, Radiowaves in the ionosphere, Cabridge: Univ. press, 1961.

Effects of Ionospheric E-Layer Dynamo Current on the Daily Geomagnetic Field Variations

Osman Özcan[1], Ali Yeşil[1], Selçuk Sağır[2], and Kadri Kurt[1]

[1]Fırat University, Science Faculty, Department of Physics, 23119, Elazığ, Turkey
[2]Department of Electronic and Automation, Technical Sciences Vocational School, Mus Alparslan University, Mus, 49100, Turkey

Introductıon. Regular geomagnetic daily variations, result from electric currents flowing mainly in the E-region of the ionosphere. The ionosphere conducts because it is ionized by electromagnetic radiation from the Sun. The ionosphere carries electric currents because winds and electric fields drive ions and electrons in different directions. By day, the most ionospheric current flows in the E-layer at 100—l30 km height. At night, E-layer ionization almost disappears, at least at middle and low latitudes [1].

In this study, the magnetic field components generated by the ionospheric dynamo current have been calculated. The ionospheric parameters required for calculations were obtained from the International Reference Ionosphere (IRI) model. Daily and seasonal variations of magnetic field components have been examined separately for maximum and minimum sunspot number. The results were compared with the magnetic field components those measured at the Kandilli magnetic observatory.

The Current Generated in The Ionosphere. The force acting on the charged particle in the ionospheric plasma is given by;

$$m_\alpha \frac{dv_\alpha}{dt} = q_\alpha(E + v_\alpha \times B) - m_\alpha \nu_\alpha (v_\alpha - U), \quad (1)$$

where ν is the collision frequency, U is the horizontal neutral wind velocity, α denotes e, and i represents the electron and ion respectively. We assumed that the z-axis of the coordinate system with its origin located on the ground is vertically upwards. The x- and the y-axis are geographically eastward and northward in the northern hemisphere, respectively.

The ambient magnetic field in the northern hemisphere is given by following equation [2];

$$\mathbf{B} = (\text{BsinD cosI})\,\hat{x} + (\text{BcosI cosD})\,\hat{y} - (\text{BsinI})\,\hat{z}. \quad (2)$$

Since the declination angle (D) of the geomagnetic field is small (≈3.5) for selected geographic coordinate (39° N, 40° E), the magnetic field becomes

$$\mathbf{B} = (\text{BcosI})\,\hat{y} - (\text{BsinI})\,\hat{z}\ , \quad (3)$$

where I is the dip angle. For the steady-state condition, the current density can be obtained from Eq.1 as follow:

$$\mathbf{J} = \frac{Ne^2}{m\nu_\alpha}\mathbf{E} + \frac{\omega_{c\alpha}}{\nu_\alpha}\mathbf{J}_\alpha \times \hat{a} + Ne\mathbf{U}\ , \quad (4)$$

where N is the electron density, $\omega_{c\alpha}$ = |eB/m| is the gyro-frequency and $\hat{a}$ is the unite vector. From the solution of the Eq. 4 one can obtain the height integrated east-west ($\mathbf{J}_{\Sigma x}$) and south-north ($\mathbf{J}_{\Sigma y}$) current densities as follow [3];

$$\mathbf{J}_{\Sigma x} = B\Sigma_1 U_x - B\frac{\Sigma_2}{sinI}U_y + \Sigma_1' E_x - \frac{\Sigma_2'}{sinI}E_y, \quad (5)$$

$$\mathbf{J}_{\Sigma y} = B\frac{\Sigma_2}{sinI}U_x + B\frac{\Sigma_1}{sin^2 I}U_y + \frac{\Sigma_2'}{sinI}E_x + \frac{\Sigma_1'}{sin^2 I}E_y, \quad (6)$$

where $\Sigma_1 = \int_{h_1}^{h_2}\frac{\nu_i}{\omega_{ci}}\sigma_1 dh$, $\Sigma_2 = \int_{h_1}^{h_2}\frac{\nu_i}{\omega_{ci}}\sigma_2 dh$, $\Sigma_1' = \int_{h_1}^{h_2}\sigma_1 dh$ and $\Sigma_2' = \int_{h_1}^{h_2}\sigma_2 dh$, σ_1 and σ_2 are ionospheric Pedersen and Hall conductivity.

The eastward (B_x) and northward (B_y) components of the magnetic field and the integrated layer current densities J_Σ are related by the following equations:

$$B_x \approx -f\mu_0 J_{\Sigma y}, \quad (7)$$

$$B_y \approx f\,\mu_0\,J_{\Sigma x}. \quad (8)$$

The value of f is about 0.5 [3].

Numerical Solutions and discussions. The magnetic field generated by the ionospheric E-layer current has been calculated at (41^0 N, 29^0 E) geographic coordinate for equinox and solstice days by using equations (7—8). The used ionospheric parameters for calculation have been obtained by using IRI-model. Since in the ionospheric E-layer $\nu_{ei} \ll \nu_{en}$ and $\nu_{ie} \ll \nu_{in}$ the electron and ion collision frequencies were taken as: $\nu_e = \nu_{en} = 5.4 \times 10^{-16} N_n T_e^{1/2}$, $\nu_i = \nu_{in} = 5.4 \times 10^{-17} N_n (T_i + T_n)^{1/2}$, where N_n, T_e, T_n and T_i are the neutral density, electron, neutral and ion temperature respectively. The expressions of the σ_1 and σ_2 conductivities of (Aydoğdu and Özcan, 1996) have been used in calculations. The eastward (E_x) and northward (E_y)

components of electric field taken from [5]. The U_x and U_y components of neutral winds have been calculated by using the equations of [4]. The height-integrated conductivities (Σ_1, Σ_2, Σ_1' , Σ_2') have been calculated by integrating the conductivities σ_1 and σ_2 with 5 m height interval from 90 to 150 km.

The eastward conponents of magnetic field produced by ionosheric dynamo current and measured geomagnetic field are given in Fig.1. As can be seen from the figures, there is a strong relationship between the magnetic field generated by the dynamo current and the measured geomagnetic field. For the selected geographic coordinates (41°N, 29°E) the sunrise and sunset times are approximately 04.00 and 16.00 UT. This result clearly shows that the source of the change of the geomagnetic field in the daytime hours is the ionospheric E-layer current.

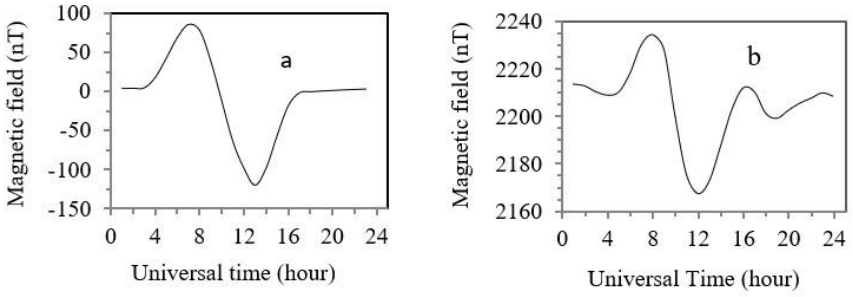

FIGURE 1. The daily variation of eastward magnetic fields producced by dynamo current and measured (b) (21 March).

The daily variation of nortward componenet magnetic fields are given in Fig. 2. As can be seen the south-north component magnetic field has not been much affected by the ionospheric dynamo current. This result is in agreement with the results of Malin et.al. [6].

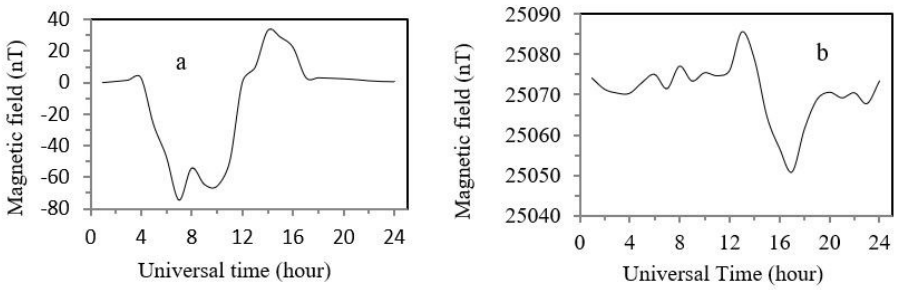

FIGURE 2. The daily variation of nortward magnetic fields producced by dynamo current and measured (b) (21 March).

The diurnal variation of eastward magnetic fiels for June 21 are given in Fig. 3. The daily variation in the magnetic field for June 21 is greater than the change on the Murch 21. This is an expected result, because the ionospheric electron density in June is greater than the values in March for the selected geographic coordinate (41 N, 29 E).

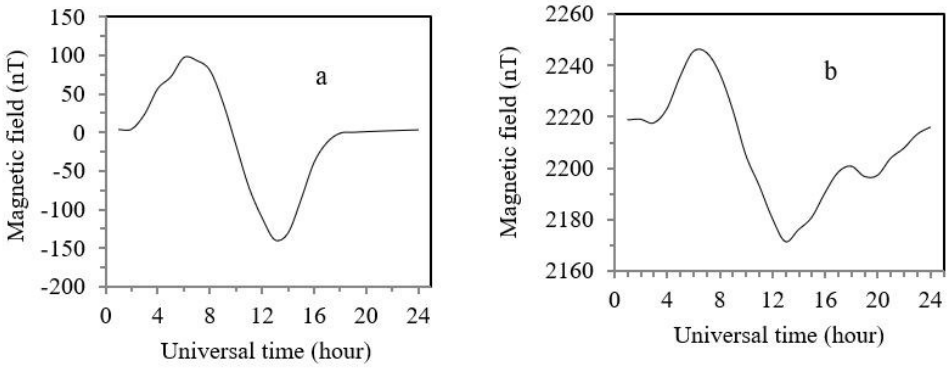

FIGURE 3. The daily variation of eastwar magnetic fields producced by dynamo current and measured (b) (21 June).

As a result, it is clear that the source of the daily variation of the geomagnetic field is the dynamo current in the ionosphere E-layer.

Acknowledgements. We are indebted to Dr. B. Tank and Dr. C. Çelik for sending the magnetic field data.

1. H. Rishbeth, The ionospheric E-layer and F-layer dynamo-a tutorial review, *J. Atmos. Terr. Phys.,* 1997, 59, pp. 1873—1880.

2. H. Rishbeth, Thermospheric winds and the F region: a review, *J. Atmos. Terr. Phys.,* 1972, 34, pp. 1—47.

3. O. Özcan and M. Aydoğdu, Possible effects of the total solar eclipse of August 11, 1999 on the geomagnetic field variations over Elazığ-Turkey, *J. Atmos. Terr. Phys.,* 2004. 66, pp. 997—1000.

4. O. Özcan and M. Aydoğdu, Electric conductivty of the topside ionospheric plasma over Turkey, *Doğa-Tr.J. of Physics*, 1991, 30, pp. 1—9.

5. J. Du and R. J. Setening, Simulating the ionospheric dynamo-I simulation model and flux tube integrated conductivities. *J. Atmos. Terr. Phys.,* 1999, 61, pp. 913—923.

6. S. R. C. Malin, O. Özcan, S. B. Tank et al., Geomagnetic signature of the 1999 August 11 total eclipse, *Geophys. J. International,* 2000, 140, F13—F16.

Comparison of F10.7 Solar Flux and QBO Effects on the Neutral Temperature of Lower Ionosphere

Selçuk Sağır[1], Ramazan Atıcı[2], Osman Özcan[3],and Ali Yeşil[3]

[1]Department of Electronic and Automation, Technical Sciences Vocational School, Mus Alparslan University, Mus, 49100, Turkey
[2]Faculty of Education, Mus Alparslan University, Mus, 49250, Turkey
[3]Department of Physics, Science Faculty, Firat University, Elazığ, 23000, Turkey

Introduction. The Earth atmosphere is divided into various regions according to temperature, physical processes and chemical components. It is defined as troposphere, stratosphere, mesosphere, thermosphere and exosphere according to temperature. According to chemical components, it has been defined as ozonosphere, ionosphere, heliosphere and protonosphere. The ionosphere is separated into D, E and F regions according to electron density; and according to latitude, into low latitude (or equator) regions (0—30 latitude), mid-latitude (30—60 latitude) and high-latitude (60—90 latitude) [1, 2]. The physical and chemical processes in each region are different [3, 4]. The processes in the equator region are more complicated than the processes in other regions. For this reason, investigating the ionosphere parameters (Tn, TEC, NmF2, τ, ..) in low latitude areas is extremely important [5]. Neutral temperature has nearly 250^{o} K value at 50 km altitude, which is the lower boundary of the ionosphere. Tn temperature starts to decrease from this altitude and gains an irregular structure at nearly 75 km altitude (the upper D region of the ionosphere), this irregularity increases between 80 and 120 km (E-region — Dynamo region) [6]. The source of neutral temperature in the E-region is mainly the Joule and particle heating [7].

Although the main source that is influential on ionosphere parameters in the upper atmosphere is the Sun, many studies were conducted on the effects of meteorological processes on this region [8—12]. It was claimed that the Tn temperature — as well as Mesosphere lower thermosphere (MLT) — is affected by thunderstorms, earthquake and atmospheric waves (Gravity, Inertia gravity, Rossby Gravity and Kelvin waves) that occur in lower atmosphere [13—19]. In addition, it was also mentioned in a previous study [20] that the effects of solar processes and meteorological processes that occur in mesosphere region on ionosphere are comparable.

In the present study, comparison of stratospheric QBO and F10.7 solar flux effects on neutral temperature in MLT region were made by statistical regression analysis. It is also aimed that MLT region parameters can obtain more accurate results by adding stratospheric QBO to the "NRLMSISE-00" model, which is widely used to obtain ionospheric parameters.

Material and Method. In this study, the linear multiple regression model has been used. In linear multiple regression model, firstly the unit root test to determine the stability of independent variables (F10.7 solar flux and QBO) and dependent variable (Tn) is made. After the stability of the variable is ensured, in the second step is checked whether there is a long-term relation between the variables with co-integration test. If there is a long-term relation between the variables, the relation coefficients of the variables are obtained with the regression model, which is the third step. The detailed information on these tests has been given Sağır et al. [17, 18]. By considering these studies as the reference, the regression equation used is given as follows:

$$Tn=\beta_0+\beta_1(F10.7)+\beta_2 D(QBO)+\varepsilon_t \quad (1)$$

where, β_0 is constant, β_s are coefficients of the independent variables, ε_t is the error term.

Results and Discussions. In this study, the Tn data received from http://ccmc.gsfc.nasa.gov/modelweb/models/nrlmsise00.php for 01/2007—08/2015 period; the F10.7 data received from http://omniweb.gsfc.nasa.gov/form/dx1.html; and the QBO data received from http://www.geo.fu-berlin.de/en/met/ag/strat/produkte/qbo/ were analyzed by statistical linear multiple regression model. As a result of the analyses, the effects of QBO and F10.7 solar flux on Tn were compared. As QBO data were obtained monthly, the other variables were also regulated monthly and used in the model.

In Fig. 1-a, it is clearly seen that in years when the western values (positive) of QBO, which is another independent variable, are maximum, there are small phase differences (approximately 0—30 days) and Tn has maximum values. It is possible to claim that, in years when QBO is maximum in eastern values (negative)-except for 2009-, all the Tn values decrease.

The changes of Tn and F10.7 solar flux parameters in time are given in Fig. 1-b. It is seen that in years when F10.7 solar cycle was minimum (2007—2011) there are small values. During this cycle, it is seen that the changes in Tn are not different from the period when F10.7 is maximum. The F10.7 and Tn changes are extremely similar in rising phase of the solar cycle (2009—2013), and in 06/2011—07/2012 period. In addition, in solar maximum years, a strong positive similarity between the variables is observed in 06/2013—08/2015.

After the stationary of the variables were ensured by stationary analysis, the issue of whether there is a long-term relation or not was investigated by the model established with Equation (1). Then, the regression coefficients that show the effects of independent variables on dependent variable (Tn) were obtained. Table 1 shows the regression analysis results for Equation 1. The values given at the bottom of the table and the values showing the significance of the coefficients (the values in brackets) indicate the accuracy of the results obtained by the model established, because the Durbin Watson test results must be between 1.5 and 2.5; and the Prob. (F-statistics) test values must be lower than 0.05; and the White Het. test results must be bigger than 0.05. It is observed here that the three tests ensure the reference values.

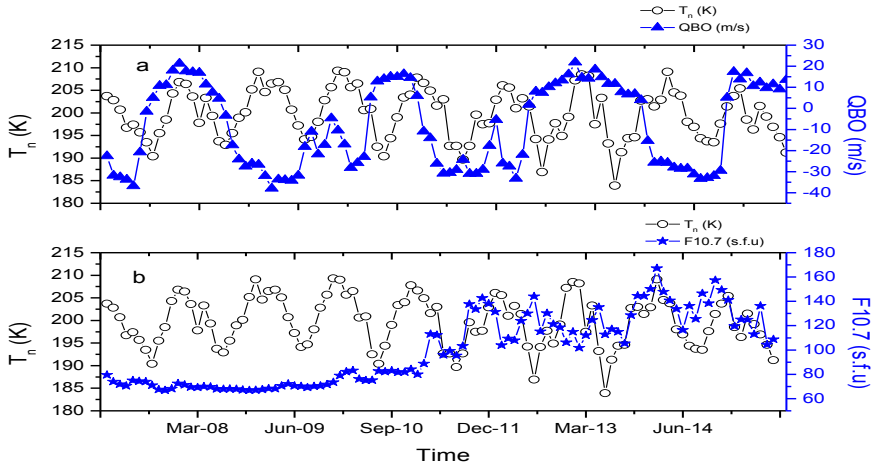

FIGURE 1. The change in time at the MLT region of neutral temperature (Tn) with QBO (a) and F10.7 solar flux (b).

TABLE 1. Regression analysis results for the Model (Eq.1).

Coefficients Model Results	
c	201.83 (0.000)*
β_1 (F10.7)	-0.028 (0.002)**
β_2 (D(QBO))	0.064 (0.094)*
R^2	0.64
Adj. R^2	0.62
Durbin Watson	1.586
Prob. (F-	(0.000)
White Het.	(0.373)

*,**,*** represents the significant level at 1%, 5%, and 10%, respectively.

As it may be observed in the table, there is a negative relation between F10.7 solar flux and Tn temperature value. This situation is stated with the negative sign of β_1 in the table. An increase/ a decrease of 1s.f.u occurred in F10.7 solar flux causes a decrease / an increase at a rate of 0.028^o K in Tn. These results show that F10.7 solar flux may influence ionospheric Tn.

It is observed that there is a positive relation between QBO and Tn. This situation is shown with the positive sign of β_1 in the table. An increase/ a decrease at a rate of 1m/s occured in QBO causes an increase/decrease at a rate of 0.064^o K in Tn. In the literature, Forbes et al. (2008) demonstrated that daily and semi-daily

migration tides caused 8—18 K and 6—14 K variations in mesospheric heights, respectively, and that these daily and semi-daily migration tides originate from QBO. Thus, QBO may have an effect as obtained in this study on the ionospheric temperature. This effect of the QBO can either be occurred by modulating the tidal waves in the MLT region or by the momentum carried by particularly small-scale gravity waves [21]. The latter option is a more likely mechanism because the QBO is known to carry as energy and momentum up to the MLT region through atmospheric waves. Also, it is expressed that QBO transported from the stratosphere to mesosphere by atmospheric waves can modulate the thermospheric dynamics [22] and the presence of a QBO signal at the amplitudes of the tides in the MLT region [23—25]. It is observed that nearly 62% of the changes that occur in neutral temperatures at 90 km altitude, which is the upper border of the D region and the lower border of the E region of ionosphere may be explained with QBO and F10.7 solar flux. This result support the assumption claiming that especially the lower regions of ionosphere are affected both by meteorological and solar processes.

In addition, these results are consistent with the results claiming that the sources coming from below are more influential than the solar sources at altitudes up to the mesosphere, and forces stemming from the Sun and the atmosphere are comparable at mesospheric altitudes [20]. In addition, [26] stated that meteo–rological processes from lower atmosphere are the most probable cause of ionospheric disturbances in the upper atmosphere and affect the dynamics of ionospheric parameters considerably.

Acknowledgments We thank OMNIweb service for F10.7 data, Freie Universitat Berlin for QBO data and Community Coordinated Modeling Center NRLMSIS-00 atmosphere model for neutral temperature data.

1. R. Schunk and A. Nagy, *Ionospheres: physics, plasma physics, and chemistry,* Cambridge university press, 2009, 628 p.

2. A. YEŞİL, S. SAĞIR, and K. Kadri, The Behavior of the Classical Diffusion Tensor for Mid-Latitude Ionospheric Plasma*, Bitlis Eren Üniversitesi Fen Bilimleri Dergisi*, 2016, **5**(2), pp. 123—127.

3. R. D. Hunsucker and J. K. Hargreaves, *The high-latitude ionosphere and its effects on radio propagation,* Cambridge University Press, 2003, 638 p.

4. S. Kumar, A. K. Singh, and J. Lee, Equatorial Ionospheric Anomaly (EIA) and comparison with IRI model during descending phase of solar activity (2005—2009)*, Adv. Space Res*., 2014, 53(5), pp. 724—733.

5. K. Venkatesh, P. V. S. Rama Rao, D. S. V. V. D. Prasad et al., Study of TEC, slab-thickness and neutral temperature of the thermosphere in the Indian low latitude sector*, Ann. Geophysicae*, 2011, 29(9), pp. 1635—1645.

6. Y. Y. Sun, K.-I. Oyama, J. Y. Liu et al., The neutral temperature in the ionospheric dynamo region and the ionospheric F region density during Wenchuan and Pingtung Doublet earthquakes*, Nat. Hazards Earth Syst. Sci*, 2011, 11, pp. 1759—1768.

7. S. Maeda, S. Nozawa, M. Sugino, et al., Ion and neutral temperature distributions in the E-region observed by the EISCAT Tromsø and Svalbard radars, *Ann. Geophysicae*, 2002, 20, pp. 1415—1427, doi: 10.5194/angeo-20-1415-2002.

8. W. Tang, X.-H. Xue, J. Lei, and X.-K. Dou, Ionospheric quasi-biennial oscillation in global TEC observations*, J. Atmos. Sol.-Terr. Phys.*, 2014, 107, pp. 36—41.

9. E. M. Apostolov, Quasi-Biennial Oscillation in Sunspot Activity, *Bulletin of the Astronomical Institutes of Czechoslovakia*, 1985, 36(2), pp. 97—102.

10. B. E. Soukharev and L. L. Hood, Possible solar modulation of the equatorial quasi-biennial oscillation: Additional statistical evidence, *J.Geophys. Res.*, 2001, 106(D14), pp. 14855—14868.

11. E. Yigit, P. Koucká Knížová, K. Georgieva, and W. Ward, A review of vertical coupling in the Atmosphere-Ionosphere system: Effects of waves, sudden stratospheric warmings, space weather, and of solar activity, *J. Atmos. Sol.-Terr. Phys.*, 2016, 141, pp. 1—12.

12. E. Yigit and A. S. Medvedev, Internal wave coupling processes in Earth's atmosphere, Adv. Space Res., 2015, 55(4), pp. 983—1003.

13. M. P. Baldwin, L. J. Gray, T. J. Dunkerton et al., The quasi-biennial oscillation, *Rev.Geophys.*, 2001, 39(2), pp. 179—229.

14. R. Atıcı, E. Güzel, M. Canyılmaz, and S. Sağır, The effect of lightning-induced electromagnetic waves on the electron temperatures in the lower ionosphere, *Kuwait J. Science*, 2016, 43(4), pp. 143—149.

15. R. Atıcı and S. Sağır, The effect of QBO on foE, *Adv. Space Res.*, 2017, 60(2), pp. 357—362.

16. K. Kurt; A. Yeşil, S. Sağir, and R. Atici, The Relationship of Stratospheric QBO with the Difference of Measured and Calculated NmF2, *Acta Geophysica*, 2016, 64(6), pp. 2781—2793.

17. S. Sağır, S. Karatay, R. Atici et al., The relationship between the Quasi Biennial Oscillation and Sunspot Number, *Adv. Space Res*., 2015, 55(1), pp. 106—112.

18. S. Sağır, R. Atıcı,O. Özcan, and N. Yüksel, The effect of the stratospheric QBO on the neutral density of the D region, *Ann. Geophysics*, 2015, 58(3).

19. J. Lastovicka, Forcing of the ionosphere by waves from below, *J. Atmos. Sol.-Terr. Phys.*, 2006, 68(3-5), pp. 479—497.

20. J. Lastovicka, On the role of solar and geomagnetic activity in long-term trends in the atmosphere-ionosphere system, *J. Atmos. Sol.-Terr. Phys*., 2005, 67(1—2), pp. 83—92.

21. D. Pancheva and P. Mukhtarov, Atmospheric tides and planetary waves: Recent progress based on SABER/TIMED temperature measurements (2002—2007), *Aeronomy of the Earth's Atmosphere and Ionosphere,* Springer, 2011, pp. 19—56.

22. A. K. Smith, Global dynamics of the MLT, *Surv. Geophys.*, 2012, 33(6), pp. 1177—1230.

23. J. Emmert, Thermospheric mass density: A review, *Adv. Space Res*., 2015, 56(5), pp. 773—824.

24. J. Oberheide, J. M. Forbes, K. Häusler et al., Tropospheric tides from 80 to 400 km: Propagation, interannual variability, and solar cycle effects, *J. Geophy.Res.: Atmospheres*, 2009, 114(D1).

25. Q. Wu, D. A. Ortland, S. C. Solomon et al., Global distribution, seasonal, and inter-annual variations of mesospheric semidiurnal tide observed by TIMED TIDI, *J. Atmos. Sol.-Terr.l Phys.*, 2011, 73(17), pp. 2482—2502.

26. O. Borchevkina and I. Karpov, Ionospheric irregularities in periods of meteorological disturbances, *Geomagn. Aeron*., 2017, 57(5), pp. 624—629.

The Trace of Matrix of the Loss-Tangent Tensor for the Cold Ionosphere Plasma in Northern Hemisphere

Ali Yeşil[1], Kadri Kurt[1], Osman Özcan[1], and Selçuk Sağir[2]

[1]Department of Physics, Science Faculty, Firat University, Elazığ, 23000, Turkey
[2]Department of Electronic and Automation, Technical Sciences Vocational School, Mus Alparslan University, Mus, 49100, Turkey

Introduction. The word "polarization" is used in two senses to mean: firstly the dipole moment per unit volume of medium; and secondly the state of polarization of wave. When there is any possibility of confusion these shall refer to two magnitudes as "the volume-polarization and the wave — polarization" respectively. It is interesting to note that the two meanings, now thought of quite differently, originated in the same idea that of producing opposite polarity at opposite ends of line. The relation to the volume polarization is obvious. In relation to wave-polarization the term arose when it was thought that light was the corpuscles in nature, and to explain the facts of double refraction it was suggested that the corpuscles acquired a polarity along a certain direction, known as the direction of polarization. From a detailed analysis of the response of the charge carriers to the oscillating **E** and **B** fields, one can deduce a linear relationship between the waves' electric field **E** and the polarization **P** [5—10].

Many researchers studied the electric currents and conductivities in ionosphere both theoretically and experimentally until today. Especially it could accept as the basic the paper of Barker, W. G. and Martyn, D. F., (1953). This paper has examined the electric conductivities and currents in ionosphere in detail such as the dynamo theory and height-integrated currents. Then, Maeda, (1977), Zhuang and Roble (1984), Takeda and Araki (1984) and Rasmussen et al. (1988) have investigated ionosphere conductivity at low latitudes. Fuller and Evans (1987), Nielsen et al. (1988) have improved some experimental models at dip equator. But all of these were used cold plasma approximation in ionospheric plasma. On the other hand, although the ionospheric plasma become a weak fluid conductive, it could show some dielectric properties with respect to some conditions. In this case, it is necessary to know in which conditions it is inductive or capacitive. About the conductivity of ionospheric plasma has been done many papers until today but there is not a considerable study about the volume polarization properties of ionospheric plasma in literature. Due to this, the studies associated with the dielectric of ionospheric plasma are lack. The real is that the dielectric structure of any medium is determiner of the refractive index of medium and diffusion properties. Therefore, it directly related to the propagation of electromagnetic waves and very important for ionospheric plasma [1—10].

1. Volume polarization tensor for cold ionosphere plasma in Northern Hemisphere. We obtained the volume polarization tensor for the cold plasma conditions in ionospheric plasma and compared the magnitudes of volume polarization constants with respect to Fig. 1. The ambient magnetic field in northern hemisphere is given by [1—4].

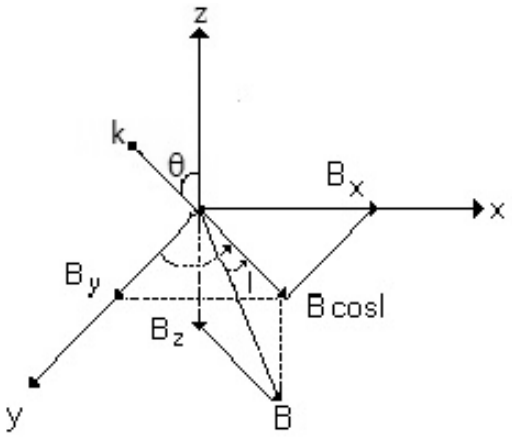

FIGURE 1. The geometry of Earth's magnetic field for Northern hemisphere [1, 2, 10].

$$\mathbf{B}=B_x\mathbf{a}_x+B_y\mathbf{a}_y+B_z\mathbf{a}_z \quad (1)$$

Where $B_x=B_0CosI\ Sind$, $B_y=B_0CosI\ Cosd$ and $B_z= -B_0SinI$. I and d are the magnetic dip and the magnetic declination angles, respectively.

The force acting on electron in the cold plasma is given by

$$m\, d\ddot{\boldsymbol{r}}/dt = -e(\boldsymbol{E}+\ddot{\boldsymbol{r}}\times\boldsymbol{B}) - mv\ddot{\boldsymbol{r}} \quad (2)$$

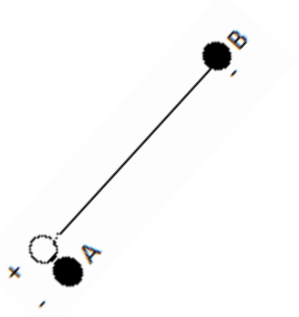

FIGURE 2. Movement of an electron from A to B is equivalent to the addition of a dipol [9].

In which **r**, **B**, **E** and ν (=electron-ion+electron-notr collisions frequency) are average electron velocity, Earth magnetic field, electric field and electron collisions frequency, respectively. In here, all of fields change like $e^{i\,(\omega t-\mathbf{k}.\mathbf{r})}$. The movement of an electron from a point A to point B is equivalent to leaving the original electron undisturbed at A and adding a dipole as shown in the Fig. 2 so that it cancels the original charge at A.

If there are N electron per unit volume, and if all move through equal distance **r**, equivalent dipole moment, which is the polarization is given by [5—9]

$$P=Ner=\varepsilon_0\chi E \quad (3)$$

The movements of the electrons and the polarization **P** is produced by the electric field of wave **E**. If there is no applied magnetic field**,** and then **P** and **E** are parallel otherwise **P** and **E** are not parallel. If we use Eqs. (1—3) together, Volume polarization for northern hemisphere is obtained by

$$(i\omega\upsilon-\omega^2)P_x-i\omega\omega_{cz}P_y+i\omega\omega_{cy}P_z=\frac{Ne^2}{m}E_x \quad (4)$$

$$(i\omega\upsilon-\omega^2)P_y+i\omega\omega_{cz}P_x-i\omega\omega_{cx}P_z=\frac{Ne^2}{m}E_y \quad (5)$$

$$(i\omega\upsilon-\omega^2)P_z-i\omega\omega_{cy}P_x+i\omega\omega_{cx}P_y=\frac{Ne^2}{m}E_z \quad (6)$$

From here,

$$P_x=\frac{a\left[(i\upsilon\omega-\omega^2)^2+\omega^2\omega_{cx}^2\right]}{A+iB}E_x+\frac{a\left[i\omega\omega_{cz}(i\upsilon\omega-\omega^2)\ -\omega^2\omega_{cx}\omega_{cy}\right]}{A+iB}E_y+\frac{a\left[-i\omega\omega_{cy}(i\upsilon\omega-\omega^2)\ -\omega^2\omega_{cx}\omega_{cz}\right]}{A+iB}E_z \quad (7)$$

$$P_y=\frac{-a[i\omega\omega_{cz}(i\upsilon\omega-\omega^2)+\omega^2\omega_{cx}\,\omega_{cy}]}{A+iB}E_x+\frac{a\left[(i\upsilon\omega-\omega^2)^2-\omega^2\omega_{cy}^2\right]}{A+iB}E_y+\frac{a\left[i\omega\omega_{cx}(i\upsilon\omega-\omega^2)\ -\omega^2\omega_{cy}\omega_{cz}\right]}{A+iB}E_z \quad (8)$$

$$P_z=\frac{a[i\omega\omega_{cy}(i\upsilon\omega-\omega^2)-\omega^2\omega_{cx}\,\omega_{cz}]}{A+iB}E_x+\frac{a\left[-i\omega\omega_{cx}(i\upsilon\omega-\omega^2)\ -\omega^2\omega_{cz}\omega_{cy}\right]}{A+iB}E_y+\frac{a\left[(i\upsilon\omega-\omega^2)^2-\omega^2\omega_{cz}^2\right]}{A+iB}E_z \quad (9)$$

If all the polarization coefficients are rearranged both real and imaginary, P_x, P_y and P_z are obtained as.

$$P_x=(\propto_{11R}-i\propto_{11S})E_x+(\propto_{12R}+i\propto_{12S})E_y+(\propto_{13R}+i\propto_{13S})E_z \quad (10)$$

$$P_y=(\propto_{21R}+i\propto_{21S})E_x+(\propto_{22R}-i\propto_{22S})E_y+(\propto_{23R}-i\propto_{23S})E_z \quad (11)$$

$$P_z=(\propto_{31R}-i\propto_{31S})E_x+(\propto_{32R}+i\propto_{32S})E_y+(\propto_{33R}-i\propto_{33S})E_z \quad (12)$$

Volume-polarization tensor could be obtained depending the permittivity coefficient (χ) of inospheric plasma as follow

$$\begin{pmatrix}P(x)\\P(y)\\P(z)\end{pmatrix}=\varepsilon_0\begin{pmatrix}\chi_{11}&\chi_{12}&\chi_{13}\\\chi_{21}&\chi_{22}&\chi_{23}\\\chi_{31}&\chi_{32}&\chi_{33}\end{pmatrix}\begin{pmatrix}E_x\\E_y\\E_z\end{pmatrix} \quad (13)$$

2. The loss-tangent tensor in the ionospheric plasma. The electric flux (**D**) of any medium is given by well-known equation as follow [5—9].

$$D=\varepsilon_0 E+P \tag{14}$$

If Eqs. (11—13) is substituted into eq.4, then the tensor for dielectric is obtained by

$$\begin{pmatrix}\varepsilon_{xx} & \varepsilon_{xy} & \varepsilon_{xz}\\ \varepsilon_{yx} & \varepsilon_{yy} & \varepsilon_{yz}\\ \varepsilon_{zx} & \varepsilon_{zy} & \varepsilon_{zz}\end{pmatrix}\begin{pmatrix}E_x\\E_y\\E_z\end{pmatrix}=\varepsilon_0\begin{pmatrix}1 & 0 & 0\\0 & 1 & 0\\0 & 0 & 1\end{pmatrix}\begin{pmatrix}E_x\\E_y\\E_z\end{pmatrix}\begin{pmatrix}\delta_{11} & \delta_{12} & \delta_{13}\\ \delta_{21} & \delta_{22} & \delta_{23}\\ \delta_{31} & \delta_{32} & \delta_{33}\end{pmatrix}\begin{pmatrix}E_x\\E_y\\E_z\end{pmatrix} \tag{15}$$

In which, the coefficients of dielectric permittivity having both the real and imaginary in ionospheric plasma are form as follow.

$$\varepsilon=\varepsilon'-i\varepsilon''. \tag{16}$$

Where, ε' defines the refractive index of medium and ε'' defines the so- called loss tangent and is related to the attenuation constant propagating any medium for electromagnetic wave. The expression of the loss-tangent is given as follow [7].

$$tan(\theta)=\frac{\varepsilon''}{\varepsilon'}$$

From here, the loss-tangent tensor with respect to eqs.(15,16) in ionospheric plasma are obtained by

$$tg(\theta)=\begin{pmatrix}tan(\theta)_{xx} & tan(\theta)_{xy} & tan(\theta)_{xz}\\ tan(\theta)_{yx} & tan(\theta)_{yy} & tan(\theta)_{yz}\\ tan(\theta)_{zx} & tan(\theta)_{zy} & tan(\theta)_{zz}\end{pmatrix} \tag{17}$$

3. Numerical analysis and results. In this study, the trace of matrix for loss-tangent was calculated both local time and latitudes by using Eq.(17) and Fig. 1 as local time for 1990 year. The ionospheric parameters used for calculation were obtained by using the IRI model. According to the accepted conditions,

For same conditions, the real and imaginer parts of the conductivity have been calculated. According to Fig. 1, in this context, the real geometry of Earth's magnetic field was used for northern hemisphere for ionospheric plasma.

At the accepted conditions, the change of the components of volume polarization tensor is given by Fig. 3 with latitude for march 21 — September 23 months. According to it, the magnitude of the diagonal elements of tensor are equal to each other ($\alpha_{xx} \cong \alpha_{yy} \cong \alpha_{zz}$) for two every seasons. The diagonal elements have maximum value around equator latitudes (10°S—10°N). The behavior of diagonal elements is similar to soliton wave form for both local time and latitudes in ionospheric plasma. α_{zx} , α_{yx}, α_{zy}, α_{xy} and α_{yx} are similar to each other as trend like (cos) function or (sin). But they are different than diagonal elements. So these are smaller than them as magnitude. All of VP(Volume-polarization) coefficients are equal to each other March 21 — Sepmtember 23 as magnitude when they have been looked at the change of latitude.

Figure 3 are given by local time the change of VP for two seasons. The magnitude of the components of VP is bigger on March 21 than September 23 as general. Besides the diagonal elements are bigger than the other components of tensor in every conditions and it is same phase with the external electric field and other components are antiphase with electric field and they have been taking the biggest value around 1200 LT(mid-day) for the accepted conditions.

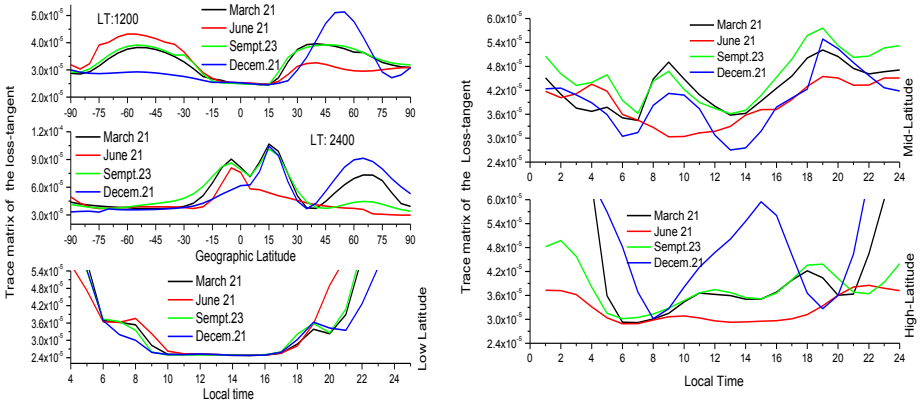

FIGURE 3. The change of trace matrix of loss- tangent with both latitudes and local time as seasonal in ionospheric plasma.

4. **Conclusions.** This manuscript investigates on the magnitude of volume polarization coefficients, for equinox conditions by using the real geometry of the Earth's magnetic field in the northern hemisphere. According to the obtained findings;

1. The diagonal elements of VP tensor are bigger than other elements for the considered conditions as magnitude, and they take maximum value around at equator and 12.00 LT. Besides the diagonal elements vibrate the same phase with electric field, but the other elements of tensor such as α_{yx} vibrates the same phase in the south hemisphere, antiphase in the north hemisphere for two every season and the whole VP tensor elements like α_{yx}(March 21) and α_{yx} (September 23) are equal to each other as magnitude. The diagonal elements have a behavior like soliton.

2. α_{yx} vibrates antiphase to electric field and maximum around 10° N. This latitude is region composed of equatorial anomaly in the ionospheric plasma in general. But for α_{zy} has maximums between –15° S—25° N hemisphere that is ; it is the same phase –15° S and antiphase 25° N. This is true for both seasons. It is possible to say that the permittivity constants of diagonal elements are bigger with respect to other tensor elements.

3. VP coefficients are bigger on March 21 than on September 23. Maybe this case could be explained with seasonal anomaly. Besides, the diagonal elements of

VP polarization are the same phase with electric field but antiphase other elements. All of the elements are maximum at 12.00 LT. Sun rays come at a right angle to Earth's surface and ionization is maximum at this time. These maximums could results from because of ionization.

1. M. Aydogdu and O. Ozcan, Effect of magnetic declination on refractive index and wave polarization coefficients of electromagnetic wave in mid-latitude ionosphere, *Indian Journal of Radio & Space Science*, 1996, 25, pp. 263—70.

2. M. Aydogdu, A. Yeşil, and E.Güzel, The group refractive indices of HF waves in the ionosphere and departure from the magnitude without collisions, *J. Atmos. Sol.-Terr. Phys.,* 2004, 66(5), pp. 343—348.

3. İ. Ünal, O. Özcan, and M. Canyılmaz, Ionospheric Absorption of HF Radio Wave in Vertical Propagation, *Iranian Journal of Science &Technology, Transaction A,* 2007, 31(4), pp. 413—419.

4. O. Ozcan, M. Aydogdu, and I. Unal, Effect of the adiabatic sound speed on the electric conductivities of the ionospheric plasma, *Balkan Physics Letters,* 1998, 6, pp. 204—213.

5. D. G. Swanson, *Plasma waves,* Academic Press, New York, 1989.

6. R. C. Whitten and I. G. Poppoff, *Fundamentals of Aeoronmy*, John Willey and Sons, New York, 1971.

7. K. G. Budden, *The Propagation of Radio Waves*, Cambridge University Press, Cambridge, 1988.

8. K. G. Buddenand G. F. Stott, Rays in magneto-ionic theory-II, *J. Atmos. Sol.-Terr. Phys.,* 1980, 42, pp. 791—800.

9. F. Richard, *The physics of Plasma*, CRC press, New York, 2014, pp. 50—140.

10. M. Aydogdu and O. Ozcan, The possible effects of the magnetic declination on the wave polarization coefficients at the cutoff point, *Progress in Electromagnetic Research, PIER,* 2001,:30, pp. 179—190.

The Earth`s Atmosphere Self-Radiation Transfer CUDA-Modeling

Konstantin G. Orlov[1], Igor V. Mingalev[1], and Ekaterina A. Fedotova[1]

[1]Polar Geophysical Institute, 26a, Academgorodok St., Apatity, Murmansk region, Russia, 184209

Abstract. The paper presents the results of simulation of the Earth`s atmosphere self-radiation in the range of frequency from 10 to 2000 $cm^{-1}$ and in the height range of 76 km from Earth`s surface. To achieve high calculations speed, in the model use is made of molecular absorption parametrizations, constructed on a certain algorithm. The calculations were carried out by video cards NVIDIA, using the CUDA technology. The results of parametrization-based calculations of the Earth`s atmosphere self-radiation field have been compared with the Line-by-Line calculations results, made with frequency resolution 0.001 cm^{-1}.

Introduction. Calculations of the self-atmospheric radiation field are necessary to solve different physical problems, in particular, to interpret the atmosphere remote sensing data, and also calculate the atmosphere heating. In modeling the global circulation of the Earth`s atmosphere, it is necessary to calculate the atmosphere heating by self-radiation in the frequency range of 10 to 3000 cm^{-1}. In doing so there appears a problem of how to speed up the calculations. To ensure the accuracy of 1—2%, the frequency resolution must not exceed 0.001 cm^{-1}. These calculations are referred to us Line-by-Line calculations.These are highly resource and time affective and so cannot be used in models of general atmosphere circulation at present and in the foreseeable future.

To solve this problem, we used the method of fast calculation of radiation transfer, which is called “correlated K-distribution” [1—5]. The main idea of this method is that narrow spectral channels are combined into groups according to a certain algorithm. Each such group is replaced by one wide model channel, which is also called a term of the k-distribution. As a result, several million narrow spectral channels are replaced by several tens or several hundreds of model channels, and in each model channel a radiation transfer equation is solved. The construction of these model channels is called the construction of the molecular absorption parametrization. To verify the accuracy of the parametrization-based calculations, the radiation field calculations in the model channels have been compared with the Line-by-Line calculations.

At present, a large number of different molecular absorption parametrizations in the Earth's atmosphere have been created within the frequency range of 10—3000 cm^{-1}.This parametrizations contain from several tens to 150—200 model channels. A common feature of these parametrizations is that it all provide good accuracy (within 0.5 Kelvin per day (K / day)) of calculations of the atmosphere heating-cooling rates due to self-radiation at troposphere and the lower stratosphere altitudes (approximately, up to 20 km). At high altitudes, the accuracy of these parametrizations deteriorates substantially. The purpose of this work is: to create a molecular absorption parametrizationsin the Earth's atmosphere that have good accuracy not only in the troposphere, but also in the stratosphere and the lower mesosphere; to create a program packages (using both CUDA and OpenMP technologies) to implement the model channels constructionalgorithm.

1. A parametrization construction general algorithm

The parametrization constructing algorithm is as follows. The interval of the spectrum is divided into wide intervals, which are referred to as the averaging intervals. These intervals should be at least 50 cm^{-1} width. In each averaging interval, narrow spectral channels are combined into wide model channels according to different algorithms, which are often called the terms of the k-distribution or the resonances carriers.

In this paper, use was made of the following algorithm for model channels construction. Consider the averaging interval $[\nu_{\min}, \nu_{\max}]$. Let the model channels number be N. This model channels are constructed for this averaging interval. The sorting height is h_c.Combined at this height into wide model channels are narrow

channels. The volume coefficient of molecular absorption in narrow spectral channels is $K^{мол}(h_k,\nu_i)$. It is calculated based on the spectroscopic database HITRAN 2012 (here h_k — the height from the Earth's surface, ν_i — the frequency). Calculated at the sorting height h_c, within the frequency interval $[\nu_{\min},\nu_{\max}]$ are the maximum and minimum values of the molecular absorption coefficient:

$$K_{\min} = \min_{\nu_i} K^{мол}(h_c,\nu_i),\ K_{\max} = \max_{\nu_i} K^{мол}(h_c,\nu_i).$$

To construct wide model channels, use was made of a grid of the molecular absorption volume coefficient values, which is constructed at the sorting height. In this paper we used a uniform grid on a logarithmic scale, given as follows:

$$K_j = (K_{\min})^{(1-j/N)} \cdot (K_{\max})^{(j/N)}, j = 1,2,\ldots,N.$$

When the grid is constructed, the narrow channels are sorted into groups combined into wide model channels. All the narrow channels, which meet the condition $K^{мол}(h_c,\nu_i) \in (K_{j-1},K_j]$, are combined into a wide model channel under the number j. The number of narrow channels included into Model channel j is M_j. A list of the numbers of the narrow channels included into Model channel j, which are written in ascending order is $\Omega_j = (i_{j,1},\ldots,i_{j,M_j})$. For each grid node along the height h_k, in wide Model channel j, the average values of Planck`s function $B(T,\nu)$ are calculated by the formula

$$B_j^{мод}(h_k) = \frac{1}{M_j}\sum_{i\in\Omega_j} B(T(h_k),\nu_i),$$

absorption volume coefficient (molecular and aerosol):

$$K_j^{мод}(h_k) = \frac{1}{B_j^{мод}(h_k)\cdot M_j}\sum_{i\in\Omega_j} K(h_k,\nu_i)\cdot B(T(h_k),\nu_i),$$

scattering volume coefficient (molecular and aerosol):

$$\alpha_j^{мод}(h_k) = \frac{1}{B_j^{мод}(h_k)\cdot M_j}\sum_{i\in\Omega_j} \alpha(h_k,\nu_i)\cdot B(T(h_k),\nu_i)$$

single-scattering albedo:

$$\omega_j(h_k) = \frac{\alpha_j^{мод}(h_k)}{K_j^{мод}(h_k)+\alpha_j^{мод}(h_k)},$$

where $K(h_k,\nu_i)$, $\alpha(h_k,\nu_i)$ — the absorption volume coefficients (molecular and aerosol) and that of scattering in a narrow spectral channel with frequency ν_i, at height h_k, $B(T(h_k),\nu_i)$ — the value of Planck`s function in a narrow spectral channel with frequency ν_i, at height h_k. The scattering indicatrix in Model channel j is calculated by the formula:

$$\chi_j^{мод}(h_k,u)=\frac{1}{\alpha_j^{мод}(h_k)\cdot B_j^{мод}(h_k)\cdot M_j}\sum_{i\in\Omega_j}\chi(h_k,\nu_i,u)\cdot\alpha(h_k,\nu_i)\cdot B(T(h_k),\nu_i),$$

where $\chi(h_k,\nu_i,u)$ — is the scattering indicatrix for radiation with frequency ν_i, at height h_k, through an angle with cosine u.

At this point, the combining of narrow channels into wide model channels and computation of the average values of optical characteristics into wide model channels is finished. Thus, hundreds of thousands of narrow spectral channels are replaced by tens or hundreds (depending on the required accuracy and speed of calculations) of wide model channels. Then, in each model channel, a radiation transfer one-dimensional equation is solved.

2. Results.

The authors of this study have developed a program package based on the parametrization constructing algorithm, described above. This program package was implemented on both CPU, by OpenMP technology, and GPU NVIDIA, by CUDA technology. The Earth's atmosphere self-radiation field parameters were determined by Line-by-Line calculation and by parametrizations of the optical characteristics of the Earth's atmosphere,based on assumption that the atmosphere is horizontal homogeneous,with the altitude being equal up to 76 km from the Earth`s surface. The calculations were made for a different number of model channels at different sorting heights. To numerically solve the radiation transfer equation, a variant of the discrete ordinates method described in detail in [6], is used. In the calculations, a uniform-in-height grid, with a step of 200 meters, and a uniform-in- zenith angles grid, with a step of less than 9 degrees, were used. Allowance was made for molecular and aerosol scattering [7—9].

The calculations used vertical temperature profiles and concentrations of the main atmospheric gases, calculated from the empirical model NRLMSISE-00 for July conditions over the North Atlantic at latitude 55 °. Three types of background aerosols are considered in the atmosphere: continental, marine and stratospheric aerosols. The optical parameters of these aerosols are taken from [10].

In Fig. 1 shows the upward and downward fluxes of the self-radiation within the frequency range of 10—2000 cm^{-1} in a cloudless atmosphere and the heating-cooling rate of atmospheric gas due to these fluxes, obtained by Line-by-Line calculations, and by calculations, when the parameterization is used. The whole range of 10—2000 cm^{-1} is divided into 40 averaging intervals, the first of which had a width of 40 cm^{-1}, and all the others had a width of 50 cm^{-1} (10—50 cm^{-1},

50—100 cm^{-1}).., 1950—2000 cm^{-1}). In each of the first ten (10—50 cm^{-1}, ..., 450—500 cm^{-1}) and of the last ten (1500—1550 cm^{-1}, ..., 1950—2000 cm^{-1}) the averaging intervals, narrow channels are combined into 20 model channels, and in each of the twenty averaging intervals (500—550 cm^{-1},..., 1450—1500 cm^{-1}) narrow channels are combined into 25 model channels. Sorting is at an altitude of 43 km. Thus, 1990000 narrow spectral channels are replaced by 900 model channels, in each of which the radiation transfer equation is solved. Fig. 1 shows that the atmosphere heating-cooling rate with the use of parametrization is very close to the reference calculations. The upward and downwardfluxes based on a parametrization, coincide with the fluxes based on Line-by-Line calculations with a relative error of less than 1%.

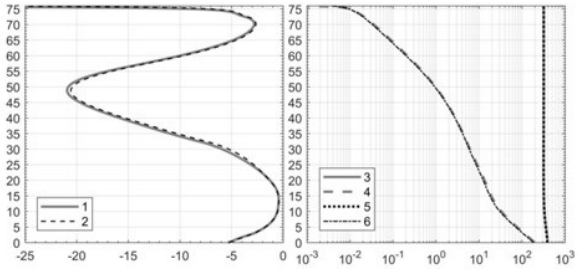

FIGURE 1. Upward and downward fluxes of the self-radiation within the frequency range of 10 to 2000 cm^{-1} in a cloudless atmosphere and the heating-cooling ratesof atmospheric gas due to these fluxes. Curve 1 is the heating-cooling rate (K/day) calculated by the parametrization, curve 2 is the same speed (K/day) obtained by Line-by-Line calculations. Curves 3 and 4 are the upward and downward fluxes of self-radiation (W/m^2) calculated by parametrization, curves 5 and 6 are the same fluxes obtained byLine-by-Line calculations.

3. Summary.

According to the calculations results, parametrization containing several hundred model channels in the spectral range 10—2000 cm^{-1}, allows us to achieve accuracy in heating-cooling rates calculations of atmospheric gas with an error not more than 0.5 K / day in the altitude range of 76 km from Earth`s surface.To achieve accuracy with an error not more than 0.2 K / day, the height at which narrow spectral channels are combined into wide model channels, should be in the range of 40—45 km. Also, the calculations results showedthat an increase in the model channels number is not always accompanied by an increase in accuracy.

1. B. A. Fomin, A k-distribution technique for radiative transfer simulation in inhomogeneous atmosphere: 1. FKDM, fast k-distribution model for the longwave, *J. Geophys. Res*., 2004, 109, D02110.

2. B. A. Fomin and P. M. Correa, A k-distribution technique for radiative transfer simulation in inhomogeneous atmosphere: 2. FKDM, fast k-distribution model for the shortwave, *J. Geophys. Res*., 2005, 110, D02106.

3. E. Mlawer et al., Radiative transfer for inhomogeneous atmospheres: RRTM, a validated correlated-k model for the longwave, *J. Geophys. Res*., 1997, 102, D14, pp. 16,663—16,682.

4. R. J. Hogan, The Full-Spectrum Correlated-k Method for Longwave Atmospheric Radiative Transfer Using an Effective Planck Function, *J. Atmos. Sciences*., 2010,doi: 10.1175/2010jas3202.1.

5. A. V. Shilkov and M. N. Gerthev, Verification of the Lebesgue Averaging Method, *Mathematical Models and Computer Simulations*, 2016, 8, 2, pp. 93—107.

6. N. I. Ignat'ev, A. V. Rodin, I. V. Mingalev, and E. A. Fedotova, A new version of the discrete ordinate method for the calculation of the intrinsic radiation in horizontally homogeneous atmospheres, *Computational mathematics and mathematical physics*, 2015, 55, 10, pp. 1713—1726.

7. B. A. Fomin, Effective interpolation technique for line-by-line calculations of radiation absorption in gases, *J. Quant. Spectrosc. Rad. Transfer*., 1995, 53, pp. 663—669,doi: 10.1016/0022-4073(95)00029-k.

8. K. F. Evans, The Spherical Harmonics Discrete Ordinate Method for Three-Dimensional Atmospheric Radiative Transfer, *J. Of The Atm. Sciences*., 1998, 55, pp. 429—446, doi: 10.1175/1520-0469.

9. K. Stamnes et al., Numerically stable algorithm for discrete-ordinate-method radiative transfer in multiple scattering and emitting layered media, *Applied Optics*, 1988, 27, 12, pp. 2502—2509, doi: 10.1364/ao.27.002502.

10. R. A. McClatchey, H. J. Bolle, and K. Ya. Kondratyev, A preliminary cloudless standard atmosphere for radiation computation, *World Climate Research Programme*, International Association For Meteorology And Atmospheric Physics, Radiation Commission, 1986, WCP 112, WMO/TD-No. 24, 60 p.

The D-region Stratification from Observation at the SURA Facility

Nataliya V. Bakhmetieva, Valery V. Vyakhirev

Radiophysical Research Institute Nizhny Novgorod State University, 25/12a, Bol'shaya Pecherskya St., Nizhniy Novgorod, 603950, Russia

Introduction. The paper presents the results of the *D*-region investigation in the altitude range of 60—90 km, obtained by resonance scattering of radio waves on artificial periodic irregularities (API) of the ionospheric plasma. In particular, the stratification of the *D*-region was found. It is shown that under certain conditions the *D*-region is two-layered. The lower layer in the altitude range up to 60 to 72—74 km is probably the *C*-layer. A similar layer was sometimes observed at an altitude between 64 and 68 km from measurements of the phase of VLF signals in South America [1, 2].

1. The method for the D-region investigation. The method of resonance scattering of radio waves on artificial periodic irregularities (API) of the ionospheric plasma developed in NIRFI [2], is the relatively new method for

ionosphere diagnostics. Many years of experimental and theoretical researches have shown the API technique is one of the most informative methods for studying of the Earth's lower ionosphere. It allows us to determine many characteristics of ionized and neutral components of the lower ionosphere with a great accuracy, including the electron density profile, the temperature and the density of the neutral atmosphere, the frequency of ion-molecular collisions, the velocity of vertical regular and turbulent plasma motions, the altitude of the turbopause, the relative density of negative oxygen ions and the density of atomic oxygen and excited molecular oxygen in the $^1\Delta_g$ state in the *D*-region. In addition, the method based on the radio waves scattering on APIs allows one to determine the parameters of internal gravity waves that affect the characteristics of scattered signals, to study the irregular structure of the lower ionosphere, including the stratification of the regular *E*-layer. The API technique allows one to detect weak sporadic ionization layers which are not available for detection by an ordinary ionosonde; to investigate the features of the sunrise and sunset phenomena and the solar eclipse phenomena in the lower ionosphere and additional layers of the electron density from the lower part of the *D*-region to the height of the maximum of the *F*-layer.

The API technique uses the effect of powerful high-frequency radio emission on the ionospheric plasma with the purpose of creating artificial periodic irregularities of the electron density, a sounding of the periodic structure with probe radio waves during the relaxation of irregularities after the heating termination, the measuring the amplitude and phase of the API scattered signal, determining from these data the characteristics of the ionosphere and the neutral atmosphere, parameters of sporadic ionization clouds, velocities and scales of wave and turbulent motions. To the APIs create and their sounding the SURA heating facility with frequencies of 4.7 and 5.6 MHz is used. For receiving the scattered signals, the receiving part of the PR facility is used. The height-temporal dependences of the API relaxation time are used to determine a large number characteristics of the ionosphere and neutral atmosphere [3,4].

2. Results of investigation of the D-region of the ionosphere by the API technique.

First, we discuss the main features of *D*-region from observations in different natural conditions.

2.1. The D-region during a solar eclipse. The reaction of the lower ionosphere to a partial solar eclipse was investigated on March 20, 2015 with a maximum phase of φ=0.586. Observations were carried out from March 16 to March 21, 2015. APIs were generated by radiation from the SURA facility to zenith of a powerful radio wave of unusual polarization at a frequency of 4.7 MHz. Amplitudes and phases of API scattered signals were measured. During the eclipse an increase in the amplitude of the scattered signals by 30—40 dB in the *E* region was registered, due to a decrease in absorption. An increase in the range of reception heights of the scattered signals was observed. Before and after the eclipse, API scattered signals in the *D*-region were comparable in amplitude with the signals from irregularities of the *E*-region. This phenomenon is extremely rare in API observational experiments. During the eclipse an increase in the height of

the scattered signals in the *D*-region and the *D*-region separation near the maximum phase of the eclipse were observed. Scattered signals with large amplitudes and a prolonged relaxation process were obtained after the termination of the ionosphere from the heights of the mesopause 86—88 km. They are usually absent due to the growth of atomic oxygen at these altitudes, which prevents the formation of APIs due to the attachment of electrons to oxygen molecules in triple collisions

In time variations of the characteristics of scattered signals and, especially, the velocity of vertical plasma motion, intense wave motion with IGW periods. [5]. Figure 1 shows the dependence of the API scattered signal on the height and time during solar eclipse.

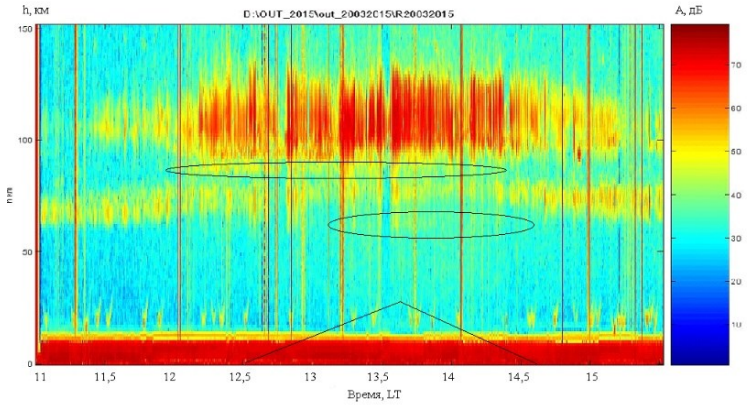

FIGURE 1. The amplitude of the API scattered signal during the solar eclipse in March 20, 2015 The time of the eclipse is marked by a triangle on the time axis. The ovals show the appearance of a signal at the height of the mesopause (upper oval) and the stratification of the D region (lower oval).

The aeronomy of the D-region. In the *D*-region APIs are formed due to the temperature dependence of the electron attachment coefficient to oxygen molecules in triple collisions. The API characteristic formation and relaxation time τ is determined by the expression $\tau=1/(\beta+\gamma)$, where β is the electron attachment rate, and γ is the rate of the detachment of electrons from negative oxygen ions. This time does not exceed 1 s. The rate of detachment, in turn, is determined by processes photo detachment and reactions with atomic oxygen and excited oxygen molecules in the $^1\Delta_g$ state. It is shown that, in the first approximation, the altitude profile of the amplitude of the API scattered signal is determined by the expression $A(h)\sim N(h)\beta(h)/[\beta(h)+\gamma(h)]$. It is obtained that in the *D*-region height profiles of the amplitude $A(h)$ and the relaxation time $\tau(h)$ of the API scattered signal are explained well on the basis of the aeronomical process model with one negative O_2^-ion. Experiments have done that height $A(h)$ and $\tau(h)$ profiles at altitudes h <65 km reacted to changes in the atmospheric density and the concentration of

molecular oxygen in the $^1\Delta_g$ state. At the height range h=75—80 km it responds to change the concentration of atomic oxygen. In this case the $A(h)$-profile of the amplitude depends also on the height $N(h)$-profile.

2.3. Sunset and sunrise phenomena in the *D*-region. The API technique was used to study the sunset and sunrise processes in the summer mid-latitude *D*-region. An example of range-time-amplitude plot of the API scattered signal on 12 — June 15, 2001 is shown in Fig. 2.

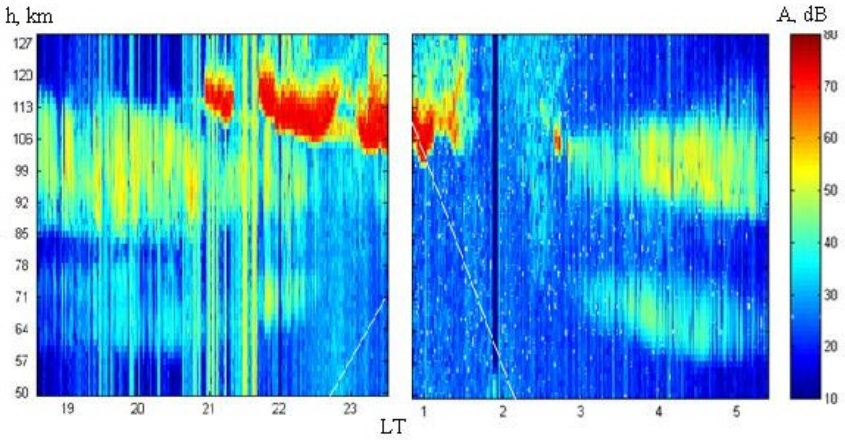

FIGURE 2. Amplitude of the API scattered signal during the sunrise and sunrise hours June 15, 2001.

The asymmetry of the altitude-time dependences of the amplitude and the relaxation time of the API scattered signal is detected. At altitudes below 65 km the signal amplitude growth at the sunrise began with a time-lag in relation to altitudes of 70—75 km, forming a kind of "step". Probably, the delay in the appearance of signals at altitudes below 65 km is due to the delay in the growth of the concentration of excited oxygen, which plays a primary role in the detachment processes at these heights. In this case the appearance of the "step" can be connected with the penetration of a part of the spectrum of solar radiation into the lower heights in the wavelength range λ=220—280 nm, which causes the appearance of oxygen molecules in the $^1\Delta_g$ state. In addition, there is a significant increase in the "dip" in the amplitude of the scattered signal at the altitudes between the *D*- and the *E*-regions at the sunrise. In the calculations it was found that the concentration of atomic oxygen should increase by 2—3 times at sunrise, and the lower boundary of the height of the appearance of atomic oxygen can be reduced by 5—7 km.

On the left panel of in the Fig. 2 one can see the *D*-region stratification and such its features as “step” and “dip”.

3. The D-region stratification. In several experiments, a nonmonotonic behavior of the altitude profile of the electron density in the *D*-region with a local

minimum at altitudes of 72—74 km was detected. It was interpreted as a stratification of the *D*-region. First we assumed that this phenomenon has a seasonal character, so the most of the data on the stratification was obtained in observations in the afternoon hours in April 2004 and 2005 [6]. In Fig. 3 the altitude profiles of the amplitude (left panel) and the relaxation time (right panel) of the API scattered signal are averaged over 15 minutes and are given (with a shift) every half hour from 12 to 15 hours of Moscow summer time.

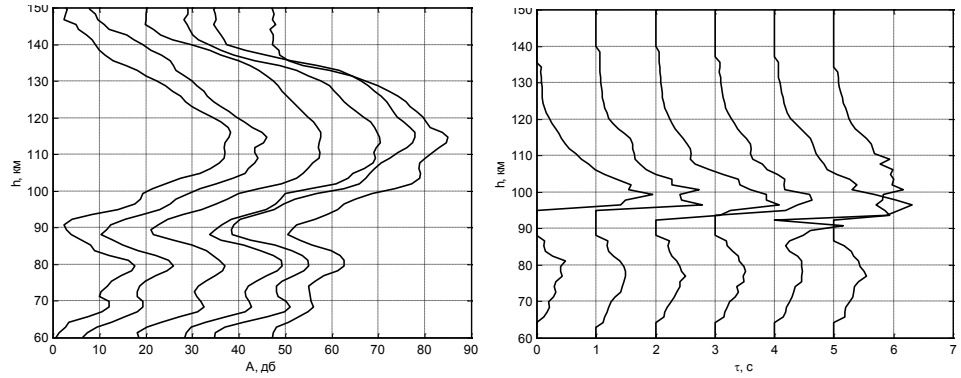

FIGURE 3. Amplitude (left panel) and relaxation time (right panel) of the signal scattered by the PID in measurements on April 6, 2005.

In the altitude profile of the amplitude, two maxima in the *D*-region are clearly visible, and the altitude variation of the relaxation time $\tau(h)$ had the form characteristic for the summer season, when in the *D* region the amplitude profile of the scattered signal had one maximum as rule. This means that the minimum in profile $A(h)$ is due to a minimum of the electron concentration at a height $h \approx 70$—75 km and, thus, the *D*-region is two-layered. From the measurements of the phase of the API scattered signal the velocities of vertical motions in the *D*-region were determined. In the lower part of the *D*-region of the velocities differed little from zero, increasing with a height up to 1—3 m/s.

Subsequently, it turned out that the two-layered nature of the dependence of the amplitude of the scattered signal occurs in the summer months. Thus, as a result of measuring the height profiles of the amplitude and phase of API scattered signals it was concluded that under certain ionospheric conditions the *D*-region is a two-layered with a minimum of electron density in the altitude range of 70—74 km. This is approximately 10 km higher than that obtained in [1, 2]. This is probably due to a change in the ionic composition of the region due to a change in solar radiation. The lower part of this region, apparently, is the *C*-layer which was also observed in [1, 2].

The work supported of the State task of the Ministry of Education and Science of the Russian Federation for Project No. 5.8092.2017/8.9.

1. J.-P. Raulin et al, Proceeding of the 3th VERSIM Workshop, 15—20 September, 2008, Tihany, Hungary.
2. F. C. P. Bertoni et al, *JGR: Space Physic*, 2013, V.118, pp. 6686—6693.
3. V.V. Belikovich, E.A. Benediktov, A.V. Tolmacheva, and Bakhmet'eva N.V., Ionospheric Research by Means of Artificial Periodic Irregularities — Copernicus GmbH, 2002. Katlenburg-Lindau, Germany, pp. 160.
4. N.V. Bakhmetieva et al, *Baltic Astronomy*, 2013. Vol. 22, No 1, pp.15—24.
5. N.V. Bakhmetieva et al, *Radiophysics and Quantum Electronics*, 2017, Vol. 59, No. 10, pp. 782—793.
6. V.V. Belikovich et al, *Geomagnetizm and Aeronomy* (in Russian), 2007, V 47, No.1, pp. 76—79.

GNSS Phase Altimetry of the Sea Level: Numerical Simulation of the Echoes from Waving Sea

Yaroslav A. Ilyushin[1,2], Artem M. Padokhin[1]

[1] Atmospheric Physics Department, Physical Faculty, Moscow State University, GSP-2, Lengory Moscow 119992 Russia
[2] Institute of Radio-engineering and Electronics, ulitza Mokhovaya, 11/7 Moscow 125009 Russia

Introduction. Dramatic changes in the natural environment, observed in the present epoch, are threatening and can be dangerous for the future of the whole world human population. Systematic monitoring of these global changes is now critical for detection of log periodic variations and long term trends such as global warming, polar ice melting, raising of the ocean level etc. Extensively developing technologies of observation of the Earth from space provide excellent possibilities for remote measurements of key physical parameters of the atmosphere, ocean and land surface. GPS reflectometry [1] is a relatively cheap technique for in situ measurements of the sea level surface, which can be implemented both at coastal stations of geodetic GPS-networks and specially organized observatories of global environmental monitoring. This technique, however, suffers from errors caused by rapid sea level perturbations, e.g. wind generated waves which can introduce not only random but also systematic biases in the measured data.

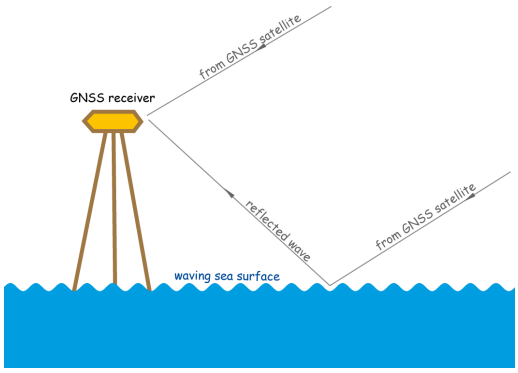

FIGURE 1. General schematic view of the GNSS reflectometric experiment.

In this study, numerical simulation of reflections of navigational space-borne radio beacons from undulating sea surface is performed at the main frequency of the Global Positioning System (GPS) L1 (1575.42 MHz). Electromagnetic field has been simulated with the Finite Difference in Time Domain (FDTD) technique [2] for different model spectra of the sea waves (2D simulation code for s-polarized waves previously used in [3]). Impact of the surface waves on the mean sea level estimate at the monitoring station location is investigated.

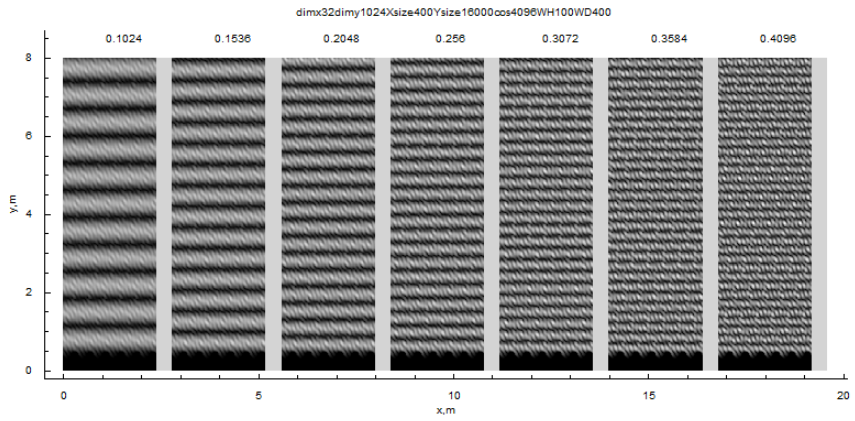

FIGURE 2. Simulated GNSS wave interference patterns over the waving sea surface. Sinusoidal wave profile, wave period 0.4 m, wave height 0.1 m. Sines of the wave grazing angle are shown with the numeric labels.

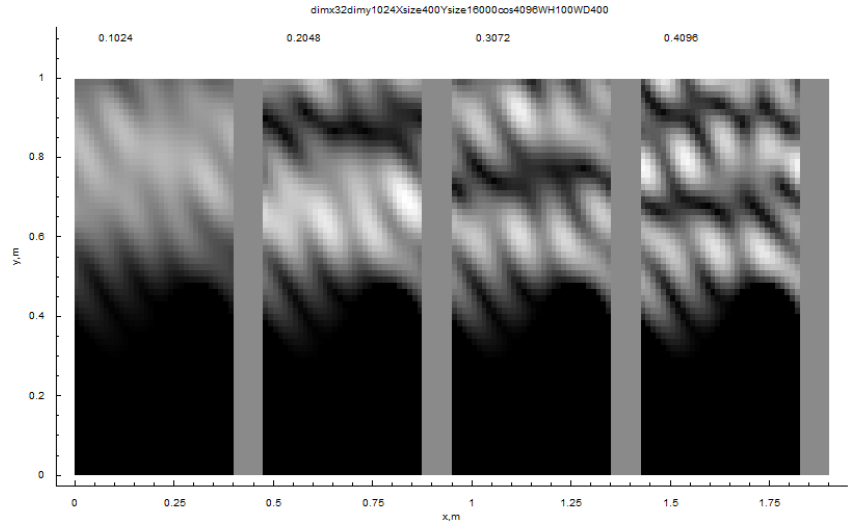

FIGURE 3. Simulated fine structure of the interference patterns. Sinusoidal wave profile, wave period 0.4 m, wave height 0.1 m. Sines of the wave grazing angle are shown with the numeric labels. Shadowing zones in the troughs of the surface profile are clearly seen.

Random and systematic errors, in particular related to partial shadowing of the undulating surface at low grazing angles of the sounding wave coming from a GPS beacon, are evaluated and estimated. Approaches to mitigation of the observational errors using auxiliary support data, including local sea waves spectra recorded in situ, context images/footage video of the surrounding aquatory, local weather conditions (wind speed and so on) are discussed.

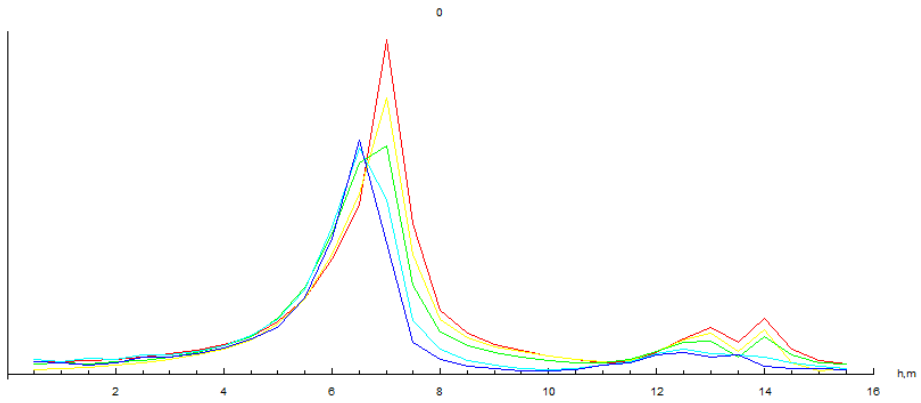

FIGURE 4. Estimates of the sea level (the receiver height over the surface) from the wave interference simulations. Systematic bias of the estimated height is due to sea waves. Red, yellow, green, cyan and blue curves correspond to wave heights 0, 0.05, 0.1, 0.15 and 0.2 m, respectively.

Acknowledgments. The research is carried out using the equipment of the shared research facilities of HPC computing resources at Lomonosov Moscow State University. Support from Russian Science Foundation with the grant 17-77-20087 is kindly acknowledged.

1. W. Liu, J. Beckheinrich, M. Semmling, M. Ramatschi et al., Coastal Sea-Level Measurements Based on GNSS-R Phase Altimetry: A Case Study at the Onsala, *IEEE Transactions On Geoscience And Remote Sensing*, 2017, 55(10), 5625 p.

2. A. Taflove, S.C. Hagness, Computational Electrodynamics: The Finite-Difference Time-Domain Method, 3rd ed. Artech House Publishers, 2005.

3. G. G. Levin, G. N. Vishnyakov, Ya. A. Ilyushin, Synthesis of three-dimensional phase images of nanoobjects: Numerical simulation, *Optics and Spectroscopy*, 2013, 115 (6), pp. 938—946.

4. V. Sadovnichy, A. Tikhonravov, V. l. Voevodin, and V. Opanasenko, ”Lomonosov”: Supercomputing at Moscow State University, *Contemporary High Performance Computing: From Petascale toward Exascale*, Boca Raton, USA, 2013, pp.283—307.

ENSO Impacts on the Middle and Upper Atmosphere in the Winter Northern Hemisphere

Alexander I. Pogoreltsev[1,2], Tatiana S. Ermakova[1]

[1]Meteorological Forecast Department, Russian State Hydrometeorological University, Russia, 192007, Saint-Petersburg, Voronezhskaya st, 79
[2]Atmospheric Physics Department, Saint-Petersburg State University, Russia, 198504, Saint-Petersburg, Ulyanovskaya st, 1

Introduction. The considerable ENSO signatures have been discovered in the northern extratropical stratosphere in the observational data [1, 2] and reproduced in simulations [3, 4]. However, the changes in forcing of stationary planetary waves (SPWs) by the latent heat release dependent on the ENSO phase and contribution of this heating to the zonally averaged thermal budget of troposphere have not been considered in these studies. SPWs generated in the troposphere propagate upward into the stratosphere, where they dissipate or are nonlinearly saturated [5] and, thus, affect the stratospheric circulation by depositing their momentum and energy to the mean flow. If the phase velocity of a wave harmonics approaches the zonal mean wind the direction of wave propagation changes due to refraction [6] or reflection [7]. The reflected waves act against the incident harmonics, which can result in changes in the zonal mean flow in the troposphere [8].

Global distributions of precipitation rates under La Nina and El Nino conditions differ substantially [9]. Latent heat release can influence SPWs at stratospheric heights in two ways: explicitly through their additional thermal forcing in the troposphere, and implicitly via altering the mean zonal flow, whose distribution determines the propagation conditions of SPWs [10]. The main purpose of the present investigation is to develop a new parameterization of atmospheric heating rates caused by latent heat release that takes into account the diurnal and longitudinal variations as well as its dependence on the ENSO phase. This parameterization has been implemented into the Middle and Upper Atmosphere Model (MUAM) [11] and a set of ensemble runs corresponding to the El Niño and La Niña conditions taking into account the differences in the lower boundary forcing of SPWs has been performed.

Heating Rates and Lower Boundary Conditions. To estimate the latent heating due to condensation, the Modern-Era Retrospective Analysis for Research and Applications (MERRA) convective precipitation data have been used [12]. The distribution of heating rates is calculated using the empirical formula suggested by [13]. This formula was obtained on the basis of the measurements [14].

In the present study the Multivariate ENSO Index (MEI) has been used. Using the table of available MEI values the following sets of Januaries of 1983, 1992, 1998, 2003, 2010 and of 1989, 1999, 2000, 2008, 2011 have been chosen, which

are representative of El Niño and La-Nina conditions, respectively. The composites for the latent heat release and lower boundary conditions for January of these years have been prepared using the MERRA and Japanese 55-year Reanalysis (JRA-55) [15] data, respectively.

The latent heating rates have been calculated at all latitudes, longitudes and altitudes on the MUAM grid points taking into account the diurnal variations (MERRA data are produced at 3-hour intervals). The longitudinal distribution of the heating rates was approximated by a set of zonal harmonics with zonal wave numbers m = 1—4. In order to take account of local (or universal) time changes in the MUAM, each zonal harmonic is presented by the stationary wave and time harmonics with periods T = 24 and 12 hours with the separation into the waves traveling to the west and to the east. Thus, the heating rates can be calculated at any model time resolving the mean zonal values, longitudinal variations (i. e., SPWs), and a set of diurnal and semidiurnal tidal oscillations. Under the La Niña conditions the maximum of heating is broader spatially and spreads into the Northern Hemisphere. The additional heating in the equatorial area leads to an increase of the latitudinal temperature gradient at the middle latitudes that causes an amplification of the jet streams in the troposphere. This strengthening, in turn, affects the efficiency of propagation of SPWs into the stratosphere. Within several days, interactions of the waves and the mean flow taking place during the intensification of SPWs results in the polar vortex weakening that can initiate SSWs. Thus it is necessary to analyze the contribution of latent heating to the forcing of these waves.

Multiple simulations with the MUAM have been conducted to investigate the ENSO signal in the middle atmosphere. Either of the two ensembles consists of 10 members for the El Niño and La Niña conditions. The method of setting up different ensemble members was the same as described in the paper [11].

Effects of the ENSO in the Northern Hemisphere Extratropics. It the present paper only the zonally averaged fields and large-scale longitudinal disturbances (SPWs) are considered. The results obtained are presented in Fig. 1. To ensure a better statistics, all composites have been calculated for the fields averaged over the middle winter months (January-February). Contours in the left panels of this figure show the composites of the zonal mean wind, temperature (Figs. 1a and 1d), SPW1 and SPW2 amplitudes in the geopotential height (Figs. 1g and 1j) simulated with the MUAM under the La Niña conditions. The shaded areas in these panels denote standard deviations that have been determined during the ensemble averaging over 10 members. The panels in the middle column of Figure 1 show the composite differences in zonal mean wind, temperature (Figs. 1b and 1e), SPW1 and SPW2 amplitudes (Figs. 1h and 1k) between the El Niño and La Niña cases obtained with the MUAM. The right panels of Fig. 1 present the results obtained using MERRA data for the selected years. The shaded areas in the middle and right panels represent the statistical significance of the differences. The comparison of the simulation results demonstrates that stratospheric polar vortex tends to be weaker and the polar region in lower stratosphere is warmer during El Niño events.

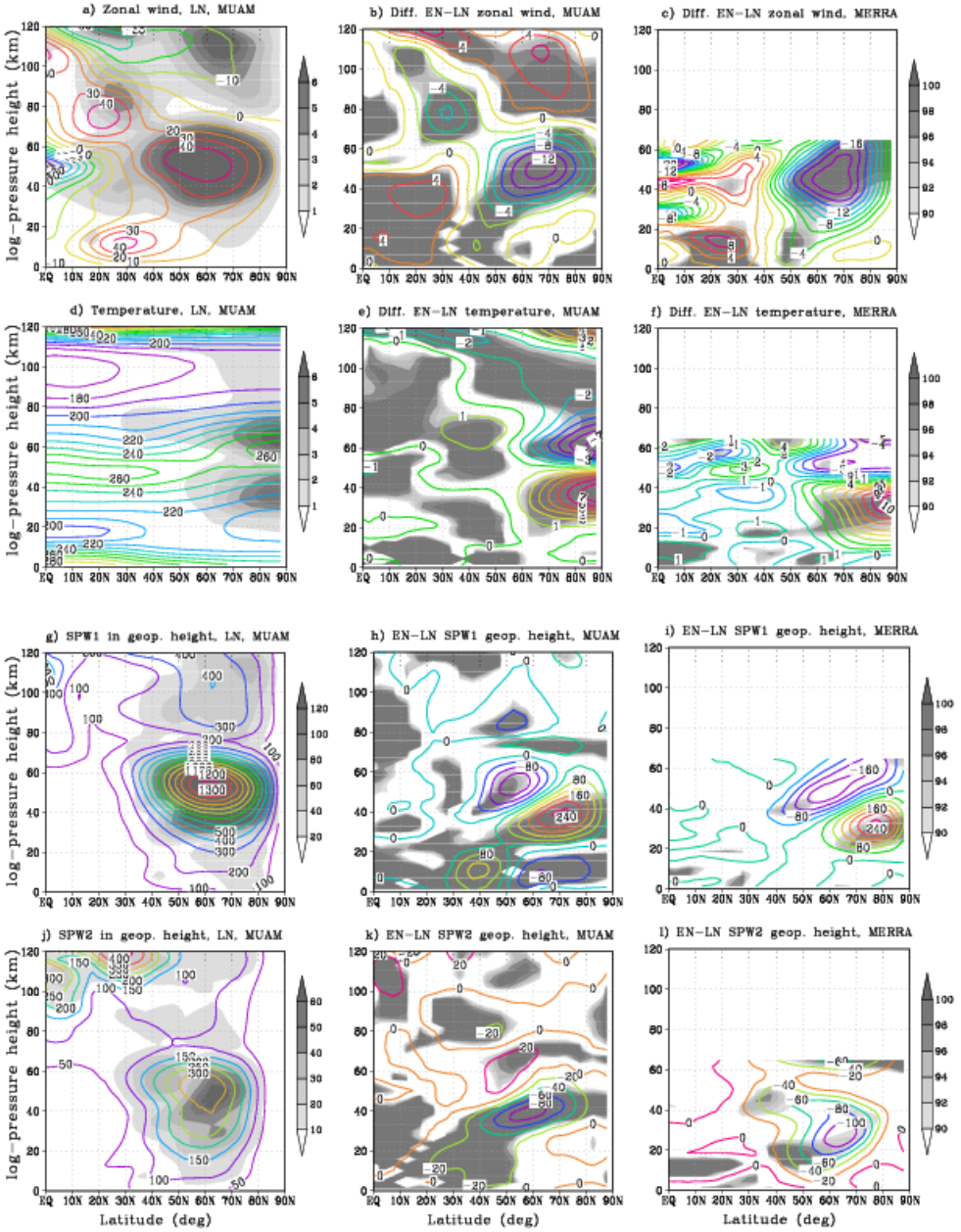

FIGURE 1. Composites of the mean zonal wind (a), temperature (d), amplitudes of SPW1 (g) and SPW2 (j) in the geopotential height obtained with the MUAM under La Niña conditions (contours). The corresponding differences (b, e, h, k) between ensembles during El Niño and La Niña (contours). The right panels show the same differences calculated using the MERRA data (c, f, i, l). The shaded areas in the left panels indicate the standard deviations obtained during the ensemble averaging. The shaded regions in the middle and right panels denote the statistical significance.

The composites of the SPW1 amplitude are smaller at higher-middle latitudes in the lower stratosphere and stronger in the upper stratosphere under the La Niña conditions. The SPW2 behaves in the opposite way and has larger amplitudes at the stratospheric levels. The results of simulations are in a good agreement with the observed differences for the zonal mean wind, temperature, and amplitudes of SPWs, as is revealed from the MERRA reanalysis data. These differences are obviously related to the changes in the forcing and propagation of SPWs associated with the ENSO-induced changes in the distributions of latent heating.

Summary and Discussion. Model experiments and the MERRA data have been used to analyze the extratropical ENSO signals in the Northern Hemisphere boreal middle atmosphere. The results of simulations with the MUAM and reanalysis data demonstrate similar ENSO manifestations in the fields of the mean zonal wind, temperature, and SPW1 and SPW2 amplitudes. Stratospheric polar vortex becomes substantially weaker and the polar region is warmer during El Niño events. At the altitudes of the upper stratosphere and mesosphere the temperature effect has the opposite sign. The composites obtained with the MUAM simulations show that the mean zonal wind in the lower thermosphere at higher-middle latitudes is stronger during El Niño. This, however, cannot be deduced from the MERRA data. The activity of SPW1 is higher in the stratosphere and weaker at middle latitudes in the region of the stratospheric jet maximum during El Niño's mid-winter. The simulated and observed SPW2 amplitude behaves in the opposite way and is larger in the stratosphere during La Niña. The obtained changes in SPW1 and SPW2 amplitudes during the transition from the La Niña to El Niño events and vice versa can affect the efficiency of the stratosphere-troposphere coupling and the influence of stratospheric processes on circulation patterns in the troposphere can be manifested at different longitudinal sectors.

In recent studies, the question concerning the difference in the frequency of SSW events under El Niño and La Niña conditions has been discussed [2, 16, 17]. The analysis of the MERRA data performed for years with different ENSO phases and the results of simulations with the MUAM show that development of SSWs during the El Niño and La Niña events proceeds somewhat differently. The main heating of the polar region during La Niña is situated in the upper stratosphere (the altitude of about 40 km) and the major SSWs could not be identified in this case basing on the analysis of the temperature and mean zonal wind behavior at 10 hPa level [18]. In particular, the SSWs in January and February 2008 under the La Niña conditions cannot be identified as major warmings according standard defining [19]. The simplest way to avoid the problem is to consider the changes of the temperature and mean zonal wind at the higher altitudes and/or averaged over some altitude range, for instance, between 30 and 50 km. However to resolve this problem the neutral ENSO phase has be considered as the next step, which helps to make a conclusion what (El Niño or La Niña) events influence extra-tropical stratosphere more significantly.

1. H. Van Loon, C. S. Zerefos, and C. C. Repapis, The Southern Oscillation in the stratosphere, *Mon. Weather Rev*., 1982, 110(3), pp. 225—229.

2. A. H. Butler and L. M. Polvani, El Niño, La Niña, and stratospheric sudden warmings: A reevaluation in light of the observational record, *Geophys. Res. Lett*., 2011, 38, L13807, doi:10.1029/2011GL048084.

3. F. Sassi, D. Kinnison, B. A. Boville et al., Effect of El Niño Southern Oscillation on the dynamical, thermal, and chemical structure of the middle atmosphere, *J. Geophys. Res*., 2004, 109, D17108, doi:10.1029/2003JD004434.

4. R. Garcia-Herrera, N. Calvo, R. R. Garcia, and M. A. Giorgetta, Propagation of ENSO temperature signals into the middle atmosphere: A comparison of two general circulation models and ERA-40 reanalysis data, *J. Geophys. Res*., 2006, 111, D06101.

5. C. Giannitsis and R. S. Lindzen, Nonlinear saturation of vertically propagating Rossby waves, *J. Atmos. Sci*., 2009, 66(4), pp. 915—935.

6. T. Matsuno, Vertical propagation of stationary planetary waves in the winter Northern Hemisphere, *J. Atmos. Sci*., 1970, 27, pp. 871—883.

7. N. Harnik, Observed stratospheric downward reflection and its relation to upward pulses of wave activity, *J. Geophys. Res*., 2009, 114, D08120, doi:10.1029/2008JD010493.

8. D. Nath, W. Chen, C. Zelin et al., Dynamics of 2013 Sudden Stratospheric Warming event and its impact on cold weather over Eurasia: Role of planetary wave reflection, *Sci. Rep*., 2016, 6, 24174, doi:10.1038/srep24174.

9. M. L. Salby, *Physics of the Atmosphere and Climate*, second edition, Cambridge University Press, 2012.

10. D. Jacqmin and R. S. Lindzen, The causation and sensitivity of the Northern winter planetary waves, *J. Atmos. Sci*., 1985, 42, pp. 724—745.

11. A. I. Pogoreltsev, A. A. Vlasov, K. Fröhlich, and Ch. Jacobi, Planetary waves in coupling the lower and upper atmosphere, *J. Atmos. Solar-Terr. Phys*., 2007, 69, pp. 2083—2101, doi:10.1016/j.jastp.2007.05.014.

12. M. M. Rienecker, M. J. Suarez, R. Gelaro et al., MERRA: NASA's Modern-Era Retrospective Analysis for Research and Applications, *J. Climate*, 2011, 24(14), pp. 3624—3648, doi:10.1175/JCLI-D-11-00015.1.

13. S.-S. Hong and P.-H. Wang, On the thermal excitation of atmospheric tides, *Bull. Geophys*., 1980, 19, pp. 56—84.

14. R. J. Reed and E. E. Recker, Structure and properties of synoptic-scale wave disturbances in the equatorial western Pacific*, J. Atmos. Sci*., 1971, 28, pp. 1117—1133.

15. S. Kobayashi, Y. Ota, Y. Harada et al., The JRA-55 reanalysis: General specifications and basic characteristics, *J. Meteor. Soc. Japan*, 2015, 93, pp. 5—48, doi:10.2151/jmsj.2015-001.

16. M. Taguchi and D. L. Hartmann, Increased occurrence of stratospheric sudden warming during El Nino as simulated by WAACM, *J Climate*, 2006, 19, pp. 324—332.

17. C. I. Garfinkel, A. H. Butler, D. W. Waugh et al., Why might stratospheric sudden warmings occur with similar frequency in El Niño and La Niña winters?, *J. Geophys. Res*., 2012, 117, D19106, doi:10.1029/2012JD017777.

18. A. I. Pogoreltsev, E. N. Savenkova, O. G. Aniskina et al., Interannual and intraseasonal variability of stratospheric dynamics and stratosphere-troposphere coupling during northern winter, *J. Atmos. Solar-Terr. Phys.*, 2015, 136, Part B, pp. 187—200.

19. A. Butler, D. J. Seidel, S. C. Hardiman et al., Defining sudden stratospheric warmings, *Bull. Amer. Meteor. Soc*., 2015, 96(11), pp. 1913—1928, doi:10.1175/BAMS-D-13-00173.1.

Modeling of Energetic Particles Impact on Ozone Layer and Atmospheric Circulation

Dmitry V. Kulyamin[1,2], Eugene V. Rozanov[2,3]

[1]Institute of Numerical Mathematics Russian Academy of Sciences, Moscow, Russia
[2]West Department of Pushkov Institute of Terrestrial Magnetism, Ionosphere and Radio Wave Propagation Russian Academy of Sciences, Kaliningrad, Russia
[3]Physikalisch-Meteorologisches Observatorium, World Radiation Center, Davos, Switzerland

Introduction. The presented work deals with one of the key open problems for the fields of atmospheric chemistry and lower and upper atmosphere coupling: the study and quantitative estimates of energetic particles precipitation (EPP) impact on Earth climate. The energetic particles, originated from magnetosphere, precipitated into the lower levels of atmosphere along the Earth magnetic field lines at high latitudes and serve as chemical sources for nitrogen oxides NOx and hydrogen oxides HOx chemical families. These components may descend to the lower layers of stratosphere and mesosphere in winter due to atmospheric general circulation structure. Basically the significant downflow of air and long lived tracers in it exists in winter polar cap region due to the presence of strong polar vortex in stratosphere and lower mesosphere, so such circulation structure allow them to reach stratosphere and ozone layer [1]. Nitrogen and hydrogen oxides both could catalytically destroy the atmospheric ozone. As HOx compounds are generally short-lived, they affect the mesospheric ozone. It was indicated recently as by the observational studies, as well as by modelling research, that the effect of energetic particle precipitation causes mesospheric ozone decrease up to 35% at long time scales [1, 2]. NOx components are longer lived and could reach winter stratosphere by described dynamical mechanism so that stratospheric ozone depletion due to their effect is estimated as 10—15% [1, 3, 4]. Since atmospheric ozone is a major radiative air component, its variability could significantly influence atmospheric general circulation and Earth climate. As term “climate” in general understanding is connected to Earth surface temperature distribution and dynamical processes and their long-term evolution, the main problem for energetic particles climate effects is to evaluate their possible influence on the surface temperature. It is generally accepted now that only the mechanism of indirect stratospheric ozone depletion considered above could significantly alter troposphere-stratosphere circulation structures and affect surface temperature. Ozone depletion in winter stratosphere directly influence the temperature, which could affect the polar vortex variability. A lot of modelling and observational studies indicate that different tropospheric weather regimes associated with polar vortex strength variability, basically the main surface variability structures at high latitudes northern hemisphere, such as Arctic oscillation (AO), are directly linked to the stratospheric variability, indicated for example by northern angular mode (NAM).

Thus in this study we try to analyze the impact of ozone loss due caused by energetic particles precipitation on the atmospheric general circulation and climate. Due to significant complexity of direct modelling of the mechanism (it requires the high-level climate-chemistry model which includes upper atmospheric layers up to lower thermosphere and reliable parameterizations of particles precipitation processes) we use the evaluated values of ozone depletion due to energetic particles in northern hemisphere [3] and prescribe it in the atmospheric general circulation model of Institute of Numerical Mathematics Russian Academy of Sciences (INM AGCM) [5, 6] using the properties of middle atmospheric circulation reproduced in model. Here we present the description of our experiment and its first results.

Methodology and model description. As the base of our investigation we use INM RAS atmospheric general circulation model. It is basically a recently developed version [5; 6] of atmospheric model unit of INMCM climate model [7], which was extensively used for many simulations within the CMIP/AMIP international projects at each of their phases (Coupled/Atmospheric Model Intercomparison Project). INM AGCM version used in this study is the separated atmospheric model which calculated the dynamical characteristics (horizontal and vertical winds), temperature and also water distribution for the altitudes from surface to mesospheric upper boundary (0.003 hPa pressure level, around 90 km). Vertical grid contains 80 levels in hybrid pressure based coordinate, resolution varies (from around 500 m to 4 km in mesosphere). The model has horizontal resolution 2°x2.5° on latitude-longitude dimensions. The time step for presented experiments were 10 minutes.

It accounts whole range of key physical process in lower and middle atmosphere by the means of various parameterizations (this include boundary layer processes, soil and vegetable effect, thermal convection, clouds, radiative processes calculation, two versions of gravity waves impact parameterizations, new, etc., for details see [5, 6] and papers cited within). The major radiative active components, such as ozone, carbon dioxide and others are prescribed by monthly mean altitude-zonal distributions. Sea level pressure on the lower boundary is also used as prescribed field interpolated during calculation between monthly mean distributions.

The main idea behind our work is to alter the prescribed ozone distribution in INM AGCM in order to take into account the effects of energetic particles precipitation according to indirect physical mechanism as close to it as possible. For that purpose we used the vertical profile of accurately evaluated in work [4] ozone multiplication factor (monthly mean values) and applied it only inside the polar vortex reproduced in model during calculation for the cap of 60—90° N.H. The detailed values and foundations behind the estimated ozone variations due to EPP are presented in [4], but the generally it is 3—7% average ozone depletion for altitudes 40—80 km during November-January period and 2—5% ozone depletion for 20—40 km levels from March till October. Thus we use this multiplication factor to correct the ozone distribution in radiative model unit during calculation.

In this study we use the 1980 year conditions for control experiment as a reference and compare the results for control and ozone altered experiments specially calculated for 5 years long each to reproduce characteristics of atmospheric calculation (seasonal cycle was applied for almost all input parameters, 2 runs differ only in ozone correction).

In order to determine the polar vortex position during model run we calculate the potential vorticity (PV) spatial distribution at rather higher stratospheric level. Here we use PV values at 600 K potential temperature isentropic surface as an indicator of stratospheric-mesospheric vortex structure. Then we define the position of maximal latitudinal vorticity gradient closest to the North Pole in the 60—90° N.H domain for each longitude, which correspond to polar vortex boundary [8]. Such approach allows us to reproduce the mechanism of NOx dynamical transport and its effect on stratospheric ozone physically justified and quite close to observational evidences [4]. The typical structure of potential vorticity spatial distribution for 600 K surface in the northern hemisphere, as reproduced by INM AGCM model in January, is shown at Fig. 1. We can clearly see the varying polar vortex boundary, indicated by abrupt change in northern high latitudes.

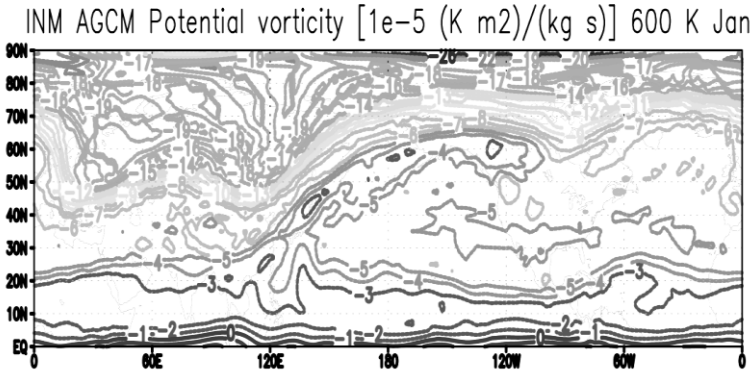

FIGURE 1. Latitude-longitude distribution of potential vorticity at isentropic surface of 600 K potential temperature in units of 10^{-5} (K m^2/kg s) calculated by INM AGCM model for January condition (hour mean for arbitrary day as a typical example).

Results and discussion. For this work we present the first preliminary results of our study. Consider the global altitudinal structure of zonal mean temperature and zonal wind distributions as reproduced by INM AGCM models for control and ozone affected experiments. Fig. 2 (top panel) demonstrates zonal mean temperature field in January for control conditions and the difference between ozone altered and control experiments results. It indicates the expected strong cooling of stratopause polar region due to ozone depletion and corresponding radiative forcing change, but as well strong warming of lower stratosphere, which

could be connected to dynamical variability. We can also determine some surface effect from this preliminary study, but more sophisticated analysis and longer model runs are required for acceptable generalization of EPP possible influence.

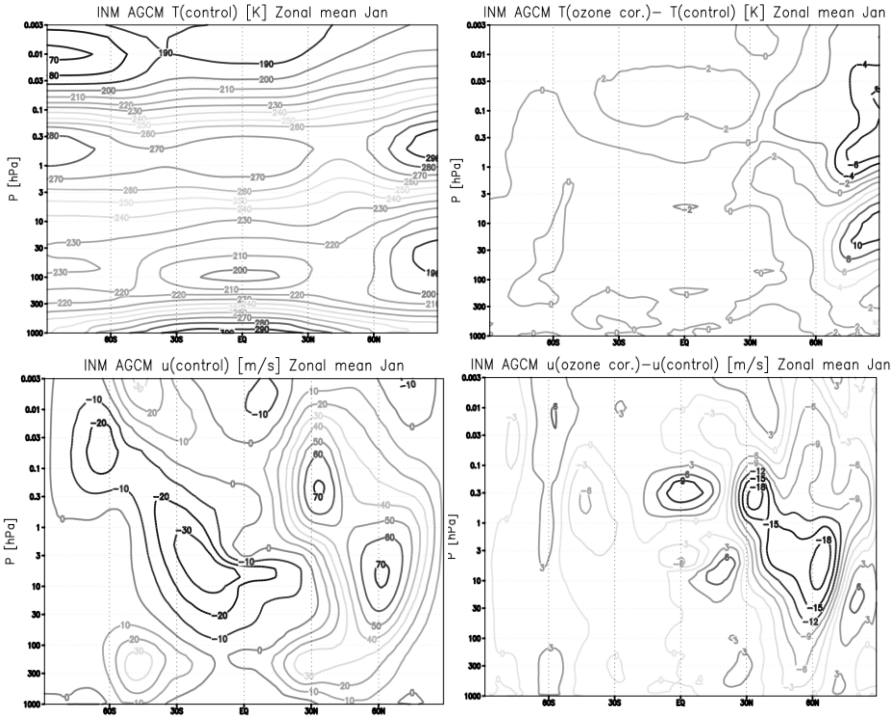

FIGURE 2. Height-latitude distributions of zonal mean temperature (top panel) and zonal wind (bottom panel) for averaged January condition calculated by INM AGCM model in control run (left figures) and the anomalies of these values between ozone corrected and control runs (right figures).

The corresponding effect in general circulation could be evaluated from the zonal wind distributions for control conditions as well as the difference between ozone corrected and control experiments, presented at Fig. 2 (bottom panel). We could indicate the significant weakening of polar vortex, caused by polar stratopause cooling and decrease in polar-equator temperature gradient, and also some changes in equatorial circulation structure. As mentioned above, in this work we present the first results and more thorough analysis is required.

The research was conducted with the financial support of Russian Science Foundation grant № 17-17-01060.

1. S. Solomon, D. W. Rusch, J. C. Gérard et al. The effect of particle precipitation events on the neutral and ion chemistry of the middle atmosphere: II. Odd hydrogen, *Planet. Space Sci.*, 1987, 29(8), pp. 885—893, doi:10.1016/0032-0633(81)90078-7.

2. K. Meraner and H. Schmidt, Climate impact of idealized winter polar mesospheric and stratospheric ozone losses as caused by energetic particle precipitation, *Atmos. Chem. Phys.*, 2018, 18, pp. 1079—1089, doi:10.5194/acp-18-1079-2018.

3. E. Rozanov, M. Calisto, T. Egorova et al. Influence of the Precipitating Energetic Particles on Atmospheric Chemistry and Climate, *Surv Geophys.,* 2012, 33, pp. 483—501, doi:10.1007/s10712-012-9192-0.

4. I. A. Mironova, K. L. Aplin, F. Arnold et al., Energetic Particle Influence on the Earth's Atmosphere, *Space Sci. Rev*., 2015, 194, pp. 1—96, doi:10.1007/s11214-015-0185-4.

5. D. V. Kulyamin and V. P. Dymnikov, The atmospheric general circulation model with a hybrid vertical coordinate, *Rus. J. of Numerical Analysis and Mathematical Modelling*, 2014, 29(6), pp. 355—373.

6. D. V. Kulyamin and V. P. Dymnikov, Modeling the lower ionosphere climate, *Izv. RAS Atm. Ocean. Phys*., 2015, 51(3), pp. 317—337.

7. E. M. Volodin, E. V. Mortikov, S. V. Kostrykin et al., Simulation of the present-day climate with the climate model INMCM5, *Climate Dynamics*, 2017, 49, 11—12, pp. 3715—3734, doi:10.1007/s00382-017-3539.

8. E. R. Nash, P. A. Newman, J. E. Rosenfield, and M. R. Schoeberl, An objective determination of the polar vortex using Ertel's potential vorticity, *J. of Geophys. Res.: Atmospheres*, 1996, 101(D5), pp. 9471—9478, doi:10.1029/96JD00066.

Peculiarities of TEC Behaviour Along the Mexican Meridian During the Weak Ionospheric Disturbances

Olga A. Maltseva[1], Maria A. Sergeeva[2,3], Tatiana V. Nikitenko[1], and J. Americo Gonzalez-Esparza[2]

[1]Institute for Physics, Southern Federal University, Stachki, 194, Rostov-on-Don, 344090, Russia.
[2]SCiESMEX, LANCE, Instituto de Geofisica, Unidad Michoacan, Universidad Nacional Autonoma de Mexico, Antigua carretera a Patzcuaro 8701, Morelia, Michoacan, C.P.58089, Mexico.
[3]CONACYT, Instituto de Geofisica, Unidad Michoacan, Universidad Nacional Autonoma de Mexico, Antigua carretera a Patzcuaro 8701, Morelia, Michoacan, C.P.58089, Mexico.

Introduction. One of the approaches to study ionosphere is the analysis of ionospheric parameters behaviour along a particular meridian. The majority of the works applying such an approach are focused on the longitude sector 100—120ºE. This work is focused on the behaviour of Total Electron Content (TEC) within the equatorial anomaly (EA) region. The issue of TEC variations in the EA zone is of a particular interest because here TEC reaches its maximal values. Due to the complexity of the dynamic processes in the equatorial and low latitude ionosphere sometimes it is difficult to explain the peculiarities of TEC behavior under quiet geomagnetic conditions, and it is even more difficult to do during the disturbances. Electric fields, thermospheric meridional winds, a "composition bulge", high latitude particle precipitation have been suggested as the possible physical

mechanisms that explain ionospheric responses to geomagnetic storms observed at different latitudes (see, for example, [1] and references therein). As it is noted in work [2], according to the generally accepted theory, the ionospheric TEC depends on the atomic/molecular ratio O/N2 [3] as well as the solar zenith angle that explain for example the features of seasonal TEC variations. Many recent works affirm that the ratio O/N2 plays an important role in TEC behaviour during disturbances [4-5].

September 2011 and February 2014 were chosen for the analysis. During these two months the disturbances of different intensity occurred including the disturbances described in [4—5]. The data of O/N2 and TEC values obtained in the IONEX format from global ionospheric maps (GIM) were used in this study. In particular, JPL GIM TEC values were obtained along the 100ºW meridian with the 2.5º step in latitude within geomagnetic latitudes between 69.2º N and 47.7º S. Absolute TEC values were compared to monthly TEC median values. Figure 1 illustrates the examples of comparison for the chosen months. The attention was focused on the EA crests presence and the possible asymmetry of the hemispheres.

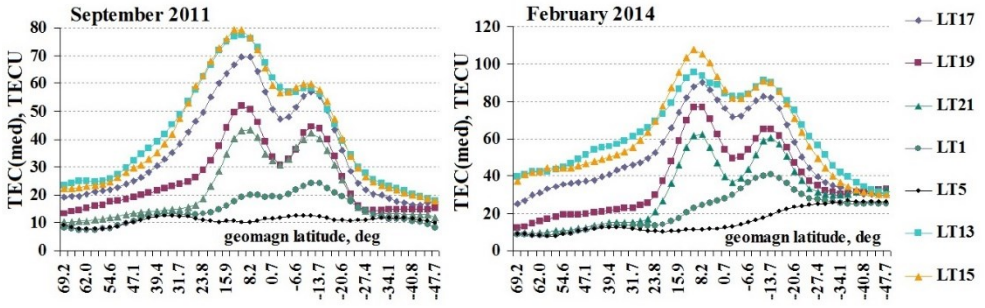

FIGURE 1. Median TEC values at different local hours (LT).

Results of observations. First, we consider September 2011 events. The month can be divided in three periods, Dst-index and TEC variations for which are shown in Fig. 2 and Fig. 3 respectively. First, let us consider the period when the most intense negative disturbance occurred on September 26th (Fig. 2, panel a). There is a positive disturbance before it, the importance of which was emphasized in [6].

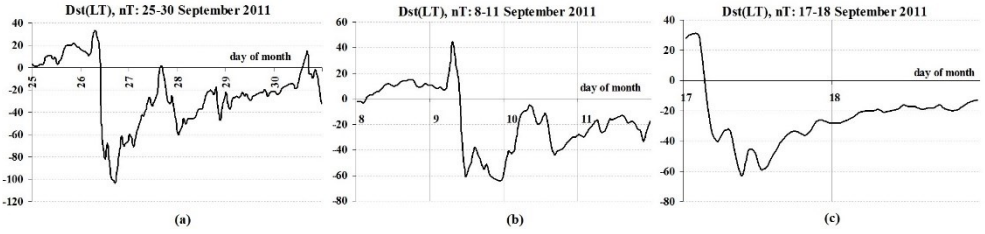

FIGURE 2. Dst-index behaviour during three chosen periods in September 2011.

The following behaviour of TEC were observed. On September 25th TEC increase in the southern hemisphere (SH) occurred at 1 and 3 LT with the ratio TEC(obs)/TEC(med) being 1.2 at the crest and 2 at the border of the SH latitude zone. On September 26th TEC increase 1.3 times at the crest and 1.8 times at the boarder zone was observed in SH at 1 LT. The positive disturbance at all latitudes of both hemispheres began at 5 LT. The large positive disturbance was in northern hemisphere (NH) at 7 LT, with twofold increase of TEC at 13 and 15 LT. TEC returned to its median values at 17 LT. On September 27th the growth of the southern crest was observed at 1 and 3 LT. At 17 LT the positive disturbance covered all latitudes. At 19 and 21 LT the crests disappeared due to the 1.5—1.9 times TEC increase at the equatorial zone. On September 28th rather intense positive disturbance was observed during (1—9) LT in SH. In the equatorial region of NH the positive disturbance occurred at 11 and 13 LT. TEC was similar to its median at 15 LT at all latitudes. The crests disappeared during (19—23) LT. On September 29th, the negative disturbance covered all latitudes of the American sector at 3 LT, and only NH — at 5 LT. The weak TEC increase in the equatorial region of NH was from 7 LT till the end of the day. On September 30th beginning from 7 LT TEC distribution was close to its median.

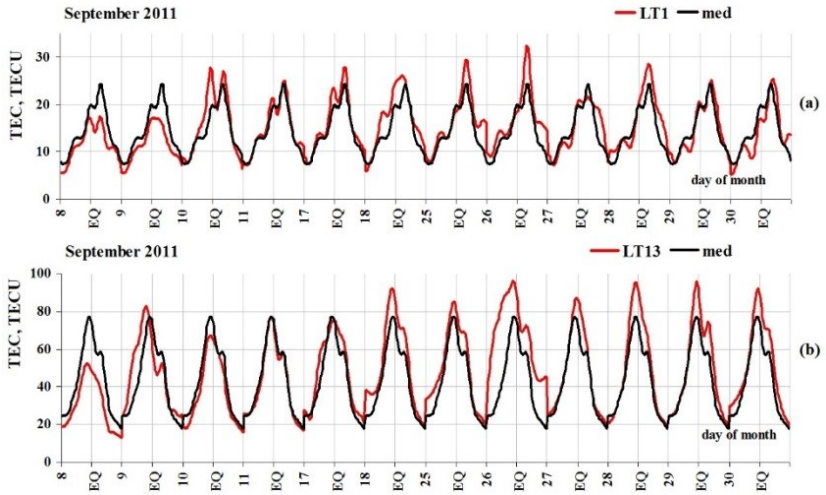

FIGURE 3. Latitudinal TEC distributions along the meridian of 100ºW for 1 and 13 LT. The days are laid off along the X-axis. The curve for each day is a dependance of TEC on a latitude in the range (69.2ºN — 47.7ºS). The letters EQ mark the location of geomagnetic equator.

Figure 2 panel "b" illustrates the case of September 8—11. On September 8th the negative disturbance was observed in both hemispheres at the background of small positive Dst during all the day. The morning hours of September 9th (1—9) LT also were marked with the negative disturbance. During (11—15) LT the positive disturbance began: first at mid latitudes of NH and then over all latitudes.

During (19—23) LT the negative disturbance occurred again. (1—5) LT hours of September 10th were characterized by the positive disturbance (TEC(obs)/ TEC(med)≈2) at the equatorial and low latitude zones of NH. TEC was similar to its median between 9 and 19 LT. The intense positive disturbance was observed at 21 and 23 LT in NH (TEC increase up to 1.5 times). On September 11th the quiet conditions were during (1—19) LT and the sharp decrease of TEC at the equator occurred at 21 and 23 LT.

During the period of September 17—18 (Fig. 2 panel c), TEC values were close to its median on the first day and showed the weak positive disturbance during the second day. Further, we consider the events of February 2014. Figure 4 shows Dst variations for this month.

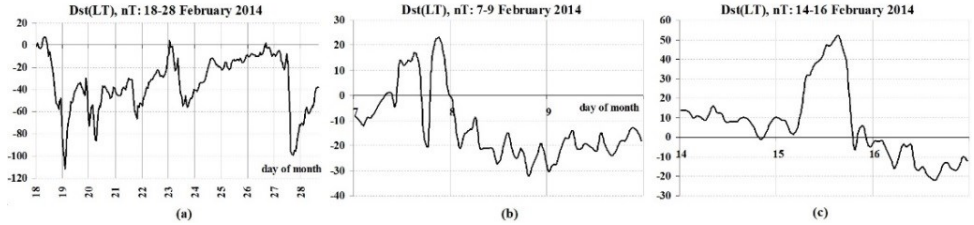

FIGURE 4. Dst-index behaviour during three chosen periods in Feburary 2014.

Global TEC distribution at 20 and 22:15 UT (13 and 15:15 LT for our region) was considered in the report [7] for February 27, 2014. The authors reported the intense positive disturbance exactly in the American sector. The large increase was observed within geographical latitudes 30—60º at the transition from 13 to 15:15 LT. Figure 5 shows the ratio of TEC(obs)/TEC(med). It is seen that the disturbance still was developing at 11 LT September 27th and was positive along the whole meridian.

The next period (Fig. 4 panel b) is characterized by the weak geomagnetic disturbance on February 8—9. The results for TEC are shown in Fig. 5 (panels b and c). Both hemispheres were covered with the positive night disturbance during which TEC can increase 2—2.5 times. In work [6] the authors considered the cases of TEC change in Mexico during the positive Dst values and showed that TEC change can be whether positive or negative in these cases. One of such cases is February 15, 2014. The curve in Fig. 5 panel "d" shows that in most cases the negative disturbance took place. The days of February 19—20 were the most disturbed during the considered period. Panels "e" and "f" of Fig. 6 illustrate TEC nighttime enhancements whose magnitude was not higher than during the weak disturbances on February 8—9. The case of February 19—20, 2014 was addressed in paper [4] with the focus on the NH polar region. The authors showed the maps of O/N2 ratio for the wide longitude zone including 100ºW. The most prominent decrease of O/N2 was higher than 40—45ºN. Our calculations show that beginning from ~11 LT till 23 LT the negative disturbance was observed higher than 30ºN.

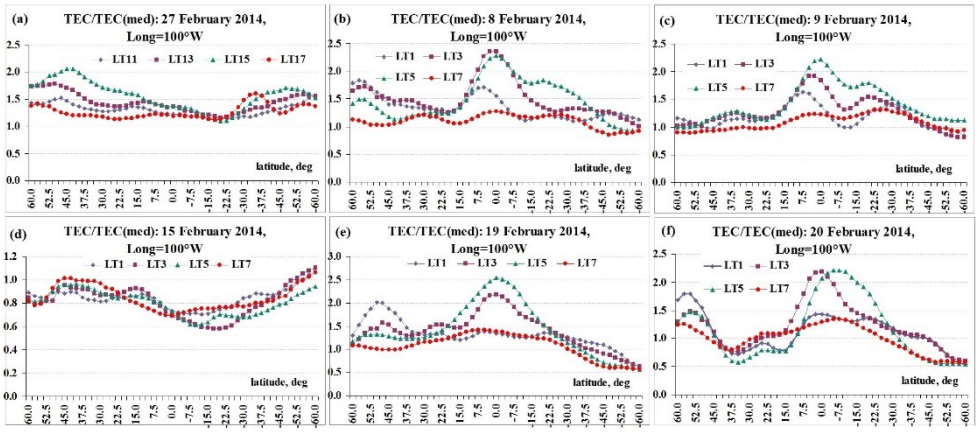

FIGURE 5. Characteristics of the disturbed ionosphere state during the chosen periods of February 2014.

Discussion and results. The results for two series of disturbed geomagnetic conditions showed the following. (1) Positive disturbances prevail both in day- and night-time. (2) TEC response to weak geomagnetic disturbances can be similar as to strong disturbances especially if they include positive Dst values. In work [6] the examples are for Dst>50nT, but the same cases are possible during the lower positive Dst values. The case of July 15—16, 2004 can serve as an additional example. This fact emphasizes the need of the continuous ionosphere monitoring with TEC. (3) It is supposed that EA crests can disappear during the strong disturbances. However, the events of September 2011 prove that this disappearance is possible under weaker disturbances. (4) Qualitatively the positive and negative disturbances correlate with increase or decrease of O/N2 ratio. (5) EA crests are registered not only for the particular days but also in the median values with the hemisphere asymmetry in the most cases. In paper [8] various “misunderstandings” of processes responsible for EA presence and maintaining were noted. However, the responsibility of variations of the neutral wind for the hemisphere asymmetry remains without changes.

Acknowledgements: *SCiESMEX is partially funded by CONACyT-AEM Grant 2014- 01-247722, CONACyT LN 269195, and DGAPA-PAPIIT Grant IN106916. The work of Maltseva O.A. was supported by grant under the state task N3.9696.2017/8.9 from Ministry of Education and Science of Russia. The authors express their gratitude to the services of IGS for the opportunity of using IONEX data via Internet.*

1. G. A. Mansilla, Moderate geomagnetic storms and their ionospheric effects at middle and low latitudes, *Adv. Space Res.*, 2011, 48, pp. 478—487, doi: 10.1016/ j.asr.2011.03.034.

2. S. P. Karia, N. C. Patel, and K. N. Pathak, Comparison of GPS based TEC measurements with the IRI-2012 model for the period of low to moderate solar activity (2009—2012) at the crest of equatorial anomaly in Indian region, *Adv. Space Res.*, 2015, 55, pp. 1965—1975, doi: 10.1016/j.asr.2014.10.026.

3. J. E. Titheridge, Changes in atmospheric composition inferred from ionospheric production rates, *J. Atmos. Terr. Phys.*, 1974, 36, pp. 1249—1254.

4. T. Durgonics, A. Komjathy, O. Verkhoglyadova et al., Multiinstrument observations of a geomagnetic storm and its effects on the Arctic ionosphere: A case study of the 19 February 2014 storm, *Radio Sci.*, 2017, 52, pp. 146 — 165, doi:10.1002/2016RS006106.

5. M. V. Klimenko, V. V. Klimenko, I. E. Zakharenkova et al., Similarity and differences in morphology and mechanisms of the foF2 and TEC disturbances during the geomagnetic storms on 26—30 September 2011, *Ann. Geophys.*, 2017, 35, pp. 923—938, doi: 10.5194/angeo-35-923-2017.

6. H. Ibarra, R. Pérez-Enríquez, R. López-Montes, and J. A. López Cruz-Abeyro, Geomagnetic activity with values of Dst ≥ 50 nT and their influence on the ionosphere at mid latitudes from 1999 to 2014, *Tenth Latin American Conference on Space Geophysics (X COLAGE)*, Cuzco, Peru, September 8—12, 2014 (PS4-16).

7. J. Berdermann, Access to multi-instrument data with focus on the ionosphere using different ESPAS data sources, *ESWW11*, Nov. 17 — 21, 2014, Liege, Belgium.

8. N. Balan,, J. Souza, and G. J. Bailey, Recent developments in the understanding of equatorial ionization anomaly: A review, *J. Atmos. Solar-Terr. Phys.*, 2017, pp. 1—9, doi: 10.1016/j.jastp.2017.06.020.

Traveling Ionospheric Disturbance Interferometry Using Geostationary Navigational Satellites

Nikita A. Tereshin, Artem M. Padokhin, and Ekaterina A. Kozlovtseva

Department of Atmospheric Physics, Faculty of Physics, Lomonosov Moscow State University, Leninskiye Gory 1-2, Moscow, 119991, Russia

Introduction. Recent developments in GNSS and SBAS and introduction of additional geostationary satellites in their constellations brought even more attention to problems of ionospheric remote sensing and allowed new remote sensing techniques to be developed. Growing networks of GNSS receivers (IGS, GEONET, ARGN and others) provide more data for experiments than there ever was. Results achieved with latest techniques have provided new knowledge about multiple ionospheric phenomena, such as the equatorial anomaly, main ionospheric trough, and various localized inhomogeneities. In particular, traveling TIDs of various origins are currently being explored by a significant number of researchers.

GeoGNSS interferometry. Among many other techniques, TIDs are currently being studied using GPS-interferometry [1—3], which requires a great deal of precision in tracking ionospheric pierce points (IPPs) due to satellite movement. Results achieved with this method usually require careful interpretation since IPP

movement velocities are usually comparable to characteristic velocities of TIDs and AGWs. Previously, in pre-GPS epoch, the same exact techniques used radio beacons installed on geostationary satellites (such as ATS-6, etc.) which circumvented the above-mentioned problem. TEC in those cases, however, was determined using Faraday rotation of signal polarization plane, leading to two major disadvantages: a) an *a priori* estimate of Earth's magnetic field was necessary for calculations, and b) acquired TEC data was less precise compared to dual-frequency GPS phase-based estimates. These two disadvantages can be eliminated using signals from geostationary GNSS satellites that can be received by existing geodetic GNSS receivers (the corresponding data is already available from IGS's MGEX, and ARGN network, for example). To the best of authors' knowledge, this experiment setup has yet to be implemented by other research groups. The proposed technique can reasonably improve the quality of data obtained by GNSS interferometry of the ionosphere.

The approach used in this work is based on the assumption that the geostationary TEC variations caused by TIDs being studied are essentially a planar wave traveling at a constant velocity. This assumption holds true when TID is significantly larger in scale than the characteristic distance between receivers in the network. TEC variations measured on three receivers relatively close to each other are expected to have similar structure of time variations with varying time offset caused by wave propagation. By examining the correlation functions between geostationary TEC data from those receivers, and therefore essentially measuring the delay between wave front transitions, an estimate of wave velocity and direction is obtained.

Results. This work presents preliminary results achieved using the above-mentioned technique. Four stations of Australian AGRN network (darw, doda, lkya, jab2) and Compass-G6 satellite were used in this study, see Fig. 1, bottom-right for the geometry. For the test day September 1, 2017, TEC variations at these four stations were considered (Fig. 1, top-left).

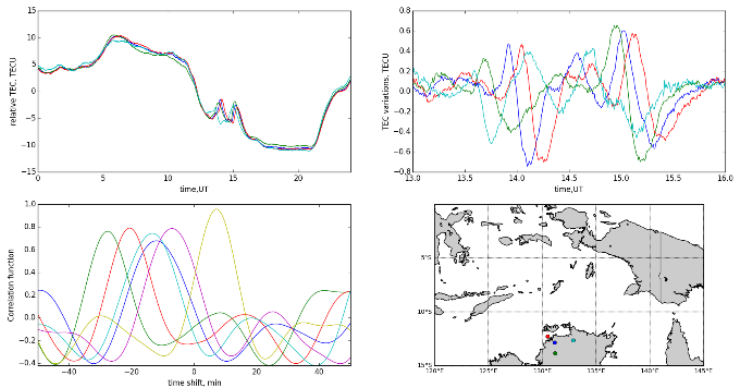

FIGURE 1. Example of LSTID detection. Top-left: relative slant TEC values (line colors correspond to receiver markers on the map). Top-right: detrended TEC variations. Bottom-left: correlation functions between TEC variations from pairs of stations, showing propagation of the TID. Bottom-right: map of the receivers used.

LSTID signatures are prominent in TEC variations (see Fig. 1 top-right) in the night sector between 13UT and 16UT. By examining correlation functions for pairs of receivers (Fig. 1, bottom-left), zonal and meridional components of TID velocity are estimated to be ~160 m/s and ~260 m/s, respectively, giving the total propagation velocity ~305 m/s in NNE direction. Obtained propagation velocity corresponds to AGW-driven TID.

The preliminary results presented in the paper show that suggested geoGNSS-interferometry approach can be capable of continuous monitoring of LSTID propagation, especially in equatorial and low-latitudes. If denser receiving networks are considered, suggested technique could also be applied to studying medium- and small-scale TIDs, requiring further research in this direction.

This work is supported by RFBR grant 18-35-00663.

1. E. L. Afraimovich, *Interference Methods of Ionospheric Radio Sounding*, Nauka, Moscow, Interferencionnye metody radiozondirovanija ionosfery, 1982, 198 p. (in Russian)

2. N. P. Perevalova, Investigation of ionospheric disturbances by the method of transionospheric GPS sounding, Irkutsk, ISZF, Issledovanie ionosfernyh vozmushhenij metodom transionosfernogo GPS-zondirovanija, 2014, 286 p. (in Russian)

3. E. L. Afraimovich, N. P. Perevalova, and S. V. Voeykov, Traveling wave packets of total electron content disturbances as deduced from global GPS network data, *J. Atmos. Solar-Terr. Phys.*, 2003, 65(11/13), pp. 1245—1262.

Appearance Frequency of GNSS Amplitude and Phase Scintillations at Mid-Latitudes

Yury V. Yasyukevich[1,2], Artem M. Vesnin[1,2], Dmitry A.Zatolokin[1], Semen V. Syrovatskii[1,2], Vladislav V. Demyanov[1,3], and Maria A. Sergeeva[4,5]

[1]Institute of Solar-Terrestrial Physics SB RAS, Irkutsk, Russia
[2]Irkutsk state university, Irkutsk, Russia
[3]Irkutsk state transport university, Irkutsk, Russia
[4]SCiESMEX, LANCE, Instituto de Geofisica, Unidad Michoacan, Universidad Nacional Autonoma de Mexico, Mexico
[5]CONACYT, Instituto de Geofisica, Unidad Michoacan, Universidad Nacional Autonoma de Mexico, Mexico

Introduction. Ionosphere impacts significantly on radio wave propagation [1]. Small-scale irregularities with size of the first Fresnel zone result in signal scattering and amplitude scintillations [2]. Phase scintillations are caused by irregular refraction on larger irregularities. For the global navigation satellite systems (GNSS) such irregularities can result in losses-of-phase lock [3] and deterioration of positioning quality [4].

Usually, S4 index [5] is used to study amplitude scintillations and σφ index [6] to study phase scintillations. Current paper is devoted to statistical analysis of phase and amplitude GPS/GLONASS scintillations at mid-latitude station in Irkutsk (52° N, 104° E).

Data and facilities. We used NovAtel GPStation-6 of Intsitute of solar-terrestrial physics SB RAS to record the scintillation data. S4 index is the signal intensity *I* standard deviation normalized to the average signal intensity:

$$S4 = \frac{\sqrt{\langle I^2 \rangle - \langle I \rangle^2}}{\langle I \rangle} \quad S4 = \frac{\sqrt{<I^2>-<I>^2}}{<I>} \tag{1}$$

σφ index is simply the standard deviation of signal phase φ:

$$\sigma\varphi = \sqrt{\langle \varphi^2 \rangle - \langle \varphi \rangle^2} \quad \sigma\varphi = \sqrt{<\varphi^2> - <\varphi>^2} \tag{2}$$

The GNSS receiver records S4 and σφ (1-sec, 3-sec, 30-sec, 60-sec) with 1-min time resolution. For analysis we used S4 and 3-sec σφ data from Aug. 2014 till Nov. 2017.

We used normalization of S4 and σφ [7] to reduce influence of elevation changing. Thus quasivertical indexes were obtained.

Results and discussion. Figure 1 shows distribution of the GPS and GLONASS amplitude scintillation index (S4). The statistics for GPS and GLONASS at L1 frequency differ slightly ($7.7 \cdot 10^6$ vs $6.3 \cdot 10^6$) due to different numbers of satellites. Bin of "1" contains all measurements when S4 >=1. Ignoring S4 <=1 the amount of records with corresponding S4 decrease exponentially with increasing S4. The factor of decreasing is different for GPS and GLONASS. The total amount of recorded GPS samples with GPS S4>=0.7 was 825 while there were only 11 such cases for GLONASS. It is rather unexpected because both GPS and GLONASS use almost the same frequency (~1.2 GHz).

Partially it can be explained with different satellites in view for GPS and GLONASS and better geometry for GLONASS satellites in high-mid and high latitudes. Another probable explanation is that GLONASS satellites radiate individual frequencies that means different scintillation pattern from one satellite to another. This difference can be especially significant for low-elevation satellites in contrast to near-zenith ones. These explanations, however can not explain difference in the general trend in S4 distribution curve for both GPS and GLONASS and need to involve GLONASS and GPS signal processing features analysis in case of their concurrent operation within one common GNSS receiver unit.

General S4 statistics for L2 is lower and contents ~ 4.2 and 3.6 million records for GPS and GLONASS correspondently. Probability distribution for S4 GPS at L2 frequency mostly exhibits gamma-distribution form. There is sharp decrease in distribution curve here with S4 increasing. There are only 114 cases when S4 >=0.2.

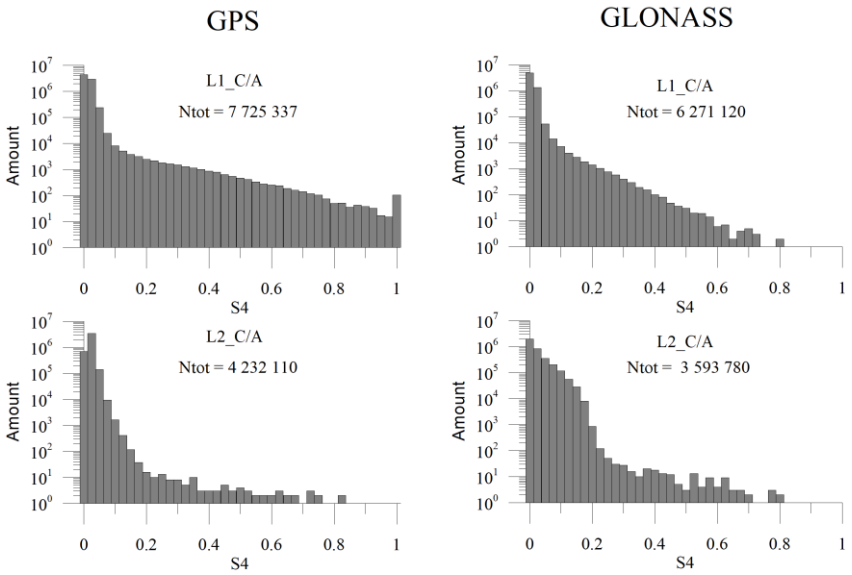

FIGURE 1. Distribution of GPS (left column) and GLONASS (right column) amplitude scintillation intensity (S4 index). Upper panels show distribution of S4 at the main frequency L1, bottom panels show those at L2. Ntot is the total number of measurements.

The significant difference in S4 at L1 and S4 at L2 is also unexpected. The irregularity sizes, which effectively result in amplitude scintillation, at L1 and at L2 differ less than 10%. It means that another explanation should be involved to understand the nature of the above mentioned results.

Taking in account all the above mentioned It would be interesting to consider the σφ at L1 and L2 frequency bands for both GPS and GLONASS. Figure 2 shows the L1 and L2 σφ distribution of the GPS and GLONASS phase scintillation intensity σφ. Bin "1.5" contains all the records with σφ>=1.5 rad.

We should note there are a lot of such records: 16571 at L1 GPS, 23377 at L2 GPS, 11251 at L1 GLONASS, 23963 at L2 GLONASS. Such records correspond probably to losses-of-phase lock. At L2 frequency there are more losses-of-phase lock due to less signal intensity.

In the majority of cases the phase scintillations had the intensity less than 0.1 rad. There were almost no scintillations with σφ>=0.6 rad. Probably, it is connected with peculiarities of signal treatment in the receiver. Standard phase recording model suggest that σφ<15° (0.26 rad.) [8]. However, receiver can measure more intense scintillations. On can see that GLONASS is characterized by higher level of phase scintillations in general (Fig. 2).

The results we obtained tell that there are certain features in GPS and GLONASS signal processing in case of their concurrent registration within one common GNSS receiver unit. In means that an analysis of GNSS combined signal

processing technique should be conducted and taking in account before the ionospheric data interpreting separately from GPS and GLONASS channels. The other important question is how to provide the correct GNSS receiver tuning before it is being used in combined ionospheric measurements involving both GPS and GLONASS channels concurrently. And, finally, intersystem biases while GPS and GLONASS units combining can arose as an important deterioration in the correct GNSS ionospheric data interpreting.

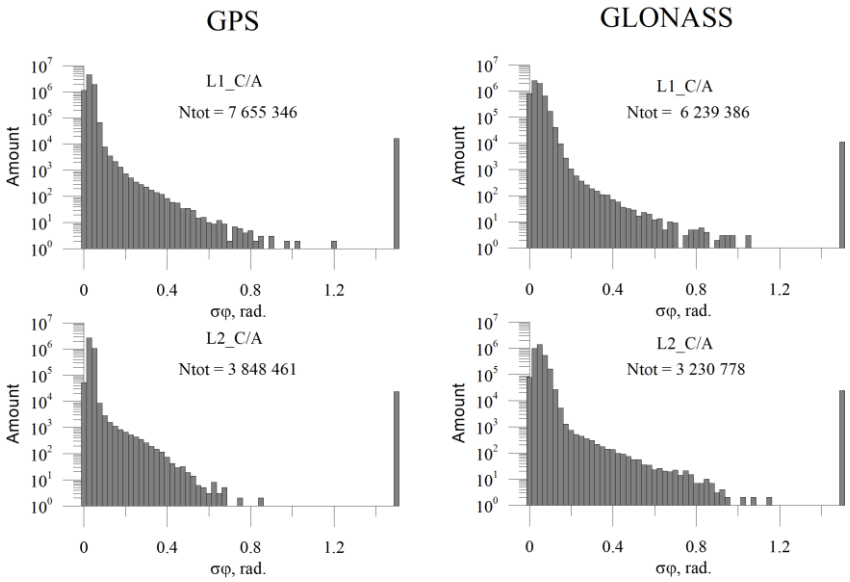

FIGURE 2. Distribution of the GPS (left column) and GLONASS (right column) 3-sec phase scintillation intensity (σφ index). Upper panels show distribution of σφ at the main frequency L1, bottom panels show those at L2. Ntot is the total number of measurements.

This work was performed under the Russian Science Foundation Grant No. 17-77-20005. Experimental data were recorded by the Angara Multiaccess Center facilities at ISTP SB RAS under program of the fundamental research of the state academies of Russia for 2013—2020 years (project No. II.16.1.1).

1. J. H. Dellinger, The role of the ionosphere in radio wave propagation, *Transactions of the American Institute of Electrical Engineers*, 1939, 58(12), pp. 803—822.

2. K. C. Yeh and C. H. Liu, Radio wave scintillation in the ionosphere, *Proc. IEEE*, 1982, 70(4), pp. 324—360, doi:10.1109/PROC.1982.12313.

3. P. M. Kintner, B. M. Ledvina, and E. R. de Paula, GPS and ionospheric scintillations, *Space weather*, 2007, 5, S09003, doi:10.1029/2006SW000260.

4. V. V. Demyanov, Yu. V. Yasyukevich, and S. Jin, Effects of Solar Radio Emission and Ionospheric Irregularities on GPS/GLONASS Performance, *Chapter in Book Geodetic Sciences — Observations, Modeling and Applications*, Prof. Shuanggen Jin (Ed.), 2013, pp. 177—222, InTech, available: http://www.intechopen.com/books/geodetic-sciences-

observations-modeling-and-applications/effects-of-solar-radio-emission-and-ionospheric-irregularities-on-gps-glonass-performance.

5. E. J. Fremouw and H. F. Bates, Worldwide behavior of average VHF-UHF scintillation, *Radio Sci.*, 1971, 6(10), pp. 863—869, doi: 10.1029/RS006i010p00863.

6. E. J. Fremouw, R. L. Leadabrand, R. C. Livingston et al., Early results from the DNA Wideband satellite experiment — Complex signal scintillation, *Radio Sci.*, 1978, 13, pp. 167-187.

7. L. Spogli, L. Alfonsi, G. De Franceschi et al., Climatology of GPS ionospheric scintillations over high and mid-latitude European regions, *Ann. Geophys.*, 2009, 27, pp. 3429—3437, doi:10.5194/angeo-27-3429-2009.

8. D. E. Kaplan and C. J. Hegarty, *Understanding GPS. Principles and Applications. Second Edition*, ARTECH HOUSE, INC., 2006, 723 p.

Tropospheric Delay of Radio Navigation Data Simulation

Alexey V. Zuev, Natalya V. Ryabova

Volga State University of Technology of Yoshkar-Ola,
424000, Lenin Sq., b. 3., Yoshkar-Ola, the Republic of Mari El, Russia

Introduction. The delay in the radio signal during the passage of the neutral atmosphere is commonly referred to as tropospheric delay, since the troposphere accounts for 80% of the total delay. Consequently, when we are talking about the troposphere applicably to the models of tropospheric delay, we mean the lowest 50 km of the neutral atmosphere.

The neutral atmosphere is divided into two components: the dry and humid components of the troposphere. The dry component of the troposphere consists mainly of dry gases. The humid component of the troposphere is the result of the water evaporation. The troposphere is the cause of the radio waves delay. The magnitude of tropospheric delay does not depend on the frequency of radio waves. Therefore, it is impossible to measure the magnitude of tropospheric delay by comparing the radio signals transmitted at two different frequencies, as is possible for ionospheric delay [1].

The aim: to carry out the modeling of tropospheric delay and to compare the simulation results with experimental values.

The overview of the most famous tropospheric models. The Hopfield model is based on a large number of measurements taken from meteorological stations in various places for several years. Helen Hopfield created the model on the basis of the assumption that the temperature change depends on the altitude with a constant speed of 0.0062 K/m. This led to the expression of a dry and wet part of tropospheric delay through a polynomial of the fourth degree.

Saastamoynen when developing their own model suggested that it is not necessary to have a detailed understanding at the temperature of the height distribution to calculate the delay integral. This simplifies the derivation of the delay formula and, paradoxically, increases the accuracy of this formula, since the height is directly proportional to the pressure in a dry atmosphere [2, 5].

Saastamoynen deduced the model, based on the following assumptions:

• water vapor behaves like an ideal gas;

• all water vapor of the atmosphere is localized in the troposphere;

• the temperature decreases linearly with altitude increasing

The third of the models considered was developed at the University of New Bruswick and is intended for use in the GPS WAAS system. This model does not require meteorological data.

For considering the dry and wet delay at the zenith, formulas similar to those of the Hopfield model are used, but the values of temperature, pressure and humidity are obtained by interpolating the mean values for latitude and day of the year.

The next model of tropospheric delay is the GCAT model (GPS Code Analysis Tool). The GCAT model was implemented in the GCAT (GPS Code Analysis Tool) software product developed by the research team of astronomy and space geodesy of the Polytechnic University of Catalonia [1]

The MOPS model was developed by EGNOS (European Geostationary Navigation Overlay Service) for use in the GPS SBAS (Satellite Based Augmentation System) correction system to the territory of Europe. It does not use terrestrial meteorological data. Instead, the average values of the meteorological data and the rate of change in the atmosphere temperature for different latitudinal belts with a step of 15 degrees and an ordinal day per year were introduced into the model [1].

Computer modeling of Hopfield, Saastamoinen, GCAT and Mops models. The second part of the study is a comparison of the tropospheric delay data with the help of four models obtained using a written program in the JavaScript language.

Figure 1 shows the algorithm of the developed program that allows calculating tropospheric delay values under conditions of altitude, temperature and atmospheric pressure changes.

Comparative analysis of theoretical and experimental data. The correlation coefficient between the experimental data obtained from the NovatelFlexPackV2 (x) receiver and the theoretical data recalculated using the Hopfield model (y) method [2—4] is determined by the formula:

$$r = \frac{\sum_i (x_i - \bar{x})(y_i - \bar{y})}{\sqrt{\sum_i (x_i - \bar{x})^2 (y_i - \bar{y})^2}}$$

Define the correlation coefficients for the remaining seasons:

TABLE 1. Correlation coefficients at different seasons

Season of the year	correlation coefficient (r)
Winter	0,86291
Spring	0,89468
Summer	0,81837
Autumn	0,88273

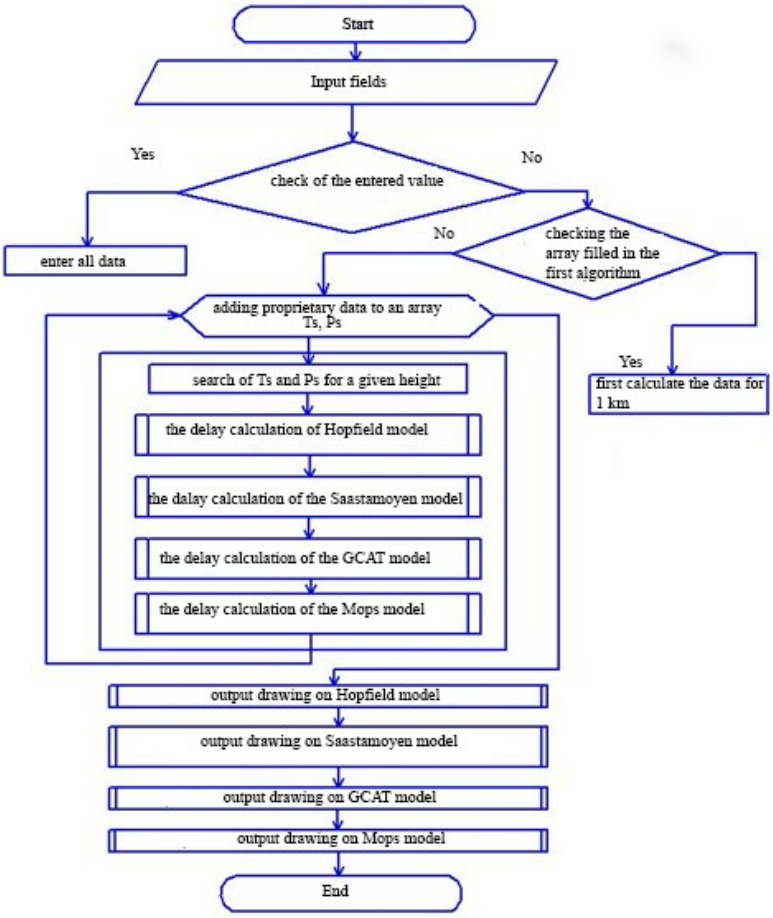

FIGURE 1. The algorithm of the program operation.

Main results of the study

1. The search for existing models of tropospheric delay was carried out, five most frequently encountered models were considered. Of the five models, the Hopfield, Saastamoynen, GCAT (GPS CodeAnalysisTool) and MOPS models were chosen, because, according to theoretical information, they are accurate for relatively simple implementation on a computer.

2. JavaScript has developed a program for modeling tropospheric delay, calculations are performed using four models (Hopfield, Saastamoinen, GCAT (GPS CodeAnalysisTool), MOPS). The program allows you to calculate the values of tropospheric delay in conditions of changes in altitude, temperature and atmospheric pressure, which is its characteristic feature.

3. The greatest correlation of theoretical and experimental data is observed in the spring period, the smallest correlation is in the summer period.

The work was supported by a grant on the project part of the government task of the Ministry of Education and Science of the Russian Federation: No. 8.2817.2017 / PP.

1. D. Yu. Pershin, Comparative analysis of models of tropospheric delay in the problem of determining the location of high accuracy in satellite navigation systems GLONASS / GPS, *Vestnik NSU.Ser. Information technologies,* 2009, 7, pp. 84—91.

2. H. S. Hopfield, Two-quartic tropospheric refractivity profile for correcting satellite data, *J. Geophys. Res.,* 1969, 74(18), pp. 487—499.

3. Product Features: FlexPak-V2, http://www.mnicglonass.ru/summary.php?id=134 — Date of circulation: 21.11.2017.

4. Multifunctional weather station (WMR200), http://www.oregonscientific.ru/catalog/mnogofunktsionalnaya-pogodnaya-stantsiya-wmr200/. — Date of circulation: 15/05/2017.

5. Yu. Saastamoynen, *Tropospheric and stratospheric corrections of the radio tracking of satellites: a textbook*, Moscow: Mir, 1975, 432 p.

Troposphere and Ionosphere Variations under Meteorological Disturbances in April 2016

Olga P. Borchevkina[1,2], Mikhail I. Karpov[1,3], Yuliya A. Kurdyaeva[1], Pavel A. Vasiliev[1] and Ivan V. Karpov[1,2]

[1] Immanuel Kant Baltic Federal University, Kaliningrad, Russia
[2] Kaliningrad branch of Pushkov Institute of Terrestrial Magnetism, Ionosphere and Radiowave Propagation, Russian Academy of Sciences, Kaliningrad, Russia
[3] Murmansk State Technical University, Murmansk, Russia

Introduction. The atmosphere is a natural geophysical fluid laboratory that can sustain to a significant degree wave generation, propagation, and dissipation processes. The associated wave-mean flow interactions produce spectacular hydrodynamical phenomena. Internal waves primarily generated in the lower atmosphere by various weather systems and various nonlinear physical processes

can propagate to higher altitudes in the atmosphere. Recently, it has been increasingly acknowledged that wave-induced vertical coupling has wider reaching implications in the momentum and energy balance of the atmosphere, in particular, at higher altitudes [1, 2]. Hypotheses about the mechanisms of the influence of processes in the lower atmosphere on the upper atmosphere and the ionosphere are based on the ideas of acoustic gravity (AGW) and gravity waves (GWs) generation which close to the Brent-Vaisela frequency in the lower atmosphere and their vertical propagation into the upper atmosphere. Meteorological storms are a source of generation of atmospheric waves in a wide spectral range [1, 3].

The paper presents the observations results of variations with AGW and small-scale GWs periods in the troposphere and the ionosphere in Baltic region in the time of meteorological storm.

The observations in the troposphere were made by lidar sensing. Frequency characteristics of troposphere parameters variations were determined from observations of the scattered lidar signal. Study of the ionosphere variability was carried out using ionosphere parameter TEC (total electron content). Observations data shows that in the spectra of scattered lidar signal presents harmonics with AGW and small-scale GWs periods witch generated in the lower atmosphere. The increasing of waves harmonics amplitudes observed in the meteorological storms time. Model study of the AGWs and GWs from meteorological storm area which propagate to the upper atmosphere shows the increasing of thermosphere temperature due the wave dissipation.

Observations in the lower and upper atmosphere.

In studies of the lower and middle atmosphere active sensing methods, in particular, lidar sounding have been widely used to study the characteristics of atmospheric parameters [4]. Lidar is an analogue of radar operating in the optical range. The source of radiation in the lidar is a laser. Observations in the lower atmosphere were conducted by lidar sounding using a two-wavelength lidar emitting at 532 and 1064 nm. The frequency characteristics of the variations in the parameters of the lower atmosphere were determined from observations of temporal changes of the intensity of the atmosphere-scattered lidar signal [4]. To study variations in the lower atmosphere was used an "E-LIS" program. The program can be used in analyses of the lidar sensing results and allows the dynamics of the scattered lidar signal and their spectral characteristics. The program includes a lidar data collection unit and modules, which allow performing harmonic analysis of observational data.

Investigation of the troposphere parameters variations in the meteorological storm period allows us to use this method.

Meteorological storm in Kaliningrad region (54˚ N, 20˚ E) was observed on March 31 — April 1, 2016. The storm is estimated at 6 points on the Beaufort scale. The maxima value of wind speed was 12 m/s. The geophysical conditions in the observed time were quiet. Figure 1 presents the changes in the spectra of the

scattered lidar signal variations on the 1064 and 532 nm wavelengths on the altitudes 5 and 10 km in this observation. In the observation analyses the main focus was on the 2—20 min. variations which caused by the generation of AGWs and small scale GWs [5].

The figure 1 shows the increasing of variations with short scale GWs periods (3—6 min.) in the spectra of scattering lidar signal data.

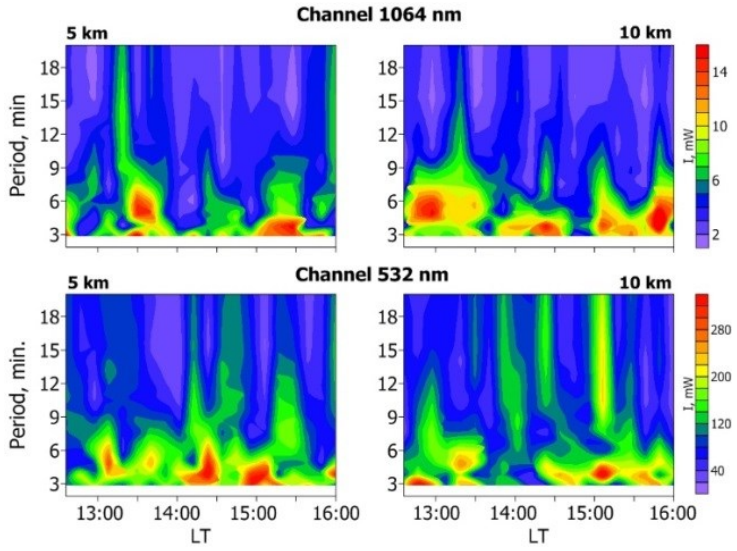

FIGURE 1. Temporal variability of the spectrum of variations in lidar signal intensity in observations in Kaliningrad at altitudes of 5, 10 km on April 1, 2016.

Figure 2 presents disturbances of the total electron content (TEC) for Kaliningrad region on March 30 — April 3, 2016. The relative TEC disturbances were calculated from the global ionosphere maps (GIM-TEC) in the IONEX format with resolution 2.5° in latitude and 5° in longitude and 2 h resolution [6] as $dTEC = \frac{TEC - TEC_0}{TEC_0} \cdot 100\%$, where TEC_0 are background values. The background values were chosen as the sliding median for the previous 15 days. In order to exclude effects of the geomagnetic activity, days with Kp ≥ 3 and Dst ≤ –40nT were not included in estimation of the background values.

Figure 2 shows the TEC relative disturbances on March 30 — April 3, 2016. In the time of the storm we can note the changes till 22.00 on March 31 to the 8.00 on April 1 in the Kaliningrad altitudes. The changes reaches up to 30% compared meteorological quite days. A numerical experiment was carried out to prove the hypothesis of the influence of the AGWs and short scale GWs propagating from the meteorological storm area, their effect on the ionization-recombination processes of the upper atmosphere.

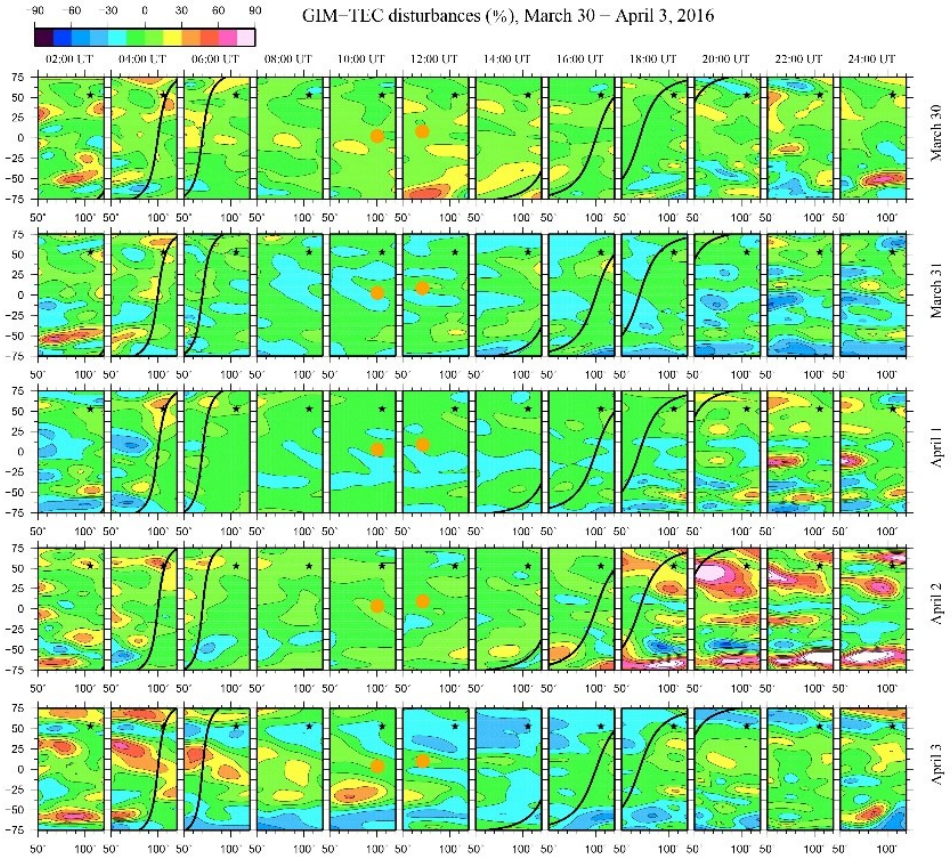

FIGURE 2. The TEC relative disturbances (%) on March 30 — April 3, 2016. The star denotes Kaliningrad, black line represents the terminator, and orange circle is sub-solar point. The maps are given in the geomagnetic coordinates.

In the calculations used a nonlinear hydrodynamic model ATMOSYM [http://atmos.kantiana.ru]. The dynamics of the atmosphere is described by a two-dimensional system of equations of thermohydrodynamics for atmospheric gas [7].

The pressure variations in the surface layer were taken as a wave source:

$$P|_{Z=0} = f_p(t), \tag{1}$$

$f_p(t)$ — the function, was determined from the results of lidar observations in the lower atmosphere during the meteorological storm. It is assumed that changes in the intensity of the signal received by the lidar reflect the pressure variations and, therefore, the pressure dependence on time can be represented in the following form:

$$p(t) = p_0 + f(t) \tag{2}$$

p_0 — background pressure, $f(t)$ — pressure variations.

The maxima amplitude changes in the intensity of the lidar signal are normalized to the amplitude of the maximum deviation of atmospheric pressure from the average value. This allows us to describe the perturbation of atmospheric pressure by expression:

$$f(t) = (I_t - I_m)\frac{p_d}{I_{max}} \tag{3}$$

I_t — changes in the intensity of the lidar signal, I_m — the average value of intensity, p_d — maximum pressure deviation (10 mm Hg), I_{max} — the maximum deviation from the average intensity value.

The wave source can be represented in the following form:

$$p(t,x) = p_0 + \exp\left(-\left(\frac{x-x_c}{L}\right)^2\right) f(t) \tag{4}$$

x_c — the coordinate that determines the position of the source at the lower boundary of the region of integration in the model's equations; L =100 km — length of source. The function *p(t,x)*, defined by the expression (4), describes the behavior of the pressure at the lower boundary of the numerical model.

Figure 3 shows spatial distributions of the change in the average temperature in the upper atmosphere created by the source at different times after the source.

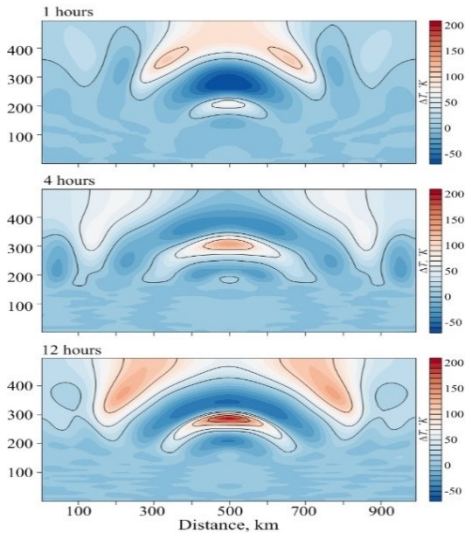

FIGURE 3. The spatial distributions of the change in the average temperature in the upper atmosphere created by the source at different times (1, 4 and 12 hours) after the source.

The propagation of AGW into the upper atmosphere is accompanied by perturbation of the background state of the atmosphere, which in turn influences

the propagation of waves in the upper atmosphere. The dissipation of AGW leads to the formation of a local thermal disturbance at altitudes of ~ 200—250 km, which expands in the horizontal direction and descends to lower altitudes, with the passage of time of the source in the lower atmosphere (Fig. 3). Local heating of the thermosphere affects the ionization balance, which in turn leads to a decrease in the TEC.

Conclusions. A complex experimental and theoretical study has revealed the features of the dynamics of atmosphere waves with AGWs and GWs periods in the lower atmosphere and the ionosphere during the meteorological storm passage. In the lidar observations there is an increase in the amplitudes of the variations with periods of 3—6 min during the meteorological storm. Confirmation of such realization of the processes of AGW propagation from sources on the Earth's surface and in the lower atmosphere can be the results of observations of variations of the TEC during the periods of the meteorological storm. A theoretical investigation of the propagation of AGWs into the upper atmosphere from the source in the lower atmosphere showed that waves with periods close to the Brent-Vaisala period effectively penetrate the upper atmosphere and, as a result of dissipation, form a perturbation of the atmosphere at altitudes of ~ 200 km.

Acknowledgments: The work is supported by the RFBR grants No. 18-05-00184 (Borchevkina O., Karpov I.) and No. 17-05-00574 (Vasiliev P., Kurdyaeva Y.).

1. E. Yiğit, P. Koucká Knížová, K. Georgieva, W. Ward, A review of vertical coupling in the Atmosphere–Ionosphere system: Effects of waves, sudden stratospheric warmings, space. *J.Atmos.Sol.-Terr.Phys,* 2016, 141, 1—12, http://dx.doi.org/10.1016/j.jastp.2016.02.011i.

2. A. Medvedev and N. Gavrilov, The nonlinear mechanism of gravity wave generation by meteorological motions in the atmosphere, *J.Atmos.Sol.-Terr.Phys*., 1995, 57, 1221—1231, doi: 10.1016/0021-9169(95)00008-P.

3. J. Laštovička, Forcing of the ionosphere by waves from below, *J.Atmos.Sol.-Terr.Phys*., 2006, 68, 479—497, doi: 10.1016/j.jastp.2005.01.018.

4. K. Baumgarten, M. Gerding and F.-J. Lübken, Seasonal variation of gravity wave parameters using different filter methods with daylight lidar measurements at midlatitudes, *J. Geophys. Res. Atmos*., 2017, 122, doi:10.1002/2016JD025916.

5. I.V. Karpov, S.P. Kshevetsky, O.P. Borchevkina, A.V. Radievsky, A.I. Karpov, Disturbances of the upper atmosphere and ionosphere caused by acoustic-gravity wave sources in the lower atmosphere, *Russian Journal of Physical Chemistry B*, 2016, 35 (1), 59—64, doi: 10.1134/S199079311601005X.

6. S. Schaer, W. Gurtner, J. Feltens, IONEX: The IONosphere Map EXchange Format Version 1, *Proceedings of the 1988 IGS Analysis Centers Workshop*, 1998, 233—247.

7. S.P. Kshevetskii, Numerical simulation of nonlinear internal gravity waves, *Comput. Mathem. and Mathem. Phys*., 2001, 41(12), 1777—1791.

Statistical Characteristics of Ionosphere Variations in the Time of Seismic Activity

Tamara V. Gaivoronskaya, Aleksandr T. Karpachev

Institute of Terrestrial Magnetism, Ionosphere and Radio Wave Propagation (IZMIRAN), Moscow, 108840, Russian

Introduction. The ionosphere of the Earth is subjected to the solar and geomagnetic influence as well as to the earthquakes, the explosions, etc. The ionosphere layer F2 is the most changeable and the modification of critical frequencies foF2 is repeatedly marked in the time of seismic events [1—3].

In contradiction to global helio-geomagnetic influence the seismic events have the local nature, therefore the comparative analysis at two and more stations, one of that is located in epicenter zone and others are away the several hundred km from it, can be productive. For example, it is compared the variations of critical frequencies foF2 at stations Petropavlovsk — Magadan and Taipei — Okinawa of Pacific coast region from January to April 1992 and from June to September 1993, when the series of earthquakes were observed near by Petropavlovsk and Taipei accordingly. The daily calculated coefficients of mutual correlation between data of two stations are close to 1 on quiet days and have sharp minimum, when the ordinal diurnal trend of critical frequencies change before earthquakes. Thus, one is able to make the conclusion that preparation of earthquakes is accompanied by breaking the correlation of ionosphere data.

The analogous result is obtained on the ionosphere parameters recorded by the Atmosphere Explorer-C (AE-C) satellite above north region of Pacific Ocean in the time of series of earthquakes with magnitudes from M=5.0 to M=6.6. The satellite moved along the elliptical descending orbits at altitude of 300—170 km from north to south. On the orbits 601—606 the plasma concentration Np, the temperature of ions Ti and the plasma drift velocity Vd were measured in situ.

The comparison of ionosphere data on the next orbits shows the considerable decrease of their correlations over seismic active zone (Table 1). The coefficient of correlation of the drift velocity K(Vd) even changes the sign, that indicates on the appearance of disturbed drift component because of the additional electric field at ionosphere.

The regular radio sounding at groud-based stations in region of seismic activity allows to execute more detailed analysis of ionosphere parameters. It is constructed the series of relative deviations of critical frequencies DfoF2(P-M) for station Petropavlovsk as compared with station Magadan, which in fact do not contain the deviations connected with geomagnetic disturbances, diurnal and season variations.

$$DfoF2(P\text{-}M) = DfoF2(P) - DfoF2(M) = [foF2(P) - foF2(M)] - [C(P) - C(M)], \quad (1)$$

where $DfoF2 = foF2 - C$, C is the moving average of the frequency over the preceding 15 days; P and M correspond to Petropavlovsk and Magadan stations, respectively. By doing so, we eliminate the identical ionospheric variations associated with the geomagnetic storms and identify the distinctions associated with the difference in seismic conditions at the stations.

TABLE 1. The coefficients of correlations of the ionosphere parameters on the orbits of the satellite AE-C.

Orbits	Coefficients of correlations		
	K(Np)	K(Ti)	K(Vd)
601—602	0.930	0.779	+0.312
602—603	0.939	0.510	–0.377
603—604	0.891	0.313	–0.055
604—605	0.794	0.412	+0.615
605—606	0.852	0.804	+0.848

Statistical distributions of the relative deviations demonstrate that they are not random values, but contain the information about anomaly structures, arising at ionosphere altitudes and preceding the earthquakes. Before strong earthquakes with magnitudes of M=6 and more the displacement X of maximum of statistical distributions towards positive values and asymmetry A of the distributions is marked,

$$X = \mathrm{Sum}\, n_i\, x_i / N, \quad A = \mathrm{Sum}\, n_i\, x_i^3 / N, \quad N = \mathrm{Sum}\, n_i, \qquad (2)$$

here x_i is the quantity of middle of each statistical interval, n_i is the number of variations that fall into interval. The summing *Sum* is realized over the all intervals *i.* Both those indexes are expressed the better the more values of magnitude M, i. e. the more energy of prepared earthquake.

In Fig.1 it is shown the results of comparison of ionospheric characteristics X and A with magnitudes M of earthquakes. The horizontal axis shows the magnitudes M of ten most strong earthquakes of 1992—1994 for which the ionospheric data were available, the vertical axis shows the displacement X of the maximum in the statistical distribution of DfoF2(P-M) calculated for the 10-day periods before the earthquakes, the asymmetry A of the distributions is marked here also. The results calculated for five seismically and geomagnetically quiet periods, each with a duration of 10 days, are shown at the mark M = 0.0. For the first time the values characterizing the seismo-ionosphere disturbance and the energy index of the earthquake is successfully compared, thereby it is confirmed that the observed ionosphere anomalies are connected just with coming earthquake.

It is noted that the scatter in the values of X and A in Fig.1 can be caused by several factors. Primarily, it can reflect the complex anomalous structure of plasma distribution in the ionosphere, which was formed under the action of the electric

fields above the seismically active area, and the Petropavlovsk station not necessarily finds itself in the area of the maximum of the positive anomaly. Besides, many factors associated with the local structure of the Earth's crust in the epicentral zone of the earthquake are impossible to account for. The seasonal features of the ionospheric processes may also contribute to this scatter.

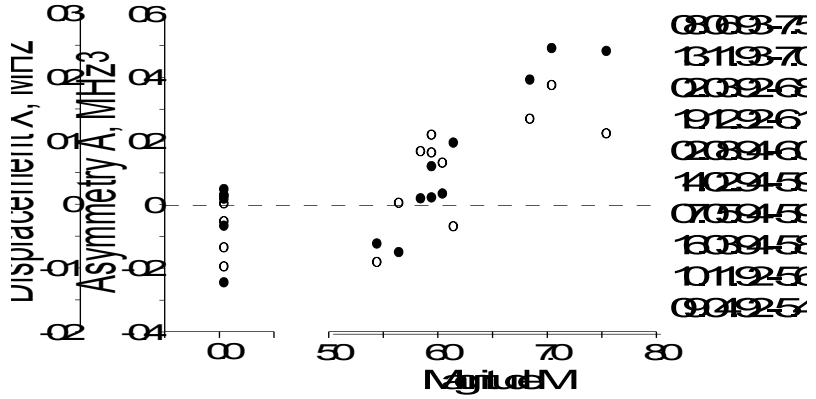

FIGURE 1. The displacement X and the asymmetry A of statistical distribution of the ionosphere variations DfoF2(P-M) as a function of the magnitude M. The dates and the magnitudes of the earthquakes are indicated on the right.

The efficiency of penetration of seismogenic electric fields into the ionosphere is low. The disturbances of the critical frequencies of the F2-layer induced by seismic activity are difficult to recognize against the daily irregular background variations, including the disturbances caused by the geomagnetic ionospheric storms. Nevertheless the analyzing the data of ionospheric radio sounding we found that the strong earthquakes in the Petropavlovsk region are typically preceded by the noticeable ionospheric anomaly. Moreover, the values of statistical characteristics X and A of ionospheric variations turns out to be correlated with the magnitude M of earthquake.

Thus, the break of correlative dependence of ionosphere parameters at several stations and the peculiarities of statistical distributions of relative deviations DfoF2 at those stations prove to be the ionosphere indicators of earthquakes.

1. T. V. Gaivoronskaya, Relative ionospheric disturbances on data of two radiosounding stations before earthquakes, Book of abstracts, *III International Conference "Atmosphere, Ionosphere, Safety"*,Kaliningrad, Russia, 2012, pp. 164—167.

2. T. V. Gaivoronskaya, Seismoionospheric effects in the F2 layer over Kamchatka, *Izvestiya, Physics of the Solid Earth*, 2012, 48(4), pp. 53—56.

3. T. V. Gaivoronskaya and A. T. Karpachev, Ionosphere indicators of seismic activity, *International scientific conference "Radiation and Scattering of Electromagnetic Waves",* Divnomorskoe, Russia, 2017.

Long (1964—2017) Data Base of Kaliningrad Ionosonde Observation

Nina A. Korenkova[1], Vladimir S. Leshchenko[1], Maxim V. Klimenko[1], Nikolay V. Chirik[1,2], Ekaterina I. Markina[2], Vladimir V. Klimenko[1], and Konstantin G. Ratovsky[3]

[1]West Department of Pushkov Institute of Terrestrial Magnetism, Ionosphere and Radio Wave Propagation, Russian Academy of Sciences, 236017, Kaliningrad, Russia
[2]Immanuel Kant Baltic Federal University, 236016, Kaliningrad, Russia
[3]Institute of Solar-Terrestrial Physics Siberian Branch of Russian Academy of Sciences, 664033, Irkutsk, Russia

Introduction. The ionosphere is a layer of the Earth's atmosphere, in which there's a sufficient level of ionization for influence on radio wave propagation. The ionosphere appears as a result of the action of ultraviolet and X-ray solar radiation on neutral particles of the upper atmosphere (thermosphere). The main parameters of the ionosphere are an electron density, ion composition and electron and ion temperatures. In solving applied problems, one of the most important parameters is the F2 layer peak electron density that can be determined from the vertical sounding of the ionosphere according to the formula describing its connection with the F2 layer critical frequency, *fo*F2. The F2 layer exists almost always, at all latitudes and longitudes, in all seasons and times. The F2 layer peak electron density and therefore *fo*F2 has strong variability even in quiet geomagnetic conditions. Temporal changes of these parameters of the unperturbed (regular) F region of the midlatitude ionosphere contain daily, seasonal and solar-cyclic variations. According to [1], the morphology of the *fo*F2 temporal variability in the mid-latitude ionosphere include: 1) an increase in *fo*F2 with a growth in the level of solar activity; 2) the smallest values of *fo*F2 occur before the local sunrise (a pre-sunrise minimum); 3) exceeding the winter daytime *fo*F2 values over the summer daytime values at similar solar activity (winter anomaly); 4) frequent occurrence of nighttime maximum in the winter *fo*F2 diurnal variation. During geomagnetic storms, sudden stratospheric warmings and meteorological storms there are significant changes in the spatial and temporal structure of the mid-latitude ionosphere [2—4].

The analysis of the solar, geomagnetic and meteorological activity contribution to the overall ionosphere variability was carried out using statistical and "case studies" approaches. The statistical approach gives approximately the same estimations of the meteorological and geomagnetic activity contributions (~ 13—15% of all the *fo*F2 disturbances in the mid-latitude ionosphere). The remaining part of the electron density disturbances (~ 70—74%) is associated with solar-cyclic and seasonal and variations [5]. The goal of this investigation is to study the influence of various factors on the temporal variability of *fo*F2 and its disturbances on the basis of the Kaliningrad ionosonde observation data. To achieve this goal,

the following problems were posed and solved: 1) the investigation of the solar and geomagnetic activity influence on the *fo*F2 variability; 2) an estimation of dependence of the *fo*F2 disturbances on the local time.

Observation data and methods of investigation. The basis of this study is an *fo*F2 observation database, accumulated from 1964 to 2017 by data from vertical sounding of the ionosphere above the mid-latitudinal station in the village of Ulyanovka (25 km from Kaliningrad (54°N, 20°E)). In different years the different ionosondes were used at this location: "Basis" (1964—1992), "AIS" (1992—2005), "Parus-A" (2007—2016). The modern Russian ionosonde "Parus-A" designed for vertical sounding of the ionosphere provides a sufficiently high signal-to-noise ratio over a wide range of sounding frequencies; it performs primary processing, storage and transfer of vertical sounding ionograms to the center of their collection and final manual (semi-automatic) processing. This type of ionosondes is built according to the classical scheme of a pulsed locator using a simple radio pulse of variable frequency in the frequency range from 1 to 20 MHz. In the present study, we used the manual scaled *fo*F2 data. To study the impact of solar and geomagnetic activity on *fo*F2 variability, we used the solar and geomagnetic activity indices: F10.7 (http://lasp.colorado.edu) and Ap (http://wdc.kugi.kyoto-u.ac.jp), respectively.

For the entire *fo*F2 observational database, 27-day moving averages, $<foF2>_{27}$ (Nday, LT), were calculated for each day (Nday) and local time (LT). Further, for each day and local time, we calculated the root mean square deviations of the *fo*F2 from their mean value:

$$\sigma(Nday, LT) = \sqrt{\frac{\sum_{i=1}^{n} (foF2_i(Nday, LT) - < foF2 >_{27} (Nday, LT))^2}{n}} \quad (1)$$

Equation (1) where n is the number of measurements for the selected 27 days for a given time; $foF2_i$ are the *fo*F2 values at a particular time on the 27-day interval under consideration. Further, absolute perturbations of the *fo*F2 with respect to their mean values were determined: $\Delta foF2$ (Nday, LT) = *fo*F2 (Nday, LT) — $< foF2>_{27}$ (Nday, LT). In the following we analyzed strong perturbations $\Delta foF2$ (Nday, LT), amplitudes of which exceeded the standard deviation σ, 2σ, 3σ, 4σ.

Results. Figure 1 shows a map of the distribution of the *fo*F2 values for all time moments and for each day for the period from 1964 to 2016. For the same years, this figure shows the annual averaged values of F10.7, Ap and *fo*F2. Data from the Kaliningrad ionosonde cover 4 cycles of 11-year solar activity and can be further used to study the *fo*F2 trends. The correlation coefficient between the annual averaged *fo*F2 and F10.7 values is 0.73. Also we note a small effect of geomagnetic activity on the *fo*F2 values with a correlation coefficient of 0.23. The annual averaged index of geomagnetic activity is not strongly dependent on solar activity (correlation coefficient 0.33). At the same time, the years of solar and geomagnetic activity maxima do not coincide and behave differently depending on a particular solar cycle.

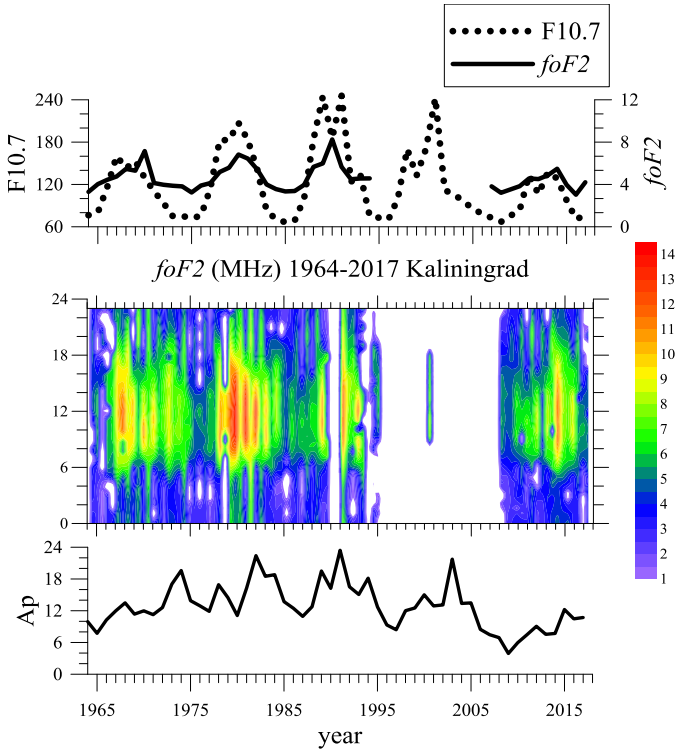

FIGURE 1. Middle panel: *fo*F2 distribution in the coordinates the day of the year — local time in hours for the whole database Kaliningrad station for the observational time interval of 1964—2017. The time periods, in which the observation data were absent, are shown by the white. The averaged over the year F10.7 and *fo*F2 values (upper panel) and Ap values (lower panel) are shown for the same years.

We carried out a study of strong *foF*2 perturbations, i. e. exceeding in the amplitude the standard deviation levels σ, 2σ, 3σ, and 4σ. Figure 2 together shows the total number of cases per year, in which *foF*2 perturbations exceeded the root-mean-square deviations of varying degrees of significance. It can be seen that the relationship between the number of statistically significant *fo*F2 disturbances and solar activity is practically absent. The connection between statistically significant *fo*F2 disturbances and solar activity was manifested only in the last solar cycle. To find out the reason for this fact, additional researches are required.

Figure 3 shows maps of daily-seasonal variations in numbers of statistically significant *fo*F2 disturbances exceeding σ, 2σ, 3σ and 4σ. The distribution of the number of measurements exceeding σ can be called uniform, from which fall October and November, as well as the pre-sunrise and post-sunset hours of December-February. There is a certain connection with the terminator line and

the number of *fo*F2 perturbations exceeding 2σ and 3σ. In general, it can be said that such disturbances are formed, mainly, in the pre-sunset hours and are practically not formed on the line of the morning terminator. The formation of the most significant perturbations in *fo*F2, exceeding 4σ, is fairly randomly distributed along time and month. Such disturbances are most often formed during the summer months in the illuminated time of day.

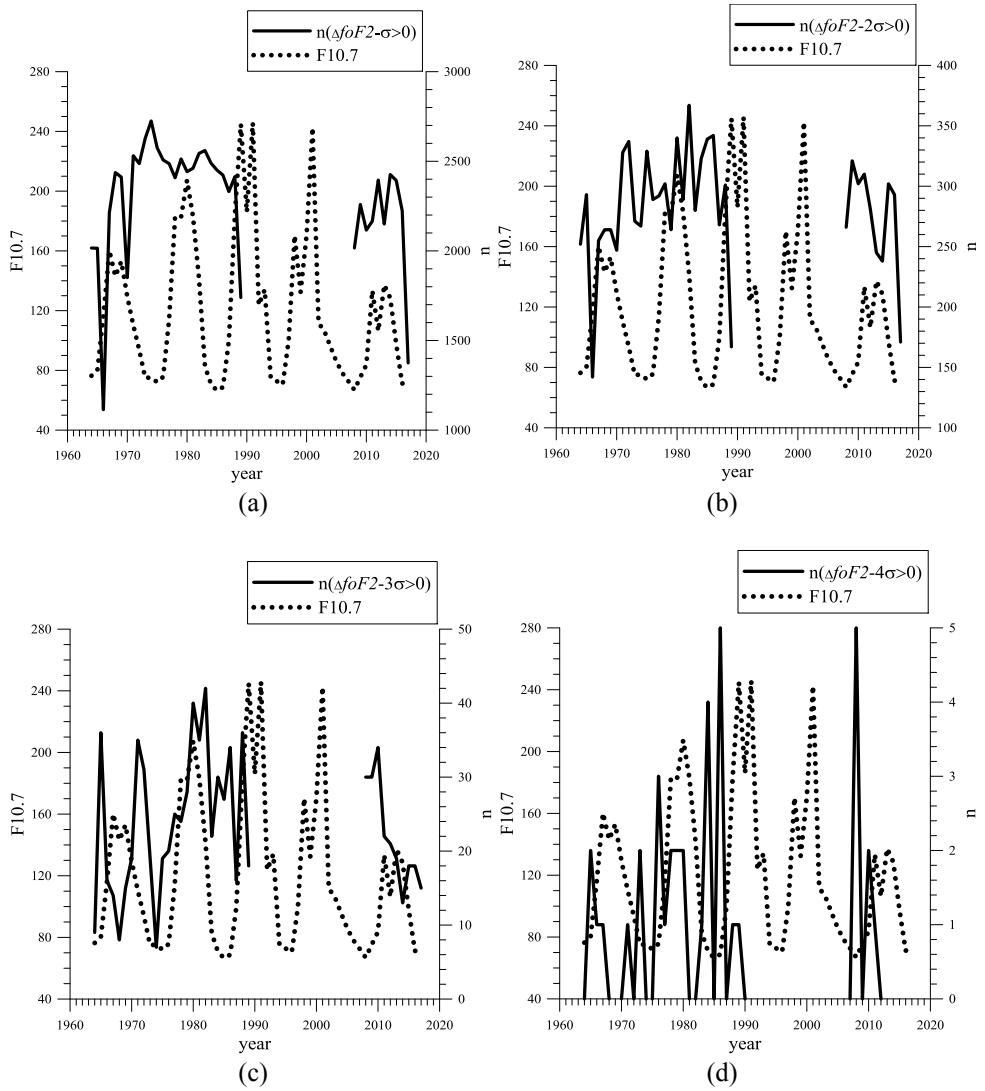

FIGURE 2. Year-to-year variations in amount of cases per year when the Δ *fo*F2 excess of over σ (a), 2σ (b), 3σ (c), and 4σ (d). Dashed lines show the annual averaged F10.7.

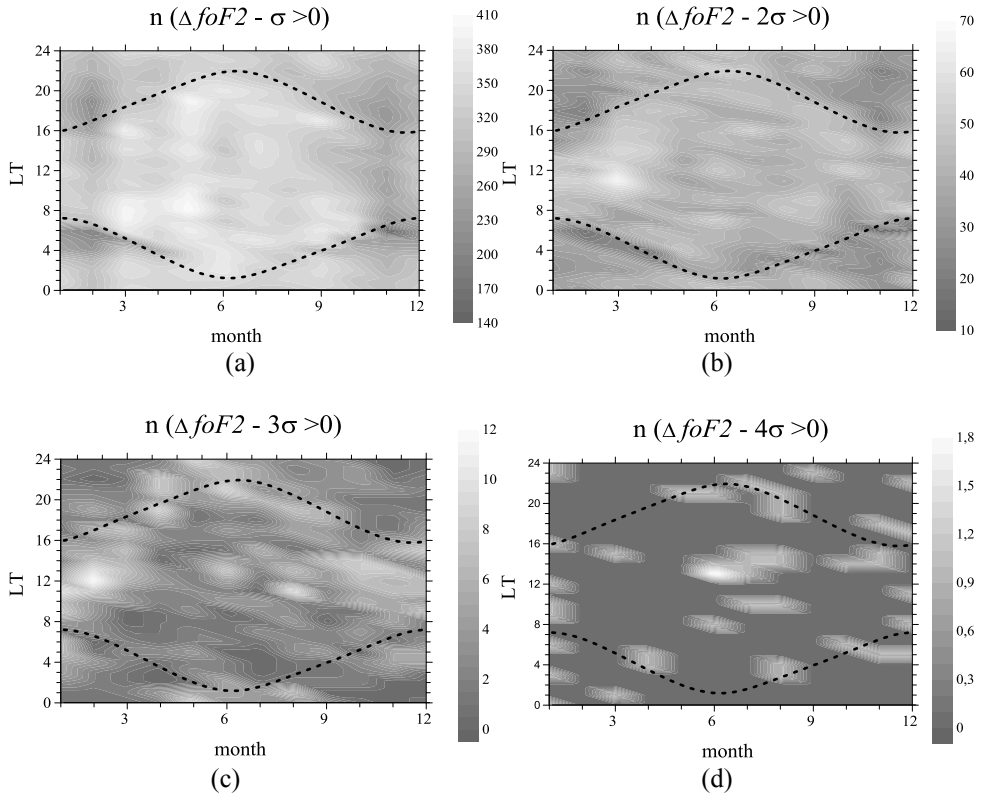

FIGURE 3. Diurnal and seasonal variations in the numbers of measurements Δ *fo*F2 perturbations, which exceed σ (a), 2σ (b), 3σ (c), and 4σ (d). Dashed curves show the terminator lines for the Kaliningrad station.

Conclusions. Based on the analysis of vertical ionospheric sounding data over Kaliningrad station for the period from 1964 to 2017, it can be noted that the annual averaged solar activity index is the determining factor for the *fo*F2 values, but not for Δ *fo*F2 disturbances. Statistically significant *fo*F2 disturbances are formed in neighborhood of the terminator line, except for the largest disturbances, which are more often formed in the summer during the illuminated time of day.

Acknowledgements. The reported study was funded by RFBR according to the research project № 18-55-52006.

1. M. N. Fatkullin, Ionospheric disturbances, *Geomagnetism and high atmospheric layers , Results of science and technology*, 1978, 4, pp. 6—107.

2. O. P. Borchevkina and I. V. Karpov, Ionospheric irregularities in periods of meteorological disturbances, *Geomagnetism and Aeronomy*, 2017, 57(5), pp. 624—629, doi:10.1134/S0016793217040041.

3. M. J. Buonsanto, Ionospheric storms — a review, *Space Sci. Rev.*, 1999, 88, pp. 563—601.

4. J. L. Chau, L. P. Goncharenko, B. G. Fejer, and H. L. Liu, Equatorial and low latitude ionospheric effects during sudden stratospheric warming events, 2012, *Space Sci. Rev.*, doi:10.1007/s11214-011-9797-5.

5. E. A. Araujo-Pradere, T. J. Fuller-Rowell, M. V. Codrescu, and D. Bilitza, Characteristics of the ionospheric variability as a function of season, latitude, local time and geomagnetic activity, *Radio Sci.*, 2005, 40, RS5009, doi:10.1029/2004RS003179.

Numerical Simulation of Sensitivity of Meridional Circulation to Impacts of Orographic Gravity Waves and QBO Phases in The Middle and Upper Atmosphere

Andrey V. Koval[1], Nikolai M. Gavrilov[1], Alexander I. Pogoreltsev[1,2], and Elena N. Savenkova[1]

[1]Atmospheric Physics Department, Saint-Petersburg State University, Ulyanovskaya st. 1, Saint-Petersburg, 198504, Russia
[2]Meteorological Forecast Department, Russian State Hydrometeorological University, Malookhtinskiy pr, 98, Saint-Petersburg, 195196, Russia

Introduction. The energy and momentum transport by internal atmospheric waves are considered as one of the important factors of dynamical interactions between the lower and upper atmosphere. For numerical modeling of the general circulation and thermal regime of the middle and upper atmosphere, it is important to take into account accelerations of the mean flow and heating rates produced by dissipating internal waves. One of the most important sources of atmospheric waves is the interaction between Earth's topography and upcoming atmospheric flow [1]. Propagation of the orographic gravity waves (OGWs), generated at the Earth's surface, into the middle and upper atmosphere can significantly affect the general circulation of the middle and upper atmosphere. Gavrilov and Koval [2] showed importance of the Earth's rotation for theoretical description of stationary OGWs. They developed a parameterization of dynamical and thermal effects of stationary OGWs, generated by the surface topography and propagating into the middle and upper atmosphere. This parameterization was implemented into a model of atmospheric general circulation [3]. The authors showed that OGW may produce substantial changes in the zonal circulation of the middle and upper atmosphere.

The influence of planetary waves (PW), OGW and gravity waves of other origin on meridional circulation in the atmosphere, was studied and evaluated in various models of general circulation (e. g., [4, 5]). The general circulation of the atmosphere in the middle and high latitudes can also be influenced by quasi-biennial oscillations (QBO), which create changes in the direction of the zonal wind in the low-latitude middle atmosphere with a period of about two years (see, for example, [6]).

In this study, we focus on the sensitivity of meridional and vertical circulation to OGW dynamical and thermal effects and to the changes in the QBO phases. The sensitivity numerical experiments are essential for better understanding of the roles of different factors in formation of global dynamical processes, in transport and mixing of atmospheric gas components, and in dynamical coupling of different layers of the lower, middle and upper atmosphere.

Numerical model and parameterizations. For numerical experiments studying dependencies of the atmospheric circulation on OGW parameterization and QBO phases we use the middle and upper atmosphere model (MUAM) [7]. Gavrilov et al. [8] described briefly the main equations and physical processes used in the model. The horizontal grid spacing is 5° and 5.625° in latitude and longitude, respectively. The model has 48 vertical levels the log-isobaric coordinate covering altitude range from 0 to 135 km.

The MUAM does not involve entire mechanisms forming QBO. To assimilate empirical data for years with different QBO phases, Pogoreltsev et al. [9] introduced additional terms to the MUAM equations for zonal wind and temperature, which are proportional to the deviations of the simulated wind and temperature from their zonal-mean climatic values at latitudes between 17.5° S and 17.5° N. Pogoreltsev et al. [9] used the UK Met Office meteorological reanalysis data [10] for January during years 1992—2011 to analyze signs of deviations of annual-mean and climatological (averaged for 20 years) zonal velocities over the equator. The positive and negative deviations correspond to the westerly and easterly QBO phases, respectively. In order to study the OGW influence on atmospheric dynamics, the recently developed parameterization of dynamical and thermal effects of stationary OGWs [2] was implemented. To calculate vertical profiles of the total vertical wave energy flux and the associated accelerations of the mean horizontal winds by stationary OGWs with ground-based observed frequencies $\sigma = 0$, the parameterization uses wave polarization relations that take into account rotation of the atmosphere.

Results of simulations. We used the MUAM model with included parameterizations of OGW dynamical and thermal effects for numerical simulations of the changes in the meridional and vertical velocities in the middle and upper atmosphere. In the experiments, the meridional and vertical components of wind velocity were simulated with and without inclusion of the OGW parameterization for conditions corresponding to the easterly and westerly QBO phases. The differences in values between these calculations demonstrate effects of OGW and QBO, respectively. Positive or negative differences indicate, respectively, increases or decreases in the corresponding quantities due to OGW effects or changes in QBO phases.

Figure 1a presents the simulated height-latitude distribution of the zonal-mean meridional velocity, averaged over January for the easterly QBO phase without OGW parameterization. Lines with arrows correspond to schematic zonal-mean streamlines calculated using the values of vertical velocity w multiplied by a factor

of 100 for the sake of illustration. A global meridional cell ascending at high and middle latitudes of the summer (southern) hemisphere and descending in winter (northern) hemisphere exists in Fig. 1a above 50—60 km. Below these altitudes, in Fig. 1a one can see additional ascend at latitudes 50—70◦N and descend at 50—70◦ forming local circulation sub-cells in both hemispheres.

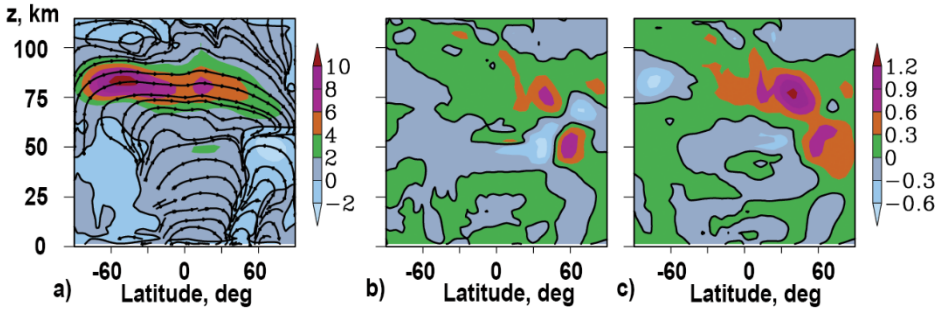

FIGURE 1. The simulated January zonal-mean meridional velocity (in ms^{-1}) and schematic streamlines for easterly QBO phase without OGW effects (a) and meridional velocity differences (in ms^{-1}) caused by inclusion of OGW effects (b) and change from easterly to westerly QBO phase (c).

Figure 2b shows simulated differences (MVD) zonal-mean meridional velocity, which are caused by the inclusion of OGW parameterization into the MUAM for the easterly QBO phase. One can see regions of increases or decreases (positive or negative MVD) in the meridional velocity after inclusion of the OGW effects. Hypotheses about nonzero differences in the meridional winds in Fig. 1b was verified using the statistical Student's t-test. Paired t-tests showed higher than 95% confidences of nonzero monthly mean meridional wind differences in latitude-altitude grid points used for plotting Fig. 1b, where their absolute values are larger than 0.1 ms^{-1}. In many cases in Fig. 1b, MVD signs are opposite to those of the meridional velocity in Fig. 1a. Therefore, OGW dynamical and heating effects may lead to a weakening of simulated zonal-mean meridional circulation fluxes. Peak MVDs in Figure 1b can reach ±(30—40)% of the zonal-mean meridional velocities at respective heights and latitudes in Fig. 1a. Simulated MVDs caused by the change from the easterly to westerly QBO phase without inclusion of OGW effects are shown in Fig. 1c. Application of paired t-tests for verification of nonzero MVDs in Figure 1c gave the same results as those described above for Figure 1b. There is the main maximum at high latitudes of the Northern Hemisphere at altitudes 40 — 60 km in Fig. 2c. This corresponds to significant weakening of the simulated southward meridional flux (up to 60%) there. The MVD minimum at altitudes 80—100 km at high latitudes of Southern Hemisphere corresponds to a decrease in the zonal-mean northward meridional velocity up to about 10%.

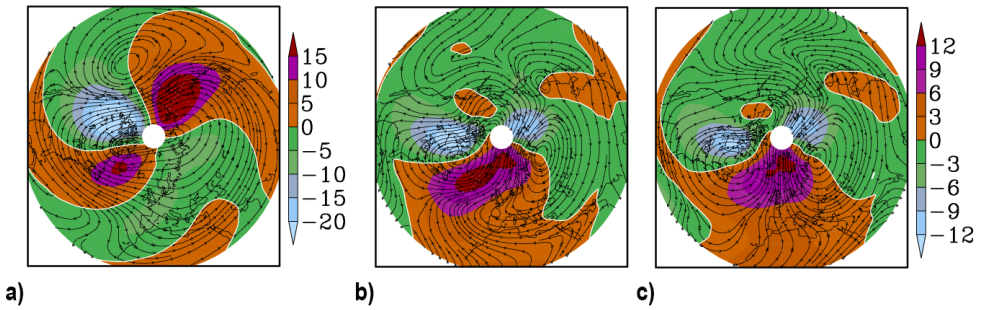

FIGURE 2. The North Pole stereographic projection at altitude 25km and latitudes 20—80 N of the simulated January mean meridional velocity (in ms^{-1}) for easterly QBO phase without OGW effects (a), meridional velocity differences (in ms^{-1}) due to inclusion of OGW effects (b) and change from easterly to westerly QBO phase (c). Contours with arrows show respective streamlines.

Figure 2a shows the North Pole stereographic projection of the simulated meridional wind (shaded areas) at altitude 25 km averaged over January without OGW effects and respective (including the zonal wind) streamlines. Fig. 2b and 2c give differences in meridional winds caused by inclusions of the OGW parameterization and change from the easterly to the westerly QBO phase. There are areas of northward meridional flux at high latitudes above Far East and North-West Atlantic and southward jets above Canada and Europe. These features make corresponding horizontal circulation cells. Inclusion of OGW parameterization as well as change of the QBO phase leads to the enhancement of northward jet above Atlantic Ocean and southward — above Canada. Fig. 3 is similar to Fig. 2 and indicates the simulated January mean vertical velocities and their differences produced by OGW effects and changes in QBO phases. Peak values of the differences in Fig. 2b, and 2c, 3b and 3c can reach up to ±(50—100)% of the respective peak values shown in Fig. 2a and 3a. Therefore, inclusion of OGW dynamical and thermal effects and changes in QBO phases in our experiments may produce substantial changes in vertical and meridional velocities in the middle atmosphere simulated with the MUAM model at middle and high latitudes.

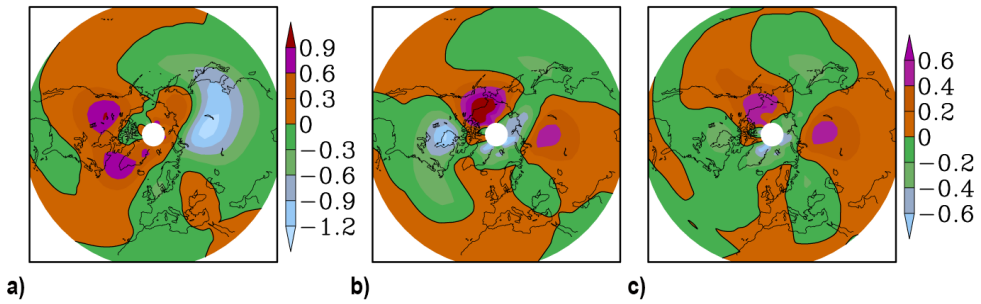

FIGURE 3. Same as Fig. 2, but for the vertical velocity (in cms^{-1}).

Conclusion. In this study, we performed numerical experiments with the MUAM model simulating the general circulation in the middle atmosphere using ten-year average meteorological information. We focused on the sensitivity of the meridional and vertical circulation in the middle and upper atmosphere to inclusion of recently developed parameterization of OGW dynamical and thermal effects for the initial and boundary conditions typical for the easterly and westerly QBO phases. The main goal was to understand the role of the processes associated with dynamical coupling between different atmospheric layers in general circulation model.

Results of numerical experiments show that global-scale meridional and vertical circulation in the MUAM model is very sensitive to OGW dynamical and thermal effects, as well as to the changes in QBO phase. Changes in meridional velocity in the middle atmosphere can reach +/- (30—40)% at high latitudes of the northern hemisphere. In the years with QBO easterly and westerly phases, the differences in meridional velocities can reach 60% at altitudes of 40—60 km. The corresponding changes in vertical velocities can reach 20—50% in the Northern Hemisphere at altitudes of 10—40 km. In addition to directly influencing dynamic and thermal processes in the atmosphere, changes in circulation at these altitudes can lead to changes in ozone fluxes, significantly changing its concentration. OGW effects and changes in QBO phases, can have a similar effect on meridional circulation in the middle atmosphere, despite the different physical mechanisms.

This study was made under financial support from the Russian Basic Research Foundation with the research grant 16-3560013 mol_a_dk.

1. E. E Gossard, W. H. Hooke, Waves in the atmosphere, Elsevier Sci. Publ. Co., Amsterdam-Oxford-New York, 1975.

2. N. M. Gavrilov, A. V. Koval, Parameterization of mesoscale stationary orographic wave impact for usage in numerical models of atmospheric dynamics, *Izv. Atm. and Ocean Phys.*, 2013, 49(3), pp. 244—251.

3. N. M. Gavrilov, A. V Koval et al., Numerical simulation of the response of general circulation of the middle atmosphere to spatial inhomogeneities of orographic waves, *Izv. Atm. and Ocean Phys.*, 2013, 49(4), pp. 367—374.

4. F. Li, J. Austin, and J Wilson, The Strength of the Brewer–Dobson circulation in a changing climate: Coupled chemistry–climate model simulations, *J. Climate*, 2007, 21, pp. 46—57, doi: 10.1175/2007JCLI1663.1.

5. N. Butchart, A. A. Scaife, M. Bourqui et al., Simulations of anthropogenic change in the strength of the Brewer-Dobson circulation, *Clim. Dyn*., 2006, 27, pp. 727—741.

6. M. P.Baldwin, L. J. Gray, Dunkerton et al., The quasi-biennial oscillation, *Rev Geophys,* 2001, 39(2), pp. 179 — 229.

7. A. I. Pogoreltsev, A. A. Vlasov, K. Froehlich and Ch. Jacobi, Planetary waves in coupling the lower and upper atmosphere, *J. Atmos. Solar-Terr. Phys.*, 2007, 69, pp. 2083—2101.

8. N. M. Gavrilov, A. I. Pogoreltsev, and Ch. Jacobi, Numerical modeling of the effect of latitude-inhomogeneous gravity waves on the circulation of the middle atmosphere, *Izv. Atm. and Ocean Phys.*, 2005, 41 (1), pp. 9 — 18.

9. A. I. Pogoreltsev, E. N Savenkova, and N. N Pertsev, Sudden stratospheric warmings: the role of normal atmospheric modes, *Geomagnetism and Aeronomy*, 2014, 54(3), pp. 357—372.

10. R. Swinbank, A. O'Neill, Stratosphere-troposphere assimilation system, *Mon Weather Rev*., 1994, 122, pp. 686—702.

Numerical Simulation of Wave Propagation from Atmospheric Pressure Variations Registered with the Microbarographs Net in Moscow and Environs

Yuliya A. Kurdyaeva[1], Sergei P. Kshevetskii[1], Sergey N. Kulichkov[2], and Elena V. Golikova[2]

[1]Immanuel Kant Baltic Federal University, A. Nevsky street, 14, Kaliningrad, 236041 Russia
[2]A. M. Obukhov Institute of Atmospheric Physics, RAS, Pyzhevsky per. 3, Moscow, 119017, Russia

In this paper, the propagation of waves from pressure variations on the Earth's surface recorded in observational experiments using a network of microbarographs is numerically modeled. On the basis of the experimental data of pressure variations on the net of microbarographs, pressure variations on the Earth's surface near the microbarograph net are approximated. These approximations of pressure variations are used in the simulations as the lower boundary condition. In the performed simulations, the effect of dissipated acoustic-gravity waves (AGWs) on all layers of the atmosphere is investigated. Simulations of wave propagation from wave pressure variations on the Earth's surface, recorded experimentally, were performed for the first time.

The propagation of AGWs originating at tropospheric heights to the upper atmosphere is one of the causes of the change in atmospheric parameters [1, 2]. Waves affect the motion of the plasma in the ionosphere and the propagation of radio waves. An investigation of the vertical propagation of AGW from the lower layers of the atmosphere and their effect on the atmosphere due to wave dissipation is necessary for describing the interaction of the layers of the atmosphere.

The processes of heating/cooling the atmospheric gas during phase transitions of water in the atmosphere are of the most important causes of generation of waves in the atmosphere [3—5]. The complexity of simulation waves from meteorological sources lies in the fact that these sources are very diverse, have a complex evolving internal structure. The available experimental information is usually not enough for a detailed description of these heat sources of waves. Uncertainty in the parameters of the wave sources, as a consequence, significantly affects the accuracy and reliability of calculations.

The processes of heat release/absorption during the formation and evolution of clouds change the atmospheric pressure [6]. These variations in pressure, recorded in observational experiments can naturally be used to calculate waves propagating upward from the surface layers of the atmosphere.

The mathematical study [7] of the problem of the propagation of acoustic-gravity waves from variations in density and temperature on the Earth's surface showed that the wave pattern is uniquely determined by the variable pressure at the Earth's surface, but does not depend on the details of the temperature and density behavior at the lower boundary. In the case of an isothermal atmosphere, the problem of the propagation of waves from a harmonic source preset at the lower boundary is solved analytically. Comparison of numerical and analytical solutions for testing the numerical model has shown good agreement between numerical solutions and analytical ones.

For numerical simulation of AGW propagation from pressure variations on the Earth's surface, real data on the pressure variations on July 17, 2016, were obtained on 4 microbarographs located in Moscow and its environs (Fig. 1, 2).

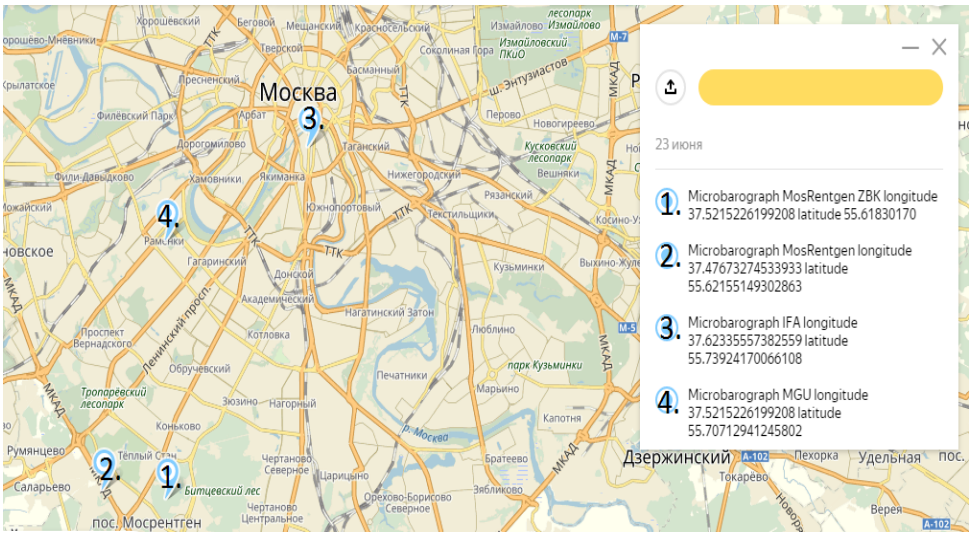

FIGURE. 1. The net of microbarographs in Moscow and around

The three-dimensional model "AtmoSym" [8], used in simulations, is available at http://atmos.kantiana.ru. The simulation of wave propagation is based on numerical solving of the complete three-dimensional system of nonlinear hydrodynamic equations for atmospheric gas in the form of conservation laws [9, 10]. The numerical method allows us to consider nonsmooth solutions and is analogous to the classical Lax-Wendorf scheme.

In numerical simulations, the spatial behaviour of variations in the pressure field in the vicinity of each of the four microbarographs is approximated by a Gaussian function.

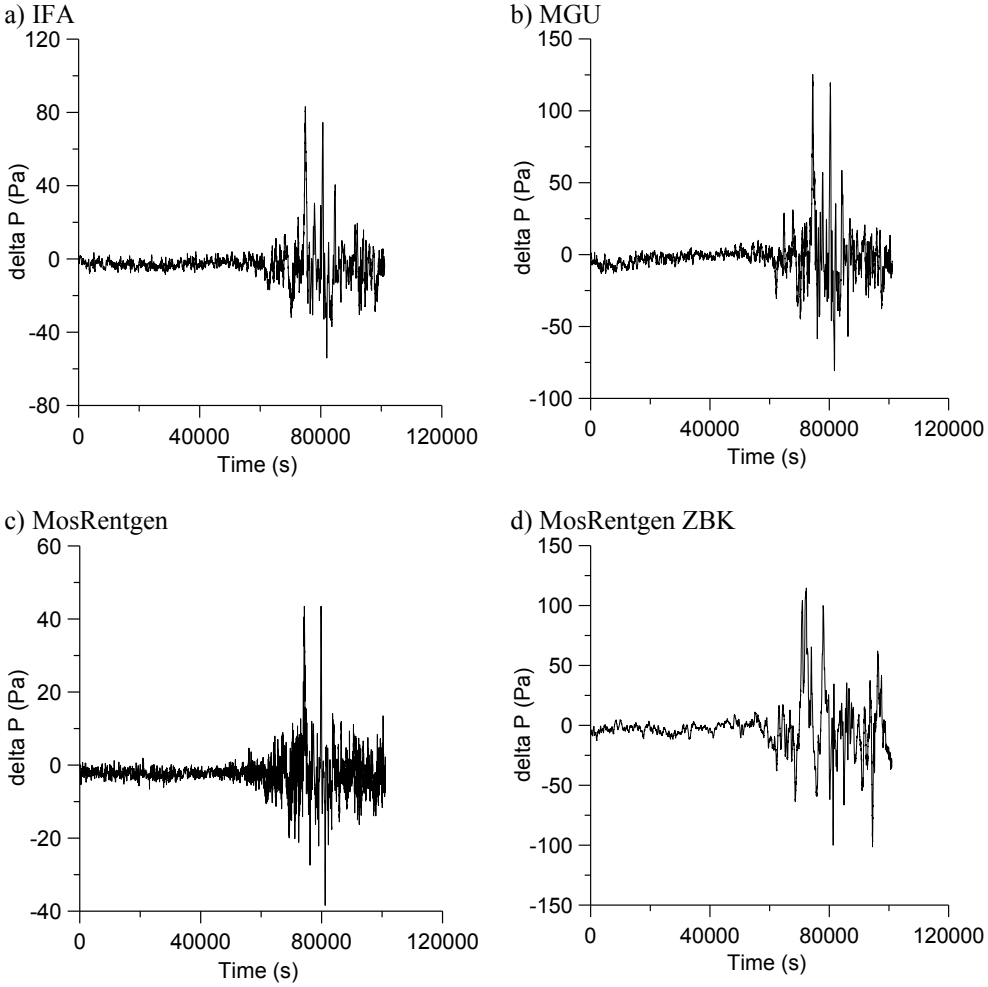

FIGURE. 2. Pressure change at 4 stations in Moscow and its environs on July 17, 2016: a- IFA (longitude: 37.62335557382559, latitude: 55.73924170066108), b — MGU (longitude: 37.5215226199208, latitude: 55.70712941245802), c — MosRentgen (longitude: 37.47673274533933, latitude: 55.62155149302863), d — MosRentgen ZBK (longitude: 37.47673274533933, latitude: 55.62155149302863).

The three-dimensional model "AtmoSym" [8], used in simulations, is available at http://atmos.kantiana.ru. The simulation of wave propagation is based on numerical solving of the complete three-dimensional system of nonlinear hydrodynamic equations for atmospheric gas in the form of conservation laws [9, 10]. The numerical method allows us to consider nonsmooth solutions and is analogous to the classical Lax-Wendorf scheme.

In numerical simulations, the spatial behaviour of variations in the pressure field in the vicinity of each of the four microbarographs is approximated by a Gaussian function.

The resulting field of pressure variations is the summation of these individual pressure fields in the vicinity of each microbarograph. If at any point the result of summing the Gaussian functions describing the pressure field in the neighborhood of each of the microbarographs exceeds unity, then it is replaced by 1; In this case, the introduced approximating pressure fields in the vicinity of the microbarographs overlap. Thus, the approximation of variations in the pressure field has the following form:

$$P_b(\mathrm{x,y,t})=\mathrm{A}_1(\mathrm{x,y}) * f_1(t)+\mathrm{A}_2(\mathrm{x,y}) * f_2(t)+\mathrm{A}_3(\mathrm{x,y}) * f_3(t)+\mathrm{A}_4(\mathrm{x,y}) * f_4(t)$$

where $A_n(x,y)$is a function describing the behavior of pressure on the lower boundary surface in the vicinity of the n-microbarograph:

$$A_n = \begin{cases} \exp\left(\frac{-\left((x-x_i)^2+(y-y_i)^2\right)}{\lambda_i^2}\right), \text{ if } \sum_{i=1}^{4} \exp\left(\frac{-\left((x-x_i)^2+(y-y_i)^2\right)}{\lambda_i^2}\right) < 1 \\ 1, \quad \text{if } \sum_{i=1}^{4} \exp\left(\frac{-\left((x-x_i)^2+(y-y_i)^2\right)}{\lambda_i^2}\right) \geq 1 \end{cases}.$$

f_n is the time dependence of pressure on the microbarograph with number n, λ is the parameter of the function approximating the pressure near the microbarograph (the width of the region), and n is number of the microbarograph.

In modeling, a three-dimensional grid is used (2000 points in z, 600 points in x, 600 points in y). The simulation area has a size of 500x750x750 km. Constructed approximating pressure variations on the Earth's surface are located in the center. The behavior of the pressure at the lower boundary corresponds to the real variations recorded on the net of microbarographs.

Figure 3 (a, b) shows the change in temperature and vertical velocity in 6 minutes from the beginning of the numerical simulation. One can see that the wave amplitudes are still small. The radiation of the waves at the lower boundary has just begun, and upon detailed consideration, one can clearly see the waves from each of the 4 sources (Fig. 3b).

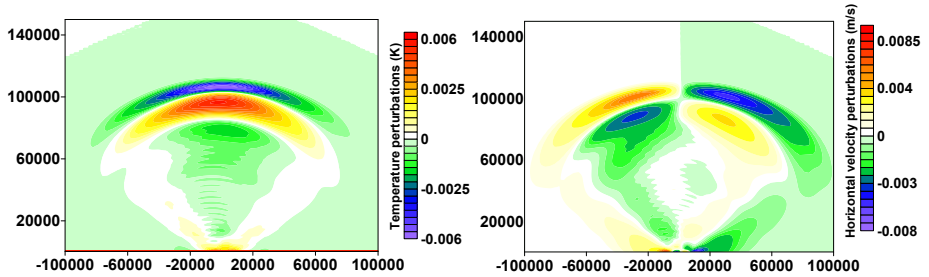

a) b)

FIGURE. 3. Cross-section by the plane x = 0 of the temperature field (a) and the horizontal velocity (b) along the x axis at t = 6 min.

Figure 4 shows the wave field in 2.2 hours after the beginning of the numerical simulation. The waves arising as a result of pressure variations in the vicinity of each microbarograph interfere and at a distance take the form of waves from a source close to a point source. The figure shows acoustic waves and internal gravitational waves. At altitudes of about 200 kilometers, the waveguide regime of wave propagation is formed.

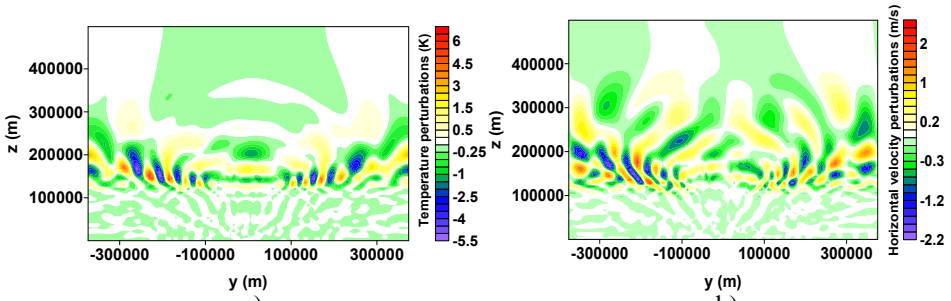

a) b)

FIGURE. 4. Cross section by the plane x = 0 of the temperature field (a) and the horizontal velocity (b) along the x axis at t = 2.2 h.

Thus, on the basis of experimental data on the pressure oscillations recorded by a microbarograph net, a field of pressure variations on the Earth's surface in the vicinity of microbarographs was constructed. The vertical propagation of acoustic-gravity waves from these pressure variations and heating by waves of the upper atmosphere is numerically modeled.

The research was supported by the RFBR grant 17-05-00574. Numerical modeling was performed on the supercomputer "Lomonosov" of the Moscow State University.

1. D. C. Fritts and M. J. Alexander, Gravity wave dynamics and effects in the middle atmosphere, *Rev. Geophys*., 2003, 41, 1003, doi:10.1029/2001RG000106.

2. D. C. Fritts, S. L. Vadas, K Wan, and J. A. Werne, J. Atmos, Mean and variable forcing of the middle atmosphere by gravity waves, *Sol.-Terr. Phys*, 2006, 68, 247—265.

3. A. S. Medvedev and N. M . Gavrilov, The nonlinear mechanism of gravity wave generation by meteorological motions in the atmosphere, *J. Atmos. Terr. Phys*, 1995, 57, pp. 1221—1231.

4. R. Ploogonven, Ch. Snyder, Inertial gravity waves spontaneously generated by jets and fronts. Part I: different baroclinic life cycles, *Journal of the Atmospheric Sciences*, 2007, 64, pp. 2502—2520.

5. R. Plougonven and F. Zhang, Internal gravity waves from atmospheric jets and fronts, *Rev. Geophys*., 52, doi:10.1002/2012RG000419 (2014);

6. E. Blanc, T. Farges, and A. Le Pichon, Gravity waves driven by thunderstorms, in *Proc. of the First ARISE Workshop*, University of Reading, 2012, 16 p.

7. Yu. Kudryaeva, S. Kshevetskii, N. Gavrilov, E. Golikova, Correctness of the problem of propagation of nonlinear acoustic-gravity waves in the atmosphere from pressure variations on the lower boundary, *Sib. Zh. Vychisl. Mat*., 2017,20(4), pp. 393—412.

8. “AtmoSym” — a multi-scale atmosphere model, http://atmos.kantiana.ru/language/en/
9. S. P. Kshevetskii, Analytical and numerical investigation of nonlinear internal gravity waves*, Nonlinear Proc. Geoph*., 2001a, 8. pp. 37—53
10. S. P. Kshevetskii, Numerical simulation of nonlinear internal gravity waves, *Comp. Math. Math. Phys*., 2001b, 12. pp. 1777—1791.

Tsunami-Driven Plane Acoustic Waves in the Atmosphere

Sergey B. Leble, Ekaterina S. Smirnova

Immanuel Kant Baltic Federal University,236041,A. Nevskogo14, Kaliningrad, Russia.

Introduction. In this work a problem of plane wave propagation from a oceansurface to atmosphere is considered. We are interested mainly with termospheric impact of tsunami waves. We suppose that the transport of energy and momentum from lower atmosphere to termospheric heights is due to acoustic waves.

In the paper [1] a general theory of acoustic and internal gravity waves with entropy mode account is presented. It includes the case of 1D exponentional atmosphere perturbations evolution with important details. There are strong arguments that phenomena that occur in oceans are an important source of waves in the thermosphere [2]. As an alternative important phenomenon, we would mention the internal waves generation by tsunami [3] with similar, but more complicated atmosphere gas perturbations.

Our model is based on 1D formulation of non-dissipative thermo-hydrodynamics, linearized with respect to perturbations. A background state is chosen as exponentially stratified along the height z. We start with a boundary problem formulation (Sec. 2), that needs two important features to take into account. First, the obvious asymmetry of basic 1D equations in respect of the derivatives: we have two z-derivative, but three t-derivatives. Second , the dispersion relations for upward and downward waves contain a-domain that gives imaginary k. The first leads to a special efforts in the entropy mode definition, compared to [1] while the second need a special interpretation related to the mentioned range of frequencies contribution. A solution is obtained via Fourier transformation of equations and boundary regime, that fix the unique solution. The inverse Fourier transform define overall acoustic wave variables field.

Basic equations. Consider the problem of propagation of acoustic waves in an exponentially stratified atmosphere. The pressure and density of the unperturbed atmosphere are described by law:

$$\bar{p}(z) = p_0 \cdot exp\left(-\frac{z}{H}\right) = \rho_0 gH \cdot exp\left(-\frac{z}{H}\right);\ \bar{\rho}(z) = \rho_0 \cdot exp\left(-\frac{z}{H}\right); \quad (1)$$

$$H(z) = \frac{T_0(C_p - C_v)}{g}.$$

Here $\bar{p}(z)$ — background pressure; $\bar{\rho}(z)$ — background density; H — height of homogeneous atmosphere; z — current height value; T_0 — background temperature.

The system of equations of hydrodynamics:

$$\frac{\partial \vec{V}}{\partial t} = -\frac{\vec{\nabla} p'}{\bar{\rho}} + \vec{a}\frac{\rho'}{\bar{\rho}}, \tag{2}$$

$$\frac{\partial p'}{\partial t} = -\vec{V}\cdot(\vec{\nabla}\bar{p}) - \gamma\bar{p}(\vec{\nabla}\cdot\vec{V}), \tag{3}$$

$$\frac{\partial \rho'}{\partial t} = -\vec{V}\cdot(\vec{\nabla}\bar{\rho}) - \bar{\rho}(\vec{\nabla}\cdot\vec{V}), \tag{4}$$

where $\vec{V}$ — the velocity of the gas flow; $\gamma = C_p/C_v$; $\vec{a}$ — the force field vector whose components in the case of gravitational forces are: $a_x = 0, a_y = 0, a_z = g$.

Further it is convenient to enter a new value φ':

$$\varphi' = p' - \gamma\frac{\bar{p}}{\bar{\rho}}\rho' \tag{5}$$

and go to the new variables:

$$P = p'\cdot exp\left(\frac{z}{2H}\right), \Phi = \varphi'\cdot exp\left(\frac{z}{2H}\right), \vec{U} = \vec{V}\cdot exp\left(-\frac{z}{2H}\right). \tag{6}$$

And we consider the one-dimensional case. Finally we have a system:

$$\frac{\partial U_z}{\partial t} = \frac{1}{\rho_0}\left(\frac{\gamma-2}{2\gamma H} - \frac{\partial}{\partial z}\right)P + \frac{\Phi}{\gamma H\rho_0}, \tag{7}$$

$$\frac{\partial P}{\partial t} = -\gamma g H\rho_0\frac{\partial U_z}{\partial z} - g\rho_0\frac{\gamma-2}{2}U_z, \tag{8}$$

$$\frac{\partial \Phi}{\partial t} = -(\gamma-1)g\rho_0 U_z\,. \tag{9}$$

Let's rewrite it in the terms of dimensionless functions and variables. For this we'll use the uniform atmosphere height H and the speed of sound $c = \sqrt{\gamma g H}$ as dimension parameters which gives us time scale $H/c = \sqrt{H/\gamma g}$ so that the new dimensionless variables are $z = H\xi$, $t = H/c\cdot\tau = \sqrt{H/\gamma g}\cdot\tau$. Functions are redefined as $U = cu = u\sqrt{\gamma g H}$, $P = p_0 p$ and, since the Φ too has the pressure as dimension (because $\varphi' = p' - \gamma\frac{\bar{p}}{\bar{\rho}}\rho'$ and $\Phi = \varphi'\cdot exp\left(\frac{z}{2H}\right)$) and $\Phi = p_0\phi$ giving us a hydrodynamic system for the one-dimensional case in dimensionless quantities:

$$\frac{\partial u_z}{\partial \tau} = \frac{\gamma-2}{2\gamma^2}p - \frac{1}{\gamma}\frac{\partial p}{\partial \xi} + \frac{\phi}{\gamma^2}, \tag{10}$$

$$\frac{\partial p}{\partial \tau} = -\gamma\frac{\partial u_z}{\partial \xi} - \frac{\gamma-2}{2}u_z, \tag{11}$$

$$\frac{\partial \phi}{\partial \tau} = -(\gamma - 1)u_z\,. \tag{12}$$

We pose the mathematical problem of propagation of the boundary regime. Consider the system of equations (8) on the half-line $\xi \in [0;\infty)$. We transform system (10), expressing u_z from the last equation of the system:

$$u_z = -\frac{1}{(\gamma-1)}\frac{\partial \phi}{\partial \tau} \tag{13}$$

Substituting it into other equations of the system and transferring the derivatives with respect to ξ to the right:

$$\frac{\partial p}{\partial \xi} = -\frac{\gamma}{\gamma-1}\frac{\partial^2 \phi}{\partial \tau^2} + \frac{\gamma-2}{2\gamma}p + \frac{\phi}{\gamma}, \tag{14}$$

$$\frac{\partial^2 \phi}{\partial \xi \partial \tau} = \frac{\gamma-1}{\gamma}\frac{\partial p}{\partial \tau} - \frac{\gamma-2}{2\gamma}\frac{\partial \phi}{\partial \tau}. \tag{15}$$

Hypothesis: Since the system (13) contains only two derivatives with respect toξ, only two boundary conditions (14) will uniquely determine the solution of the system

$$u_z(0,\tau) = F(\tau), p(0,\tau) = G(\tau), \tag{16}$$

where F, G — arbitrary functions.

The solution of the problem of propagationof the boundary regime. We use the Fourier transform for the basic quantities of the system (13):

$$p(\xi,\tau) = \frac{1}{\sqrt{2\pi}}\int_{-\infty}^{\infty} e^{i\omega\tau}\,\tilde{p}(\xi,\omega)d\omega, \tag{17}$$

$$\phi(\xi,\tau) = \frac{1}{\sqrt{2\pi}}\int_{-\infty}^{\infty} e^{i\omega\tau}\,\tilde{\phi}(\xi,\omega)d\omega. \tag{18}$$

We substitute (15), (16) into system (13) and have:

$$\frac{\partial \tilde{p}(\xi,\omega)}{\partial \xi} = -\frac{\gamma}{\gamma-1}\omega^2\tilde{\phi}(\xi,\omega) + \frac{\gamma-2}{2\gamma}\tilde{p}(\xi,\omega) + \frac{\tilde{\phi}(\xi,\omega)}{\gamma}, \tag{19}$$

$$\frac{\partial \tilde{\phi}(\xi,\omega)}{\partial \xi} = \frac{\gamma-1}{\gamma}\tilde{p}(\xi,\omega) - \frac{\gamma-2}{2\gamma}\tilde{\phi}(\xi,\omega), if\ \omega \neq 0. \tag{20}$$

We also find the equation of the relationship between u_z and ϕ in ω-space:

$$u_z(\xi,\tau) = \frac{1}{\sqrt{2\pi}}\int_{-\infty}^{\infty} e^{i\omega\tau}\,\tilde{u}_z(\xi,\omega)d\omega; \tag{21}$$

$$\tilde{u}_z(\xi,\omega) = -\frac{i\omega}{(\gamma-1)}\tilde{\phi}(\xi,\omega). \tag{22}$$

The system (20) is a linear homogeneous system of ordinary differential equations with constant coefficients that depend on the parameter

Theorem: The general solution of a linear homogeneous system of ordinary differential equations with constant coefficients depending on the parameter exists in the form:

$$\tilde{p}(\xi,\omega) = C_1(\omega)e^{\lambda_1(\omega)\xi} + C_2(\omega)e^{\lambda_2(\omega)\xi}, \tag{23}$$

$$\tilde{\phi}(\xi,\omega) = C_3(\omega)e^{\lambda_1(\omega)\xi} + C_4(\omega)e^{\lambda_2(\omega)\xi}. \quad (24)$$

where$\lambda_1$and λ_2 — roots of the characteristic equation for equation. For our case:

$$\lambda_1(\omega) = \sqrt{1/4+\omega^2}, \lambda_2(\omega) = -\sqrt{1/4+\omega^2}. \quad (25)$$

Substitutng solutions into the system, we find the coupling equations between $C_1(\omega), C_2(\omega)$ and $C_3(\omega), C_4(\omega)$:

$$C_3(\omega) = \frac{(\gamma-1)\left(2\gamma\sqrt{1/4+\omega^2}-\gamma+2\right)}{2(\gamma-1-\omega^2\gamma^2)} C_1(\omega), \quad (26)$$

$$C_4(\omega) = \frac{(\gamma-1)\left(-2\gamma\sqrt{1/4+\omega^2}-\gamma+2\right)}{2(\gamma-1-\omega^2\gamma^2)} C_2(\omega). \quad (27)$$

Let us find the boundary regimes in ω-space:

$$\tilde{p}(0,\omega) = \frac{1}{\sqrt{2\pi}}\int_{-\infty}^{\infty} e^{-i\omega\tau}\, G(\tau)d\tau, \quad (28)$$

$$\tilde{u}_z(0,\omega) = \frac{1}{\sqrt{2\pi}}\int_{-\infty}^{\infty} e^{-i\omega\tau}\, F(\tau)d\tau. \quad (29)$$

We take into account the coupling equation and find the boundary regime for$\tilde{\phi}$:

$$\tilde{\phi}(0,\omega) = \frac{i(\gamma-1)}{\omega}\frac{1}{\sqrt{2\pi}}\int_{-\infty}^{\infty} e^{-i\omega\tau}\, F(\tau)d\tau. \quad (30)$$

We set $\xi = 0$ in solutions and equate them to the boundary regimes in the ω-space:

$$\tilde{p}(0,\omega) = C_1(\omega) + C_2(\omega) = \frac{1}{\sqrt{2\pi}}\int_{-\infty}^{\infty} e^{-i\omega\tau}\, G(\tau)d\tau, \quad (31)$$

$$\tilde{\phi}(0,\omega) = C_3(\omega) + C_4(\omega) = \frac{i(\gamma-1)}{\omega}\frac{1}{\sqrt{2\pi}}\int_{-\infty}^{\infty} e^{-i\omega\tau}\, F(\tau)d\tau. \quad (32)$$

Let the boundary regime be given by an impulse of the form of the Gaussian function:

$$u_z(0,\tau) = Ae^{-(\tau-\tau_0)^2/\alpha};\ p(0,\tau) = Be^{-(\tau-\tau_0)^2/\alpha} \quad (33)$$

We also apply the Fourier transform for the boundary regime to find the boundary regime for the Fourier system:

$$\tilde{u}_z(0,\omega) = A\sqrt{\frac{\alpha}{2}}e^{-\frac{\alpha(\omega-\omega_0)^2}{4}}; \quad (34)$$

$$\tilde{p}(0,\omega) = B\sqrt{\frac{\alpha}{2}}e^{-\alpha(\omega-\omega_0)^2/4}.$$

Using (30) we can find:

$$\tilde{\phi}(0,\omega) = \frac{i(\gamma-1)}{\omega}A\sqrt{\frac{\alpha}{2}}e^{-\alpha(\omega-\omega_0)^2/4}. \quad (35)$$

Then:

$$\tilde{p}(0,\omega) = C_1(\omega) + C_2(\omega) = B\sqrt{\frac{\alpha}{2}}e^{-\alpha(\omega-\omega_0)^2/4}; \quad (36)$$

$$\tilde{\phi}(0,\omega) = C_3(\omega) + C_4(\omega) = \frac{i(\gamma-1)}{\omega} A \sqrt{\frac{\alpha}{2}}\, e^{-\alpha(\omega-\omega_0)^2/4}. \qquad (37)$$

Using (26) and (27) we solve (36) and (37) with respect to $C_1(\omega)$, $C_2(\omega)$:

$$C_1(\omega) = \left[\left(\frac{1}{2} + \frac{\gamma-2}{4\gamma\sqrt{1/4+\omega^2}}\right) B + \frac{i(\gamma-1-\omega^2\gamma^2)}{\omega 2\gamma\sqrt{1/4+\omega^2}} A\right] \sqrt{\frac{\alpha}{2}}\, e^{-\alpha(\omega-\omega_0)^2/4}; \qquad (38)$$

$$C_2(\omega) = \left[\left(\frac{1}{2} - \frac{\gamma-2}{4\gamma\sqrt{1/4+\omega^2}}\right) B - \frac{i(\gamma-1-\omega^2\gamma^2)}{\omega 2\gamma\sqrt{1/4+\omega^2}} A\right] \sqrt{\frac{\alpha}{2}}\, e^{-\alpha(\omega-\omega_0)^2/4}. \qquad (39)$$

The solutions in the ω-space can be write down in forms (23) and (24) with using of (25), (26), (27), (38) and (39). To find solution in the τ-space the inverse Fourier transform (17) and (18) should be applied to the solution in the ω-space.

Conclusion. We derived general formulas for acoustic field, generated in 1D exponential atmosphere by boundary regime at the Earth level. The field is expressed via integrals by frequency and may be evaluated by asymptotic formulas at large time range as integrals of rapidly oscillating functions. The resulting formalism may be used in one-point diagnostics by means of projecting operators [4].

Acknowledgement. The work is supported by grant RFFI 18-05-00184.

1. S. Leble and A. Perelomova, Problem of proper decomposition and initialization of acoustic and entropy modes in a gas affected by the mass force, *Applied Mathematical Modelling*, 2013, 37, pp. 629—635.

2. N. A. Zabotin, O. A. Godin, and T. W. Bullett, Oceans are a major source of waves in the thermosphere, *J. Geophysical Research: Space Physics*, 2016, 121(4), pp. 3452—3463.

3. M. P. Hickey, G. Schubert, and R. L. Walterscheid, Propagation of tsunami-driven gravity waves into the thermosphere and ionosphere, *J. Geophys. Res.*, 2009, 114, A08304.

4. S. Leble, General remarks on dynamic projection method, *Task Quarterly*, 2016, 20(2), pp. 113—130.

Absolute Vertical Total Electron Content from Galileo, Beidou, GLONASS and GPS

Anna A. Mylnikova[1], Yury V. Yasyukevich[1,2], and Ilya V. Zhivetiev[1,3]

[1]Institute of Solar-Terrestrial Physics of Siberian Branch of Russian Academy of Sciences, Irkutsk, 664033, Lermontov Street 126a, p/o box 291, Russia
[2]Irkutsk State University, Irkutsk, 664003, Karl Marks Street 1, Russia
[3]Institute of Cosmophysical Research and Radiowave Propagation, FEB RAS, 684034 Kamchatka Krai, Elizovsky region, Paratunka village, Mirnaya Street 7, Russia

Introduction. The ionosphere is a highly dynamical medium. Significant advances in ionosphere studies were achieved with sounding based on global navigation satellite system (GNSS) [1]. There are several techniques to estimate

absolute total electron content based on GNSS data from network [2] or single station [3]. We have developed an algorithm to estimate the ionospheric absolute vertical total electron content (TEC) based on the Taylor space-and-time expansion of GNSS measurements (TayAbsTEC) [4].

In this paper, we analyze efficiency of the algorithm when different satellite systems are used. We used American GPS, Russian GLONASS, European Galileo and Chinese Beidou systems. We estimated the absolute vertical TEC, its gradients, and its time derivative.

TayAbsTEC algorithm. The algorithm to estimate the vertical TEC, the TEC gradients, time derivative, and the DCBs involves:

1. Calculating TEC based on the code I_P and phase $I\varphi$ measurements from GNSS.
2. Dividing the data into continuous samples.
3. Detecting and eliminating the influence of outliers and cycle slip parameters in the TEC data [5].
4. Eliminating the phase measurement ambiguity: $\text{const} = \frac{1}{N}\sum_{i=1}^{N}\left(I_p - I_\varphi\right)$, where N is the number of measurements over a continuous interval.
5. Estimating the DCBs by a simple measurement model and determining the model parameters based on minimizing the model data root-mean-square deviation.

Experimental result. We estimated absolute vertical TEC (TayAbsTEC TEC) I near Irkutsk region, using LIST station (104.8 E 51.8 N). We used data from all the available navigation satellite systems: GPS, GLONASS, Galileo and Beidou.

Figure 1a presents absolute vertical TEC using only GPS data (dashed and dotted line), only GLONASS data (dashed line), only Beidou data (long dashed line) and GPS+GLONASS data (thin solid line).

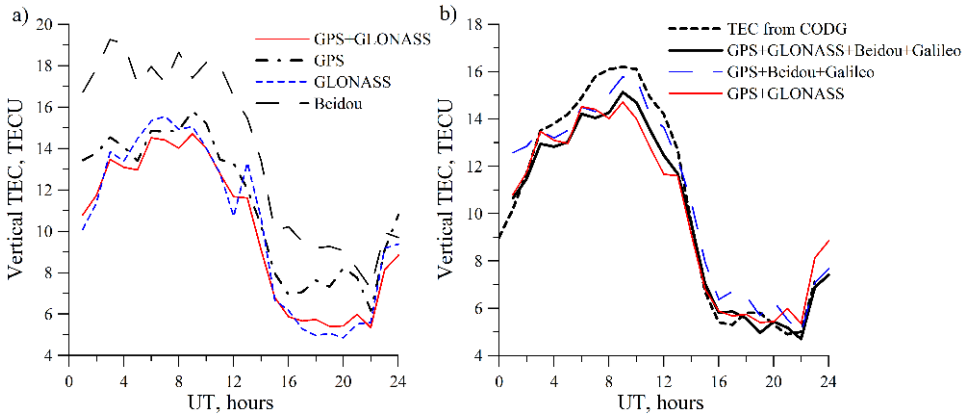

FIGURE 1. a) Absolute vertical TEC based on GPS data (dash and dot line), GLONASS data (dash line), Beidou data (long dashed line) and GPS+GLONASS data (thin solid line). b) Absolute vertical TEC based on GPS+GLONASS data (thin solid line), GPS+GLONASS+Beidou+Galileo data (bold line), GPS+Beidou+Galileo data (dashed line) and absolute vertical TEC from CODG (bold dashed line). September 7, 2017.

On the figure, one can see big difference between TEC evaluation using only GPS data and TEC evaluation using joint GPS and GLONASS data, mean difference 1.27 TECU. For TEC evaluation using only GLONASS data this difference less: mean value 0.64 TECU. It can be concluded, in that case, that using only GPS data or only Beidou data TEC evaluated worse than using joint GPS and GLONASS data. Figure 1b shows TayAbsTEC TEC using data from all the available navigation satellite systems in different combinations, GPS+GLONASS data (denoted asGPS_GLO in tables), GPS+GLONASS+Beidou+Galileo data (GPS_GLO_Bei_Gal), GPS+Beidou+Galileo data (GPS_ Bei_Gal) and absolute vertical TEC from CODG in compare with absolute vertical TEC from CODG, which based on data from IGS (International GNSS Service) stations. On the figure one can see good agreement TayAbsTEC TEC with CODG TEC. Values of mean vertical TEC difference ($<I_{mean}>$) present in table 1.

TABLE 1. Mean differences for TayAbsTEC TEC with CODG TEC.

	CODG-GPS_GLO_Bei_Gal	CODG-GPS_Bei_Gal	CODG-GPS_GLO
$<I_{mean}>$	1.2	1.5	1.1

Figure 2 presents absolute vertical TEC (a), time derivation (b) and spatial gradients (c, d), based on GPS data, GLONASS data, GPS+GLONASS data (GPS_GLO), GPS+GLONASS+Beidou+Galileo data (GPS_GLO_Bei_Gal). On the figure one can see good TEC evaluation when using several systems together, in our case it are GPS+GLONASS+Beidou+Galileo systems, for its time and spatial derivatives difference is larger. In table 2 presents mean difference for TEC, gradients and time derivation evaluated using data of various combinations of systems. Difference calculated from GPS+GLONASS+Beidou+Galileo data evaluation.

TABLE 2. Mean differences for TEC based on various GNSS data.

Difference GPS_GLONASS_Bei_Gal	<ΔI>	<ΔG_lon>	<ΔG_lat>	<ΔG_t>
with GPS_GLO	0,44	0,023	0,034	0,8
with GPS	1,4	0,039	0,12	1,1
with GLO	0,87	0,068	0,1	1,2
with GPS_ Bei_Gal	0,7	0,028	0,07	0,6

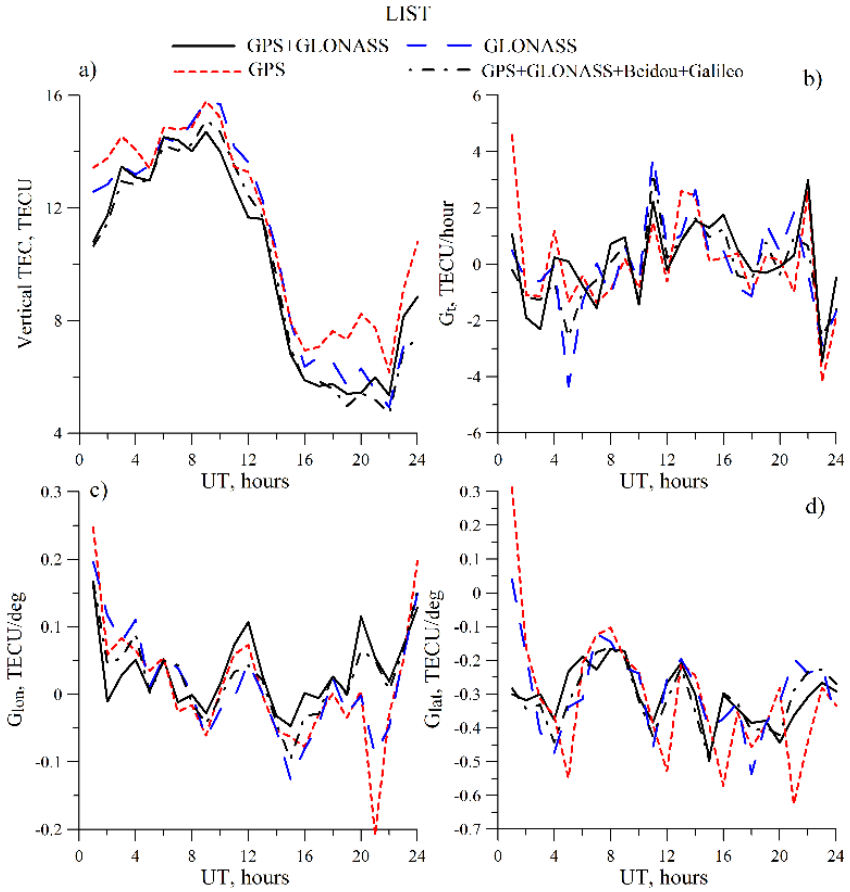

FIGURE 2. Absolute vertical TEC (a), time derivation (b) and spatial gradients (c, d), based on GPS data (frequent dotted line), GLONASS data (dotted line), GPS+GLONASS data (solid line), GPS+GLONASS+Beidou+Galileo data (dashed and dotted line). September 7, 2017.

Conclusion. We analyzed absolute vertical TEC, its time and spatial derivatives. The data is based on dual-frequency GPS, GLONASS, Beidou and Galileo measurements from LIST station (104.8 E 51.8 N) on September 7, 2017. We should note that each separate system (except the Galileo) allow estimating the absolute vertical TEC with appropriate precision. Difference between absolute vertical TEC, time derivation and spatial gradients evaluated based on data of several GNSS was shown. The main problem is at interval boundaries. Maximal differences in different TEC estimations correspond to 0 and 24 UT. It was found that using several GNSS systems improves the quality of TEC estimation. There is a significant problem with TEC gradients: different solutions have a different sign sometimes. This problem needs additional analyzing. Also there is an effect of 0 UT.

The work is supported by President of Russian Federation (grant No MK-1097.2017.5). The work is carried out within base financing of FR program II.16.

1. B. Hofmann-Wellenhof, H. Lichtenegger, and J. Collins, *Global Positioning System: Theory and Practice,* Springer-Verlag, Wien, New York, 1992, 327 p.

2. S. Schaer, G. Beutler, and M. Rothacher, Mapping and predicting the ionosphere, *Proc. IGS AC Workshop*, Darmstadt, Germany, February 9—11, 1998, pp. 307—320.

3. G. E. Lanyi and T. Roth, A comparison of mapped and measured total ionospheric electron content using global positioning system and beacon satellite observations*, Radio Sci.*, 199, 23(4), pp. 483—492.

4. Yu. V. Yasukevich, A. A. Mylnikova, V. E. Kunitsyn, and A. M. Padokhin, Influence of GPS/GLONASS differential code biases on the determination accuracy of the absolute total electron content in the ionosphere*, Geomagn. Aeron.*, 2015, 55(6), pp. 790—796, doi:10.7868/S0016794015060176

5. G. Blewitt, An automatic editing algorithm for GPS data, *Geophys. Res. Lett*., 1990, 17(3), pp. 199—202.

Absolute Total Electron Content Driven by the Single-Frequency GNSS Measurements

Anna A. Mylnikova[1], Yury V. Yasyukevich[1,2], Vsevolod B. Ivanov[2], and Artem M. Vesnin[1,2]

[1]Institute of Solar-Terrestrial Physics of Siberian Branch of Russian Academy of Sciences, Irkutsk, 664033, Lermontov Street 126a, p/o box 291, Russia
[2]Irkutsk State University, Irkutsk, 664003, Karl Marks Street 1, Russia

Introduction. The first investigations of daily dynamics of the ionosphere total electron content (TEC) based on global navigation satellite systems (GNSS) were carried out in the late 1980s [1]. On the one hand, progress in such investigations results in creation of global ionosphere maps GIM [2]. GIM led to significant progress in ionosphere studies [3—5], as well as to develop new ionospheric models [6]. On the other hand, such investigations led to a large number of papers devoted to estimating the vertical TEC over a station [7, 8].

Data from dual-frequency receivers are commonly used, because single-frequency measurement TEC much noisy. However, we can expect that the TEC estimations based on single-frequency measurements are quite adequate due to averaging. Single-frequency measurement frequency opens great opportunity to increase GNSS-receiver capability networks many times by using devices never used for this application such as smart-hones with built-in GNSS receivers. The In current paper we present the developed technique based on the single-frequency

data for estimating the absolute TEC, its gradient and the time derivative, as well as the ambiguity of phase measurements for individual slant TEC rows along the "satellite-receiver" line-of-sight.

Technique for estimating absolute ionospheric parameters based on single-frequency data. To estimate the absolute TEC, its gradient and the time derivative, as well as to eliminate the ambiguity of phase measurements for individual slant TEC rows based on GPS/GLONASS single-frequency data, we used the similar technique which we developed for dual-frequency data [8].

1. The calculation of TEC based on the pseudo range and phase measurements $I_{p\varphi}$.

$$I_P = \frac{1}{2}\frac{f_1^2}{40.308}\left[\left(P_1 - L_1\lambda_1\right) + K + aLP\right], \quad (1)$$

where f_1 is the primary operating frequency of GNSS (GPS, GLONASS, or others.); P_1 is additional radio wave path caused by group delay in the ionosphere, m; $L_1\lambda_1$ — additional radio wave path caused by phase delay in the ionosphere, m; L_1 is the number of the phase turns on the primary GNSS frequency; λ_1 is wavelength in meters; K is a constant determined by phase ambiguity and signal propagation time in the satellite and the receiver equipment; aLP is the total noise of the phase and group measurements at the primary frequency. We used 10° elevation cutoff. Simultaneously with the calculation of the TEC, we calculated elevations and azimuths of satellites.

2. The division of data into continuous samples.

3. The detection and elimination of the influence of outliers and cycle slip parameters in TEC data [9].

4. The estimation of DCBs by a simple measurement model, based on second-order Taylor expansion and determination of model parameters based on minimization of the experimental and model data root-mean-square deviation. Simultaneously, measurement ambiguity K is evaluated.

5. The correction of the TEC series obtained at point 3 to eliminate ambiguity.

Experimental results. For analysis, we used data from IGS network of dual-frequency GPS/GLONASS receivers [10] in the Asian and American sectors of the Northern hemisphere (IRKJ, 52.2 N, 104.3 E; NRC1, 45.5 N, 104.4 W). The use of such data makes it possible to obtain both single-frequency vertical TEC and dual-frequency those.

Figure 1 shows the results of the algorithm described above in comparison with the results obtained by TayAbsTEC [8]. Also we shown vertical TEC data from the GIM CODE [2] (ftp://cddis.gsfc.nasa.gov/gps/products/ionex/). Time resolution is 1 hour for the data obtained from a single station, and is 2 h for GIM data.

The dynamics of vertical TEC obtained by various techniques are qualitatively and quantitatively similar. Maximal difference for this example between single-frequency and dual-frequency data is ~2 TECU. At the same time, in some cases bigger errors appear. However, the differences with the CODE data are usually higher.

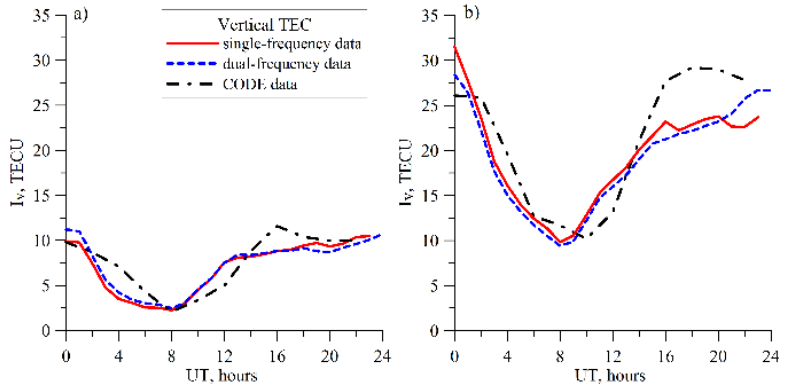

FIGURE 1. The daily TEC dynamics over NRC1 station (45.5 N, 104.4 W) May 20, 2009 (a) and May 20, 2014 (b).

To estimate errors, we considered the distribution of differences between single-frequency and dual-frequency vertical TEC. To do this, we calculated vertical TECs for each day of 2009 and 2014 for IRKJ and NRC1 stations. Temporal resolution was 1 hour. The results are shown in Fig. 2. The histograms are normalized by the total number of measurements N_{total}.

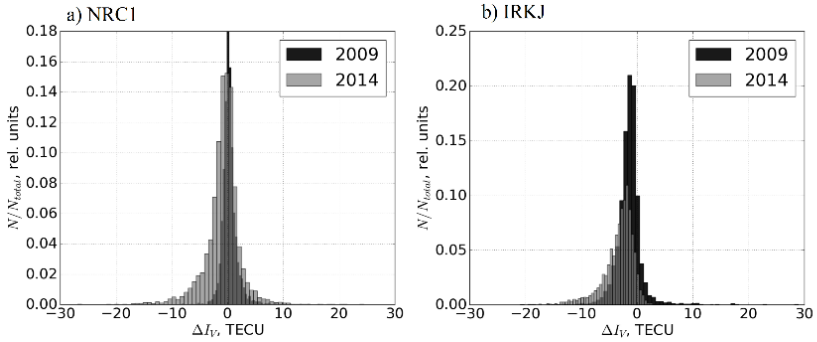

FIGURE 2. Distributions of the differences between the vertical TECs obtained by single-frequency and dual-frequency measurements at NRC1 (a) and IRKJ (b), for 2009 (black) and 2014 (gray).

For NRC1 station one can see a systematic component of ~ 0.5 TECU and RMS of ~1.5 TECU for low solar activity and ~ –0.5 TECU and RMS ~3.5 TECU — for high solar activity. For IRKJ station these values are higher: the systematic component is of ~ –1.5 TECU and RMS is ~ 2.5—3 TECU. It should be noted that the differences correspond to the overall noise level. Besides, these errors (deviations) correspond on the order-of-magnitude to the systematic deviations between different laboratories, published GIM maps. In this context, derived deviations can be considered as quite acceptable.

Figure 3 shows how to obtain the absolute slant TEC. Original single-frequency slant TEC is shown by black solid line, single-frequency slant TEC with removed ambiguity is shown by gray curve, dual-frequency phase slant TEC with removed phase ambiguity is shown by dashed curve. One can see that for the selected satellite after correction measurements are positively defined in contrast to original data. Actually, the final data are "pure" measurements without filtering effects. Figure 3 show that single-frequency absolute slant TEC data agree with dual-frequency those.

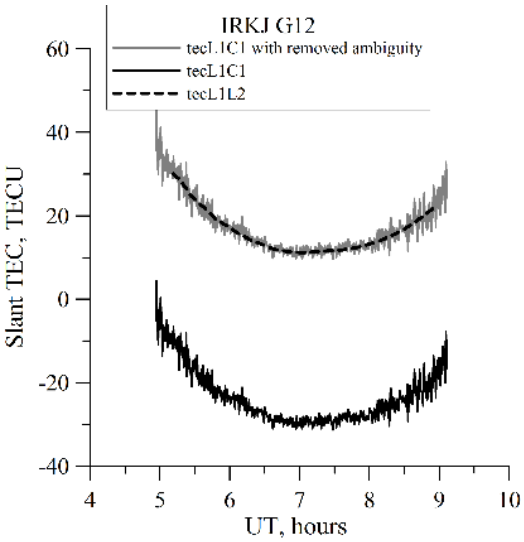

FIGURE 3. Slant TEC along the «PRN12 satellite — IRKJ station» line-of-sight.

Conclusion. We analyzed data on vertical TEC dynamics based on dual-frequency and single-frequency data from NRC1 and IRKJ receivers for the whole 2009 year and the whole 2014 year. It was found that the daily dynamics of the absolute vertical TEC obtained by the single-frequency data qualitatively agree with those obtained by the dual-frequency data. Statistical comparison of the vertical TEC for whole 2009 and 2014 showed that there is a systematic difference between single-frequency and dual-frequency TEC. For NRC1 station the difference is ~0.5 TECU with RMS ~ 1.5 TECU for 2009 year (minimum of solar activity) and ~ –0.5 TECU with RMS ~ 3.5 TECU — for 2014 year (maximum of solar activity). For IRKJ station these values are higher: the systematic difference is ~ –1.5 TECU with RMS ~ 2.5—3 TECU. It should be noted that the differences correspond to the overall noise level of initial measurements. Besides, these differences correspond to the order of the systematic deviations between laboratories published Global Ionospheric Maps. In this context, derived deviations can be considered as quite acceptable. The reason for the discrepancy probably is a non-Gaussian shape or pseudorange measurements error distribution offset. This issue requires a detailed study.

Getting the absolute values of the TEC for single-frequency measurements is good prospects for the development of the ionosphere monitoring, especially in the Russian Federation, where the number of dual-frequency receivers is not as great as, for example, in Japan or in the United States. This algorithm and capability id the modern smart-phones, that allow navigation signal raw measurement give great opportunity to create “volunteer” GNSS receiver network. To do so we should enhance algorithm to: a) work with non-static receiver data, b) coherently process data from multiple smart-phones/receivers to improve data quality. These are topic

for further investigation. Our analysis shown that quality of the single-frequency measurements of the vertical TEC differs not so much from the same estimates based on the dual-frequency data. It also allows obtaining absolute slant TEC along the "satellite-receiver" line-of-sight. Such data can be used for ionospheric correction to be employed in radio communication systems [11, 12].

The authors are grateful to A. M. Padokhin for fruitful discussion. We acknowledge IGS [Dow et al., 2009] for used GPS/GLONASS data. The work is carried out within base financing of FR program II.16. The work is supported by the RFBR grant No. 18-35-00218 mol_a.

1. G. E. Lanyi and T. Roth, A comparison of mapped and measured total ionospheric electron content using global positioning system and beacon satellite observations, *Radio Sci.*, 1988, 23(4), pp. 483—492, doi:10.1029/rs023i004p00483.

2. S. Schaer, G. Beutler, and M. Rothacher, Mapping and predicting the ionosphere, *Proc. IGS AC Workshop*, Darmstadt, Germany, February 9—11, 1998, pp. 307—320.

3. E. L. Afraimovich, E. I. Astafyeva, A. V. Oinats et al., Global electron content: A new conception to track solar activity, *Ann. Geophysicae*, 2008, 26(2), pp. 335—344, doi:10.5194/angeo-26-335-2008.

4. K. Hocke, Oscillations of global mean TEC, *J. Geophys. Res*., 2008, 113, A04302, doi:10.1029/2007JA012798.

5. T. L. Gulyaeva and I. S. Veselovsky, Two-phase storm profile of global electron content in the ionosphere and plasmasphere of the Earth, *J. Geophys. Res*., 2012, 117, A09324, doi:10.1029/2012JA018017.

6. V. B. Ivanov, G. D. Gefan, and O. A. Gorbachev, Global Empirical Modelling of the Total Electron Content of the Ionosphere for Satellite Radio Navigation Systems, *J. Atmos. Solar-Terr. Phys.*, 2011, 73, pp. 1703—1707, doi:10.1016/j.jastp.2011.03.010.

7. D. R. Themens, P. T. Jayachandran, and R. B. Langley, The nature of GPS differential receiver bias variability: An examination in the polar cap region, *J. Geophys. Res. Space Physics*, 2015, 120, pp. 8155—8175, doi:10.1002/2015JA021639.

8. Yu. V. Yasyukevich, A. A. Mylnikova, V. E. Kunitsyn, and A. M. Padokhin, Influence of GPS/GLONASS differential code biases on the determination accuracy of the absolute total electron content in the ionosphere, *Geomagn. Aeron.*, 2015, 55(6), pp. 790—796, doi:10.7868/S0016794015060176.

9. G. Blewitt, An automatic editing algorithm for GPS data, *Geophys. Res. Lett.*, 1990, 17(3), pp. 199—202, doi:10.1029/GL017i003p00199.

10. J. M. Dow, R. E. Neilan, and C. Rizos, The International GNSS Service in a changing landscape of Global Navigation Satellite Systems, *J. Geodesy*, 2009, 83, pp. 191—198, doi:10.1007/s0019000803003.

11. E. L. Afraimovich and Yu. V. Yasukevich, Using GPS-GLONASS-GALILEO data and IRI modeling for ionospheric calibration of radio telescopes and radio interferometers, *J. Atmos. Sol.-Terr. Phys*., 2008, 70(15), pp. 1949—1962, doi:10.1016/j.jastp.2008.05.006.

12. V. B. Ovodenko, V. V. Trekin, N. A. Korenkova, and M. V. Klimenko, Investigating range error compensation in UHF radar through IRI-2007 real-time updating: Preliminary results, *Adv. Space Res*., 2015, 56(5), pp. 900—906, doi:10.1016/ j.asr.2015.05.017.

Towards Automated Computer Evaluation of Seismo-Assosiated Ionosphere Total Electron Content Disturbances: Problems and Challenges

Oleg V. Zolotov, Maria A. Knyazeva

Laboratory for Computer Modeling of the Near-Earth Environment Physical Processes, Murmansk Arctic State University, Murmansk, 183038, Russia

Introduction. Searches for ionosphere disturbances possibly associated with forthcoming seismic activity last for more than 4 decades but no accepted solution having been yield till nowadays. Many papers consider ionosphere total electron content (TEC) as main subject to analyze due to availability of huge openacces arrays of TEC data, especially, NASA Global Ionosphere Maps (GIM). Nevertheless, it should be noted that the most of the researches being published are *case studies*. Case studies allow one to determine some ionosphere TEC features preceding concrete strong seismic events but require additional justification of applicability of the results in general case. A number of papers that consider a dozen of seismic events is rather small. We expect this is due to the fact that the task of ionosphere TEC (and GIMs as one of the cases) analysis is very man-power consuming when not automated. Analysis of ionosphere disturbances considered as possible precursors to earthquakes is not automated in the majority of the researches.

Methods in use. A review of the available publication does not allow to name the one concrete method that is generally accepted as reference ones for seismo-ionosphere disturbances' discrimination. Here we provide a list of the most frequent ones in use. (1) The use of empirical model (e. g., different versions of the International Reference Ionosphere model — IRI) to calculate the undisturbed variation [1]. (2) The use of the nearest quite-day variation as reference one [2]. (3) The use of different filter-like techniques, including averages [3—4], wavelet transformations, Kalman filters, interquartile analysis [5—6], principle component analysis [7], artificial neural networks [8], genetic algorithms [9], etc. Different averages are widely in use, the sliding (running) window size typical values are 7, 15 [10—11], 27 [12], or 30 [13—14] days and each day is supposed to be of the same weight in calculations. The sliding window may be placed before, after or centered relatively to the calculation moment.

Problems and Challenges. All the mentioned above techniques suffer from a few drawbacks that we discuss in this section.

(1) Non-consistent data transformation. As an example, a linear interpolation of the initial GIM TEC data (time resolution 2 h) is applied to obtain 1 h resolution data. It is not evident that the linear interpolation does not change the statistical properties of the resulting set in contrast to the original one.

(2) Some statistical properties of the initial data set are implicitly assumed but never verified. The most often one is the normal (Gauss) distribution of the dataset.

(3) Background variation is calculated without any justification of the method being used. Different number of days are taken into account but no investigation of the results' dependency on the running window width is performed. An example of such dependency and valuable changes of the results are presented in Fig. 1—2.

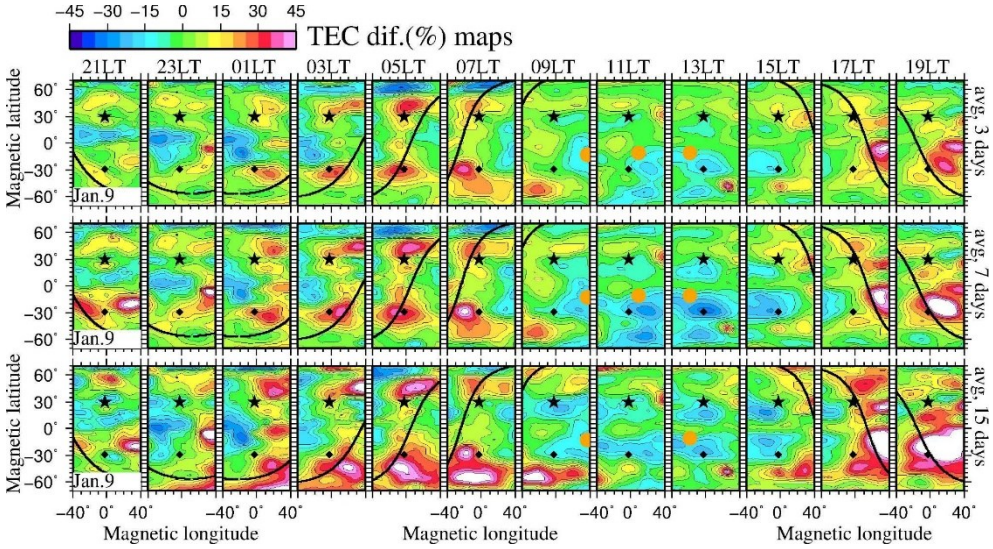

FIGURE 1. Maps of relative TEC disturbances (%) for Jan. 9, 2010. Reference (undisturbed) variations are calculated as running averages for 3, 7 and 15 (from top to bottom), correspondingly.

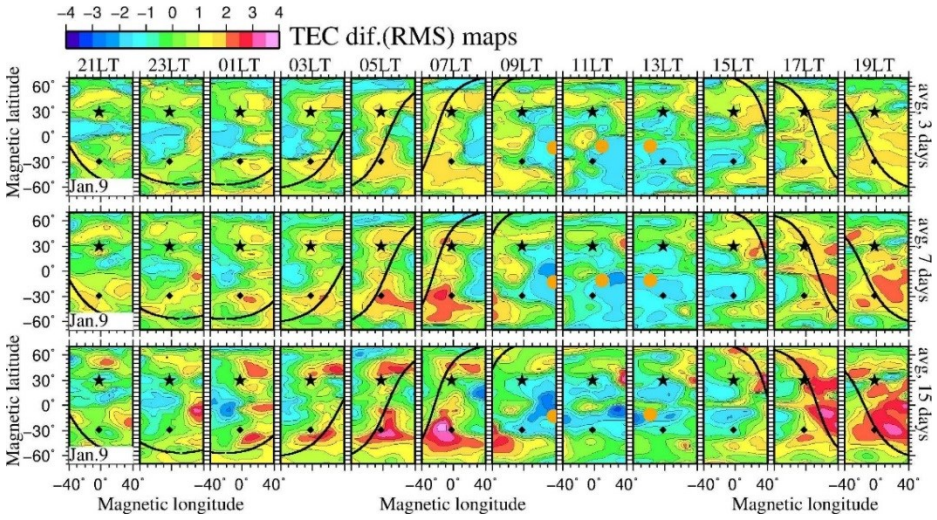

FIGURE 2. Maps of relative TEC disturbances (normalized by RMS) for Jan. 9, 2010. Reference (undisturbed) variations are calculated as running averages for 3, 7 and 15 (from top panel to bottom), correspondingly.

(4) Definition of the anomalies' criteria. This problem is strictly bound to the background variation definition problem (see also Fig. 1—2). Discrimination of the "anomalies" in the data requires the concrete quantitative criteria or the "threshold" definition. The "threshold" is usually taken as some fixed value or is defined by the analogy with confidence interval. In the latter case the values outside interval are assumed to be anomalous. The interval ranges are defined as M(X)±K*sigma, where M(X) is the sample mean (or sample expectancy), sigma is the standard deviation, k is a value that is usually taken in many paper as 1, 1.5, 2, 2.5, or 3. Formally, the k value, if such a criteria is applicable, should depend on the sample size, distribution law of the sample data and desired confidence level. Therefore, the value of k might depend on the number of days that are taken into consideration to calculate the reference variation, and the resulting disturbances for the same k but different sliding window sizes will have different linear sized and amplitudes (see Fig. 1—2). Moreover, many researchers use different criteria to calculate and define the anomalous disturbances and that make the results incomparable, at least directly. It also make difficulties in determining the common features of the anomalies.

(5) Many papers restrict to the 1D data analysis only. Even papers considering NASA TEC GIMs most often assume them as a "bunch of" 1D data series (variations at the each grid node is analyzed independently of other grid nodes variations). This assumption does not allow to take into account spatial characteristics of the anomalies in consideration. A few papers that consider joint variations at different points also have some limitations: they require the GPS-recievers to be places on the same (or very close) magnetic latitude and the magnetic longitude should not differ too match; or actually analyze data in a single grid node or two nodes performing cross-correlation analysis of a pair of neighboring receivers.

(6) The geomagnetic activity is not taken into account. The most of the papers are "considering" geomagnetic activity by excluding the disturbed days from analysis. Papers [15—16] are a few researches that try to deal with disturbed period.

(7). No one paper take into account the RMS (root-mean-square) data supplied with the NASA TEC GIMs, or, at least we could not find such publications at all. Any paper we saw that analyze NASA TEC GIMs just omits the RMS data. Therefore, no estimation of the revealed disturbances over the "natural variability" is done basing on the observations' uncertainties.

Discussion and conclusions. Basing on the problems named in the previous section we are able to formulate a few principles. Any data transformation that is not compulsory and can be avoided should be avoided to prevent potential inclusion of the properties not presented in the original dataset. Any transformation should be carefully described and justified before being applied. An investigation of the disturbances dependence on the reference variation should be preformed to be able to compare the results of different researches. The option to use the same approach is not discussed and is unreachable nowadays.

The criteria to define anomalous variation from inequality $X - k*L < X < X + k*L$ seems reasonable but require some extra discussion, where X is somehow estimated reference variation (possibly expected value E(x), some empirical model fitted value, Neural network forecast, etc.), L is some measure of variability and k is the factor (to be able to calibrate) that should depend both on L, sample size and the desired confidence. Here we do not discuss the X value determination and consider E(x) as a good starting point. But we think the L value worth its own discussion as it is close to the problem of the natural variability accounting. As a special case of this problem we can propose a few estimations to take RMS data into account for anomalies discrimination:

$$L_1 = \Sigma\, RMS_i, \tag{1}$$

$$L_2 = (\Sigma\, RMS_i^2)^{1/2}, \tag{2}$$

$$L_\infty = \max(RMS_1, RMS_2, \ldots, RMS_n), \tag{3}$$

$$L^*_E = (1/N)\Sigma\, RMS_i, \tag{4}$$

$$L^*_\sigma = (1/M)(\Sigma\, RMS_i^2)^{1/2}. \tag{5}$$

The L_1 and L_2 estimation seems to be very pessimistic. L_1 is a direct analogy to the absolute errors' addition rule for the imprecise values and it presents the worst case neglecting any possibility of errors' cancellation. L_2 estimation is an analogy to the Euclid distance. L_1 and L_2 estimations seem not to be very practical due to the very pessimistic approach. L_∞ approach may be unstable due to very high sensitivity to random outliers. Therefore L_∞ may require some outliers' removal. L^*_E and L^*_σ are mean-like and dispersion-like estimations. The M multiplier in equation (5) is expected to be N or N-1 (where N is a sample size) by the analogy with biased and unbiased sample dispersion. We expect L^*_E and L^*_σ to be more suitable for the practical purposes.

1. I. E. Zakharenkova, I. I. Shagimuratov, N. Yu. Tepenitzina, and A. Krankowski, Anomalous modification of the ionospheric total electron content prior to the 26 September 2005 Peru earthquake, *J. Atm. Solar-Terr. Phys.*, 2008, 70(15), pp. 1919—1928, doi:10.1016/j.jastp.2008.06.003.

2. I. E. Zakharenkova, A. Krankowski, and I. I. Shagimuratov, Modification of the low-latitude ionosphere before the 26 December 2004 Indonesian earthquake, *Nat. Haz. Earth Syst. Sci.,* 2006, 6(5), pp. 817—823, doi:10.5194/nhess-6-817-2006.

3. J. Y. Liu, Y. J. Chuo, S. J. Shan et al., Pre-earthquake ionospheric anomalies registered by continuous GPS TEC measurements, *Ann. Geo.,* 2004, 22(5), pp. 1585—1593, doi:10.5194/angeo-22-1585-2004.

4. J. Y. Liu, Y. I. Chen, Y. J. Chuo, and C. S. Chen, A statistical investigation of preearthquake ionospheric anomaly, *J. Geophys. Res.,* 2006, 111, A05304, doi:10.1029/2005JA011333.

5. M. Akhoondzadeh and M. R. Saradjian, TEC variations analysis concerning Haiti (January 12, 2010) and Samoa (September 29, 2009) earthquakes, *Adv. Space Res.,* 2011, 47(1), pp. 94—104, doi: 10.1016/j.asr.2010.07.024.

6. M. R. Saradjian and M. Akhoondzadeh, Thermal anomalies detection before strong earthquakes (M > 6.0) using Interquartile, Wavelet and Kalman filter methods, *Nat. Haz. Earth Syst. Sci.,* 2011, 11(4), pp. 1099—1108, doi:10.5194/nhess-11-1099-2011.

7. J.-W. Lin, Two-dimensional ionospheric total electron content map (TEC) seismo-ionospheric anomalies through image processing using principal component analysis, *Adv. Space Res.,* 2010, 45(11), pp. 1301—1310, doi:10.1016/j.asr.2010.01.029.

8. M. Akhoondzadeh, A MLP neural network as an investigator of TEC time series to detect seismo-ionospheric anomalies, *Adv. Space Res.,* 2013, 51(11), pp. 2048—2057, doi: 10.1016/j.asr.2013.01.012.

9. M. Akhoondzadeh, Genetic algorithm for TEC seismo-ionospheric anomalies detection around the time of the Solomon (Mw = 8.0) earthquake of 06 February 2013, *Adv. Space Res.,* 2013, 52(4), pp. 581—590, doi: 10.1016/j.asr.2013.04.012.

10. S. A. Pulinets and K. G. Tsybulya, Unique variations of the total electron content in the preparation period of Haitian earthquake (M7.9) on January 12, 2010, *Geomagn. Aeron.,* 2010, 50(5), pp. 686—689, doi: 10.1134/S0016793210050166.

11. H. Le, J. Y. Liu, and L. Liu, A statistical analysis of ionospheric anomalies before 736 M 6.0+ earthquakes during 2002—2010, *J. Geophys. Res.,* 2011, 116(A2), A02303. doi:10.1029/2010JA015781.

12. T. Xu, Zhi Chen, Chunbin Li et al. GPS total electron content and surface latent heat flux variations before the 11 March 2011 M9.0 Sendai earthquake, *Adv. Space Res.,* 2011, 48(8), pp. 1311—1317, doi:10.1016/j.asr.2011.06.024.

13. S. A. Pulinets, V. G. Bondur, M. N. Tsidilina, and M. V. Gaponova, Verification of the concept of seismoionospheric coupling under quiet heliogeomagnetic conditions, using the Wenchuan (China) earthquake of May 12, 2008, as an example, *Geomagn. Aeron.,* 2010, 50(2), pp. 231—242, doi:10.1134/S0016793210020118.

14. B. A. Carter, A. C. Kellerman, T. A. Kane et al., Ionospheric Precursors to Large Earthquakes: A Case Study of the 2011 Japanese Tohoku Earthquake, *J. Atm. Solar-Terr. Phys.,* 2013, 102, pp. 290—297, doi:10.1016/j.jastp.2013.06.006.

15. D. V. Davidenko, PhD thesis, Diagnostic of ionosphere disturbances ove seismic regions, Moscow, 2013. URL: http://ipg.geospace.ru/ref/20130716/auto_Davidenko.pdf (in Russian)

16. L. He, L. Wu, S. Pulinets et al., A nonlinear background removal method for seismo-ionospheric anomaly analysis under a complex solar activity scenario: A case study of the M9.0 Tohoku earthquake, *Adv. Space Res.,* 2012, 50, pp. 211—220, doi:10.1016/j.asr.2012.04.001

Nonlinear Interaction of Wave Processes in the Middle and Upper Atmosphere

Ksenia A. Didenko[1] and Alexander I. Pogoreltsev[1,2]

[1]Department of Atmospheric physics, St Petersburg University, St.Petersburg-Petrodvorets,198904, Russia
[2]Department of Meteorological Forecasting, Russian State Hydrometeorological Universty, St.Petersburg,195196, Russia

Introduction. In the stratosphere, there is anti-correlation between changes in the amplitudes of stationary planetary waves with zonal wave numbers 1 and 2 (SPW1 and SPW2). This negative correlation is mainly due to the nonlinear wave-wave interactions within the stratosphere. To interpret the observed behavior of

SPW amplitudes, it is useful to consider the nonlinear interactions of SPWs with the zonal mean flow and between the SPWs with different zonal wave numbers. Using this approach, the conservation of the perturbed potential enstrophy is investigated. When the amplitude of the SPW considered changes, the transfer of energy or enstrophy to another wave numbers is a necessary condition for the maintenance of the conservation requirements. In this case the terms responsible for the wave-wave interaction in the balance equation of the potential enstrophy (Ertel's potential vorticity squared) are calculated [1].

To obtain the balance equation of potential enstrophy, we use the linearized equation of conservation of the potential vorticity and multiply it by its eddy component and include the source and/or sinks term Q:

$$q' \times \quad D_t q' + v' \, \bar{q}_\varphi / a + w' \, \bar{q}_z = Q' \tag{1}$$

where

$$D_t \equiv \partial/\partial t + (\bar{u}/a \cos\varphi) \, \partial/\partial\lambda \tag{2}$$

$$Q = \frac{Rf}{H\rho} \frac{\partial}{\partial z} \frac{\rho D}{N^2} \tag{3}$$

(here R is the gas constant of dry air, f is Coriolis force, H is height scale, ρ is the background density, D is the rate of temperature change due to diabatic heating and N represents the buoyancy frequency.

The result is the general form of the eddy enstrophy balance:

$$\frac{\partial}{\partial t} \frac{\overline{q'^2}}{2} + \overline{\frac{q'u'}{a\cos\varphi} \frac{\partial q'}{\partial\lambda}} + \overline{\frac{q'v'}{a} \frac{\partial q'}{\partial\varphi}} + \overline{\frac{q'v'}{a}} \frac{\partial \overline{q}}{\partial\varphi} = \overline{q'Q'} \tag{4}$$

where q' is the perturbation of the quasi-geostrophic potential vorticity, u' and v' are perturbations of the zonal and meridional geostrophic winds, and Q' represents the perturbation of diabatic sources and sinks and terms describing the subscale contributions to the momentum equation. All other symbols have their conventional meaning: a is the Earth's radius, λ and φ are the longitude and latitude. The first term in left-hand side denotes the wave transience. The two next terms describe the wave-wave interactions. The last term in the left-hand side describes the eddy enstrophy changes due to wave-mean flow interaction. The term in the right-hand side gives the changes in eddy enstrophy due to the diabatic heating and subscale contributions to the momentum equation including momentum deposition by gravity and inertial-gravity waves [1].

Decomposing into series potential vorticity, zonal and meridional winds and diabatic heating for the zonal wavenumbers 1, 2, 3 and substituting to Equation (4) we can calculate the contribution of different terms to the eddy enstrophy balance for SPW1 and SPW2 (in a similar way with the expressions that was suggested by Smith (1983, Appendix [1])). The terms describing the interactions SPW1 and SPW2 may be written as follows:

$$+\frac{1}{4a\cos\varphi}[2U_2 Q_1^2 Q_1^{*2} + U_2^*(Q_1^{*2} - Q_1^2)] +$$

$$+\frac{1}{4a}\left[(V_2 Q_1 + V_2^* Q_1^*)\frac{\partial}{\partial\varphi} Q_1 + (V_2^* Q_1 - V_2 Q_1^*)\frac{\partial}{\partial\varphi} Q_1^*\right] \tag{5}$$

while Smith et al. (1984) suggested that this term can be rewritten in a different way using the quasi-geostrophic eddy continuity equation for SPW2 [2]:

$$+\frac{1}{8a\cos\varphi}\frac{\partial}{\partial\varphi}\{[V_2(Q_2^1 - Q_1^{*2}) + 2V_2^*(Q_1 Q_1^*)]\cos\varphi\} \quad (6)$$

Comparison of the results obtained using expressions (5) and (6) shows that there are significant differences between them (at least in the middle latitudes of the winter stratosphere, where the nonlinear wave-wave interactions are strong). [3]

For a correct description of nonlinear interactions, it is necessary to refuse the quasi-geostrophic approximation. A quasi-geostrophic potential vortex which perturbation is used for calculating the perturbation of the potential enstrophy is not an approximation of the Ertel's potential vorticity. It is just its analogue (even the dimension is different). Taking into account the expression for the absolute vorticity $\omega_a = rotV+2\Omega$, $\Omega = \{0, \Omega\cos\varphi, \Omega\sin\varphi\}$ and neglecting $2\Omega\cos\varphi$ in comparison with the vertical derivative of the zonal wind u_z, we obtain the expression for the Ertel's potential vorticity $P = \omega_a \cdot \nabla\theta / \rho_0$, which is usually used in atmospheric dynamics, particularly in "primitive" equations in a spherical coordinate system [4]. To compare the results obtained with the quasi-geostrophic approximation and without it, we should use $P' \cdot \frac{\rho_0}{\theta_z}$ instead of q' in the eddy enstrophy balance equation (4).

In order to show the behavior of different terms in the balance of potential enstrophy using q' or $P' \cdot \frac{\rho_0}{\theta_z}$, it was decided to consider an example of simulation with the middle and upper atmosphere model (MUAM) when a strong sudden stratospheric warming (SSW) was observed (simulated). Wave activity usually intensifies during this phenomenon. Fig. 1 demonstrates the results of simulation with the MUAM (a set of the ensemble runs for El-Nino conditions have been performed and one of the ensemble runs was selected). One can see a strong increase in the amplitude of the SPW1 on the 10th of January, which was accompanied by reversal of the zonal mean flow in the stratosphere. As a consequence, the sudden stratospheric warming was observed several days later.

Using the results of simulation, the terms of Equation (4) were calculated and visualized. The values have been averaged over the middle latitude region from 57.5 to 72.5°N, using cosine of latitude weighting. The results in Fig. 2a and 3a shows that the time changes of eddy potential enstrophy for SPW1 and SPW2 are almost independent on the type of the potential vorticity is used. The run of the curve showing the interaction between waves with different wave numbers looks similar (weather we use q' or $P' \cdot \frac{\rho_0}{\theta_z}$), but the intensity is noticable different. The most interesting situation is formed when considering the interaction of the SPW1 or SPW2 with the mean flow. In the panel (d) of Fig. 2 and 3 one can see, that the values of interaction terms for quasi-geostrophic potential vorticity and Ertel's potential vorticity are out of phase.

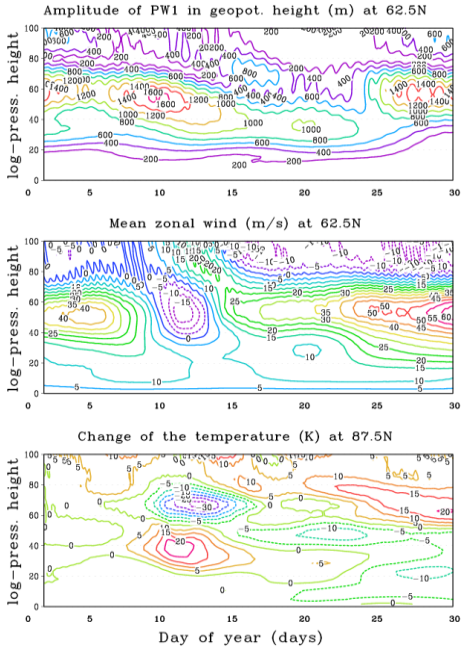

FIGURE 1. The time-altitude cross-sections of the amplitude of zonal harmonic with zonal wave number m = 1 in the geopotential height and the mean zonal wind at latitude 62.5N (upper and middle panels) for January; the changes of the zonal mean temperature during this month at 87.5N are shown in the lower panel. MUAM data.

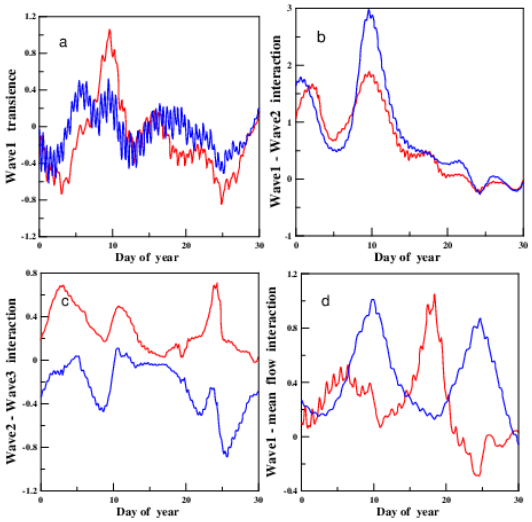

FIGURE 2. Terms contributing to the eddy enstrophy balance (using quasi-geostrophic potential vorticity — red lines (grey lines in black-and-white), Ertel's potential vorticity — blue ones (black lines in black-and-white)) for SPW1 at 30 km for January: (a) transience, (b) wave1-wave2 and (c) wave2-wave3 interaction and (d) wave–mean flow interaction. Units are 10^{-15} s^{-3}.

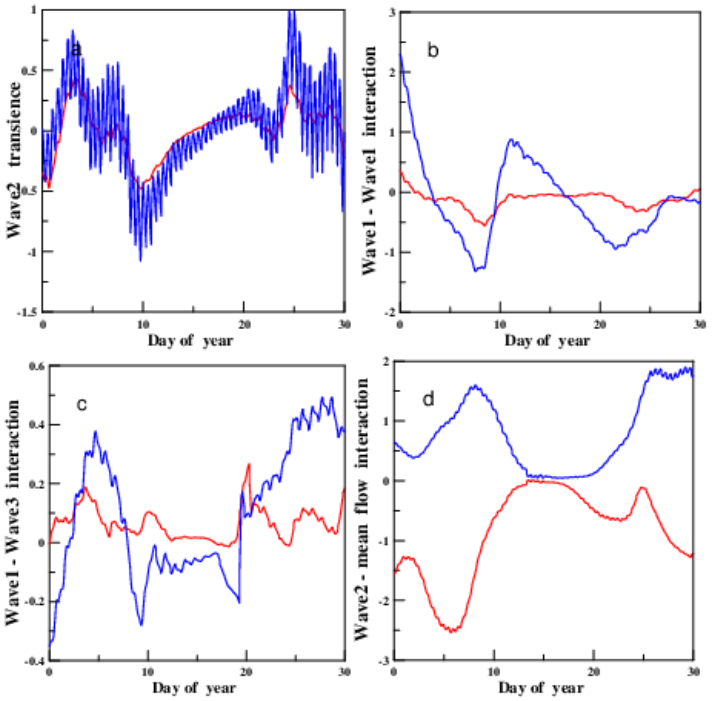

FIGURE 3. Terms contributing to the eddy enstrophy balance (using quasi-geostrophic potential vorticity — red lines (grey lines in black-and-white), Ertel's potential vorticity — blue ones (black lines in black-and-white)) for SPW2 at 30 km for January: (a) transience, (b) wave1-wave1 and (c) wave1-wave3 interaction and (d) wave-mean flow interaction. Units are 10^{-15} s^{-3}.

Conclusion. The results of calculation the terms in the eddy potential enstrophy balance equation demonstrate substantial differences between the quasi-geosptrophic approximation and when we use the Ertel's potential vorticity expression. It is important to consider in more details the interaction of SPW1 and SPW2 with the mean flow separately. Moreover, terms containing a vertical velocity were not considered in this research. These terms can provide a contribution to the balance during the SSW events and/or in the case of nonlinear interaction between higher-frequency planetary waves (for instance, the atmospheric tides). This problem will be the subject of a further research.

1. A. K. Smith, *J. Atmos. Sci*., 1983, vol 40, pp. 2484—2493.

2. A. K. Smith, *J. Atmos. Sci*., 1984, vol 41, No.3, p. 365.

3. A. I. Pogoreltsev, E. N. Savenkova, O. G. Aniskina, T. S. Ermakova, W. Chen, K. Wei, *J. Atmos. Solar-Terr. Phys.,* 2015, pp. 191—194.

4. D. G. Andrews, J. R. Holton, B. L. Conway, *UK: ACADEMIC PRESS INC. (LONDON) LTD*, 1987, pp. 120—122.

ENSO Influence on the Polar Temperature and Ozone Mixing Ratio in the Springtime Stratosphere

Ekaterina A. Drobashevskaya[1], Alexander I. Pogoreltsev[1,2], and Sergei P. Smyshlyaev[1]

[1]Russian State Hydrometeorological University, St.Petersburg,
Russia 192007, Saint-Petersburg, Voronezhskaya st, 79
[2]Atmospheric Physics Department, Saint-Petersburg State University,
Russia, 198504, Saint-Petersburg, Ulyanovskaya st, 1

Introduction. Stratospheric ozone plays an important role in climate formation and the Earth's radiation budget. The ozone content in the stratosphere varies over the seasons and years; it is influenced by both dynamical and chemical processes. Planetary wave activity, formation of circumpolar vortex are among the factors that influence the ozone content [1, 2]. Furthermore, in recent years the studies dedicated to the ENSO impact on the global ozone variations have been performed [3, 4]. In this study, we are focusing on the ENSO impact on the polar ozone and temperature during springtime transition.

The study. The dramatic ozone loss, observed in Arctic during spring in 2011 [1, 2] corresponds to La Niña conditions. To make more statistically significant conclusions about a possible impact of the ENSO events on the ozone mixing ratio (OMR) and temperature in the stratosphere, we selected 5 years under El Niño phase and 5 years under La Niña phase. March-April time interval has been considered, which corresponds to the springtime transition [5]. To accomplish the study, the Multivariate ENSO Index (MEI) [6] for March and April has been used. According to the MEI values, El Niño phase in March/April was observed in 1983, 1987, 1992, 1993, 1998 and La Niña phase corresponds to 1989, 1999, 2000, 2008, 2011 years. The OMR and the temperature observed during these years have been processed using the MERRA data [7].

The OMR and temperature have been averaged over 5 years selected for both El Niño and La Niña phases. Figure 1 shows the differences in the OMR and the temperature between El Niño and La Niña cases averaged over March and April. Statistical significance is indicated by the shaded areas. There is a significantly lower OMR under El Niño conditions in the middle stratosphere at the low latitudes and higher OMR in the polar middle stratosphere. The analysis of the temperature difference shows significantly higher temperature in the upper stratosphere at the high latitudes. Figures 2, 3 are provided to demonstrate in more details the evolution of the polar temperature and OMR during selected time interval. Upper panels of Figs. 2 and 3 show the OMR relative differences (%), averaged over latitudes 67.5N—87.5N for El Niño and La Niña events,

respectively. Climatic values of the OMR have been averaged over 1976—2016. Lower panels of Figs. 2 and 3 demonstrate the differences of the temperature (K) between 5 years averaged values observed under the El Niño and La Niña conditions and corresponding climatic values (averaged over 1980—2016).

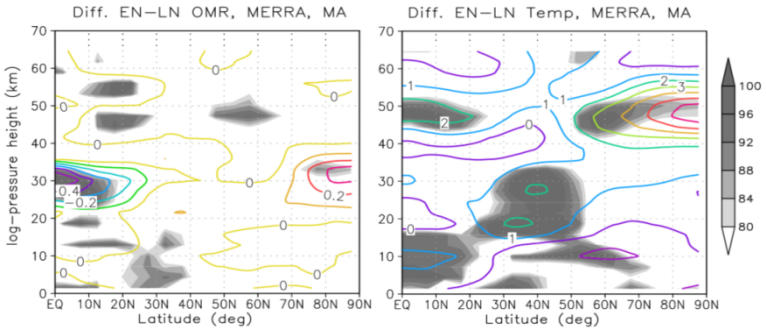

FIGURE 1. Left panel: averaged over March-April, difference in the OMR (ppmv) between El Niño and La Niña conditions (contours) and the statistical significance (shaded). Right panel: averaged over March-April, difference in the temperature (K) between El Niño and La Niña conditions (contours) and the statistical significance (shaded).

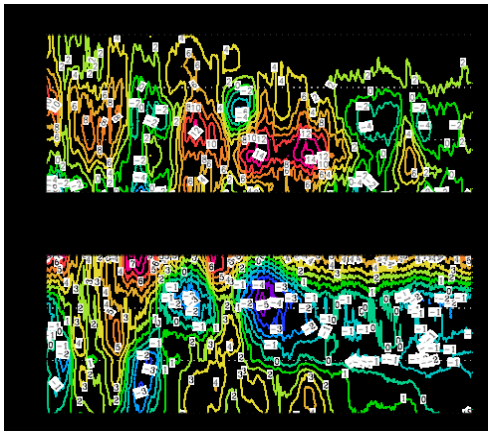

FIGURE 2. Upper panel: relative difference (%) between values of OMR observed under El Niño conditions and OMR climatic values, averaged over latitudes 67.5N—87.5N in March and April. Lower panel: difference of the temperature (K) between values observed under El Niño conditions and climatic values, averaged over latitudes 67.5N—87.5N in March and April.

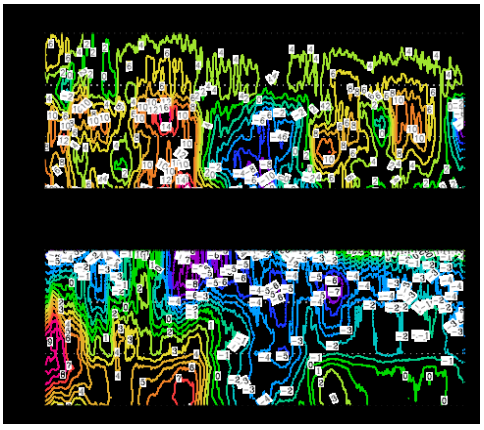

FIGURE 3. Upper panel: relative difference (%) between values of OMR observed under La Niña conditions and OMR climatic values, averaged over latitudes 67.5N—87.5N in March and April. Lower panel: difference of the temperature (K) between values observed under La Niña conditions and climatic values, averaged over latitudes 67.5N—87.5N in March and April.

Figure 2 shows the biggest positive deviations of the OMR observed under El Niño conditions from the OMR climatic values at the beginning of April. The deviation goes up to 14%. In its turn, Fig. 3 shows the inverse situation for La Niña phase, where the negative deviation reaches the value of -10% during the same time interval. Considering the deviations obtained, we can conclude that the difference in the OMR between El Niño and La Niña can reach values of more than 20%. At the same time, there is a cooling in the upper stratosphere (a negative deviation from the climatic values) under La Niña conditions. Conversely, we observe higher temperatures with respect to climatic values in the lower stratosphere under El Niño conditions.

Summary. The results obtained demonstrate that the most important changes in the OMR and the temperature are observed during the time interval approximately corresponding to the mean date of the springtime transition (6 of April) [8]. The question requires the additional research, involving more years for the examination to get the better statistics.

The work was performed under the state assignment of the Ministry of Education and Science of the Russian Federation. Project 5.6493.2017/8.9.

1. S. P. Smyshlyaev, A. I. Pogoreltsev, E. A. Drobashevskaya, A.Yu. Kahukhina, Influence of dynamical factors on the ozone anomalies in Arctic, *Proceedings of the Russian State Hydrometeorological University*, 2015, No 41, pp. 136—148.

2. S. P. Smyshlyaev, A. I. Pogoreltsev, V. Ya. Galin, E. A. Drobashevskaya, Influence of Wave Activity on the Composition of the Polar Stratosphere, *Geomagnetism and Aeronomy*, 2016, Vol. 56, No. 1, pp. 95—109.

3. F. Xie, Li J., Tian W, Zhang J, and J. Shu, The impacts of two types of El Niño on global ozone variations in the last three decades, *Adv. Atmos, Sci.*, 2014, 31(5), pp. 1113—1126, doi:10.1007/s00376-013-3166-0.

4. F. Xie, Li J, Tian W., Zhang J., and C. Sun, The relative impacts of El Niño Modoki, canonical El Niño, and QBO on tropical ozone changes since the 1980s, *Environ. Res. Lett.*, 2014, 9(6), 064020, doi:10.1088/1748-9326/9/6/064020.

5. A. I. Pogoreltsev, and E. N. Savenkova, Interannual and climatic variability of the spring transition date of the stratospheric circulation, *Proceedings of the Russian State Hydrometeorological University*, 2009, 11, pp. 53—62.

6. Bimonthly MEI values, NOAA Earth System Research Laboratory, https://www.esrl.noaa.gov/psd/enso/mei/table.html

7. M. M. Rienecker, et al. (2011), MERRA: NASA's Modern-Era Retrospective Analysis for Research and Applications, *J. Climate*, 24 (14), pp. 3624—3648. doi:10.1175/JCLI-D-11-00015.1.

8. E. N. Savenkova, A.Yu. Kahukhina, A. I. Pogoreltsev, E. G. Merzlyakov, Variability of the springtime transition date and planetary waves in the stratosphere, *J. Atmos. Solar-Terr. Phys.,* 2012, V. 90—91, pp. 1—8, doi:10.1016/j.jastp.2011.11.001.

Influence of the Madden — Julian oscillation on Extratropical Atmosphere Circulation

Kanykei K. Kandieva[1], Alexander I. Pogoreltsev[1,2], and Olga G. Aniskina[1]

[1]Meteorological Forecast Department, Russian State Hydrometeorological University, Voronezhskaya st. 79, Saint-Petersburg, 192007, Russia
[2]Atmospheric Physics Department, Saint-Petersburg State University, Ulyanovskayast, 1, Saint-Petersburg, 198504, Russia

Introduction. The Madden-Julian oscillation (MJO) is the dominant mode of tropical intraseasonal variability [0]. As its convection center propagates from the Indian to Pacific oceans, the MJO affects various weather and climate phenomena [0]. In particular, during the wintertime in the Northern Hemisphere the MJO impacts on the stratospheric polar vortex [0]. The phase of the MJO in which convection is propagating into the tropical central Pacific leads to a weakened vortex, while suppressed MJO convection in this region is associated with a stronger vortex. It was found that the MJO has stronger relationship for vortex-split than for vortex-displacement during sudden stratospheric warmings (SSW) [0]. The MJO can be modulated by the stratospheric QBO [0]. Specifically, the boreal winter MJO amplitude is typically stronger than normal during the easterly QBOat 50 hPa and weaker than normal during the westerly QBO at 50 hPa.

Motivated by these studies, we intend to study what change of extratropical stratospheric circulation refers to the MJO during different QBO phases. Numerical experiments have been performed using the general circulation model and obtained results have been compared to the reanalysis data.

Data and Method. The middle and upper atmosphere model (MUAM) [0] has been used to investigate impact of the MJO on stratospheric dynamic during January and February (JF) months. Four ensemble-run have been conducted, each ensemble consists of 10 runs with different initial conditions (two experiments for different QBO phases, and two experiments for different QBO phases including the MJO into consideration).

The MJO model was introduced in the MUAM as an additional heating source and has the following form:

$$Q(x,y,z,t) = A\left[1 + cos\left(m\lambda - \frac{2\pi}{T}t\right)\right] exp\left(-\left(\frac{x-x_0}{x_0}\right)^2 - \left(\frac{y}{y_0}\right)^2 - \left(\frac{(z-z_0)}{z_0}\right)^2\right)$$

Here A is the averaged heating rate 1.5 K/day, zonal wavenumber m=2, the period of oscillation$T$=45 days. The heating anomaly has an elliptical form moving eastward along the equator, with maximum on the longitude x_0 = 120 E, at altitude z_0=7 km, they are confined to north and south by the latitude y_0 = 15 degrees. The heating anomaly propagates eastward with the average phase speed of about 5 m/s.

The QBO was introduced in the model as an additional nudging term in the prognostic equation for zonal wind component. The value of this term is proportional to the difference of observed and climatic mean zonal wind for the easterly and westerly QBO.

To verify model results with observational data the MJO index was computed as described by [0]. The method of the MJO index calculation is based on empirical orthogonal function (EOF) analysis of the combined fields of outgoing longwave radiation (OLR) and zonal winds in the upper and lower troposphere. Projection of the daily observed data on the pair of EOFs generates two principal components (PC1 and PC2). The data of daily averaged OLRzonal wind at 200 and 850 hPa are obtained from the Japanese 55-year Reanalysis [0] for the period from 1958 to 2016. Data from the 1959 to 1988 period are used to define the EOFs. Figure 1 shows longitudinal structure of the pair of EOFs. The first EOF has a strong convective cloud centered across Indonesia with two circulation cells connected to convective zone. The second EOF represents an eastward shift of this pattern; it has convective cloud centered over the western Pacific.

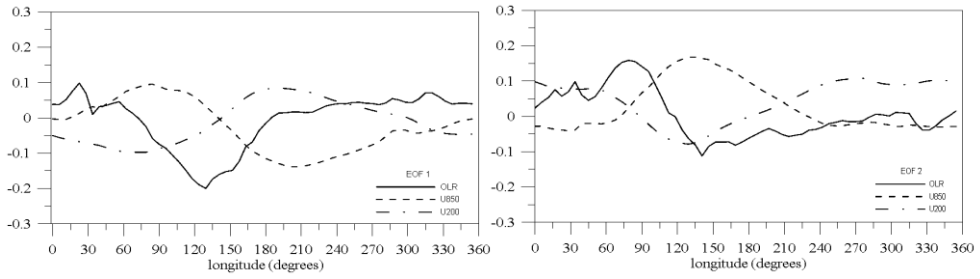

FIGURE 1. Longitudinal structure of the pair of EOFs. The vertical axis is a value of the eigenvector for OLR (solid line), 850 hPa zonal wind (dashed line), 200hPa zonal wind (dash-dot line).

The two series (PC1 and PC2) may be equivalently expressed as a daily amplitude (i. e., $\sqrt{PC1^2 + PC2^2}$). Thus, depending on the amplitude of the MJO index, the JF time interval has been considered as a period with strong (weak) MJO impact if the mean JF amplitude is greater (less) than mean amplitude averaged over 1958—2016. To determine the significance of the obtained results Welch's t-test has been used.

Results. To understand contribution of the equatorial oscillation in atmosphere circulation of the Northern Hemisphere a set of numerical experiments with and without considering the MJO in the model has been performed. The left panels of Fig. 2 demonstrate the effects of MJO including into the model. The right panels of Figure 2 show differences in observed zonal wind and temperature for strong and weak MJO events.

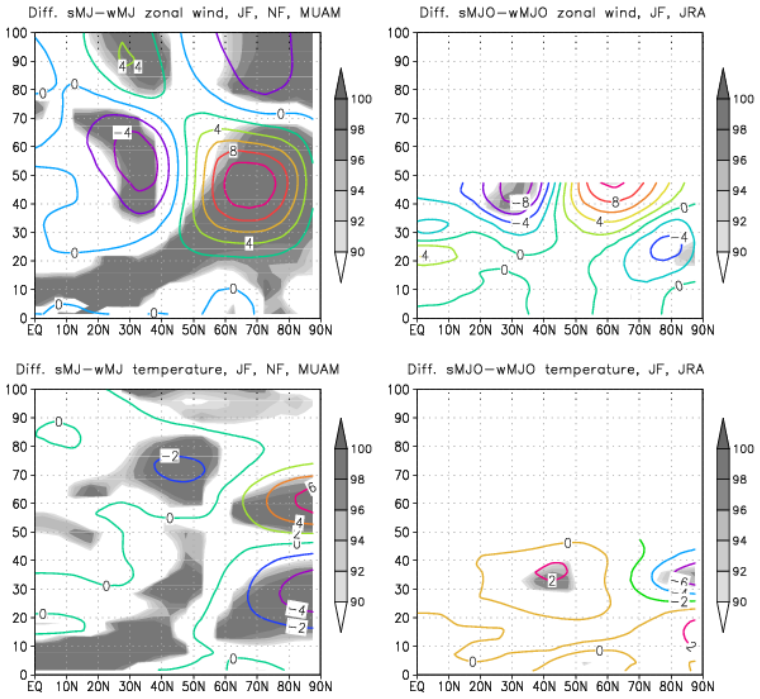

FIGURE 2. Changes of the mean zonal wind and temperature caused by the MJO obtained using the MUAM model (left panels) and observed in JRA reanalysis (right panels). Shaded contours mark the areas where the differences are statistically significant at the 90% confidence level based on the Welch's t-test.

Obtained patterns of the zonal wind and temperature distributions presented in Fig. 2 (left panels) and the magnitude of change of meteorological parameters caused by the MJO are quite similar to results obtained using JRA reanalysis (right panels). One can conclude that magnitudes of the zonal wind and temperature fluctuate with the QBO period. Figure 3 shows the impact of the MJO on the mean zonal wind distribution during the easterly (upper panels) and westerly (lower panels) QBO phases. Changes of the zonal wind caused by the MJO are calculated as difference of runs with and without accounting the MJO in the model separately for two QBO phases. To verify results obtained with simulation, the observations from 1958 to 2016 were divided into two groups with the easterly and westerly QBO phases. In each group it was selected years with weak and strong MJO influence depending on the deviation of the observed MJO amplitudes from the mean amplitude (averaged over whole time interval considered).

Impact of the MJO on zonal wind during easterly QBO is quite negligible in contrast to impact of the MJO during westerly QBO. Consistency of the model and observational results during westerly QBO is better than during easterly QBO.

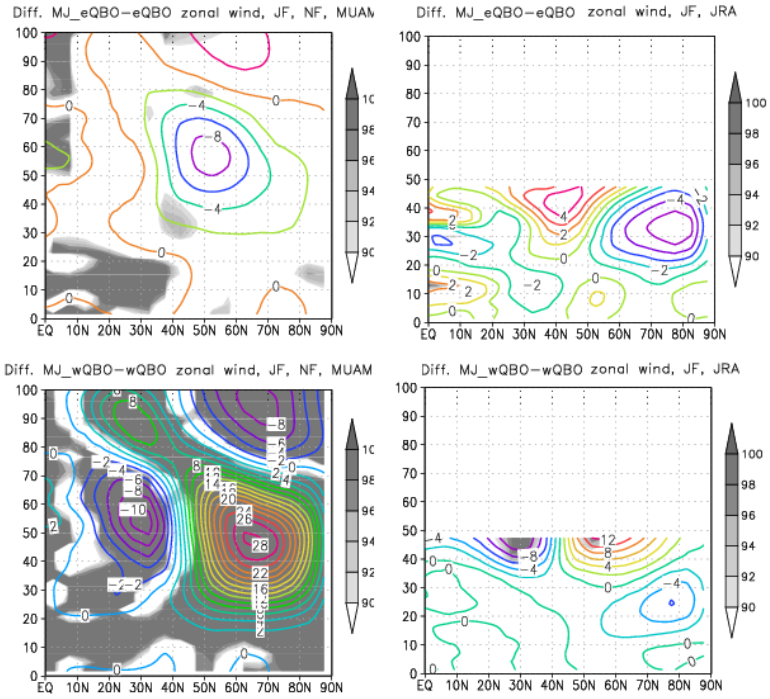

FIGURE 3. Changes of the mean zonal wind caused by the MJO obtained withthe MUAM model (left panels) and JRA reanalysis (right panels) during different QBO phases. Shaded contours mark the areas where the differences are statistically significant at the 90% confidence level based on the Welch's t-test.

Conclusion. Analysis of the MJO influence on dynamical processes in the extratropical stratosphere depending on the QBO phases has been performed. The results obtainedshow that during easterly QBO the MJO decreases the mean zonal wind that may lead to occurrence of the SSW.The opposite situation exists during westerly QBO when the MJO intensifies the mean zonal wind and diminishes occurrence of the SSW events.

1. R. A. Madden and P. R. Julian, Detection of a 40—50 day oscillation in the zonal wind in the tropical Pacific, *J.Atmos.Sci*, 1971, 28, pp. 702—708.

2. C. Zhang, Madden-Julian Oscillation: Bridging weather and climate, *Bull. Am. Meteorol. Soc.*, 2013, 94, pp. 1849—1870, doi:10.1075/BAMS-D-12-00026.1.

3. C. I. Garfinkel, J. J. Benedict , E. D. Maloney,Impact of the MJO on the boreal winter extratropical circulation, *Geophys. Res. Lett.*, 2014, 41, pp. 6055—6062, doi:10.1002/2014GL061094.

4. C. Liu, B. Tian, K.-F. Li et al., Northern Hemisphere mid-winter vortex-displacement and vortex-split stratospheric sudden warmings: Influence of the Madden-Julian Oscillation and Quasi-Biennial Oscillation, *J. Geophys. Res. Atmos.*, 2014, 119, 12, pp. 599—12, 620, doi:10.1002/2014JD021876.

5. C. Yoo and S.-W. Son, Modulation of the boreal wintertime Madden-Julian oscillation by the stratospheric quasi-biennial oscillation, *Geophys. Res. Lett*., 2016, 43, pp. 1392—1398, doi:10.1002/2016GL067762.

6. A. I. Pogoreltsev, Forcing of the normal atmospheric modes by stratospheric vacillations, *Izvestiya, Atmospheric and Ocean Physics*,2007, 43(4), pp. 28—40.

7. M. C. Wheeler and H. H. Hendon, An all-season real-time multivariate MJO index: Development of an index for monitoring and prediction, *Mon. Wea. Rev.,* 2004, 132, pp. 1917—1932, doi:10.1175/1520-0493(2004)132<1917:AARMMI>2.0.CO.

8. S. Kobayashi, TheJRA-55 reanalysis: General specifications and basic characteristics, *J. Meteor. Soc. Japan*, 2015, 93, pp. 5—48, doi:10.2151/2015-001.

X-Ray Increase while Precipitation as an Atmosphere Phenomenon

Yury V. Balabin, Aleksei V. Germanenko, Boris B. Gvozdevsky

Polar Geophysical Institute, 26a, Academgorodok St., Apatity, Russia

Introduction. At present gamma-ray detectors are placed by the Laboratory of Cosmic Rays, Polar Geophysical Institute (PGI) at six stations: Barentsburg (78°N, the Spitsbergen archipelago), Tixie (71° N, the Laptev Sea), Apatity (68° N, the Kola peninsula), Yakutsk (62°N, East Siberia), the Houlougay-Sha peak (52°N, the Sayan mountains, 3000 m), Rostov-on-Don (47° N, the middle latitude plain). Except for the Alpine Houlougay station, other stations are located at sea-level. At all the stations, soft gamma radiation monitoring (20—400 KeV) is carried out by means of uniform calibrated scintillation detectors NaI(Tl), Ø60×20, which are made at PGI. These detectors placed into a lead shield, with walls thickness of 5 cm and opened from the top, get radiation only from the upper hemisphere. At Apatity and Barentsburg stations observations have been continuously carried out since 2010, at other stations, since 2016. The two stations are equipped with a complex to monitor the main secondary components of cosmic rays, such as hadronic, charged and electromagnetic ones.

It was revealed from the first observations that, in precipitating, the gamma radiation flow increases by tens of percents (up to 70%), which is being observed all the year round. Also it has been found out from the observation data (Apatity and Barentsburg) [1—3] that only an electromagnetic component increases. No increase is observed in a charged particles (electrons, positrons, muons) flux. As gamma radiation increases, we do observe a 2—4% increase on the charged component detectors. However, it can be explained by the fact that Geiger-Muller (G-M) counters are known to be low sensitive (1—2%) to gamma radiation, as well as by the fact that radiation is capable to knock electrons out of the material the cover is made of (~1 %). As other gamma radiation variations are also observed (for example, a daily variation of 2—3%), a threshold increase has been assumed to be equal to 5%, an increase of less than 5% has not been taken into consideration as an event.

The phenomenon discovered by the authors is being closely investigated. It has been found that energetic spectrum of gamma radiation inducing an increase, has exponential form and extends up to 2.5—3 MeV, having no characteristic lines of elements. These spectral measurements are made at Apatity station on a scintillation spectrometer (a crystal NaI(Tl), Ø150×110). The time of measuring of a differential energetic spectrum of gamma radiation over the range of 0.2—8 MeV is 30 minutes

Experimental measurements. Each station records, on the average, more than one hundred events with a > 5% amplitude increase a year. More than 90% of increase events occur under precipitating. In summer, it is rain, and in winter, these are snow or frosty fog. Observed under long-lasting overcastting precipitation are the events with many local maxima corresponding to an increase in precipitation intensity. These data have been obtained at Apatity station, where relative intensity of precipitation is measured, with resolution of 1 minute by an auxiliary precipitation detector, Unfortunately, absolute measurements of precipitation intensity are possible to be made at a meteorological station only every three hours.

Discussion. At present the mechanism of gamma radiation generation in precipitating has not clearly established yet; other groups of researchers offer different hypotheses. The authors consider that increase events are not related to any radionuclides of a natural or anthropogenic origin, which are present in precipitation.

Firstly, once during hard raining in Apatity, when the gamma radiation flux was intensively increasing, a vessel with rain-water (5 litres) running from the roof of a laboratory building was placed on an additional detector. This detector was placed indoors and could record no increase because radiation was completely absorbed by the roof of the building. No changes in the detector's counter have been recorded even after the vessel with rainwater was placed above the detector. It should be noted that the water volume of 5 litres is the volume of all the drops contained simultaneously in the air at a height of 100 m over the detector [4]. The atmosphere pass of gamma-ray quanta with energy of 100 KeV is also about 100 m [5]. Therefore such a quality experiment can be considered as a representative one.

Secondly, the detector being placed on the roof of a building (Fig. 1) at a height above the soil and exposed to open air and wind makes the hypothesis of radon gas origination of increases groundless.

Finally, in our opinion a convincing demonstration of the above said is the analysis of all the conditions accompanying a gamma radiation flux increase. Let us take quite an ordinary event taking place in 05.04.2012 in Apatity as an example (Fig. 2). The beginning of April is still a cold winter period in this region. The maximum depth of snow cover is recorded in the middle of April [6]. The day time temperature is in the range of –5° C to –10° C, at night it is of –20° C, the snow cover's depth is about 1 m, below it is the frozen soil.On April, 5th the weather is changeable, a bit windy. Three snowfalls (short snow storms) follow each other, lasting for a short period of time, about half an hour. Each of these results in about a 1—3 cm snow layer, covering the one formed before.

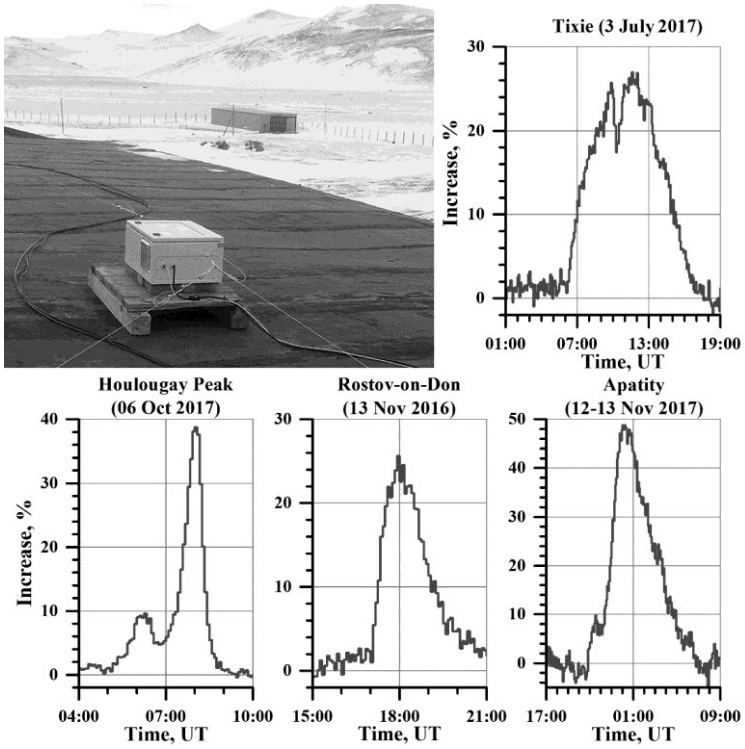

FIGURE 1. Top: the scintillation detector at Tixie and one of the gamma radiation flow increase events. The lead shield with the detector inside is placed into a thermo-stabilized box. Soft gamma radiation is strongly absorbed by the material of a cover, so the detector is placed outside. Bottom: The examples of the increase events at stations Houlougay, Rostov and Apatity. The zero level corresponds to the radiation flux at a good weather the day before.

The precipitation intensity measuring data are based on measuring an IR-radiation flux reflected from snowflakes. Therefore the signal depends on the shape of snowflakes. But within one storm it is possible to consider that snowflakes are similar in shape and the signal is proportional to the precipitation intensity. A small amount of fresh-fallen snow cannot induce gas emanation through frozen soil and a dense snow layer of 1 m thick.

In addition, a thorough analysis has shown that the fresh-fallen snow contains no radionuclides. After each snow storm, snow is on the roof of the building. In this case the gamma-background intensity decreases with characteristic time of $\tau \approx 1$ hour. If we assume that an increase and the subsequent drop are caused by radionuclides present in fresh-fallen snow, then τ is also their life-time. Hence, radionuclides are to get into a cloud, be transferred in it to be falling with snow onto the observation point for no more than 2—3 τ, otherwise all the radionuclides are decayed on their transportation. At the average cloud velocity of 15 km/s, the distance from the radionuclides source to the observation point cannot be more than 100 km. In addition, it must constantly produce these short-lived

radionuclides, and source intensity will be more many times. In this case, clear dependence of increase on wind velocity would be observed. However, it is absent. If we consider a short-lived isotope to be a daughter one to a natural radionuclide (for example, uranium, like in [7]), then, according to the secular equilibrium equation, the activity of the initial (uranium) and daughter radionuclides must be equal. As uranium is a long-lived radionuclide, a half decrease in intensity would be observed. Figure 2 shows that after its increase, the level of gamma radiation flux decreases to the initial one. Moreover, a permanent, thick and dense snow cover in the region in winter prevents ground and rock particles from getting into the atmosphere.

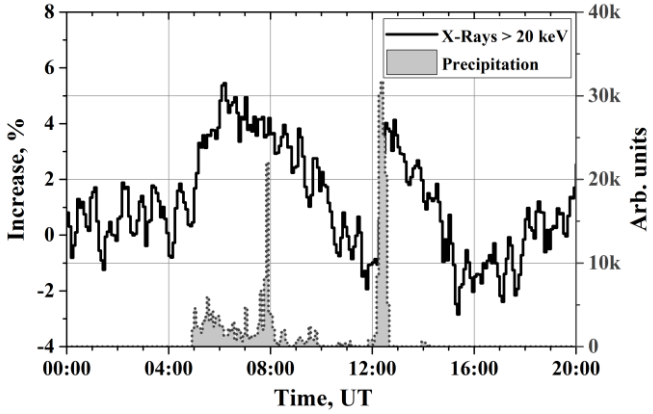

FIGURE 2. The profiles of a gamma radiation increase in the channel of >100 KeV (black solid line, the left-hand scale), April 5, 2012 and the precipitation velocity (dotted grey line, the right-hand scale).

Conclusions. The fact that the phenomenon of increase is observed everywhere(Barentsburg is located in the island, at the distance of about 1000 km to the continent; Tixie is in a sparse populated coastal part of the Eastern Siberia; the Houlougay peak is in the Sayany mountains, at an altitude of 3000 m, inside the continent) and the effect is similar (the increase amplitude is 30—50%) means that one reason inducing it is present. It is most likely that some physical conditions inside the atmosphere change the processes of interaction between the secondary cosmic rays and the atmosphere, resulting, in result, in an increase in the gamma radiation intensity. The phenomenon has been poorly studied at present, and its role in affecting the atmospheric processes is not clear. It is necessary to extend the studies.

1. A. V. Germanenko, Yu. V. Balabin, B. B. Gvozdevsky, L. I. Schur, Nature of Gamma Radiation Variations During Atmospheric Precipitation, *Solar-Terrestrial Physics*, 2016, 2(1), p. 78—88.

2. A. V. Germanenko, Y. V. Balabin, E. A. Maurchev et al., The Continuous Detection of Gamma (X-Ray) Spectra Registered During Atmospheric Precipitations, *Journal of Physics: Conference Series,* 2013, 409(1), p. 012240.

3. A. V. Germanenko, Y. V. Balabin, B. B. Gvozdevsky and E. V. Vashenyuk, Features of the Flux of Gamma-Radiation in the Lower Atmosphere During Precipitation, *Journal of Physics: Conference Series*, 2013, 409(1), p. 012241.

4. L. T. Matveev, Fundamentals of General Meteorology: Physics of the Atmosphere, Israel Program for Scientific Translations, Jerusalem 1968, 712 p.

5. Yu. M. Shirokov, N. P. Yudin, Nuclear Physics, Nauka, Moscow, 1980, 728 p.

6. Weather Forecast, https://rp5.ru

7. E. Yu. Yakovlev, S. V. Druzhinin, V. M. Bykov, Impact of the Short-Lived Radon Decay Products on Change of Gamma Background During Precipitation on The European North of Russia, *Advances in current natural sciences*, 2017, 6, p. 123—129.

Generation of the Electromagnetic Ion Cyclotron Waves by the Artificial Ionospheric Source

Dmitry S. Kotik[1], Ekaterina V. Orlova[2], and Vladimir A. Yashnov[2]

[1]Radiophysical Research Institute, Nizhny Novgorod, 603005, Russia
[2]Department of Radiophysics, Nizhny Novgorod State University, Nizhny Novgorod, 603950, Russia

Fast magnetosonic waves (FMS) and electromagnetic ion cyclotron (EMIC) waves are important for electron acceleration and loss from the radiation belts [1,2]. These waves are generated usually in the region of magnetic equator by unstable energetic particles distributions that form during geomagnetically disturbed conditions [3—5]. It is known that a significant number of heavy ions such as He^+ and O^+ exist in the upper ionosphere. The dispersion relations for multiple-ion plasmas in the presence of heavy ions have been theoretically calculated [4—8]. However, there is not much experimental work to confirm the theory (see [9]). It is shown that the evolution of normalized wave frequency with wave vector is similar to the analytical results obtained under the linear dispersion theory for L mode waves.

Since the early 1970s active experiments on ionospheric modification by high-power radio waves (RF: 1—10 MHz) have been conducted at different ionospheric heating facilities [10]. The low frequency waves in ULF, ELF and VLF bands were observed at all known heating facilities (see [10—14]).

The purpose of this paper is to consider the idea that magnetosonic waves generated by the artificial ionospheric source in the F-region of ionosphere could propagate a large distance and provide the source of energy EMIC waves as a result of propagation and a process of linear mode conversion. The linear conversion takes place in the region of upper ionosphere where the frequency of a wave approaches the so-called crossover frequency.

In this paper the properties of ULF-ELF waves in ionospheric plasma are carefully investigated basing on the magneto-ionic theory using the international

models like IRI-2016 — for ionosphere, MSIS-E-00 — for atmosphere and DGRF/IGRF — for geomagnetic field. The components of permittivity tensor, collisional frequencies, refractive index, polarization, peculiarities of group velocity and wave normal surfaces of two normal modes have been calculated. The particles composition and electron collisional frequencies for the Sura facilities (0.0 LT) are shown on the Fig.1.

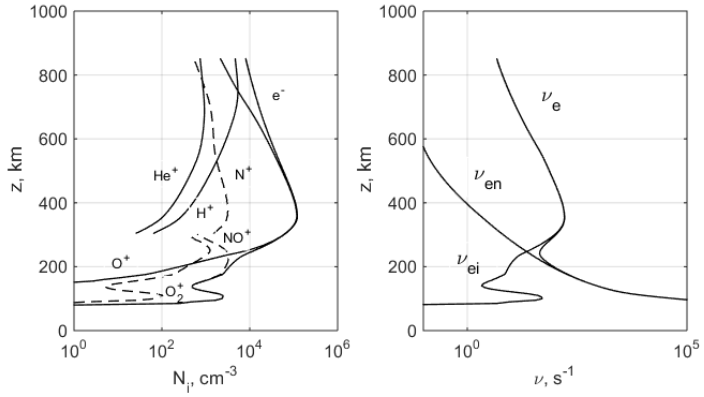

FIGURE 1. Profiles of particles composition (left) and collisional frequencies (right).

The dispersion curves of Alfven (A) and FMS modes were calculated for ionosphere parameters presented in Fig.1. Refraction indices vary with frequency f and wave normal angle θ. Red curves in Fig. 2 (θ = 18°) correspond A mode and blue — FMS mode at the altitude 645 km. The form of curves near the crossover frequency is shown on the right panel. It is seen that the dispersion curves touch each other at the crossover frequency and the wave energy can be transferred from one wave mode to another.

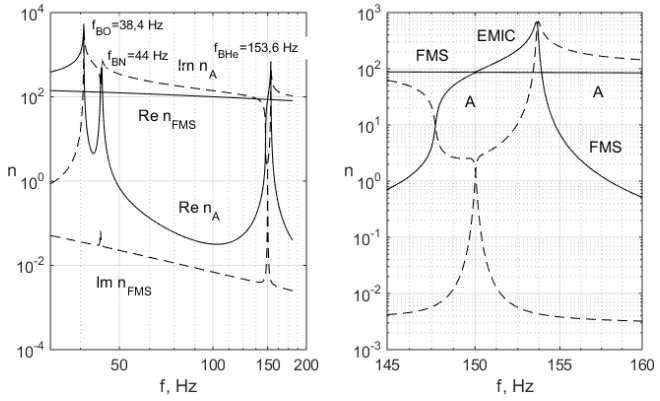

FIGURE 2. Refractive index as a function of frequency for altitude 645 km.

The vertical structure of real Re(n) and imaginary Im(n) parts of local refraction coefficients for Alfven (A) and FMS modes for vertically incident waves is shown in Fig. 3 for 150 Hz frequency. In the right panel the region where mode conversion can take place are presented in details. The analysis of dispersion curves shows that the energy of FMS mode is partially transformed to A mode and EMIC mode.

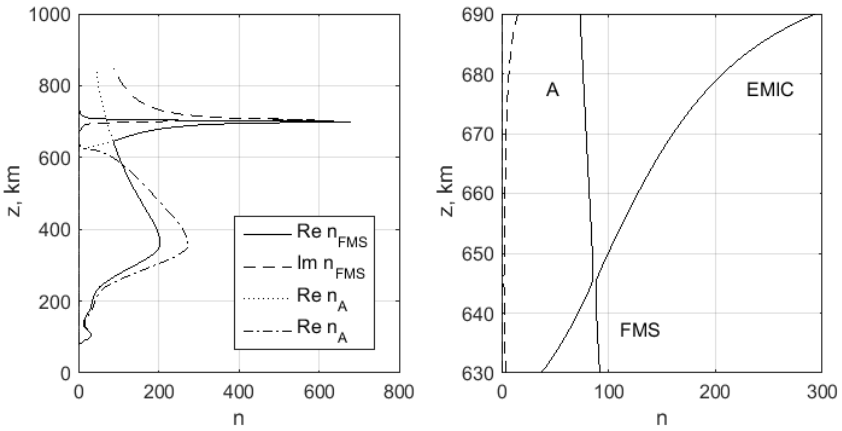

FIGURE 3. The vertical structure of local refraction coefficients for A and FMS modes.

Change of polarization of normal waves with height is shown on Fig 4. FMS mode is left-hand polarized (L) below the crossover frequency and right-hand polarized (R) above. Alfven mode is right-hand polarized below the crossover frequency and left-hand polarized above. But both modes are linearly polarized in the crossover region.

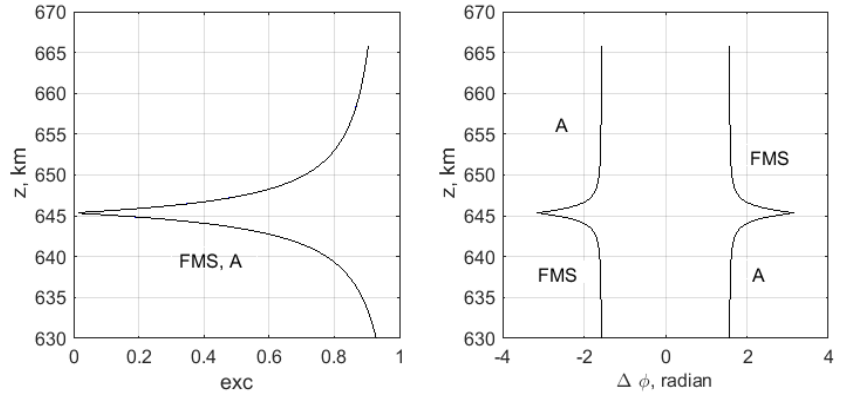

FIGURE 4. The polarization of A and FMS modes. Eccentricity (left) and phase shift (right) versus height.

The four first-order differential equations governing the propagation of electromagnetic waves in the stratified ionosphere may be presented in the form [16]

$$\frac{d\vec{e}}{dz} = ik_0 \hat{T}\vec{e}\,, \qquad \vec{e} = \left(E_x, E_y - \zeta_0 H_x, \zeta_0 H_y\right)^T, \tag{1}$$

where E_x, E_y, H_x, H_y — horizontal components of electric and magnetic fields, ζ_0 — free space impedance. Expressions for matrix components are presented in [16]. The solution is found by means of a simple and rapid numerical method based on thin-film optics [17]. By this method the ionosphere is divided into a large number of thin layers, all partial reflections within a given layer are summed, and the process is then extended layer by layer to include the entire ionospheric region. The iterative procedure is started above linear conversion region and extended downward to terminate at the level below this region. Then the iterative process repeats upside-down. Variations of amplitudes upward-propagating modes with height under conditions $A_{A0} = 0$, $A_{FMS0} = 1$ (left panel) and $A_{A0} = 1$, $A_{FMS0} = 0$ (right panel) a presented on Fig. 5. Here A_{A0} and A_{FMS0} — initial values of amplitudes A and FMS modes at height 630 km. It is seen that in the conversion region (near $z = 645$ km) energy of FMS mode is converted to energy of A mode and vice versa. At the same time the considerable part of energy of FMS mode passes into EMIC mode. Amplitudes of backward-propagating waves in this case have negligible values.

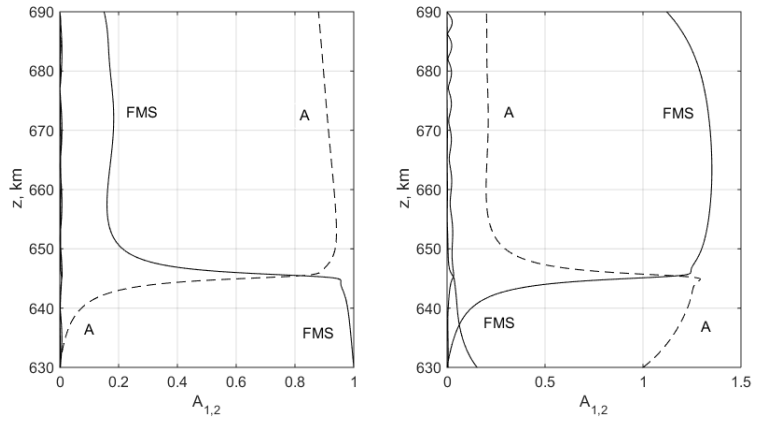

FIGURE 5. The amplitudes of A and FMS modes as a function of height.

It is shown that the energy of FMS waves can be transformed to energy for EMIC waves in the resonance region (helium band) as a result of upward propagation and linear mode conversion near the height where wave frequency is equal crossover frequency. At this height both modes (FMS and A) have linear polarization and there is a polarization change upon transition through this region (L to R for FMS mode and R to L for A mode). The height where linear transformation takes place depends on wave frequency, increasing when the frequency decreases.

The work was supported by Russian Science Foundation (project no. 14-12-00706).

1. Y. Y. Shprits, D. A. Subbotin, N. P. Meredith, and S. R. Elkington, Review of modeling of losses and sources of relativistic electrons in the outer radiation belt II: Local acceleration and loss, 2008, 70, pp. 1694—1713, doi:10.1016/j.jastp.2008.06.014.

2. B. J. Fraser, H. J. Singer, W. J. Hughes et al., CRRES Poynting vector observations of electromagnetic ion cyclotron waves near the plasmapause, *J. Geophys. Res.*, 1996, 101, pp. 15331—15343, doi:10.1029/95JA03480.

3. D. Summers and R. M. Thorne, Relativistic electron pitch-angle scattering by electromagnetic ion cyclotron waves during geomagnetic storms, *J. Geophys. Res.*, 2003, 108, p. 1143, doi:10.1029/2002JA009489.

4. W. Li, Y. Y. Shprits, and R. M. Thorne, Dynamic evolution of energetic outer zone electrons due to wave-particle interactions during storms, *J. Geophys. Res.*, 2007, 112, A10220, doi:10.1029/2007JA012368.

5. R. L. Smith. and N. Brice, Propagation in Multicomponent Plasmas, *J. Geophys. Res.*, 69, pp. 5029—5040.

6. D. T. Young, S. Perraut, A. Roux et al., Wave-particle interactions near He^+ observed on geos 1 and 2, 1. propagation of ion cyclotron waves in He^+-rich plasma, *J. Geophys. Res.*, 1981, 86, pp. 6755—6772.

7. D. G. Swanson, Plasma Waves, Institute of Physics Publishing, Bristol and Philadelphia, 1989.

8. R. B. Horne and R. M. Thorne. Ion cyclotron absorption at the second harmonic of the oxygen gyrofrequency, *Geophys. Res. Lett.*, 1990, 17, pp. 2225—2228.

9. I. P. Pakhotin, S. N. Walker, Y. Y. Shprits, and M. A. Balikhin, Dispersion relation of electromagnetic ion cyclotron waves using Cluster observations, *Ann. Geophys.*, 2013, 31, pp. 1437—1446.

10. G. G. Getmantsev, N. A. Zuikov, D. S. Kotik et al., Combination frequencies in the interaction between high-power short wave radiation and ionospheric plasma, *JETP Lett.*, 1974, 20, pp. 101—102.

11. D. S. Kotik. ELF/VLF emissions generated in the ionosphere by heating facilities—A new tool for ionospheric and magnetospheric research, *Radiophys Quantum Electron*., 1994, 37, 460, https://doi.org/10.1007/BF01088656.

12. K. Papadopoulos, A. S. Sharma, and C. L. Chang, On the Efficient Operation of a Plasma ELF Antenna Driven by Modulation of Ionospheric Currents, *Comm. Plasma Phys. And Cont. Fus.*, 1989, 13(1), pp. 1—17.

13. K. Papadopoulos, N. Gumerov, X. Shao et al., HF driven currents in the ionosphere, *Geophys. Res. Lett.*, 2011, 38, L12103, doi:10.1029/2011GL047368.

14. P. Stubbe, Review of Ionospheric Modification Experiments at Tromso, *J. Atmos. Terr. Phys.*, 1996, 58, pp. 349—368.

15. K. Papadopoulos, C. L. Chang, J. Labenski, and T. Wallace, First Demonstration of HF-driven Ionospheric Currents, *Geophys. Res. Lett.*, 2011, 38, L20107, doi:10.1029/2011GL049263.

16. K. G. Budden, The Propagation of Radio Waves: The Theory of Radio Waves of Low Power in the Ionosphere and Magnetosphere, Cambridge University Press, Cambridge, 1985.

17. C. Altman, H. Cory, The Simple Thin-Film Optical Method in Electromagnetic Wave Propagation, *Radio Science*, 1969, 4 (5), pp. 449—457.

Comparison of Global Ionospheric Maps with Data Obtained Using Vertical Sounding of the Ionosphere

Inna R. Petrova, Vladimir V. Bochkarev, and Adel D. Akchurin

Institute of Physics, Kazan Federal University, Kremlevskay str., 18, Kazan, Russia

Introduction. Various methods and equipment are used to study ionospheric processes such as ionosondes of vertical sounding, incoherent scattering radars and transionospheric sounding using signals from GPS navigation satellites. The development of these methods and equipment allows performing continuous and almost global monitoring of the Earth's ionosphere. One of the methods of using GPS data for ionospheric studies is the construction of global maps of the total electronic content (TEC). Global ionospheric maps (GIM) is a new powerful tool for studying the global structure of the ionosphere and large-scale ionospheric processes. The use of GIM allows performing quantitative analysis of TEC with a low spatial-temporal resolution corresponding to global diurnal variations in the electron concentration of the ionosphere. The researchers had the opportunity to trace the evolution of the global structure of the ionosphere, analyse the dynamics of large-scale processes and, most importantly, the interrelationship of various processes in the atmosphere [1].

The problem of using GIM maps for ionospheric studies is spatial interpolation used for construction of maps. Uneven distribution of GPS receivers around the globe and the need to obtain TEC values on a uniform grid for constructing global maps results in different data quality in different regions. The following factors influence the accuracy of map construction near the GPS receiver: multipath signal propagation, hardware errors in the receiver and transmitter; interpolation errors. In regions where are no GPS receivers, the TEC value at a specific node of the map grid at a specific moment of local time is determined by measurements obtained at the same local time by the receivers which geomagnetic latitude is close to this node. Therefore, the TEC values shown on the maps are accurate for regions with a large number of GPS receivers and are unreliable for areas where there are only a few receivers.

There are only a few sources of GPS data used to construct global ionospheric maps (GIM) in European part of Russia. In this case, it is recommended to use data of ground-based radio-sounding of the ionosphere to correct the regional component of the global distribution of TEC obtained using the GIM technology. Implementation of such an integrated approach requires preliminary analysis of features and compatibility of the used data. In this paper, we performed the correlation analysis of the TEC maps and the data of the vertical sounding of the ionosphere in order to develop the most effective methods for their integrated use.

The experimental data. GIMs are constructed according to the data of the international network of GPS receivers in various scientific centres such as Centre

for Orbit Determination in Europe (CODE), Jet Propulsion Laboratory of California Institute of Technology (JPL), Grup Universitat Politecnica de Catalunya (UPC), European Space Agency Group (ESA). A special format IONEX has been developed to store and transfer GIM in digital form. Data in this format are available on the Internet at ftp://cddis.gsfc.nasa.gov/gps/products/ionex/. Each IONEX file contains TEC values for one day with a 2-hour average. The spatial range of maps is from –180 to 180 in longitude and from –87.5 to 87.5 in latitude. The algorithms for obtaining GIM are described, for example, in [2].

Experimental data obtained at Kazan Federal University using the "Cyclone" ionosonde [3] were used for comparison with the GIM. To perform the analysis, a series of fxF2 values obtained during the continuous experiment of 2011—2012 were selected. fxF2 is the critical frequency of the X component reflected from the F2 layer. The sampling interval is 1 min.

Discussion of the obtained results. We compared the obtained fxF2 values with the TEC values. The values of fxF2 were averaged over two-hour intervals to obtain a series synchronized with the TEC values series. The TEC values at the Cyclone ionosonde location were calculated using the corresponding maps applying linear interpolation.

Direct comparison of the total amount of available data shows an unexpectedly low degree of statistical connection — the value of correlation coefficient for data obtained at different processing centres range between 0.51—0.55. Relatively low correlation of these data is seen in Fig. 1-a which shows the scattering diagram of fxF2 and TEC values (according to UPC data).

Then, we performed comparison separately for different time of a day. Only the values relating to the selected hour were chosen from the entire set of available data. Then, the Spearman correlation coefficient was calculated. Dependence of the correlation coefficient between fxF2 and TEC, according to the data of different centres, is shown in Fig. 1-b. It can be seen that relatively high values (up to 0.81) of the correlation coefficient are observed during a considerable part of the day. At that, the correlation decreases round about midday.

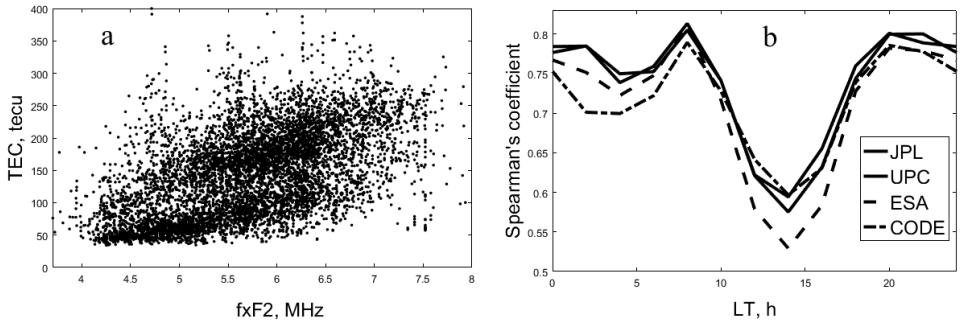

FIGURE 1. a) Scattering diagram of fxF2 and TEC values, according to UPC data, b) Values of the correlation coefficient of fxF2 and TEC for different time of a day.

The best correlation is observed for data submitted by the UPC and JPL processing centres, with some advantage of UPC. The correlation for data presented by ESA is significantly lower especially at noon. On the contrary, a significantly smaller correlation is obtained for the CODE data in the night, morning and evening hours.

Figures 2a and 2b show scatter diagrams of fxF2 and TEC values (according to the UPC) for hours when the maximum (8 am local time) and minimum (2 pm local time) correlation of these parameters are observed. Firstly, it can be seen that the nature of the relationship between fxF2 and TEC differs at different times of the day. Secondly, significantly larger relative variation in the values of one of the considered parameter values is observed at noon. Thus, a small average statistical relationship between fxF2 and TEC is due to both change in the character of the relationship between these parameters during the day and, in particular, lower predictability of their values at around the midday.

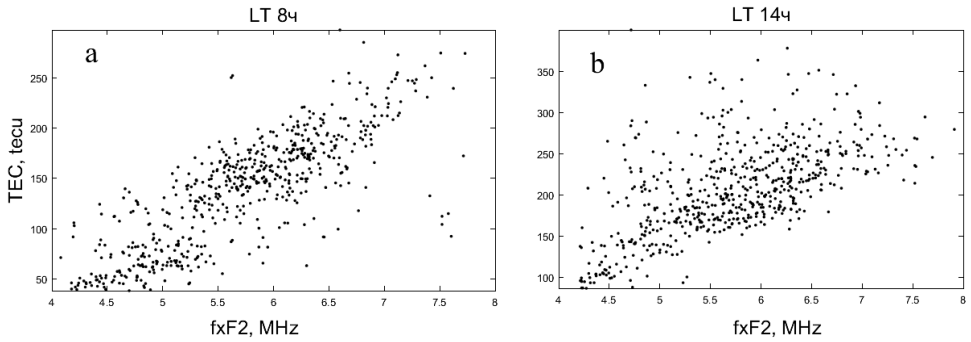

FIGURE 2. a) Scattering diagram of fxF2 and TEC values for 8 am local time, b) Scattering diagram of fxF2 and TEC values for 14 am local time.

Conclusion. Thus, based on the conducted analysis, the following approaches can be proposed for joint use of GIM and vertical ionospheric sounding. The degree of correlation of the analyzed data varies significantly for different time of a day, therefore, different methods should be used at different time of the day. Despite the use of a universal algorithm for obtaining TEC, the data presented by different processing centres have obvious differences. The highest correlation coefficients were obtained for the “Cyclone” ionosonde data and GIM presented by the UPC and JPL data processing centres, which is probably due the improved spatial interpolation algorithms they use.

1. I. Azeem, S. L. Vadas, G. Crowley, and J. J. Makela, Traveling ionosphericdisturbances over the United Statesinduced by gravity waves from the 2011Tohoku tsunami and comparison with gravity wave dissipative theory, *J. Geophys. Res. Space Physics*, 2017, 122, pp. 3430—3447, doi:10.1002/2016JA02365 9.

2. A. J. Mannucci, B. D. Wilson, D. N. Yuan et al., A global mapping technique for GPS derived ionosphere TEC measurements, *Radio Sci.,* 1998, 33(3), pp. 565—582.

3. A. D. Akchurin, V. V. Bochkarev, V. R. Ildiryakov, and K. M. Usupov, TID selection and research of its characteristics on ionograms, *in 30th URSI on General Assembly and Scientific Symposium*, IEEE, Istanbul, Turk, 2011, p. GP1.23.

Seasonal and Interannual Variability of Temperature and Gravity Wave Intensity from Hydroxyl Emission Observations in Alma Aty

Andrey A. Popov[1], Nikolai M. Gavrilov[1], Alexey B. Andreev[2], and Alexander I. Pogoreltsev[3]

[1]Saint-Petersburg State University, Department of atmospheric physics, Saint Petersburg, Russia, 198504
[2]Science Center KIT, "Institute for Ionosphere", Almaty, plateau Kamenskoye, Kazakhstan, 050020
[3]Russian State Hydrometeorological University, Department of meteorological forecasts, Saint-Petersburg, Voronezhskaya Str., 98

Introduction. Currently, the study of internal gravity wave (IGW) studies are of interest. Their sources are located mainly in the lower atmosphere and, propagating upwards, IGWs are able to transfer energy and momentum to the middle and upper atmosphere, thus influencing the thermodynamic regime of the atmosphere.

Measurements of intensity and rotational temperatures of nightglows is a way for monitoring the dynamics and composition of the upper atmosphere. Authors [1] studied temperature variability in the mesopause region using spectral observations of hydroxyl emission at the Zvenigorod station. The problem of changes in the mesopause region during sudden stratospheric warming was analyzed in [2]. The study [3] deals with seasonal changes of temperature obtained from hydroxyl emission observations and their dependence on solar activity.

Recent studies reveal the presence of long-term changes of the upper atmosphere characteristics [e. g., 4]. Authors [5] used a simple differential filters and analyzed seasonal and interannual changes in the mean winds and IGW intensity at altitudes 80—100 km from observations of the ionospheric drifts at Collm Observatory in Germany.

In this paper, the method of digital differential filtering is applied for analyzing observations of the rotational temperature hydroxyl nightglows at altitudes of 85—90 km with the SATI devise in Alma-Aty, Kazakhstan in years 2010—2017. We study seasonal and interannual changes in the average temperature and in the intensity of variations with periods 1.7—5 hours, which may be associated with IGWs in the mesopause region.

The device and method of data analysis. Information about hydroxyl nightglow at altitudes of 85—90 km is obtained at the Institute of Ionosphere in Alma-Aty, Republic of Kazakhstan. The device SATI (Spectral Airglow

Temperature Imager) is installed at the foothills of the Tien Shan mountain region. The SATI is a Fabry-Perot spectrometer, which uses narrow-band interference filters and a CCD camera detector. The SATI can variations of the intensity and rotational temperature in the bands of OH emission. To select them, the SATI uses interference filters for the spectral region of the OH Meinel bands [6]. The exposure time is 2 minutes. The use of the SATI for IGW studies ~~of~~ in the lower thermosphere is described in detail in [7].

The SATI measures the intensity and vibrational temperature of OH emission at the average altitude of 87 km at 12 sky points along almucantar with a zenith angle of 30°. During primary processing, measured values are averaged over all 12 sky points and over hourly time intervals.

To estimate the intensity of short-period perturbations near the mesopause, we used the method described in [5]. To obtain variations with mesoscale time periods, a numerical filtering was applied by calculating the difference between consecutive hourly average values of temperature

$$T'_i = (T_{i+1} - T_i)/2, \tag{1}$$

where i is the number of hourly interval with the middle time t_i. It is shown in [5] that the difference between the average hourly values is equivalent to a numerical frequency filter having the transmission function

$$H^2 = \frac{\sin^4(\sigma\tau/2)}{(\sigma\tau/2)^2}, \tag{2}$$

where σ is frequency, $\tau = t_{i+1} - t_i$ is the time step of the hourly data. Figure 1 shows the transmission function of the filter (2) for τ = 1h. The H^2 maximum in Fig. 1 corresponds to the period about 2.7 h and the half-width of H^2 at the level of 0.5 of the maximum value gives the filtered period interval of 1.7—5.1 h.

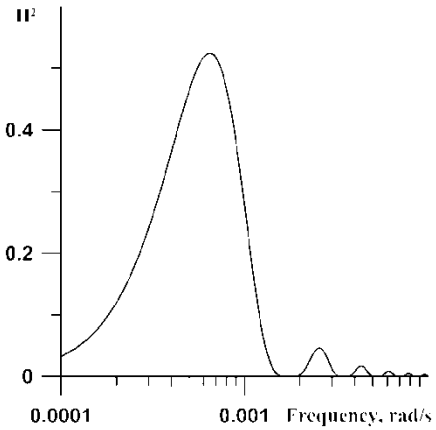

FIGURE 1. Transmission Function of the hourly-difference filter (2).

To improve statistical reliability of results, the filter (2) was applied only to pairs of hourly intervals with at least 40 individual temperature measurements. To study the seasonal and inter-annual changes, the mean temperatures and relative variances of the hourly differences (2) over monthly intervals were calculated.

Results. The method described previously was applied to the data of ground-based observations of the rotational temperature of the OH band (6—2) with the SATI device in Alma-Aty during the interval from May 2010 to April 2017. The polarization relations of the theory of atmospheric IGW [8] allow to obtain the following formula for the amplitude of horizontal velocity variations, U, and potential wave energy, E_p:

$$U = \frac{g}{N}\sqrt{\frac{T'^2}{T_0^2}}; \qquad E_p = \frac{U^2}{2}, \tag{3}$$

where g is the gravitational acceleration, N is the Brund-Vaisala frequency, T_0 is the montly-mean temperature.

Figure 2 shows seasonal changes of the analyzed parameters averaged over years 2010—2017. The mean temperature near the mesopause in Fig. 2a has a maximum in winter and minimum in June. The intensity of mesoscale temperature variations in Fig. 2b and IGW characteristics in Figs. 2c and 2d. have maxima in spring and autumn, also minima in winter and summer. Similar seasonal variations of IGW intensity were obtained from medium-frequency radar observations of winds at altitudes of 80—100 km [9].

Figure 3 presents interannual changes of the analyzed characteristics between years 2010 and 2017. The monthly-mean temperature near the mesopause in Fig. 3a demonstrates quasi-sinusoidal changes in accordance with seasonal changes shown in Fig. 2a. The thin line in Fig. 3a shows the linear regression with parameters presented in the first line of Table 1. The slope of the regression line in Fig. 3a corresponds to the rate of temperature decrease near the mesopause about 20±10 K/decade. This is significantly higher than temperature trends in at altitudes of 80—100 km determined from satellite and other ground-based measurements [e. g., 4]. A reason for the differences could be possible long-term changes in the SATI characteristics.

Figures 3b—3d show interannual changes in the characteristics of mesoscale variations with periods of 1.7—5 h. These changes do not show such expressed quasi-sinusoidal behavior as the mean temperature in Fig. 3a. This is due to the more complex seasonal variations of IGW characteristics having two maxima and two minima in Figs. 2b—2d and their instability in different years. Thin lines in Figs. 3b—3d show linear regression of analyzed values, and parameters are presented in Table 1. The slopes of the regression lines in Figs. 3b—3d correspond to increasing intensity of mesoscale perturbations near the mesopause. Similar positive multi-year trends in IGW intensity were obtained in [10].

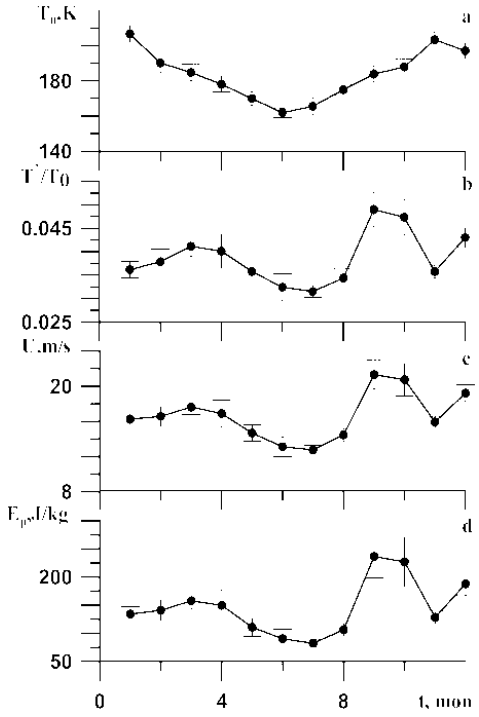

FIGURE 2. Seasonal variations of temperature (a), relative hourly-difference temperature variance (b), amplitude of horizontal velocity perturbation (c) and potential wave energy (d) averaged over years 2010—2017.

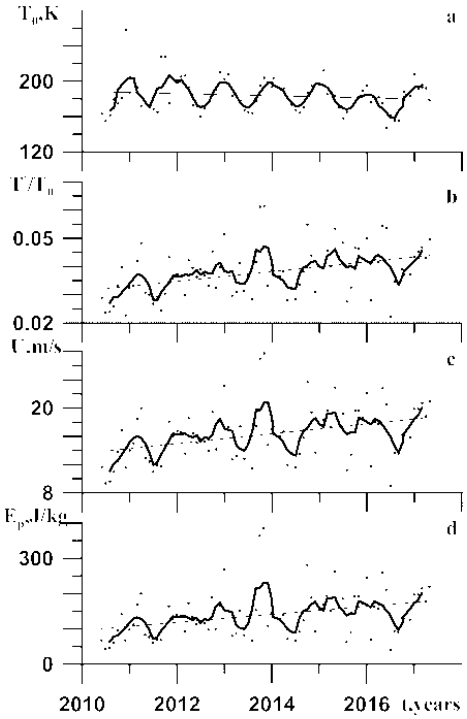

FIGURE 3. Interannual changes of the monthly-mean temperature (a), relative temperature variance (b), amplitude of horizontal velocity perturbations (c), potential wave energy (d). Thin lines shows linear fits.

TABLE 1. Coefficients of multy-year regression lines expressed in the form of $f=a_0+a_1(t-t_0)/10$ for characteristics shown in Fig. 3. Here t is time in years, $t_0 = 2010$.

Parameter	a_1	a_0
T_0	-20±10 Kdec^{-1}	200±100 K
$\lvert T`/T_0 \rvert$	0.017±0.004 dec^{-1}	0.06±0.01
U	6±2 ms^{-1}dec^{-1}	13±4 ms^{-1}
E_p	110±30 J kg^{-1}dec^{-1}	80±30 J kg^{-1}

Conclusion. The method of digital differential filters (2) is applied to the analysis of observations of the rotational temperature of hydroxyl nightglow at altitudes of 85—90 km with the SATI device in Alma-Aty, Kazakhstan in years

2010—2017. Analyzed are interannual and seasonal changes in the monthly-mean temperature and characteristics of temperature perturbations with mesoscale periods, which may be associated with IGW in the mesopause region. To obtain variations with time periods of 1.7—5 h a numerical filtering was used by calculating the differences between consecutive hourly-mean temperature values. The mean temperature near the mesopause has a maximum in winter and minimum in June. IGW intensities maximize in spring and autumn and minimize in winter and summer. The slopes of regression lines in Figs. 3b—3d correspond to multi-year increasing intensity of mesoscale perturbations near the mesopause.

This study was supported by the Russian Basic Research Foundation (#17-05-00458).

1. V. I. Perminov, A. I. Semenov, I. V. Medvedeva, and N. N. Pertsev, The temperature change in the area of the mesopause by observation of hydroxyl emission in the mid-latitudes, *Geomagn. Aeron.*, 2014, 54(2), pp. 230—239.

2. I. V. Medvedeva, A. B. Beletskii, V. I. Perminov et al., Variations in atmospheric temperature at heights of the mesopause and lower thermosphere during periods of stratospheric warming, according to ground and satellite measurements in different longitude sectors, *Sovremennyye problemy distantsionnogo zondirovaniya Zemli iz kosmosa*, 2011, 8(4), pp. 127—135 (in Russian).

3. A. M. Ammosova and P. P. Ammosov, Seasonal variations of temperature and emission intensities of mesopause on variation of solar activity, *Proceeding of SPIE, Eighteenth International Symposium on: Atmospheric and Ocean Optics/Atmospheric Physics*, 2012, 8696, 86960S, doi: 10.1117/12.2008792.

4. J. Lastovichka, A review of recent progress in trends in the upper atmosphere, *J. Atmos. Sol.-Terr. Phys*., 2017, 163, pp. 2—13.

5. N. M. Gavrilov, C. Jacobi, and N. Kurshcner, Drifts and their short-period perturbations in the lower ionosphere observed at Collm during 1983 — 1999, *Phys. Chem. Earth*, *Part C: Sol.-Terr. Planet. Sci.*, 2002, 26, pp. 459—464.

6. M. J. Lopez-Gonzalez, E. Rodrıguez, R. H. Wiens et al., Seasonal variations of O2 atmospheric and OH(6–2) airglow and temperature at mid-latitudes from SATI observations, *J. Atmos. Sol.-Terr. Phys*., 2007, 69, pp. 2379—2390.

7. R. H. Wiens, A. Moise, S. Brown et al., SATI: A spectral airglow temperature imager, *Adv. Space Res.*, 1997, 19, pp. 677—680.

8. E. E. Gossard and W. H. Hook, *Waves in atmosphere*, 1978, M.: Mir, 530 p.

9. N. M. Gavrilov, D. M. Riggin, and D. C. Fritts, Medium-frequency radar studies of gravity-wave seasonal variations over Hawaii (22°N, 160°W), *J. Geophys. Res*., 2003, 108(D20), 4655, doi:10.1029/2002JD003131.

10. N. M. Gavrilov, S. Fukao, T. Nakamura et al., Comparative study of interannual changes of the mean winds and gravity wave activity in the middle atmosphere over Japan, Central Europe and Canada, *J. Atmos. Sol.-Terr. Phys*., 2002, 64, pp. 1003—1010.

Propagation of Stationary Planetary Waves to the Thermosphere at Different Levels of Solar Activity

Andrey V. Koval[1], Nikolai M. Gavrilov[1], Alexander I. Pogoreltsev[1,2], and Nikita O. Shevchuk[1]

[1]Saint-Petersburg State University, Department of atmospheric physics, 198504, Saint-Petersburg, Russia
[2]Russian State Hydrometeorological University, Department of meteorological forecasts, Saint-Petersburg, Russia

Introduction. Large-scale wave disturbances in the atmosphere contribute to the energy transfer between different atmospheric layers and play significant role in the formation of the general circulation of the middle and upper atmosphere [1]. According to Haynes et al. [2], wave disturbances in the upper mesosphere and thermosphere are the most prominent driving force affecting the extratropical circulation. Due to the rapid development of computer technology and the improvement of numerical models of the atmospheric general circulation, interest in a more accurate study of the dynamical and thermal effects produced by wave motions, in particular, by planetary waves (PW) at different atmospheric layers is constantly increasing.

The incoming solar radiation and heating depend on the solar activity (SA), which undergoes cyclic changes with a period of about ~ 11 years [3]. Changes in the SA can affect the temperature and circulation, changing the conditions for the propagation and reflection of PW in the upper atmosphere [4, 5]. In order to investigate the effect of SA changes on the global circulation and characteristics of SPW, the numerical experiments with MUAM model [6, 7] were performed. The MUAM solves the standard set of hydrostatic equations in spherical coordinates, the horizontal grid has 36 nodes in latitude and 64 nodes in longitude. The vertical grid has 56 levels covering the heights from the Earth's surface to of about 300 km.

At the lower boundary, the amplitudes of the SPW are set in the model according to geopotential height distributions in the lower atmosphere taken from the JRA-55 (Japanese 55-year Reanalysis) database [8] for January averaged over the years 2005—2014. The radiative block of the MUAM takes into account the dependence of solar radiation on the SA. The main indicator of SA is the solar radio flux at the wavelength of 10.7 cm (F10.7). The F10.7 flux changes during the 11-year solar activity cycle. Our analysis of F10.7 observations during the last six solar cycles (Royal Observatory of Belgium, 2013) leads to values of F10.7 = 70, 130, 220 sfu (1 sfu = 10—22 W/(m2Hz)), which are taken here to characterize the low, medium and high SA levels, respectively. The main purpose of this study is to consider effects of SA changes occurring in the thermosphere only (see above). Therefore, different F10.7 values in the radiation and thermospheric blocks of the MUAM were set only at altitudes above 100 km.

To take into account the effects of ionospheric charged particles on the neutral gas motion, ionospheric conductivities with their latitudinal, longitudinal and temporal variability [9] are taken into account in the MUAM.

Figure 1a, 1b and 1c show, respectively, the altitude-latitudinal distributions of the zonal-mean wind, temperature and meridional temperature gradient averaged over January-February and 12 model runs for high and low SA along with differences between them. At the altitudes higher than 160—180 km, the zonal wind is significantly stronger (up to 50%) at a high SA. Between 140 and 180 km in the Southern Hemisphere the zonal wind is stronger under the high SA (see positive wind differences in the right panel of Fig. 1a), which is connected with corresponding positive differences of the meridional temperature gradient in the right panel of Fig. 1c. At altitudes below 100 km, there are minor differences in zonal wind in the right panel of Fig. 1a. This shows that modifications of thermospheric parameters caused by SA change at altitudes above 100 km can influence the global circulation at the middle atmosphere heights.

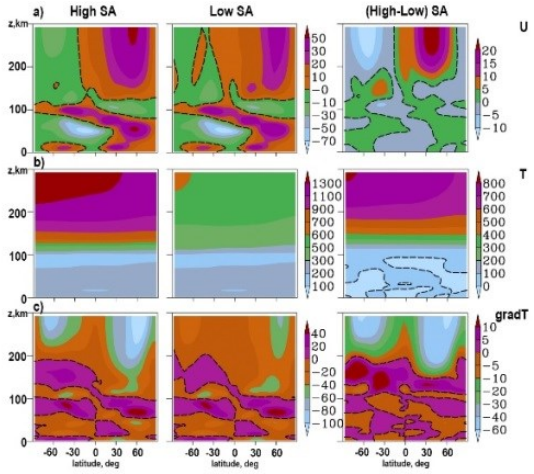

FIGURE 1. High-latitude distributions of averaged over January-February and 12 model runs the zonal-mean zonal wind in m/s (a), temperature in K (b) and meridional temperature gradient in K/deg (c) for the high (left) and low (center) SA along with and differences between the corresponding values (right). Dashed contours correspond to zero values.

Altitude-latitude distributions of the amplitudes of SPW1-SPW4, having zonal wavenumbers m = 1—4, their refractivity index and EP-fluxes are shown in Figs. 2a — 4a, respectively. The amplitudes are calculated using the longitude-time Fourier transform with the least squares fitting of the geopotential heights averaged over January-February and two 12-member ensembles. Left and right panels of figure 3 reflect distributions of mean-zonal quasi-geostrophic complex refractivity index (RI) sqared and vertical component of the Eliassen-Palm flux (EP-flux) vector,

respectively. An upward direction of EP-flux vector relates to the northward wave heat flux, while downward EP-flux relates to the southward wave heat flux. The divergence of the EP-flux shows the net drag of the zonal-mean flow by PWs.

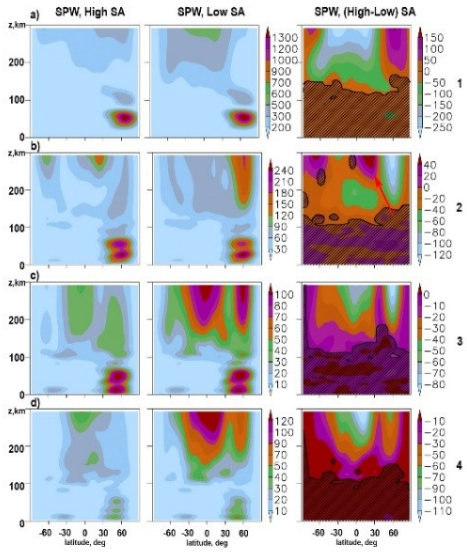

FIGURE 2. Amplitudes of the geopotential height variations (in g.p.m.) caused by SPW1-SPW4 (a—d, respectively) under the high SA(left), low (center) SA, and their differences (right) for January-February, averaged over 12-members ensembles. Dashed contours correspond to zero values.

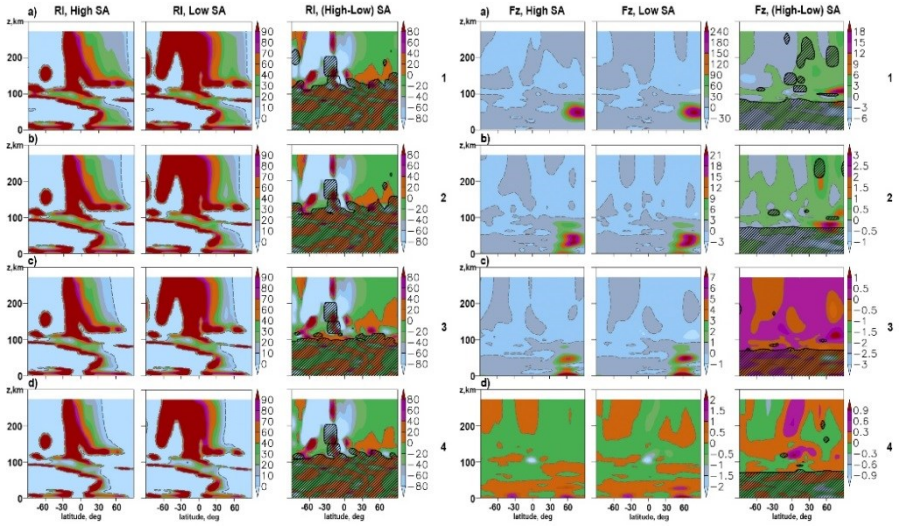

FIGURE 3. The same as Fig. 2, but for the SPW refractivity index squared (left panel) and for the vertical component of the EP-flux vector in 10^{-2} m^3/s^2 (right panel).

Conclusion. Using a thermospheric version of the mechanistic MUAM model, the ensemble of 12 pairs of simulations of general circulation and amplitudes of the SPW with the zonal wavenumbers m = 1—4 were performed at high and low SA levels for January-February at altitudes from the Earth's surface to 300 km. The SA changes are taken into account in calculations of solar heating and ionospheric conductivity at thermospheric heights above 100 km only. The influence of thermospheric SA effects on SPW characteristics in the atmosphere is studied.

Numerical experiments have shown that changes in the thermal and dynamical regimes in the thermosphere with a changing SA can significantly affect the SPW propagation and reflection in the atmosphere. At altitudes above 140 km, SPW amplitudes are generally larger under the high SA than those under the low SA. This can be explained by significant SA influences on meridional temperature gradients lead to the changes in the vertical profiles of the zonal wind, and the SPW propagation conditions. In the thermosphere, the relative differences in SPW1 amplitudes between high and low SA can be up to 30%. For SPW2, the differences in SPW2 amplitudes can reach 50%, and those for the SPW3 and SPW4 could be more than 50%. Values of the refractive index squared in the thermosphere is generally smaller and respective SPW waveguides are narrower at high SA. At altitudes above 70—80 km, SPWs can propagate along waveguides not only in the Northern, but also in the Southern Hemisphere, where the SPW amplitudes in the thermosphere are larger under the low SA level.

The SA effects at altitudes above 100 km can produce statistically significant changes in the mean zonal wind up to 3 m/s in the mid-latitude Northern Hemisphere at altitudes 30—100 km. They can be associated with corresponding differences in SPW amplitudes, refractive index and EP-fluxes. This give evidences that changes in thermospheric characteristics caused by changing SA can make differences in SPW propagation and reflection conditions, and, thus, influence the circulation and wave characteristics in the middle atmosphere. However, the statistical confidence of differences in SPW characteristics between the high and low SA is smaller than 95 % at altitudes below 100 km. More statistically reliable simulations are required, which could involve not only thermospheric influence, but also effects of changes in solar irradiance and cosmic rays intensity on the thermal regime and dynamics of the middle atmosphere.

The work was supported by the Grant Council of the President of the Russian Federation (grant MK-1424.2017.5).

1. J. R. Holton, *The dynamic meteorology of the stratosphere and mesosphere*, Meteorological monograph, 1975, 15(37), 218 p.

2. P. H. Haynes, M. E. McIntyre, T. G. Shepherd et al., On the “downward control” of extratropical diabatic circulations by eddy-induced mean zonal forces, *J. Atmos. Sci.*, 1991, 48(4), pp. 651−678.

3. D. H. Hathaway, The Solar Cycle, *Living Rev. Solar Phys.*, 2010, 7(1), [Online Article]: http://www.livingreviews.org/lrsp-2010-1

4. M. A. Geller, J. C. Alpert, Planetary wave coupling between the troposphere and the middle atmosphere as a possible Sun-weather mechanism, *J. Atmos. Sci.*, 1980, 37, pp. 1197—1215.

5. N. F. Arnold and T. R. Robinson, Solar cycle changes to planetary wave propagation and their influence on the middle atmosphere circulation, *Ann. Geophysicae*, 1998, 16, pp. 69—76.

6. A. I. Pogoreltsev, Production of electromagnetic field disturbances due to the interaction between acoustic gravity waves and the ionospheric plasma, *J. Atmos. Terr. Phys.*, 1996, 58(10), pp. 1125−1141.

7. A. I. Pogoreltsev, Production of electromagnetic field disturbances due to the interaction between acoustic gravity waves and the ionospheric plasma, *J. Atmos. Terr. Phys.*, 1996, 58(10), pp. 1125−1141.

8. S. Kobayashi, Y. Ota, and H. Harada, The JRA-55 Reanalysis: General Specifications and Basic Characteristics, *J. Meteorol. Soc. Jpn*., 2015, 93, pp. 5−48, doi:10.2151/jmsj.2015-00.

9. N. O. Shevchuk and A. I. Pogoreltsev, Upper Atmosphere Conductivity Model and Conductivities Effects on Modeling of Atmospheric Tides, *Proc. Intern. Conf. "Atmosphere, ionosphere, safety" (AIS-2016)*, Kaliningrad, Russia, June 19−25, 2016, pp. 500—504.

Dependence of the Stimulated Electromagnetic Emission Behavior on Relative Location of the Ionosphere HF-pumped Volume and Groundbased Receiving Sites — on the Base of 2011 Experiments at HAARP

Vera P. Smolina, Savely M. Grach, Evgeny N. Sergeev, and Alexey V. Shindin

Radiophysics Faculty, Lobachesky University, Gagarin Avenue 23, Nizhny Novgorod, 603950, Russia

Introduction. In the experiments at the HAARP heating facility near Gakona, Alaska (62.4º N, 145.15ºW) for HF ionosphere pumping at a frequency f_0 near 4th electron cyclotron harmonic $4f_{ce}$ it was found an excitation of descending layers of additional ionization [1].This had been confirmed by three independent diagnostic methods: measurements of the Stimulated Electromagnetic Emission (SEE) from the HF-pumped volume of the ionosphere, registration of ionospherically reflected short diagnostic pulses, and observation of enhanced plasma line radar echoes by the radar MUIR located at HAARP. Particularly, the new SEE spectral feature, the dynamic Broad Upshifted Maximum (BUM_D) had been discovered. The BUM_D is believed to be generated in the "fresh" newly created plasma. In the same experiment we have obtained new data on properties of the "traditional" SEE spectral features, such as "ponderomotive" and "thermal" Narrow Continua (NC_p and NC_t), Downshifted Maximum (DM) and "stationary" Broad Upshifted Maximum (BUM_S), generated in the background ionospheric plasma, see [2] and

references there]. In this paper we present the results concerning mainly a dependence of these features behavior on a relative location of the HF-pumped volume of ionosphere and the receiving sites.

The paper is organized as follows. In the second section we briefly describe the experimental setup and known properties of the SEE spectral features. The third section contains newly obtained results on the temporal evolution of the SEE features.

Experimental setup. The experiment was run on 28 March, 2011 between 1500 and 1600 AST. The HF beam was pointed vertically (V) during the first 30 min and toward the magnetic zenith (MZ), i. e., along the geomagnetic field. Injections of O-mode pump waves were made at full pump power P_0= 1.8GW ERP (effective radiated power) and pump frequencies f_0, stepping by 30 kHz every 5 min. from 5730 to 5880 kHz. Each 5-min interval was comprised of three pumping periods followed by 30 s off. The first (1) and third (3) periods consisted of low-duty pulses of duration τ_p =20 ms and an interpulse period T_p =1 s (mode p), for a total of 30 and 180 s, respectively. The second (2) period consisted of τ_q = 160 ms pulses separated by 40-ms pauses (mode q, T_q= 0.2 s), for a total of 60 s. The short 100 μs diagnostic pulses were transmitted 20 ms prior each mode p pulse and in the middle of each mode q pause. Note the difference in average radiated power $P_{p,q}= P_0\ \tau_{p,q}/T_{p,q}$ between mode p (0.036 GW ERP) and q (1.44 GW ERP). During the experiment, the critical frequency f_{OF2} during the 30-s off periods varied in the limits $f_{OF2} \approx$ 6.2—6.5 MHz, the pump nominal reflection altitude was ≈210—220 km. The observational sites were located along the meridian to the south of the HAARP facility at about 11 km (A), 83 km (B), and 113 km (C). Site A (B) was nearly under the heated volume during injections at vertical (MZ). Some details of the receiving systems one can find in [1]. In the present paper we use only data obtained at the sites A and B.

A sample of the SEE spectrograms for the pump frequency f_0=5820 kHz obtained during experiment at the receiving sites A (right) and B (left) are presented in the Fig. 1 for 5-min intervals on pumping in vertical (V) and magnetic zenith (MZ) directions. Figure 2 exhibits samples of the SEE spectra for different f_0 registered at different time after start of 5-min pumping interval.

SEE has been being studied extensively since its discovery in 1982. The SEE features regularly present in the spectrum in the frequency range near $4f_{ce}$-include: the narrow continuum (NC) in the range of negative frequency shifts from the PW frequency, $\Delta f_{NC} = f_{SEE} - f_0 \approx$ (– 40) – 0 kHz (at the maximum powers of the HAARP facility, Δf_{NC} can reach (– 80) kHz); the downshifted maximum (DM) with a sharp peak at frequency shifts $\Delta f_{DM} \approx$ (– 9) — (– 12) kHz and its satellites 2DM at double frequency shifts, and the upshifted maximum (UM) with $\Delta f_{UM} \approx$ (– 7) — (– 10) kHz almost symmetric to DM with respect to f_0; the broad upshifted maximum (BUM_S) with $\Delta f \approx$ (– 12) — (–120) kHz for $f_0 > 4f_{ce}$. The BUM peak is known to be at $\Delta f_{BUM} \approx f_0 - 4f_{ce} + \delta f$ ($\delta f \approx$ 10 — 15 kHz) in the SEE spectrum. These features are marked in the Figs. 1, 2.

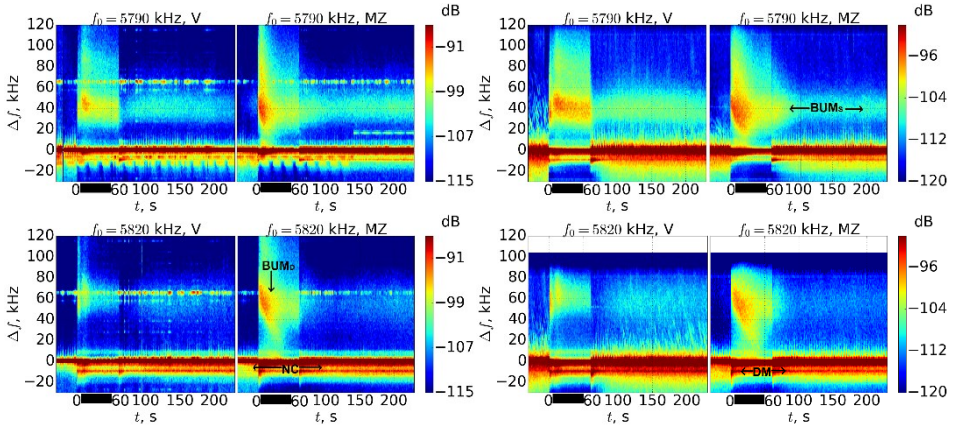

FIGURE 1. SEE spectrograms obtained for f_0=5790 and 5820 kHz at A (right) and B (left) receiving sites for pumping in V and MZ directions. $\Delta f = f_{SEE} - f_0$.

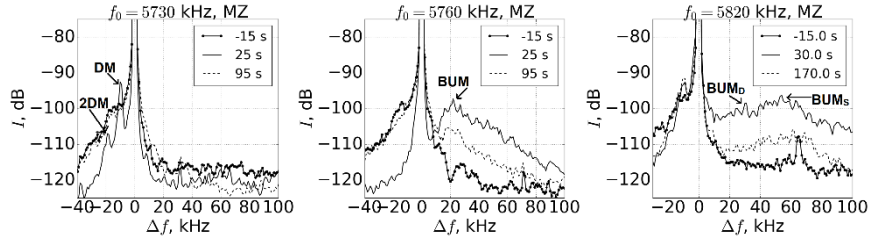

FIGURE 2. Samples of the SEE spectra for f_0=5730 kHz, 5760 kHz and 5820 kHz registered at different time after start of 5-min pumping interval. Time of spectra registration after 5-min pumping interval for 18 ms time window and 250 samples for FFT are shown in the panels. Individual spectra are shifted by 5 dB for clarity. SEE spectral features NC, DM, BUM_D and BUM_S are marked.

At the initial stage of pumping (1—20 ms) the SEE spectrum contains only the NC component (NC_p).This is well seen in the Fig. 1 for $-30<t<0$ s (pulse mode p, t=0 corresponds to the pump transition to the mode q) and in the Fig. 2 for the spectra marked as "–15 s". The NC_p is associated with the development of Ponderomotive Parametric Instability near the O-polarized pump wave reflection altitude, where $f_0 = f_{pe}$ ($f_{pe} = (e^2 N_e/\pi m_e)^{1/2}$ is the plasma frequency) and generation of Langmuir waves propagating along the geomagnetic field [2].

Quasicontinuous (q-mode) pumping produces so called "upper hybrid (UH) related" SEE features, viz. the DM, its satellites 2DM and UM and BUM_S. These features are related to the thermal parametric instability (TPI) developing during 0.5—5 s near the UH resonance altitude of the pump wave where $f_0 = (f_{pe}^2 + f_{ce}^2)^{1/2}$, the excitation of magnetic field aligned small-scale irregularities of plasma density (striations) and UH waves, and anomalous absorption (AA) of the electromagnetic waves (pump wave and SEE) due to conversion to the UH waves on striations. The

reverse process (conversion of the UH waves to electromagnetic ones) provides the SEE generation. Simultaneously, NC_p intensity decrease and become inapparent against the background of the DM due to AA. The UH-related "thermal" narrowband component, NC_t predominates at the shifts $\Delta f_{NC} = (-7) - 0$ kHz.

In addition to traditional SEE features, in the same experiment [1], the dynamic BUM_D with a peak approaching to the pump wave frequency in time during quasicontinuous pumping in the MZ direction was revealed (see Fig. 1, 2).

After transition from q-mode to p-mode pumping at t=60 s (from period 2 to period 3), the average pump power drops by 40 times. This leads to quick (1—2 s) disappearance of artificial ionization layers, and ionosphere comes back to the background state. The decay of striations as well the total decay of the UH-related SEE features and recovery of the NC_p takes much longer time. Moreover, the *p*-mode pumping can essentially prolong the striation lifetime.

Experimental results. In the paper [1] we focused on the SEE dynamics only during period 2 (mode *q*). In contrary, in the present paper we study all three periods and focus on properties of traditional SEE components and their dependence on the direction on pump wave radiation (vertically or to MZ) and position of the receiving sites. Figures 1 and 2 exhibit few samples of the SEE spectrograms and individual SEE spectra during the experiment. Temporal behavior of the NC at Δf_{NC} = (– 5) — (– 7) kHz and DM at Δf_{DM} = (– 9) — (– 10) kHz for both receiving sites, different f_0 for both V and MZ pumping during corresponding 5-min intervals are presented in Figs 3 and 4, respectively. An analysis of the Figs 1—4 allows making some conclusions pump-induced turbulence in the ionosphere. Unfortunately, it's impossible to present (spectrograms and SEE temporal behavior at individual Δf) for all experimental sessions due to insuffisient room of the paper.

Recall, that all UH-related SEE features strongly depend on the mismatch $f_0 - 4f_{ce}$ and are suppressed when $f_{SEE}=f_0+ \Delta f \approx 4f_{ce}$. In the experiment presented the BUM was seen at $f_0 \geq 5760$ kHz, so we conclude that $5730 < 4f_{ce} < 5760$ kHz in the interaction region. Furthermore, the absence of the DM for f_0 =5760 kHz (Fig. 2, f_0 =5760 kHz) indicates that the DM frequency matches fourth gyroharmonic at the UH altitude, i. e. $f_{DM} \approx 4f_{ce} \approx 5750$ kHz.

The results obtained can be summarized as follows.

During the period 1 the NC_P is the only feature in the SEE spectra (Figs. 1,3,4, t<30 s, Fig. 2 spectra marked '–15 s'). The NC_p intensity is essentially (by ~7 dB)) larger for $f_0<4f_{ce}$ (f_0=5730 kHz) then for $f_0>4f_{ce}$. For $f_0>4f_{ce}$ it practically does not depend on f_0, except from last 5—10 s for f_0=5820, 5850 and 5880 kHz. During this interval the UH-related SEE features begin to develop because average radiated power exceeds the threshold of the UH-turbulence (striations and UH-waves), and DM and NC_t (but not BUM!) SEE feature. In period 2 (*q*-mode) for $f_0 \leq 4f_{ce}$ (5730 and 5760 kHz) SEE essentially drops for both directions of pumping and both receiving sites, and recovers after transition back to *p*-mode (period 3). Note also that at both sites NC intensity during *p*-mode is larger for V pumping then for MZ, but is approximately the same in *q*-mode. For $f_0>4f_{ce}$ NC exhibits an

overshoot effects (initial growth and following decrease) at the transition from *p*- to *q*- and from *q*- to *p*-modes. In the period 3 (*p*-mode) after the overshoot the NC intensity in noticeably larger than in the period 1 (f_0 in range 5790—5880 kHz).

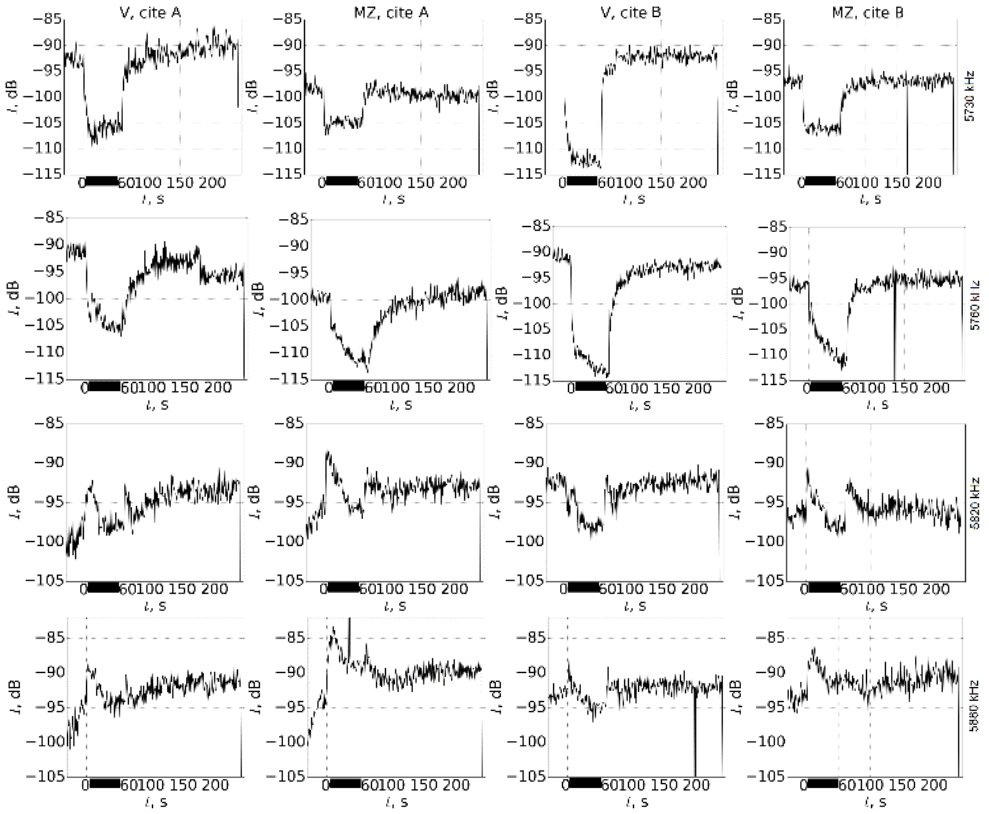

FIGURE 3. Temporal evolution of the NC SEE component obtained at the cites A (left) and B (right) for vertical (V) and magnetic zenith (MZ) pumping at different pump frequencies.

The DM feature appears in the SEE spectra during *q*-mode for all f_0 except for $f_0 \approx 4f_{ce}$ (Figs. 1, 2) and "survives" in the period 3 (p-mode) till 30 s off interval for $f_0 > 4f_{ce}$ (see Fig. 2 for f_0=5820 kHz and Fig. 4). The DM intensity exhibits overshoots similar to ones for NC. It noticeably increases with growth of f_0, stronger during q-mode pumping in MZ direction. For $f_0 \leq 4f_{ce}$ the DM is not shown up in the SEE on the enhanced NC background Difference in DM behavior for V and MZ pumping for f_0=5730 kHz (upper row of Fig. 4 (the suppression for V and growth for MZ) is related, most probably, to larger $f_0 - 4f_{ce}$ for MZ pumping.

Notice finally that temporal behavior of the NC, DM and BUM features is similar to one at the "Sura" facility with lower power (100—150 MW). However during period 3 these features achieve minimum of the intensity after the overshoot

and begin to grow again (Figs. 1, 3, 4). The BUM intensity in this time is noticeably less than during *q*-mode, and its spectral shape is different. Such an effect can be attributed, most probably, to excitation of "additional" portion of UH turbulence in "preconditioned" ionosphere. The intensity minimum of the SEE during the period 3 appears faster at vertical than at MZ pumping.

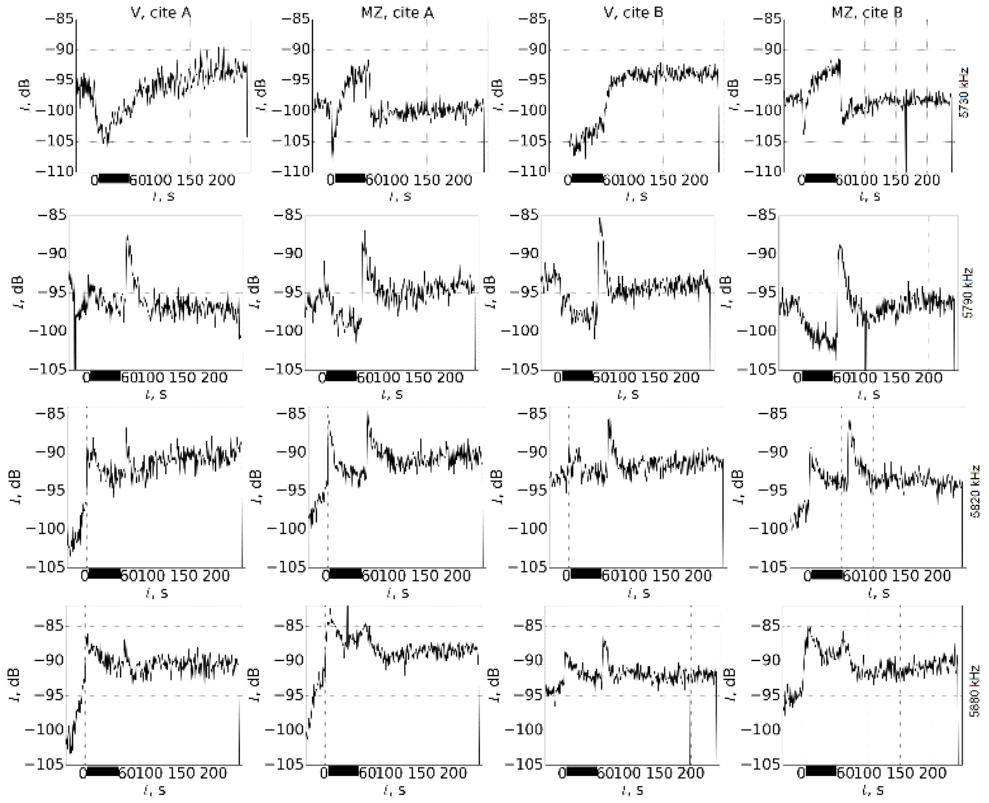

FIGURE 4. Temporal evolution of the DM SEE component obtained at the cites A (left) and B (right) for vertical (V) and magnetic zenith (MZ) pumping at different pump frequencies.

The work was supported by Russian Science Foundation, grant 14-12-00706.

1. E. Sergeev, S. Grach, and A. Shindin, Artificial Ionospheric Layers during Pump Frequency Stepping Near the 4th Gyroharmonic at HAARP, *Phys. Rev. Lett.*, 2013, 110 (6), 065002, doi: 10.1103/PhysRevLett.110.065002.

2. S. M. Grach, E. N. Sergeev, E. V. Mishin, and A. V. Shindin, Dynamic properties of ionospheric plasma turbulence driven by high-power high-frequency radiowaves, *Physics — Uspekhi*, 2016, 59(11), pp. 1091—1128, doi:10.3367/UFNe.2016.07.037868.

Comparative Analysis of the Ray Path and Amplitude Characteristics of the Normal Modes of HF Waves Propagating in the Ionosphere

Kristina V. Tatarinova, Veniamin E. Zakharov

Immanuel Kant Baltic Federal University, 236041 Kaliningrad, Russia.

The numerical experiments are performed to estimate how much the non-uniform structure of HF waves propagating in the ionosphere is evolved. It is also estimated the behavior of the wave amplitude and phase along the ray paths. The radio propagation environment is supposed to be non-uniform and anisotropic. The propagation of extraordinary HF waves is investigated in dependence on geophysical conditions.

Introduction. The theoretical basis of the research is the method of geometric optics of inhomogeneous media [1]. A review of the results of modeling the propagation of short radio waves in the ionosphere was made in [2]. As the main method for modeling the propagation of radio waves in the ionospheric plasma, the extended bi-characteristic system described in [3] is presented. The extended system makes it possible in calculating each ray trajectory, to calculate the Jacobian of the transformation from the ray coordinates to the geographic coordinates of the ray. The equations of bi-characteristics for the unknown derivatives are obtained by differentiating the initial ray equations from the geographic coordinates of the ray.

Features of the propagation of the ordinary and extraordinary mode of short waves in the presence of local in homogeneities in the ionosphere were studied in [4]. Diagnostics of the heterogeneous structure of the ionosphere according to the satellite radio sounding of the ionosphere was carried out in [5]. In [6] the formation of ray trajectories and absorption of short waves in the ionosphere during magnetic storms was investigated. In [2] the results of modeling the factor of attenuation of the amplitude of short waves along ray trajectories by the method of bi-characteristics are presented.

The application of the bicharacteristic method assumes that in addition to the attenuation factor due to the ray divergence factor, we can additionally find the attenuation factors due to the action of other factors. For instance, in [7] it was shown that the calculation of the ray trajectories makes it possible to calculate the phase, take into an account of the absorption along the trajectories and the rotation of the polarization vector.

The purpose of this paper is to construct a numerical model for the propagation of short waves in the ionosphere, suitable for describing not only the beam trajectories and absorption, but also the amplitude and polarization's characteristics of the signals. The application of the developed model is realized by means of numerical calculations of the variation of the parameters of the complex wave amplitude along the chosen hypothetical radio paths.

1. Description of the radio-wave distribution model. The ionosphere is a three-dimensional inhomogeneous and anisotropic medium. The anisotropy of the ionosphere plasma is due to the geomagnetic field. A numerical model of the ray trajectories of normal modes of short waves in the ionosphere is used for calculations [8]. The calculation of each ray trajectory reduces to solving six characteristic equations for coordinates and momenta. Characteristic equations are integrated numerically by the Runge-Kutta method in a spherical geomagnetic coordinate system. The refractive indices of normal modes in a three-dimensionally inhomogeneous anisotropic ionosphere, at altitudes from 60 to 1000 km, are calculated using the cold-plasma permittivity tensor [9]. The experimental models of the neutral atmosphere MSIS86 [10] and the ionosphere IRI2012 [11] were used to determine the parameters of the neutral atmosphere gas and the ionosphere plasma. The geomagnetic field is described in the dipole approximation.

The development of the short-wave propagation model in the ionosphere [8] is carried out by applying the transfer equation of the complex wave amplitude vector [1]. The electric E and magnetic H field strengths of the distinguished normal wave are expressed as

$$E = \Phi f, \qquad H = \sqrt{\frac{\varepsilon_0}{\mu_0}}\, p \times E,$$

where Φ and f are the complex amplitude and polarization vector of the wave field, p — is the momentum, $\varepsilon_0$and μ_0 are the permittivity and magnetic permeability of the vacuum, respectively. Using the normalization condition ff*=1, where the sign "*" means the operation of complex conjugation, we find that the components of the polarization vector f at each observation point in the ionosphere satisfy the system of homogeneous equations

$$(p^2\delta_{im} - p_i p_m - \varepsilon_{im}) f_m = 0, \quad i, m = 1,2,3,$$

where the summation is implied by the twice-occurring index m, are the components of the tensor of the complex relative permittivity of the ionosphere plasma, and δ_{im} is the Kronecker symbol.

Let us write the equation of energy transfer in a wave taking into an account of the absorption in the medium:

$$div(\sigma|\Phi|^2) - (1/2)i\omega\, \varepsilon_0 \varepsilon_{im}^a f_i f_m^* |\Phi|^2 = 0, \qquad (1)$$

where $\sigma = (1/4)\sqrt{\varepsilon_0/\mu_0}\,[f \times (p \times f^*) + f^* \times (P \times f)]$, and $\varepsilon_{\mathrm{im}}^{\mathrm{a}}$ are components of the non-Hermitian part of the tensor of the complex relative permittivity of the plasma of the ionosphere.

We express the complex amplitude of a quasiplane wave in the normalized form as

$$\Phi = |\Phi| exp(ju)$$

The phase change u = argΦ of the complex amplitude along each selected beam is described by equation

$$(\sigma\nabla)u = (1/4)\sqrt{(\varepsilon_0/\mu_0}\, I_m(f^* rot(pf) + p \times frotf^*). \quad (2)$$

Integration of equation (2) should be taken into an account.

2. Numerical algorithm. Let the point source be located, for example, on the Earth's surface at a point with a geographical latitude φ and a longitude λ. The radiation direction of the reference ray is given by the elevation angle β and the azimuth γ. In the vicinity of the reference ray, we single out a beam of rays with a narrow angular solution (Δβ, Δγ) at the radiation point. In numerical simulation, the beam is approximated by a finite number of rays. At first stage, the ray trajectories of the extracted beam are calculated. The second stage calculates the field characteristics at the points of the difference grid of the reference ray with taking the data obtained for all rays of the extracted beam into an account. We introduce the attenuation factor

$$V_3 = 20\lg\left(|\Phi|/|\Phi_0|\right)$$

where $|\Phi_0|$ is the amplitude of the wave when the beam enters the ionosphere at altitude h = 60 km. Integrating equation (1) along the reference ray, we find

$$V_3 = V_1 + V_2 = -2{,}17j\omega\varepsilon_0 \int_{s_0}^{s} (1/|\sigma|)\, \varepsilon_{im}^{a} f_i f_m^* ds - 10\lg(|\sigma|S/|\sigma_0|S_0)\,,$$

where V_1 is the contribution to the attenuation factor due to the absorption of the wave in the ionosphere, V_2 is the contribution to the attenuation factor from the divergence of the rays in the extracted beam, s — is the length along the reference beam, S = S (s) is the cross section of the beam, and for the narrow beam

$$div\sigma \approx (1/S)\partial(S|\sigma|/\partial s)$$

Integrating equation (2) along the reference ray, we find

$$u = (1/4)\sqrt{\varepsilon_0/\mu_0} \int_{x_0}^{x} (1/|\sigma|) I_m(f^* rot(p \times f) + p \times frotf^*) ds\,,$$

where it is given $u(s_0) = 0$.

The ray tube is divided into cells by means of sections. Each section is a piecewise smooth surface composed of triangular elements. The current cross-section is calculated as the projection of the surface area vector from the triangular elements to the direction of the group velocity vector of the wave in the reference beam node. The numerical calculation of the values of u in the nodes of the difference grid at the reference ray is based on the application of finite-difference approximation of the Stokes formula to calculate $rot\,(p \times f)$ and $rot\, f^*$. For greater accuracy of the wave field representation, it is possible to increase the number of beams in a narrow beam.

3. Results of the calculations and conclusions. The calculations were made for solstice conditions at high solar activity (F10,7 =150). Day number of the year

is set N=172. The universal time is given as UT = 16,65 hour. The geographic coordinates of the transmitter on the Earth's surface are the latitude $\varphi = 15°$, and the longitude $\lambda = 290°$.

Figure 1 represents the integral attenuation factor of the wave amplitude (dB) along the reference ray. Coordinate grid: h is the height above the Earth's surface, and s is the length counted along the ray. The elevation angle $\beta = 30°$, and the azimuth $\gamma = 90°$ are set the direction of the reference ray at the location point of transmitter. The angular solution of the beam emitted by transmitter is chosen as $\Delta\beta = 2°$, and $\Delta\gamma = 2°$ in the vicinity of the reference ray.

The choice of the values of $\Delta\beta$ and of $\Delta\gamma$ is justified by numerical experiments. Calculations were carried out for an extraordinary wave at a frequency f = 10 MHz. Figure 1 shows the results of calculations.

Curve 2 (see Fig. 1a) has a local maximum in the region where the ray tube turns due to the ionospheric refraction. This maximum is related to the local minimum of the cross section of the tube. As the reference ray penetrates deeper into the ionosphere, the group velocity is reduced (see Fig. 1b). The change in the phase of the complex amplitude has a non-monotonic character. The maximum phase change in Fig. 1b is of the order of magnitude 10 degrees.

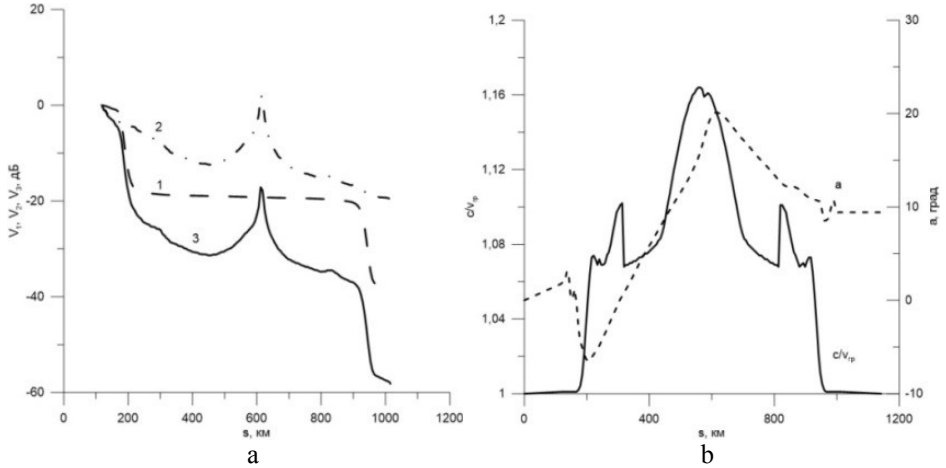

a b

FIGURE 1. (a) — the attenuation factor (V3, curve 3) and the contributions to it from absorption (V1, curve 1) and the divergence of the rays in the tube (V2, curve 2) for an extraordinary wave; (b) — dependence of the ratio c/vpp of the wave on s and the change in phase complex amplitude for an extraordinary wave (a = argΦ).

1. Yu. A. Kravtsov, Yu. I. Orlov, *Geometrical optics of inhomogeneous media*, Springer-Verlag, Berlin, 1990, 312 p

2. D. S. Lukin, E. A. Palkin, E. B. Ipatov et al., Deveopment of Mathematical Modeling of Radio Wave Propagation in the Earth's Ionosphere on the Basis of Wave Catastrophe Theory and Canonical Maslov's Operator, *Physical sciences and astronomy*, 2016, 1, pp. 40—50.

3. A. S. Kryukovsky, D. S. Lukin, and K. S. Kiryanova, Method of Extended Bicharacteristic in Propagation Ionospheric Plasma, *Communications technology and electronics*, 2012, 57(9), pp. 1039—1045.

4. A. S. Kryukovskii, D. S. Lukin, and D. V. Rastyagaev, Investigation of Peculiarities of Distribution of Short Radio Waves in the Inhomogeneous Anisotropic Ionosphere, *Electromagnetic waves and electronic systems*, 2009, 14(8), pp. 17—26.

5. A. T. Karpachev, G. A. Zhbankov, and V. A. Telegin, Region of Permanent Generation of Large-Scale Irregularities in the Daytime Winter Ionosphere of the Southern Hemishere, *Geomagn. Aeron.*, 2016, 56(1), pp. 69—76.

6. D. S. Kotova, M. V. Klimenko, V. V. Klimenko, and V. E. Zakharov, Numerical Simulation of the Influence of the May 2—3, 2010 Geomagnetic Storm on HF Radio-Wave Propagation in the Ionosphere, *Radiophysics and Quantum Electronics*, 2014, 57(7), pp. 467—477, doi: 10.1007/s11141-014-9529-2.

7. D. S. Lukin and E. A. Palkin, *Numerical canonical method in problems of diffraction and propagation of electromagnetic waves in inhomogeneous media*, MIPT, Moscow, 1982, 159 p. (in Russian)

8. V. E. Zakharov, A. A. Chernyak, Numerical model of radio paths of HF radio waves in the ionosphere, *Bulletin of the RGU. I. Kant, Physics and mathematics*, 2007, 3, pp. 36—40. (in Russian)

9. B. E. Brunelli and A. A. Namgaladze, *Physics of the ionosphere*, Nauka, Moscow, 1988, 528 p. (in Russian)

10. A. E. Hedin, Extension of the MSIS thermospheric model into the middle and lower atmosphere, *J. Geophys. Res.*, 1991, 96(A1), pp. 1159—1172.

11. D. Bilitza, D. Altadill, Y. Zhang et al., The International Reference Ionosphere 2012 — a model of international collaboration, *J. Space Weather and Space Clim.*, 2014, 4(A07), doi:10.1051/2014004.

ELEMENTARY PROCESSES IN THE UPPER ATMOSPHERE AND IONOSPHERE

Ab Initio Study of Singlet and Triplet Valence-Rydberg Electronic States of N_2 Molecule

Sergey O. Adamson[1,2], Veronika V. Kuverova[3], Georgy K. Ozerov[4], Gennady V. Golubkov[2], Yuri A. Dyakov[5,6], and Maxim G. Golubkov[2]

[1] Laboratory of Molecular Structure and Quantum Mechanics, Department of Chemistry, Lomonosov Moscow State University, Moscow, Russia
[2] Semenov Institute of Chemical Physics, Russian Academy of Sciences , Moscow, Russia
[3] Center of Chemical Physics of Atmosphere, Moscow, Russia
[4] Skolkovo Institute of Science and Technology, Moscow, Russia
[5] Genomics Research Center, Academia Sinica, Taipei, Taiwan
[6]Karpov Institute of Physical Chemistry, Moscow, Russia

Nitrogen molecule N_2 is a strongly bound diatomic system which is the main part of the upper atmosphere. Even several years ago the literature describing electronic excited states of N_2 was surprisingly brief except than studies of $^1\Sigma_u^+$ and $^1\Pi_u$ symmetry. Few experimental studies have probed the Rydberg series of triplet and gerade symmetry that underline the first ionization limit with some theoretical treatments. Lofthus and Krupenie [1] gave a comprehensive summary of the observed electronic spectra of N_2 considering the lowest 15 electronic states, later updated by Huber and Herzberg [2]. After that numerous experimental studies were carried out. Few of them investigated experimentally transitions involving $^1\Sigma_u^+$ and $^1\Pi_u$ states. More recently, Lewis *et al* [3] have measured the $^3\Sigma_u^+$ and $^3\Pi_u$ states. Last decades, many of theoretical calculations were concerned with modelling the Rydberg states. Spelsberg and Meyer [4] give a particularly detailed *ab initio* study of the interaction between Rydberg and valence states, albeit only for $^1\Sigma_u^+$ and $^1\Pi_u$ symmetries.

Recently, Guberman [5] presented potential energy curves for studies low-temperature dissociative recombination (DR) of slow electrons with N_2^+ ions in the ground vibrational state (v=0). The interactions of these states with bound Rydberg configurations of the system are very important for DR studies. It was shown by Guberman [5] that triplet $^3\Pi_u$ ones make the main contribution to DR cross

section. This result motivated Little and Tennyson [6] to perform very extensive calculations of potential energy curves for electronically excited states of molecular nitrogen using three different *ab initio* procedures. The most comprehensive one involves scattering calculations, performed at negative energy using the UK molecular *R*-matrix method. These calculations were carried out to characterize all the Rydberg states of N_2 with $n < 7$, as well as a lot of higher excitations including the states assigned to the $A^2\Pi_u$ (N_2^+) Rydberg series. The only problem was that the results of Guberman [5] and Little and Tennyson [6] differs from each other. Sometimes, the discrepancy between them reaches 0.5 eV in energy.

The present ab initio study of potential curves and non-adiabatic coupling functions of the N_2 molecule were carried out using the multi-reference configuration interaction method (cMRCI) [7]. The set of atomic orbitals (AO) was constructed by the addition of the s-f type diffuse functions (ζ_s = 0.33,0.1, 0.03,0.01; ζ_p = 0.5,0.15,0.045, 0.0125; ζ_d = 0.33,0.11.0.033; ζ_f = 0.66.0.24) to the atomic natural orbitals basis set created by Widmark et al. (ANO). The natural orbitals created by means of the multiconfigurational SCF calculations with the averaging on the ground states N_2 and N_2^+ were chosen as the set of molecular orbitals (MO). The model space for the cMRCI calculations was generated using the two steps routine. At the first, a zero-order Hamiltonian was constructed using the complete active space, spanned by MO's, correlated with 2s2p AO on the dissociation limit together with the $4\sigma_g^+$ $4\sigma_u^+$ Rydberg orbitals. Then, the configuration state functions with the weights >0.005 obtained by diagonalization of the zero-order Hamiltonian were included into the model space.

Equilibrium energies (E_e) and positions (R_e) are tabulated in Table 1 with a comparison to available experimental data and previous theoretical calculations. All energies are given relative to the equilibrium energy of the N_2^+ ground state. Table 1 also gives a comparison with Rydberg states of N_2. Due to the interaction with valence states some of the equilibrium positions of the Rydberg states are strongly perturbed. This contributes to the disparity with spectroscopic values if this coupling was not included when the original spectroscopic constants were fitted to the experimental data. Due to the top down approach of our calculation we have presented the energies as being relative to the ion ground state as this gives the best comparison with experimental data.

TABLE 1. Equilibrium binding energies E_e and equilibrium positions R_e for excited valence and Rydberg states of N_2 molecule. A comparison was made for the states for which experimental and other theoretical data are available.

State	This work		Experiment			Other theories		
	E_e, eV	R_e, Å	E_e, eV	R_e, Å	Refs.	E_e, eV	R_e, Å	Refs.
$X^2\Sigma_g^+$	0.000	1.125	0.000	1.116	[2]	0.000	1.125	[6]
$^3\Sigma_u^-(3d\pi_g)$	-0.239	1.178	-	-	-	-0.237	1.183	[6]
$^3\Delta_u(3d\pi_g)$	-0.269	1.178	-	-	-	-0.296	1.197	[6]

Continue of table 1

State	This work		Experiment			Other theories		
	E_e, eV	R_e, Å	E_e, eV	R_e, Å	Refs.	E_e, eV	R_e, Å	Refs.
$3\,^3\Sigma_g^-$	-0.662	1.455	-	-	-	-0.456	1.518	[6]
$4\,^3\Delta_g$	-0.980	1.844	-	-	-	-1.195 -1.277	1.692 1.736	[5] [6]
$2\,^1\Pi_g$	-0.992	1.952	-	-	-	-0.893	1.886	[6]
$3\,^3\Delta_g$	-0.994	1.848	-	-	-	-	-	-
$c_5'\,^1\Sigma_u^+$ $(5p\sigma_u)$	-1.060	1.124	-1.217	-	[8]	-1.241	1.136	[6]
$^3\Delta_u$ $(4f\delta_u)$	-1.089	1.123	-	-	-	-0.861	1.125	[6]
$2\,^3\Delta_g$	-1.103	2.762	-	-	-	-	-	-
$2\,^3\Sigma_g^+$	-1.123	1.829	-	-	-	-	-	-
$4\,^3\Pi_u$	-1.155	1.492	-	-	-	-	-	-
$x\,^1\Sigma_g^-$ $(3p\pi_u)$	-1.304	1.174	-1.526	1.173	[2]	-1.539	1.179	[6]
$^3\Sigma_g^-(3p\pi_u)$	-1.310	1.174	-	-	-	-1.349	1.181	[6]
$2\,^3\Sigma_g^-$	-1.322	1.943	-	-	-	-1.438 -1.375	1.729 1.821	[6] [9]
$y^1\Pi_g$ $(3p\sigma_u)$	-1.328	1.175	-1.418	1.177	[2]	-1.253	1.175	[6]
$k^1\Pi_g$ $(3d\pi_g)$	-1.330	1.128	-1.480	1.109	[2]	-1.465	1.128	[6]
$^3\Pi_g$ $(3d\pi_g)$	-1.342	1.120	-	-	-	-1.494	1.124	[6]
$z^1\Delta_g$ $(3p\pi_u)$	-1.342	1.174	-1.278	1.169	[2]	-1.331	1.155	[6]
$1^1\Delta_g$	-1.352	1.744	-	-	-	-1.504	1.732	[6]
$^3\Delta_g$ $(3p\pi_u)$	-1.364	1.176	-	-	-	-1.486	1.196	[6]
$3\,^3\Pi_u$	-1.369	1.359	-	-	-	-	-	-
$^3\Sigma_g^+(3p\pi_u)$	-1.402	1.176	-	-	-	-1.482	1.189	[6]
$2\,^1\Sigma_g^+$	-1.450	2.328	-	-	-	-0.959	1.700	[6]
$d_3\,^1\Sigma_g^+(3d\sigma_g)$	-1.466	1.121	-1.699	-	[10]	-1.633	1.125	[6]
$^3\Sigma_g^+(4s\sigma_g)$	-1.488	1.125	-	-	-	-1.680	1.129	[6]
$b'^1\Sigma_u^+$	-1.988	1.737	-2.634	1.444	[2]	-2.794 -2.780	1.499 1.463	[5] [6]
$o_3\,^1\Pi_u$ $(3s\sigma_g)$	-2.123	1.151	-2.464	1.178	[2]	-2.182	1.170	[6]
$H^3\Phi_u$	-2.123	1.485	-2.483	1.488	[2]	-2.534 -2.358 -2.210	1.506 1.512 1.499	[5] [6] [9]
$F^3\Pi_u$ $(3s\sigma_g)$	-2.184	1.183	-2.555	1.176	[3]	-2.254	1.168	[6]
$2\,^3\Pi_u$	-2.335	2.834	-	-	-	-	-	-

Continue of table 1

State	This work		Experiment			Other theories		
	E_e, eV	R_e, Å	E_e, eV	R_e, Å	Refs.	E_e, eV	R_e, Å	Refs.
$c_3{}^1\Pi_u$ ($3p\pi_u$)	-2.427	1.120	-2.637	1.116	[2]	-2.488	1.140	[6]
$G^3\Pi_u$ ($3p\pi_u$)	-2.431	1.124	-2.696	1.113	[3]	-2.660	1.127	[6]
$c_4'{}^1\Sigma_u^+$ ($4p\sigma_u$)	-2.460	1.125	-2.635	-	[8]	-2.628	1.127	[6]
$D^3\Sigma_u^+$ ($3p\pi_u$)	-2.515	1.124	-2.603	1.108	[2]	-2.724	1.124	[6]
$1^1\Gamma_g$	-2.571	1.727	-	-	-	-2.765 -2.821 -3.100	1.636 1.609 1.600	[6] [9] [11]
$b^1\Pi_u$	-2.769	1.330	-2.984	1.284	[2]	-3.158 -3.200	1.381 1.340	[5] [6]
$a''{}^1\Sigma_g^+$ ($3s\sigma_g$) inner	-3.109	1.122	-3.190	1.122	[2]	-3.165 -3.698	1.128 1.114	[6] [9]
$C'{}^3\Pi_u$	-3.187	1.522	-3.396	1.514	[2]	-3.698 -3.755 -3.286	1.535 1.534 1.527	[5] [6] [9]
$1^3\Sigma_g^-$	-3.240	1.704	-	-	-	-3.659 -3.467	1.631 1.619	[6] [9]
$E^3\Sigma_g^+$ ($3s\sigma_g$)	-3.303	1.123	-3.705	1.117	[2]	-3.575 -3.700	1.127 1.127	[6] [9]
$1^3\Sigma_g^+$	-3.450	2.818	-	-	-	-	-	-
$2^3\Sigma_u^+$	-3.524	2.883	-	-	-	-	-	-
$a''{}^1\Sigma_g^+$ outer	-4.056	1.549	-	-	-	-4.570 -4.553 -4.367	1.574 1.572 1.557	[5] [6] [9]
$C^3\Pi_u$	-4.173	1.159	-4.539	1.149	[2]	-4.583 -4.703 -4.401	1.160 1.162 1.154	[5] [6] [9]
$G^3\Delta_g$	-4.419	1.670	-4.692	1.611	[2]	-4.608 -4.876 -4.466	1.618 1.637 1.618	[5] [6] [9]
$w^1\Delta_u$	-6.468	1.266	-6.651	1.268	[2]	-7.763 -6.786 -6.470	1.280 1.282 1.295	[5] [6] [9]
$a^1\Pi_g$	-6.817	1.228	-7.000	1.220	[2]	-7.043 -7.088 -6.915	1.226 1.235 1.223	[5] [6] [9]
$a'{}^1\Sigma_u^-$	-6.915	1.273	-7.140	1.276	[2]	-7.274 -7.031	1.292 1.278	[6] [9]
$B'{}^3\Sigma_u^-$	-7.192	1.282	-7.373	1.278	[2]	-7.667 -7.349	1.292 1.283	[6] [9]

End of table 1

State	This work		Experiment			Other theories		
	E_e, eV	R_e, Å	E_e, eV	R_e, Å	Refs.	E_e, eV	R_e, Å	Refs.
$W^3\Delta_u$	-8.000	1.282	-8.175	1.300	[2]	-8.147 -8.499 -8.243	1.285 1.293 1.283	[5] [6] [9]
$B^3\Pi_g$	-8.001	1.222	-8.198	1.213	[2]	-8.242 -8.494 -8.106	1.218 1.227 1.220	[5] [6] [9]
$A^3\Sigma_u^+$	-9.222	1.291	-9.336	1.287	[2]	-9.460 -9.946 -9.392	1.291 1.310 1.292	[5] [6] [9]
$X^1\Sigma_g^+$	-15.432	1.104	-15.590	1.098	[2]	-15.997 -15.590	1.107 1.104	[6] [9]

Figures 1—4 show the diabatic potential energy surfaces of the Rydberg and valence states of the nitrogen molecule as a function of interatomic distance. Data are presented for even and odd singlet and triplet potential curves. The N_2^+ ion ground $X^2\Sigma_g^+$ state is shown with the lowest seven vibrational levels (v = 0—6). The energy is measured from the ground vibrational level of the ion. The data obtained can be used directly to calculate the partial and total DR cross sections and rate constants with the participation of electrons and nitrogen molecular ions.

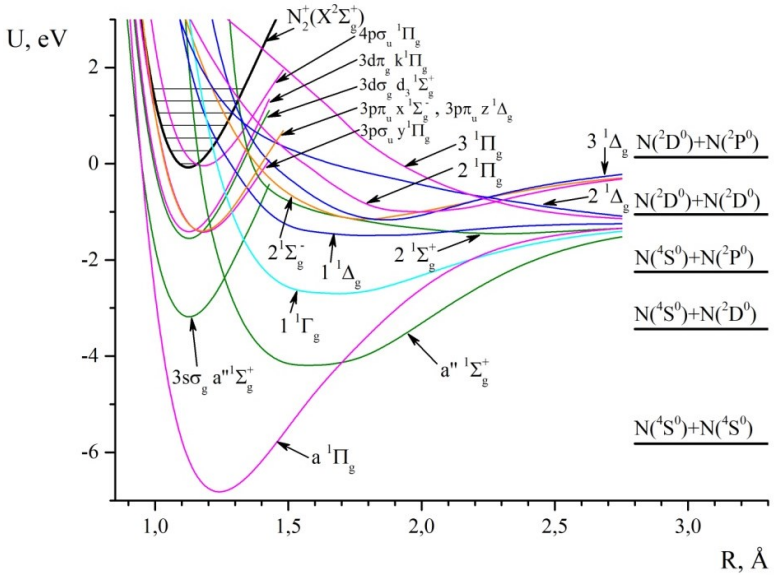

FIGURE 1. Diabatic potential energy curves of even Rydberg and valence singlet states of N_2 molecule. The N_2^+ ion ground $X^2\Sigma_g^+$ state is shown with the lowest seven vibrational levels (v = 0—6). The energy is measured from the ground vibrational state of the ion.

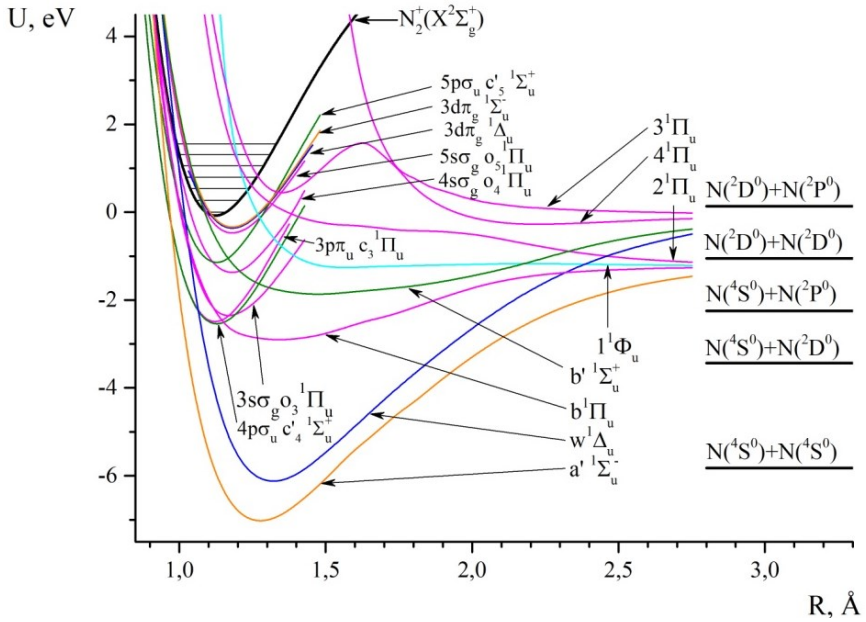

FIGURE 2. Diabatic potential energy curves of odd Rydberg and valence singlet states of N_2 molecule.

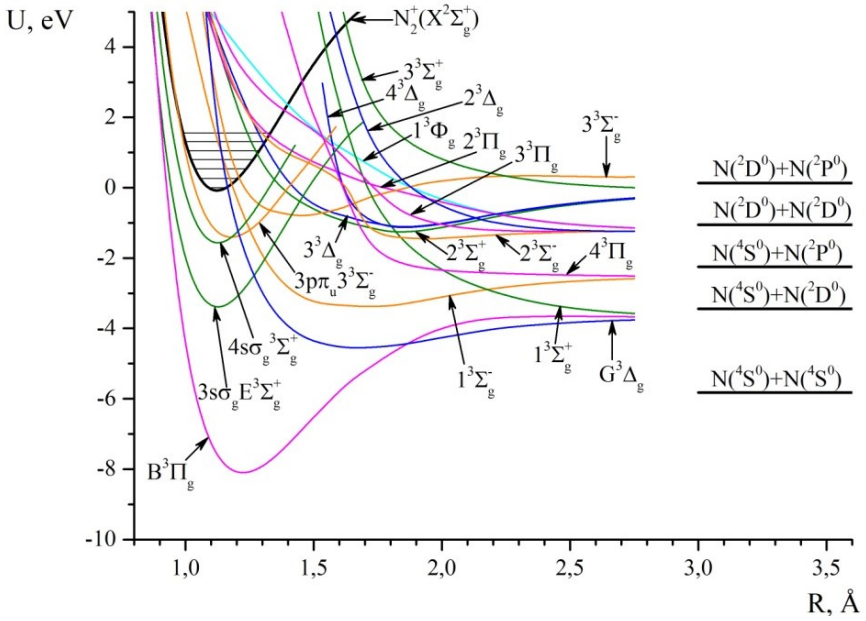

FIGURE 3. Diabatic potential energy curves of even Rydberg and valence triplet states of N_2 molecule.

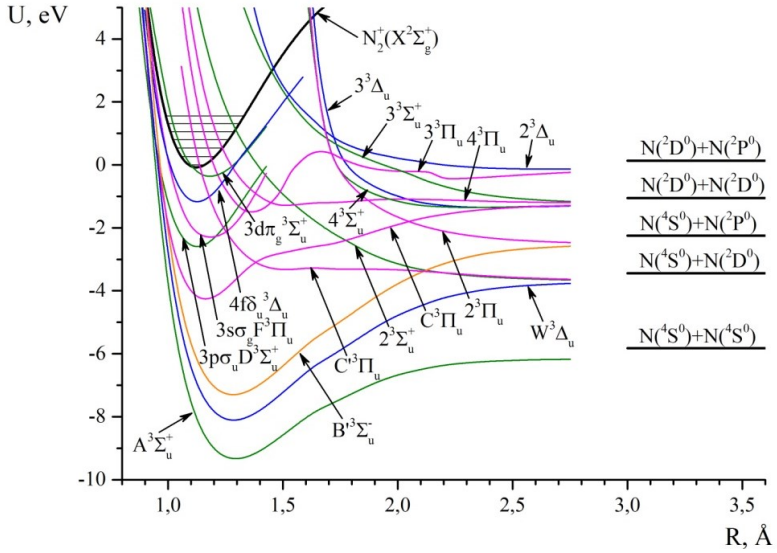

FIGURE 4. Diabatic potential energy curves of odd Rydberg and valence triplet states of N_2 molecule.

Acknowledgements. *This work was carried out in the framework of State Assignment of Russian Federal Agency of Scientific Organizations (project 0082-2018-0001, registration code AAAA-A17-117112240026-5).*

1. A. Lofthus, P. H. Krupenie, The spectrum of molecular nitrogen, *Journal of Physical and Chemical Reference Data*, 1977, 6, 1, pp. 113—307.

2. K. P. Huber and G. Herzberg, Constants of Diatomic Molecules, New York: Van Nostrand-Reinhold, 1979.

3. B. R. Lewis, A. N. Heays, S. T. Gibson et al., A coupled-channel model of the $^3\Pi_u$ states of N_2: Structure and interactions of the $3s\sigma_g$ F_3 $^3\Pi_u$ and $3p\pi_u$ G_3 $^3\Pi_u$ Rydberg states, *The Journal of Chemical Physics,* 2008, 129, 16, 164306, 11 p.

4. D. Spelsberg and W. Meyer, Dipole-allowed excited states of N_2: Potential energy curves, vibrational analysis, and absorption intensities, *The Journal of Chemical Physics*, 2001, 115, 14, pp. 6438—6449.

5. S. L. Guberman, Spectroscopy above the ionization threshold: Dissociative recombination of the ground vibrational level of N_2^+, *The Journal of Chemical Physics*, 2012, 137, 7, 074309, 16 p.

6. D. A. Little and J. Tennyson, An ab initio study of singlet and triplet Rydberg states of N_2, *Journal of Physics B*: *Atomic, Molecular and Optical Physics*, 2013, 46, 14, 145102, 14 p.

7. H. J. Werner, P. J. Knowles, G. Knizia et al., MOLPRO, version 2010.1, a package of *ab initio* programs, see http://www.molpro.net.

8. K. P. Huber and Ch. Jungen, High-resolution jet absorption study of nitrogen near 800 Å, *The Journal of Chemical Physics*, 1990, 92, 2, pp. 850—842.

9. M. Hochlaf, H. Ndome, D. Hammoutene, and M. Vervolet, Valence-Rydberg electronic states of N_2, *Journal of Physics B: Atomic, Molecular and Optical Physics*, 2010, 43, 24, 245101, 7 p.

10. D. Cossart and C. Cossart-Magos, New Rydberg-Rydberg transitions N_2. Identification of the $d_3\ ^1\Sigma_g^+$ state, *The Journal of Chemical Physics*, 2004, 121, 15, pp. 7148—7152.

11. H. H. Michels, Identification of Two Low-Lying Non-Rydberg States of the Nitrogen Molecule, *The Journal of Chemical Physics*, 1970, 53, 2, pp. 841—842.

Spin Dependent Processes in Three Spin Systems. Radical Triads and Quantum Dots

Aleksandr. S. Letuta, Vitaliy L. Berdinskiy

Department of Biophysics and Solid State Physics, Orenburg University, Pobedy av. 13, Orenburg, 460018, Russia

A new mechanism of spin evolution in three spin systems is proposed. Spin dependent recombination in radical triads and Pauli spin blockade in triple quantum dots have been shown to be able to induce spin evolution without physical (Zeeman, contact, and exchange) interactions. This evolution is accompanied by singlet-triplet conversion in radical pairs and triads in quantum dots. As a result of pairwise spin correlation changes these processes in radical triads and in others carriers of uncoupled electrons open new channels of recombination processes. In triple quantum dots this mechanism removes spin prohibitions on transfers of electrons.

An Effect of Orientational Isomerism of the Small Neutral Water Clusters on their Thermodynamic Functions and Concentrations in a Gas Phase

Ekaterina A. Shirokova[1], Stanislav K. Ignatov[1], and Alexey G. Razuvaev[2]

[1]Faculty of Chemistry, Lobachevsky State University of Nizhni Novgorod, 23 Gagarina prospect, 603950, Nizhny Novgorod, Russia
[2]Institute of Information Technology, Mathematics and Mechanics, Lobachevsky State University of Nizhni Novgorod, 23 Gagarina prospect, 603950, Nizhny Novgorod, Russia

Introduction. Water clusters are now widely studied both theoretically and experimentally. These objects are of great interest because they take part in such important processes in the atmosphere as energy distribution, hydrolysis and hydration reactions, and propagation of electromagnetic radiation. As a result, multi-molecular complexes of water, being contained everywhere in the Earth's atmosphere, play an important role in climate formation and change.

By now, a structure and thermodynamic functions of these clusters are found for water clusters $(H_2O)_n$ with $n = 2 \div 5$ only [1]. Theoretical estimations of the parameters of more complex water clusters and their comparison with experimental data are highly varied [2—4]. That makes theoretical modeling of chemical reactions in the atmosphere more difficult. This problem is even more complicated because there exist different types of oxygen "skeletons" for $(H_2O)_n$ water clusters, and each of these "skeletons" has many orientational isomers.

A standard way to find the water clusters concentration is to perform thermodynamic calculations of a structure with the lowest energy. However, this way seems to be not correct because (a) structural diversity of water clusters and (b) an effect of different isomers on thermodynamic parameters and concentrations are not taken into account here.

In this paper, an effect of orientational isomerism of the neutral water hexamers on their state functions and concentrations in a gas phase is studied.

Calculation details. The thermodynamic functions are calculated for 96 isomers $(H_2O)_6$ of *book* conformer, 27 isomers of *cage* conformer, and 10 isomers of *prism* conformer. The initial structures are selected using an original computer program generating orientational isomers for a given "skeleton" of oxygen atoms. Full optimization of geometry and calculation of oscillation frequencies and state functions have been performed for all 133 considered isomers using DFT (B3LYP/6-311++G(2d,2p)) and G4 methods. For each isomer, values $\Delta_r E^\circ_{298\,K}$, $\Delta_r (E + ZPE)^\circ_{298\,K}$, $\Delta_r U^\circ_{298\,K}$, $\Delta_r H^\circ_{298\,K}$, $\Delta_r G^\circ_{298\,K}$ of reaction of the water hexamer formation

$$6H_2O \rightarrow (H_2O)_6 \tag{1}$$

have been calculated.

The individual calculation results have been averaged using 2 weighting schemes.

1. The arithmetic mean:

$$\langle \Delta\varepsilon \rangle_{av} = \frac{1}{k} \sum_{i=1}^{k} \Delta\varepsilon_i \,, \tag{2}$$

where $\Delta\varepsilon_i$ is a change of one of the state functions, mentioned above, in reaction (1) for the *i*th isomer, and *k* is a number of the structures for which values $\Delta\varepsilon_i$ are averaged.

2. The average with the Boltzmann weight factors:

$$\langle \Delta\varepsilon \rangle_{td} = \frac{\sum_{i=1}^{k} \Delta\varepsilon_i \exp\left(-\frac{\Delta\varepsilon_i}{RT}\right)}{\sum_{i=1}^{k} \exp\left(-\frac{\Delta\varepsilon_i}{RT}\right)}, \tag{3}$$

where R is the gas constant, and T is temperature. Application of formula (3) allows us to take into account distribution of the structures over energy.

To perform the further calculations, the results obtained using DFT method are corrected. The corresponding correction term is calculated as a difference of values $\Delta_r H^\circ_{298\,\mathrm{K}}$, found using G4 and DFT methods, for the most energetically profitable structure.

An equilibrium constant of the reaction and concentration of clusters $(H_2O)_6$ are calculated from the found values $\Delta_r G^\circ_{298\,\mathrm{K}}$ of reaction (1).

In addition to quantum mechanical calculations, direct molecular dynamics simulations of the water clusters formation have been performed in *DL_POLY 4.03*. A cubic box (its edge equals 520 Å, the periodic boundary conditions are used) that contains 324 water molecules under pressure P = 24 mmHg is considered. SPC model of the water molecule is used for calculations. The first computation is done for NVE ensemble, and the second one is done for NVT ensemble (the Nosé–Hoover thermostat, T = 298.15 K). The integration time is 10 ns for the time step 0.1 ns (LeapFrog/Shake integrator). The number of iterations is therefore equal to 100 million. Analysis of the calculation results is done using the original program for search of collisions of the water molecules in the box on the basis of their trajectories data.

Results. Five types of oxygen "skeletons" have been obtained during optimization of geometry. Two of them are different from the initial *book*, *cage*, and *prism* conformers (see Fig. 1).

Presence of structures 4 and 5, that are usually not considered as the most stable isomers $(H_2O)_6$, can be explained by the fact that the hexamer is transformed into the circular pentamer with lower energy (oxygen atoms 1, 2, 4, 5, and 6) that is additionally connected to another water molecule (oxygen atom 3). This molecule is later evaporated from the cluster. The molecule that tends to evaporate is such that both its protons are not connected to other molecules by hydrogen bonds. A similar phenomenon for clusters $(H_2O)_4$ и $(H_2O)_{10}$ is described in paper [4], and structures 4 and 5 were previously described in paper [5].

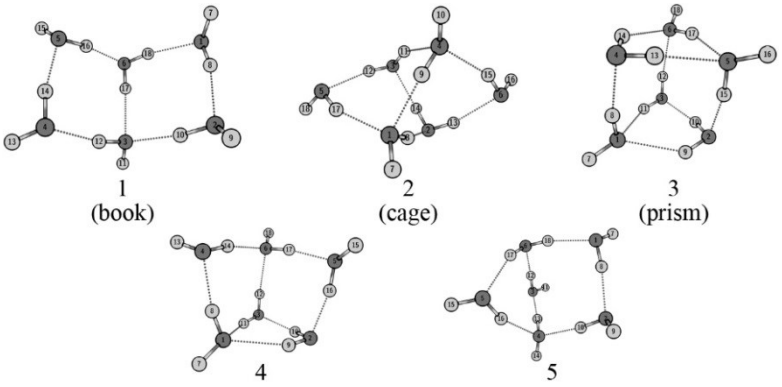

FIGURE 1. Types of the oxygen "skeletons" obtained from optimization of geometry of the initial structures.

The results of calculation of $\Delta_r G^\circ_{298\,K}$ of reaction (1) are shown in Fig. 2. The correction mentioned above allows us to make the DFT results significantly closer to the G4 results.

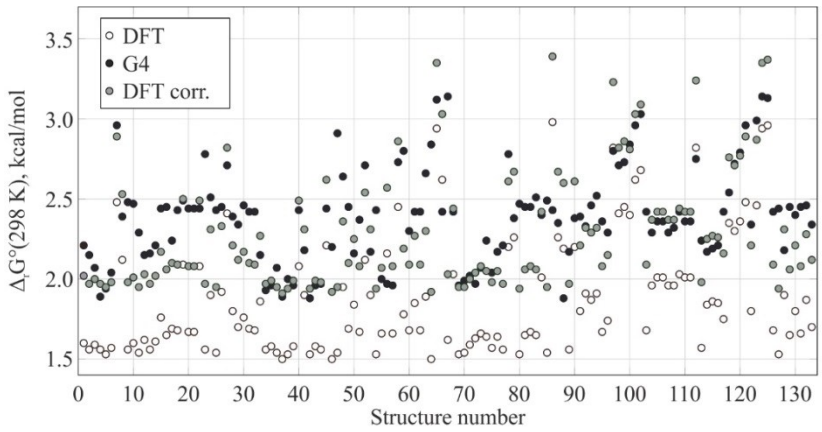

FIGURE 2. The results of calculation of $\Delta_r G^\circ_{298\,K}$ of reaction (1) for all the sampling of isomeric structures.

The averaged results of the thermodynamic calculations for reaction (1) are shown in Table 1.

TABLE 1. The averaged values of the state functions of reaction (1), kcal/mol.

		$\Delta_r E^\circ_{298\,K}$	$\Delta_r (E+\mathrm{ZPE})^\circ_{298\,K}$	$\Delta_r U^\circ_{298\,K}$	$\Delta_r H^\circ_{298\,K}$	$\Delta_r G^\circ_{298\,K}$
DFT	$\langle\Delta\varepsilon\rangle_{av}$	-6.69	-4.55	-4.70	-5.19	2.03
	$\langle\Delta\varepsilon\rangle_{td}$	-7.09	-5.07	-5.07	-5.57	1.84
G4	$\langle\Delta\varepsilon\rangle_{av}$	-7.21	-4.58	-4.58	-5.38	2.39
	$\langle\Delta\varepsilon\rangle_{td}$	-7.23	-4.59	-4.59	-5.40	2.38

Using the state functions, concentration of the water clusters in a gas phase has been calculated. The results are shown in Table 2.

Calculations from the state functions of the structure with the lowest energy leads to underestimation of concentration by 1—2 orders of magnitudes. A significant contribution to concentration of the water clusters in a gas phase is done by the isomeric structures, and their existence is not taken into account in the standard method of the concentration estimate. Orientational isomers $(H_2O)_n$ affect concentration as more as *n* goes up.

The maximal concentration is found for *book* conformer. This can be explained by the facts that (a) this type of the oxygen "skeleton" is the most stable, and (b) this "skeleton" produces more orientational isomers.

TABLE 2. Concentration of clusters in a gas phase ($T = 298.15$ K, $P = 24$ mmHg; columns 1 show the results of conventional calculations for a structure with the lowest energy, columns 2 show the results where the orientational isomerism is taken into account), molec./cm^3.

	DFT corr.		G4	
	1	2	1	2
1 (book)	$1.12 \cdot 10^2$	$1.34 \cdot 10^3$	$7.67 \cdot 10^2$	$1.86 \cdot 10^4$
2 (cage)	$8.55 \cdot 10^0$	$7.96 \cdot 10^1$	$2.08 \cdot 10^1$	$1.63 \cdot 10^2$
3 (prism)	$1.28 \cdot 10^0$	$3.06 \cdot 10^1$	$1.04 \cdot 10^1$	$4.21 \cdot 10^1$
4	$3.52 \cdot 10^0$	$2.24 \cdot 10^1$	$5.75 \cdot 10^1$	$2.74 \cdot 10^2$
5	$1.32 \cdot 10^{-2}$	$1.32 \cdot 10^{-2}$	$1.97 \cdot 10^2$	$3.81 \cdot 10^3$

Molecular dynamics modeling. It has been found 274 molecular collisions during the integration period. They lead to forming of dimers with lifetime more than 2 ps. According to the obtained results, the water dimer represents 2 molecules that simultaneously rotate around their center of mass and move in translational motion. The typical values of the approach radius and time of rotation around the center of mass are 2.5 Å и 2—3 ps, respectively. The trajectory and parameters of one of the found dimers are shown in Fig. 3. The dimers concentration estimate (according to their lifetime) is about 0.04 %, and that is in agreement with G4 calculations.

However, during the same integration time, only one collision of a molecule with the water dimer has been found (see Fig. 3), and this collision does not lead to the trimer forming. Therefore, direct molecular dynamics simulations seem to be ineffective for more complex water clusters.

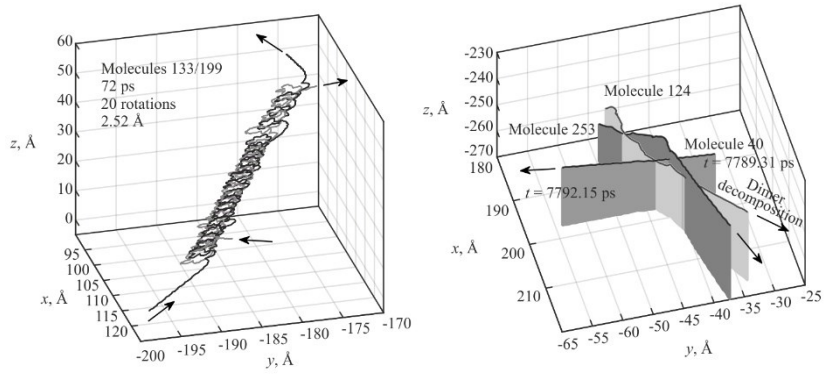

FIGURE 3. The water dimer and trimer.

Conclusion. According to our calculations, concentration of hexamers in a gas phase at temperature $T = 298$ K are $1.86 \cdot 10^4$, $1.63 \cdot 10^2$, $4.21 \cdot 10^1$, $2.74 \cdot 10^2$, and $3.81 \cdot 10^3$ molec./cm^3 for isomers 1, 2, 3, 4, and 5, respectively. It has been shown that existence of the large number of isomeric multi-molecular water complexes

has a significant contribution to their concentration in a gas phase. When calculating concentration of clusters $(H_2O)_n$ with $n > 2$, it is necessary to take into account a phenomenon of orientational isomerism. The standard approach, when concentration is calculated for the most energetically profitable structure, leads to underestimation of concentration by 1—2 orders of magnitudes.

The work is supported by the Russian Foundation for Basic Research (project 17-03-00912).

1. S. V. Drozdov and A. A. Vostrikov, Structural Features and Energy of Small Water Clusters, *Tech. Phys. Lett.*, 2000, 26(5), pp. 397—399, doi: 10.1134/1.1262888.

2. M. E. Dunn, E. K. Pokon, and G. C. Shields, Thermodynamics of forming water clusters at various temperatures and pressures by Gaussian-2, Gaussian-3, complete basis set-QB3, and complete basis set-APNO model chemistries; implications for atmospheric chemistry, *J. Am. Chem. Soc*., 2004, 126(8), pp. 2647—2653, doi: 10.1021/ja038928p.

3. R. J. Saykally and D. J. Wales, Pinning Down the Water Hexamer, *Science*, 2012, 336(6083), pp. 814—815.

4. C. Pérez, M. T. Muckle, D. P. Zaleski et al., Structures of Cage, Prism, and Book Isomers of Water Hexamer from Broadband Rotational Spectroscopy, *Science,* 2012, 336(6083), pp. 897—902, doi: 10.1126/science.1220574.

5. E. D. Belega, K. Tatarenko, D. N. Trubnikov, and E. A. Cheremukhin, The dynamics of water hexamer isomerization, *Rus. J. Phys. Chem. B*., 2009, 3(3), pp. 404—409.

Ab Initio Calculations of Surface Catalytic Recombination of heat Flow Stimulating of Spacecraft in the Upper Atmosphere

Andrey S. Vetchinkin

Semenov Institute of Chemical Physics, 4 Kosygina Street, Building 1, 119991, Moscow, Russia

Introduction. The great practical interest to the study of interaction between multicomponent gas mixtures and catalytic thermal barriers is connected with creation of reusable spacecrafts and promising hypersonic aircrafts. Such space/aircraft experience non-equilibrium flow conditions in high-heat parts of the flight path in the atmosphere, and application of low-catalytic coatings reduces heating several times due to heterogeneous catalytic atom recombination. Considerable reduction of heat flows allows reducing the thermal protection weight and increasing the payload and safety [1]. High-frequency induction plasmatrones are efficient experimental facilities for studying thermal barrier catalytic properties [2] Metal (often copper) sensors are used in them for the purpose of flow diagnostics [3] The flow parameter values to be determined to a great extent

depend on the sensor material catalytic activity degree. At mathematical problem setting the catalytic activity of the surface is included into the boundary condition for a set of equations describing the multicomponent chemically reacting flow at the surface. Heterogeneous catalytic recombination effects are normally considered by introduction of recombination coefficients γi showing the share of atoms recombining on the surface. Coefficients γ_i depend both on the surface properties, and the gaseous phase conditions. These dependences include many parameters. Rather a detailed review of the results of experiments that consisted in measuring the possibility of heterogeneous recombination of oxygen atoms γO on copper and its oxides is given in paper [4] In 300—600 K surface temperature range a high level of oxygen atom heterogeneous recombination possibility ($\gamma \approx 0.1$—0.5) on CuO and Cu_2O surfaces is observed, and the values for Cu_2O are somewhat exceed the values for CuO.

Providing the appropriate selection of elementary step rate coefficients, theoretical models accounting for a detailed mechanism of heterogeneous catalytic reactions and based on Langmuir adsorption layer theory, allow satisfactory description of aerodynamic heating both the windward surface of reusable spacecrafts along their entire descending trajectory in the Earth atmosphere, and models in experimental facilities [1] But the mentioned coefficients have a number of parameters determined when compared with heat flow experimental data, and this approach can be ambiguous ammbiguous in case with multiparameter dependence. Approaches based on quantum mechanics and molecular dynamics methods allow better understanding of heterogeneous catalytic process mechanism and determination of elementary step rate coefficients without using experimental data.

In this paper the cluster approach is applied to dissociated oxygen interaction with Cu_2O copper oxide surface. Using quantum mechanics methods geometric, energy and vibrational properties of oxygen atom heterogeneous recombination are calculated. The Schrodinger equation in adiabatic approximation was solved by application of the density functional theory (DFT) methods using the GAUSSIAN software package. The elementary step rate coefficients were calculated depending on the temperature basing on the transition state theory of Eyring and Polanyi. The above was the basis for determination of γ_O recombination coefficient values in a wide range of conditions change at the surface. The obtained results are consistent with the experimental data.

Modeling recombination processes and structure of material surface. When copper sensors are used as parts of a highfrequency induction plasmatrones in dissociated air, cuprous oxide Cu_2O is produced on their surface. This is a red–brown crystalline substance. Its crystalline structure can be represented as a body-centered cubic lattice with oxygen atoms in the nodes, and an interpenetrating facecentered lattice of the same size but with copper in nodes, one quarter-shifted along the body diagonal. Copper coordination is equal to two, oxygen coordination — to four. Cell dimension a_0=4.26 Å. The melting point is 1236 °C, the

break-down temperature is 1800 °C (the highest among all copper oxides). Both the impact and the associative mechanisms of heterogeneous recombination were taken into account on Cu_2O surface, and the rate coefficients of the respective elementary steps were calculated oxygen atom adsorption/desorption

$$O + (S) \leftrightarrow (O\text{-}S)$$

Eley–Riedel (ER) mechanism of recombination (impact recombination)

$$O + (O\text{-}S) \leftrightarrow O_2 + (S)$$

Langmuir–Hinshelwood (LH) mechanism of recombination (associative recombination)

$$(O\text{-}S) + (O\text{-}S) \leftrightarrow O_2 + 2(S)$$

Here (S), (O–S) are symbols of free adsorption sites and adsorbed oxygen atoms. Since chemisorbed particles bound to the surface by short-range forces are involved into heterogeneous catalytic reactions on the surface, the cluster approach is rather efficient for description of local interactions. A cluster is a relatively small part of a solid body lattice consisting of a finite number of surface and near-surface layer atoms. The study of interactions with it reveals the possibility of direct application in the calculations of quantum mechanics methods dealing with molecular systems limited in terms of size. The Cu_2O copper oxide surface was modeled by three near-surface layers (Fig. 1).

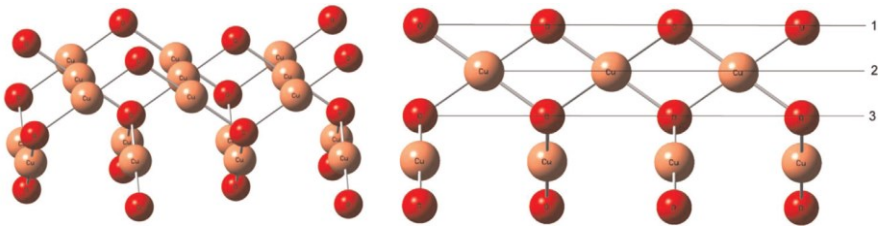

FIGURE 1. Cu_2O copper oxide crystal structure (on the left) and side view (on the right).

The Schrodinger equation was solved using the DFT method with Becke's three parameter hybrid functional, supplemented with Lee–Yang–Parr exchange–correlation functional (B3LYP), and using Pople splitvalence basis 6—31G* [5]. The calculations were carried out using the GAUSSIAN software package. potential energy surface, geometry and frequency of cluster vibration in transition state and energy barriers of reactions were determined. These findings were used for calculation of rate coefficients of elementary reactions on the surface. The specific type of elementary step rate coefficients obtained using the transition state theory of Eyring and Polanyi.

Results. The calculation showed that adsorption on the active centers of the first type was much faster than on the centers of the second type. On the Cu_2O

surface two types of active surface centers were accounted for. It was also revealed that the Eley–Riedel reaction was almost barrierless on active centers of the second type. That is why the Langmuir–Hinshelwood reaction rate was determined by the product of rates of surface diffusion from the firsttype centers to the second-type centers and impact recombination on the second-type centers. Since adsorption centers have staggered arrangement on the surface, the minimum distance between the adsorption centers is the distance between the neighboring centers of different types equal to 3.01 Å.

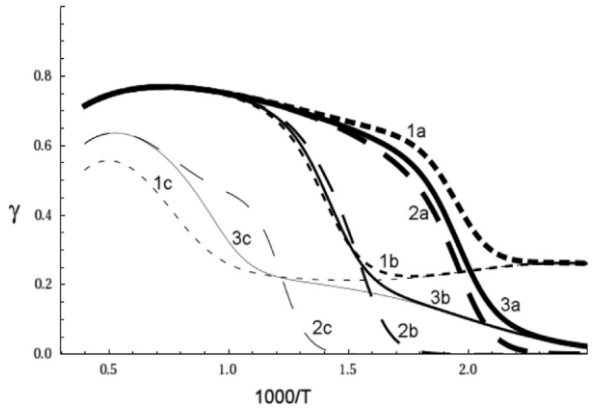

FIGURE 2. Dependence of recombination effective coefficient on partial pressure of atomic oxygen a,b,c (0.1, 100, 105 Pa, respectively) and temperature taking into account joint and individual ER (1) and LH (2) reactions (3).

The relative contribution of various recombination mechanisms is shown in Fig. 2. It is evident that impact recombination prevails at T<1000 K, and the associative one-at T>850 K. The calculation showed that a high degree of copper oxide catalyticity at high and medium temperatures (T>500 K) was conditioned by barrierless impact recombination on the centers of the second type. The calculations also showed that in this system impact recombination processes on the second-type centers was of primary importance at low temperatures. Dependences of recombination effective coefficient γ on the temperature for partial pressures p_O = 0.1, 10^2 and 10^5 Pa are shown in Fig. 3. A significant dependence of the recombination effective coefficient both on the temperature and partial pressures can be observed. It can be seen that at p_O=0.1 Pa and p_O=10^2 Pa the recombination effective coefficient reaches its maximum value γ_{max}=0.8 at T=1430 K. At p_O=10^5 Pa maximum value γ is reached at higher temperatures. Temperature decrease causes exponential decrease of γ, and in this case its value does not depend on the partial pressure any more. The obtained results are consistent both with earlier experimental data given in [6—9] and the last experimental work. It stands to mention that in [6—10] γ=0.01 at T=310 K. As a result of our calculations γ=0.008 at this temperature.

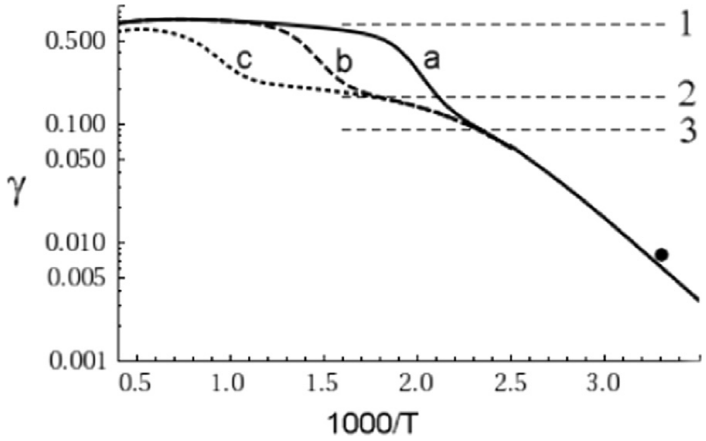

FIGURE 3. Dependence of recombination effective coefficient on partial pressure of atomic oxygen a, b, c (0.1, 100, 105 Pa, respectively) and temperature. Lines 1, 2, 3 and point are experimental data [6—10].

1. V. L. Kovalev, *Hetergenous Catalytic Processes in Aerothermodynamics*, FIZMATLIT, Moscow, 2002, 224 p.

2. A. N. Gordeev, A. F. Kolesnikov, and V. I. Sakharov, Numerical and experimental study of flow and heat exchange of bodies with supersonic underexpanded air jets on the VGU-4 induction plasmatron (Institute of Problems in Mechanics of Russian Academy of Sciences) with partitioned discharge channe, *J. Russ. Acad. Sci. Fluid Dyn*., 2011, 3, pp. 113—125.

3. A. N. Gordeev, A. F. Kolesnikov, and V. I. Sakharov, Heat transfer in underexpanded non-equilibrium carbon dioxide jets: experiment in induction plasmatron and extrapolation in the conditions of entry into the Martian atmosphere, *Phys.–Chem. Kinet. Gas Dyn.*, 2014, 15(4), pp. 1—18.

4. V. D. Berkut, V. M. Doroshenko, V. V. Kovtun, and N. N. Kudryavtsev, *NonEquilibrium Physical and Chemical Processes in Hypersonic Aerodynamics,* Energoatomizdat, Moscow, 1994, 400 p.

5. P. C. Haharan and J. A. Pople, The influence of polarization functions on molecular orbital hydrogenation energies, *Theor. Chem. Acta*., 1973, 28, pp. 213—222.

6. E. L. Winkler and R. E. Sheldalh, Influence of calorimeter surface treatment on heat transfer measurements in arc-heated test streams, *AIAA J.*, 1966, 4(4), pp. 715—716.

7. R. A. Hartunian, Measurements of catalytic efficienty for oxigen atoms and the O–O2 diffusion coefficients*, J. Chem. Phys.*, 1965, 43(11), pp. 4003—4006.

8. P. G. Dickens and H. B. Sutcliffe, Reactins of oxygen atoms on oxide surfaces, *Trans. Faraday. Soc.*, 1964, 60, pp. 1272—1285.

9. A. Nawaz, D. Driver, and I. Terrazas-Salinas, Surface Catalysis and Oxidation on Stagnation Point Heat Flux Measurements in High Enthalpy Arc Jets, *AIAA Paper*, 2013, 15 p.

10. G. Park, Oxygen catalytic recombination on cooper oxide in tertiary gas mixtures, *J. Spacecr. Rockets,* 2013, 50(3), pp. 540—555, doi:10.2514/1.A32312.

Ab Initio Calculation of the Lowest ^2S Resonance of He^- by Complex Absorbing Potential Method

Sergey O. Adamson[1] and Darja D. Kharlampidi[2]

[1]Laboratory of Molecular Structure and Quantum Mechanics, Department of Chemistry, Lomonosov Moscow State University, Leninskie Gory, 1, Moscow 119991, Russia
[2]General Chemical Department of Institute of biology and chemistry, Moscow State Pedagogical University, Kibalchicha street, 6/2, Moscow 129164, Russia

A specific feature of the complex absorbing potential (CAP) method is the possibility of its application to the calculation of the resonance energies and widths for molecules and their ions [1—3]. In this method the initial Hamiltonian $\hat{H}_0$ is replaced by the modified one $\hat{H} = \hat{H}_0 - i\eta W(r; R_0)$, where $W(r; R_0)$ is a non-negative potential defined in the region $r>R_0$ and η — real scaling factor, called "CAP strength" [4, 5]. The resonance energy E_{res} and half-width $\Gamma/2$ in the CAP framework can be estimated as the real and imaginary parts of the complex eigenvalue $E(\eta)$ obtained at the point corresponding to the minimum value of the function $f(\eta) = |\eta dE(\eta)/d\eta|$ [4]. Unfortunately, the application of this technique leads to significant differences between the experimental and calculated E_{res} and Γ values, for example, such as in paper [4]. The attempts to improve this situation have not been very successful [1, 2].

Recently the resonance parameters extraction method based on the averaging of complex eigenvalues on closed paths of η-trajectories was applied to the lowest ^1S resonance in H^- [6]. It was found that this technique provides more reliable estimations of the E_{res} and Γ values in comparison with the earlier used techniques. Now this method is applied to the lowest ^2S resonance of He^-.

In our calculations the absorbing potential $W(r; R_0)$ has been taken in the form

$$W(r; R_0) = \eta(r - R_0)^2, \qquad r \geq R_0, \tag{1}$$

with the logarithmic strength parameter $-8.9 \leq \ln\eta \leq 8.0$ and step 0.1.

As in the previous work [6], the parameters of the ^2S resonance were estimated by the averaging over the closed paths of the η-trajectories (Method A) and by the minimum of $f(\eta) = |\eta dE(\eta)/d\eta|$ function (Method B). The details of the Schrödinger equation solution can be found in earlier works [7, 8]. The η-trajectories have been obtained using the (4,2)/(23,1) (Basis I) and (5,2)/(22,1) (Basis II) bases of single-particle functions (orbitals) in the terms of [9]. The scaling factor for the basis functions is varied over the interval $1.90 \leq b \leq 2.3$ (with 0.1 step).

It is found that the resonance parameters depend on the choice of the scaling factor (Fig. 1—2).

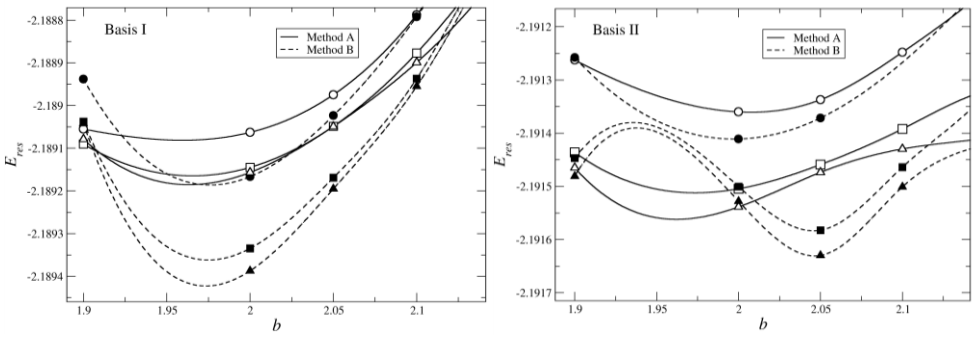

FIGURE 1. Resonance energies (a.u.), ○ − R_0=20, □ − R_0=25, Δ − R_0=30 a.u.

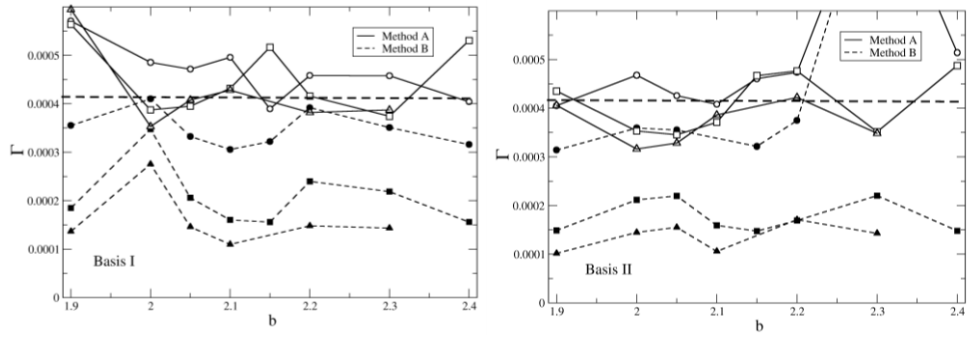

FIGURE 2. Resonance widths (a.u.), ○ − R_0=20, □ − R_0=25, Δ − R_0=30 a.u. The horizontal dotted line corresponds to the experimental value [10].

The better agreement with the reference values [10—13] is observed for the scaling factor b value which corresponds to the minimum energy of the lowest excited state ^3S of *He* atom (b_{min}=2.20 for Basis I and b_{min}=2.17 for Basis II). Increasing of the internal part of the basis set affects strongly the energy of the resonance and slightly affects the widths (Tab.1, Fig. 1—2). It should be pointed out that the similar results were observed in stabilization calculations [9]. Better estimations of the resonance widths were obtained by Method A for the $25 \le R_0 \le 30$ while both methods yields the close values of the resonance energies (Tab. 1). Thus the Method A is more accurate than the Method B.

TABLE 1. Energies and widths of the lowest ^2S resonance state of He^- (in a.u.).

Method	R_0	Basis I		Basis II	
		$-E_{res}$	$\Gamma*10^5$	$-E_{res}$	$\Gamma*10^5$
Scaling factor b_{min} corresponds to the minimum energy of 1^3S state of He					
A	20	2.188020	46.17	2.191085	46.32
	25	2.188332	41.17	2.191310	48.20
	30	2.188352	38.14	2.191410	42.56
B	20	2.187995	39.39	2.191062	32.67
	25	2.188361	24.24	2.191272	15.33
	30	2.188153	14.85	2.191421	14.14
Averaging over scaling factor interval $1.90 \le b \le 2.30$					
A	20	2.188119	46.68	2.191031	50.64
	25	2.188240	45.19	2.191246	41.08
	30	2.188627	42.55	2.191383	36.78
B	20	2.188126	34.80	2.191101	43.75
	25	2.188300	20.86	2.191277	17.80
	30	2.188687	15.98	2.191454	13.68
Reference values[a]					
Experiment[b]		E_{res}= -2.19208±0.00004, $\Gamma=(41.2\pm1.8)\cdot10^{-5}$			
R-matrix (19 states)		E_{res}= -2.19171, $\Gamma=43.0\cdot10^{-5}$ [c]			
Complex rotation		E_{res}= -2.19202, $\Gamma=31.6\cdot10^{-5}$ [d]			
R-matrix with pseudostates (RMPS) (41 states)		E_{res}= -2.19204, $\Gamma=39.3\cdot10^{-5}$ [e]			
Stabilization method, basis (4,2/23,1)		E_{res}= -2.18901±0.00010, $\Gamma=(51\pm7)\cdot10^{-5}$ [f]			
Stabilization method, basis (5,2/22,1)		E_{res}= -2.19144±0.00005, $\Gamma=(42\pm4)\cdot10^{-5}$ [f]			

[a] The present values are calculated as the sum of electron incident energy and ground ^1S state energy of *He*; conversion factor is 1 a.u. = 27.2116 eV.

[b] Ref. [10]. [c] Ref. [11].

[d] Ref. [12]. [e] Ref. [13].

[f] Values for $23.9 \le R_{res} \le 25.8$ a.u. averaged over $1.65 \le b \le 2.15$ interval, Ref. [9].

The financial support was provided by the Russian Foundation for Basic Research (grant No. 15-03-03582). Also we would like to thank Useinova A. R., who helped with the calculations.

1. D. Zuev, T.-C. Jagau et al., *J. Chem. Phys.*, 2014, 141, 024102-1, doi: 10.1063/1.4885056.

2. T. C. Jagau, D. Zuev, K. B. Bravaya et al., *J. Phys. Chem. Lett.*, 2015, 5, 310, doi: 10.1021/jz402482a.

3. Y. Sajeev, M. Sindelka, and N. Moiseyev, *Chem. Phys.*, 2006, 329. 307, doi: 10.1016/j.chemphys.2006.08.008.

4. U. V. Riss and H. D. Meyer, *J. Phys. B*, 1993, 26, 4503, doi: 10.1088/0953-4075/26/23/021.

5. G. Jolicard, C. Leforestier, and E. J. Austin, *J. Chem. Phys.*, 1988, 88, 1026, doi: 10.1063/1.454269.

6. A. A. Preobrazhenskaya, S. O. Adamson, D. D. Kharlampidi, and A. I. Dementiev, AIS-2016: Atmosphere, ionosphere, safety. Proceedings of V International conference, Supported by RFBR; ed. I. V. Karpov. Kaliningrad, 2016, 102.

7. S. O. Adamson, D. D. Kharlampidi, and A. I. Dementiev, *Prog. Theor. Chem. Phys*., 2013, 27, 101, doi: 10.1007/978-3-319-01529-3_5.

8. A. A. Preobrazhenskaya, S. O. Adamson, and D. D. Kharlampidi, *Russ. J. Chem. Phys.*, 2016, 35, 65, doi: 10.1134/S1990793116010115.

9. S. O. Adamson, D. D. Kharlampidi, A. A. Preobrazhenskaya, and A. I. Dement'ev, *Russ. J. Phys. Chem. B,* 2017, 11, 894, doi: 10.1134/S199079311706015X.

10. A. Gopalan, J. Bömmels, S. Götte et al., *Eur. Phys. J. D,* 2003, 22, 17, doi: 10.1140/epjd/e2002-00219-7.

11. W. C. Fon, K. A. Berrington, P. G. Burke, and A. E. Kingston, *J. Phys. B.: At. Mol. Opt. Phys.,* 1989, 22, 3939, doi: 10.1088/0953-4075/22/23/016.

12. M. Bylicki, *J. Phys. B: At. Mol. Opt. Phys,* 1991, 24, 413, doi: 10.1088/0953-4075/24/2/009.

13. K. Bartschat, E. T. Hudson, M. P. Scott et al., *Phys. Rev. A,* 1996, 54, R998, doi: 10.1103/PhysRevA.54.R998.

Noncovalent Hydrogen Isotope Effects in the van der Waals Complexes

Natalia N. Breslavskaya[1], Anatoly L. Buchachenko[2,3], Lubov A. Wasserman[4], and Irina I. Barashkova[2]

[1]Institute of General and Inorganic Chemistry RAS, Leninskii pr.31, Moscow 117907, Russia
[2]Institute of Chemical Physics RAS, 4 Kosygin str., Moscow, 119991, Russia
[3]Scientific Center in Chernogolovka, Chernogolovka, 142432 Russia
[4]Institute of Biochemical Physics RAS, 4 Kosygin str., Moscow, 119991, Russia

Introduction. The difference in zero-point energy (ZPE) of isotopic molecules (with H and D atoms, for instance) produces the main contribution into the covalent isotope effects. However, there are many observations of the anomalious properties of the effects. Thus, the magnitudes of experimentally measured isotope effects IE in the H/D atom abstraction reactions were shown to depend on the solvent and presence of the third substances, besides of the pair of reactants. IEs measured in the reactions of individual compounds, differ from those measured in their mixture. In many cases enormously large isotope effects were observed at the mild conditions (room temperature, liquids).

Analysing these discouraging isotope anomalies it is worthy to keep in mind that there exist noncovalent isotope effects, which are controlled by ZPEs of the intermolecular, noncovalent vibrations in weakly bound complexes of reactants with solvent or with other, foreign molecules. The chemistry of van der Waals complexes plays an important role in the troposphere. At this paper $H_2O^{\cdots}O_2$ and water dimers were studied; these complexes are interesting due to its possible

contribution to the atmospheric absorption of solar radiation [1, 2]. ZPEs of the noncovalent bonds for H_2O O_2 and water dimers were calculated due to evaluate noncovalent isotope effects on the equilibrium constants for the complex formation and to estimate their contribution into the experimentally measured isotope effects. Early [3, 4] similar calculations were performed for different types of weak molecular complexes (water-hydrogen, protonated biwater, water-methane, $(CH_3)_2NO\cdots H_2O$, $H_2O\cdots HO_2$).

Calculation procedure. Calculations of the energy characteristics with full optimization of geometry for all structures were performed at second-order Møller-Plesset perturbation theory (MP2) and coupled-cluster singles doubles correction (CCSD) with the use of Dunning's correlation-consistent aug-cc-pVDZ and aug-cc-pVTZ basis sets. The calculations were carried out using the Gaussian 2009 program. The results of vibration frequency calculations of all complexes characterize the optimized structures as the energy minima.

Results

Reaction kinetics in terms of noncovalent interactions. In the hydrogen (deuterium) atom abstraction reactions by radical $r^{\bullet}$ from the molecules RH and RD

$$r^{\bullet} + RH \xrightarrow{k_H} rH + R^{\bullet} \quad (1)$$

$$r^{\bullet} + RD \xrightarrow{k_D} rD + R^{\bullet} \quad (2)$$

both molecules may be complexed with solvent molecules S:

$$RH + S \rightleftharpoons^{K^H} [RH\cdots S] \quad (3)$$

$$RD + S \rightleftharpoons^{K^D} [RD\cdots S] \quad (4)$$

By assuming that the complexation prevents reactions of [RH···S] and [RD···S], i. e. only free, not solvated molecules RH and RD are able to react, one can derive the equation for the total, experimentally measured isotope effect IE:

$$IE = (k_H/k_D)(K^D/K^H) \quad (5)$$

The equation (5) may be generalized for the cases, when solvent molecules are protiated or deuterated (particuarly, if the reaction is carried out in protiated and deuterated water). In these cases radical $r^{\bullet}$ may also be solvated:

$$r^{\bullet} + S(H) \rightleftharpoons^{K_r^H} [r^{\bullet}\cdots S(H)] \quad (6)$$

$$r^{\bullet} + S(D) \rightleftharpoons^{K_r^D} [r^{\bullet}\cdots S(D)] \quad (7)$$

where S(H) and S(D) are protiated and deuterated solvents. Then the total isotope effect is expressed by equation:

$$IE = (k_H / k_D)(K^D / K^H)(K_r^D / K_r^H) \quad (8)$$

Furthermore, the molecules RH and RD may be solvated by S(H) and S(D) differently as shown in next equations:

$$RH + S(H) \underset{}{\overset{K^{RH}_{S(H)}}{\rightleftharpoons}} [RH\cdots S(H)] \quad (9)$$

$$RH + S(D) \underset{}{\overset{K^{RH}_{S(D)}}{\rightleftharpoons}} [RH\cdots S(D)] \quad (10)$$

The similar equations are valid for the RD molecules:

$$RD + S(H) \underset{}{\overset{K^{RD}_{S(H)}}{\rightleftharpoons}} [RD\cdots S(H)] \quad (11)$$

$$RD + S(D) \underset{}{\overset{K^{RD}_{S(D)}}{\rightleftharpoons}} [RD\cdots S(D)] \quad (12)$$

Keeping in mind isotope effects in these equations one can derive a total equation for the summary isotope effect IE:

$$IE = (k_H / k_D)(K^D / K^H)(K^D_r / K^H_r)(K^{RH}_{S(D)} / K^{RH}_{S(H)})(K^{RD}_{S(D)} / K^{RD}_{S(H)}) \quad (13)$$

Further we will consider particular, but the most important case of solvation presented by equations (2) and (3). We will calculate the ratios (K^D/K^H) for the various types of intermolecular interactions and different types of complexes.

Noncovalent isotope effects. In general, the isotope effect, i. e. the ratio K^D/K^H, is determined as

$$K^D/K^H = \exp(\Delta H_H - \Delta H_D) \quad (14)$$

where ΔH_H and ΔH_D are the enthalpies for equilibrium (3) and (4). Note, that

$$(\Delta H_H - \Delta H_D) = \varepsilon(H) - \varepsilon(D)$$

where ε(H) and ε(D) are the differences of ZPEs of reactants:

$$\varepsilon(H) = ZPE(RH\cdots S) - ZPE(RH) - ZPE(S) \quad (15)$$

$$\varepsilon(D) = ZPE(RD\cdots S) - ZPE(RD) - ZPE(S) \quad (16)$$

These values, ε(H) and ε(D), determine intermolecular, noncovalent ZPEs for the [RH···S] and [RD···S] complexes; they are ZPEs of noncovalent bonds and characterize intermolecular potential of the atom-atom contact in complex or compound molecule. The contribution of the noncovalent ZPEs into the isotope effect is determined by equation

$$K^D/K^H = \exp(\Delta\varepsilon_0) \quad (17)$$

where

$$\Delta\varepsilon_0 = \varepsilon(H) - \varepsilon(D) \quad (18)$$

Since $\Delta\varepsilon_0 > 0$, the ratios $K^D/K^H > 1$, that is deuterated molecules RD are more tightly bound with solvating molecules, than the protiated molecules RH. These values — ε(H) and ε(D), denoted further as simply ε, as well as $\Delta\varepsilon_0$ and K^D/K^H — will be presented below in the Tables**.**

Water dimers. The global minimum has been determined to be C_s structure (Figure *a*) [5 and references therein]. Their parameters calculated at CCSD/aug-cc-pVDZ level of theory are shown in Table 1. They result to the isotope effects K^H/K^D in the equilibrium

$$H_2O + HOD \overset{K^H}{\rightleftharpoons} [H_2O\cdots HOD]$$

$$H_2O + DOH \overset{K^D}{\rightleftharpoons} [H_2O\cdots DOH]$$

$$D_2O + HOH \overset{K^D}{\rightleftharpoons} [D_2O\cdots HOH]$$

in the range 1.1−1.6. Quatitavely similar effects were detected in cromatography [6]. In order to control accuracy of calculations we have computed the energy of noncovalent bond in the water dimer $(H_2O)_2$; it was found to be 5.2 kcal/mol, a standard magnitude for hydrogen bond; it is not strongly different from those found in other works, from 5.0 to 6.0 kcal/mol [7, 8].

TABLE 1. Water dimers.

Dimer	ZPE, kcal/mol	ε, kcal/mol	$\Delta\varepsilon_0$, cal/mol	K^D/K^H (300 K)
$H_2O\cdots H{-}OH$	28.99	2.11	–	–
$D_2O\cdots H{-}OH$	25.15	1.93	180	1.35
$H_2O\cdots D{-}OH$	26.90	1.83	280	1.59
$H_2O\cdots H{-}OD$	27.11	2.04	70	1.12

As seen in Table 1 the main contribution into the ZPE difference results from the deuterium atoms directly involved in noncovalent binding; the others, distant from noncovalent bond, do not contribute markedly.

a *b*

FIGURE. Selected computed structures of complexes with noncovalent bonds: $H_2O\cdots H{-}OH$ (*a*); $H_2O\cdots O_2$ (*b*). The figures refer to the bond lengths (Å) and angles.

Water-oxygen complexes. The C_s structure of $H_2O\cdots O_2$ (Figure *b*) is the global minimum [2 and references therein]. Parameters calculated at MP2/aug-cc-pVTZ level of theory are shown in Table 2. Isotope effect on the complexation of water molecule with oxygen, which seems to be important in the Earth's atmosphere [1], is slightly larger but does not exceed 10—20%.

TABLE 2. $H_2O\cdots O_2$ complexes.

Complex	ZPE, kcal/mol	ε, kcal/mol	$\Delta\varepsilon_0$, cal/mol	K^D/K^H (300 K)
$H_2O\cdots O_2$	16.48	0.96	–	–
$HOD\cdots O_2$	14.60	0.89	70	1.12
$D_2O\cdots O_2$	12.70	0.84	120	1.22

Zero-point energies of intermolecular, noncovalent vibrations presented in hydrogen bonds are not negligible; they contribute markedly into the experimentally measured isotope effects and can not be ignored. Noncovalent IEs should be taken into account to make correct and substantiated conclusions on the reaction mechanisms. The kinetic equations are derived for the total isotope effects, which include noncovalent IEs as additive factors. Noncovalent isotope effects are also the means to elucidate intriguing isotopic phenomena. The latter are understandable in terms of noncovalent ZPEs and noncovalent isotope effects.

Acknowledgments: This work was financially supported by Russian Fund for Basic Research (Grant 17-03-00166, registration code AAAA-A17-117041310106-5), the Russian Academy of Sciences in terms of Program № 38. The support of FASO of Russia (project 082-2014-0018, registration code AAAA-A17-117040610311-3) is also acknowledged.

1. Y. Kasai, E. Dupuy, R. Saito et al., The H_2O-O_2 water vapour complex in the Earth's atmosphere, *Atmos. Chem. Phys*., 2011, 11, 8607, doi:10.5194/acp-11-8607-2011.

2. K. M. Dreux, G. S. Tschumper, Anchoring the potential energy surface of an important atmospheric van der Waals dimer, the $H_2O\cdots O_2$ complex, *Comp. Theor. Chem.*, 2015, 1072, 21, http://dx.doi.org/10.1016/j.comptc.2015.08.022.

3. A. L. Buchachenko, N. N. Breslavskaya, Noncovalent Hydrogen Isotope Effects, *Rus. J. Phys. Chem. A*, 2018, 92(2), 315, doi:10.1134/S003602441802005X.

4. A. L. Buchachenko, L. A. Wasserman, N. N. Breslavskaya, I. I. Barashkova, Noncovalent hydrogen isotope effects in paramagnetic molecules, *Rus. J. Phys. Chem. B*, 2018, in press.

5. X. Huang, B. J. Braams, J. M. Bowman, Ab Initio Potential Energy and Dipole Moment Surfaces of $(H_2O)_2$, *J. Phys. Chem. A* 2006, 110(2), 445, doi:10.1021/jp053583d.

6. A. Valleix, S. Carrat, C. Caussignac et al., Secondary isotope effects in liquid chromatography behaviour of ^2H and ^3H labelled solutes and solvents. *J. of Chromatography A*, 2006, 1116, 109, https://doi.org/10.1016/j.chroma.2006.03.078.

7. J. Ceponkus, P. Uvdal, B. Nelander, Intermolecular vibrations of different isotopologs of the water dimer: Experiments and density functional theory calculations, *J. Chem. Phys.* 2008, 129(19), 194306, https://doi.org/10.1063/1.3009620.

8. F. N. Keutsch, J. D. Cruzan, R. J. Saykally, The water trimer, *Chem. Rev.*, 2003, 103(7), 2533, doi:10.1021/cr980125a.

Calculation of Electromagnetic Dipole Radiation in the Wave Zone with Vector Potential

Leonid S.Chudnovskiy[1], Maxim A. Aborin[1], and Vladimir T.Polyakov[2]

[1]Open Joint-stock Company "Research-and-Production Corporation "Precision System and Instruments", Aviamotornaya street. 53, Moscow, 112250, Russia
[2]Russian New University (RosNOU), Radio Street, 22, Moscow, 195005 Russia

The proposed method makes it possible to estimate the electromagnetic field of a dipole of any extent in the wave zone using the Green's function for the vector potential. The calculation is correct to within grad φ.

Let us consider the radiation of a short dipole, when the delay from the small radiating elements of the dipole can be neglected. Let us find the expression for the field strength E (t) in terms of the vector potential A (t).

We set the current density in the dipole

$$j(t) = \delta\left(t - \frac{r}{c}\right)[\eta(r) - \eta(r - L)] - \delta\left(t + \frac{r}{c}\right)[\eta(-r) - -\eta(-r + L)], \quad (1)$$

where: δ (t) is the delta function, η (r) is the unit function, *c* is the speed of light, and *L* is the dipole length.

For a short dipole at L / c << ω_{max}^{-1}, where ω_{max} is the maximum frequency of the radiation, the expression for the current density is simplified

$$j(t) = \delta(t)\{[\eta(r) - (r - L)] - [\eta(-r) - (-r + L)]\}. \quad (2)$$

The vector potential of the Green's function of a short dipole for the direction of radiation perpendicular to a dipole will be

$$g(t) = \delta(t)L(2\pi\varepsilon_0 c^2 R)^{-1}, \quad (3)$$

where ε_0 is the permittivity of vacuum; c is the speed of light; R is the distance between correspondents.

For the current I (t) in a short dipole for the electric field strength of a short dipole, we obtain:

$$E(t) = \frac{dA(t)}{dt} = \frac{d}{dt}[I(t) * g(t)] = \frac{dI(t)}{dt}L(4\pi\varepsilon_0 c^2 R)^{-1}, \quad (4)$$

where * — is the convolution operation.

Expression (4) is obtained for the wave zone to within gradφ, whose value decreases with distance as R^{-3}.

For a sinusoidal signal, expression (4) takes the following form:

$$E(\omega) = L(2\pi\varepsilon_0 c^2 R)^{-1} i\omega I(\omega) \quad (5)$$

Expression (5) is a well-known formula for the electromagnetic radiation of a short dipole in the wave zone.

With the help of expression (1), one can simply estimate the electric field strength of an extended dipole. Calculation of the radiation of a vertical antenna with grounding is carried out analogously without the second additive term in expression (1).

Low-Temperature Exchange Reactions Involving O, N, O_2, N_2, and Rydberg Particles in Orbitally Degenerate States

Veronika V. Kuverova[1], Gennady V. Golubkov[2], Nikolay S. Malyshev[2], Sergey O. Adamson[2,3], Fedor S. Bessarab[4,5], Inna Y. Yurova[6], Maxim G. Golubkov[2]

[1]Center of Chemical Physics of Atmosphere, Moscow, Russia
[2]Semenov Institute of Chemical Physics, Russian Academy of Sciences, Moscow, Russia
[3]Laboratory of Molecular Structure and Quantum Mechanics, Department of Chemistry, Lomonosov Moscow State University, Moscow, Russia
[4]Kaliningrad branch of Pushkov Institute of Terrestrial Magnetism, Ionosphere and Radiowave Propagation, Russian Academy of Sciences, Kaliningrad, Russia
[5]Immanuel Kant Baltic Federal University, Kaliningrad, Russia
[6]Physics Department, Saint-Petersburgh State University, Saint-Petersburgh, Russia

Exchange reactions involving Rydberg atoms and molecules

$$N_2^{**} + O \to N_2^+ O^- \to NO^{**} + N, \quad (1)$$

$$O_2^{**} + N \to O_2^+ N^- \to NO^{**} + O, \quad (2)$$

$$O^{**} + N_2 \to O^+ N_2^- \to NO^{**} + N, \quad (3)$$

$$N^{**} + O_2 \to N^+ O_2^- \to NO^{**} + N, \quad (4)$$

are of great interest for the radiochemical physics of the upper atmosphere. These reactions flow most efficiently through the harpoon mechanism with the formation of an intermediate complex in the ion configuration, when the resonance energies E_r for the fragments diluted to infinity are located in the continuous spectrum. Below the ionization boundary the states of the complex are stable, but higher they are autoionizing ones. In the first stage of the reactions (1)—(4), the Rydberg states quenched, where the acceleration of the fragments in the Coulomb potential plays the decisive role. At the second stage of the process, the complex decays into the final state of the system. This mechanism is due to the fact, that the ionization

potential of the NO molecule to the ground $X^1\Sigma^+$ state of the ion (I_{NO} = 9.66 eV [1]) is smaller than the ionization potentials of unexcited N_2, O_2, and O particles, given in Table 1.

TABLE 1. Ionization potentials of NO, N_2 and O_2 molecules [1].

Molecules	Ionization potentials (eV) and electronic states		
NO	9.66 ($X^1\Sigma^+$)	16.36 ($b^3\Pi$)	16.88 ($w^3\Pi$)
N_2	15.58 ($X^2\Sigma_g^+$)	16.71 ($A^2\Pi_u$)	18.75 ($B^2\Sigma_u^+$)
O_2	12.08 ($X^2\Pi_g$)	16.12 ($a^4\Pi_u$)	17.05 ($A^2\Pi_u$)

As a result, the total cross section of the exchange reaction will be equal to the product of the quenching cross section of the intermediate complex in the energy region below the ionization boundary of the *NO* molecule by the probability of its decay due to direct interconfiguration transitions with the formation of *NO*** molecule (see Fig.1). Note, that the reactions (1)—(4) should be accompanied by the Penning ionization process with the formation of ions, whose contribution to the overall picture must also be taken into account.

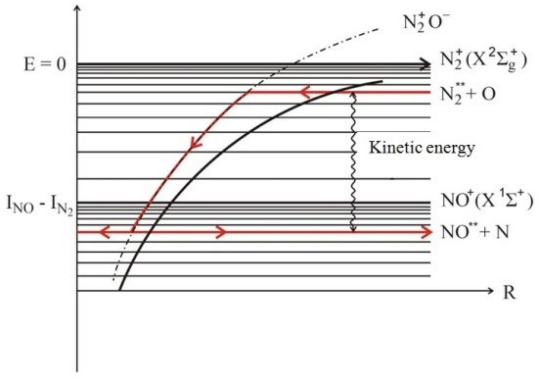

FIGURE 1. Scheme of harpoon mechanism for reaction (1).

Reaction (1)

The positive energy of the electron affinity in the negative ion $O^-(s^2p^4)$ is equal to 1.46 eV and corresponds to the bound state [2]. Resonances in the elastic scattering cross-section (i. e., negative affinity energies) are located starting from the electron energy of 9.82 eV and higher [3]. The ionization potential of N_2

molecule for the ground $X\,^2\Sigma_g^+$ state of N_2^+ ion is equal to 15.58 eV, for the first excited state is equal to 16.70 eV, and for the second one is equal to 18.75 eV, respectively (see Table 1). Therefore, for the $A\,^2\Pi_u$ configuration, only the excited vibronic Rydberg states with vibrational quantum number $v \geq 2$ contribute to the reaction (1). For $B\,^2\Sigma_u^+$ configuration, the resonance energy is $E_r = 1.51$ eV. Thus, two configurations of electronically excited states of the ion core participate in the process, which form a complex resulting picture of the spectrum. In this case, the total wave function of the intermediate ion configuration is a superposition of these states. The coefficients of the expansion of this function in the motion of fragments in the Coulomb potential behave randomly, i. e. there is a typical dynamic chaos with a lot of pseudo-intersections. Moreover, if we can use the modified optical potential theory to describe the first stage of the process (1) [4], a statistical approach will be required for the second decay stage.

Reaction (2)

The nitrogen atom does not have a positive affinity for the electron. The first resonance state $1s^2\,^2S^2\,2p^3$ (^{3}P), which was found experimentally, is located at $E_r = 0.057$ eV with resonance width $\Gamma_r = 0.0013$ eV [5]. It is this (shape) resonance that is dominant in the cross section for the elastic scattering of electrons by nitrogen atoms from the threshold to an energy of 0.5 eV [6], which is of the greatest interest to us. The positions of $2p^4\,^1D$ and $2p^4\,^1S$ resonances are 1.513 eV and 2.91 eV, respectively [7]. According to Table 1, in reaction (2), in addition to the vibronic electron-excited states $X\,^2\Pi_g\,(v>0)$ of the ion core of the O_2 molecule, electron-excited states $a\,^4\Pi_u$ and $A\,^2\Pi_u$ of O_2^+ ion and the excited states $b\,^3\Pi$ and $w\,^3\Pi$ of the ion core of NO molecule can also participate, followed by quenching of the ion complex $O_2^+ N^-$. In addition, non-adiabatic transitions must occur between autoionization states in the continuous spectrum, which must be accompanied by ionization with the formation of positive molecular ions. The spectrum of intermediate states here becomes more complicated than in the previous case, which will require further modification of the theory [4].

Reaction (3)

The nitrogen molecule (also like the nitrogen atom) does not have a positive affinity for the electron. In the elastic scattering of a slow electron by N_2 molecule, there is a well-known (shape) resonance $N_2^-(^2\Pi_g)$ with an energy of 12.3 eV [8]. There is also a series of resonances corresponding to vibrational excitation of the N_2 molecule [9]. The exchange reaction (3) with respect to the harpoon mechanism can occur here only with the participation of the Rydberg series, converging to the limit $O^+(2s^2\,2p^3\,^2P^0)$, the excitation energy of which, measured from the ground

state of the ion, is 5.01 eV [10]. The excitation energy of the next ion limit $O^+(2s2p^4\,{}^4P)$ is equal to 15.87 eV and considerably exceeds the energy of $^2\Pi_g$ resonance of N_2^- ion. Therefore, the cross section for reaction (3) will be much smaller than the cross sections for Penning and impact ionization and is of little interest.

Reaction (4)

Molecular ion $O_2^-(^2\Pi_g)$ has a positive affinity for an electron whose energy is 0.44 eV [1]. The first three vibrational states are bound. Higher vibrationally excited states exit into a continuous spectrum and are autoionization states. They make the main contribution to the reaction (4).

Note the most important features of the reactions (1)—(4). All of them are exothermic and are accompanied by the release of the kinetic energy of the products, which greatly exceeds the average temperature of the medium. Therefore, radiative processes involving NO^{**} molecules will lead to an additional broadening of the emission spectrum.

Aknowledgements: This work was supported by Russian Foundation for Basic Researches (Grant No. 16-05-00052-a).

1. G. V. Golubkov and G. K. Ivanov, Rydberg states of atoms and molecules and the elementary processes with their participation, Moscow: URSS, 2001.

2. Y. Itikava and A. Ichimura, Cross Sections for Collisions of Electrons and Photons with Atomic Oxygen, *J. Phys. Chem.Ref. Data*, 1990, 19, 3, pp. 637—651.

3. Yang Wang, Ya-Jun Zhou, and Li-Guang Jiao, Resonances in Electron Impact on Atomic Oxygen, Chin., *Phys. Lett*., 2008, 25, 6, pp. 2027—2029.

4. G. V. Golubkov, A. Z. Devdariani, M. G. Golubkov, Rydberg Atom A** Collision with an Atom in the Ground Electronic State. Optical Potential, *Journal of Experimental and Theoretical Physics*, 2002, 95, 6, pp. 987—997.

5. P. G. Burke, R. A. Berrington, M. Le Dourneuf et al., The $^3P^e$ Resonance in the Low-Energy Scattering of Electrons by Atomic Nitrogen, *J. Phys. B: At. Mol. Opt. Phys.,* 1974, 7, 18, pp. L531—L535.

6. P. G. Burke, R-Matrix Theory of Atomic Collisions. Application to Atomic, Molecular and Optical Processes, Berlin, Heidelberg: Springer, 2011.

7. T. Andersen, Atomic Negative Ions: Structure, Dynamics and Collisions, *Phys. Rep*., 2004, 394, pp. 175—313.

8. C. J. Gillan, O. Nagy, P. G. Burke et al., Electron Scattering by Nitrogen Molecules, *J. Phys. B: At. Mol. Opt. Phys.*, 1987, 20, 17, pp. 4585—4603.

9. C. J. Gillan, J. Tennyson, B. M. McLaughlinx et al., Low-Energy Electron Impact Excitation of the Nitrogen Molecule: Optically Forbidden Transitions, *J. Phys. B: At. Mol. Opt. Phys*., 1996, 29, 6, pp. 1531—1547.

10. R. R. Laher, F. R. Gilmore, Updated Excitation and Ionization Cross Sections for Electron Impact on Atomic Oxygen, *J. Phys. Chem. Ref. Data*, 1990, 19, 1, pp. 277—305.

ELECTROMAGNETIC AND OPTICAL PHENOMENA IN THE ATMOSPHERE INCLUDING LONG-LIVED AND PLASMA OBJECTS

Electromagnetic Radiation of Expanding Plasma in Air Environment

Leonid S. Chudnovskiy, Vladimir Yu. Krylov

Open Joint-stock Company "Research-and-Production Corporation "Precision System and Instruments", Aviamotornaya street. 53, Moscow, 112250, Russia

It was shown that thermionic currents of expanding plasma generate radial electrostatic field on its border which induce charge at microscopic dipoles in vapor drops of air environment. In this, emission area dimensioned in km is forming.

Electromagnetic radiation in the air of a high-temperature plasma is formed by electron-initiated fluxes: gamma rays, X-rays, thermionic emission, in the process of collisions of high-energy molecules.

The radiations of the Compton and delta electrons induced by the absorption of gamma quanta in the air are well studied and systematized in [1, 2]. Such emissions include:

— geomagnetic impulse (twisting Compton electrons in the Earth's magnetic field [1]);

— surface component of radiation (asymmetry of Compton currents up on reaching the Earth's surface [1]);

— barometric component (variation of the mean free path of gamma quantum with height [1]);

— an asymmetric component (the inhomogeneity of the emission of gamma quantum from the solid angle [1]);

— microdipole component (the appearance of an electron-ion microdipole at the moment of molecule ionization [2]).

The effect of air conduction on the formation of the radiation of the listed components was analyzed in [3].

However, the most energy component is the low-frequency radiation of high-temperature plasma [4]. In our opinion, electromagnetic radiation in the very low frequency range has a wider application, for example, electromagnetic radiation of collapsing fireballs in the Earth's atmosphere, radiation of an respond ball lightning etc. Let us consider a model of such radiation.

We shall assume that the plasma formation is spherically homogeneous with a sharply defined boundary changing its boundaries in time. With an increase in the plasma temperature, electrons will be injected from its boundary: collisions of high-energy molecules, thermionic emission, X-ray radiation. The scalar potential caused by the motion of an electron in the air at the point R will be [5] $\varphi(R) = = \frac{Ve}{c4\pi\varepsilon_0 \boldsymbol{R}}$ here **V** — velocity of the electron; **e** — electron charge; c is the speed of light; $\boldsymbol{\varepsilon_0}$ — dielectric constant of the vacuum. Since the emission of electrons with respect to the plasma radius $\boldsymbol{R_п}$ — spherically symmetric, we should expect a decrease in the scalar potential

$$\varphi_{\Sigma}(R) \approx \frac{\tau\rho VeR_{п}^{3}}{3Tc\varepsilon_0 R^2}, \quad (1)$$

$\frac{\tau}{\mathrm{T}}$ — the ratio of the electron $\boldsymbol{\tau}$ lifetime to one second T; $\boldsymbol{\rho}$ — change in the electron flux from the plasma boundary in time.

Expression (1) was obtained on the assumption of very low frequencies, when the influence of the time lag $\frac{2R_{п}}{\mathrm{c}}$ can be neglected. Expression (1) does not take into account the effect of the conductivity of the plasma on the potential component on the rear side of the spherical formation. However, taking into account the smallness $\frac{2R_{П}}{cf_{max}}$ expression (1) can be considered valid for further calculations. The vector potential can be ignored, since it is equal to [4] $A = \frac{V}{c}\varphi_{\Sigma}(R)$ and the ratio $\frac{V}{c} < 10^{-4} - 10^{-2}$ (for the energy of the emitted electrons is less than 10 eV).

The radiation of the system (1) will be high-frequency and insignificant in amplitude, but the presence of water molecules in the air medium can greatly enhance the electromagnetic radiation itself and transform its spectrum into a low-frequency region. In the air medium there are suspended droplets or single water molecules that are oriented along the electric field strength lines (1) and create electromagnetic microdipole radiation that form the electric field strength back to the distance from the source.The size of the radiation zone of such microdipoles is a few kilometers, which creates significant electromagnetic radiation at large distances. Under the influence of the potential (1), a dipole moment is formed on a droplet of water of size $\boldsymbol{l}$

$$d = \frac{4\pi\rho\tau e\varepsilon R_{п}^{3} l^3}{3TcR^3}, \quad (2)$$

here $\boldsymbol{\varepsilon}$- relative permittivity of water

At large distances L> R, the dipole radiation at the observation point L will be equal to

$$E(t) = \frac{d^{"}(t)}{4\pi c^2 |L-R|\varepsilon_0} \quad (3)$$

To estimate the radiation of the system of dipoles (2, 3), we take into account the change in the concentration of droplets with height **z** in a spherical coordinate system:

$$l(z) = l^3 e^{-\frac{z}{H}} = l^3 e^{-\frac{r\cos\theta}{H}} e^{-\frac{h}{\text{H}}}, \quad (4)$$

where: H = 6.3 km is the reduced height of droplet concentration in the atmosphere [6].

The value of the volume density $\boldsymbol{l^3}$ is estimated from the distribution of specific humidity 2—4 g / kg [6].

Figure 1 shows oscillograms of electromagnetic radiation for $\tau\rho V R_{\text{п}}^3 = = At^2 \exp\left(\beta t^{\frac{2}{3}}\right)$. The data in Fig. 1 show a change in the polarity of the radiation for altitudes of about 1.5 — 2 km, an increase in the radiation duration with the height of the source. The characteristic times of the radiation change are about 10 μs, which corresponds to the size of the emitted zone over 3 km.

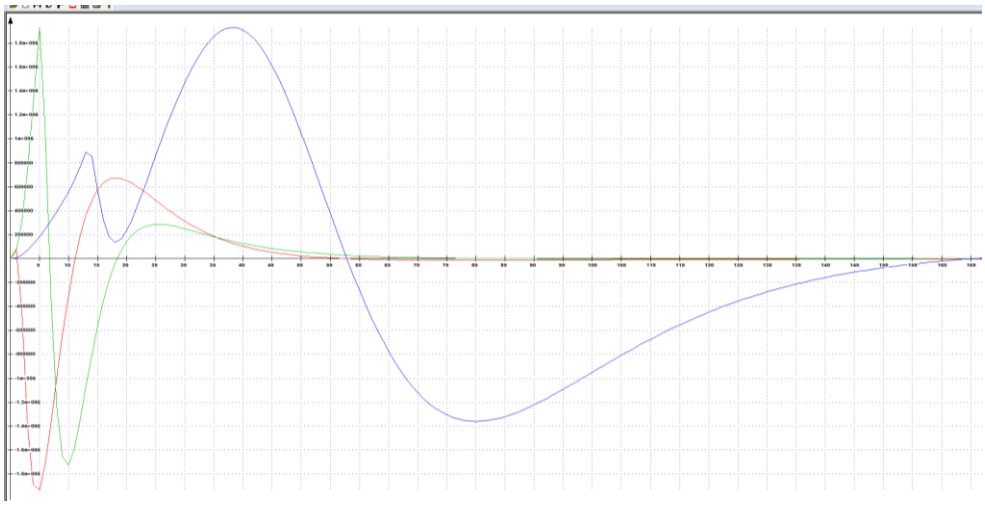

FIGURE 1. Electromagnetic radiation of high-temperature plasma in air for a source height of 700 m (the first pulse is negative), 3 km (the first pulse is positive), and a height of 8 km (the first pulse is positive with two maxima). Time in μc.

1. L. Chudnovsky, Electromagnetic Pulse in the Air by a Pulsed Flow off Gamma Rays, *AIS-2012 «Atmosphere, Ionosphere, Safety»*, Kaliningrad, July 24—30, 2012, pp. 136—142.

2. L. Chudnovsky, K. Mozgov, and S.Panov, Microdipole electromagnetic radiation induced by a powerful pulse of gamma quanta, *Chemical Phys.*, 2013, 32(11), pp. 23—25.

3. L. Chudnovsky and G. Golybkov, Forming of Conductivity of Airspace Exited by Pulse Streams of Gamma Rays, *AIS-2012 «Atmosphere, Ionosphere, Safety»*, Kaliningrad, July 24—30, 2012, pp. 217—219.

4. V. Kuvshinnikov, V. Pankov, and A. Shvedov, Electromagnetic momentum of a ground-based nuclear explosion, *Physics of nuclear explosion*, 1997, 1, pp. 85—119.

5. V. Levich, *Course of theoretical physics, vol.1, Theory of the electromagnetic field. Theory of relativity. Statistical physics. Electromagnetic Processes in Matter*, M.: Nauka, 1969, 969 p.

6. A. Matveev, *Fundamentals of General Meteorology. Physics of the Atmosphere*, Leningrad, 1965, 876 p.

The Humming and Motion of Ball Lightning I: Atmospheric Maser Spiking

Peter H. Handel and Klara E. Splett

Department of Physics and Astrnomy & Center for Nanoscience
University of Missouri-St. Louis, St. Louis MO 63131, USA

Introduction. Our Maser-Soliton theory of Ball Lightning (BL) was first introduced [1] in 1975. It was further developed in several conference proceedings papers [2] and in JGR [3]. This theory easily and accurately explains all observed properties oF BL as a solitonic and cavitonic repeated (quasi-periodic) spiking discharge in a huge atmospheric maser of several cubic miles, usually pumped by a streak lightning flash. The population inversion happens most likely in the energy levels of the atmospheric water molecules and aggregates.

The theory was further developed by the author in a 10-year cooperation with Russian scientists from the Kurchatov Scientific Center, which successfully verified the various steps in its derivations, and underpinned the analytical formulas of this author with extensive numerical calculations at the Kurchatov computer center. This cooperation involved Jiltsov and Skovoroda from the Kuchatov plasma institute, who were also responsible for the ITER plasma source, as well as the theoretician Timofeev and other members of that institute. It also involved Manykin, head of the Kurchatov solid state and superconductivity institute and his team.

Although it was known and described since antiquity and in spite of having been seen by 5% of the world's population, BL was never understood, giving rise to superstitions in some countries. Now we are able for the first time to understand its fascinating nature on the basis of our Maser-Soliton Theory (MST). BL is explained as a nonlinear quasistationary state of plasma and trapped electromagnetic field (Langmuir soliton), representing a high frequency (HF) discharge. The latter is in an antinode of a standing electromagnetic wave, fed by an atmospheric (most likely H_2O) maser that can be many cubic miles in volume and is caused by a field pulse associated with lightning. Due to a strange first property of BL that is explained for the first time by the MST, it was almost never seen by workers in the field of atmospheric electricity, causing them to become frustrated and to even doubt its existence, as it happened with Karl Berger in Switzerland. That property is its occurrence only when lightning strikes in a flat area, and its absence at high peaks of buildings or of the landscape.

Another, second, property of BL, now understood with the MST, prevented its generation in the laboratory. It is a peculiarity of large atmospheric masers, of their unusual load-line and ultra-short spiking rise time that allows for a new type of pulsed low-temperature electric HF discharge, even at atmospheric pressure. This is a unique low-temperature discharge at atmospheric pressure. Because of its low

temperature and negligible buoyancy force, and because of the mentioned second special property of the large volume maser, it remains quasi-stationary at an antinode of the standing wave generated by the maser, and only moves along the antinode in the direction of the decreasing degree of population inversion, as shown below. Finally, the peculiar final explosion that is often associated with the demise of open air BL, is also explained by the MST, as a final spiking phenomenon caused by the sudden disappearance of the load represented by the BL cavitonic soliton. BL provides our first contact with the awesome power of low frequency masers of very large volume, and with their mind-boggling properties caused by practically instantaneous avalanches of photons. The maser is most often caused by the very wide-spread field pulse associated with lightning on a flat landscape.

The new type of discharge will have countless civilian and military applications. The solution of the BL puzzle will allow us better protection against, and control of, the BL discharge. Furthermore, it will shine light on some other ill-understood natural phenomena such as larger luminous formations usually classified as luminous UFOs or radar angels. The MST will allow scientists from the fields of plasma physics, quantum electronics, nonlinear dynamics, for the first time to return to this field of atmospheric electricity, and atmospheric physics with a clear sense of purpose and mission. It will allow them to meet both the true dedicated scientists like Grigoriev, who have collected enormous data bases with observations of BL and those who have developed various models trying to explain the phenomenon, such as Nikitin and Bychkov. Together they now stand a better chance than ever before to successfully forge a new cooperation, to fully develop the science of BL, and to put it in the service of mankind.

Nonlinear System of Maser and HF Soliton. When lightning strikes on flat terrain, a strong homogeneous electric field pulse is present simultaneously in a large volume of moist air, of the order of cubic miles. As shown earlier [*Handel* 1988, 1989], this pulse can lead to homogeneous population inversion in the rotational energy levels of the H_2O molecule. Close to mountain tops, the electric field and the ensuing population inversion is limited to a cone-shaped volume, so this pulse does not lead to maser action without cavity walls. On flat terrain this field pulse will sometimes lead to maser action for a period of the order of seconds, due to the low rate of forbidden transitions between closely spaced pairs of rotational energy levels of the water molecule. The condition for this maser action to take place is that the gain G exceeds the loss L in the number of photons per time unit

$$dn/dt = G\text{-}L > 0, \qquad (1)$$

resulting in a net increase in the number of photons n first in a certain, well defined standing wave mode of oscillation of the decimetric electromagnetic spectrum, or in small number of modes of the same frequency. The loss term can always be represented in terms of an effective cavity lifetime τ_c, and in terms of an effective load lifetime τ_b, the load being represented by the caviton, i.e., by the visible ball

lightning (BL). In the open air case there are no cavity walls, at best some reflecting objects, such as the trees lining an opening in the forest. In the absence of any cavity walls and reflecting objects or boundaries, τ_c assumes the lowest value, of the order of L/c, where L is the diameter or characteristic size of the inverted volume which can be of the order of several miles. With L = 3 km we get τ_c = 3 km /(3 10^5 km/s) = 10^{-5} s, better than for resonant cavities with copper walls. The resonator theory was further done by Carlson [4]. On the other hand, on a high peak, such as K. Berger's observatory on Mount San Salvatore in Lugano (Switzerland) we have l≈10m and $\tau_c \approx 3\ 10^{-8}$ s, which precludes maser action. This explains why Berger never saw ball lightning. He acknowledged this in a personal letter to me.

Collisional deexcitation of molecules is in competition with stimulated emission. The latter wins sometimes because it is faster when it happens to go into a high-gain field mode.

The gain G is from stimulated emission, being proportional to the number N_2 of molecules present in the upper maser level E_2, and to n+1, i.e., roughly to the number of photons already present in the mode under consideration

$$dn/dt = K(n+1)N_2 - n/\tau_c - n/\tau_b \quad (2)$$

$$dN_2/dt = -KnN_2 - N_2/\tau_2 + R_e\,, \quad (3)$$

where we added also the rate equation for the upper maser level population N_2 in terms of the relaxation time τ_2 ($>>\tau_c$) of the upper maser level, a time which can be as long as a second or a minute, because the transition is, in fact, one of the many well-known strongly forbidden transitions between pairs of nearly coincident rotational energy levels of the H_2O molecule and is becoming only weakly allowed under the influence of perturbing fields. We also included an effective pumping rate R_e describing the rate by which in some cases the population inversion is replenished by various processes (such as, e.g., a circulation of inverted air through a barn, or recuperation of a hole burned into an inhomogeneously widened gain profile in the frequency domain).

In the quasi-stationary regime the time-derivatives are zero in equations (2)—(3). We can then eliminate N_2 and solve the resulting quadratic equation for n, with the result

$$n = (p/2)\{ r-1 + [(r-1)^2 + 4r/p]^{1/2}\} \approx p|r-1|\{\theta(r-1) + r/p(r-1)^2\}, \quad (4)$$

where $p = 1/K\tau_2$, $r = R_e/R_t$ is the reduced pump rate close to 1, $R_t = 1/\tau_2 K\tau$ is the threshold pump rate, and $\tau^{-1}=\tau_c^{-1}+\tau_b^{-1}$. We have introduced $\theta(x)$ which is 1 for $x>0$ and 0 for $x<0$. Here p is close to the number of field modes within the width of the maser line. This width is very large in our case. Therefore, p is a very large number of the order of 10^{20} and equation (4) describes an explosive growth of the number of photons n as a function of r, whenever r exceeds unity even by very little. Indeed, from the last form of Eq. (4) obtained for $p>> 4r/(r-1)^2$, we see that for $r>1$ but close to 1, we get $n \approx p(r-1)$ which is an enormously large number of the order of 10^{20}, for $r<1$ we get $n \approx r/1-r$ which may be a number from 1 to 1,000 for example, and for r=1 we have $n=\sqrt{p}$.

Precisely this explosive growth as a function of r (and also in time) is what happens at the start, at each of its fast spiking re-births, and also in the explosion often observed at the demise of an open air BL discharge. The demise causes τ_b to become suddenly infinite and therefore r to exceed unity considerably. A similar first spike thus initiates even the creation of the BL discharge, when the original population inversion is established by the initial lightning-generated field pulse.

In the hypothetical stationary case of a HF electric discharge at atmospheric presure Eqs. (2)—(3) an effective heat diffusion equation describing the BL must be added. The simplest form considered is

$$P = \alpha(T-T_o), \tag{5}$$

where α is a heat exchange coefficient and T_O is the ambient temperature of about 300K. Here we have introduced the power P absorbed by the BL from the standing wave of the main maser mode. This power is assumed to be ohmic as in previous experiments of Ohtsuki & Ofuruton (1991) as well as Zhil'tsov et al. (1995), although other forms of absorption such as multiphoton field-ionization of neutral atoms in the BL will also be present:

$$P = v\sigma_T nh;\ \omega/V = v\sigma_o(n/V)h;\ \omega e^{-I/2kT} = v\sigma_o(n/V)h;\ \omega e^{-I/2k(P/\alpha + T_o)}. \tag{6}$$

Here we have used the relation $E^2 = 8\pi nh;\ \omega/V$ connecting the squared electric field amplitude with the photon concentration n/V, where V is the volume of the atmospheric maser divided by a factor larger than 1 describing the solitonic localized electric field enhancement in the BL, and v is the BL volume. I is the ionization energy and k is Boltzmann's constant. We have assumed thermal ionization equilibrium at the temperature T in calculating the conductivity σ_T, although this is not likely to be exact for the cold (orange-colored) form of BL. Nevertheless, this approximation will give us already an approximate basis for developing the BL theory. The curve

$$n = [VP/v\sigma_o h;\ \omega]e^{I/2k(P/\alpha + T_o)}. \tag{7}$$

has a maximum, a minimum and a linear asymptote as shown in Fig 1. Indeed, setting dn/dP=0 we obtain

$$kP^2 + (2kT_o - I/2)\alpha P + k(\alpha T_o)^2 = 0 \tag{8}$$

with the discriminant

$$\Delta = I(I/4 - 2kT_o) > 0. \tag{9}$$

This inequality is satisfied, since I is of the order of 10 eV, much larger then kT_o which is 0.025 eV. Therefore we get the root

$$P_1 \approx \alpha I/2k \qquad \text{and} \qquad P_2 \approx (\alpha T_o)^2/[\alpha I/2k] = 2k\alpha T_o^2/I. \tag{10}$$

These roots define two branches of the curve in Fig. 1, corresponding to the two forms of BL.

Note that in our theory, P is related to T through a simple linear transformation and can be considered an equivalent variable with T. On the other hand, n is equivalent to the external power incident on the BL, Pi. Switching the axes, we obtain the T versus Pi diagram shown in Fig. 1 of the companion paper discussion.

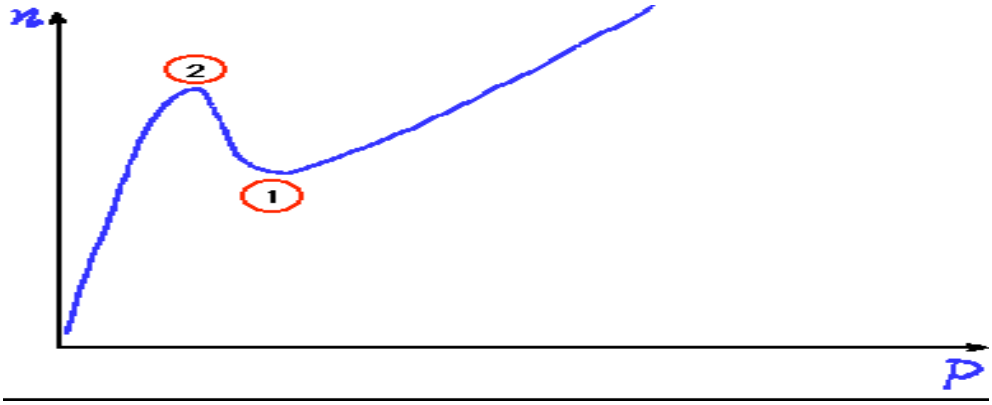

FIGURE 1. Photon number n of the maser versus power P absorbed in the BL.

Note also that replacing Eq. (5) with the other extreme case, energy transfer by radiation with $\beta(T^4-T_o^4)$, does not change the situation qualitatively, although the maximum and minimum are less pronounced and less separated.

1. P. H. Handel and J. F. Leitner, Development of the Maser-Caviton Ball Lightning Theory, *J. of Geophys. Research*, 1994, 99 (10), pp. 689—691.

2. P. H. Handel,"Maser-Caviton Ball Lightning Mechanism, *Proc. VIII Int. Conf. on Atmospheric Electricity*, Institute of High Voltage Research, Uppsala University Press, Uppsala, Sweden, 1988, pp.177—182.

3. P. H. Handel, New Approach to Ball Lightning, *Science of Ball Lightning (Fire Ball*), World Scientific Publ. Co., Yoshi-Hiko Ohtsuki, Editor,1989, pp. 254—259.

4. P. H. Handel, Maser-Caviton Ball Lightning Model: Comparison with the Known Observational Evidence, Maser Condition and Spiking, Proc. *II Int. Symposium on Ball Lightning*, 1990.

5. P. H. Handel, Development of the Maser-Caviton Ball Lightning Model, *Proc. 9th International Conference on Atmospheric Electricity,* 1992, pp. 826—829.

6. P. H. Handel, The Maser-Caviton Theory and Ball Lightning Phenomenoligy, *Proc. III. International Symp. on Ball Lightning, UCLA,* Springer Verlag, Inc., New York, Editor S. Singer, 1992.

7. Glenn A. Carlson, Handel's maser-soliton theory of ball lightning: the creation of stable three-dimensional cavitons by an atmospheric maser within an open resonator, *PhD Thesis, Univ. of Missouri -St. Louis*, 2012.

8. P.H Handel and K. E. Splett, *The Humming and Motion of Ball Lightning II*.

The Humming and Motion of Ball Lightning II: Discussion and Motion

Peter H. Handel, Klara E. Splett

Department of Physics and Astronomy & Center for Nanoscience
University of Missouri-St. Louis, St. Louis MO 63131, USA

Introduction. This paper derives the motion of Ball Lightning (BL) and then continues the discussion of the nonlinear system of a huge atmospheric maser and the BL soliton (caviton), started in the preceding (I) companion paper [1] present in this volume.

Consider the quasi-stationary state of ball lightning in open air, on flat terrain. In general, the occupation of the energy levels that are subject to possible population inversion due to a sudden, large, but short electric field pulse caused, e. g., by lightning, will not be perfectly uniform. As seen from the location of the BL, the population inversion may be slightly stronger in the cubic km on one side (#1) of the BL, than in the similar volume on the other side (#2) of the BL. Considering the direction of the gradient **g** of the population inversion in the region containing the BL, the side #1 is that, to which the small vector of the gradient points.This definition is applicable also in the absence of a population inversion.In that case, the gradient **g** points to where the absorption coefficient is lower.

In our Maser-Soliton theory [1]—[6], [8], [15], open air BL is a nonlinear (solitonic) system of plasma and field, fed by a giant atmospheric maser of several cubic km, usually caused by a lightning flash over flat terrain. The maser causes a standing electromagnetic wave in the space with population inversion. The solitonic HF discharge is initially ignited in one of the antinodes of this standing wave by a mechanism of resonance as was described in an earlier paper [11]. It then continues as a rapid sequence of extinctions and re-ignitions in the same antinodal place, with a repetition frequency close to the natural spiking frequency of the maser.

Standing waves. In particular, the waves originating in region #1 with **k** parallel to **g**, will be superposed on those coming from region #2, forming a standing wave **E**

$$\mathbf{E} = \mathbf{E}_o \exp i[\mathbf{k}\cdot\mathbf{r} - (\omega+s)t] + \mathbf{E}_o \exp i[-\mathbf{k}\cdot\mathbf{r} - (\omega-s)t]. \quad (1)$$

Here we neglect the slight difference in the amplitudes $\mathbf{E}_o$, and focus instead on the phases. We have denoted by ω the average frequency of waves generated in the maser volume. As is known, this frequency is slightly lower due to damping in the absence of a population inversion. When population inversion prevails, causing "negative damping", it is higher. This will be proven in Sec. 3 below by calculating the part of the phase velocity that is proportional to the population inversion.Assuming for simplicity the BL to be in the middle of the region

occupied by the standing wave, in Eq. (1) we have denoted by s the small deviation of the frequency ω+s of the waves in the #1 region from its average over both regions, ω.Then -s is a good approximation for the deviation from ω that is noticed in the #2 region..We can define the component parallel to k of a vector v, such that

$$s = \boldsymbol{k}\cdot\boldsymbol{v}; \qquad or v_k = s/k. \tag{2}$$

Then, the elementary standing wave becomes

$$\mathbf{E} = \mathbf{E}_o \exp i[\mathbf{k}\cdot(\mathbf{r} - \mathbf{v}\,t) - \omega t] + \mathbf{E}_o \exp i[-\mathbf{k}\cdot(\mathbf{r} - \mathbf{v}\,t) - \omega t] = 2\mathbf{E}_o\{\cos[\mathbf{k}\cdot(\mathbf{r} - \mathbf{v}\,t)]\}\exp i\omega t \tag{3}$$

This is a standing wave that is moving with a velocity v_k given by Eq. (2).The component of **v** perpendicular to **k** is left arbitrary. It can be determined by other factors, such as the direction of a prevailing wind, and by the boundary conditions affecting the standing wave at the surface of the earth and at the limit of the space occupied by the cloud and by the polarization catastrophe, if present.

Choosing the origin of the coordinate system at the location of the BL, for s=0 we can express the total electromagnetic field of the standing wave, including the BL, in terms of a cosine- Fourier integral, or packet of standing waves

$$E_{tot} = \int E(\boldsymbol{k}) \cos \boldsymbol{k}\cdot\boldsymbol{r}\, d^3x \tag{4}$$

centered on the origin. This is possible due to the assumed symmetry. With a small s different from zero, considering Eq. (2), this will become

$$E_{tot} = \int E(\boldsymbol{k}) \cos[\boldsymbol{k}\cdot(\boldsymbol{r} - \boldsymbol{v}t)] d^3x, \tag{5}$$

and the BL will start to move with velocity **v**, as we have shown, in the opposite direction of the gradient of the population of levels, defined above.

In general, therefore, we conclude that BL tends to move away from the region of larger population inversion, or towards the region with larger absorption coefficient. This may explain the seemingly erratic motion of BL, often along horizontal antinodal planes. It may also explain why open air BL is often seen descending from the clouds, in which 80% of the streak lightning activity is known to take place.Indeed, the population inversion is likely to be larger above.

For the motion of BL close to ground, the boundary conditions that determine the antinodal areas must be taken into account.This is true also for BL inside closed spaces, such as inside airplanes.

In general, in airplanes, the boundary conditions restrict the BL to the centerline in the passenger room. There is a general motion of the air from front towards the back of the plane.If there is a population inversion in that air, it will decay while the air slowly drifts to the end of the plane. Therefore, BL will move toward the back, away from the higher population inversion, with a speed that is likely to exceed the speed of the airflow.

Molecular Formulation. The preceding formulation can be expressed also more explicitly in terms of the dielectric function and quantum mechanical matrix elements. The permitivity is

$$\varepsilon = \varepsilon_o[1 + \chi(\omega)] = \varepsilon_o[1 + \chi'(\omega) + i\chi''(\omega)] \tag{6}$$

The susceptibility introduced by a population inversion N_n-N_m per unit volume on a molecular transition of frequency ω_{mn} and damping γ is

$$\chi(\omega) = -3i[e^2F_{nm}(N_n-N_m)]/\{m\varepsilon_o\omega_{mn}[\gamma_{rad} +2i(\omega-\omega_{mn})]\}, \quad (7)$$

where $\gamma_{rad} =1/\tau_{rad}$ must be replaced by the total linewidth $\Delta\omega_{mn}$ to include all forms of broadening. The oscillator strength F_{nm} is related to the molecular quantum mechanical matrix element r_{nm} and to the real molecular damping rate τ_{mn}

$$F_{mn} = 4\pi m\omega_{mn}r_{mn}^2/3h = \tau_{rad} /\tau_{mn} \quad (8)$$

The phase velocity is $v=c/n=c/\varepsilon_r^{1/2}$.Therefore, for $\chi<<1$ it can be written as

$$v=Re[c/(1+\chi'/2+i\chi''/2)]\approx c[(1+\chi'/2)]/[(1+\chi'/2)^2+\chi''^2/4]\approx[c/(1+\chi'/2)]\{1-\chi''^2/4(1+\chi'/2)^2\};$$

$$s\approx-c\chi''^2/4(1+\chi'/2)^3 - <-c\chi''^2/4(1+\chi'/2)^3>, \qquad \mathbf{v_k} = s\mathbf{k}/k^2. \quad (9)$$

The small difference present in $\omega=kv$ is given by the term χ''.The average $< >$ is over the whole maser volume of many cubic kilometers. Thus, we obtain $\mathbf{v_k} = = s\mathbf{k}/k^2$, with

$$\chi'/2=3[F_{nm}e^2(N_n-N_m)(\omega-\omega_{mn})]/\{m\varepsilon_o\omega_{mn}[(\Delta\omega_{mn})^2+4(\omega-\omega_{mn})^2]\}$$

$$\chi''=3[F_{nm}e^2(N_n-N_m)\gamma_{rad}]/\{m\varepsilon_o\omega_{mn}[(\Delta\omega_{mn})^2+4(\omega-\omega_{mn})^2]\} \quad (10)$$

This is proportional to (N_n-N_m).It proves the assertion made in Sec. (2) above, that the phase velocity contains a small term increasing with the population difference between the levels involved in the maser effect. The linear absorption/amplifica-tion coefficient is $\alpha =\omega\chi''/2c$.For balanced maser conditions, the losses caused by the end reflection coefficient r must equal the maser gain: $r^2\exp(-2\alpha L)=1$, or $\alpha L=\log r$. Therefore, we get $\chi''=(2c/\omega L)\log r$. Substituting into $\mathbf{v_k}$,

$$\mathbf{v_k}=-c(\mathbf{k}/k)[\ \chi''^2/4(1+\chi'/2)^3]=-(\mathbf{k}/k)[c^3(\log r)/\omega^2L^2(1+\chi'/2)^3] =$$

$$= -(\lambda/2\pi L)2[c(\log r)2/(1+\chi'/2)^3]. \quad (11)$$

With $\lambda = 0.5$ m, L =1 km, and $(1+\chi'/2)^3=2$, this yields v_k= 1m/s, in agreement with observations.

We conclude that the main cause of BL motion is the phase difference that can occur between the components of the standing wave feeding the BL. This has its cause in turn in small spatial variations of the level population difference, or population inversion. A 1m/s BL speed is found. The BL moves to lower inversion.

Discussion of the nonlinear system of maser and BL soliton (continuedfrom I).In the previous (I) companion paper [1], based on the simple assumptions of a linear heat diffusion relation $P=\alpha(T-T_0)$ for the absorbed standing wave power P and the temperature increase of the BL above the ambient T_0, we derived an energy balance equation (7) of I,$n = [VP/v\sigma_o h,' \omega]e^{I/2k(P/\alpha +T_o)}$. This n has a maximum, a minimum and a linear asymptote as shown in Fig 1 of that previous paper. By switching the axes, we obtain the T versus P_i diagram shown in Fig. 1 below of the

present paper. Here, as before, we have used the relation $E^2 = 8\pi nh,' \omega/V$ connecting the squared electric field amplitude with the photon concentration n/V, where V is the volume of the atmospheric maser divided by a factor larger than 1 describing the solitonic localized electric field enhancement in the BL, and v is the BL volume.I is the ionization energy and k is Boltzmann's constant. We have assumed thermal ionization equilibrium at the temperature T in calculating the conductivity σ_T, although this is not likely to be exact, in particular for the cold (orange) form of BL, since field ionization is always important in continuously resurrecting the BL.

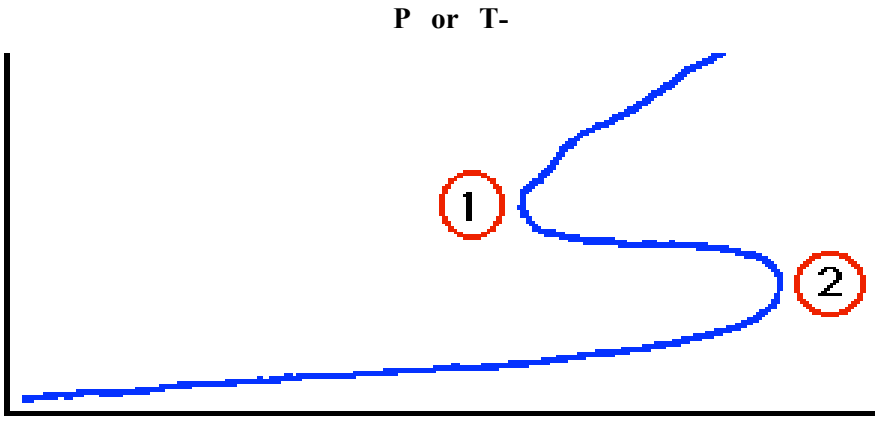

FIGURE 1. Relative temperature of BL discharge as a function of incident power or maser photon number n.

The roots $P_1 \approx \alpha I/2k$ and $P_2 \approx (\alpha T_O)^2/[\alpha I/2k] = 2k\alpha T_o^2/I$, from Eq. (10) of I define two branches of the curve in Fig. 1 above, corresp. to the two forms of BL.

Note that in our model, P is related to T through a simple linear transformation and can be considered an equivalent variable with T. On the other hand, n is equivalent to the external power incident on the BL, P_i. Switching the axes of the figure in paper I, we obtain the T or P versus n or P_i diagram shown in Fig. 1 above.

Let us assume now that we have r just slightly larger than 1 with a BL present as a load.Then n=(r-1)p. Since h; $\omega n/\tau_b$ is the load $P = v\sigma_o(n/V)h$; $\omega e^{-I/2k(P/\alpha+T_o)}$, we can identify τ_b as$1/\tau_b = \sigma_o(v/V)e^{-I/2k(P/\alpha +T_o)}$.

This result is substituted into the expression of R_t present in I, in the definition of r there, yielding

$$n = (r-1)p = p[r_o/(1+v\tau_c\sigma_T/V) - 1], \qquad (12)$$

where we introduced $r_o = R_eK\tau_2\tau_c$ as the reduced rate corresponding to a given pumping rate R_e in the absence of the BL load (for $\tau_b=\infty$).

Equating the two expressions of n in Eqs. (7) of I and in (12), we obtain the fundamental stationary BL equation

$$p[r_o/(1+v\tau_c\sigma_T/V) - 1] = VP/v\sigma_T h;\ \omega, \qquad (13)$$

or, for the linear heat diffusion case,

$$p[r_o/(1+vV^{-1}\tau_c\sigma_o e^{-I/2k(P/\alpha + T_o)}) - 1] = [VP/v\sigma_o h;\ \omega]e^{I/2k(P/\alpha + T_o)}. \qquad (14)$$

This equation determines the reduced equivalent pumping rate $r_o = R_e K\tau_2\tau_c$ that an atmospheric maser must have in order to sustain a stationary BL discharge with power dissipation P, heat convection coefficient α and volume v at an ambient temperature T_o.Substituting the roots defined in Eq. (10) of I, we obtain two limiting values of r_o, one for white and one for orange BL. These are the values corresponding to the end points of the hot (white or "1"-type) and cold (orange or "2"-type) BL state-branches, present in both Figs. 1, here and in I. More calculations are found in [10], also showing that the “forbidden” branch between points 1 and 2 of Fig. 1 can be stabilized with special feedback, as from masers. Instability is obvious there, because $dT/dn<0$.

1. P. H. Handel and E. K. Splett: "The Humming and Motion of Ball Lightning I: Atmospheric Maser Spiking" The companion paper in this volume.

2. P. H. Handel: “Ball Lightning and Atmospheric Masers” Subm. to JGR and Z. für Physik in 1975, so far unpublished.

3. P. H. Handel, Maser-Caviton Ball Lightning Model: Comparison with the Known Observational Evidence, Maser Condition and Spiking, Proc. *II Int. Symposium on Ball Lightning*, 1990.

4. P. H. Handel, Development of the Maser-Caviton Ball Lightning Model, Proc. 9th International Conference on Atmospheric Electricity, St. Petersburg, Russia, 1992, pp. 826—829.

5. P. H. Handel, The Maser-Caviton Theory and Ball Lightning Phenomenoligy, *Proc. III. International Symp. on Ball Lightning, UCLA,* Springer Verlag, Inc., New York, Editor S. Singer, 1992.

6. P. H. Handel and J. F. Leitner, Development of the Maser-Caviton Ball Lightning Theory, *J. of Geoph. Research*, 1994, 99, 10, pp. 689—10,691.

7. M. A. Uman, P. H. Handel, and J. Lowke,See the Scientific American Web Site www.sciam.com/askexpert/physics/physics30.html

8. P. H. Handel and J. F. Leitner, Theory of the Stationary Nonlinear Ball Lightning System of Fireball and Atmospheric Maser, *5th Internatl. Symp. on Ball Lightning, Aug. 26—29,* 1997, Tsugawa Town, Niigata Prefecture, Japan, Daito Insatsu Kogyo Co., Ltd. 1997, pp. 114—119.

9. P. H. Handel, Nonlinear Dynamics of the Polarization Catastrophe in Clouds and of the Atmospheric Masers feeding Plasma Solitons, *Proc. of the Internatl. Symp. on Nonconventional Plasmas, Niigata University, Niigata, Japan, Aug. 31 — Sept. 1*, 1997, pp. 1—2.

10. A. V. Zvonkov, A. B. Timofeev and P. H. Handel, On the Stability of Low temperature States of the VHF discharge at High Pressure, *Plasma Physics Reports*, 2000, 26(9), pp. 801—808.

11. P. H. Handel, New Approach to Ball Lightning, *Science of Ball Lightning (Fire Ball*), World Scientific Publ. Co,1989, pp. 254—259.

The Humming and Motion of Ball Lightning III: Experiments on the Maser-Soliton Theory and a New Cloud Electrification Process

Peter H. Handel and Klara E. Splett

Department of Physics and Astronomy & Center for Nanoscience
University of Missouri-St. Louis, St. Louis MO 63131, USA

Introduction. Our Maser-Soliton theory of Ball Lightning (BL) easily and accurately explains all observed properties of BL as a solitonic and cavitonic repeated (quasi-periodic) spiking discharge in a huge atmospheric maser of several cubic miles, usually pumped by a streak lightning flash [1—3]. The periodic extinction and reignition of the solitonic discharge causes the humming sound often observed at the spiking frequency of the large atmospheric maser, e. g., in the 50—100 Hz range. The description as a caviton emphasizes the self-trapping of the electromagnetic field and the expulsion of ions in the nonlinear dynamical system of plasma and field that defines the soliton ignited by the large atmospheric maser. The initiation of the solitonic discharge in the maser-generated standing electromagnetic wave is described in [4]. The quasi-stationary states of the plasma solitons are described [2] based on a nonlinear "Schrödinger" Eq. in a way similar to [5].The stability of these plasma solitons with size above a certain limit of the order of about 2 cm is proven in [6]., Finally, the experimental verification of the ability of these HF and microwave discharges to pass through glass panes of considerable thickness was demonstrated by Ohtsuki and Ofuruton [7].The study of similar solitonic discharges at lower pressure was performed by Schneider and Handel [8—10].

Experiments Suggested for the Maser-Soliton BL Theory.

Outdoors Experiment. Both during a thunderstorm and in cloudy, humid, weather without a thunderstorm, we will measure atmospheric absorption in the 300—1,000 MHz frequency region. This way we will determine the reduction in the ab-sorption coefficient, caused by the thunderstorm, as a function of frequency, as shown below in Fig. 1. The absorption coefficient could go to zero or even change sign at a certain frequency. This will identify the maser molecular transition of BL.

Pulse Experiment. We plan to apply a strong electric field pulse or other similar pumping agent inside a large metallic container with high H_2O vapor content, tunable as a resonator, and

a) Listen to VHF signals right after the pulse;

b) Measure a reduction in the absorption at certain frequencies, close to the resonance frequencies of the H_2O asymmetric rotor molecule;

c) Repeat the experiment with various levels of constant superposed electric field that may cause the many forbidden transition frequencies of H_2O vapor to become weakly allowed through Stark effect.

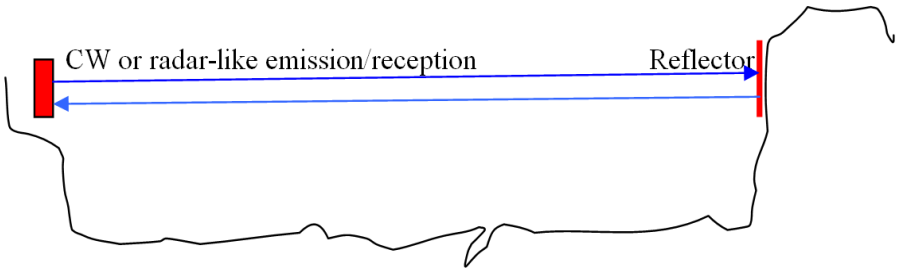

FIGURE 1. Atmospheric absorption spectrum measurements during thunderstorms, e.g. over a distance of 1 km, in a flat area, using a tunable VCO (voltage-controlled oscillator), or other generators.

At atmospheric pressure the resonance frequencies are broadened into oblivion by the large frequency of intermolecular collisions.We count in all cases on the frequency narrowing phenomenon present at high Q-factors of the cavity employed.The narrowing corresponds in the time domain to snatching the energy out of the "jaws" of the collisions due to the large volume of an atmospheric maser.The large volume causes both a large Q even without cavity walls, and an extremely short rise time of the maser signal (or spike).That ultra-short rise time is needed, in order to extract the energy before the collisions can dissipate it.

d) Therefore, in order to get an initial value of the practically important resonance frequencies, we plan to do the points a-c above also at low pressures, and with additional gain in the tunable resonance loop.That will allow tuning of the cavity to the resonance frequencies at lower collision frequencies, and will increase the chances of success as we gradually increase the pressure up to the atmospheric domain.Note that the collision frequencies scale like the square of the density, or pressure.We also plan to add electron-scavenging impurities to the H_2O vapor, in order to discourage the formation of electric discharges in the applied electric fields.

Wind Tunnel Experiment. This repeats a previously successful exploratory experiment of the author with 2 students at the McDonnell Douglas Lightning Research Facility (no longer existent here at Boeing) in the mid-seventies, and is in essence a different, stationary flow based, implementation of points a-d explained above for the static case.In this case moist air is rushed through a portion of a wind tunnel between a pair of capacitor plates parallel to the flow.The portion of the wind tunnel right after the plate has metallic walls and represents a tunable high Q electromagnetic Helmholtz resonator, from which the signal is coupled out, as in points a-d above.

Laboratory Ball Lightning Generation. The author's Maser-Soliton BL theory allows for the first time not only to understand the natural phenomenon, but also to emulate it in the laboratory.This represents a new type of discharge.

This experiment is based on a 10—20KW Klystron amplifier with negative feedback, trying to simulate the behavior of the atmospheric maser.The klystron is

connected through a directional coupler to a tuned resonator that serves as discharge chamber. From there, a wave guide completes the loop, as shown in Fig. 2. An optical feedback strengthens the natural tendency of the klystron to spike almost instantaneously when the load decreases. The discharge sought is a glow at atmospheric pressure, at much lower temperature than the lowest temperature arch discharge ever obtained so far at normal pressure.

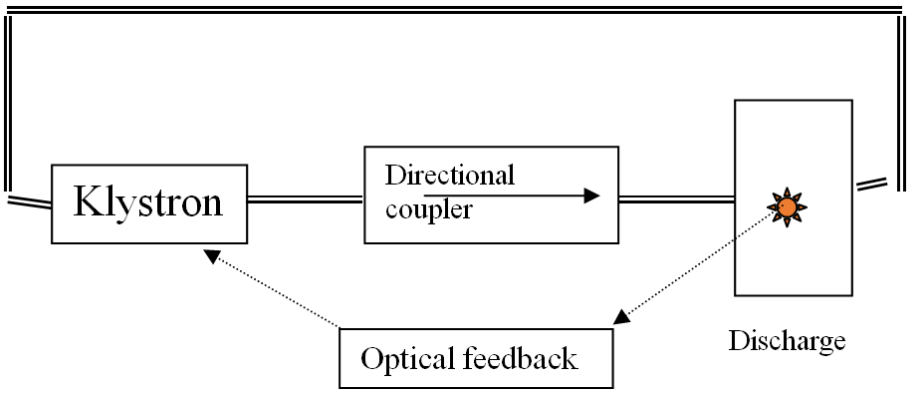

FIGURE 2. Scheme of laboratory ball lightning generation, emulating the atmospheric maser with a klystron.

At these low temperatures there are no electrons that could sustain the discharge. However, right when the discharge is dying, a powerful klystron spike is automatically caused by the sudden decrease of the load. This extracts electrons through cold (Fowler) emission, and rekindles the discharge. However, like in the case of the atmospheric maser, the presence of the large spike automatically stops the klystron power. The optical feedback is responsible in part for the fast reaction. Then the spiking cycle repeats itself. The continued quasi-periodic cycle of successive extinctions and re-ignitions causes the perceived "***humming***" of BL, often reported by direct observers.

The present BL maser-soliton theory can be expanded to explain the nature and the behavior of UFO-type luminous effects in the atmosphere and "radar angels."

New Cloud Electrification Mechanism. The maser-soliton theory of BL has to be considered together with the polarization catastrophe (PC) theory of cloud and thundercloud electrification [11]. This clarifies also the origin of the positive ionospheric potential and the origination of sprites, elves and blue jets, as we show below, after the description of our suggested BL experiments.

Submicron and micron size ice crystallites, all nucleated heterogeneously on aerosol dust particles (e. g., SiO_2 nano- or submicron crystals advected from desert areas) have a giant ferroelectric saturation polarization. Our theory is based on research by Hentschel [12], Hipolito [13], Minagawa [14] and Dengel [15], which was neglected so far. Therefore, when the concentration c of submicron ice

particles in a cloud exceeds $c_o=2.5\cdot10^{21}/\nu^2$ per cubic cm, where ν is an average number $\nu\cong10^{11}$ of water molecules per crystallite, i. e., for $c>c_o= 0.25/cm^3=25/l$, the PC occurs. Then the ice crystallites, all nucleated heterogeneously on aerosol dust particles (e. g., SiO_2 nano- or submicron-crystals, advected, e. g., from desert areas) align their dipole moments in the same direction. Thus, a large polarization vector field **P**(**r**) appears in the cloud. It has negative polarization charges –div**P** on top, positive on the bottom, since it was initially induced by the fair-weather field.

Due to the large average number ν of water molecules in a crystallite, the PC (Fig. 3) is present in practically all clouds, lowering the free energy. The PC gradually grows in size from raising moist air, together with the whole cloud, in the fair weather field. It will be continuously compensated by masking charges, up to the charge density divP, which compensates the polarization charge, during the few hours while the cloud grows: positive masking charges on top and negative at the bottom (Fig. 3). In cumulo-nimbus (or thunder) clouds with large vertical convection, the collapse of the PC is rapid, with the remaining masking charges leading to IC and CG lightning, and in the upper atmosphere also to sprites, elves, and blue jets. In the quiescent stratus clouds, however, the PC collapse is slow, and only leads to dark currents that also contribute to charging the earth negatively.

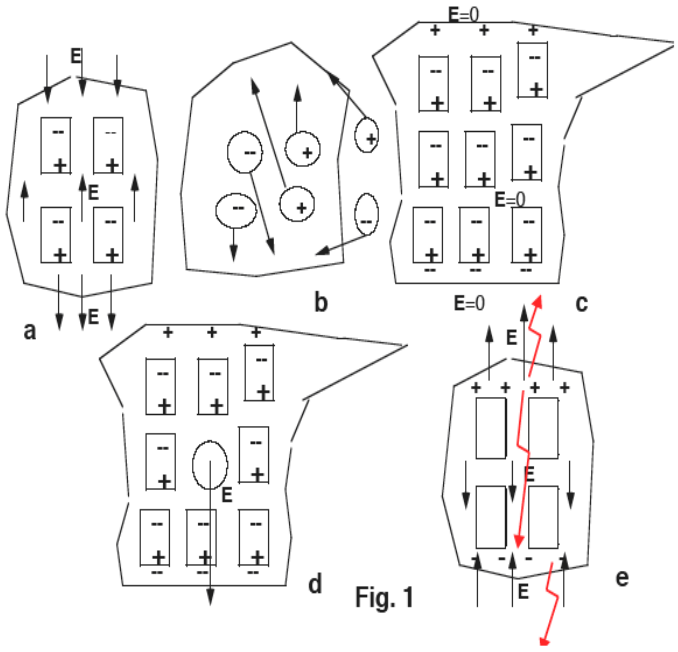

FIGURE 3. Generation ***a*** of the PC in the pre-existing fair weather field, masking charges ***b*** hiding it for hours ***c***, a large electric field E present ***d*** in a cavity betraying it, and the sudden colloidal instability setting free the masking charges ***d,*** thus contributing to atmospheric electricity ***e***.

The PC leads to reverse polarity in growing clouds (plus on the bottom, negative on top, because of the growing excess polarization charge), as compared with dissipating clouds (minus on the bottom, because of the growing uncompensated masking charges). This helps explain early, thin, charge-layers in terrestrial clouds, even with low rain rate, without excluding contributions from other mechanisms. It explains and proves as a natural instability the formation of many narrow horizontal space charge layers as detected with balloon-based instruments in the stratiform trailing region of mesoscale convective systems [16]. It also explains the electrostatic discharges in the C-ring of Saturn [17].

1. P. H. Handel, Maser theory of BL, *Bull. Am. Phys. Soc. Ser. II,* 1975, 20, 26.

2. P. H. Handel, New approach to ball lightning, *Science of Ball Lightning*, World Scientific, London, 1989, pp. 254—259.

3. P. H. Handel, and J. F. Leitner, Development of the Maser-Caviton Ball Lightning Theory, *J. Geophys. Res*., 1994, 99, 10, pp. 689—691.

4. P. H. Handel and R. T. Schneider, Nature of resonances leading to high-pressure cavitons, *Fusion Technology,* l985, 7, pp. 320—324.

5. V. E. Zaharov, Zh. Eksp. Teor. Fiz. 1972, 62, 1745 p.

6. E. W. Laedke, and K. H. Spatschek, Stable three-dimensional envelope solitons, *Phys. Rev. Lett.* 1984, 52, pp. 279—282.

7. E. W. Laedke, and K. H. Spatschek, Stability properties of multidimensional finite-amplitude solitons, *Phys. Rev.,* 1984, *A30,* pp. 3279—3288.

8. Y. H.Ohtsuki andH. Ofuruton, Plasma fireballs formed by microwave interference in air, *Nature,* 1991, 350, 139 p.

9. R. T. Schneiderand P. H. Handel, Neutron Emission by Plasma Cavitons, *Proc. of the 1982 IEEE Int. Conf. on Plasma Science*, IEEE Catalog No. 82CH1770-7, 97 p.

10. R. T. Schneider and P. H. Handel, Neutron Emission by Plasma Cavitons, *Fusion Technology,* 1985, 7, pp. 316—319.

11. R. T. Schneider and P. H. Handel, Fusion Reactions in RF Plasma Cavitons, *Proc. V. Topical Conf. on RF Plasma Heating*, Madison WI, 1983, pp. 109—112.

12. P. H. Handel, Polarization catastrophe theory of cloud electricity, *J. Geophys, Res*, l985, 90, pp. 5857—5863.

13. H. G. E. Hentschel, Ferroelectric Transition in Ice I_h, Molec. Phys. 1979, 38, 401 p.

14. O. Hipolito and R. Lobo, A study of Brout's Model for ferroelectrics; investigations on hexagonal ice, *Ferroelectrics,* 1970, 1, 169 p.

15. I. Minagawa, Ferroelectric phase transition & ε anisotropy in ice I_h, *J. Phys. Soc. of Japan,* 1981, 50*,* pp. 3669—3676.

16. O. Dengel, , U. Eckener, H. Plitz, and N. Riehl, Ferroelectric behavior of ice, *Phys. Lett,* 1964, 9, 291 p.

17. P. H. Handel, Proof of Cloud Instability With Respect to the Formation of Several Horizontal Space Charge Layers, *Proc. Chauzy & Laroche Eds.*, 2003, pp. 193—196, ISBN 2-7257-0008-6

18. P. H. Handel and P. B. James, Polarization Catastrophe Model of Static Electrification and Spokes in the B-Ring of Saturn, *Geophys. Res. Lett*., 1983, 10, pp. 1—4.

Ball Lightning — Heterogeneous Charged Plasmoid with Chemical Transmutation Reactions

Anatoliy I. Klimov

Laboratory for Heterogeneous Plasma Flow, Joint Institute for High Temeperature RAS, Izhorskaya str., 13 bld. 2, Moscow, 127415, Russia

Introduction. It is well-known that ball lightning (BL) decay or its explosion are connected with a creation of sub-micron particles, thin threads, ash particles and aerogel clumps (clots). These artefacts are named "angel hair" [1, 2]. It was reported that BL decay products are not stable. There is a chemical element transmutation of these decay samples at their heating in vacuum conditions. For example, initial chemical elements, such as, the aurum Au, the argentum Ag, the niccolum Ni, the cobaltum Co, the magnum Mn, the praseodymium Pr, the iridium Ir are transmuted to the molybdenum Mo, the beryllium Be, the sulfur S and others at their heating up to the temperature 2800 K. Some decay samples have strong magnetic properties. For example, the strong magnetized silicon plates were found after plasmoid's death [1].

We suppose that a real BL is a charged heterogeneous plasmoid (HP) and it consists of solid particles (liquid particles) and plasma halo. These charged solid particles interact each other and form a local dense kern inside plasmoid. So, plasmoid's kern stabilizes BL's spherical shape.Chemical element transmutation reactions are realized in this plasmoid's kern namely, [1]. These reactions are connected with energy release and high-energy charged particle creation (such as α-particles and β-particles). Radioactive BL with unstable radioactive isotope transmutation may be observed in nature. This radioactive BL can emit of neutron flux and γ-ray flux.

These hypothesizes connected with a creation of a natural HP and an artificial HP in laboratory conditions are discussed in the present work. Note that the physical properties of long-lived high energetic HPs were studied in our previous works [2—5]. It was revealed that these HPs have physical properties closed to BL's ones.

Experimental Set up. Plasma- chemical vortex reactor (PVR) for HP creation was considered in our work [3—5] in detail. This PVR consists of a swirl flow generator, a test section with electrodes, an output nozzle, a power supply and a diagnostic instrumentation. The following gas flow mixture is used in this reactor: water steam+argon. Maximal gas flow velocity is about of 30 m/s in this experimental set up. Tangential velocity of this swirl flow equals to its axial velocity.Static pressure is about of 1—2 Bar in the test section. Pulse repetitive electric discharge is used in this PVR to create heterogeneous plasma in test

section. The typical parameters of this discharge are the followings: mean electric input power 100÷1000W, pulse duration 2÷10000 μs, pulse repetitive frequency 1÷50 kHz, pulsed current 2÷20Amp, pulsed voltage — 1÷4 kV. The following parameters are controlled in our experiments: mass flow rate of a gas mixture M_g, electrical power N_e, mass erosion rate of a cathode material M_e, output heat power connected with heterogeneous plasma flow Q_T.

Experimental results. The typical HPs obtained in this PVR are shown in the figures 1. One can see that a constricted electric discharge (1) is obtained in swirl gas flow in the test section. This pulsed discharge streamer (1) strikes a cathode and produces its considerable erosion. Pure nickel (99.99%) electrodes and pure gas mixture (water steam+argon) are used in this work. This discharge creates many micro-metal droplets (2, cathode's erosion). These tiny droplets (2) interact with plasma discharge and they are evaporated.Plasma halo (3) consisted of metal nano-clusters is created around metal micro-droplet (2). In a result, spherical HP (4) with kern-droplet (2) and plasma halo (3) are created near cathode. The typical HP's diameter is about of several mm ÷ cm. This HP is a negative charged formation. The typical electrical potential of this HP is about of (2—4) kV. This charged HP moves against swirl flow from a cathode to an anode in the external electric field. It is revealed that this charged HP is a virtual cathode of a pulsed discharge. Really, anode streamer strikes HP in the first step and then it strikes a real cathode in the second step, figure 1. Analysis of high-speed video proves this conclusion. This streamer finds and strikes any HP arranged in any local position of a test section (near axis of discharge or far from this line).It is revealed that there is a transmutation of the chemical elements in a local HP (4) namely. For example, it was obtained that there are the optical lines of the cuprum Cu I in HP shown in the figure 1 (but not nickel optical lines). High-speed video frames of HP's evolution in time and space are shown in the figure 1. One can see that there is a destruction of HP's plasma halo and a formation of naked droplet nuclear.

We use a sedimentation method in water bathto accumulate nano-cluster particles from HP. Heterogeneous plasma flow from PVR's nozzle moves through water bath and dusty particles are separated from gas flow. Then water with these dusty particles is evaporated and nano-cluster sediment is analyzed by a chemical method, SIMS method and IMS method.The typical chemical composition of the dusty particles from HP is shown in the table 1. One can see that there are considerable concentrations of the cuprum Cu, the silicon Si, the ferrum Fe, and other component (but not nickel atoms only). Remind that pure nickel electrodes used in our experiments.

It is revealed that there isan extra heat power Q_T in this reactor (comparing with input electrical power N_e). The typical value of extra heat power Q_T is about of 2÷10 N_e. The flow mass rate of erosive cathode material M_e is about of 1 mG/s. So, the typical value of a specific heat release $q= Q_T/M_e \sim 1$ KeV/atom. This value is much higher than the typical one connected with traditional chemical reactions.

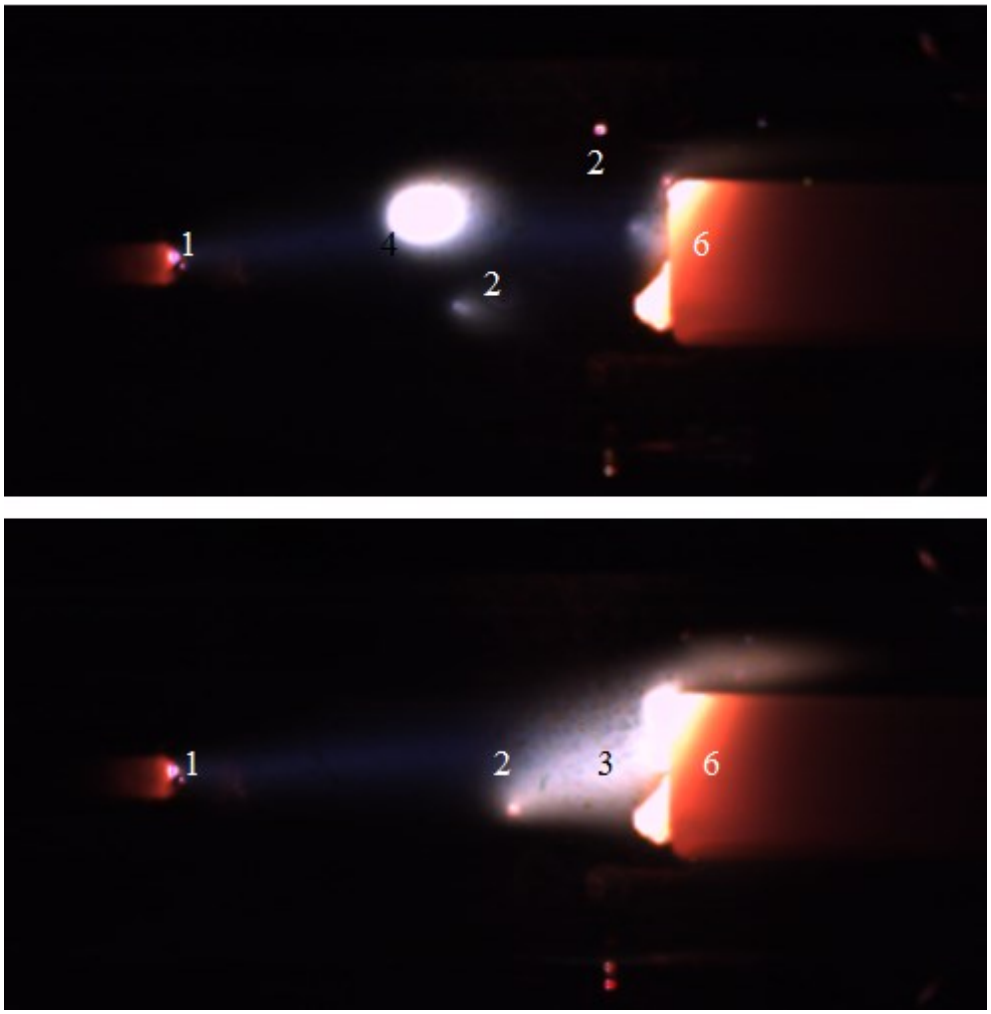

FIGURE 1. HP's evolution in the PVR test section. Swirl flow velocity — 10m/s. Mean electric power — 500 W. Gas mixture: argon+water steam= 1:1. Anode streamer — 1, plasma halo — 3, micro-droplet — 2, HP — 4, cathode — 6.

TABLE 1. Composition of dusty particles from PVR. IMS method. Nickel electrodes (99.99%)

	Si	Ni	Fe	C	Al	Cu	Co	K	Mg
Atom concentr., %	50	14,7	8,9	8,8	6,2	5,1	1,8	1,3	0,4

Soft X-ray radiation from HP was recorded by spectrometer X-123 [5]. Analysis of X-ray spectra shows that there is a continuous spectrum with the

maximum pike E ~ 1÷1.5 KeV and the separate Kα- lines ofdifferent chemical elements, such as the carbon C, the oxygen O, the nitrogen N, the fluorine F and others. The first three lines are connected with excitation of air molecules near reactor's nozzle, but the fourth line may be connected with the oxygen transmutation. It is important to note that extra heat release in PVR is obtained at maximal X-ray radiation from HP. So, X-ray sensor can record optimal regime operation of the PVR reliably.

The measurements of warm neutral particles (like neutrons) from HP by He3 – sensors and standard neutron radiometer "KRAN" are fulfilled today. High value of neutral particle flux 50000 imp/s is recorded by these sensors. This value is higher the background one more than 1000 times. This maximum value of a neutral particle flux is recorded by these sensors at the definite additives in nickel electrode such as the cadmium Cd, the lithium Li, the indium In and others. Remind that these chemical elements have enormous cross sections of warm neutron capture namely.

It is revealed that some HP have very strong magnetic properties.This plasmoid attracts with external magnetic field very effectively. The value of a magnetic induction used in this experiment is small one about of B=0.1T.

It is obtained that there is a cheap hydrogen production in this PVR. Its commercial coast is about zero.The cheap hydrogen production connected with two main factors:- non-equilibrium water steam dissociation by fast discharge electrons and a considerable plasma heating up to 4000—5000K by the interaction of hydrogen ions with metal nano-clusters.

Discussion. Hydrogen atoms and ions play important role in HP's physics. It was revealed that interaction of hydrogen ions accelerated in a cathode region with metal nano-clusters is responsible for an extra heat energy release, a soft X-ray radiation and strong magnetic properties of HP namely. Two main physical mechanisms help us to explain of unusual HP's properties.

Mechanism #1.The existence of a bound state of a proton and a heavy atom is predicted in the work [6]. The electrons screen the field of the proton, which suppresses the repulsive force between the proton and the atomic nucleus. On the other hand, the force of attraction between the proton and the electrons is directed along the electron density gradient (towards the nucleus). It is found that the potential energy minimum of the proton with a depth of several tens eV (or hundreds eV) lies in the range of negative energies (attraction). It is proposed that such a system be referred to as a binuclear atom. It is emphasized that in contrast to molecules, in which binding with the hydrogen atom is ensured by a rearrangement of the states of the outer shell (valence) electrons, a binuclear atom is formed as a result of the collective response of the system of inner electrons to the proton potential. This mechanism may be responsible for soft X-ray radiation in our experiment.

Mechanism #2. Hydrogen atom is transformed into hydrino's state by the help of "resonant catalysis" with resonant partner atom [7]. This partner atom can obtain a considerable mechanical energy from hydrino during their interaction. Then this partner atom transforms this mechanical energy to thermal gas energy. The typical

values of hydrino's energy levels are about of 100—10000 eV. The minimal hydrino's diameter closes to Compton's diameter. This thermal energy connected with "resonant catalysis" can explain a large value of extra heat energy release obtained in the PVR. This mechanism may be responsible for unusual optical spectra from HP also [5].

Acknowledgemens. Author thanks my colleagues for the help in this experimental work and fruitful discussions: prof. Bychkov V., prof. Nikitin A., prof. Bazhutov Yu., Tolkunov B., Belov N.

1. Multilingual, Web-Based, Free-Content Encyclopedia, wp.wiki-wiki.ru/wp/index.php/*Incedent on height 611*

2. V. Bychkov, A. Klimov, A.Gridin, On the Nature of the Artificial Ball Lightning, *High Temperature*, 1994, 32, pp. 190—194.

3. A. Klimov, Vortex Plasmoids Created by High_Frequency Discharges, *Atmosphere and Ionosphere: Dynamics, Processes, Monitoring*, Springer, Berlin, 2013, pp. 251—271.

4. A. Klimov, N. Evstigneev, I. Moralev et.al., Vortex Control by Combined Electric Discharge Plasma, *AIAA Paper 2013-1046*, 51th AIAA Aerospace Sciences Meeting, Dallas, Texas, 2013, pp. 1—15.

5. A. Klimov, A. Grigorenko, A. Efimov, et.al.,High-energetic Nano-Cluster Plasmoid and Its Soft X-ray Radiation, *J. Condensed Matter Nucl. Sci*, 19, pp. 1—10.

6. V. Chalyi, V. Gurevich, M. Pogorelsky, Binuclear Atom as the Bound State of a Proton and Heavy Atom, *Techn. Phys*., 2009, 54(2), pp. 159—164.

7. R. Mills, Hydinos and BlackLight Process, *Proc. Intern. Workshop*, Milan, Italy, 2003, pp. 1—95.

Natural and Artificial Long Living Luminescent Objects

Vladimir L. Bychkov

Lomonosov Moscow State University, Moscow, Russia, e-mail: bychvl@gmail.com

Nowadays one can attribute several types of phenomena to natural long living luminescent objects (LO) in atmosphere besides flashes of thunderstorm lightnings, and sprites and elfs, typical for middle atmosphere. They are: ball lightning (BL), St. Elmo's fires (SEF), Hessdallen and other lights, complex phenomenon accompanied with appearance of crop circle (CC), UFO, and gelatinous meteors (GM). We call them all (LO). This report is devoted to short review of the last events of LO observation, their analysis, experiments on their modeling and theoretical models.

During the last two years since 2016 (the previous symposium) events have occurred with varying intensity devoted to the study of these phenomena. We will discuss the works known to us. The collection of observational data on ball

lightning continued in [1—3]. Every year, in personal interviews, in the Internet or in the literature, there are 10—15 cases that were not previously described in the scientific literature. Of the interesting can be noted: the passage of BL through the walls and glass without visible traces in a wide variety of conditions; frequent interactions of CMM with humans and animals, leading to their death and injury. In [4] information appeared about strange luminous objects in the PO river valley in northern Italy. These objects were observed in a variety of forms, colors and durations, depending on the location. The author connects the appearance of BL and anomalous luminous formations in the atmosphere, both with the presence of hydrocarbons in the environment, and with continuing tectonic activity.

In [5], properties of BL were investigated on a basis of photographs of BL. Methods for the analysis of such information have been developed.

In [6], experiments were carried out to simulate an interaction of BL with a glass by heat release in some definite area, when cylindrical pieces of glass fall out as a result of the interaction. Studies have shown that BL should have a number of properties (including the high thermal power in the interaction) and a method of contact with the glass. In [7], was studied a glass through which the BL had passed without leaving a visible trace. Studies have shown that an opening with a diameter of ~ 0.2 mm emerged through the interaction, through which the BL consisting of small elements could flow.

In [8—9], investigations of the interaction of capillary discharges with various metallic samples were continued with the aim of obtaining LO possible analogues of BL. It is shown that in some cases objects with a shell of a metal filled with a vapor appeared. The aim of the research is to elucidate the physical conditions under which a shell of a luminous object appears under nonequilibrium plasma conditions.

In [10], a study of the Gatchina discharge, which was often advertised as BL, was continued. Experimental studies in which volt and ampere characteristics were obtained in time and a detailed video survey parallel to a numerical simulation showed that the luminous object is a vortex of a gas heated in the discharge near the upper electrode area.

The paper [11] is devoted to the analysis of high-energy BL. It is shown that BL is a unipolar object. On it, in the presence of a shell, a polarization of charges in the shell can occur under the action of the BL charge, and the conditions can be realized for which the Coulomb repulsion force of the charges is smaller than the polarization compression force. It is shown that such properties are possessed by BL of the dynamic capacitor type [11] and BL, which has a shell filled with a vapor [12].

In the case of UFO, which are currently considered as products of the existence and destruction of aircrafts/cosmic apparatus or optical illusions, the BL models developed in [11—12], which do not have size limitations, show that BL can be one of the UFO types.

Studies of corona discharges [13] interaction with liquids, components of the Earth ground and some materials show that luminous formations can be generated on protrusions and needles, as well as on the surface of charged liquids, with the development of electro-hydrodynamic instabilities [14]. The luminous structures

appearing at the same time, can represent luminous drops of destructible fluid structures which in [14] are considered as one of the SEF type. However, in our [13] experiments, large luminous formations of 1 cm or more were not obtained.

Recently [15], attention has been attracted to, so-called, crop circles, arising in the summer during a thunderstorm activity, often with the appearance of BL. It was shown in [16—17] that such phenomena can be associated with the appearance of strong electric fields as a result of the polarization of plant stems in external electric fields of the Atmosphere. In this case, local heating can occur due to the plasma-chemical processes in the resulting plasma, which ultimately lead to the destruction of the stems.

A similar reason can have the Hesdallen lights and other known lights, when local formation of plasma at the tips of subjects can cause air heating and subsequent ignition of the subject.

During the period under review, there were no fundamentally new data on gelatinous meteors [18], and no new models of this phenomenon have appeared.

1. Bychkov V.L., Toporov A.A., Yakovlev A.Y. Ball lightning Description of observations, 2015. *Materials of 22-nd Russian conference on cold transmutation of chemical elements nuclei and ball lightning*. Dagomys, Sochi, Krasnodar area, Sept.27 — Oct. 4, 2015, Moscow -2016, M: AIR, 2016. P. 204—216.

2. Bychkov V.L., Bikmukhametova A.R., Nikitin A. I., Nikitin A. I. Observation of Ball lightning, 2016. *Materials of 23-d Russian conference on cold transmutation of chemical elements nuclei and ball lightning*. Dagomys, Sochi, Krasnodar area, June.19—26, 2016, Moscow -2017, M: MATI, 2017. P. 176—189.

3. Bychkov V.L., Bikmukhametova A.R., Nikitin A. I., Nikitin A. I. Observation of Ball lightning, 2017. *Materials of 24-th Russian conference on cold transmutation of chemical elements nuclei and ball lightning*. Dagomys, Sochi, Krasnodar area, Sept.17—24, 2017, Moscow -2017, M: MATI, 2017. P. 30.

4. Straser V. Ball lightning, oilfields and earthquakes *New Concepts in Global Tectonics Journal*, V. 4, No. 3, September 2016. www.ncgt.org.

5. Nikitin A. I., Velichko A. M., Nikitina T. F., and Stepanov I. G. Methods of determination of ball lightning parameters based on the analysis of their photos. *2-nd International Symposium on Lightning and Storm — Related Phenomena Aurrillac*. 10 — 11 May 2017. France. 2017.

6. Bikmukhametova A.R., Bychkov V.L.,Nikitin A.I., Nikitina T.F., Velichko A.M., Stepanov I.G. Experimental modeling of ball lightning interaction with window glasses. *Proc. of 24 Intern. Conf. Electromagnetic field and Materials*. Moscow 16—19 Nov. 2016. P. 260—263.

7. Bychkov V. L., Nikitin A.I., Ivanenko I.P., Nikitina T.F., Velichko A.M., Nosikov I.A. Ball lightning passage through a glass without breaking it. *Journal of Atmospheric and Solar–Terrestrial Physics*. 2016. V. 150—151, P. 69—76.

8. Bychkov V.L., Chernikov V.A., Osokin A.S., Vaulin D.N. Energy of long –fife luminescent formations created with a help of the capillary discharge. *Abstracts.15th Intern. Workshop on Magneto-Plasma Aerodynamics*. Moscow. April 19—21. 2016. P. 185—186.

9. Bychkov V.L., Chernikov V.A., Taranenko S.O., Abakumov V.I., Vaulin D.N. Obtaining of long-lived luminous formations under an influence of erosive discharge plasma on metals. *XLIY International Zvenigorod Conference on Plasma Physics and Controlled Thermonuclear Fusion*. 13—17 February. 2017. Zvenigorod. Moscow. ZAO NTC "PLAZMAIOFAN", 2017, P.287.

10. Bychkov V.L., Anpilov S.V., Savenkova N.P., Stelmashuk V., Hoffer P. On modelling of “plasmoid” created by electric discharge. *Euler readings, MGOU-2017*. Nov.21—22. Moscow. 2017

11. Nikitin A. I., Bychkov V. L., Nikitina T. F., Velichko A. M., and Abakumov V. I. The sourcesand components of bases of ball lightning theory. *Euler readings, MGOU — 2017*. Nov. 21—22. Moscow. 2017.

12. Bychkov V.L., Abakumov V.I. Model of thermal ball lightning. Complex systems of charged particles and their interactions with electromagnetic radiation. 15-th Intern. Workshop. Moscow. Russia. April. 5—7. 2017. P.46. OOO «Online copy ». *Abstracts.15th Intern. Workshop on Magneto-Plasma Aerodynamics.* Moscow. April 19—21. 2016. P. 185—186.

13. Bychkov V.L., Abakumov V.I., Bikmukhametova A.R., Chernikov V.A. On electro-hydrodynamic effects over liquids under influence of corona discharge. *Euler readings, MGOU-2017*. Nov.21—22. Moscow.2017.

14. Grigor’ev A.I., Sinkevich O.A. On a possible mechanism of St. Elmo lights appearance. *ZhTF*. 1984. V. P. 1276—1283.

15. Abakumov V.I., Bikmukhametova A.R., Bychkov V.L., Safronenkov D.A., Chernikov V.A., Mikhaylovskaya T.O., Dolgoruky A.M., Shvarov A.P. Interaction of long-lived luminous formations with the Earth's surface. *Materials of the 25th International Conference "Electromagnetic Field and Materials"*. Moscow on November 24—25, 2017. Moscow. Infra M.S.538-554.

16. Ardelyan N.V., Bychkov V.L., Golubkov G.V., Kosmachevskii K.V. Air plasma parameters in seismic conditions. *Proc. 16th Workshop on Magneto-Plasma Aerodynamics. Ed. V.A. Bityurin*. Moscow, JIHT RAS, 2017. P. 118.

17. Ardelyan N.V., Bychkov V.L., Kosmachevskii K.V. Theoretical Analysis of Ionization in Long-Term Air Discharge Plasmas at Atmospheric Pressure. *IEEE Transactions on Plasma Sci. 2016*. V. 44. N. 11. P. 2530—2535.

18. Bychkov V.L., Atmospheric gelatinous meteors. The Atmosphere and Ionosphere: Elementary Processes, Monitoring and Ball Lightning. Eds. V. Bychkov, G. Golubkov, A. Nikitin. Springer. 2014. P. 369—384.

Production of Long-Lived Plasma Structures Using Capillary Discharge

Victor. I. Abakumov, Vladimir L. Bychkov, Adliya R. Bikmukhametova, Vladimir A. Chernikov, and Daniil A. Safronenkov

Faculty of Physics, Lomonosov Moscow State University, 119234, Moscow, Russia

Introduction. Investigation of large (up to 2 cm and more in diameter) luminescent heterogeneous structures, the so-called long-lived plasma formations (LLPF), is of significant interest for low-temperature plasma physics [1], both in terms of determining conditions and thermodynamics of such structures creation in non-equilibrium conditions, and from a point of view of their possible applications in plasma aerodynamics [2].

In this paper, a heterogeneous luminescent formation with a thin shell under action of an erosive plasmatron plasma jet on various materials, including metals covered with a film of alcohol or glycerin, was performed. A scheme of the experimental device is shown in Fig. 1.

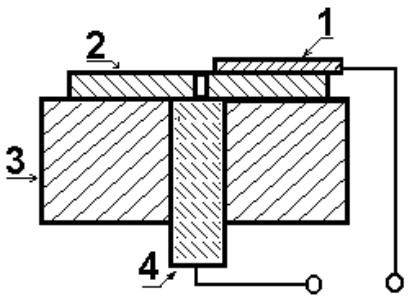

FIGURE 1. Capillary plasmatron: 1, 4 — electrodes, 2 — dielectric plate with a capillary (discharge chamber), 3 — a base of plasmatron of organic glass.

We identified conditions under which a lifetime of objects with a shell and a vapor nucleus reaches 4 seconds. Experiments were carried out to obtain LLPF based on the alloy of tin and lead, pure tin, pure lead and pure copper using the erosion plasmatron with energy input of about 190 J during an action a time of ~ 10 ms. A dependence of the number of LLPF on parameters of the installation was studied.

Conditions (a diameter of a plasmatron channel, an angle of the jet action on a metal target) at which several dozen LLPF arise are determined. It was found that when the plasmatron jet interacts with materials moistened by various liquids, a number of LLPF and their size change. In particular, glycerol leads to increase both of an amount and size of LLPF, while alcohol, on the contrary, reduces these characteristics.

In Fig. 2 typical trajectories of LLPF obtained in experiments are presented. Fig. 3 shows traces of the molten droplets and tracks of explosive LLPF. According to [3] it is the cover (shell) presence that allows to explain LLPF explosion when it falls on a substrate.

FIGURE 2. Typical paths of LLPF.

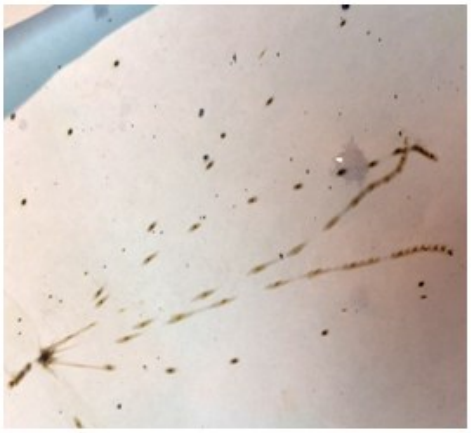

FIGURE 3. LLPF tracks.

Because of the objects fragility we studied various conditions and ways of LLPF shell conserving. In Fig. 4 one of the experimental setup arrangement variants is shown. It allows to separate fragile formations and to conserve objects with a strong shell.

The plasmatron capillary was directed downwards, and shells of LLPF, produced by interaction of a plasma jet with metal samples at LLPF contact with a liquid have been destroyed; only the strongest left.

Experiments were also conducted when the erosive plasmatron capillary was directed upward (Fig. 5). We tried to conserve whole shells by catching LLPF by various liquids (alcohol, glycerin, water).

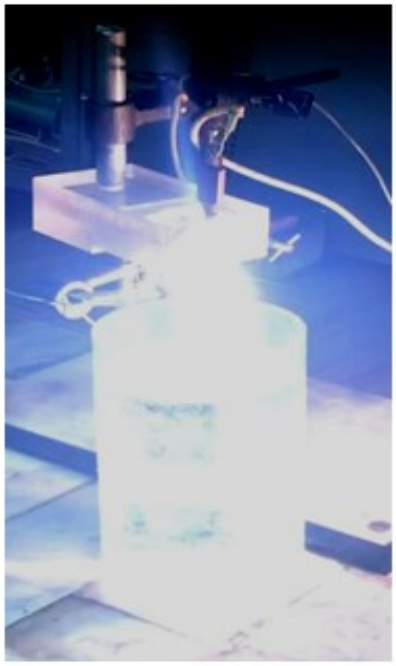

FIGURE 4. Plasmatron capillary directed downwards.

FIGURE 5. Capillary upwards.

In Fig. 6 the resulting cover of LLPF is presented, and in Fig. 7 the shell and the "core" from the solder POC-61 dropped out of it.

In Fig. 8 conserved shells and tracks obtained over these liquids are shown. It was possible to keep the whole shells for a week, after which they have been destroyed. Oil and glycerin were used to save the whole shells.

Some experiments were carried out with thin polymer membranes, with one side sputtered by a metal. Principal differences were found at plasma jet interaction with the sputtered side and with the side of the polymer membrane. In case when

the polymer side is closer to the jet, the membrane melts, but does not burn; when the side of the metal sputtering is closer, it burns out. In Fig. 9 the interaction result is presented.

FIGURE 6. The envelope of the LLPF.

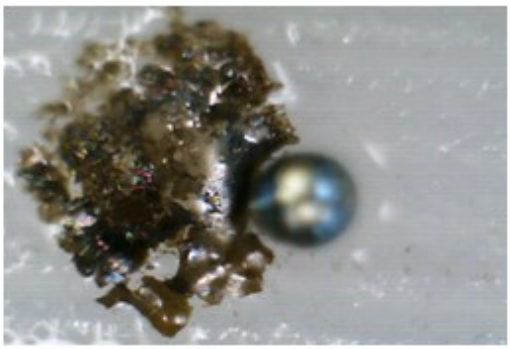

FIGURE 7. Shell and "core" (of~600 mcm diam.)

FIGURE 8. Saved shells and tracks of LLPF.

FIGURE 9. Results of interaction of a jet with a thin membrane.

Experiments have been carried out on interaction of the capillary discharge plasma with soil and soil-like objects of various compositions. Parameters of heating and plasma, under which it can affect the soil, are determined. Natural studies of the monolith of chernozem of the pre-Caucasian leached and model studies of typical chernozem, clay and sand have been carried out and changes in electrical conductivity and other soil properties have been revealed.

As a result of the experiments, changes of the electrical conductivity value of the treated samples were revealed, it changed from 1.2 to 7 times (with respect to the control one), depending on f the plasma jet action time on the soil. The longer the plasma was in contact with the surface of the samples, the greater became the electrical conductivity.

It was also found that the effect of noticeable conductivity increase was at interaction of dry samples with the plasma (Fig. 10), the conductivity increase ranged from 194 to 676 mS/cm.

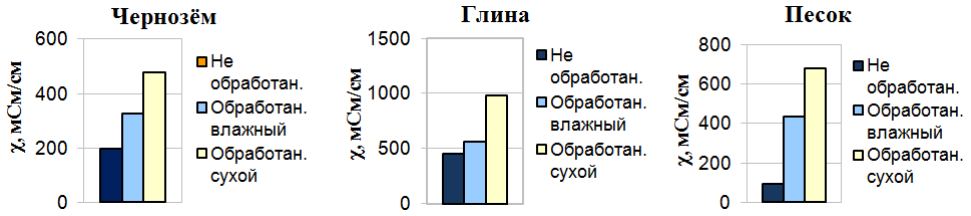

FIGURE 10. Growth of electrical conductivity of samples: left to right- chernozem, clay, sand. Dark blew — non proceeded by plasma, bleu-wet sample proceeded by plasma, yellow- dry sample proceeded by plasma.

1. Stakhanov I.P. *The physical nature of ball lightning,* M .: Nauchny mir. 1996.

2. Bychkov V.L., Nikitin A.I. *Ball Lightning: A New Step in Understanding. In: The Atmosphere and Ionosphere. ElementaryProcesses, Monitoring, and Ball Lightning.* Eds. Bychkov V.L., Golubkov G.V., Nikitin A.I. Springer, the Netherlands, 2014. P. 201—367.

3. Bychkov V. L. Ball Lightning with a Cover Filled by a Vapor. *IEEE Trans. Plasma Sci.* vol. 42, N. 12, 2014, 3912 — 3915.

On Spectral and Energetic Characteristics of Erosional Plasma on the Basis of a Tin Alloy and of "Jumping Fireballs"

Alexei L. Pirozerski, Alexandr I. Nedbai, Vladimir A. Reznikov, Elena L. Lebedeva and Anastasia S. Khomutova

Saint-Petersburg State University, Saint-Petersburg, 198504, Russia

The ball lightning (BL) is one of the most enigmatic natural phenomena. Despite the long history of investigations its physical nature remains unknown. Experimental modeling of BL is one of the ways to resolve this problem. While up to now nobody was able to create real BL in laboratory in controlled and reproducible way, different researchers have developed several methods to generate long-living autonomous luminescent objects which resemble the natural

phenomenon in some properties. One type of such objects is so-called “jumping fireballs” (JF), discovered and studied in [1], which are generated via impact of an erosional plasma jet, ejected from a polymethylmethacrylate capillary discharger, onto a tin anode. JFs had spherical shape with diameter of ~1—2 mm, glowed with bright yellow-reddish light, after falling on a surface they jumped up and down up to several tens times. Also JFs leaved aerogel tails which did not diffuse in the air but shrank into thin threads. Further studies of objects of the same class but generated without use of polymers were performed in [2].

In this paper we present the results of the spectral studies of erosive discharge with tin alloy electrodes and of the generated JFs, and experimentally determine internal energy of JFs using the calorimetric technique.

Simplified schematic diagram of the experimental setup is shown in Fig. 1a. The discharge circuit consists of a pulse storage capacitor ~1 mF x 5kV, an inductance L~0.25 mH integrated with a pulse ignition transformer, a protective discharge gap, main discharger and shunt resistor for measurements of the discharge current. The voltage on the main discharger was measured by a frequency-compensated divider. Oscillograms of the voltage and the current were registered using a Rigol DS2202A oscilloscope.

The main discharger included a dielectric plate with two adjustable dielectric supports carrying metallic guides for electrodes. Two piece of an industrial tin-copper alloy wire of length about 5 cm were used as the electrodes. The alloy composition was 97% Sn and 3% Cu. The electrodes were aligned opposite each other with a gap of 12 mm between their ends. The discharger was mounted at a height of about 30 cm over a support on which either a calorimeter described below or a vessel to collect the objects generated via the discharge were placed. Additionally, pyramidal or conic concentrators could be installed around or below the discharger.

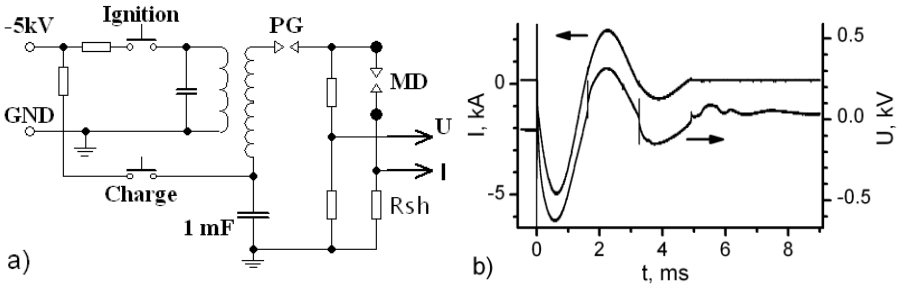

FIGURE 1. (a) Simplified schematic diagram of the experimental setup. PG — protective gap; MD — main discharger. (b) A typical oscillogram of the discharge current and the voltage on the main discharger.

Video recording of the experiments were performed via a Nikon 1 S1 digital camera. Spectra of the discharge and of JFs were recorded by a camcoder Sony HDR-HC9 using a modernized version of the original spectrograph [3]. The

spectral range was 4000—6700 Å, with the maximal spectral resolution of ~1.5 Å. As a reference source a He-Hg lamp with a reflector was used. The spectral images were taken via the same spectrometer with the input slit removed.

To measure the energy of the jumping fireballs a simple calorimeter was constructed which consisted of a box made of 50 μm-thick copper foil surrounded by a thermal insulation. The temperature at several parts of the box was measured using a two junction copper-constantan thermocouple with the reference junction placed into melting ice. The calorimeter was calibrated with hot water.

As a result of the discharge a luminous plasmoid and a multitude of fast moving bright small point-like JFs are generated. The plasmoid fade away quickly and turns into a dust cloud. JFs fall on the laboratory table, some of them getting to the installed vessel or the calorimeter. The JFs leave bluish-gray thread-like tails consisting of tin oxide which are floating up in the atmosphere. The tails undergo a gradual turbulization, break up into smaller pieces and shrink. After falling on surface, JFs are actively moving on it either gliding or jumping to height up to few centimeters. Structure of the generated aerogel threads on the scales from hundreds microns to tens nanometers, and interaction of JFs with different targets were discussed elsewhere [2].

An oscillogram taken at a typical experiment is shown in Fig. 1b. The initial voltage of the capacitive storage was 3.3 kV. As it may be seen from the figure, the main stage of the discharge include three half-period of oscillations and has the duration of ~4.9 ms with maximal absolute magnitude of the current being ~5 kA. The fact that voltage on the discharger did not return to zero after this time means that a weak current flows in the discharge circuit for a longer time. Final voltage of the capacitive storage was usually of the opposite polarity that the initial one. Integration of the oscillogram gives the total energy input to the discharge at its main stage to be of 2.99 kJ, which, at the decrease of the electrode mass at the discharge being of 0.186 g, means about 19.8 eV/at. It is an upper estimate, in particular, due to energy losses for heating remaining parts of the electrodes and constructional materials of the discharger).

The discharge spectrum in visible spectral range is shown in Fig. 2. Several lines are present superimposed on a sufficiently bright continuous spectrum. Most of noticeable line marked in Fig. 2 was identified using [4—6] and found to belong to tin and copper atoms and first ions, see Table 1, in accordance with the alloy composition. Note that lines of Cu II and Sn II have the excitation energies of about 15—17 eV and 9—11 eV, respectively. Taking into account that ionization energies for copper and tin are 7.72 eV and 7.34 eV, respectively, this implies the presence in the erosive discharge plasma of excited states with energies up to 25 eV. Taking into account that the discharge occurs in the ambient conditions this is very unusual. For example, in spectroscopic studies of the interaction of the capillary discharge jet with the metal foils [7] no lines of atomic ions were observed. To elucidate mechanisms responsible for the formation of these excited states further investigations are required.

Because the luminescence of the JFs themselves is sufficiently lower, it was difficult to obtain their spectra in normal mode, i. e. with the input slit installed.

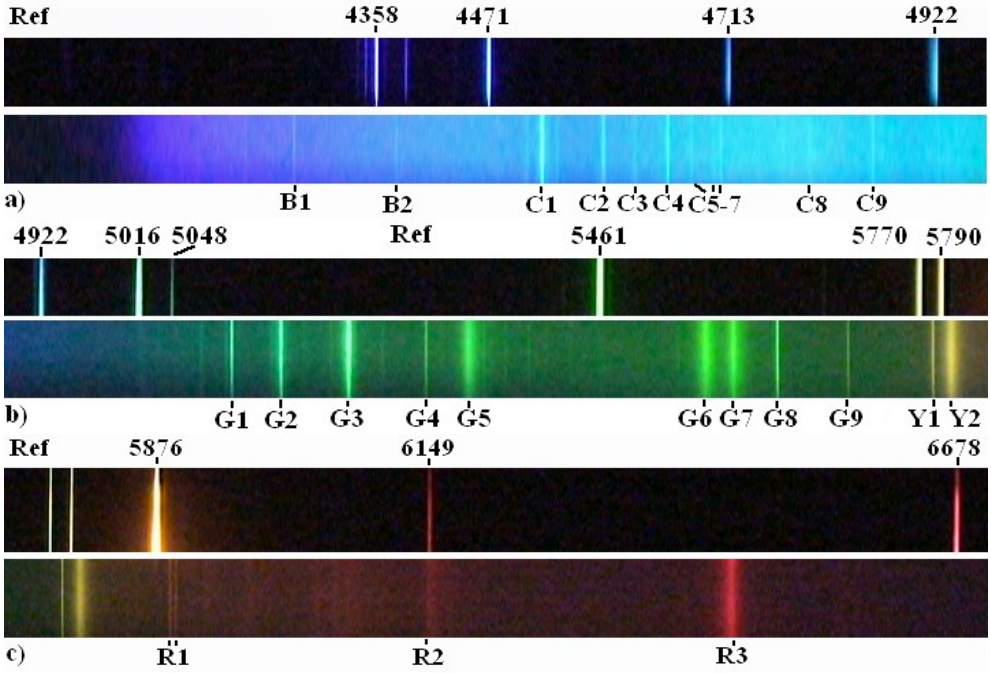

FIGURE 2. The discharge spectra in violet-blue (a), blue-yellow (b) and yellow-red (c) spectral ranges. Upper images (marked as Ref) are reference spectra of the He-Hg lamp installed behind the discharger, lower images are the discharge spectra. The wavelengths are given in angstroms. Noticeable lines or cants are marked by capitals letters with numbers in the bottom of each image.

TABLE 1. Noticeable lines in the spectrum of the erosive discharge with the tin alloy electrodes.

Line	Ion/ atom	Wave-length, Å	Excitation energy, eV	Line	Ion/ atom	Wave-length, Å	Excitation energy, eV
B1	Cu I	4275.13	7.74	G4	Cu I	5292.5	7.74
B2	Cu I	4378.2	7.8	G5	Cu II	5331.63	16.0
					Sn II	5332.3	11.19
C1	Sn I	4524.74	4.87	G6	Sn II	5561.9	11.20
					Cu II	5560.6	17.22
					Cu II	5562.07	16.85
					Cu II	5562.64	16.66
C2	Cu I	4586.95	7.8	G7	Sn II	5588.81	11.07
C4	Cu I	4651.13	7.74	G8	Sn I	5631.71	4.33
C5	Cu I	4674.76	7.8	G9	Cu I	5700.24	3.82
C6	Cu I	4698.7	7.88	Y1	Cu I	5782.13	3.79
C7	Cu I	4704.6	7.74	Y2	Sn II	5796.66	11.07
					Sn II	5798.86	11.07
					Cu II	5801.13	15.53

End of table 1

Line	Ion/ atom	Wave-length, Å	Excitation energy, eV	Line	Ion/ atom	Wave-length, Å	Excitation energy, eV
G1	Cu I	5105.54	3.82	R1	Cu II Cu II	5890.4 5897.97	16.75 16.56
G2	Cu I	5153.24	6.19	R2	Cu I	6147.31	16.56
G3	Cu I	5218.20 5220.7	6.19 6.19	R3	Sn II	6453.58	8.97

Hence, taking into account the small size of the JFs, the slit was removed and the spectral images were registered instead of spectra, see Fig. 3. At that, a conic concentrator was used to make JFs be closer to the normal slit position. It should be noted that despite of a blur due to both the finite size and the motion of JFs, and also a distortion of the wavelength calibration due to offset of the mean position of JFs, spectral images reproduce to some extent the features of the spectrum. As seen from Fig. 3, the spectral images show no signs of any spectral lines or cants, so we assume that JFs have continuous spectra.

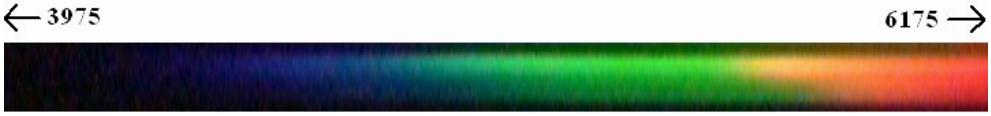

FIGURE 3. The spectral image of a jumping fireball. The wavelengthes (in angstroms) corresponds to the left and right edges of the corresponding spectrum which would be taken with the input slit installed.

For direct measurements of the JF energy calorimetric studies were carried out. The calculated idealized sensitivity of the calorimeter was ~0.46 K/J. However, the calibration of the calorimeter using hot water showed that the heat recovery coefficient (i.e., the ratio of the energy evaluated as maximal calorimeter temperature increase divided by the idealized sensitivity to real value of the energy) was only ~0.15.

Mass of the JFs hitting upon the calorimeter found by weighing was of order of milligrams or tens milligrams. Calculated specific internal energy of the JFs (taking into account the heat recovery coefficient) varies from ~1 to 7 eV/at. The higher values correspond to the greater JF masses and, therefore, seem to be more reliable. Note, that the specific energy required to heat the tin from room temperature to the melting one (505.08 K) is ~0.06 eV/at, the specific melting heat is ~0.07 eV/at, the specific energy to heat the melt from melting temperature to the boiling one (2875 K) is >0.7 eV/at, the specific energy of the vaporization is ~3.1 eV/at. The sum of all this energies is >4 eV/at. The enthalpy of formation of tin oxide (IV) from solid tin and gaseous oxygen is ~6 eV/at. Taking into account uncertainty of the heat recovery coefficient and its possible dependence on mass of the objects and places where they hit into the calorimeter box, the present results can not give

unambiguous answer whether the available chemical and thermal energy of JFs is sufficient to account for the result of the calorimetric measurements or a fraction of the internal energy of JFs is stored in some other form.

In conclusion, the present studies show the presence of excited ions with excitation energies of order 20—25 eV in the plasma of the erosional discharge with tin alloy electrodes. Luminescence of JFs has continuous spectrum, and its internal energy, determined via calorimetric studies, is of the same order of magnitude as their available thermal and chemical energy, however the presence of other forms of energy storage cannot be excluded definitely.

1. S. E. Emelin, V. S. Semenov, V. L. Bychkov et al., Some objects formed in the interaction of electrical discharges with metals and polymers, *Tech. Phys.*, 1997, 42(3), pp. 269—277.

2. A. L. Pirozerski, V. Yu. Mikhailovskii, E. L. Lebedeva et al., Artificial fireball generation via an erosive discharge with tin alloy electrodes*, Int. J. Appl. Eng. Res.*, 2014, 9(24), pp. 24047—24055, preprint: http://arxiv.org/abs/1504.01120.

3. S. E. Emelin, A. L. Pirozerski, and N. N. Vassiliev, Dust-gas fireball as special form of electric erosive discharge afterglow*, Proceedings of ISBL-06*, Eindhoven, The Netherlands, 16—19 August 2006, preprint: http://arxiv.org/abs/physics/0604115.

4. A. N. Zajdel, V. K. Prokofiev, S. M. Rajskij et al., *Tables of spectral lines. The reference-book,* Nauka, Moscow, 1977, 800 p. (in Russian)

5. A. Kramida, Yu. Ralchenko, J. Reader, and NIST ASD Team, *NIST Atomic Spectra Database (ver. 5.5.1),* National Institute of Standards and Technology, Gaithersburg, MD, 2017, https://physics.nist.gov/asd.

6. N. S. Sventickij, *Visual methods of emission spectral analysis,* Moscow, 1961, 344 p. (in Russian)

7. D. L. Kirko and A.S. Savjolov, Characteristics of capillary discharge upon adding metal atoms to plasma*, High Temperature*, 2015, 53(6), pp. 921—923.

Traces of Ball Lightning Interaction with Glass as a Proof of Its Material Nature

Anatoly I. Nikitin[1], Vladimir L. Bychkov[2], Ilya G. Ivanenko[2], Tamara F. Nikitina[1], Alexander M. Velichko[1],Adlia R. Bikmukhametova[1,2], and Ilya G. Stepanov[1]

[1]Talrose Institute for Energy Problems of Chemical Physics, RAS, Moscow, Russia
[2] Lomonosov Moscow State University, Moscow, 111111, Russia

In the long history of the ball lightning (BL) theory development is a struggle of two concepts [1, 2]. According to one of them, the BL is an electrical discharge, burning in the air due to the action of an alternating electric field, generated by an external source of energy [3, 4]. According to the second one, the BL is the

material body, storing energy within itself [5, 6]. Data banks of BL observations give evidence that it can pass through the glass, leaving no traces on them [7]. Supporters of the first concept consider this as the proof of the correctness of the "electric field nature" of the BL. Here we present results of investigation of the window glass, from which, according to observer, BL freely passed. On the part of glass, located in the place where BL has penetrated inside a room, we found a region of 1—2 mm dimensions, at the centre of which a cavity of diameter 0.24 mm was located. It indicates that the glass was heated up to boiling temperature, and BL elements have passed through the orifice, which then was partly closed. This gives evidence to a "material" nature of BL.

Events of BL interaction with glass can be divided into three types. The first type is the passage of BL through holes and cracks, existing in the glasses. The size of the holes are often by 10—100 times smaller than the diameter of the BL. BL when passing through a slot changes its shape, sometimes stretching into a filament or tape [7]. The second type is the active influence of the BL on the glass, leading to the formation of holes in it [8, 9]. The most mysterious of the types is the third one, when the BL passes through the glass, "as if not noticing it". In July 2004 in the city of Pustoschka, Pskov region of Russia, during a storm a spherical luminous object of 20 cm diameter before a boy's eyes went through the window glass as if there was no obstacle for it. Entering the room, the ball, after making some "vibrations", was drawn into the electrical socket.Visual inspection of the glass showed that it remained whole [10].

The glass with sizes 530 mm × 350 mm × 2 mm, through which BL has passed, was taken out of the frame and it was investigated by us. There were no cracks and defects on the glass of sizes comparable with the size of the BL. However, by careful examination of the glass with a help of the magnifying glass, in the place of the BL entering the room, which is about 15 cm from the edge, we found a defect, resembling a gnarl of low quality window glasses. Fig. 1 shows a photograph of the outer (side streets) surface of the glass made by the optical microscope with a magnification of ×200. It turned out that the BL left a cylindrical hole with a diameter of 240 microns in the glass. It was not a through hole. In Fig. 1 one can see a dark lentil like figure with size 430 × 800 μm around the cavity, which is surrounded by the glass area of the same shape with size of 1200 × 750 μm with slightly reduced transparency. The cavity in the glass has a conical shape; the diameter of its bottom located approximately 1 mm from the surface is 160 microns.

FIGURE 1. A photo of the outdoorside of the glass. Magnification. ×200.

To investigate changes in the optical characteristics of the glass occurred in the area of its contact with the BL linearly polarized beam of He-Ne laser with a diameter of 1 mm (632.8 nm wavelength) perpendicularly to the glass surface was transmitted. The glass could be moved in the horizontal plane in mutually perpendicular directions. It has been found that the area of the glass in the vicinity of the cavity acts as a converging lens with a focal length of 5 cm. It was found that the transmittance of light in the center of the cavity is by 9.4 times smaller than the light transmission of the intact glass, and the size of the region where the transmittance decrease is observed (about 5×5 mm^2) considerably exceeds the diameter of the cavity (240 microns). Fig. 2a shows how changes the transparency of the glass near the cavity. For this picture the glass was cut so that the cutting plane passed at a distance of 1 mm from the axis of the cavity. The glass in the left side of the image (near the cavity) seems to be darker than in the right side of the picture. The area of reduced transparency represents a flat-convex lens. To the right is adjacent the flat concave lens diverging lens of undamaged glass. Fig. 2b shows a diagram of the path of rays in the compound lens. Located to the left flat- convex lens is formed of the glass area with a modified structure and unknown refractive index n_x. According to Fig. 2a, the diameter of the lens is 4 mm, and thickness is 1mm. From the triangle OAB the beam, traveling parallel to the optical axis at angle α to the perpendicular to the spherical surface of the lens, after coming out of the lens in the undamaged part of the glass will go under angle β to this perpendicular. For these angles $\sin\alpha / \sin\beta = n_g / n_x$, where n_g is the refractive index of the glass, $n_g = 1.5$. At point C inside the glass the beam intersects the surface of the glass at the angle $\gamma = \beta - \alpha$ to the perpendicular to the surface, and the angle between the beam emitted in the air and this perpendicular is δ. The relationship between angles γ and δ is defined as $\sin\delta / \sin\gamma = n_g / n_a$, where n_a, refractive index of air, is $n_a = 1$. From the angle CDF we find $\sin\delta \approx \mathrm{tg}\delta = CD/DF$. Taking DF equal to 50 mm (focal length of the lens), and $CD = 2$ mm (the radius of the lens), we get $\sin\delta = 2/50 = 0.04$. Hence $\sin\gamma = \sin\delta / 1.5 = 0.0267$ and $\gamma = 1.528^0$. From the triangle OAB $\sin\alpha = AB / OA = 2 / 2.5 = 0.8$ and $\alpha = 53.13^0$. Knowing the angles α and γ, we find the angle $\beta = \alpha + \gamma = 54.658^0$ and $\sin\beta = 0.8157$. The refractive index of the left lens material $n_x = n_g \cdot (\sin\beta / \sin\alpha) = 1.5295$, that is, it is changed by 0.0295, or for about 3%. The reason for this change is not clear. Perhaps this is connected with appearance of particles with size of about 1 micron inside the glass, which were discovered in the photo of the glass surface area, remoted for 1 mm from the edge of the cavity. On the area of the surface with sizes 22×22 μm^2 were about 22 spherical inclusions ranging in size from 1 micron to 3 microns. From here follows that in the segment length of 22 μ is $22^{1/2}=4.69$ "balls", and in the interval of 1 cm their number is equal to $4.69/22 \cdot 10^{-4}=2.132 \cdot 10^3$.Thus, in the volume of 1 cm^3 can be $N = (2.132 \cdot 10^3)^3=10^{10}$ spherical inclusions. The volume of the "ball" with the diameter of 2 μm is

$4.2 \cdot 10^{-12}$ cm^3, and the total volume of $N = 10^{10}$ balls is $4.2 \cdot 10^{-2}$ cm^3. So, the "balls" occupy about 4% of the volume of the glass. It is somehow correlates with three percent change in the refractive index "of the damaged glass" found by us.

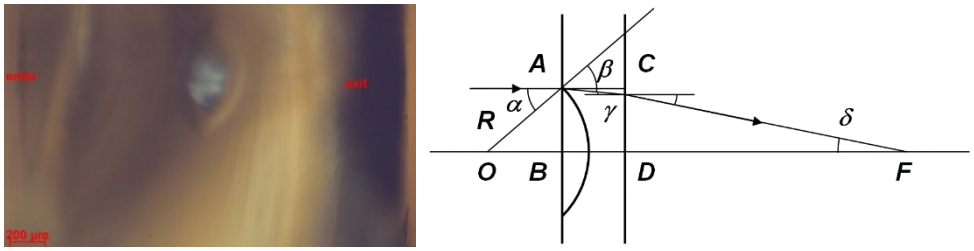

a) b)

FIGURE 2. a) Side view of the region near the cavity. On the left — a place of BL entry. b) Scheme of the beams in the vicinity of the cavity region.

The above leads to the univocal conclusion that BL is a material body, which is able to pass through the obstacle, in particular, through the glass window. However, (as opposed to the trivial case of electromagnetic waves passing through the dielectric) there should be fulfilled several conditions. (1) BL has to have a certain energy limit (not less than 10 kJ), to heat the material of the obstacles [9]. Based on the results of observations, when the BL volatilized circular metallic objects (rings, bracelets, and so on), one can assume that the heating of the glass was carried out by a powerful pulse of electromagnetic radiation [11, 12]. (2) Since the BL of 10—15 cm in size is capable to pass through the hole of 1—5 mm (or less) in size, it means that the size of its core elements or surface elements does not exceed 0.1—1 mm. This conclusion is confirmed by real observations of the core structure of BL and conclusions of some models of ball lightning [6, 7, 12, 13]. Concerning significant decrease in the optical transparency of the glass may be indicative of a sharp rise in the temperature of the glass up to its boiling point (1700^0—1800^0 C). Hatched there embedding size of 1—3 microns, it appears to be bubbles containing silica crystals. Since heated to boiling inner heating region was isolated from atmospheric oxygen, it has not occurred chemical reactions which could alter the ratio of basic glass components. The most natural reason for appearing of a force, pulling BL through a glass, is the presence of non-compensated electric charge in its elements [6, 14, 15]. Let a radius of this element is R = 1 mm and a charge $q = 4 \cdot 10^{-7}$ C. In the electric field of a storm cloud $E=10^5$ V/m a force, acting on the element, is $F = qE = 4 \cdot 10^{-2}$ N. At $T = 1700°$C a dynamic viscosity of a glass is $\eta = 1$ N $\cdot$ s $\cdot$ m^{-2} [16]. A velocity v of the ball of radius R = 1 mm motion through a melted glass is $v = F / 6\pi R\eta = 2$ m/s. The ball can pass through a glass of 2 mm thickness at time 10^{-3} s. It is possible that the channel, laid in the glass by the first "ball", will not close at once and the "balls", following it, will experience minimal friction and therefore will move with greater speed. Elements of the BL core passing through the glass, somehow gather in a common shell material of which has also to pass through the hole in the glass. The

BL due to the electric field, which "pulled" its elements through the glass, will separate from the window. The resulting hole will close due to the pressure difference outside of the hole (pressure of liquid) and inside the hole (gas pressure). An increase in viscosity of the glass when it cools can prevent the process of holes closing. It is possible that this was the scenario of events left marks on the glass samples investigated by us.

So the dispute whether the BL is an electric discharge at the antinode of a stationary electromagnetic wave [3] or a material body, can be considered as finished. The winning point of view on BL is that it is a physical body made of molecules, ions and electrons. This fact poses for proponents of "material" hypothesis of BL a number of difficult questions. Firstly, it is necessary to explain how BL can carry an electric charge, which field several orders higher than the breakdown field strength of air. Secondly, a structure of BL elements and their interaction with the shell of BL must be explained. Thirdly, a "mechanism" of electromagnetic radiation generation in optical and radio-frequency regions must be developed. The concepts for solving of these problems one can find in [6, 12, 14, 15]. Thus, the results of this work open wide field of activity to BL researchers.

1. S. Singer, The Nature of Ball Lightning, Plenum, New York, 1971.

2. M. Stenhoff, Ball Lightning. An Unsolved Problem in Atmospheric Physics, Kluwer/Plenum, New York, 1999.

3. P. L. Kapitsa, On a Nature of Ball Lightning, *Dokl. Akad. Nauk,* 1955, 101**,** pp. 245—248.

4. Y.-H. Ohtsuki and H.Ofuruton, Plasma Fireballs Formed by Microwave Interference in Air, *Nature,*1991, 350**,** pp. 139—141.

5. G. C. Dijkhuis, A Model for Ball Lightning, *Nature,* 1980, 284**,** pp. 150—151.

6. A. I. Nikitin, An Electrical Capacitor as the Element of the Power Core of Ball Lightning, *Electrical Technology Russia*, 1998, No. 4, pp. 70—85.

7. A. I. Grigoriev, Ball Lightning, Yaroslavl State University publishers, Yaroslavl, 2006.

8. D. J. Turner, The Interaction of Ball Lightning with Glass Window Panes. *J. Meteorology,* 1997, 22**,** pp. 52—54.

9. A. I. Nikitin, V. L. Bychkov, T. F. Nikitina, and A. M. Velichko, Modeling of Ball LightningInteraction with Window Glasses, *Khimicheskaya Fizika,* 2006, 25, pp. 98—105.

10. V. L. Bychkov, A. I. Nikitin, I. P. Ivanenko et al., Ball lightning passage through a glass without breaking it, *Journ. of Atmospheric and Solar-Terrestrial Physics*, 2016, 150, pp. 69—76.

11. I. Imiyanitov and D. Tikhyi, At the Edge of the Scientific Laws, Atomizdat, Moscow, 1980.

12. V. L. Bychkov, A. I. Nikitin, and G. C. Dijkhuis, Ball lightning investigations, *The Atmosphere and Ionosphere, Dynamics, Processes and Monitoring*, 2010, pp. 201—373.

13. A. I. Nikitin, Small-sized and Composite Ball Lightning. *Intern. Journ. "Unconventional Electromagnetics and Plasmas" (UEP)*, 2012, 4, pp. 105—116.

14. A. I. Nikitin, Electrodynamic Model of Ball Lightning, *Khimicheskaya Fizika*, 2006, 25**,** pp. 38—62.

15. A. I. Nikitin, V. L. Bychkov, T. F.Nikitina, and A. M.Velichko, High Energy Ball Lightning Observations. *IEEE Trans. Plasma Sci.,* 2014*,* 42, pp. 3906—3911.

16. B. M. Tareyev, Physics of Dielectric Materials, Energiya publishers, Moscow, 1973.

Energy, Charge, And Radio-Waves Emission as The Base Principles for Development Of Electrodynamical Model of Ball Lightning

Anatoly I. Nikitin, Alexander M. Velichko, Tamara F. Nikitina, and Ilya G. Stepanov

Talrose Institute for Energy Problems of Chemical Physics, RAS, Moscow, Russia

In the article [1], on the basis of analysis of ball lightning (BL) observation results, its basic properties, which can be taken as a principle of its model developing, were defined: its high energy, ability to generate a powerful radio-frequency radiation and a presence of non-compensated electric charge. The analysis of cases when BL got into a tank with water, allowed to estimate limiting value of energy density of its substance as $\rho_E = 10^{10}$ J/m^3. In literature cases when BL evaporated ring metal subjects or lighted the incandescent lamps, switched off from a network, are described. It is possible to explain this by its ability to generate microwave electromagnetic radiation, which power can reach 10 MW. Sometimes BL, passing over heads of people, forces to lift their hair "fan". Such action can make a body, which electric charge is equal to 10^{-5}—10^{-4} C.

It is shown in [1] that it is possible to combine the specified BL characteristics if to assume, that it consists of the certain core, possessing a surplus electric charge Q, which is placed inside a spherical cover from dielectric. Due to action of electric field of the charge, a polarization of the cover substance take place and a force F_{sh}, shrinking the BL core, arises:

$$F_{sh} = [Q\sigma a\ (2R+a)] / [\varepsilon_0 (R+a)^2]. \quad (1)$$

Here R is an internal radius of the cover, a is the cover thickness, σ is a density of electric dipoles on the cover surface, ε_0 is electric constant. A force F_{em}, with which charges stretch the cover, is:

$$F_{em} = Q^2 / (4\ \pi\varepsilon_0 R^2). \quad (2)$$

Because the force F_{sh} is proportional to the first degree of Q, and the force F_{em} is proportional to a square of charge Q^2, in interval from $Q = 0$ to Q_{max} $F_{sh} > F_{em}$. These forces are equal at

$$Q_{max} = [4\pi R^2 \sigma a\ (2R+a)] / (R+a)^2. \quad (3)$$

At $Q < Q_{max}$ the cover is capable to sustain, except the Coulomb force of charges pressure F_{em}, as well a force F_k, caused by movement of charge carriers with total kinetic energy E_k:

$$F_k = 2E_k/R. \quad (4)$$

In 1998 in the article [2] the electrodynamical model of BL was proposed [3—5]. In this model it is supposed that the space inside the ball lightning cover is filled with certain "plasmoids", possessing not compensated electric charge. The

plasmoid is meant as a system of moving charges, kept together by own electric and magnetic fields [6]. However it was proved that stabilization of the plasmoid only by internal forces is, basically, impossible. Any external force, for example, force of gravitation, is necessary for this purpose [7]. In our case a role of this external force is played by the force of the cover compression.

As a prototype of our plasmoid "the hydromagnetic plasma condenser", invented in the fifties of 20th century, is served [8]. This condenser represents a disk of plasma, placed in a strong magnetic field. In this field positive and negative charges are separated: electrons move in an orbit of small radius around a magnetic field direction, and positive ions move in an orbit of the big radius. Basically, for existence of similar system of moving charges a presence of an external magnetic field is not obligatory. Really, let us imagine a certain ring of electrons, moving in a closed orbit of radius r in magnetic field H, which is created by the positive ions, rotating in an orbit of big radius R. These electrons are kept in the orbit, making drift movement in mutually perpendicular fields H and E, where E is an intensity of electric field between the internal electronic ring and the external ionic ring. Ions are kept in the orbit thanks to their attraction to the electronic ring (due to action on them the field E).

Equating a centripetal force $F_e = eE$ to centrifugal force $F_c = (m_p v_p)^2/R$, we find an orbital velocity of an ion $v_p = (eER/m_p)^{1/2}$. Here m_p is a mass of proton (of the most light positive ion), $m_p = 1.673 \cdot 10^{-24}$ kg; $e = 1.602 \cdot 10^{-19}$ C is a proton charge. We consider not relativistic case, therefore an intensity of electric field at $R = 10^{-6}$ m should not exceed $E = 10^{14}$ V/m, and at $R = 10^{-2}$ m must be $E<10^{10}$ V/m. Rotation frequency of proton is $f_p = v_p/2\pi R = (eE/4\pi^2 m_p R)^{1/2}$. If the total charge of all protons is equal to Q_p, a current I_p, created by their movement, is $I_p = Q_p \cdot f_p = = (Q_p^2 eE/4\pi^2 m_p R)^{1/2}$. This current generates in the centre of the proton orbit a magnetic field intensity $H_p = I_p/2R = (Q_p^2 eE/16\pi^2 m_p R^3)$. As rough approach let us accept that electric field E, created by an electronic ring with charge Q_e, is equivalent to a field of a point charge. In this case

$$E = Q_e/4\pi\varepsilon_0 R^2 \text{ (V/m)}. \tag{5}$$

For such E

$$H_p = (Q_p^2 e Q_e/64\pi^3 m_p \varepsilon_0 R^5)^{1/2}. \tag{6}$$

Movement of electrons in the mutually perpendicular electric E and magnetic H fields occurs in a cycloid [9]. For the way of electron was closed, it is necessary that the magnetic field was strong enough and the condition $H_p \geq (\varepsilon_0/\mu_0)^{1/2} E$ was satisfied [10]. Here $\mu_0 = 1.257 \cdot 10^{-6}$ V·s/A·m is a magnetic constant. In this case we find from formulae (5) and (6) the relation between values of total charges of protons Q_p and electrons Q_e:

$$Q_p^2 \geq (4\pi m_p R Q_e)/e\mu_0 = 0.1 R Q_e. \tag{7}$$

The analysis shows, that at $Q_e = 10^{-6}$ C the inequality (7) is carried out at $R > 10^{-4}$ m, and at $Q_e = 10^{-3}$ C for its performance it is necessary, that there were

$R > 10^{-2}$ m. It means that in this area of values Q_e and R the total charge of protons exceeds a total charge of electrons, so the plasmoid (the dynamic electric condenser) is positively charged. For a movement of the charged particles was not being braked due to its collisions with air molecules, a high vacuum should be exist inside the cover. Simultaneously the vacuum carries out a role of an electric insulator between the dynamic condenser and the ball lightning cover. The radius of the proton orbit aspires to increase. The expansion of the orbit may be constrained by mutual impacts of dynamic condensers (if there are many condensers inside the cover) or by their impacts with the cover wall. Due to losing of the core charge the cover also becomes positively charged, this promotes process of "plasmoids" reflection from its wall.

Now let us discuss how BL characteristics will vary at reduction of a size of its elements. Kinetic energy of the proton, hold in an orbit by field E, created by the electronic ring (see formula (5)), is $w_p = m_p v_p^2/2 = eQ_e/8\pi\varepsilon_0 R$, and a total kinetic energy N_p of protons ($N_p = Q_p/e$) is:

$$W_p = w_p \cdot N_p = Q_e Q_p / 8\pi\varepsilon_0 R = 4.5 \cdot 10^9 \, Q_e Q_p / R. \qquad (8)$$

Considering a relation between values of total charges of protons and electrons (7), the formula (8) can be copied in a kind:

$$W_p \le \left(\frac{m_p}{16\pi\varepsilon_0^2 e \mu_0} \right)^{1/2} \cdot \frac{Q_e^{3/2}}{R^{1/2}} = 1{,}45 \cdot 10^9 \cdot \frac{Q_e^{3/2}}{R^{1/2}} \text{ (J)}. \qquad (9)$$

Accepting the plasmoid volume equal to $V_c = 4\pi R^3/3$, we find an average density of kinetic energy of protons: $\rho_w = W_p/V_c = 0.35 \cdot 10^9$ ($Q_e^{3/2}/R^{7/2}$) (J/m^3). We see that at decrease of the plasmoid radius R the density of total kinetic energy grows. For example, for ball lightning with internal radius of cover R = 1 mm and a charge $Q_e = 10^{-6}$ C its diameter will be $2(R+a)$ = 2.64 mm, kinetic energy of protons W_p = will reach 46 J, and energy density — $\rho_{ws} = 5 \cdot 10^9$ J/m^3. A quantity of these small ball lightnings can appear inside a big container with a dielectric wall. If a total volume of such ball is equal to 1 litre (it is a typical volume of "macroscopic" ball lightning), than their total energy will be nearby 5 MJ. If the cover of this container — a "composite" ball lightning — appears to be transparent, then these small ball lightnings can be seen with naked eyes [11].

As one of the basic properties of ball lightning its ability to soar freely in air is marked [11—14]. Let us check, whether a considered model of ball lightning in the form of hollow sphere with internal radius R = 5 cm and a cover thickness a = 1 cm is capable to such action. We will assume that the cover consists of the substance, which density is close to density of liquid water $\rho_w = 10^3$ kg/m^3. Volume of the cover of our ball lightning is $V_{sh} = 4\pi [(R+a)^3 - R^3]/3 = 3.8 \cdot 10^{-4}$ m^3, and its mass $m_{sh} = \rho_w \cdot V_{sh}$ = 0.38 kg. Weight of the cover is $P_{sh} = m_{sh} \cdot g$ = 3.74 N. Let an area inside the cover is filled with carriers of positive charge, which total value is $Q = 10^{-3}$-10^{-2} C. We will assume that charge carriers are protons. In this case their quantity in cover is $N_p = Q/e = 6.25 \cdot 10^{15} - 6.25 \cdot 10^{16}$, and a total weight

$M_p = m_p \cdot N_p = 10^{-8}$–$10^{-7}$ kg. Near the ground surface an electric field always presents. At fine weather its intensity is nearby E_{gw} = 100—150 V/m, and during thunder-storms it can be more than E_{gw} at 100—1000 times [15]. For creation of the elevating force, equal to a weight (P_{sh} = 3.74 N) of ball lightning with charge $Q = 10^{-2}$ C, an electric field with intensity $E = P_{sh}/Q = 3.74 \cdot 10^2$ V/m is need. Because of leaking of ball lightning charge into a space around it a cloud of charges appears. Repelling of ball lightning from this cloud can provide it soaring over conductors [11—14; 16, 17] and existence of groups of ball lightnings [18]. Elements of ball lightning core represent magnetic dipoles. Because of chaotic movement of these elements inside a cover of a ball lightning it has no macroscopic magnetic moment [4]. However in an external magnetic field there can be a partial ordering of the moments of separate dipoles. Likely this can explain a case of lifting by ball lightning in air of horseshoe-shaped magnets [16].

As the generator of electromagnetic radiation of ball lightning electric charges (electrons and protons), moving on the closed orbits, apparently, serve. At performance of condition $H_p \geq (\varepsilon_0/\mu_0)^{1/2} E$ velocity of electrons appears to be close to light velocity. Such electrons become a source of synchrotron radiation which frequency appears n times more than frequency of their orbital movement $f_e = c/2\pi r$ (r — is a radius of an electronic orbit). Harmonic number n_{max}, on which a maximum of radiation intensity falls, is [19]:

$$n_{max} = (3/2) \cdot (1 - \beta^2)^{-3/2}. \qquad (10)$$

Here $\beta = v_e/c$ — is a ratio of electron velocity to the light velocity. A power of synchrotron radiation is inversely proportional to product of squares of radius of the electron orbit r and a parameter $\alpha = 1 - \beta$ [19]. Calculations show, that if there is a "mechanism" of transfer of kinetic energy of protons to electrons, then a full energy of ball lightning should "be highlighted" by electrons during 10^{-3}—10^{-2} s [3]. However this conclusion concerns only a case of radiation of light by a single electron or by an electron bunch. If electrons will be located along an orbit absolutely in regular intervals, they will not radiate light [9]. In our system with the large number of electrons they will aspire to be distributed in an orbit in regular intervals. The wave length, on which a maximum of intensity of radiation falls, depends on electrons velocity and may be different. Therefore a color of ball lightning may be any. At infringement of uniformity of electrons arrangement along an orbit ball lightning can radiate energy in the form of a short pulse. Apparently, the specified mechanism of ball lightning radiation is realized not only in an optical range, but also in a radio range.

The most probable reason of ball lightning formation is a discharge of linear lightning (or, strictly speaking, any channel of enough strong current). Usually a voltage between a storm cloud and the earth makes $U = 10^9$ V. A discharge of average lightning transfers to the earth a charge Q_l = 5 C, from here its energy is $W_l = U \cdot Q_l = 5 \cdot 10^9$ J. At energy density $\rho_{bl} = 10^{10}$ J/m^3 ball lightning with a volume $V_{bl} = 10^{-3}$ m^3 possesses energy 10^7 J, that makes 0.2 % of a linear lightning energy. According to the "scenario", described in [3, 4, 20, 21], ball lightning is generated

near to a bend of a linear lightning channel at passage through it of several return strokes. It is considered that thanks to action of the first return stroke in a space near to the bent channel the vacuum cavity is formed and there is air ionisation. At passage through the channel a current of the next discharge a pulse of magnetic field with duration of forward front nearby 10 μs and with duration of a falling down part nearby 50 μs is generated. In a phase of increase of a magnetic field eddy electric field is generated. Under the influence of this field a separation of charges takes place: electrons are injected inside a vacuum cavity, and positive ions (protons) remain near its walls. During reduction of intensity of magnetic field the direction of the vector of eddy electric field changes on reverse. As a result of action of electric and magnetic fields acceleration of protons takes place, and a part of electrons, moving along magnetic field lines, leaves the area near to the channel of a lightning. As a result a positively charged system of moving charges (the dynamic electric condenser) is formed: an electronic ring, round which protons rotate. In electric field of non-compensated charge from water drops a cover can be formed. The single double ring of moving charges is thermodynamically unstable: according to the law of growth of entropy it is favorable for it to separate into elements of small size, which will fill in regular intervals a space inside the cover. The minimum size of these elements can be about 1 mm [3, 4].

1. A. I. Nikitin, V. L. Bychkov, T. F. Nikitina, and A. M. Velichko, High-energy ball lightning observations, *IEEE Transactions on Plasma Science*, 2014, 42(12), pp. 3906—3911.

2. A. I. Nikitin, Electrical capacitor as the element of the power core of ball lightning, *Electr. Technol. Russia*, 1998, 4, pp. 70—85.

3. A. I. Nikitin, The electrodynamic model of ball lightning, *Khimicheskaya Fizika*, 2006, 25(3), pp. 38—62.

4. A. I. Nikitin, A. M. Velichko, and T. F. Nikitina, The principles of search of conditions of creating of ordered plasma structures*, Proc. RAS. Energetics*, 2008, No. 2, pp. 115—132.

5. A. I. Nikitin, A new approach for solving of ball lightning problem — change of the paradigm, *Vestnik RAEN*, 2012, No. 2, pp. 19—30.

6. W. H. Bostik, Experimental study of ionized matter projected across a magnetic field, *Phys. Rev.,* 1956, 104(2), pp. 292—299.

7. V. D. Shafranov, About stable magneto-hydrodynamic configurations, *Journ. Exp. Theor. Phys*., 1957, 33, 3(9), pp. 710—722.

8. O. Anderson, W. R. Baker, A. Bratenahl, H. P. Furth, W. B. Kunkel, Hydromagnetic capacitor, *J. Appl. Phys.,* 1959, 30(2), pp. 188—196.

9. L. A. Artzimovich and S. Yu. Lukianov, *Motion of Charged Particles in the Electric and Magnetic Fields*, Nauka, Moscow, 1978.

10. L. D. Landau, and E. M. Lifshits, The Theory of Field, Nauka, Moscow, 1961.

11. A. I. Grigoriev, Ball Lightning, YarGU Publisher, Yaroslavl, 2006.

12. I. P. Stakhanov, About Physical Nature of Ball Lightning, Nauchny Mir, Moscow, 1996.

13. M. Stenhoff, Ball Lightning. An Unsolved Problem in Atmospheric Physics, Kluwer/Plenum, New York, 1999.

14.W. Brand, Der Kugelblitz, H. Grand, Hamburg, 1923.

15. M. A. Uman, Lightning, McGraw-Hill, New York, 1969.
16. I. Imyanitov, and D. Tikhiy, Beyond Boundary of Science Laws, Atomizdat, Moscow, 1980.
17. A. I. Nikitin, T. F. Nikitina, and A. M. Velichko, Corona discharge and levitation of ball lightning, *Electrichestvo*, 2010, 3. pp. 16—22.
18. A. I. Nikitin, A. M. Velichko, T. F. Nikitina et al., *Observation and analysis of ball lightning group flights,* Proc. 5th International Conf. "Atmosphere, Ionosphere, Safety" (AIS-2016), Kaliningrad, 2016, pp. 274—278.
19. I. M. Ternov, V. V. Mikhailin, V. R. Khalilov, Synchrotron Radiation and its Applications, MGU Publisher, Moscow, 1980.
20. A. I. Nikitin, The principles of developing the ball lightning theory, *Journ. Russian Laser Research,* 2004, 25(2), pp. 169—191.
21. A. I. Nikitin, Creation of ball lightning at developing of linear lightning, *Electrichestvo*, 2000, No. 3, pp. 16—23.

Features of the Mitino's Ball Lightning Motion near the Transmission Line

Anatoly I. Nikitin, Alexander M. Velichko, Tamara F. Nikitina, and Ilya G. Stepanov

Talrose Institute for Energy Problems of Chemical Physics, RAS, Moscow, Russia

On 27 July 2015 in the region Mitino, northwest district of Moscow, during a west-east storm front, ball lightning (BL) was observed for 4—5 minutes. This event was simultaneously recorded by three observers (Sokolov (S), Chichin (C) and Novosyolov (N)). A strong wind blew into their faces at shooting. BL at first was moving before the wind, and then within a minute it was sweeping across the region bounded by an angle of about 4 degrees, as if it didn't feel the wind. After that it rose to the approaching cloud front and flew eastward with it.

In [1] BL position and height above the ground were defined by triangulation at three characteristic points of its path. BL diameter was estimated as D_c = 0.73 m, minimum height was 40 m, the horizontal velocity v_g = 12 m/s, lift speed v_{up} = 4.74 m/s, the time of its hanging out in the "pit" — 80 s. The movement of BL in the last phase of observations (during its rise to the cloud) can be explained by the combined effect of the electric field of the cloud and of the wind pressure. However, the reason for its stay in a limited area of space before going up remains unclear. One of the possible assumptions about the reasons for the special nature of BL motion is the presence of a 500 kV electric transmission line near this region.

Computer analysis of video frames of the observers (S) and (C) allowed us to define more accurately the height of BL above the ground and the distance to the transmission line. This is due to the fact that in the video recordings of these two observers there are landmarks, the scale of which is either known, or can be determined from the map of the area. In Sokolov's film it is the house 38 Baryshiha street and in the movie of Chichin — transmission tower and nearby garages. Thus,

by comparing the coordinates of the reference points (with reference to the BL coordinates) in the videos and on the map there can be determined both the position of BL on the map, and its height above the ground. We have identified in both films a time interval of about 40 s, during which BL was in the first phase. (Two minima B_1 and B_2 of BL height above ground fall into this period of time [1]). We have broken this gap into frames and determined BL position in each frame. With landmarks one can determine the point on the map through which a line of observation of the operator passes, and knowing his location on the map (place of recording) a straight line can be drawn on the map through these two points, which determines the direction to BL. The intersection point of the observation lines of two operators uniquely determines the coordinates of BL. Calculating so for the entire period of time, we have found the path of BL motion. The initial phase of lifting of BL to the cloud was analyzed on the basis of processing of the films made by operators (N) and (S). This has been done due to the fact that in this period of time in the Novosyolov's film (N) there was visible the transmission tower which dimensions were known. This helped us to determine BL trajectory in this range. Both ranges of BL stay are marked on the map [2] (see. Fig.1). From the Sokolov's film (S) one can also determine the BL height, knowing the altitude of Sokolov's position, the height of the house 38 Baryshikha street, as well as the coordinates of these objects and BL on the map.

As can be seen from Fig. 1, the BL trajectory in the "trap" fills a slightly curved region 12 m wide and 100 m long. The second part of BL stay is separated from the first one because it was impossible to determine BL trajectory between these parts (there was an image of BL, recorded only by a single operator, at this time). The distance between the point (1) lying on the edge of the first part, and the power line wires is l_1= 202 m, and for point (2) l_2 = 173 m. The height of BL at these points was equal to, respectively, 41.5 and 39.6 m.

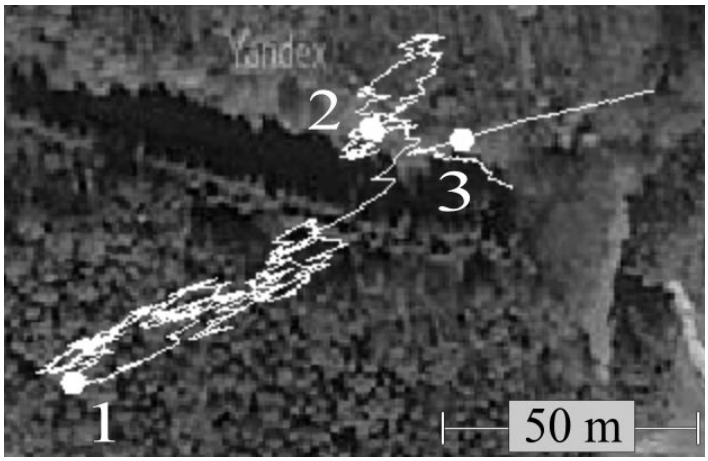

FIGURE 1. Motion of ball lightning in the "trap" in the vicinity of the power line. (1), (2) and (3) — the position of the BL at a minimum height [2]

Let us determine the magnitude of the intensity of an alternating electric field (with a frequency 50 Hz) produced by the transmission line at these points. Since the wires of the line, which we regard as infinite straight-line conductors, are located near the surface of the earth (conducting medium), the line field will be created not only by the charges of wires, but also by the charges of their mirror images. The total electric-field vector will then be equal to the geometric sum of electric-field vectors of all the charges [3]:

$$E = \sqrt{E_x^2 + E_y^2},$$

where

$$E_x = \frac{CU_\phi}{4\pi\varepsilon_0}\sqrt{(2u_1 - u_2 - u_3)^2 + 3(u_2 - u_3)^2};$$

$$E_y = \frac{CU_\phi}{4\pi\varepsilon_0}\sqrt{(2v_1 - v_2 - v_3)^2 + 3(v_2 - v_3)^2}.$$

U_ϕ is effective value of phase voltage, u_i, v_i are coefficients, determining, respectively, the horizontal and vertical projection of electric-field vectors for 3 phases of power line:

$$u_i = \frac{x_i}{m_i^2} - \frac{x_i}{n_i^2}; v_i = \frac{H+h}{n_i^2} - \frac{H-h}{m_i^2}.$$

Here x_i, m_i, n_i are the shortest distances from BL to the axis of each phase, the phase itself and to its image, respectively, H is BL height above the ground, h is a height of the power line wire above the ground. The capacity of phase per unit length of the line is determined for a three-phase power line by the following expression:

$$C = \frac{2\pi\varepsilon_0}{\ln\dfrac{2hd}{r_{экв}\cdot\sqrt[3]{(4h^2+d^2)\sqrt{h^2+d^2}}}}$$

For a line with horizontal wires relative to earth the capacity of each phase is the same. Here $r_{экв} = \sqrt[3]{r\cdot a^2}$. The phase of 500-kV transmission line near the Baryshikha street consists of 3 splinted wires with a radius r = 0.019 m, placed in a triangle with a distance a = 0.3 m between them. The distance between adjacent phases is d = 10 m. In this case, we have neglected the conductor sag, i. e. we considered the height of the wires above the ground to be the same. Taking h = 18.4 m, we find $C = 1.21 \cdot 10^{-11}$ F / m.

Calculations have shown that the electric field at the point (1) didn't exceed 16 V/m, at the point (2) it was about 25 V/m, and at the point (3) is was less than 34 V/m. The values of these fields can be compared with the characteristic values of the electric field strength in the atmosphere. The electric field of "fine weather" is about 100 V/m; a field, created by a thundercloud charge (Q_{cl} = 5 C) at a

distance L = 1000 m, is $4.5 \cdot 10^4$ V/m. This field is 1000 times stronger than the electric field generated by the power line with a voltage 500 kV. And unlike the field of a power line, it is constant or slowly changes. Therefore, it makes sense to try to explain the special character of BL motion in the "trap" by the influence of the electric field of a thunderstorm cloud. According to observations, BL has an uncompensated electric charge [4, 5]. Usually the lower part of a thunderstorm cloud is charged negatively. If BL possesses a positive charge, then a force appears that tends to lift BL upward. Let us consider the diagram (Fig. 2) when the storm cloud, carrying charge Q_c = 5 C, is at a height A = 1000 m and is offset horizontally from BL to L = 1000 m. From right to left a wind blows, acting on the BL and on the cloud. The cloud moves with the wind velocity v_g = 12 m/s, and in 1000 m/(12 m/s) = 83 s, it will appear above the BL and raise it up. At the beginning of analysis the charge of the cloud is at a distance of 1400 m from the BL and pulls it upwards at an angle of 45^0 to the horizontal. Suppose that BL is not carried away by a wind because the force of wind pressure on it F_f is compensated by the force of its attraction to the cloud F_{el}.

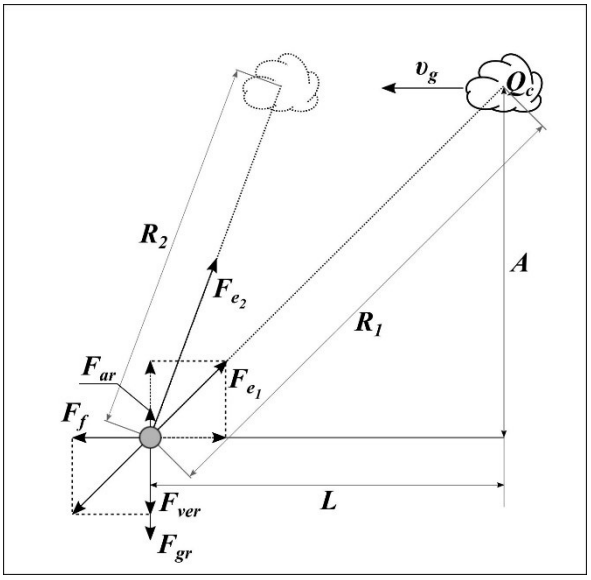

FIGURE 2. Diagram of the forces acting on BL in the "trap". (The ball does not rotate).

On a still ball with a diameter of 0.73 m streamlined by a flow of air with velocity v_g = 12 m/s, the force of friction is acting $F_f = C_x \cdot (\rho v_g^2/2) \cdot (\pi D_c^2/4) =$ =10 N (C_x = 0.3, ρ=1.13 kg/m^3 is air density) [6]. Let the force F_f is compensated by the force of BL attraction to the charge of the approaching cloud. Electric field of the charge at a distance 1400 m from it is equal to $E = 2.29 \cdot 10^4$ V/m. To compensate the horizontal friction force F_f = 10 N, force of BL attraction to the cloud must be F_{el} = 14 N. Hence, we find the charge of BL $Q_{bl} = F_e/E = 6.11 \cdot 10^{-4}$ C.

BL height above ground is H = 40 m. The strength of the "mirror" attraction of the charge to ground $F_{mir} = Q_{bl}^2/4\pi\varepsilon_0(2H)^2$ = 0.52 N. This is about 5% of a vertical component of the force F_{ver} = 10 N. Therefore, the force F_{mir} can be neglected. The vertical component of the force is a gravity force, which is directed against the buoyancy force $F_{ar.}$ We could find the Archimedean force, determining the weight of the air displaced by the ball of radius R_{bl}=0.365 m: $F_{ar}=(\rho g \cdot 4\pi R_{bl}^3)/3$ = 2.2 N.

Mass of BL $m_{bl}=(F_{ver}+F_{ar})/g$=1.24 kg ($g$ is a free fall acceleration). The surface area of BL is $S=4\pi(D_c/2)^2$ = 1.67 $m^{2.}$ Let the density of the shell material is ρ_s=1000 kg/m^3. Then a shell mass (equal to the mass of BL) is $m_{bl} = \rho_s \cdot S \cdot a$. The thickness of the shell $a=0.74\cdot10^{-3}$ m.

Coulomb force of the BL charge pressure on the shell wall is $F_Q= Q_{bl}^2/2\pi\varepsilon_0(D_c)^2 = 0.67\cdot10^4$ N [7]. "Gradient" force, shrinking the shell, is $F_{sh}=(4\sigma a Q_{bl})/\varepsilon_0 D_c = 4.48\cdot10^5$ N. $\Delta F = F_{sh} - F_Q = 4.41\cdot10^5$ N. One can assume that ΔF is the pressure on the wall of the particles (charge carriers) possessing a kinetic energy. They push the wall with a force $\Delta F/S=2.64\cdot10^5$ N/$m^{2.}$ This value is equal to the energy density of BL: $\rho_E = 2.64\cdot10^5$ J/$m^{3.}$ In addition, the particles pressure must compensate atmospheric pressure $P_a = 10^5$ N/m^2. Hence the complete energy density of BL substance is ρ_{ET} =$3.64\cdot10^5$ J/$m^{3.}$ Volume of the internal sphere cavity $V = (4\pi R^3)/3$ = 0.2 $m^{3.}$ The total energy of BL $E_T = \rho_{ET} \cdot V = 0.74\cdot10^5$ J. This is the minimum estimate of BL energy. If the shell wall thickness a is larger in ten times (a= 0.74 cm), BL energy will be about 0.74 MJ.

When the cloud approaches to the location of BL, the force of attraction of BL to it becomes greater, but at the same time the horizontal component of this force reduces. Fig. 3 shows the variation with a distance L between BL and thundercloud of the values of vertical component of the force F_e of BL attraction to the cloud (dotted line) and a horizontal force component F_e (solid line). BL is on the left in zero coordinate, and the cloud approaches it from right to left.

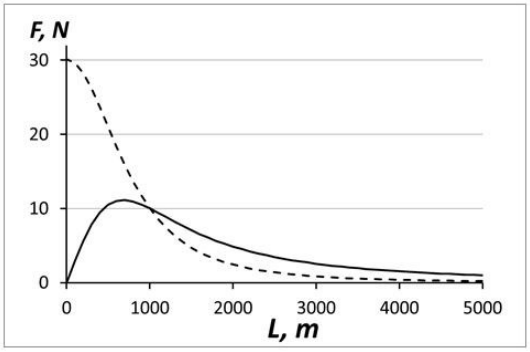

FIGURE 3. The dependence on the distance L between BL with the positive charge $Q_{bl} = 6.11\cdot10^{-4}$ C and thundercloud with a negative charge Q_c=5 C, flying at an altitude 1000 meters, of force F_e components, acting on BL. The solid line is the horizontal component of the force F_e, the dashed line is the vertical component of this force.

It's clear that at distances L>2000 m BL is practically unaffected by the cloud, and it moves, carried by the wind. However, in the region of L=400—1000 m horizontal component of the force F_e reaches its maximum and remains substantially constant over time. We can assume that this is the interval of distances L, when the force F_f of wind action on BL is compensated by a horizontal component of the electric force F_e, and BL appears inside a "trap". However, at the same time the vertical component of the force F_e continues to grow (it is increasing from 10 N to 25 N). The force compensating this increase can be an "anti-lifting force" that may occur in the presence of BL rotation. Indeed, at a height of about 40 m BL is moving in the boundary layer of air, wherein the wind velocity increases with height, and there are numerous eddies. Due to this BL can acquire a torque. In this case, it will be rotated around a horizontal axis in the direction in which the upper part of the ball is moving along the wind, and the bottom — against the wind. As a result, the force F_{rot}, directed downward, will act on the ball. The magnitude of this force is $F_{rot}=v_g \rho D_c \Gamma$, where v_g is wind speed (12 m/s), ρ is air density (1.13 kg/m^3) and Γ is a velocity circulation ($\Gamma = \pi D_c v_{rot}$) (v_{rot} is a linear speed of ball rotation) [6]. Substituting into this formula the numerical values of the parameters, we obtain F_{rot} = 22.7$v_{rot.}$ This means that if BL during its stay in the "trap" has increased the speed of rotation from v_{rot} = 0 to v_{rot} = 0.7 m/s, a force, pulling it to the ground, could be increased by 15 N.

Thus, the nature of BL motion inside the "Mitino trap" may be generally accounted, considering it as an ordinary material body possessing an electric charge. The effect on this charge of the alternating electric field of a nearby power line is negligible. Indeed, consider the limiting case, when the charge $Q_{bl} = 6 \cdot 10^{-4}$ C is affected by the electric field E_e = 100 V/m for $\Delta t = 10^{-2}$ s (a half period of AC 50 Hz). With the mass of BL 1 kg acceleration of BL equals $6 \cdot 10^{-2}$ m/s^2. For $\Delta t = 10^{-2}$ s BL will have time to shift to a distance of 3 μm. It is not possible to notice such an offset.

1. A. I. Nikitin, A. M. Velichko, T. F. Nikitina and I. G. Stepanov. Ball lightning observation in Mitino, the northwest district of Moscow, *Proc. 5th Intern. Conf. "Atmosphere, Ionosphere, Safety",* Kaliningrad, Russia, 2016. pp. 278—283.

2.Yandex Maps, https://maps.yandex.ru/213/moscow/?ll=37.341979%2C55.851214&z=17&l=sat&rl=37.34298797%2C55.85334908

3. P. A. Dolin, Basics of Industrial Safety in Electric Installations, Energoatomizdat, Moscow, 1984, pp. 310—318.

4. A. I. Grigoriev, Ball Lightning, YarGU Publishers, Yaroslavl, 2006.

5. A. I. Nikitin, T. F. Nikitina and A. M. Velichko, Radio-emission of corona discharge and ball lightning, *Elektrichestvo*, 2013, 9, pp. 12—22.

6. L. G. Loytzyansky, Mechanics of Liquid and Gas, Nauka, Moscow, 1987.

7. A. I. Nikitin, V. L. Bychkov, T. F. Nikitina, and A. M. Velichko, High-energy ball lightning observations, *IEEE Trans. on Plasma Science*, 2014, 42(12), pp. 3906—3911.

On Particle Acceleration and Relaxation in Ball Lightning

Geert C. Dijkhuis

Rotterdam, The Netherlands

Abstract Gamma flashes from lightning in Japan bear out early data from India and the UK. Multiple ball lightnings in Neuruppin, Germany repeat those in Amiens, France. For unstable nuclei in air we take runaway protons as alternative to gamma photons. Length of Lissajous-type loops defines elliptic integrals for particle acceleration in lightning channels by photonic response on structured surfaces. We present a canonical eigenstate solution for ball lightning with chiral characteristics.

Conclusive data from ground-based stations, airborne detectors and satellites establish lightning and thunderclouds as natural particle accelerators [1]. Enoto's team reports γ-rays beyond thresholds for atmospheric neutron production by photonuclear reactions.

Figure 1 shows leading decay channels for nitrogen nuclei including neutron capture, positron emission and electron-positron annihilation. During a winter thunderstorm in 2017, lightning struck near the monitor station at Kashiwazaki-Kariwa, Japan. Its γ-flash peak and afterglow decayed in 50 milliseconds, followed by line emission at 0.511 MeV lasting one minute. Observed decay rates and spectral cutoff agree well with laboratory data on γ-rays from electron-positron annihilation and nuclei excited by neutron capture.

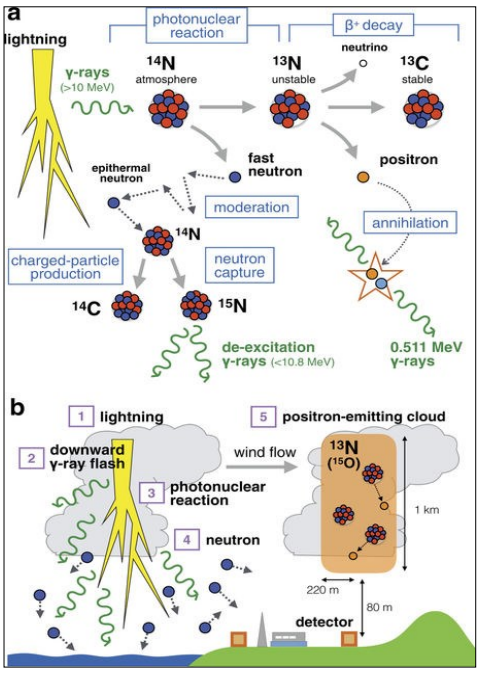

FIGURE 1. Photonuclear reactions in air from lightning in Japan [1].

Already in 1985 Shah et al. reported neutron counts from lightning near the Himalayan cosmic ray station in Kashmir, India [2]. Their experiment found 10^7—10^{10} neutrons per stroke from 11,200 events recorded over a 3-year period. Even earlier Ashby & Whitehead installed similar equipment near Abingdon, UK, for detection of atmospheric γ-flashes. Out of 4 events in one year, one event links 0.511 MeV photons from electron-positron annihilation with severe thunderstorm activity [3].

Recently, Boerner correlated ball lightning events with positive cloud-to-ground strokes in winter [4]. A spectacular case occurred during winter thunderstorm in Neuruppin, Germany. Its current peaked at 370 kA, creating multiple ball lightnings in maritime air of polar origin. One observer saw huge blue streamers or leaders driven sky-high near the impact point. Other observers report sudden indoor formation of ball lightnings, irregular motion, passage through curtains and windows etc..

As in Neuruppin a 1884 winter thunderstorm in Amiens, France, created several *foudres globulaires* after a flash that illuminated the whole city [5]. One fireball measuring 2—3 cm exploded softly after more than a second behind the scene of an ongoing theater performance. Decharme's report carefully details a hole left in window pane, showing edges free of any signs of melting. For such events Boer-ner considers atmospheric electricity above laboratory breakdown field 3 MV/m necessary.

By Altschuler's 1970 ball lightning model unstable nuclei come from capture of runaway protons [6]. Resulting oxygen and fluor isotopes copy the γ-ray profiles from β-decay channels in Figure 1. Our bosonic model treats ball lightning as filamentary plasma state self-confined by electrons circulating at the quantum limit [8]. Particle acceleration comes from vortex tubes stretching at constant volume, for linear growth of circulation energy with tube length. As smooth flux loop uniformly spiraling the unit sphere in Fig. 2 we define:

$$\{\cos(n\theta)\sin(\theta), \sin(n\theta)\sin(\theta), \cos(\theta)\} \qquad (1a)$$

$$L = 4E(-\mathrm{n}^2) \;\; ; \;\; L_0 = 2\pi \;\; ; \;\; L_\infty \to 4n \qquad (1b)$$

where elliptic integral E scales loop length L by quarter turns n. For n=0 the loop is a meridian circle with length 2π. Stretching by external torques shears loops into twin spirals smoothly joined at the poles as shown in Fig. 2. As tube radius shrinks for conservation of volume, particles accelerate for conservation of circulation. Conversely, shrinking flux loops decelerate circulating particles, releasing energy for sustained luminosity after ball lightning formation.

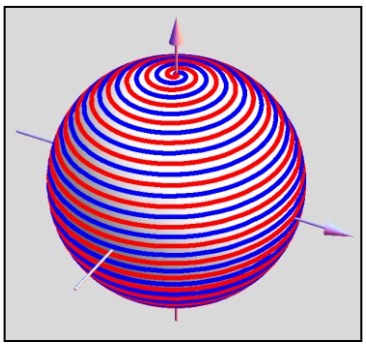

FIGURE 2. Sheared flux loop winds a double helix on the unit sphere. Colors highlight reversed currents.

Our quantum flux lattice extends reversible energy storage in ball lightning plasma beyond classical virial limitations. Perfect spherical shape as in Fig. 2 matches the iconic ball lightning event witnessed by R. C. Jennison after lightning impact on a commercial airliner [9]. High-energy aspects of ball lightning are unmistakable in the outdoor case witnessed by M. T. Dmitriev on the banks of Onega River in Russia after intense lightning [10]. By data from stellar evolution, fusion of atmospheric deuterium leads as nuclear process from particle acceleration in air. Flux tubes with one Bohr radius as core radius already open fusion regimes for deuterium nuclei. Notably their charged reaction products carry 2 and 4 cm in air, just as the widths of violet and blue shells seen around Dmitriev's ball lightning.

Flux tubes in our monolayer solution in Fig. 2 combine chiral geometry with knot-free field topology. Instead A. F. Rañada connects ball lightning with magnetic knots seen in nuclear fusion plasmas [11]. Their linked flux tubes conserve helicity in force-free states aligning currents with magnetic fields.

Recent work on Hopf fibrations treats evolution of similar knots by Maxwell's equations [12]. Spherical harmonics plot their relaxation towards force-free forms, including doubly linked trefoil knots.

From electromagnetic knots in optical laser light we return to Pendry's photonic microwaves for formation of ball lightning [13]. At Boerner's electric field threshold, exchange interaction between conduction electrons results from breakdown in air [8].

Hereby London depth replaces Debye screening as length scale, and circulation at quantum limit replaces collision frequency. Photonic plasma needs surfaces structured for surface plasmons. For lightning plasma our Lissajoux-type formula plots photonic surfaces through:

$$\{r\cos(m\varphi), r\sin(m\varphi), \sin(n\varphi)\} \ , \ m/n = 9/8 \qquad (2a)$$

$$L = \psi\, E(2\pi n, 1/\psi^2) \ ; \ \psi = \sqrt{(1 + 4m^2/n^2)} \qquad (2b)$$

with phase angle φ weighted by m=9 for horizontal planes, and n=8 for vertical ones in Fig. 3. Here elliptic integral E defines length L of the outer border-line. Arrows on the rim show alter-nation of ascending and descending field directions. Initial values m=0 and n=1 start the rim as vertical 2×2 square centered on the cylinder axis. Opposing axial torques at large m stretch flux loop length linearly with n as in Eq. 1.

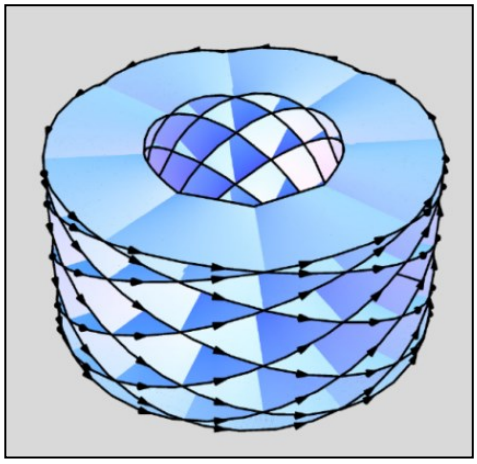

FIGURE 3. Radial channel structure from Eq. 2a for photonic response in lightning plasma.

Alternative surfaces structured for surface plasmons shown in Figs. 4a, b require minor changes in Lissajous formula Eq. 2a. With cylinder coordinate z in Eq. 3a, and colatitude θ in Eq. 3b axial channels in Fig. 4a and toroidal channels in Fig. 4b result through:

$$\{r_n \cos(m\varphi), r_n \sin(m\varphi), \mathrm{z}\} \quad , \quad 2r_n = 3 + \cos(n\varphi) \qquad (3a)$$

$$\{r_m \cos(\varphi), r_m \sin(\varphi), \sin(\mathrm{n}\theta)\}, \quad 2r_m = 3 + \cos(m\varphi) \qquad (3b)$$

with phase angle φ again weighted by m=9 and n=8 for channel systems in the same plasma volume as Fig. 3.

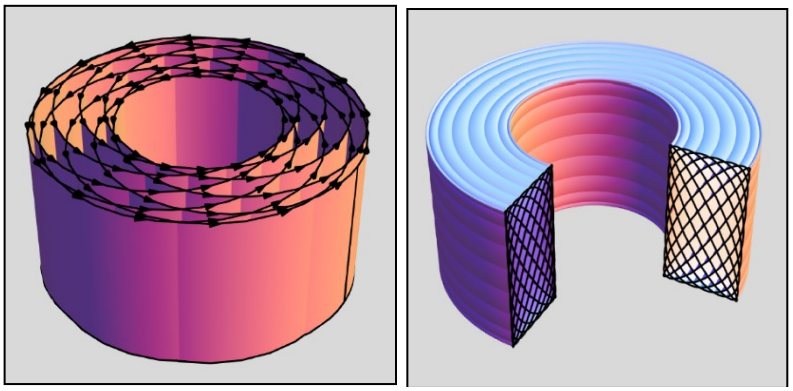

(a) (b)

FIGURE 4. (a) — Axial channels from Eq. 3a. (b) — Toroidal channels by Eq. 3b.

Like Pendry's wire grids our plasma channels foster photonic response in microwave regimes, including reversal of refraction angles, Doppler effects, Cherenkov radiation etc. as left-handed solutions of Maxwell's equations found by Veselago [14]. But his search for natural substances with simultaneously negative values of ε and μ was in vain. Today such materials exist for microwaves as man-made arrays of split-ring resonators, Swiss roll capacitors etc. At the same time inherent chirality characterizes our canonical solutions for the natural ball lightning [7,8]. Below we present one such canonical eigenstate.

Our real matrix method extends planar potential field and flow solutions into 4D quaternion space. Regular quaternion space has elliptic geometry, furnishing static solutions as given in refs. 8, 15. Related split-quaternion space has hyperbolic geometry for the kinematic solutions given in ref. 7. Symplectic symmetry of the respective matrices qualify their solutions as Hamiltonian dynamics.

Starting point for (split-)quaternion field solutions are the eigenstates of (split-)complex planes as in Fig. 5. Standard conformal maps serve for various symmetries and boundary conditions as in Fig. 6. Lastly spherical solutions as result from stereographic projection as used in cartography.

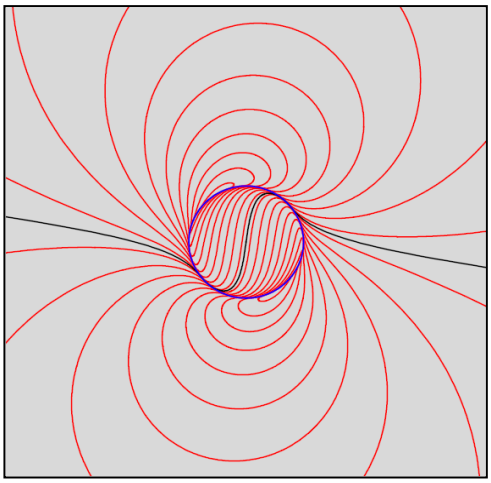

FIGURE 5. Swirling field lines of chiral eigenstate in the split-complex plane.

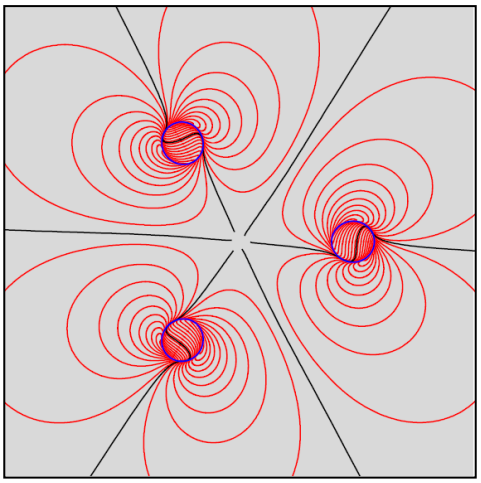

FIGURE 6. Complex cube root map for triples state with threefold axis.

Let independent variables φ, ψ in Eqs. 4 parametrize swirling characteristics of the split-quaternion eigenstate shown in Fig. 5. Their domains secure real values for coordinates in Eqs. 4. Tangent junctions on the unit boundary circle connect external curves from Eq. 4a with internal curves from Eq. 4b. Chirality χ changes sign across the circle. By Eqs. 4c the separatrix curve divides Fig. 5 in two equal parts.

$$\{x,y\} = \{\varphi + \chi\psi,\ \psi - \chi\varphi\}/r^2 \quad , \quad r^2 = \varphi^2 + \psi^2 \qquad (4a)$$

$$\{\xi,\psi\} = \{\varphi - \chi\psi,\ \psi + \chi\varphi\} \quad , \quad \chi^2 = 1 - r^2 \qquad (4b)$$

$$\{1, +\chi_s\}\varphi \quad , \quad \{1, -\chi_s\}/\varphi \quad , \quad \chi_s^2 = 1 - \varphi^2 \qquad (4c)$$

The complex cube root in Eqs. 5 maps nested flux loops in Fig. 6 that remain smooth and preserve the original topology.

$$x_1 = \mathrm{Re}\left[(x + \mathrm{i}y)^{1/3}\right] \ , \ y_1 = \mathrm{Im}\left[(x + \mathrm{i}y)^{1/3}\right] \qquad (5a)$$

$$\xi_1 = \mathrm{Re}\left[(\xi + \mathrm{i}\psi)^{1/3}\right] \ , \ \psi_1 = \mathrm{Im}\left[(\xi + \mathrm{i}\psi)^{1/3}\right] \qquad (5b)$$

Three unbounded separatrix curves partition the complex plane sector-wise. The threefold central symmetry requires prior translation and intrinsic rotation of the original eigenstate.

The circle radii and distances offer additional design freedom.

Hereby stereographic projections in Eq. 6 map circle centres on vertex points of the regular tetrahedron.

Now bounded separatrix curves intersect at both poles, and they also partition the unit sphere sector-wise.

$$2\,\{-x_1, -y_1, n-1\}/n \quad , \quad n = x_1^2 + y_1^2 + 1 \qquad (6a)$$

$$2\,\{-\xi_1, -\psi_1, \nu-1\}/\nu \quad , \quad \nu = \xi_1^2 + \psi_1^2 + 1 \qquad (6b)$$

Quartic roots in Eqs. 5 provide for extension to full tetrahedral symmetry as in carbon chemistry [8]. Our basic split-complex eigenstate in Fig. 5 also fits partitions shown as (semi-)regular and zonohedral solids in ref. 8. Here the 14-plane zonohedron stands out for 6:8 imbalance in spin directions.

In ref. 16 two merging eigenstates define a smooth footprint that covers the unit sphere by a baseball grid. Similar applications appear viable for calculation of electron states in stable Rydberg atoms [17].

1. T. Enoto et al., Photonuclear reactions triggered by lightning discharge, *Nature*, 2017, 551, pp. 481—484.

2. G. N. Shah et al*., Neutron generation in lightning bolts, Nature*, 1985, 313, pp.773—775.

3. D. E. Ashby and C. Whitehead, Is ball lightning caused by anti-matter meteorites?, *Nature*, 1971, 230, pp. 180—1822.

4. H. *Boerner, Analysis of conditions favorable for ball lightning creation, 2016,* 11 p, arXiv:1606.04421.

5. C. Decharme, Orage et coup de foudre en fragments globulaires. La Lumière électrique, *Journal Universal d'Electricité*, XI, 1885, pp. 551—553, http://cnum.cnam.fr/CGI/redir.cgi?P84.

6. M. D. Altschuler, L. L. House and E. Hildner, Is ball lightning a nuclear phenomenon?, *Nature*, 1971, 230, pp. 180—182.

7. G. C. Dijkhuis, On canonical eigenstates for ball lightning, *Second International Symposium on Ball, Lightning and Storm-related Phenomena (ISL-SRP)*, Aurillac, France, May 2017, (in press).

8. V. L. Bychkov, A. I. Nikitin and G. C. Dijkhuis, Ball lightning investigations. In: The Atmosphere and Ionosphere: Dynamics, Processes and Monitoring, Springer, 2010, pp. 201—373.

9. R. C. Jennison, Ball lightning, *Nature*, 1969, 224, 895 p.

10. M. T. Dmitriev, Stability mechanism for ball lightning, *Soviet Physics-Technical Physics*, 1969, 14, pp. 284—289.

11. A. F. Ranada, M. Soler and J. L. Trueba, Ball lightnings and force-free magnetic knots. *Proc. 6th International Symposium on Ball Lightning (ISBL-99)*, Antwerp, Belgium, 1999, pp. 102—107.

12. W. T. M. Irvine and D. Bouwmeester, Linked and knotted beams of light, *Nature Physics*, 2008, 4, pp. 716—720.

13. J. B. Pendry, L. Martin-Moreno and F. J. Garcia-Vidal, Mimicking surface plasmons with structured surfaces, *Science*, 2004, 305, pp. 847—848.

14. V. G. Veselago, The electrodynamics of substances with simultaneously negative values of ε and μ. *Sov. Phys. Usp*., 1968, 10, pp. 509—514.

15. G. C. Dijkhuis, On 3D potential field solutions for atmospheric charge distributions, PIERS Online, 2010, 6, pp 300—306**.** piers.org/piersonline/piers.php?volume=6&number=4&page=300

16. G. C. Dijkhuis, On ball lightning formation by soliton waves. *Proceedings, 13th International Symposium on Ball Lightning*, Zelenogradsk, June 2014.

17. G. V. Golubkov, M. G. Golubkov and M. I. Manzhelii, Rydberg states in the D layer of the atmosphere and the GPS positioning errors, *Russian Journal of Physical Chemistry B*, 2014, 8, pp. 103—115.

A Model for Ball Lightning Derived from an Extension of the Electrodynamics Equations

Daniele Funaro

Dipartimento di Fisica, Informatica e Matematica,
Università di Modena e Reggio Emilia, 41125 Modena, Italy

Forewords. Most of the results here presented come from the extension of the equations of electrodynamics developed in [1], [2]. This is basically the coupling of the Maxwell's model with the equations ruling fluid motion. The new formulation strictly includes the classical one, allowing for an impressive enlargement of the space of solutions. Before starting, it is important to remark that we are in vacuum, without the presence of sources, such as for instance given currents or magnets. Thus, our aim is for the moment to describe pure EM radiations. The novelty is to suppose that the divergence of the electric field may get values different from zero. Failing to accept this assumption, brings back to the standard Maxwell's equations, making our extension useless. Thus, interesting situations will be examined with the requirement that div**E** is not vanishing.

The model. As usual **E** and **B** denote the electric and magnetic field, respectively. We set by definition: $\rho = \mathrm{div}\mathbf{E}$. In addition, we have a new velocity field **V**, which has the role of indicating direction and speed of the energy flow (a sort of generalization of the Poynting vector). The system of equations is:

$$\begin{aligned}
\frac{\partial \mathbf{E}}{\partial t} &= c^2 \mathrm{rot}\mathbf{B} - \rho\mathbf{V} \\
\frac{\partial \mathbf{B}}{\partial t} &= -\mathrm{rot}\mathbf{E} \\
\mathrm{div}\mathbf{B} &= 0 \\
\rho\left(\frac{\partial \mathbf{V}}{\partial t} + (\mathbf{V}\cdot\nabla)\mathbf{V} + \mu(\mathbf{E}+\mathbf{V}\times\mathbf{B})\right) &= -\nabla p \\
\frac{\partial p}{\partial t} &= \mu\rho\,\mathbf{E}\cdot\mathbf{V}
\end{aligned}$$

where c denotes the speed of light and, up to dimensional scaling, the scalar p acts as a pressure. The constant μ has the dimension of charge divided by mass and has been estimated to be approximately 2.85×10^{11} Coulomb/Kg. A charge density can be defined by setting $\varepsilon_o\rho$, where ε_o is the dielectric constant in vacuum. Formally, it is also possible to introduce a density of mass as $\varepsilon_o(\rho - p/c^2)/\mu$, although there is no real matter for the moment. This setting is fully consistent with all the relevant physical properties (see again [1], [2]). We recognize the Euler's equation with a forcing term given by the vector $\mathbf{E} + \mathbf{V} \times \mathbf{B}$, which recalls the Lorentz's law. By taking the divergence of the first equation, we get the continuity equation for the charge density, so that such a constraint does not need to be imposed

independently. The last relation says that pressure may raise as a consequence of a lack of orthogonality between **E** and **V**. The revised set of equations is similar to that ruling plasma physics (see e. g. [3], chap.10), with the difference that no effective matter is present in our case. We trivially return to the Maxwell's case in vacuum by imposing $\rho = 0$ and $p = 0$. The important fact here is that the vector field **V** is one of the unknowns and it is not directly related to the product **E** × **B**, as suggested by the classical theory.

Free waves. A special case is obtained when D**V**/Dt=0 and p=0. In this circumstance we have (recall that ρ = div**E**):

$$\frac{\partial \mathbf{E}}{\partial t} = c^2 \mathrm{rot}\mathbf{B} - \rho\mathbf{V}$$
$$\frac{\partial \mathbf{B}}{\partial t} = -\mathrm{rot}\mathbf{E}$$
$$\mathrm{div}\mathbf{B} = 0$$
$$\rho\,(\mathbf{E} + \mathbf{V} \times \mathbf{B}) = 0$$

This version (see Fig. 1) produces solutions called *free waves*. In this situation, it is possible that **V** is a gradient of a potential Ψ. Since the constancy of the speed of light leads to the *eikonal* equation: |**V**|=|gradΨ|=*c, here* the waves exactly follow the rules of geometrical optics. The main consequence is the possibility of simulating 'photons' (i. e., non-diffusive EM emissions behaving like particles) in the framework of classical theories, reopening the discussion on the problem of wave-particle duality. Such solutions are not present in the standard Maxwell's theory (ρ = 0). It is shown that the integral (extended on the support of a photon) is zero, for both the density of charge and mass, in agreement with expectations.

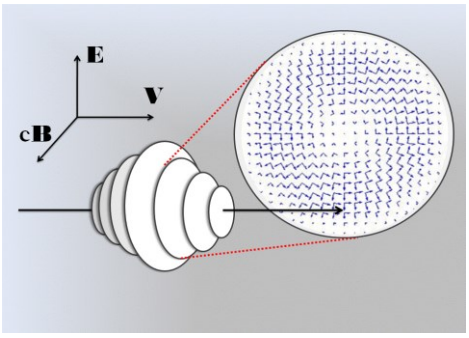

FIGURE 1. A special subset of solutions is obtained by requiring that **V** has no acceleration. Non-dissipative compact-support EM waves, travelling straightly at the speed of light, can be now modelled. Each travelling front displays orthogonal EM fields with div**B**=0, however div**E** is not necessarily equal to zero.

Vortex rings. Since the new model equations are the results of the coupling with fluid equations, other more complicated structures may be taken into consideration. Among these, *vortex rings* have a special attention due to their extreme stability (see Fig. 2). In [1], [2], [4], solutions representing EM waves trapped in rings have been proposed. These are in general the mathematical combination of a dynamical component and a stationary one. The two pieces sum up linearly in simple situations, but they are mixed up in more serious cases. Each one cannot exist without the other. The dynamical component is somehow transparent, by meaning that the evolution of

the corresponding EM fields displays zero average in space and time. The stationary component is needed for stability and provides the object with effective electric and magnetic properties. It displays a field **B**, whose lines are closed and turn around the main axis of the ring, and a radial electric field **E**. The stationary component, however, may contribute only in part to the whole energy. Again, here we are talking about pure EM waves (in the extended meaning of the term, according to the new model equations), since no charged massive particles have been introduced so far.

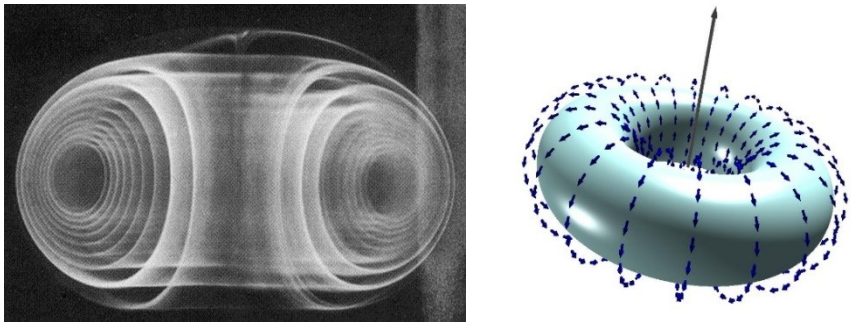

FIGURE 2. Fluid vortex ring colored with dye (courtesy of T. T. Lim, Nat. Univ. of Singapore). Similar behavior is obtained in the framework of EM waves with the help of the new set of equations.

Stability of EM ring structures may be deduced through very classical arguments. Each point of the rotating immaterial fluid, described by the velocity **V**, can be imagined to be an infinitesimal entity carrying density of charge different from zero. A magnetic field is present, so that the stream evolves along curbed lines due to the Lorentz's force. This force actually acts on the points, since they also carry a non vanishing density of mass. An internal pressure is generated and the surface of the ring is characterized by having the gradient of pressure equal to zero.

Another way to explain stability is to argue in terms of general relativity. The model equations are obtained by energy and momentum preservation. In fact, they are recovered from the sum of the EM stress tensor with a suitable mass type tensor (see [1]). This sum can be put on the right-hand side of Einstein's equations in order to get the metric. It turns out from the theory that the scalar curvature R of the metric is proportional to the pressure potential p. If it happens that the geodesics are the stream lines of the ring, then the structure should be stable. Thus, some photons are following the space-time geodesics created by their own motion. Such peculiar situations are not always obtained, but only when suitable conditions of energy and geometry are satisfied. Note that in the case we are discussing there are no classical masses at all, by the way the curvature of the space-time is a consequence of the presence of a nontrivial right-hand side in Einstein's equations.

We denote by η the major diameter of the ring and by q its global charge. Combining (105) and (111) in Appendix G in [2], one arrives at the following relation:

$$| q | \approx 42.35\ \eta\ \varepsilon_o\ c^2/\mu \approx 1.18\ \eta\ 10^{-4} \qquad (1)$$

For example, when η is of the order of 10^{-15} meters, one finds that $|q|=e$ is approximately the charge of the electron. In this situation, by integrating the mass density on the volume one finds the global mass, which agrees with that of an electron. Of course, *spin* is directly related to the rotation of the dynamical part of the wave. This suggests the possibility of modelling electrons within a pure EM context. Toroid models of the electron are present in the literature (see [2], section 2.1, for a review). The proposal discussed here seems to fulfil all the basic features.

Plasma dynamics. We can now improve a bit our knowledge about plasmas in this new framework. We first introduce electrons and ions in the model. This is easily done through the standard equations (see [3]) and by suitably adding terms such as **V**div**E**. In this fashion we have the combined action of the density of charge carried by the particles (moving at speed **v**) and that of the radiation evolving at speed **V**. Indeed, it is not surprising that the electric field in the void interspace between charged particles may assume values of ρ different from zero. This is a consequence of the finiteness of the speed of light, especially when high frequencies or fast movement of particles are involved. It is true that Coulomb's law guarantees div**E**=0 between particles, nevertheless it requires the information to travel at infinite speed. Therefore, in the new version, the Gauss theorem should be interpreted in milder form. The movement of massive particles is now fully coupled with the exchange of EM radiations. It is like dealing with three species (electrons, positive ions, pure waves). Of course, this extension is made in such a way that for div**E**=0 one returns to the usual plasma model.

Ball lightning. According to what has been said above, a pure EM vortex ring carries an intrinsic internal density of charge. Real charged particles (i. e., made of matter) can enter the toroid and find their equilibrium. They can move relatively slow, or they can even remain steady. Everything is ruled by the model that combines the standard plasma development with the exchange of EM information. As a consequence, the total charge comes from averaging the contribution of the actual physical charges with that naturally generated at the interior of the ring itself. The whole structure is stable for the reasons we specified before. For example, assuming that a negative density of charge is responsible for the stability of the ring, a certain number of positive ions can be stored into it, without reciprocal repulsion. We recall once again that we have a confined plasma into a container that has no physical boundaries. There is indeed an internal pressure that arrives with zero gradient at the border. These statements are waiting however to be confirmed by numerical experiments. If the object has a diameter $\eta \approx 10^{-1}$ meters (typical magnitude of a BL), we get from (1) that q is of the order of $10^{-5} \div 10^{-4}$ Coulomb (in rough agreement with observations, see e. g. [5], [6]).

By computing the energy of the stationary component plus that of the ions, we get a quantity far below the level of what it is measured in BL. We have to remember however that a dynamical component (having $\rho = 0$, see [4]) also exists and may carry a large amount of energy. We guess that a BL is the addition of a very energetic EM rotating wave (with zero kinetic energy) with the stationary part mentioned above. The two combine in order to stay confined in a portion of space. Exact computations can be performed for rings having the minor diameter much smaller than the major one. In this case, the coupling between the stationary and dynamical parts is very mild, so that the last quantity can in principle reach arbitrary intensities. By impacting with the environment a BL can dissipate electromagnetic energy and diminish the magnitude of the dynamical rotating component. Radio waves are emitted during this process. Their frequency is inversely proportional to the diameter η and are of the order of GHz when $\eta \approx 10^{-1}$ meters (the wave-length of such a cavity). When most of the energy is dissipated, the dynamical part of the trapped wave does not provide anymore a good support to the stationary part, so that the object becomes unstable. Without the negative constraining force, the positive ions tend to repel creating an explosion.

Other comments. Due to viscosity, fluid vortex rings tend to shift naturally in the direction of the axis. This is expected to be true also for plasma rings. Moreover, these structures are charged, so that they may follow specific (invisible) electric patterns in the atmosphere, especially if air conditions are favorable. Rings can take the shape of a ball (but showing a different topology, however) when their hole is reduce to a segment (Hill's vortex). In this situation, the study of the coupling of the different components (stationary and dynamical EM parts, plus ions) becomes rather involved. We have no conjectures at the moment about the reason why BL emit radiations in the visible range. Earlier models describing BL as EM bubbles were discussed for instance in [7], [8], but turned out to be not fully satisfactory. In our opinion, if we want to follow this direction of research in BL, the extension of the EM equations is a necessary step to reach more convincing results.

1. D. Funaro, Electromagnetism and the Structure of Matter, *World Scientific*, Singapore, 2008, ISBN: 978-981-281-451-7.

2. D. Funaro, From Photons to Atoms, *The Electromagnetic Nature of Matter*, 2012, arXiv:1206.3110v1

3. J. D. Jackson, *Classical Electrodynamics*, II Edition, John Wiley & Sons, 1975.

4. C. Chinosi, L. Della Croce and D. Funaro, Rotating electromagnetic waves in toroid-shaped regions, *Int. J. Modern Phys*. C, v.21, n.1 (2010), pp. 11—32.

5. A. I. Nikitin, The principles developing ball lightning theory, *J. Russian Laser Res*., v.25 (2004), pp. 169—191.

6. V. L. Bychkov et al. (Editors), The atmosphere and Ionosphere, Elementary Processes, monitoring and Ball Lightning, *Springer*, 2014, ISBN: 978-3-319-05238-7.

7. V. G. Endean, BL as electromagnetic radiation, *Nature*, v.263 (1976), pp. 753—755.

8. G. A. Dawson and R. C. Jones, Ball lightning as a radiation bubble, *Pure and Appl. Geophys*, v.75 (1969), pp. 247—262.

Long-range Interaction in Processes of Heat Transfer and the Atmosphere

Dmitriy S. Baranov[1,2], Valeriy N. Zatelepin[2]

[1]Joint Institute for High Temperatures RAS, Russia, Moscow,125412, Izhorskay, 13
[2]INLIS Laboratory, Russia, Moscow,127521, 8 proezd Marinoy Roschi, 30

Introduction. In modern physics for the calculation of heat transfer processes introduces the concepts of thermal energy and of the vector flow of heat energy. The application of these concepts in the equation of energy in the mechanics of fluid and gas is given in [1]. There are three components of the heat flow vector: convective, conductive and radiation heat flows. For the present work it is essential that an experimental specimen of the substance can be protected from all three components of the heat flux with the help of thermal insulating panels.

The specimen in our experiments was a small piece of lead weighing 10^{-2} kg (10 g) and a total surface area of 10^{-4} m^2 (1 cm^2). As a heat insulator, pressed mineral heat insulator with the following thermophysical parameters was used: density 130 kg/m^3, thermal conductivity 0.044 W/m° C, heat capacity 800J/kg° C. Panel thickness of the insulator in Experiment 1 was 10 cm. For sure isolated from the long-wave radiation panel of the heat insulator was covered with aluminum foil. The sample temperature was measured by chromel-alumaloy a K-type thermocouple and were recorded with an electronic thermometer ATT2036 with a time step of 10 seconds. The temperature measurement accuracy was of 0.1° F (about 0.05° C).

Experiment 1. The scheme of Experiment 1 is shown in Fig. 1. A specimen with attached to it the thermocouple is located behind the panel of a heat insulator. Firs we reach a thermal equilibrium with the environment during the 1—1.5 hours. The equilibrium temperature (room temperature) is about 26° C. After that, at the area at a distance of 1.5 m in front of the insulator panel the man (heated object) came in. After 5 minutes the man came out of that area.

The black curve in Fig. 2 shows the results of temperature measurements in Experiment 1. The appearance of a person (abscissa 10) leads to an immediate increase in the temperature of the sample at 0.15° C. After 200 seconds (abscissa 30) people left the area in front of the screen. The temperature of the sample returned to its initial value.

Evaluation of the characteristic warm-up time of the thermal insulating plate, the parameters of which are specified above, by 0.15° C when the radiation heat flow to the side of the plate facing the person, gives a value of 1700 sec. This time is much longer than the time of a standing person in the area in front of the screen. In addition, the return of temperature to the initial value indicates that the heat insulator does not warm up.

In the second phase of Experiment 1 near the thermocouple (Fig. 1) electrical motor is placed. The electrical motor rotates a metal (Fe) disk (10 cm diameter) with a frequency of 3500 rpm. The temperature of the specimen placed near the rotating disc is shown in Fig. 2 with the red curve. Similar to the previous case at some moment (abscissa 10) into the area behind the screen a person (heated object) came in . This leads to a more intense increase in the sample temperature in comparison with the case without rotating disc. It is seen from the comparison of the red and black curves in Fig. 2.

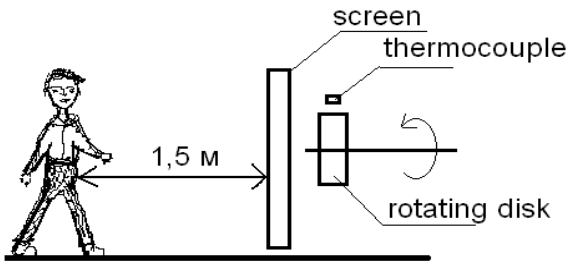

FIGURE 1. Scheme of the Experiment 1.

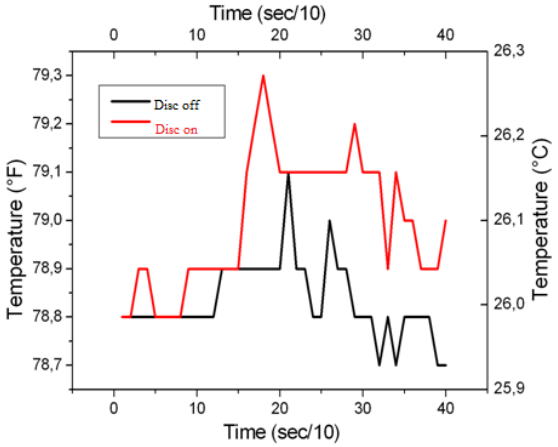

FIGURE 2. Change the temperature of the specimen when the heated body appears in front of insulating panel: the rotating disk is switched on (red curve) and off (black curve).

To explain experiments let suppose that not only conductive heat flow participates in the process of heat exchange through the insulating panel to bring the power to the specimen, but also the penetrating “ether substance”, filling the entire space around. When a heated object appears, the flow of the ether moving to the specimen becomes more heated and increases the temperature of the specimen.

The rotating disk increases the flow of the heated ether substance entering the sample during the flight through it, which leads to an even more noticeable increase in the temperature of the specimen.

Experiment 2.The Fig. 3 shows a diagram of the Experiment 2. Ceramic cylinder with Nickel-hydrogen mixture is heated by electric current and is blown by air flow from the right to the left of the cylinder for cooling. Above the cylinder is a thermal insulating plate. Several thermocouples are used in the experiment.

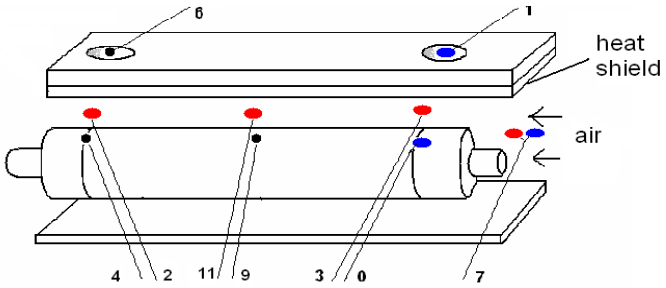

FIGURE 3. Scheme of Experiment 2.

In this case, we will analyze the readings of thermocouples marked in blue (thermocouples 0, 1 and 7). On the Fig. 4 on the x-axis shows the number of measurement temperature (1/10 sec). and y-axis — temperature: the black curve is air cooling, red — the surface temperature of the heated cylinder, green — temperature at 15 mm depth inside the insulator on the cylinder. The total time of the experiment is more than 6 hours. For more than one hours of work the following distribution of temperatures was reached: air cooling — 103.5° F, the internal area of the insulator — 106.5° F, the temperature at the surface of the ceramic tube — 107.6° F. This distribution is understandable, because the surface of the tube, inside of which the heater is placed has the highest temperature.

At some point (abscissa 1300) the intensity of flow of the blowing air is increased. This leads to that the temperature inside the heat insulator exceeds the temperature on the surface of the tube: the surface of the tube (red curve) — 103.3° F, inside the heat insulator (green curve) — 103.7° F. This distribution of temperature is stationary, because it remains stable during for several hours. At point 2850, the cooling air velocity decreases and the temperature distribution is returned to its initial value.

We may understand the nature of the temperature distributions , if we assume that throughout of the electric heater (inside the tube) moves the heated penetrating “ether substance”. It provides its heat energy to the thermocouple passing through it and its heat energy passing through insulator substance. This can be interpreted as the presence of an internal heat source in the substance proportional to the volume of the substance.

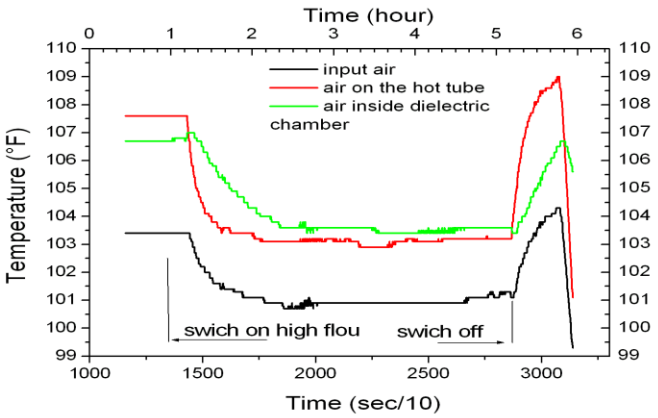

FIGURE 4. Time dependence of the temperatures.

Qualitative considerations on the effect of "ether substance" on heat transfer in the atmosphere. It should be borne in mind that perhaps the "ether" consists of at least two components: light and heavy. In this work, we will talk about the "ether" of the second type with a greater mass. Perhaps an "ether substance" consists of penetrating of small size particles with large magnetic moment. A particle of the ether substance fills all space, moving in different directions and interact rather weakly with ordinary matter. The particles of the ether substance participate in an electromagnetic interaction and react more strongly with the moving charged particles (electric current) when interacting with a conventional matter. The "hydrino" and the so called " the atom Barut-Vigier" [2] can be considered as a candidate for ether. We prefer to call the ether substance by the term "coronium", which was introduced by D. I. Mendeleev in his article [3].

Presented in this work results help for evaluation of coefficient of interaction "coronium" with an ordinary matter. For such estimates, the ideology of energy loss calculation when a beam of particles is passing through a substance can be used. When heavy particles pass through the substance, energy loss by mass braking capacity is introduced [4]. We introduce a similar value in our case by the relation $K = (dE/dx)/(E\rho)$. Then assuming that the theermocouple temperature changing (0.15° C) in Fig. 2 is connected with the growing thermal energy of "coronium" when it is passing through the heated body (the characteristic density 10^3 kg/m^3, the typical size of heated body is 0.3 m, a characteristic temperature difference between heated body and room temperature is 10° C) we get an estimate of $K = 0.5\times10^{-4}$m^2/kg.

"Coronium" should well retarded by a dipole medium, such as clouds, consisting of water vapors. In order to assess the cooling of the air by the flow mass "coronium" coming from space at a temperature T = –270° C, it is necessary to know the flow density of "coronium" and its heat capacity. We do not know

these values yet. But to estimate the horizontal heat exchange between air masses with temperatures (T1-T2) = 10, the characteristic size L= 10^3 m is sufficient to use the coefficient K

$$dT = K\times 1{,}03\times(T1\text{-}T2) \times L = 0.5^\circ C$$

The mechanism of heat exchange, which is considered in this paper, is not taken into account in the modern physics of the atmosphere. The coronium flow, especially the vertical flow, provided the cool "coronium" to the Earth, can significantly influence the formation of the temperature field in the atmosphere. In particular, freezing on the ground on a clear night may be associated with cooling the ground by the flow of the cosmic ether.

1. L. G. Loytsyanskiy, *Fluid and Gas Mechanics*, Moscow, 1973, 257 p. (in Russian)

2. A. Dragic, Z. Maric, and J. P. Vigier, New quantum mechanical tight bound states and "cold fusion" experiments, *Physics Letters A*, 2000, 265, pp. 163—167.

3. D. I. Mendeleev, An attempt of chemical understanding of the ether, 1902, (in Russian)

4. I. S. Grigoriev and E. Z. Meylikhova, *Physical magnitudes*. Handbook. Moscow, Atomizdat, 1991, 1332 p. (in Russian)

Electro-Hydrodynamic Phenomena over Liquids under Influence of Corona Discharge

Victor. I. Abakumov, Vladimir L. Bychkov, Adliya R. Bikmukhametova, Vladimir A. Chernikov, and Daniil A. Safronenkov

Faculty of Physics, Lomonosov Moscow State University, 119234, Moscow, Russia

Introduction. Present investigations are devoted to formulation and undertaking of experiments with corona discharges realized over surfaces of different liquids. Investigations when a surface of one of the electrodes is covered by a liquid or is an electrode itself are of interest for hydrocarbon fuel activation, search of undesirable liquids elimination in engines, problems of ecology and disinfection. They are of a fundamental interest, since the corona discharge allows to obtain new information on phenomena connected with development of electro-hydrodynamic instabilities in new, earlier unrealized conditions. Such investigations are developing now, that is a reason for undertaking of these ones. In this work we are concentrated on electric-hydrodynamic features of corona discharges which are practically uninvestigated yet. However, there is limited information about any discharges over surfaces of liquids [1, 2] and it is obtained mainly for

electrolytes or water. From the application point of view it is interesting to know how a surface of a liquid fuel acts under an impact of gas discharges. Therefore our work is devoted to investigations of electric-hydrodynamic (EHD) effects caused by corona discharges over liquid. We made several series of experiments with positive and negative coronas over surfaces of tap water, distilled water, alcohol, glycerin, and their mixtures.

Electro-hydrodynamics phenomena with corona discharges. Corona discharges are typically obtained by applying of a high potential between a small diameter needle, charged positively or negatively and plate or coaxial cylinder [3] charged oppositely.

The principle scheme of the experimental device is represented in Fig.1.

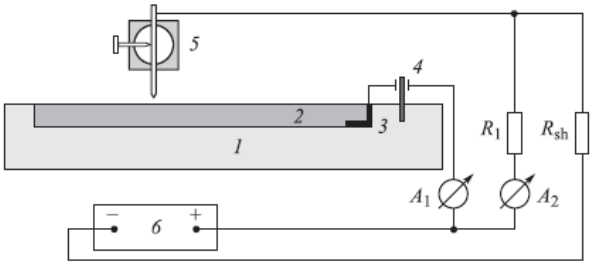

FIGURE 1. Principle scheme of the experimental device. 1 — Ditch, 2 — Liquid (water, alcohol, kerosene), 3 — Anode, 4 — Post, 5 — Cathode, 6 — Power supply

It consists of a ditch filled with a liquid (water, alcohol, kerosene, etc), and electrical circuit. A current in a discharge was measured by a milliampere meter A_1, a voltage was measured by a chain consisting of resistance R_1 and a milliampere meter A_2.

Experiments have been carried out with a help of different cavities: rectangular — dielectric, cylindrical — dielectric and steel. Sizes of the rectangular cavity, were 70×20×15 mm (length, width and depth). Characteristics of cylindrical cavities were ∅125, 10 mm and ∅185, 20 mm, respectively. An investigating liquid was poured into a cavity, a negative or positive electrode was located directly over the liquid, a distance between the electrode and the liquid could be varied in a range (1—30) mm. The needle diameter was 3 mm, a radius of a tip was 0,4 mm. An electrode of another polarity was located directly in the liquid. (The metallic cavity was used as the electrode). It was connected with a feeding source through a hermetic unit. In this case the liquid becomes the second electrode.

A high voltage generator was used as the feeding source, it allowed to measure a voltage on the electrodes from 2 kV to 25 kV with a step of 1 kV. Typical range of the voltage was 5—25 kV. Appearance of the spark discharge was accompanied with a drop of the voltage at the capacity, which was detected by the voltmeter. In this device we used a ballast resistance, which value was 510 MΩ. Typical values of a current were 1—50 μ A.

Experiments with discharges over tap water. Our experiments have shown that application of negative and positive corona discharges over water surfaces in plastic or metallic cavities lead to appearance of a rotating funnel, it was evidently caused by the ion wind, see Fig. 2.

FIGURE 2. Appearance of a funnel over the water surface covered with the wooden powder, metallic cavity, a distance between the upper electrode and a surface is 5 mm, electrode is in central position, positive corona.

Vortices over surfaces of liquids appeared in case of non-central position of the upper electrode with respect to the cavity or in rectangular cavities.

Fig. 2 represent appearance of a funnel over the water surface covered with the wooden powder. Fig. 3 represent a funnel over the alcohol surface.

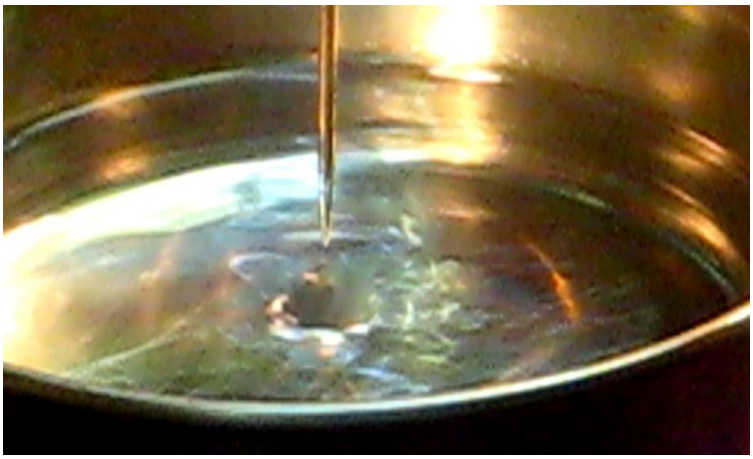

FIGURE 3. Appearance of a cavity over the alcohol surface, metallic cavity, a distance between the upper electrode and a surface is 5 mm. Positive corona.

Experiments with alcohol. In case of alcohol in the plastic or metallic cavities corona discharges lead to appearances of different EHD effects over the surface of the liquid.

Funnels appeared at both polarities of the upper electrode. In Fig. 3 we represent such a phenomenon. In case of the positive upper electrode firstly a rotating funnel usually appeared (it was evidently caused by an ion wind). This process finishes by an appearance of liquid columns Fig. 4. The development of the process finally finishes by appearance of the arc. Usually this takes place at high applied voltage (15—25 kV). These columns are either standing in the funnel center or on a side of a funnel.

FIGURE 4. Appearance of a flat column over the alcohol surface, metallic cavity, a distance between the upper electrode and a surface of the liquid is 7 mm. Positive corona.

Liquid columns have usually a widening at the tip. Sometimes a violet-bleu glow on the tip appears. It speaks about the breakdown field realization near the tips. Images were obtained with a help of a digital video camera Canon Digital IXUS 70 with frame duration 33 ms.

Similar phenomena are known in EHD [4—6]. They are connected with a development of Rayleigh, Taylor, Tonks and Frenkel electrostatic instabilities on surfaces of charged drops and jets when Coulomb forces of accumulated charges become greater than the surface tension force.

Special interest represents experiments with the metallic (Al_2O_3) powder with a particle size about 30 μm on a liquid surface. In this case which is shown in Fig. 5. When applied voltage exceeds a value of 7 kV vortices that mix the liquid very intensively appear.

Experiments with dry and wet clay were also conducted. Some of them have interesting results (Fig. 6), such as arise of a clay column, covered with metallic powder that provides a possibility to deeper understand a way of EHD instabilities development.

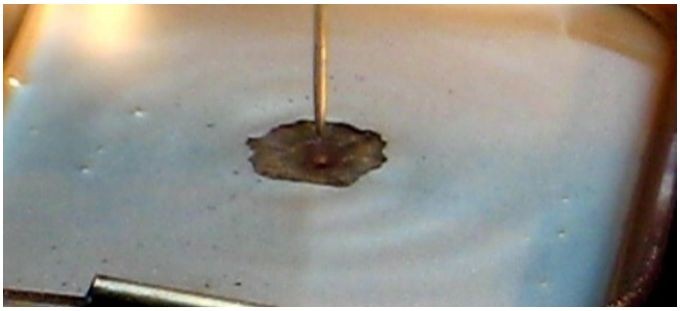

FIGURE 5. Appearance of curls which are remixing liquid, a distance between the upper electrode and a surface 7 mm. Positive corona.

FIGURE 6. Column has a length of 7 mm and a diameter 1 mm.

Conclusions. Creation of corona discharges has been realized over tap and distilled water, alcohol, glycerin and their mixtures.

Conducted experiments and their analysis show that the corona discharge over liquids can cause different hydrodynamic phenomena including appearance of the ion wind and different hydrodynamic instabilities. Funnels appear both in positive and negative coronas.

Appearance of liquid jets and columns is a result of the Tonks — Frenkel instability in conditions of positive and negative corona [4, 5]. This phenomenon depends on a value of electric field strength and is better realized in liquids with low density and surface tension.

Separation of these jets and columns in drops are connected with instabilities of charged drops.

These experiments help to clarify modes of discharges realization and their connection with appearance of funnels on the surfaces of liquids and columns in case of alcohol.

Luminescence over tips and columns manifests the discharge creation there and can be the cause of St. Elmo's fires origination.

1. *Encyclopedia of low temperature plasma. Applied Plasma Chemistry*. Ed. Lebedev Yu. A., Plate N. A., Fortov V. E., 2009, Yahys-K publishers, Moscow

2. V. Bychkov, V. Chernikov, A. Ershov, I. Esakov, A. Kostiuk, *Corona discharge over a surface of a liquid*, AIAA-2009-1554. 47th AIAA Aerospace Sciences Meeting. 5—8 January 2009, Orlando World Center Marriott. Orlando. Florida.

3. Yu. P. Raizer, Gas discharge physics, Nauka, Moscow, 1992.

4. V. A. Saranin, Equilibrium of liquids and its stability, Institut Kompiuternykh Issledovanii Publishers, Moscow, 2002.

5. L. D. Landau, E. M. Lifshitz, Electrodynamics of continuous media, Moscow, Nauka, 1982.

Interaction of Plasma with Earth Surface

Victor. I. Abakumov[1], Vladimir L. Bychkov[1], Adliya R. Bikmukhametova[1], Vladimir A. Chernikov[1], Daniil A. Safronenkov[1] Tamara O. Mikhailovskaya[2], Aleksandr P. Shvarov[2]

[1]Faculty of Physics, Lomonosov Moscow State University, 119234, Moscow, Russia
[2]Faculty of Soil Scvience, Lomonosov Moscow State University, 119234, Moscow, Russia

Introduction. Experiments on thermal and plasma effects on soil have been carried out to determine possible parameters of interaction of natural objects such as thunderstorm discharges plasma and long-lived luminous formations (LLPF) with soil and vegetation cover. Experiments have been carried out on the interaction of the capillary and corona discharge plasma with the soil and soil-like objects of various compositions. The parameters of heating and plasma, under which the latter can affect the soil, are determined. Natural studies of the monolith of chernozem of the pre-Caucasian leached and model studies of typical chernozem, clay and sand have been carried out and changes in electrical conductivity and other soil properties have been revealed. Investigations of the interaction of the corona discharge with the surface of liquids, simulating the effect of the flows of charged particles created in the pre-thunderstorm atmosphere, on the soil cover have been carried out.

One of the little-studied areas of knowledge related to the study of atmospheric electricity and its interaction with the Earth's surface and soil is the problem of such interaction with the participation of LLPF and ball lightning (BL) [1]. They have high energy [2], which follows from the analysis of the traces of their impact on the Earth's surface with the creation of slag areas and molten surface areas. Another possible manifestation of their interaction with the Earth's surface is the so-called "crop circles (CC)" in fields that arise during vegetation of plants.

However, the interaction of LLPF and BL with soil has not been described so far in known literature. At the same time, studies of this interaction results allow to evaluate certain features of these natural phenomena.

Modeling studies of thermal and plasma effects on typical black clay and sand have been carried out to identify mechanisms of natural LLPF effect, and changes in electrical conductivity and other soil properties have been revealed.

Description of the event and sample parameters. The place of the investigated impact of LLPF with the soil is the field in the area of the village of Dondukovskaya of the Gyaginsky district of the Adyghe republic, Russia.

Samples were provided by observers. In the soil under the place of appearance of LLPF, according to eyewitnesses, a hole had appeared. The hole parameters are shown in Fig. 1 and Fig. 2.

FIGURE 1. A hole in the soil.

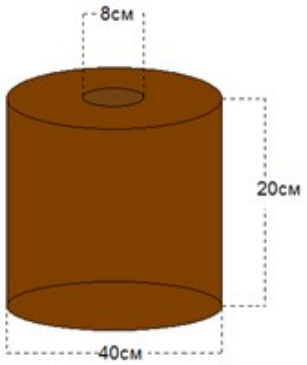

FIGURE 2. Monolith parameters.

The volume of the monolith is 21.56 dm^3, the mass of the monolith is 28.59 kg, the density of addition is 1.33 g /cm^3. Objects of this type have not been previously investigated, neither from points of view of physics and soil sciences.

Methods used by us to study the samples: electrical conductivity of the samples measurements, the waxing (determination of the porosity of the samples), the magnetization measurement. Experimental action of the capillary plasmatron plasma on samples of chernozem, at inputted energy of about 190 J, at an exposure time of 10 ms was carried out. Experiments were conducted with corona discharges in order to obtain pictures of ion the wind effect on the surface of liquids and liquids coated with metal and wood powders. Experimental action of the corona discharge plasma on the soil at different polarity of the corona.

As a result of the studies, the electrical conductivity change of the soil samples exposed to LLPF was found to be more than 2.5 times (see Fig. 3). The density of the monolith decreased from 1.9 g/cm^3 to 1.5 g/cm^3 as it moved from the dense wall of the hole in the monolith to the periphery of the piece of soil, to external control (see Fig. 4). The value of the maximum density exceeds the value of the external control density by 1.2 times (see Fig. 5).

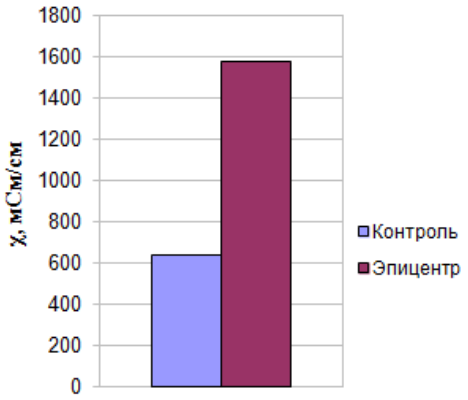

FIGURE 3. Difference in the mean conductivity of samples from the epicenter, (mSm/cm) Violet-control, crimson-epicenter.

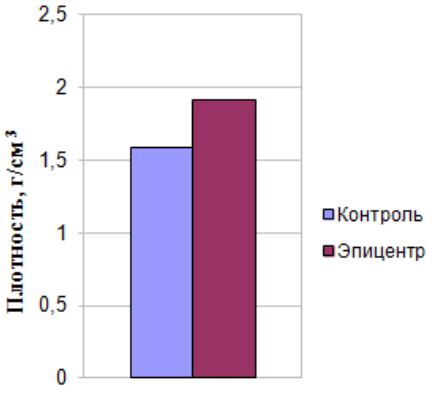

FIGURE 4. Difference in the values of the maximum density of samples from the epicenter, (g/cm^3) Violet-control, crimson-epicenter.

The porosity of the aggregates as a result of compaction was reduced by an average of 17%. An investigation of the magnetic characteristics with a vibration magnetometer (see Fig. 6) also showed a change in the magnetization curve for samples exposed to LLPF, as compared to chernozem external monitoring (see Fig. 7 a, b).

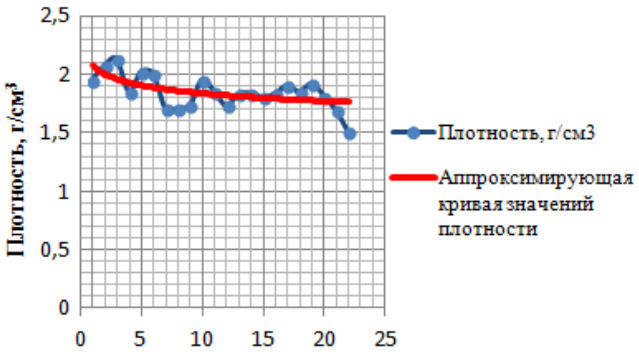

FIGURE 5. Change in density of the samples as the distance from the wall (g/cm^3).

FIGURE 6. Sample in a variational magnetometer.

Analysis of possible analogies for the study of objects on the soil surface (possible effect of LLPF and BL plasmoids) should account two features. Observers state [5] that CCs of natural origin take a form of round rings or rings connected by straight lines. In this connection, attention should be paid to soil

cover studies from aircraft boards [5]. They showed that buried underground remains give out their presence through growing crops or wild grasses above them. Above the former ditches and other depressions, where the soil is more fertile, the moisture is greater and the roots are easier to penetrate into the depths, the vegetation is lush, higher and thicker. Proceeding from these facts, it can be assumed that the emergence of CC, is connected with the fluxes of charged particles to the Earth's surface in a strongly charged thunderstorm atmosphere and the processes going on inside the Earth and the soil cover can participate. So within the soil cover, due to various physical and chemical processes, as well as in the places of activity of ancient people, with the construction of various local objects of life and objects of the cult with the use of various materials, an electrode system arises that concentrates local ion fluxes and accelerates them, directing to a quasi-electrodes that are formed under the Earth. In this case, the form of circles and lines becomes unsurprising, because they are inherent the forms of channels, the place of rites and roads of ancient people.

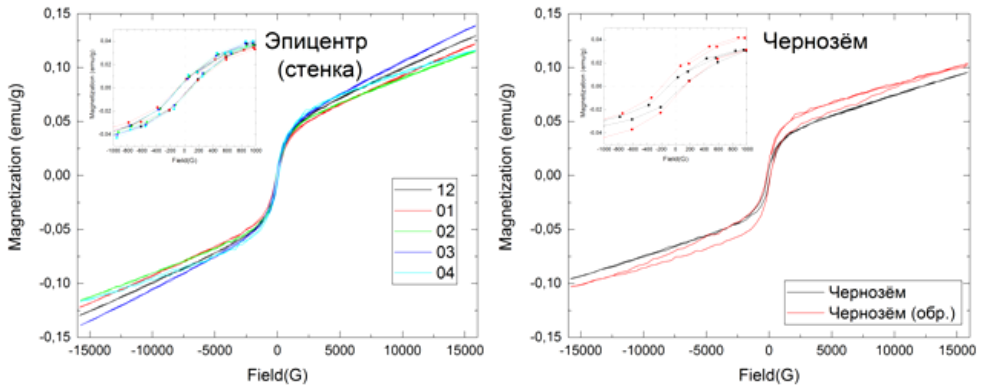

FIGURE 7. Magnetization curves of samples: a — monolith walls, b — chernozem external control.

It is possible to select from plasma devices the corona discharges (CD) as the devices that create similar effect on the processing material under them. The corresponding are the experiments with CD over various powders covering liquids [3—4]. In this case, the soil is modeled by a liquid and the powder is the soil cover.

Experimental research.

As a result of the experiment with the erosive plasmatron plasma, changes in the value of the electrical conductivity of the treated samples were revealed, increase from 1.2 to 7 times, depending on the time of action of the plasma jet on the soil. The longer the plasma was in contact with the surface of the samples, the greater the electrical conductivity, respectively. (Definite parameters are presented at the Conference in the special paper)

Studies using corona discharges.

As a result of the experiment, changes in the value of the electrical conductivity of the processed samples were revealed in comparison with the control, and with positive corona discharge (CD) polarity (lower electrode grounded, potential on the needle) the electrical conductivity increases more noticeably (Fig. 8) than with the negative polarity (potential at the bottom electrode, needle grounded) (Fig. 9). (Definite parameters are presented at the Conference in thespecial paper)

FIGURE 8. Changing of samples conductivity with a positive conductivity polarity of CD.

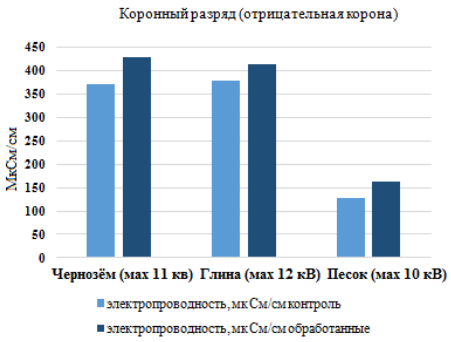

FIGURE 9. Changing of samples with a negative polarity of CD.

It can be assumed that the development of plasma processes on the Earth's surface covered with grasses in conditions of thunderstorm activity, when there LLPF, causes the appearance of crop circles can strongly influence the Earth surface properties. The appearance of the hole can also be connected with the release of energy and the effect of plasma ion-wind currents on the soil under complex atmospheric electricity conditions, when LLPF plays the role of an upper electrode, and the subsoil layer is the complex lower electrode of the natural corona discharge.

1. Stakhanov I. P. On physical nature of ball lightning, Moscow: Nauchnyi mir. 1996.

2. Bychkov V. L., Nikitin A. I. *Ball Lightning: A New Step in Understanding. In: The Atmosphere and Ionosphere. ElementaryProcesses, Monitoring, and Ball Lightning.* Eds. V. L. Bychkov, G. V. Golubkov, A. I. Nikitin. Cham: Springer, 2014. P. 201—367.

3. Bychkov V. L., Ershov A. P., and Chernikov V. A., *Negative Corona Discharge Over a Surface of Alcohol*. IEEE Transactions on Plasma Science, Volume 36, Issue 4, Part 1, Aug. 2008 Page(s):1140 — 1141.

4. Bychkov V. L., Chernikov V. A., Volkov S. A., Bychkov D. V., and Kostiuk A. A. *Corona Discharge Over liquids with Powder Addition.* IEEE Transactions on Plasma Science. 2011, V. 39, Issue 2. P. 2640—2641.

5. Abakumov V. I., Bikmukhametova A. R., Bychkov V. L., Safronenkov D. A., Chernikov V. A., Mikhailovskaya N. O., Shvarov A. P., Interaction of long-lived luminescent formations with Earth surface. Proc. 25-th Intern. Conf. “Electromagnetic field and materials”, Moscow. November 24—25, 2017. Moscow. Infra M. P. 538—554.

Whether it is Possible to Describe a Ball Lighting Within The Standard Model?

Andrey V. Chistolinov

Joint Institute for High Temperatures of the Russian Academy of Sciences,
Izhorskaya st.13 bd.2, Moscow,125412, Russia

Introduction. This year marks 180 years since the publication of the famous work of Francois Arago [1], dedicated to ball lightning. At that time, ball lightning was considered one of the manifestations of atmospheric electricity. In recent years, tremendous progress has been made in many areas of physics; however, the nature of ball lightning has remained a mystery. And although its connection with atmospheric electricity has been proven to date, the ball lightning seems to have a much more complex nature. The accumulation of observational data on ball lightning collected over the years speaks in favor of the fact that it is a long-lived autonomous self-luminous formation that freely floats in air, which retains its volume and has surface energy [2—5].

Paradoxically, this object moves with a sufficiently high speed even in calm air. According to [2], the average speed of motion of the ball lightning is 4 m/s. In most models it is assumed that the motion of ball lightning is caused either by air currents or by electric fields. However, this is contradicted by numerous cases when the ball lightning moves along an almost closed trajectory in the calm air in the room. For example, when it enters the room through an open door or window, and then leaves it through the same entrance [3]. Since the work of electrostatic forces along a closed contour is zero, they obviously cannot be the cause of such a motion.

In addition, at such large movement speeds in a closed room, the ball lightning, it would seem, must very quickly end its life, faced with some obstacle. But observations show that the ball lightning can be in the room for a period of time substantially exceeding the ratio of the maximum linear dimension of the room to its speed. This is a consequence of one more surprising property of ball lightning — the ability to bypass obstacles. But the most surprising property of ball lightning is its ability to pass through the glass without damaging it, which was first described in Brandt's book [4]. This property directly indicates that ball lightning can not at all be a compact object consisting of ordinary matter. Previously, this property was challenged, appealing to insufficient statistics of observations [3] or simply trying not to notice it [2]. However, to date, an increase in the statistics of observations has confirmed that ball lightning can indeed pass through the glass without damaging it [5], as it was described by Brandt [4]. The following data are given in Grigoryev's book [5]: from 5315 previously unknown descriptions of ball lightning collected in the Center at the Yaroslavl University in

42 cases, ball lightning passed through the glass without damaging it and only in 26 was the passage of ball lightning through the glass was made through the hole. This data is statistically significant. And one can conclude from it that the passage of ball lightning through the glass without damaging it is not only a fairly frequent phenomenon, but also the predominant mechanism of interaction of ball lightning with glass.

The main provisions of the model. Steady levitation of ball lightning in the air indicates that the substance of ball lightning has a density close to or less than the density of air, at the same time the ball lightning can freely change its shape, but retains its volume. These properties of ball lightning indicate that the most suitable model for describing it is a fluid model with a density of close or lower than air density. On the other hand, the ability of ball lightning to pass through the glass without damaging it indicates that this fluid must have the ability to pass through a conventional atomic substance. That is, it must be a liquid that interacts very weakly with the atomic substance. So weak that it could move through the substance, experiencing only a slight resistance.

Such liquid we will call tied matter (TM).

Since the motion velocities of the ball lightning are relatively small, for tied matter one can use the approximation of an incompressible fluid. Also we will not take into account the thermal expansion of the tied matter. In addition, we assume that the internal friction in the tied matter is small in comparison with the volume friction between the TM and the atomic substance. With these approximations taken into account, we obtain the following system of equations describing the behavior of the ball lightning substance or tied matter:

$$\begin{cases} \rho\left(\frac{\partial \vec{u}}{\partial t} + (\vec{u}\cdot\nabla)\vec{u}\right) = -\nabla P + \rho\vec{g} - \underline{\mu n(\vec{u}-\vec{v})} + \underline{\nabla(\gamma n)} & (1) \\ \nabla\vec{u} = 0 & (2) \\ \rho c_p\left(\frac{\partial T}{\partial t} + \vec{u}\nabla T\right) = \nabla(\varkappa\nabla T) - \underline{\varepsilon n} & (3) \end{cases}$$

where, c_p — is the heat capacity of the TM at constant pressure; ρ — density of tied matter; P — pressure of tied matter; $\varkappa$ — the coefficient of thermal conductivity of the TM; μ — the coefficient of friction of a TM with an atomic medium, calculated per molecule of atomic matter; n — the concentration of molecules of the atomic medium; $\vec{u}$ — TM velocity; $\vec{v}$ — atomic medium velocity; γ — the binding energy of one molecule of the atomic medium with TM, that is, the work that must be done to separate them; $\varepsilon = \varepsilon(T, T_a)$ — the heat flux from tied matter to atomic matter per molecule of atomic matter; T — temperature of tied matter; T_a — temperature of atomic matter.

The parameters μ>0, γ>0, ε determine the interaction of the tied matter with the atomic matter. Equation (1) is the Euler equation, in which two new terms appear that characterize the interaction of tied matter with an atomic substance (underlined terms). The first of them characterizes the volume friction that occurs when the tied

matter moves relative to the atomic matter. The second characterizes the binding energy of a unit volume of tied matter with the unit volume of atomic matter. It is essential that this quantity is positive.

Equation (2) is the continuity equation for an incompressible continuous medium.

Equation (3) is the heat transfer equation for a fluid in which one new term (an underlined term) appears, characterizing the volumetric heat flux between the tied and atomic matters.

In equation (1), inertial and gravitational terms that contain a small factor ρ can be neglected. As a result, after simple transformations we arrive to the system:

$$\begin{cases} \vec{u} = \vec{v} + \dfrac{\nabla(\gamma n - P)}{\mu n} \\ \nabla\vec{u} = 0 \\ \rho c_p \left(\dfrac{\partial T}{\partial t} + \vec{u}\nabla T\right) = \nabla(\varkappa \nabla T) - \varepsilon n \end{cases} \tag{4}$$

With boundary conditions:

$$P = \sigma\left(\frac{1}{R_1} + \frac{1}{R_2}\right) \tag{5}$$

$$\frac{\partial T}{\partial n} = 0 \tag{6}$$

where, σ — the coefficient of surface tension of the tied matter; R_1, R_2 — the main radii of curvature at a given point on the surface; $\frac{\partial T}{\partial n}$ — the derivative of T in the direction of the normal to the surface.

The boundary condition (5) is the Laplace equation, which determines the surface pressure of the liquid.

The boundary condition (6) is the condition for the absence of heat flux through the surface.

Equation (4), which is obtained from equation (1), is Darcy's law — the equation of fluid filtration through a porous medium, whose role is played by atomic matter.

Equation (3) requires some explanation. It characterizes the processes of heat exchange between TM and atomic matter. If the TM is in thermodynamic equilibrium with atomic matter, then in fact it will not manifest itself in any way and we will not see any effects like a glow or ionization of a gas which are characteristic for the ball lightning. It is a different case if the temperature of the tied matter T is much greater than the air temperature T_a. So, if T were to reach several thousand K, then not only heating, but also ionization and glow of gas in the TM volume is possible. But, since the interaction between TM and atomic matter is assumed to be weak, the relaxation time of the system to thermodynamic equilibrium can be significant. This determines the long lifetime of ball lightning.

The non-equilibrium state of TM can arise, for example, when it hits a discharge channel of linear lightning. And what we see after this in the form of a glowing ball is the process of slow relaxation of the TM to an equilibrium state. If the temperature gradients in TM are small, then equation (3) can be rewritten as:

$$\rho c_p \frac{\partial T}{\partial t} = -\varepsilon n \tag{7}$$

This equation determines the lifetime of ball lightning when it is quietly extinguished. In this case it is necessary to take into account that both c_p and ε are functions of the TM temperature.

Main results. A small ball of tied matter for which the gradient n varies little on its dimensions will move as a whole, obeying the equation (8), which is obtained from (4) by averaging over the volume of the ball:

$$\vec{u} = \vec{v} + \frac{\gamma}{\mu}\frac{\nabla n}{n} \tag{8}$$

Or, given that $n = \frac{P_a}{kT_a}$, this expression can be rewritten as:

$$\vec{u} = \vec{v} - \frac{\gamma}{\mu}\frac{\nabla T_a}{T_a} \tag{9}$$

where, T_a — temperature of the gas.

In the general case, T_a depends on the energy flux density transferred from the tied matter to the atomic matter. Therefore, it is necessary to solve the joint system of equations for TM and atomic environment. As a result of solving such a system for the case of homogeneous air, we obtain:

$$|\vec{u} - \vec{v}| = \sqrt{\frac{2}{7}\frac{\gamma}{\mu}\frac{\mu}{kT_a}} \tag{10}$$

The physical meaning of this result is that the ball lightning during its movement through the air, itself creates a temperature gradient, which in turn is the cause for its movement.

One of the consequences of the model is the dependence of the motion of ball lightning on temperature inhomogeneities. Perhaps this explains the strange nature of the movement of ball lightning, in particular, its ability to bypass obstacles.

Different physical bodies can often have a higher temperature than the ambient air. For example, as a result of absorption of thermal or solar radiation. Then, near such bodies, there is a temperature gradient that can lead to a change in the direction of motion of the ball lightning before it comes in contact with them.

In case the body temperature does not exceed the temperature of the surrounding air, the ball lightning can approach it up to the point of contact. In this case the repulsive force will also arise, but it will arise due to the direct contact

with the body. In fact, the interaction of ball lightning with the surface of a solid body leads to the heating of the latter, and hence to the heating of the near-surface layer of air. The temperature gradient arising in this case is the cause of the appearance of the repulsion force of ball lightning from the surface of solids.

This effect, apparently, explains the repulsion of ball lightning from the surface of dielectrics and, in particular, the deformation of ball lightning as it passes through narrow slits and openings in dielectric partitions.

Discussion. The proposed model of ball lightning is phenomenological and is based solely on observational data of ball lightning. Not surprisingly, therefore, that it is in a pretty good agreement with this data. In fact, such key properties of ball lightning as the preservation of volume, surface tension, long glow time, the ability to pass through the glass without damaging it, are simply postulated in this model. It is important, in this case, that other properties of ball lightning, such as the ability to move in stationary air in a room along an almost closed path, avoid obstacles, bounce off the surface of solid bodies at contact, and pass through small diameter holes in this model are obtained without any additional assumptions. Naturally, the reliability of this model hinges on the reliability of observational data of ball lightning, on which it is based.

But, let's assume that this data is reliable and further collection of observational data of the ball lightning will only confirm it. Then it is appropriate to ask the question — what is tied matter and how does it relate to the modern physics of elementary particles? First of all, it is obvious that TM cannot consist of particles that have an electric charge, since in this case there cannot be any talk of permeability with atomic matter. But if so, then TM cannot be a baryonic matter at all, and moreover it can be shown that it cannot consist of some known particles described by the Standard Model.

In principle, there is nothing unusual in this. It is well known that the Standard Model is not the final theory. It does not describe gravity, does not explain the baryon asymmetry of the Universe, does not predict neutrino oscillations, and it contains no particles from which dark matter could consist, whose mass in the Universe, according to modern astronomical data, is 6 times greater than the mass of baryonic matter.

Does this mean that a study of ball lightning can open a way to expand the Standard Model? The observations of ball lightning indicate that this possibility cannot be ruled out. And this means that this issue requires the most serious study.

1. Arago F. Thunder and lightning. Paris. 1838. St. Petersburg. 1885.
2. Smirnov B. M. The problem of ball lightning. M. Science. 1988. 208 p.
3. Stakhanov I. P. On the physical nature of ball lightning. M. Scientific world. 1996.
4. Brand W. Der Kugelblitz. Hamburg. H.Grand. 1923. 170 p.
5. Grigoryev A. I. Ball lightning. Yaroslavl. YarSU. 2010. 200 p.

Ball Lightning Observations Analysis of "The Mitino Trap 2015"

Andrei I. Shchedrin

Undependent researcher, Shipilovskaya str., 6-1-123, 115569, Moscow, Russia

The ball lightning (BL) observations in the area Mitino district on Nord West of Moscow 27.07.2015 are unique for its informativeness and reliability. Videos of the phenomenon posted at least three independent observers on the Internet, brief information about these videos is given in Table 1.

TABLE 1.

	1	2	3
URL http:/	www.youtube.com/ watch?v= frTCqnz8-Bg	www.youtube.com/ watch?v= IyO_XFeSMzQ	www.youtube.com/ watch?v= eyRL0BimsHM
author	Egor Chickin	Dmitry Novoselov	Vladimir Sokolov
address	Baryshikha str. 34, parking building 39 on the video	Baryshikha str. 40-1, ETL-pole on the video	Angelov lane 9, building 38 (Baryshikha str.) is in front of BL on the video
duration (min.sec.)	2.21	1.16	2.05
distance	400m	500m	600m

The distance to the BL and its dimensions. Observation of BL with three different points gave the possibility to determine its exact location during the filming. This helped by satellite images Google Map and landmarks that are present in all three videos. Point and viewing direction are shown on the map, see Fig. 1. The numbering of the observation points in accordance with Table 1.

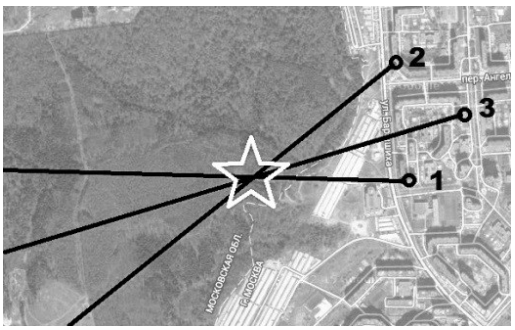

FIGURE 1. The BL location during the filming.

Video 3 allows to determine the size of the BL. In Fig. 2 the angular size of the BL can be compared with the width of the attic window, which is 1 m. Thus, the angular size of the BL in the plane of the visible walls of the building number 38 on the street Baryshikha is about 25 cm, and real, given the distance from the observer to the BL 600 m to the building 38 — 170 m — is about 80 cm.

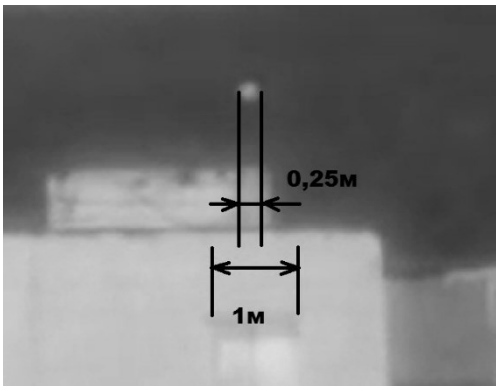

FIGURE 2. The BL size determination.

BL life time. Observer No. 3 noted that watched the BL for about 15 minutes before the shoot began. Given the objective duration of filming about 2 minutes, it is possible to estimate the lifetime of observed BL as from 2 to 15 minutes.

The character of the movement. At the beginning of all three videos we see that at least one minute BL is "loafing about" in a some potential hole from which it can't get out in despite of huge random disturbances, which caused its intense "Brownian motion". The trajectory was drawn using the frame-by-frame processing of video, see Fig. 3. The scale is defined similarly to the definition of the diameter of the BL on the visible landmarks in the foreground, the dimensions are in meters.

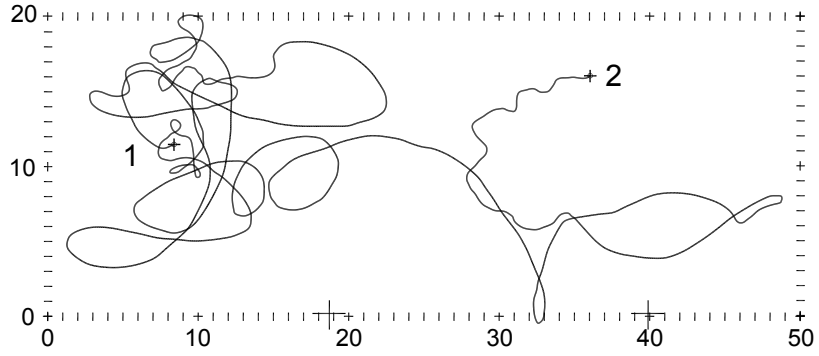

FIGURE 3. The BL trajectory (observer 3, time 0.00—0.48).

Draw attention to a quasi-harmonic character of the movement, similar to a periodic loops or sine waves, that is very character to the potential hole in which the position of the BL shows some stability. This fact allows to conclude that the nature of the motion of the BL in this case is determined mainly NOT by the Coulomb forces as in accordance with Earnshaw's theorem, the system of free interactive charges cannot be stable.

Assuming electromagnetic (i. e. with variable fields), the nature of BL, one should look for the large-scale electric origin of this potential hole. The cause for this is easily found on the map in the form of powerful 220kV 50Hz electric transmission lines (ETL) having each phase of the three splited wires plus two upper lightning protection wires.

Most notable in this ETL is its location topology in the BL observation region. It is shown in Fig. 4, where the triangles marked the ETL mast position.

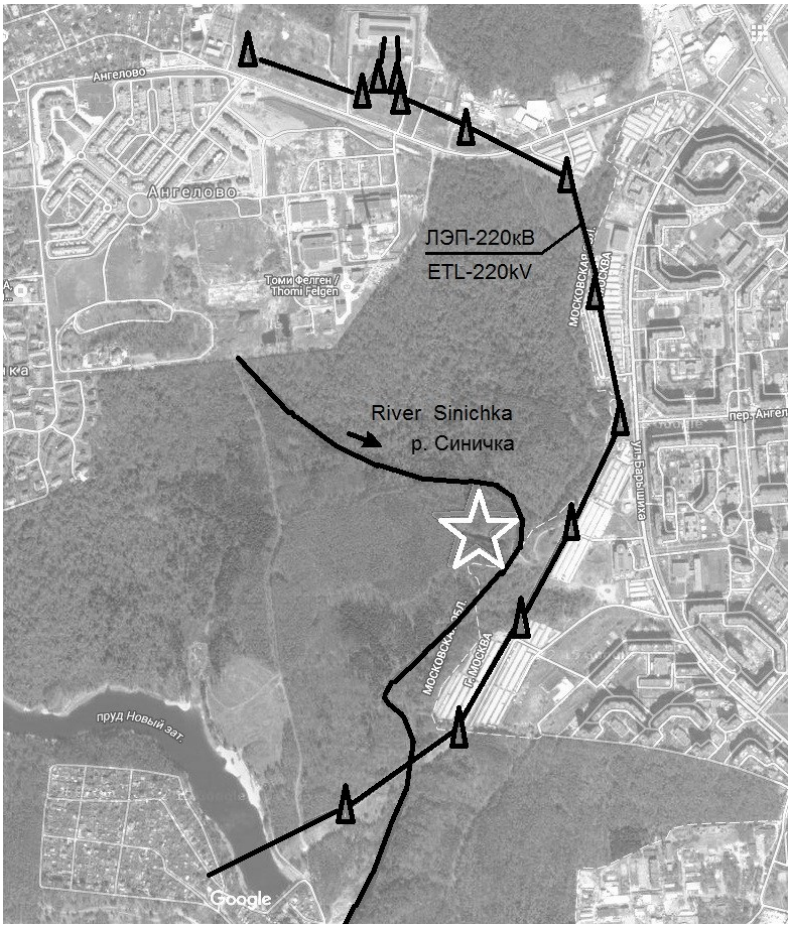

FIGURE 4. River and ETL 220kV topology.

It is clearly seen that ETL as broken line is very similar to parabola. And the observation point of the BL is located near the focus of this parabola, at a minimum distance of about 200 m from the ETL wires. Thus, it is likely that the interaction of precessing magnetic BL dipole (if that) with the ETL wires creates mentioned potential hole for this dipole, which ensured the stabilization of the BL in space with a precision of fluctuations of external disturbances, the main of which was a wind of approaching tunderstorm front.

The detailed landscape study showed a deep ravine with a small Sinichka river tracks around the place of the BL observation. Given that the ravine is deep and with the presence of water, and the soil above is a sandy loam with conductivity considerably less than water and swampy bed of the river, this relief is also an important inhomogeneity in the electrical point of view. In addition, you may notice that the "focus" of the ravine river much more accurately coincides with the place of BL trap location in comparison with the ETL "focus".

After BL leaving from its "traps" it evenly began to move in the direction of the wind with increasing height. Taking video from the beginning of a sharp BL rise and to passing over the observer, we can estimate its speed as 100 km/h, which most likely coincides with the wind speed.

Having data on the size, speed and location of the BL, we can estimate the order of forces magnitude that could explain the nature of its movement.

1. The aerodynamic pressure of the wind — 100N. Calculated by the classical formula of the aerodynamic drag for the ball diameter of 80 cm when the speed of the oncoming wind 100 km/h. It is possible that due to the special surface properties of the BL (e. g. presence of interlayer plasma) or due to less wind speed — this pressure is several times smaller.

2. The Archimedes force is 1N on the basis of the volume of a sphere with a diameter of 80 cm.

3. The strength of the electrostatic attraction towards the conducting surface of the earth is $2.5 \cdot 10^{-3}$N, on the basis of the maximum possible value of uncompensated electric charge of BL equal to $5 \cdot 10^{-5}$C, which is calculated under the assumption that the electric field strength near BL does not exceed the limit of the dielectric strength of air. I. e., the tension on the BL border is accepted to be equal 30 kV/cm. BL altitude is taken equal to 50 m.

4. The strength of the electrostatic effects of a tunderstorm cloud — less than 2.5N, based on the maximum field strength 50 kV/m (the above is already happening lightning, but we see not it there). It is likely that this value is actually less in two orders of magnitude.

5. The force of gravity is less than 1N, based on the fact that in the area of free flight BL floated up.

It is obvious that among these forces p. 2—5 listed above there is NO real reason, which would explain the compensation of the HORIZONTALLY directed aerodynamic pressure of the wind on BL within a few minutes at the distance of

50m from the ground surface and 400 m from the walls of nearby buildings. Such force may be the strength of the electromagnetic interaction of the BL with the conductors of the ETL and the river bed.

Assuming BL as a magnetic dipole with a diameter of 80 cm, we can estimate a magnitude of electric current therein, which when interacting with the conductors of the ETL would lead to a compensating force order of 100N.

This was made following assumptions. ETL arc lines with a diameter of 1500 m is assumed to be closed loop, as on high frequency it is "shorted" by parasitic inter-turn capacity of substation transformers and linear capacity of the conductors themselves to the earth. The impedance of the ETL we consider a purely inductive, as the estimated inductance of the considered conductors is about 5 mH (for calculation formulas) and the impedance is equal to the ohmic resistance of the wires only at frequencies below a fraction of a Hertz.

Calculating the magnetic flux from the precessing dipole through said ETL circuit, it is possible to find the EMF in the circuit and then assuming the inductance — amperage. The last is not frequency-depended and is directly proportional to the BL dipole current. Further, for a rough estimate, it was assumed that the force acting on the BL from the ETL conductors just equal to the force acting on a conductor with a length equal to the BL diameter, and with a BL dipole electric current. It turns out that the magnitude of the aerodynamic pressure of the wind in the 100N this force will compensate at a dipole current 300 MA (MegaAmperes)! This result is consistent with the BL model [1] although in reality there can be 1—2 orders of magnitude lower due to resonance phenomena in ETL and in the river bed, just as it happens in radio antennas.

Due to the fact that the distances "BL trap — river bed" and "river bed — ETL" are almost identical and amount to about 100 m, there is a natural assumption for any radio engineer that these conductive systems played the role of a Yagi-type antenna. In this case, first, lower frequency, geometrical resonance will be observed at a distance from the first reflector (river bed) to BL equal to 1/4 the wavelength of the radiation, and with the same distance between the two reflectors (the river bed and ETL). Therefore, the maximum BL emission wavelength is to these assumptions — 400 m, and the minimum frequency of precession is 0.75 MHz.

On the data of Mitino trap BL we can rate the power and energy of the BL in accordance with paper [2], and will receive 50 MW and $5 \cdot 10^{10}$ J.

In the final stage of observations became prevalent, apparently, electrostatic forces and/or the Archimedes force, which tore the BL from this unique "trap" and dragged on after the tunderstorm front. Earlier, these forces have ensured the displacement of the center of the trap 50 m up above the ground and up above ETL plane.

1. A. Shchedrin, *Proc. 9th Intern. Symp. on Ball Lightning, ISBL06*, The Netherlands, Eindhoven, 16—19 August 2006, p. 210.

2. A. I. Shchedrin, To the question about the energy and lifetime of ball lightning, *Scientific review*, 2013, 5, p. 124.

Proposed Formation Mechanism of Ball Lightning in Nature

Andrei I. Shchedrin

Undependent researcher, Shipilovskaya str., 6-1-123, 115569, Moscow, Russia

Model of ball lightning (BL), proposed by the author in [1] gives no direct information on the possible mechanism of BL formation in natural conditions. However, there are a number of observations of witnesses that contain some details that could shed light on this mechanism. The most valuable, in the author's view, is the observation which was made by Tar [2].

According to this observation, the BL occurred after 2 seconds in close proximity to the place of a strong discharge of linear lightning. As in the observations of some other witnesses, the BL "came from nothing" in the air. But before the observer noticed a local wind type motion of the air, which then arose glowing rotating region, shaped like a horizontal Crescent. This area after 0.3 s was curled up in a bright ball with a diameter of 30—40 cm. Despite heavy rain and wind the ball began uniform motion at a distance of approximately 1.2 m from the ground against the wind. Based on this and some other observations, we propose the following mechanism for the formation of BL, consisting of several stages.

Step 1. The generation of a large local vortex electric field (VEF). Places of localization correspond to the areas of magnetic field lines concentration, for example inside of the lightning channel bending or current-carrying conductor loops, see Fig. 1, and also near to the place of linear lightning impact to the ground.

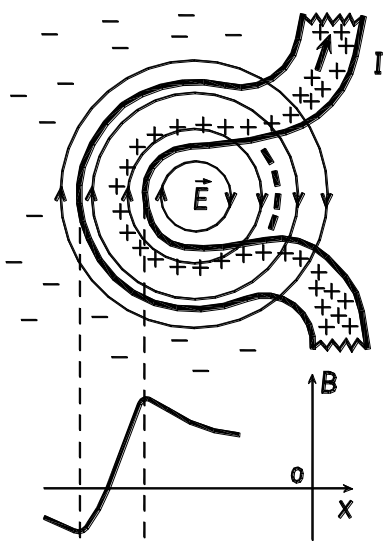

FIGURE 1. The vortex electric field localization.

VEF occurs in moments of strong change of the electric current. Moreover, the moment of the current increasing at the beginning of the lightning discharge and the corresponding VEF are not essential to the described mechanism, as in the beginning there are no sufficient quantity of free ions and electrons in the ambient air. After the linear lightning discharge a large number of ions and free electrons there are formed around through air photoionization. End of the discharge is characterized by a sharp decrease of electrical current and VEF peak.

Step 2. Electrically charged particles acceleration and their separation under the action of the VEF. In the local area VEF power lines are closed and look like ellipses or circles. Under the influence of this field the charged particles start to move by unwinding spirals, see Fig. 2.

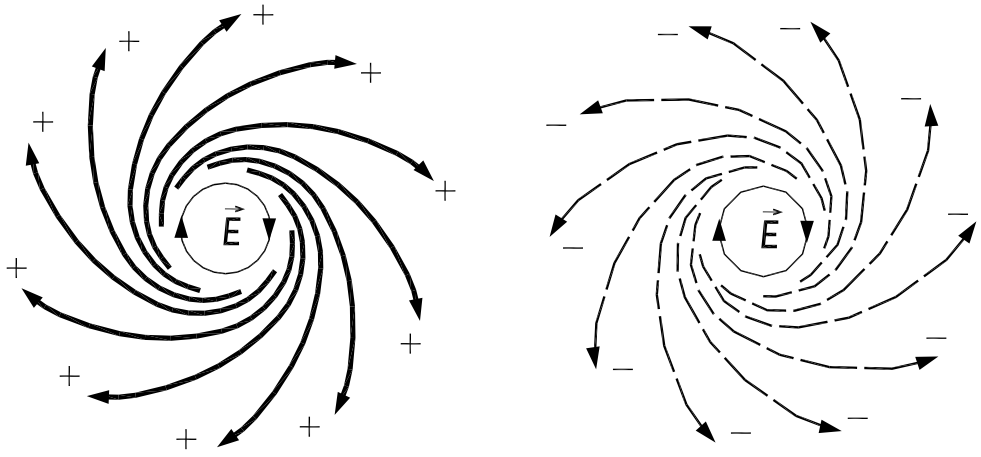

FIGURE 2. The movement of charged particles under the action of vortex electric field, the same system depicted separately for ions and for electrons.

Positively charged ions (nitrogen, oxygen) due to the significant mass and size while actively act on neutral air molecules, forcing them to move at the same time. Unlike positive ions, neutral molecules of air are not emitted by spirals from the center of rotation, and spun in a conventional aerodynamic mini-tornado. Most likely, this process was described by Tar [2] in the form of "wind type motion of the air", which led to the formation of horizontal mini-tornado in the form of a Crescent. Due to the known properties of the air vortex its inside pressure begins to decrease, and this leads to the electric breakdown of this area by VEF. The central area begins to glow. This breakdown leads to the generation a lot of ions and electrons, which are unwinding spirals away from the center of rotation. Thus, there is almost a vacuum cavity in which electrons are free to accelerate to relativistic velocities. This is fundamentally important, because in accordance with the model [1], such a cylindrical system of rotating particles can be stable under certain conditions. Before the VEF expiration a rotating core of electrons accumulates an energy.

Step 3. The positive ions collection and the BL formation. After the VEF expiration, the runaway positive ions are attracted to the toroidal e-core due to the Coulomb interaction. Their initial speed is low and comparable to a thermal motion speed of air molecules. But now, moving to the center, the ions begin to twist in converging spirals in the other direction under the action of the Lorentz force due to magnetic field of the e-core. Thus, the core electrons and the positive ions of the outer shell — revolve now in one direction. Due to the opposite sign of electric charge, magnetic dipole moments of the core and the shell are oppositely directed

and will seek to line up their vectors. Due to the presence of the moment of inertia a precession will arise. Initially cylindrical or toroidal rotating system of electrical charges, when trying to turn in the nature of things forms a ball.

Step 4. Fixing the BL size. The Coulomb force of attraction compresses the outer ion shell. Whereas the last compresses the inner electron core by magnetic field. This process occurs as long as the packing density of the outer shell ions reaches the limit of incompressible liquid state of matter.

Thus, the proposed BL model [1] and the possible formation mechanism of BL describe it as some macroscopic model of "inside-out" of the hydrogen atom. Moreover, outer shell of natural BL, apparently, consists of extremely ionized liquid nitrogen.

1. A. Shchedrin, *Proc. 9th Intern. Symp. on Ball Lightning, ISBL06*, The Netherlands, Eindhoven, 16—19 August 2006, p. 210.

2. D. Tar, *Proc. 9th Intern. Symp. on Ball Lightning, ISBL06*, The Netherlands, Eindhoven, 16—19 August 2006, p. 223.

Experimental and Theoretical Research of Electric Dipoles Interaction Inside the Shell of Ball Lightning

Anatoly I. Nikitin, Alexander M. Velichko, and Tamara F. Nikitina, and Ilya G. Stepanov

Talrose Institute for Energy Problems of Chemical Physics, RAS, Moscow, Russia

Discovery of the theoretical possibility of confinement of a charged plasmoid inside a dielectric spherical shell [1, 2] enabled to begin the development of a consistent model of ball lightning (BL) with a high energy density [3]. The electric field of the charge inside the shell polarizes the shell material. For example, if particles with a total positive electric charge Q_{bl} are placed inside the shell, then due to polarization the inner surface of the shell turns out to be covered with the ends of electric dipoles with a negative charge, and the outer surface — by the ends of positive charges. In a sufficiently strong electric field, a complete polarization of shell material takes place, and the number of elementary charges (e =1.6·10^{-19} C) per unit area of the shell surface can be assumed equal to the surface density of polarized molecules. If the shell consists of water, then the density of charges on the inner and outer surfaces of the sphere is σ=1.6 C/m^2. The charges located on the inner surface of the shell are acted upon by a force, directed toward the center of the sphere, while the charges on the outer surface are acted by a force, directed from the center. The first (shrinking) force is greater than the second (stretching) force, as a result the envelope is shrunk by the force $F_{sh} = (4\sigma f Q_{bl})/\varepsilon_0 D_c$, where D_c is the inner diameter of the sphere, and f is the shell thickness [3]. However, this

formula is valid only for large diameters of the sphere, when the angle between adjacent dipoles (oriented in the direction of the sphere center) is very small. For BL of small size, the interaction of dipoles in the shell must also be taken into account. To understand the mechanism of this interaction, first consider what forces act in a simple system, consisting of three dipoles (see Fig. 1a). Let us define the forces, acting on the dipole (1—2) from the other two dipoles (3—4) and (5—6), located to the left and to the right of it. Since the dipoles are rigid, we must not take into account the force that acts on charges 1 and 2 from another charge of the same dipole. Thus, we can assume that charges 1 and 2 are acted upon by forces of charges 3, 4, 5 and 6. The total force that acts on the central dipole (1—2) can be represented in the form $\boldsymbol{F}=\boldsymbol{F}_{1\text{-}3}+\boldsymbol{F}_{1\text{-}4}+\boldsymbol{F}_{1\text{-}5}+\boldsymbol{F}_{1\text{-}6}+\boldsymbol{F}_{2\text{-}3}+\boldsymbol{F}_{2\text{-}4}+\boldsymbol{F}_{2\text{-}5}+\boldsymbol{F}_{2\text{-}6}$, where $\boldsymbol{F}_{i\text{-}j}$ is the force, acting on charge i from the charge j. We can decompose each of these forces into two components: a vertical force, directed along the (1—2) axis, and a horizontal force, directed perpendicular to this axis. In view of symmetry of the presented construction, the total force, acting on the dipole (1—2) in the horizontal direction, will be zero, since the force, acting in this direction from the dipole (3—4), will be balanced by the force from the dipole (5—6). Thus, in order to obtain an expression for the force, pushing a single dipole out of the shell, it is sufficient for us to consider two neighboring dipoles, taking into account that the horizontally directed force is zero, and the vertically directed force must be doubled.

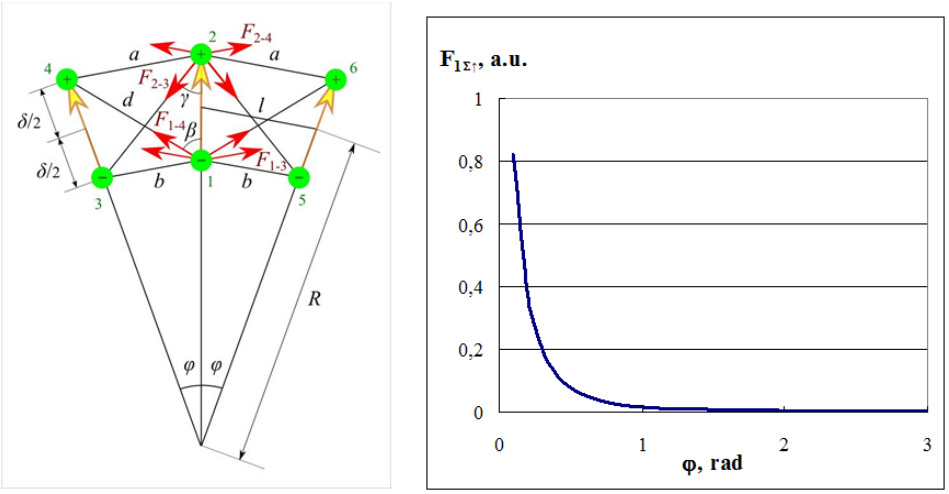

(a) (b)

FIGURE 1. Scheme of forces, acting in the system of three electric dipoles (a); Dependence of the force, acting on the dipole 1—2 along its axis, on the angle φ between the adjacent dipoles (b).

In this connection, it suffices to consider the forces, acting in the system of two dipoles, for example, (1—2) and (3—4). Let δ is the length of the dipole, R is the distance from the center of the dipole to the center of the circle and φ is an angle between the adjacent dipoles. We assume that distance l between the centers of

neighboring dipoles is fixed. It is not difficult to show that $l = 2R \sin(\varphi/2)$. The distance between charges 2 and 4 is $a = 2(R+\delta/2) \sin(\varphi/2)$, and the distance between charges 1 and 3 is $b = 2(R-\delta/2) \sin(\varphi/2)$. We assume that forces, acting between the charges, are subject to the Coulomb law. Let denote the absolute values of the charges by the letter q, then the modulus of the force F, acting between the charges, located at a distance r from each other, is $F = C(q_n q_m / r_{nm}^2)$ (n, m=1—4). We are interested not in the total forces, acting between the charges, but their projections on the vertical axis: $(F_{13})_\perp = C(q^2/b^2) \cos[(\pi-\varphi)/2]$; $(F_{24})_\perp = = C(q^2/a^2) \cos[(\pi-\varphi)/2]$; $(F_{14})_\perp = C(q^2/d^2) \cos\beta$; $(F_{23})_\perp = C(q^2/d^2) \cos\gamma$ (see Fig. 1a). The total force $(F_{tot})_\perp$, acting on the dipole 1—2 in the vertical direction, will be the vector sum of these four forces multiplied by 2 (taking into account the effect of the dipole 5—6). Figure 1b shows the dependence of the force $(F_{tot})_\perp$ on an angle φ between the neighboring dipoles. One can see that the force, acting on the dipole 1-2 along the radius direction, quickly decreases with increasing of the angle φ.

Of greater practical interest is the situation when dipoles, oriented by a centrally symmetric field, are located on the surface of a sphere. To understand the nature of their interaction, consider the problem when the dipoles are located in a plane along a circle of radius R. We agree that when R varies, the distance l between them does not change (this means that for each value of R there exists a discrete number of dipoles N, located on the circle $S = 2\pi R$. Let divide the circle into $2n$ identical sectors, where $2n = N$, then the angle at the vertex of each sector will be equal to $\varphi = \pi/n$. Let us determine the force, acting on one particular dipole from the remaining dipoles. As before, consider the total effect on the selected dipole of the remaining dipoles located on the left half of the circle. To find the value of the component of the force, directed along the radius, the result must be multiplied by 2. For each particular pair of dipoles, lying on the semicircle, the values of the angle between them are $\varphi_k = k\varphi = k\pi/n$. Solving this problem is similar to the one considered above, in which the letter a denotes the distance between the ends of the dipoles, lying on the outer circumference, the letter b is the distance between the ends of the dipoles on the inner circle, and d is the distance between the charges of the dipoles at the ends of the diagonals of the trapeze 1-2-4-3, we find:

$$a_k = (R + \frac{\delta}{2}) \cdot \sqrt{2 \cdot (1 - \cos\varphi_k)}$$

$$b_k = (R - \frac{\delta}{2}) \cdot \sqrt{2 \cdot (1 - \cos\varphi_k)}$$

$$d_k = \sqrt{\delta^2 + a_k b_k}$$

$$\beta_k = \arccos \frac{\delta^2 + d_k^2 - a_k^2}{2 \cdot \delta \cdot d_k}$$

$$\gamma_k = \arccos \frac{\delta^2 + d_k^2 - b_k^2}{2 \cdot \delta \cdot d_k}.$$

Here δ is the length of the dipole, β_k is the angle between the vertical axis (on which the dipole is located) and the end of the dipole k, lying on the outer circumference, γ_k is the angle between this axis and the end of the dipole k, lying on the inner circle. Knowing these quantities, one can find the projection on the vertical axis of the force, acting on the central dipole 1—2 from the k-th dipole:

$$(F_{\Sigma k})_\perp = (F_{1\text{-}3k})_\perp + (F_{2\text{-}4k})_\perp + (F_{1\text{-}4k})_\perp - (F_{2\text{-}3k})_\perp.$$

The total force, acting on the selected dipole from the other dipoles, located on the circle, is:

$$F_\Sigma = 2\sum_{k=1}^{n-1} F_{\Sigma k} + F_{\Sigma n}.$$

In Fig. 2, solid line shows the dependence of the force F_Σ (pushing out the selected dipole along the radius R) on the radius of the circle, passing through the centers of the dipoles. One can see that this force decreases with increasing of diameter D (note that in this case the distance l between the centers of the dipoles was considered to be constant).

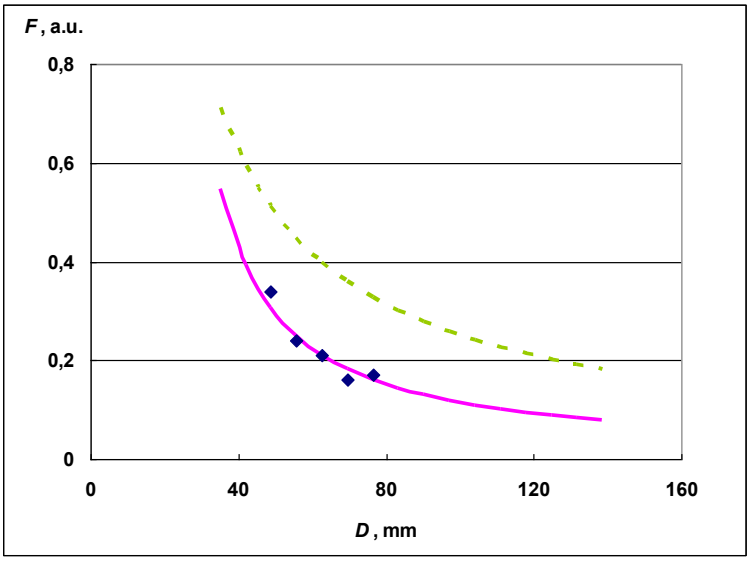

FIGURE 2. Dependence of the force F_Σ, acting on the selected dipole from other dipoles, located on a circle of diameter D, on the diameter value. The solid line is the results of calculation and the points are the results of the measurements. The dashed line is a dependence on D of the "gradient" force F_{sh}, pulling the dipoles to the center of the sphere. (Note that the forces F_Σ and F_{sh} are directed in opposite sides).

For experimental verification of the law of computed dependence, we have carried out experiments on the measurement of the force, acting on a movable dipole from dipoles, fixed on a circle of diameter D. As dipoles, we used linear magnets with a length of 12 mm. These magnets were pasted on the substrate along the circle, and in each case the distance between the centers of the neighboring magnets was kept the same. The movable magnet was placed on a trolley, which allowed the magnet to move freely only along one selected axis. Figure 3 shows a picture of the installation. The force, pushing the movable magnet out of the system, was compensated by the component of the gravitational force $mg \sin \alpha$, where m is a mass of the trolley with magnet, g is the acceleration of gravity and α is the angle between the horizontal plane and the plane along which the trolley moved. In Fig. 2, the points show the results of measuring the force, pushing out the movable magnet, with a different number of magnets on the circumference: M=14 (D=48.8 mm), M=16 (D=55.7 mm), M=18 (D=62.6 mm), M=20 (D=69.5 mm), M=22 (D=76.4 mm). One can see that the agreement between the results of the experiment and the calculation within the limits of the coinciding part of the curves is quite satisfactory. The dashed line in the figure shows the form of the dependence on the diameter D of the "gradient" force $F_{sh} = C_x / D$.

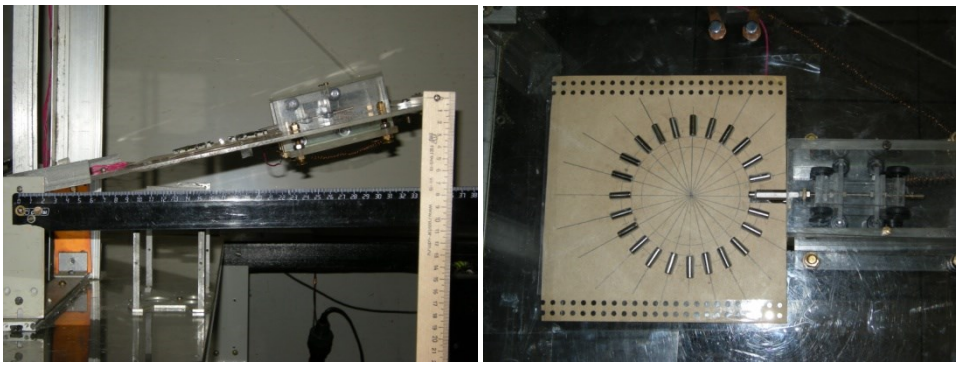

a) b)

FIGURE 3. Installation for measuring the interaction force of magnetic dipoles. a) side view, b) top view.

It can be assumed that the nature of the dependence of the force of the dipole-dipole interaction F_{Σ}, found by us for the plane case, will be qualitatively the same for the case of the arrangement of dipoles on the sphere. This force, like the "gradient" force F_{sh}, decreases with increasing radius of the sphere. However, the "efficiency margin" of the dipole-dipole force is much less than for the "gradient" force. Indeed, the limit of its growth is the value of the maximum surface density of charges of dipoles on the surface of the BL shell, when this force ceases to depend on the charge Q_{bl} of BL (when, figuratively speaking, the charge field has "completed its work", polarizing the shell up to saturation). At the same time, the "gradient" force F_{sh} can increase indefinitely with increasing of charge Q_{bl} and can

significantly exceed the force F_{Σ}. Processes of interaction of dipoles in shells, formed by molecules, polarized in the field of the central charge, investigated in this paper, may be useful for analyzing the structures of clusters, formed in the electric field of ions.

1. A. I. Nikitin, An electrical capacitor as the element of power core of ball lightning, *Electrical Technology Russia*, 1998, 4, pp. 70—85.

2. A. I. Nikitin, The dynamic capacitor model of ball lightning. *Proc. 6th Intern. Symp. on Ball Lightning. Antwerp*, Belgium, 1999, pp. 91-95.

3. A. I. Nikitin, V. L. Bychkov, T. F. Nikitina and A. M. Velichko, High-energy ball lightning observations, *IEEE Transactions on Plasma Science*, 2014, 42(12), pp. 3906—3911.

The EMF in the Stuart-Tolman Experiment

Vladimir L. Bychkov[1], Fedor S. Zaitsev[1], and Vladimir A. Chizhov[2]

[1]M.V. Lomonosov Moscow State University, Moscow, Russia
[2]LLC «Processing of energy materials», Moscow, Russia

Introduction. As now stated, an electric current in metals is a movement of electrons, and metal ions do not take part in the transfer of electric charge. It is claimed [1, 2] that the most convincing proof of the electronic nature of the current in metals was obtained in experiments with electron inertia. The idea of this experiment was expressed in 1913 by Mandelstam and N.D. Papaleksi [2]. Then this experiment was proposed by G. Lorenz and carried out with quantitative results by Tolman and Stuart in 1916 [3]. The purpose of this work is to consider results of this experiment from the point of view of classical electrodynamics with using of general form of electromotive force (EMF) equation.

The Stuart-Tolman Experiment

T. Stewart and R. Tolman [3] conducted the following experiment. A coil with a large number of turns of a thin wire was driven into a rapid rotation around its axis (the total length of the turns of the winding was up to 530 m, and the linear speed of the wire reached 56 m/s [5]). The ends of the winding were connected to a sensitive galvanometer using long flexible wires. After unwinding the coil, it was sharply braked by a special device. In this case, a short-time current appeared in the circuit, and the direction of the current corresponded to the direction of motion of the coil. See reasoning [1], explaining the participation of electrons and their role. When the coil brakes according to [3], the inertia force acts on the electrons, which is, in this case, an external force. When accelerating dv/dt a wire one electron with the mass m is acted upon by a force

$$F = -m\,dv/dt. \tag{1}$$

The force per unit charge, i. e. field strength of the external forces E' equals to

$$E' = -\frac{m}{e}\frac{dv}{dt},$$

e is the electron charge.

Using without any justification a simplified formula for EMF of a closed contour [1], without taking into account the rotation of the circuit, an expression for the EMF was obtained

$$\varepsilon = \bigcirc \qquad \frac{v}{t} L,$$

which develops in the circuit when the coil brakes, where L is the length of the coil wire.

If R is the resistance of the circuit, then the current produced by this EMF is equal to

$$i = -\frac{m}{e}\frac{dv}{dt} L / R \tag{2}$$

Therefore, the magnitude of the charge passed along the circuit for the total braking time of the coil is given by

$$q = \int_{v_0}^{0} i \cdot dt = -\frac{m}{e} L / R \int_{v_0}^{0} dv = \frac{m}{e} L / R \cdot v_0.$$

Whence, measuring the charge q and knowing the remaining quantities v_0, R, L, one can find the value of the specific charge of the electron

$$\frac{e}{m} = v_0 \cdot L / (R \cdot q).$$

To measure the charge in the experiments, a ballistic galvanometer was used (an ammeter measuring the current in time t). The measured charge is equal to $q = i \cdot t$, where i is the instantaneous current that appears in the coil when the inert electrons are decelerated. Then substituting this product for q, one determines the specific charge of the electron

$$\frac{e}{m} = v_0 \cdot L / (R \cdot i \cdot t). \tag{3}$$

Using the circuit parameters, the authors of the experiment [3] found values e/m for a number of elements, which turned out to be close to those obtained in other experiments.

Let us analyze formula (3). Recall that j is the current density, s is the wire cross section, and the resistance is expressed in terms of the resistivity of the

material ρ_0, the length of the sample - in our case L, the cross section of the sample α, the coefficient of variation of the resistivity of the material with temperature T. Then $R = (1+\alpha \cdot T)\rho_0 \cdot L / s$. Substituting this expression in (3), one obtains

$$\frac{e}{m}\rho_0 = v_0 /(t \cdot j \cdot (1+\alpha \cdot T)) \quad (4)$$

Following the logic of the research [3, 5] within the framework of the Lorentz and Drude theories [4], the current density in the wire is $j = e \cdot N_e \cdot w$, where N_e is the electron concentration in the wire, which is completely determined for a given material, and w is the velocity of electrons in the wire. In this case, because the electrons participate in the inertial motion, their velocity must be proportional to the speed of the wire, or equal to it $w = \eta \cdot v_0$ where η is some coefficient of order unity.

Substituting the expressions for the current density and the velocity of the electrons in the wire into the formula (4), one gets

$$\frac{e}{m}\rho_0 = v_0 /(e \cdot N_e \cdot w \cdot t \cdot (1+\alpha \cdot T)) = 1/(e \cdot N_e \cdot \eta \cdot t \cdot (1+\alpha \cdot T)), \text{ or}$$

$$\frac{e^2}{m}\rho_0 \cdot \eta = 1/(N_e \cdot t \cdot (1+\alpha \cdot T)).$$

In this formula there are characteristics on the left that do not depend on the properties of the circuit, and it turns out that the system must be adjusted to the metal temperature, and the electron concentration in the metal and the accumulation time of the charge, which is unlikely. The role of the length of the conductor and the length of the coil in the motion of the electrons becomes unclear.

Consider another objection. The volume of copper in a conductor 1 m long and 1 mm^2 cross section is 1 cm^3. The concentration of copper atoms $N_a = 0.85 \times 10^{23}$ cm^{-3} (which gives the average distance between atoms $L \sim 2 \times 10^{-8}$ cm). Taking into account the copper divalence, we obtain the number of free electrons in a given section of the chain of $2 \cdot 10^{23}$ electrons. The free range of electrons in the wire $\lambda = (N_a \cdot \sigma)^{-1}$ ($\sigma \sim 10^{-16}$ cm^2 is the characteristic electron scattering cross section) then $\lambda \sim 5 \cdot 10^{-8}$ cm. We see that $L \sim \lambda$ and no free motion of electrons in the sample will be associated with the lattice atoms and cannot perform inertial motion.

The basic law of electromagnetic induction. EMF

The definitions of the vectors of the magnetic and electric field strengths **B** and **E** from the point of view of continuum mechanics are given in [7] as a rotor and a convective derivative of the physical vacuum (ether) flux density

$$\mathbf{B} \equiv c\nabla \times (\rho \mathbf{u}) \quad (5)$$

$$\mathbf{E} \equiv (\mathbf{u}\cdot\boldsymbol{\nabla})(\rho\mathbf{u}) = \frac{1}{\rho}(\rho\mathbf{u}\cdot\boldsymbol{\nabla})(\rho\mathbf{u}) = \frac{1}{\rho}\left(\frac{1}{2}\boldsymbol{\nabla}(\rho\mathbf{u})^2 - \rho\mathbf{u}\times\left(\boldsymbol{\nabla}\times(\rho\mathbf{u})\right)\right) =$$

$$= |\mathbf{u}|\boldsymbol{\nabla}(\rho|\mathbf{u}|) - \frac{\mathbf{u}}{\mathrm{c}}\times\mathbf{B} \qquad (6)$$

Here $\mathrm{c}\rho\mathbf{u}$ is the vector potential known from electrophysics, which in continuum mechanics [7] is a product of the rate of vacuum flow and its density.

The relationship between the flow parameters, the electric field, the external force **F** and the pressure gradient is given by

$$\frac{\partial\rho\mathbf{u}}{\partial t} = -\mathbf{E} + \frac{\mathbf{F}+\boldsymbol{\nabla}P}{k_{m,0}}. \qquad (7)$$

Consider the time derivative of the magnetic flux Φ in a general form, in contrast to the simplified approach [1, 2], starting from the well-known definition of Φ

$$\frac{d\Phi}{dt} = \frac{d}{dt}\int_{S(t)}\mathbf{B}\cdot\mathbf{n}\,ds.$$

We use the well-known integral identity [7]

$$\frac{d}{dt}\oint_{L(t)}\mathbf{A}\cdot d\mathbf{l} = \oint_{L(t)}\left(\frac{\partial\mathbf{A}}{\partial t} - \mathbf{V}\times(\boldsymbol{\nabla}\times\mathbf{A})\right)\cdot d\mathbf{l},$$

In accordance with the representation of the magnetic field (5) and the Stokes formula, we have

$$\frac{d\Phi}{dt} = \frac{d}{dt}\int_{S(t)}\boldsymbol{\nabla}\times(c\rho\mathbf{u})\cdot\mathbf{n}\,ds = \frac{d}{dt}\oint_{L(t)}c\rho\mathbf{u}\cdot d\mathbf{l}, \qquad (8)$$

where the contour $L(t)$ bounds the surface $S(t)$, the direction of traversal $L(t)$ is determined from the vector **n** by the right screw.

We apply this formula for $\mathbf{A} = c\rho\mathbf{u}$:

$$\frac{d\Phi}{dt} = \int_{L(t)}\left(\frac{\partial c\rho\mathbf{u}}{\partial t} - \mathbf{V}\times\left(\boldsymbol{\nabla}\times(c\rho\mathbf{u})\right)\right)\cdot d\mathbf{l}. \qquad (9)$$

We use equation (9) and definition (7)

$$\frac{d\Phi}{dt} = \oint_{L(t)}\left(c\left(-\mathbf{E} + \frac{\mathbf{F}+\boldsymbol{\nabla}P}{k_{m,0}}\right) - \mathbf{V}\times(\boldsymbol{\nabla}\times\mathbf{B})\right)\cdot d\mathbf{l}.$$

Here **V** – speed of the contour at a point of the contour.

Taking into account that the term $\boldsymbol{\nabla}P$ does not contribute to the integral (since $\boldsymbol{\nabla}\times(\boldsymbol{\nabla}P) = 0$), we obtain

$$\frac{1}{c}\frac{d\Phi}{dt} = -\mathcal{E}(t),\ \mathcal{E}(t) \equiv \oint_{L(t)}\left(\mathbf{E} + \frac{\mathbf{V}}{c}\times\mathbf{B} - \frac{\mathbf{F}}{k_{m,0}}\right)\cdot d\mathbf{l}. \qquad (10)$$

The function $\mathcal{E}(t)$ is called the electromotive force of induction (EMF), and formula (10) is the basic law of electromagnetic induction. In contrast to [1, 2], this

law was obtained here not as a generalization of experiments, but as a formal mathematical consequence of the equations of the physical vacuum (ether) motion [7], that is, the continuity equation and Newton's second law.

We emphasize that formulas (9) and (10) show that the EMF of induction appears in the circuit as the magnetic field or contour changes with time, and also in the presence of an electric field. And the contribution to $\mathcal{E}(t)$ is provided only by the non-potential component of the vector E, since the integral over the closed contour from the potential component is zero. The question of applying the expression for the magnetic flux in the circuit, when the magnetic field and the configuration or the arrangement in the field changes, was raised in [6], where the expression (10) was obtained from qualitative considerations only without taking into account the force and the pressure gradient.

Tolman-Stewart experiment results from the standpoint of continuum mechanics

To explain the results of the Tolman-Stewart experiment, let us turn to the description of the experiment [4] and to the formula (10). In the absence of a pressure gradient in the circuit and external force one has

$$\mathcal{E}(t) \equiv \oint_{L(t)} \left(\mathbf{E} + \frac{\mathbf{V}}{c} \times \mathbf{B}\right) \cdot d\mathbf{l}.$$

In it, the second term in the integral takes into account the rotation of the contour. Let us estimate its influence on the interpretation of the experiment. In the experiment, it was believed that the vertical magnetic field of the Earth was reduced due to a fixed coil wound in the opposite direction compared to the rotating coil and located above it. According to the authors, when using coils with currents passing through them, the horizontal component of the earth's magnetic field and the vertical component of the Earth's field were reduced to 1% of the original value. However, it is doubtful that the vertical component of the Earth's field was suppressed as a result of using a fixed coil.

In this experiment, according to [5], the length of the wire wound on the coil was 529 m, and the rotation speed was 56.4 m / s (~ 40 rpm). These data are not available in [3]. In addition, in [3] there is no data on the magnitude of the currents in the coil and the voltages at the contacts.

Assuming that the total length of the circuit is equal to the length of the wire in the rotating coil and the rotation speed of the coil is perpendicular to the earth's magnetic field for EMF, we obtain the following. At $\mathbf{B} = 5.5 \cdot 10^{-5}$ T, a typical value of the vertical field of the Earth in California, where the experiment was performed at the indicated values of the speed and length of the contour $\mathcal{E}$= 1.6 V, and for $\mathbf{B} = 5.5 \cdot 10^{-7}$ T $\mathcal{E} = 1.6 \cdot 10^{-2}$ V. These are quite large voltages. At the same time, measures to reduce the impact of the vertical component of the Earth's magnetic field were insufficient, since the authors of the experiment struggled with the influence of induction and self-induction, and did not take into account the EMF in the moving contour.

Conclusion. In this work from the point of view of the methodology of continuum mechanics, the results of the Tolman-Stewart experiment are analyzed. The derivation of the expression for EMF is given with allowance for the motion of the electric circuit in a magnetic field. The values of this EMF are obtained in the magnetic field of the Earth, realized in this experiment, which turned out to be noticeable. This allows us to reconsider the interpretation of the results of this experiment without invoking the hypothesis that it is the electrons that participate in the inertial motion in the conductor.

1. S. G. Kalashnikov, Electricity , Moscow : Nauka, 1964, 667, p.

2. D. V. Sivukhin, General course of physics, V.3, Moscow: Nauka, 1977, 688 p.

3. R. C. Tolman, T. D. Stewart, The electromotive force produced by the acceleration of metals, Phys. Rev. V.8, N.2, 1916, pp. 97—116.

4. N. Ashcroft, N. Mermin, Solid state physics, V.1, Moscow: Mir, 1979, 400 p., S. Barnett, UFN, V.18, № 3, 1937, pp. 392—452.

5. N. N. Grinchik, A. P. Dostanko, Influence of thermal and diffusion processes on propagation of electromagnetic waves in layered materials, Nat.Acad. Sci. Belarus, A. V. Lykov Int. Heat and mass exchange, Minsk, 2005, 150 p.

6. V. L. Bychkov, F. S. Zaitsev, Mathematical modeling of electromagnetic and gravitation phenomena by mythology of mechanics of continuous media, Moscow, Maks-press. 2016, 232 p.

Interaction of Long-Living Plasma Formations with the Earth Surface

Vladimir L. Bychkov, Adliya R. Bikmukhametova, Nikolay V. Ardelyan, and Konstantin V. Kosmachevskii

M. V. Lomonosov Moscow State university, Mosow, Russia, bychvl@gmail.com

One of the poorly studied areas of knowledge related to the study of atmospheric electricity and its interaction with the Earth's surface and soil is the problem of interaction during the thunderstorm electricity, long-lived luminous formations (LLO) and ball lightning (BL) with soil. To manifestation of such an interaction with the Earth's surface, so-called, "circles" in the fields that arise during the vegetation period can lead. Therefore, studies of these interaction results allow us to evaluate certain features of these natural phenomena.

In connection with the registration of anomalous soil properties as a result of the action of natural LLO on the soil and vegetation cover in the conditions of the Republic of Adygea, experiments were carried out on the thermal and plasma effects on the soil in order to determine the possible parameters of the interaction of LLO with soil. In the same place, natural studies of the monolith of chernozem of the pre-Caucasian leached, taken from the place of impact of LLO on the soil

cover, were carried out. These experiments [1] showed a significant effect of LLO or conditions of their formation on the soil, namely [1]: the increase in the electrical conductivity of samples of chernozem in the epicenter of contact of LLO in comparison with the surrounding landscape is 1.7—2.5 times. In the epicenter of contact of LLO with soil, an increase in the aggregate density of 0.22 g/cm^3 was recorded. The porosity of aggregates as a result of compaction is reduced by an average of 17%. The effect of LLO on soil samples under laboratory conditions increases the electrical conductivity compared to the control by 1.2 to 7 times. The effect of increasing electrical conductivity is more pronounced as a result of the interaction of air-dry samples with LLO. The greatest effect of electrical conductivity growth after interaction with LLO was fixed on dry sand, while the increase in conductivity was 94 to 676 mS/cm. Therefore, it can be assumed that the source of heat was affected by soil with anomalous properties in the sense of soil impact.

Possible analogs The following considerations indicate the possibility of studying the effect of LLO and BL. Crop circles or pictograms (P) and holes in the ground and soil cover, according to observations [2], appear during the vegetative period of plants, in the period — May-July, i. e. in the period of maximum appearance of LLO and BL [3]. In Europe and North America, this period corresponds to the greatest thunderstorm activity, accompanied by the flow of ions to the surface of the Earth, which are captured by plants. It is obvious that the grass fields become huge antennas for ion absorption.

Collected in the P ears under a microscope showed that the stems are deformed as if the inside of the stalk was heated rapidly, as if electromagnetic energy heated the liquid inside the plant, converting it into steam, which when heated caused an explosion in the nodules of the stem and, as a result, its explosion in this place [2]. These phenomena are analogous to explosions of the bark of trees during the motion of CM along their surface [2, 3]. I. e. when heavily electrically charged objects passing near the trees.

Soil analysis showed that in the P area there are two types of dust deposits. In the first type there is a magnetic iron ore in 600 greater concentration than in normal conditions. Another type of deposition is silicon SiO_2, but not in the form of particles of ordinary sand, but in the form of small spheres, as if silicon crystals would be melted by a powerful flux of energy. In the dark, such a powder emits yellow-green light, this radiation can be explained by assuming that silicon crystals were excited by an external source during a short time.

Observers also argue [2] that Ps of natural origin take a form of circular rings or rings connected by straight lines. P were observed in the UK in areas where there are megalithic structures of ancient people, and in the Krasnodar Territory — near mounds in a form of hills. In this connection, attention should be paid to soil cover studies from aircraft boards [3], which showed that buried underground remains give out their presence through growing crops or wild grasses above them. It is quite obvious that subsoil conditions can be favorable or unfavorable for plants. Above the former ditches and other depressions, where the soil is more

fertile, the moisture is greater and the roots are easier to penetrate into the depths, the vegetation is lush, higher and thicker. And above the stone floors, the foundations of buildings or over powerful roads, it is noticeably scarcer and weaker. Vegetative signs are especially well manifested due to plants with a branched root system, whose roots extend far into all depressions with more fertile (i. e., once disturbed) soil. In this respect, all cereals are good. Beetroot, etc., reacts well.

Proceeding from thestated facts, it can be assumed that in the emergence of P, both the fluxes of charged particles to the Earth's surface in a strongly charged thunderstorm atmosphere and the processes going on inside the Earth in the soil cover can participate. I. e. within the soil cover, due to various physical and chemical processes, as well as in the places of activity of ancient people, with the construction of various local objects of life and objects of the cult with the use of various materials (metals and dielectrics), an electrode system arises that concentrates local ion fluxes and accelerates them, directing to a quasi-electrode that is formed under the Earth. In this case, the form of circles and lines becomes unsurprising, since they are inherent in the forms of channels, the place of rites and roads of ancient people.

Of the plasma devices in which ions of air play an important role at the same time, the medium into which they enter is different from air and the electrodes, it is possible to separate corona discharges from the surface of liquids [5—6]. This is especially true for discharges with a surface covered with various powders. In this case, the soil cover and its interaction with the ion fluxes are modeled.

Experimental studies with the help of corona discharges

The scheme of the experimental device is shown in Fig. 1 [4]. It consists of a cuvette filled with liquid (water, alcohol or kerosene) and an electrical circuit. The upper electrode, 0.9 mm in diameter (with a tip radius of 0.2 mm) or 2 mm (with a tip radius of 0.4 mm) was placed at a height of 5—15 mm above the surface of the liquid. The electrodes were under a positive or negative potential. The cuvettes were made of metal or dielectric. The metal cuvettes were as follows: cylindrical diameter 130 mm, height 18 mm, and rectangular 37×70×122 mm; The dielectric plastic cuvette was rectangular 45×95×130 mm.

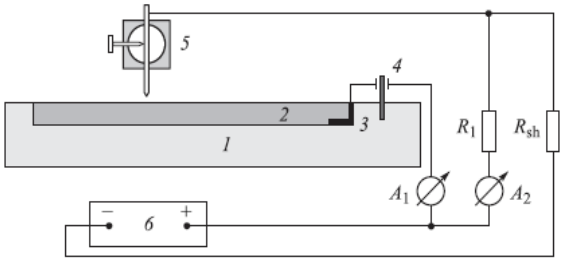

FIGURE 1. Schematic diagram of the experimental setup. 1 — cuvette, 2 — liquid (water, alcohol, kerosene), 3 — anode, 4 — stand, 5 — cathode, 6 — power source.

The current in the discharge was measured by the milliammeter A1, the voltage was measured by a circuit consisting of resistance R1 and milliammeter A2. To visualize the processes on the surface of the liquid of these experiments, we used aluminum powder of grade PAP-1, GOST 5494. The aluminum particles in the powder are plate-shaped and covered with a thin oxide and fatty film. The powder is a product of silvery-gray color, which does not contain the foreign impurity visible to the naked eye. The bulk density of the powder is about 0.15—0.30 g/cm^3, the content of active aluminum is 85—93%. The average thickness of the petals is approximately 0.25—0.50 μm, and the average linear dimension is 20—30 μm. We added 1 and 2 ml of aluminum powder to the liquid. Because of the hydrophobic property, the powder was always on the surface of the liquid. It practically did not sink to the bottom of the dish with water, but with stirring he sank to the bottom of the dish with kerosene. In all liquids, a film of aluminum powder was created. In water, the powder dissolved slightly — almost all the powder remained on the surface, most of it was removed from the surface of the water, leaving a thin film. The aluminum powder was completely dissolved in alcohol and kerosene.

Fig. 2 shows a picture of a corona discharge on the surface of an alcohol with a negative polarity of the upper electrode, the depth of alcohol is 12 mm, the height of the upper electrode above the surface of the liquid is 7 mm, 2 ml aluminum powder. On the left in Fig. 2a a funnel is visible, on the right in Fig. 2b a liquid column and traces of convective fluid motion are visible. One can see the complex structure of the funnel.

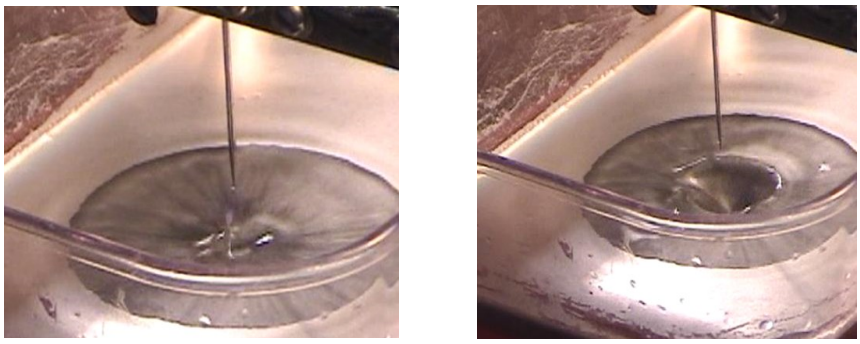

a b

FIGURE 2. Corona discharge over the surface of alcohol. Negative polarity of the upper electrode. The depth of alcohol is 12 mm. The height of the upper electrode above the liquid surface is 7 mm. 2 ml of aluminum powder.

Analysis of the measurement results shows that when adding aluminum powder to alcohol, the appearance of a funnel and charged columns is observed. Fig. 2a shows the motion of the convective fluid in the volume. The photograph of Fig. 2b shows the growth of a charged column of liquid appearing under the action of the field of the upper electrode. It can be seen from the figures that the thickness of the

aluminum film affects the pattern appearing on the surface of the liquid. Thus, the presented experimental material shows that the development of plasma conditions of the corona discharge type leads to the appearance of various figures on a charged surface.

Modeling of the environment heating, leading to the destruction of herbide cover. Plasma chemistry of humid air.

To study the chemical kinetics of humid air, we applied our plasma-chemical code. It takes into account air chemistry and electron-molecular reactions in an external electric field in air and water gas. We used reactions involving 27 plasma components and 23 reagents containing hydrogen, including: positive ions O+, O_2+, O_4+, O_6+, O_8+, H+, H_2+, OH+, HO_2+, H_2O+, O_2+(H_2O), H_3O+, H_3O+(H_2O), H_3O+(OH), H_3O+(H_2O)$_2$, H+(H_2O)$_2$, H+(H_2O)$_3$, H+(H_2O)$_4$ negative ions O-, O_2-, O_3-, O_2-(H_2O), O_2-(H_2O)$_2$, H-, OH-, atoms O and H, molecules H_2, O_2, H_2O, O_3, free radicals OH, HO_2, H_2O_2, O($^1D_1$), O($^1S_0$), electrons and molecular components of air, including hydrogen. The number of reactions in dry air is about 200 and more than 250 for humid air components containing hydrogen.

The role of herbal sharpening. Looking at Fig. 3 one easily understands that there should be some mechanism which can rise electric field near blades of grass in order to insure appearance of plasma and heating of air by this plasma. Let us consider blades of grass for this role.

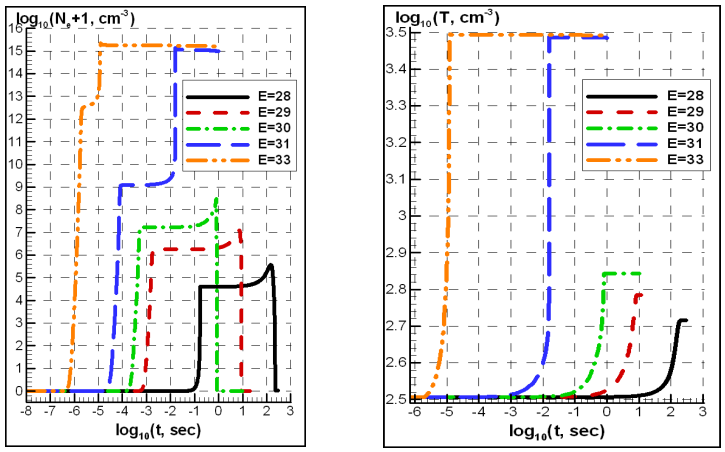

a) b)

FIGURE 3. The time dependences a) of the electron concentration are left and b) the gas temperature is directly at a power G=100(cm^3 s)$^{-1}$. E, kV/cm. Humid air air.

We estimate the parameters of a pointed object (blade) in an external electric field near which ionization in an electric field in the gas increases. To do this, we use known data on the increase of local electric fields due to polarization. In accordance with this, near the ends of the conducting spheroids in the electric, where the electric field strength E_{surf} is the field at the tip of the spheroid

$$E_{surf} = E_{ext} \cdot k$$

E_{ext} is the external electric field. The coefficient k is related to the length **a** and thickness **b** of the spheroid as (Landau 1968):

$$k \approx (b/a)^{-2} \cdot \left(\ln\left(4/(b/a)^2\right)/2 - 1\right)^{-1}$$

In pre-thunderstorm conditions external electric field under clouds can reach E = 20—40 V/cm. If a length of an object (the stem of the plant) is 20 cm and the thickness 2 mm, then (a / b) ≈ 100 , and k ≈ 2000, this is enough to realize a strong field near the blade of grass and the area is heated to the temperature at which this object will explode.

So we see that the appearance of the strong field in the conditions of ion fluxes can cause the dropping of the spikelets in the fields, and the discharge over a complex physicochemical substrate serves to form the circles on which the ears are located under the action of ions.

Conclusion. It may be assumed that development of physicochemical processes over the Earth's surface covered with grass is the cause of the appearance of crop circles. The appearance of the hole can also be associated with the release of energy and the action of streams of plasma of the ion-wind type on the soil in the difficult conditions of atmospheric electricity, when the LLO plays the role of the upper electrode, and the subsoil layer of the complex lower electrode of the natural corona discharge. A model is presented that relates the processes in an electrically disturbed atmosphere to processes similar to those in the corona discharge and to the processes of plasma formation in a strong thunderstorm field near pointed objects of the grass cover. This model shows a complex sequence of processes in a thunderstorm atmosphere and with the participation of DSO, which can lead to the appearance of crop circles.

1. D. Fiorani, Circles in the fields, Moscow: BINOM, 2014. 128 C.

2. I. P. Stakhanov, On the physical nature of ball lightning, M .: The scientific world, 1996, 203 p.

3. V. L. Bychkov, A. I. Nikitin, Ball Lightning: A New Step in Understanding. In: The Atmosphere and Ionosphere. ElementaryProcesses, Monitoring, and Ball Lightning. Eds. V. L. Bychkov, G. V. Golubkov, A. I. Nikitin. Cham: Springer, 2014, pp. 201—367.

4. L. Deuel., Flights into yesterday, London, 1969.

5. V. L. Bychkov, A. P. Ershov, and V. A. Chernikov, Negative Corona Discharge Over a Surface of Alcohol. IEEE Transactions on Plasma Science, Volume 36, Issue 4, Part 1, Aug. 2008, pp. 1140—1141.

Noise Electromagnetic Radiation Flare

Leonid S. Chudnovskiy, Kirill E.Tyupikov

Open Joint-stock Company "Research-and-Production Corporation "Precision System and Instruments", Aviamotornaya street. 53, Moscow, 112250, Russia

An estimate is obtained for the mean-square intensity of the electromagnetic field of the flame at a fuel consumption of 0.1 kg/s of the exhaust gas velocity of $1{,}5 \cdot 10^3$ m/s and a fuel temperature of 500 K.

The emission spectrum is near to broadband white noise with a spectral density of $E(f) = 2\,\frac{\text{мкВ}}{\text{м МГц}}$ for the distance between correspondents of 100 km.

Let us pass to the analysis of the accompanying electromagnetic radiation. The jet flame at the exit from the nozzle represents ionized gas mixtures in which recombination and electron production takes place. These processes lead to the appearance of high-frequency electromagnetic radiation. Let us pass to the evaluation of this electromagnetic radiation.

At a fuel consumption of 0.1 kg/s [1], the exhaust gas flow rate will be $1{,}5 \cdot 10^3$ m/s. For the mass of a gas mixture molecule of 10^{-26} kg and a temperature of 500 K, its energy will be 7 eV, which is insufficient for ionization processes and the appearance of free electrons, becausefor the average ionization energy of the molecule, about 15 eV is required. To ionize an electron, it is necessary that the energy of the molecules W be higher than E_{ion}=30 eV [2]. This probability can be estimated as a thermionic component

$$P(W > 2E_{\text{ion}}) = \frac{2}{\pi^{\frac{1}{2}}} \int_{\frac{2E_{\text{ion}}}{W_{\text{м}}}}^{\infty} x^{1/2} e^{-x} dx, \text{ where } x = \frac{2E_{\text{ion}}}{W}$$

The ratio $\frac{2E_{ion}}{W} = 4{,}4$, therefore, we can use the following approximation

$P(W > 2E_{ion}) \approx \frac{2}{\pi^{\frac{1}{2}}} \left(\frac{2E_{ion}}{W_{\text{м}}}\right)^{\frac{1}{2}} exp\left(-\frac{2E_{ion}}{W_{\text{м}}}\right)$. Thus, the probability of producing an electron is P $(W > 2E_{\text{ион}}) \approx 0{,}09$. In one second, when the mass is 0.1 kg/s, the total amount of ejected molecules of the gas mixture is 10^{25} units/s and the number of generated electrons is about 10^{24} s^{-1}, which is equivalent to a direct current of about 10^5 A. However, the oriented directional current in such a system does not arise, therefore, the rms current level is 330 A. We will carry out a further evaluation of the electromagnetic radiation for the average energy of the ionized electron of 3 eV with a velocity of motion $V_e = 10^6$ m/s and a lifetime $\tau = 10^{-12}$s.

Let us now consider the electromagnetic radiation of one electron. Its dipole moment is:

$$d(t) = eV_e t\{\eta(t) - \eta(t - \tau)\} \quad (1)$$

Here **e** — electron charge, **V** — electron velocity, **t** — time, and **η(t)** -unit function.

The intensity of the electric field of radiation

$$E(t) = e\,(4\pi\varepsilon_0 c^2 R)^{-1}\frac{d^2\{d(t)\}}{dt^2} = eV_e\,(2\pi\varepsilon_0 c^2 R)^{-1}\{\delta(t) - -\delta(t-\tau)\} \quad (2)$$

Here: $\boldsymbol{\varepsilon_0}$ — dielectric constant of the vacuum, c is the speed of light, **R** — distance between the correspondents, and **δ** (...) — delta function.

The spectral density of the radiation (2) will be

$$E(\omega) = eV_e\,(2\varepsilon_0 c^2 2R)^{-1}\{1 - \exp(-i\omega\tau)\} \quad (3)$$

For the total electron flux N_e=10^{24} s^{-1}, participating in electromagnetic radiation, the spectrum of the electric field strength of the radiation will be

$$E(\omega) = eV_e\,(2\varepsilon_0 c^2 R)^{-1}\{1 - \exp(-i\omega\tau)\}\{1 - \exp(-i\omega N_e\delta t)\}\{1 - \exp(-i\omega\delta t)\}^{-1}, \quad (4)$$

here $\delta t \approx 10^{-24}$ s. For frequencies below 10 GHz, expression (4) is simplified

$$E(\omega) \approx \frac{e\tau V_e}{2\pi\delta t R c^2 \varepsilon_0} \quad (5)$$

The spectrum of electromagnetic radiation is close to white noise to frequencies below 10 GHz and at a distance between correspondents R = 100 km is equal to $E(f) = 2\frac{\text{мкВ}}{\text{м МГц}}$

Considering the wide spectrum of radiations, the location of such radiation is possible at large distances [3].

1. Characteristics of the engine TRDD-50, http://www.vonovke.ru/s/trdd-50-harakteristiki dvigatelya trdd-50

2. K. Shimoni, *Physical electronics*, M. Energia, 1977, 608 p.

3. A. Chudnovsky and V. Ageev, Passive location of transient electromagnetic radiation from a beam electron radiator, *Chemical Physics*, 2013, 32(11), pp. 17—32.

CONTENTS

ATMOSPHERIC-IONOSPHERIC RELATIONS

ELEMENTARY PROCESSES IN THE UPPER ATMOSPHERE AND IONOSPHERE

ELECTROMAGNETIC AND OPTICAL PHENOMENA IN THE ATMOSPHERE INCLUDING LONG-LIVED AND PLASMA OBJECTS

ATMOSPHERE, IONOSPHERE, SAFETY

Proceedings
of VI International conference

Part 1

Компьютерная верстка *Ю. И. Блазаренаса*

Подписано в печать 22.05.2018 г.
Формат 70×100 $^{1}/_{16}$. Усл. печ. л. 29,3
Тираж 500 экз. (1-й завод 70 экз.). Заказ 137

Издательство Балтийского федерального университета им. И. Канта
236022, г. Калининград, ул. Гайдара, 6